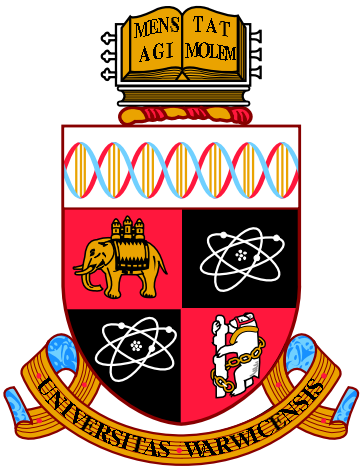

Bone Scaffolds with Controllable Porosity

by

James Winnett

Thesis

Submitted to the University of Warwick

for the degree of

Doctor of Philosophy

Supervisors: C. Dancer; G. Gibbons

WMG

April 2015

THE UNIVERSITY OF WARWICK

In *Memoriam*

DR. KAJAL K. MALLICK

6 March 1950 - 25 December 2013

'Learn from yesterday, live for today, hope for tomorrow. The important thing is not to stop questioning'

Albert Einstein

FRANCIS S. WINNETT

31 January 1924 - 29 July 2014

'If you can keep your head when all about you; are losing theirs, and blaming it on you'

Rudyard Kipling

Contents

List of Figures

List of Tables

Acknowledgments

I would first like to thank Dr Kajal Mallick (dec.), without whom I would probably not have decided to undertake this PhD, for all his support.

For continuing the supervision, I would like to thank Dr Greg Gibbons and Dr Claire Dancer. The different areas of expertise they have has enabled me to consider the research from different angles and has improved my research greatly.

Within the University of Warwick, I would like to extend my thanks to the technicians within WMG for their assistance in the production of components used in different parts of the PhD and with the mechanical testing. Furthermore, for undertaking the microCT scanning and analysis, I would like to thank Professor Mark Williams and Dr Jay Warnett. I would also like to thank the Department of Physics for assistance with the firing and sintering of structures in inert atmospheres, staff within the Materials and Analytical Science department for their assistance with XRD, and staff within the School of Engineering for their assistance with SEM.

I would also like to thank Dr Gwendolen Reilly and Dr William Van-Grunsven at the Department of Materials Science and Engineering at the University of Sheffield for undertaking preliminary biological evaluations. Furthermore, the assistance provided by Professor Liam Grover and Dr Neeraj Jumbu within the TRAILab at the University of Birmingham (Department of Chemical Engineering) has proved invaluable in my carrying out the remainder of the viability assays.

I also thank the Engineering and Physical Sciences Research Council for providing the funding for this research.

Finally, I would like to thank my friends and family for all their support, and in particular my wife and parents.

Declarations

This thesis is submitted to the University of Warwick in support of my application for the degree of Doctor of Philosophy. It has been composed by myself and has not been submitted in any previous application for any degree, although it follows on from from the background material in Section 3.1.5.1 which was previously submitted for a Masters of Engineering degree (University of Warwick, 2011).

The work presented (including data generated and data analysis) was carried out by the author except in the cases outlined below:

- Preliminary cell viability tests and analysis (Section 6.4.1), carried out by collaborators at the University of Sheffield (Department of Materials Science and Engineering)
- MicroCT scanning and analysis (Section 6.2.4), carried out by collaborators at the University of Warwick (WMG)

Parts of this thesis have been published by the author as detailed in the List of Publications immediately following this declaration

List of Publications

Journal Articles

1. Winnett J, Mallick KK, Comparative analysis of hydroxyapatite and titanium based bioscaffolds fabricated via adaptive foam reticulation, *Ceramic Transactions*, Accepted.

2. Winnett J, Mallick KK, Parametric Characterisation of Porous 3D Bioscaffolds Fabricated by Adaptive Foam Reticulation, *Journal of the Minerals, Metals and Materials Society*, special issue Thin Films and Interfaces, 66 (4):pp.590-597, 2014.

3. Winnett J, Mallick KK. Porous 3D Bioscaffolds by Adaptive Foam Reticulation. *Bioinspired, Biomimetic and Nanobiomaterials*, 4:4-14, 2014.

4. Mallick KK, Winnett J, van Grunsven W, Lapworth J, Reilly G. 3-D Porous Bioscaffolds for Bone Tissue Regeneration: Fabrication via Adaptive Foam Reticulation and Freeze Casting Techniques, Characterisation and Cell Study, *Journal of Biomedical Materials Research: Part A*, 100 (11):pp.2948-2959, 2012.

5. Mallick KK, Winnett J. Preparation and Characterization of Porous Bioglass® and PLLA Scaffolds for Tissue Engineering. *Journal of the American Ceramic Society*, 95 (9):pp.2680-2686, 2012.

6. Mallick KK, Winnett J. Porous Biodegradable Scaffolds for Hard Tissue Engineering. In: Narayan, R. (ed.), *Biomaterials Science - Processing, Properties, and Applications*, Volume 228. John Wiley & Sons, Inc., pp.57-66, 2011

Book Chapters

1. Mallick KK, Winnett J. Bioceramic foams for Tissue Engineering. In: Mallick KK (ed.), *Bone Substitute Biomaterials*, Woodhead Publishing, Chapter 6, pp.118-141, 2014.

Oral Presentation at Conferences

1. Winnett J. Comparative Analysis of Hydroxyapatite and Titanium-based Bioscaffolds Fabricated via Adaptive Foam Reticulation. Presented at *Materials Science and Technology (MS&T) '13.* Montreal, Canada, 27-31 October 2013.

2. Winnett J. Processing and Characterisation of Titanium Based Alloy Scaffolds by Adaptive Foam Reticulation. Presented at *8th Pacific Rim International Conference on Advanced Materials and Processing (PRICM 8).* Waikoloa, Hawaii, 4-9 August 2013.

3. Winnett J. Parametric characterisation of porous 3D bioscaffolds fabricated by Adaptive Foam Reticulation technique. Presented at *TMS 142nd Annual Conference and Exhibition.* San Antonio, Texas, March 3-7 2013.

4. Mallick KK, Winnett J, Reilly G, van Grunsven W, Lapworth J. Fabrication Approaches and Characterization of Porous 3D Bioscaffolds for Hard Tissue Augmentation. Presented at *Materials Science and Technology (MS&T) '11.* Ohio, USA, October 16-21 2011

Poster Presentation at Conferences

1. Winnett J, Development of Scaffolds with Controllable Pore Sizes – Adaptive Foam Reticulation. Presented at *11th International Conference on Materials Chemistry (MC11).* Coventry, UK, 8-11 July 2013.

2. Winnett J. Development of Titanium based Bioscaffolds – Controllable Pore Sizes via Adaptive Foam Reticulation. Presented at *UK Society for Biomaterials Annual Conference.* Birmingham, UK, 24-25 June 2013.

3. Winnett J. Fabrication of Porous Bone Scaffolds – a Novel Adaptive Foam Reticulation Technique. Presented at *WMG Annual Materials and Manufacturing Theme Group Conference.* Coventry, UK, 28 May 2013.

Abstract

The Adaptive Foam Reticulation (AFR) technique, a combination of foam reticulation and freeze casting, has been investigated for producing bone repair bioscaffolds from hydroxyapatite (HA), titanium (Ti) and titanium-aluminium-vanadium (Ti-6Al-4V). Scaffolds have a network of macropores of diameter between 94 and 546 μm, with struts 20 to 118 μm thick. The structure was dependent on the template from which structures were produced, the number of coats of slurry applied to the template and the sintering temperature. The struts contained numerous micropores, the size of which was increased from 2-5 to 20-30 μm by decreasing the freezing temperature. Whilst the size of individual micropores was independent of the amount of porogen in the slurry, there was some coalescence at higher percentages.

Scaffolds exhibited porosities of between 76 and 96%, with porosity consistently decreased by increasing the number of coats from one to five. The mechanical strength of all samples was determined theoretically by the novel incorporation of a shape factor conventially used for microporous structures into an existing equation used to calculate the yield stress of porous structures. In most cases this agreed with the experimentally obtianed yield stress. With compressive yield stresses of 0.002 to 0.18MPa and 0.002 to 1.8 MPa respectively, HA and Ti structures are only suitable in non-load bearing situations. However Ti-6Al-4V scaffolds had yield stresses of 0.21-13.7 MPa, within the range of cancellous bone.

AFR-fabricated HA scaffolds offered greater *in-vitro* cell viability than a commercially available porous HA disc. Including a porogen offered no improvement in viability compared to structures fabricated without porogen, except at the highest inclusion where a statistically significant increase was observed. The weak compressive strength of scaffolds needs improving, and fabrications require *in-vivo* analyses. However, AFR could offer a viable alternative to other manufacturing techniques.

NOMENCLATURE

3DP 3D printing

3T3 cell line Undifferentiated pre-fibroblastic mouse cells

ρ Density

λ Wavelength

μ Mean (of a sample set)

$\mu\varepsilon$ Microstrain

μ_0 Shape factor

σ Yield stress

σ_e Standard error

σ_{er} Standard error of the mean

σ^2 Variance (of a sample set)

AFR Adaptive foam reticulation

Al_2O_3 Aluminium oxide, alumina

ALM Additive layer manufacturing

ALP Alkaline phosphatase

ANOVA Analysis of variance

at.% Atomic percentage

BCC Body-centered cubic

BCP Biphasic calcium phosphate

bMSC Bone marrow stromal cells

BMUs Basic multicellular units

C Carbon

Ca Calcium

CAD-CAM Computer aided design and manufacture

CaO Calcium oxide

CaP Calcium Phosphate

CCD Charge-coupled device

Co-Cr Cobalt-Chromium

COD Crystallography Open Database

CS CellSupports commercially available porous HA disc

CT Computed tomography

DAPI 4',6-diamidino-2-phenylindole

DCP Dicalcium phosphate

DCPA Dicalcium phosphate anhydrous, monetite

DCPD Dicalcium phosphate dihydrate, brushite

DMC Dimethyl-carbonate

DMEM Dulbecco's Modified Eagle's Medium

DNA Deoxyribonucleic acid

DTA Differential thermal analysis

E Young's modulus

ECM Extracellular matrix

FBS Foetal bovine serum

FCC Face-centered cubic

FCT Face-centered tetragonal

FDA Food and Drug Administration

FDM Fused deposition modelling

FWHM Full-width at half-maximum

HA Hydroxyapatite

HCL Hydrochloric acid

HCP Hexagonal close-packed

HEPES 4-(2-hydroxyethyl)-1-piperazine-1-ethanesulfonic acid

HIP Hot isostatic pressing

hOBs Human osteoblasts

ICDD International Centre for Diffraction Data

JCPDS Joint Committee on Powder Diffraction Standards

mbar Milibar

MC3T3 Undifferentiated pre-osteoblastic mouse cells

MCPA Monocalcium phosphate anhydrous

MCPM Monocalcium phosphate monohydrate

Mg Magnesium

MG63 Undifferentiated pre-osteoblastic human cells

micro-CT Micro-computed tomography

mol.% Molar percentage

MTS 3-(4,5-dimethylthiazol-2-yl)-5-(3-carboxymethoxyphenyl)-2-(4-sulfophenyl)-2H-tetrazolium, inert salt

MTT 3-(4,5-dimethylthiazol-2-yl)-2,5-diphenyl tetrazolium bromide

NaCl Sodium chloride, salt

NaOH Sodium hydroxide

ng/mL Nanograms/mililitre

Ni Nickel

OCP Octacalcium phosphate

OH Hydroxide

OHAP Oxyhydroxyapatite

P Phosphorous

P_o Porosity

P_r Probability

PBS Phosphate buffered solution

PCL Polycaprolactone

PDF Powder diffraction file

Pen/Strep Penicillin/Streptomycin

PGA Poly-glycolic-acid, poly-glycolide

Phalloidin-TRITC Phalloidin, Tetramethylrhodamine B isothiocyanate

PI Propidium iodide

PLA Poly-lactic-acid, poly-lactide

PLGA Poly-lactic-co-glycolic acid, poly-lactide-co-glycolide

PMMA Polymethyl methacrylate

PMS Phenazine methosulphate

pNPP p-nitrophenyl phosphate

PO_4^{3-} Phosphate ion

ppi Pores per inch

PSZ Partially-stabilized-zirconia

PU Polyurethane

PVA Poly-vinyl-alcohol

RIR Reference intensity ratio

RNA Ribonucleic acid

SD Standard deviation

SEM Scanning electron microscopy

Si Silicon

SLA Stereolithography

SLS Selective laser sintering

STA Simultaneous thermal analysis

Ta Tantalum

Ta_2O_5 Tantalum oxide

TBA Tertiary-butyl-alcohol

TCP Tricalcium phosphate

TCPM Tetracalcium phosphate monoxide, hilgenstockite

TGA Thermogravimetric analysis

Ti Titanium

Ti-6Al-4V Titanium-aluminium-vanadium

Ti-C-N Titanium-carbide-nitride, Ti_5CN_4

Ti_2 α-titanium

Ti_4 β-titanium

TiC Titanium-carbide

TiH_2 Titanium hydride

TiO_2 Titanium oxide, titania

tm Micropore size

tp Macropore size

ts Strut thickness

vol.% Volume percentage

WD Working distance

wt.% Weight percentage

XRD X-ray diffraction

XTT 2,3-bis(2-methoxy-4-nitro-5-sulfophenyl)-5-[(phenlyamino)carbonyl]-2H-tetrazolium hydroxide

Y_2O_3 Yttrium oxide, yttria

Zr Zirconium

ZrO_2 Zirconium oxide, zirconia

Part I

Background

Chapter 1

Introduction to Bone Repair

This chapter provides an overview of why scaffolds aimed at aiding bone repair are necessary and the challenges behind their design.

1.1 Current Aids to Repair

Grafting is the relocation of healthy tissue to the site of defects unable to repair themselves. There are three types of bone grafts: autogenous bone graft, where bone from the same body is used; allogenous bone graft, where bone from the same species is used; and xenogeneic bone grafts, where bone from similar species, such as porcine (from pigs) or bovine (from cows), is used [1, 2].

Cancellous bone grafting is the most common type of bone relocation and accounts for 10 % of orthopaedic surgeries [3]. Cortical bone can also be grafted although it instigates regrowth at a slower rate [2]. The iliac crest, found on the pelvic bone, is the most popular location for donor tissue as it houses cells with the highest osteogenic potential. The tibia (lower leg), tarsus (cluster of 7 bones in the upper foot) and femur (upper leg) are also suitable, with the location of potential donor sites shown in Figure 1.1.

Autografts are considered the optimal grafting procedure as they have the greatest osteogenic capacity, inherent biocompatibility and the lowest risk of stimulating an immune response [1, 2]. However, they are limited by the lack of available tissue,

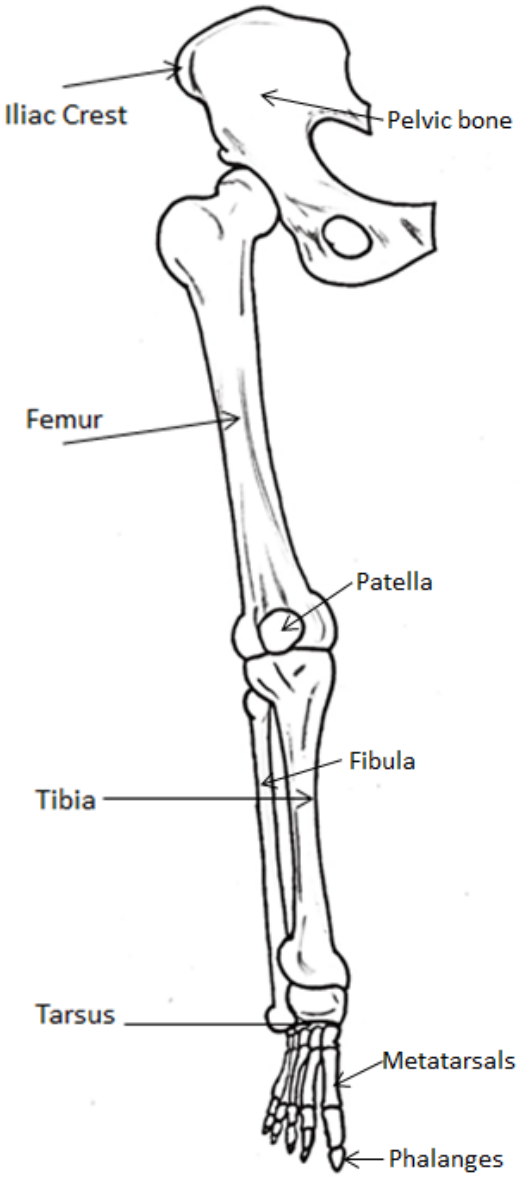

Figure 1.1: Overview of bones in the leg suitable for donating bone for autologous grafts are the iliac crest, found on the pelvic bone, the femur in the upper leg, the tibia in the lower leg and the tarsus in the foot. The remaining lower limb bones are also labelled [2, 3]

donor site morbidity and the risk of musculoskeletal infections [1–7], which occur in 3 % of operations and of which 50 % result in death [7]. Finally, the resorption rate of bone is not completely understood and cannot be predicted. This means that complete dissolution of the implant is possible before sufficient regrowth occurs.

Allografts are the next best alternative after autografts. However, they have a lower osteogenic capacity, larger immunogenic responses, stimulate regrowth at a much slower rate whilst exhibiting greater biodegradation, undergo less revascularisation and present a much larger risk of transferring infections [4–6]. Additionally, there is a donor shortage and stored bone must be sterilized, causing a loss in immunogenicity [1]. Xenografts are not considered suitable for bone grafts due to the acute immune response they initiate, causing the graft to fail [1–3]. However, work with mammalian extracellular matrix (ECM) to initiate soft tissue regrowth may generate interest in similar procedures for hard tissues [8, 9].

Grafting operations could be made much cheaper and safer through the implantation of synthetic scaffolds at the fracture location, Figure 1.2. The field of tissue engineering seeks to develop materials and structures that help guide bone repair, with current research aimed at improving the anchoring, load distribution, augmentation and scaffold strength [2, 10].

1.1.1 Bioscaffold Requirements for Reparative Applications

There is a wide range of scaffold requirements which constructs must adhere to in order to be successful in initiating growth. The scaffold must be constructed of a 3D interconnected porous network of pore sizes within different ranges. Macropores, 100-900 μm, are required to allow for the movement of cells and other essential nutrients throughout the structure [2, 5, 6, 12–15]. Micropores, 1-50 μm, should also be present as they provide attachment sites for the cells [2, 16] as well as facilitating capillary growth [2] and cell development [17–19]. Surface topography has a strong impact on initial cell morphology, which in turn affects the ability of the cells to

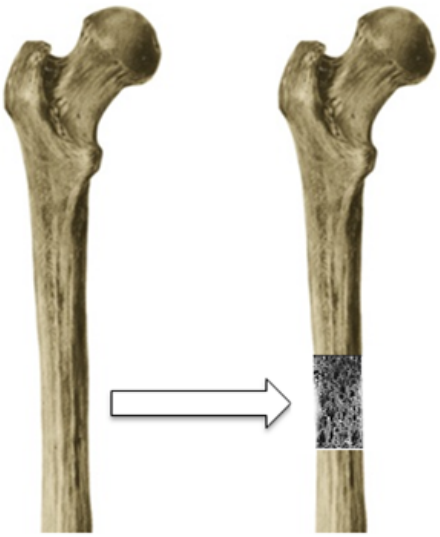

Figure 1.2: Fractured bone can be replaced by scaffold structures that encourage bone repair [11]

attach to the surface and proliferate [16, 20–22]. The requisite level of topography is material dependant [17, 19], although *in-vitro* testing of microgrooved surfaces has suggested that grooves with widths similar to the size of the cell (approximately 8 μm) and a depth of approximately 10 μm elicited the strongest cell responses [17–21].

The structure must be biocompatible and must not elicit any adverse inflammatory response [1, 2, 5, 6]. This is mainly material dependent, as is bioactivity [1, 2, 5], the property denoting the recruitment of stem cells and other biological agents that initiate bone growth to the implant site. In many cases bioresorbability, the ability to be broken down by the body, is also desirable [1, 5, 6]. The rate of bioresorption needs harmonization with the growth rate of new bone so that the scaffold is only completely removed as the repair process completes [5,6,23]. Finally, the mechanical properties of the scaffold must be matched to those of natural bone to ensure the scaffold is of sufficient strength for regrowth whilst avoiding problems with stress shielding as discussed in Section 1.2.2.

1.2 The Biology of Bone

To produce a suitable structure, it is necessary to understand what the final use will be and the environmental conditions in which it will be used. Thus, knowledge of the biology of bone is a prerequisite in the design of bone scaffolds.

1.2.1 Structure

Bone has a complex structure that has not yet been fully replicated synthetically. It is a highly specialized tissue that provides the body with an internal support network, a reservoir for minerals, protection to internal organs and attachment sites for muscles [24]. It is a composite consisting of organic and inorganic components, with the exact composition specific to the location of the bone within the body. The organic matrix constitutes 20-30 % of the total mass and consists of approximately 90 % Type I collagen [25,26], with smaller amounts of Types III, V, X, XII and some non-collagenic proteins necessary for osteoblast differentiation, tissue mineralisation, cell adhesion and bone remodeling [25–28]. The inorganic components of bone account for 60-70 % of the total mass and are predominantly calcium phosphate (CaP), with small amounts of potassium, sodium and magnesium; the remaining 10 % is water [2, 25, 26].

The major factor limiting the complete replication of bone is that it has a hierarchical structure. This can be broken down into macro (cancellous and cortical bone), micro (10-500 μm; Haversian systems, osteons, trabeculae), sub-micro (1-10 μm, lamellae), nano (1 nm-1 μm; fibrillar collagen and embedded mineral), and sub-nano (below 1 nm; mineral, collagen and non-collagenous proteins) regions [2, 24–27, 29, 30] as shown in Figure 1.3.

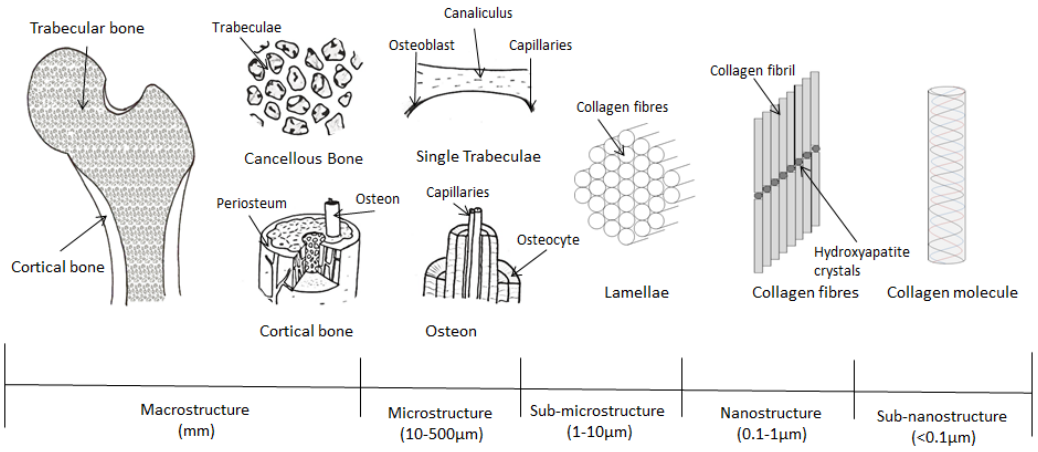

Figure 1.3: Hierarchical structure of bone. There are 5 major scales used, ranging from mm (macrostructure) to smaller than 0.1 nm (sub-nanostructure) in size (redrawn from [29, 31])

There are 2 macroscopic types of bone: cortical and cancellous (or trabecular). Although they take up similar volume, cortical bone accounts for 80 % of the total mass due to an osteonic construction that provides a compact and orthotropic structure [31] and generates low porosity and high compressive strength; the Young's modulus is 17 GPa [32]. Cancellous bone has a high porosity of 50-90 % depending on the location within the body. Although this reduces the strength by up to a factor of ten, it allows for the even distribution of loads and the flow of oxygen, cells and other nutrients throughout the structure [2, 3, 25, 32, 33]. It is constructed of a 3D, interconnected network of trabeculae that give it anisotropic mechanical behaviour [31].

The microstructure consists of osteons and Haversian systems in cortical bone [24–26, 29], and trabeculae in cancellous bone [25, 29]. Groups of osteons are clustered around a central Haversian canal. An osteon is made up of concentric lamellae around a central canal, the osteonic canal, forming a cylinder 200-250 μm in diameter that runs parallel to the long axis of bone [25, 26].

At the sub-microstructure, there are different arrangements of lamellae depending on the bone type: parallel fibre, as found in parallel fibre bone; woven, as in woven

bone; lamellar array, as in lamellar bone; and radial as in dentin [25, 26, 28]. The most common array in load bearing and impact resistant bones is lamellar. This consists of neighbouring fibrils that rotate about a central canal with a bimodal distribution of angles, progressively rotating sub-layers by 30 °, with the sub-layer thickness and orientation being location specific [24–26, 28].

The nanostructure is made up of mineralised collagen fibrils called lamellae. Collagen fibres are organized into parallel arrays, with plate-shaped carbonated apatite crystals between fibres. This allows the limited growth of discrete and continuous crystals. Osteoblasts secrete type I collagen molecules that self-assemble into fibrils with 67 nm periodicity and 40 nm gaps forming a matrix that acts as a reservoir for calcium and phosphate ions [24, 25, 28].

This highly complex architecture is difficult to replicate in its entirety. However for bone replacement constructs, it is important to attempt to mimic this structure and hence ensure that the different roles of each hierarchical level is minimally compromised during regrowth. Furthermore, bone is more likely to grow successfully on scaffolds that provide it with a more natural environment.

1.2.2 Remodeling and Repair

Bone repair is a multi-stage process starting with the formation of a soft fracture callus immediately after the break that welds bone fragments together. This is then replaced by pockets of lamellar bone, before remodeling occurs to leave the bone fully functional [34]. remodeling is an important, continuously occurring mechanism whereby small pockets of bone are replaced [35, 36]. Although bone that has been damaged is preferentially targeted, healthy bone is also remodeled so that 3-5 % of the total bone is always being remodeled [37]. Teams of osteoclasts and osteoblasts known as basic multicellular units (BMUs) remodel over a period of 120 days [37,38]. Osteoclastic resorption removes cylinders of old bone into which osteoblasts deposit

a layer of non-mineralised extracellular matrix which is mineralised to integrate into existing bone [37, 38], Figure 1.4.

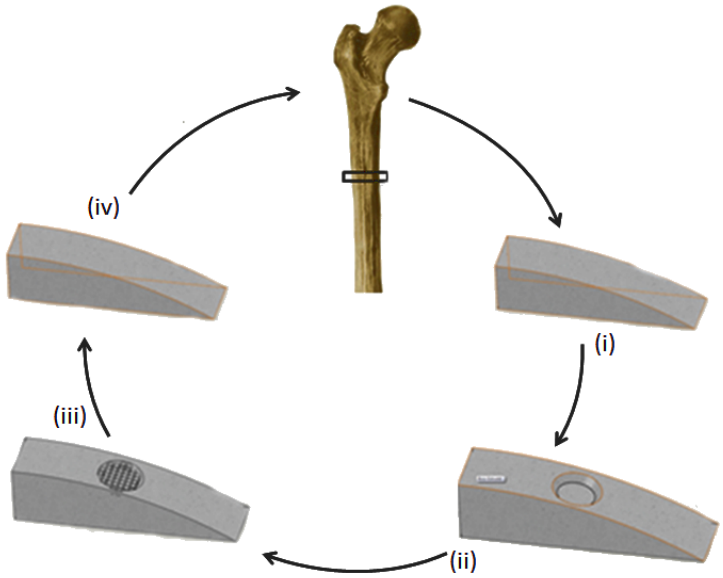

Figure 1.4: Bone undergoes remodeling, whereby a small, plate-shaped mass undergoes osteoclastic resorption (i-ii), osteoblastic synthesis (ii-iii) and integration with existing bone (iii-iv) [11]

Mechanosensitivity is the characteristic causing the mass architecture to be remodeled in response to mechanical loading [34, 39–41]. The response of bone to strains placed upon it is shown in Figure 1.5. Based on Wolff's Law, the Utah Paradigm and Mechanostat hypothesis [39, 41, 42] state that if the strain a bone experiences is below a certain level, less bone is produced than is required leading to a weakened structure; conversely if the strain is too great, then excess bone is produced and stress shielding occurs. This is the phenomenon whereby regions of high strength absorb more stress than surrounding regions, thus this surrounding bone regenerates under the assumption that it needs to be weaker than it should and hence less bone is produced than necessary.

The different levels of bone growth can be explained in terms of the level of microstrain ($\mu\varepsilon$)($\varepsilon \times 10^{-6}$) it experiences. Briefly, between 1500-2500 $\mu\varepsilon$ is the adapted

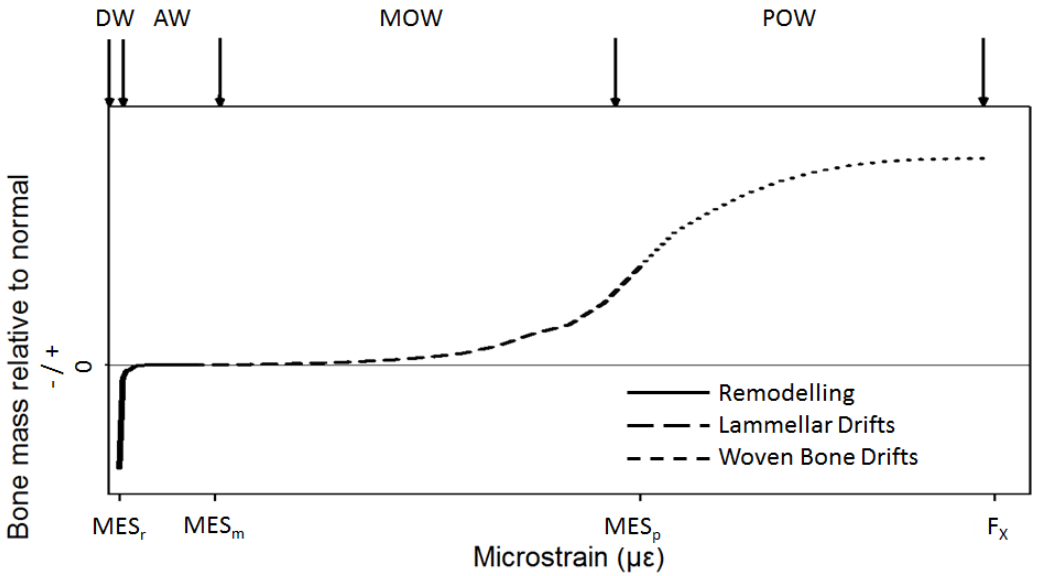

Figure 1.5: Strain affects the remodeling of bone. In the adaptive window (AW), mechanically controlled modelling (MES_m) causes no net change in bone strength; below the lower remodeling threshold (MES_r), bone is in the disuse window (DW) and experiences a loss in mass; between the upper limit of the AW and the operational fatigue microdamage threshold (MES_p) it is within the mild overload window (MOW) where any damage is reversible; above this, up to fracture (F_x) is the pathological overload window (POW) within which bone sustains permanent damage (redrawn from [31])

window (AW) and mechanically controlled modeling (MES_m) causes no net change in bone strength. If the strain is below the lower remodeling threshold range (MES_r) of 100-300 με, it is in the disuse window (DW) and more bone is removed than is produced, decreasing the bone mass and strength. Above the AW, and up to the operational fatigue microdamage threshold (MES_p) of 3000 με is the mild overload window (MOW), within which bone is remodeled with no lasting damage. Above this, up to fracture (F_x) at 25000 με, the bone is within the pathological overload window (POW) and sustains permanent, irreversible damage [31, 34, 39, 41, 42].

This emphasizes the importance of ensuring the mechanical properties of the scaffold are matched to those of bone, given in Table 1.1 for a human femur. If the scaffold is too weak, it may fail leading to costly and difficult corrections being required; if it is too strong, stress shielding will cause implant loosening [3, 38].

Table 1.1: Average mechanical properties of human femur [32, 33, 43]

Mechanical Property	Value
Elastic modulus (transverse/radial) (GPa)	11.9
Elastic modulus (longitudinal) (GPa)	15.8
Shear Modulus (GPa)	3.3
Ultimate tensile strength (longitudinal) (MPa)	133
Ultimate tensile strength (transverse) (MPa)	51
Ultimate compressive strength (longitudinal) (MPa)	195
Ultimate compressive strength (transverse) (MPa)	133

1.3 Summary

Bone is one of the more commonly grafted physiological substances, with autografting still the most popular technique in instances where bone requires a reparative aid. However this is associated with a multitude of issues such as the lack of available tissue or the risk of infection, and as such bone scaffolding is seen as a potentially viable alternative. There are many requirements that such bioscaffolds must adhere to in order to be successful. Furthermore, the hierarchical nature of bone and its inherent capabilities must also be fully understood to enable the design and manufacture of a suitable replacement. One potential method of varying the scaffold properties such that they meet the requirements is through the use of materials with appropriate characteristics. Thus the currently used and potential materials are outlined in the following chapter.

Chapter 2

Bone Repair Biomaterials

A wide range of materials can be used as bioscaffolds, with inert metals such as titanium and stainless steel traditionally the most popular clinically, although bioactive ceramics such as apatites and Bioglass®, and polymers such as poly-lactide and poly-glycolide have undergone significant research and are beginning to be used surgically. At present, research aims to overcome the limitations of currently used materials and enhance their biological response. Although many more materials than those discussed here are used, for brevity only those relevant to this work are included.

2.1 Metals

Due to their suitable mechanical properties, metals have traditionally been used for bone repair components in a variety of situations. Conventionally, solid components are used even though they have a high stiffness exceeding that of bone. All metals used clinically are corrosion resistant, biocompatible, chemically stable and readily formable into components [3, 44–46]. Stainless steel and cobalt-chromium (Co-Cr) alloys were more prevalent in orthopaedic surgeries [45–51], however there has been a recent trend towards transition metals such as titanium (Ti), tantalum (Ta) and zirconium (Zr) [3]. Porous metallic scaffolds with reduced strength compared to monolithic constructs can be produced and used as the reinforcement in polymer-metal composites. These have increased bioactivity and more suitable mechanical properties than bulk products [3, 52–54].

2.1.1 Traditionally Used Metals

Stainless steels are the most popular material for use in orthopaedic situations due to low costs, high processability and the ability to optimise the mechanical properties [3, 44, 55–58]. However, localised corrosion can occur resulting in some of the ions (carbon (C), manganese (Mn), Cr, nickel (Ni), molybdenum (Mo), sulphur (S), silicon (Si), phosphorous (P) [44]) being leached into the body, any of which are toxic at elevated levels [44, 55–63]. As yet any attempt to prevent such corrosion has not yielded an optimal solution causing this issue to still be a clinical concern [55–59,62,63]. Co-Cr alloys are also used due to good wear and corrosion resistances and high fatigue strength. As with stainless steel, there is also the potential for toxic ion leakage from Co-Cr alloys, particularly regarding particulate Co and Ni [3,44,58]. Thus there has been research into and commercialisation of the use of other metals, with transition metals and their alloys exhibiting encouraging results, as discussed below in Sections 2.1.2 - 2.1.5.

2.1.2 Titanium and Titanium-Based Alloys

Titanium is widely used in orthopaedic medical situations for fixation elements and total hip replacements. It has good biocompatibility, corrosion resistance and fatigue strength, coupled with a low modulus and density, although it also has low wear resistance and shear strength [3, 44, 64]. Commercially pure titanium (CP-Ti) is available in 4 grades depending on the levels of iron and oxygen. Of the many alloys, titanium-aluminium-vanadium (Ti-6Al-4V) is the most popular for medical applications due to enhanced biocompatibility and corrosion resistance, and a modulus more closely matched to that of bone [3,44], with titanium-aluminium-niobium (Ti-6Al-7Nb) and titanium-aluminium-iron (Ti-5Al-2.5Fe) also suitable. Introducing porosity to CP-Ti and Ti-6Al-4V structures has led to mechanical properties even more suited to bone reparation [49–54, 65–68].

2.1.3 Zirconium

Zirconium is used in knee arthroplasty components due to its biocompatibility and high strength. Post production, it is commonly subjected to surface oxidation by heating to 600-700 K and passing oxygen over it to increase its abrasion resistance, strength and toughness [3,69,70]. The mechanical properties can also be increased by manufacturing components with ultrafine Zr grains [71]. It forms a stable interface with bone [3], and Uchida et al [72] enhanced bioactivity by subjecting structures to surface sodium hydroxide (NaOH) treatment.

2.1.4 Tantalum

Tantalum is also suitable for use as a bone repair biomaterial due to its biocompatibility, corrosion resistance, high density and coefficient of friction, and mechanical similarity to bone [73–81]. It has a highly stable interface with bone that encourages new growth via the formation of a passive oxide layer [82], tantalum oxide (Ta_2O_5), especially after NaOH pre-treatment [78]. There is currently a lack of long term studies evaluating the stability of scaffolds which is important due to the unknown biocompatibility of tantalum particles [77]. Ta nanoparticles are biocompatible, yet at present only used for imaging purposes due to their high cost and density [83].

A commercially available porous tantalum for clinical use, Trabecular Metal ^{TM} (Zimmer, USA) is produced via a 2-stage process, where polyurethane foams are pyrolised to carbon skeletons onto which tantalum is deposited using chemical vapour deposition and infiltration techniques [73–75,78,79]. Thus scaffolds with a fully interconnected porosity of 75-80% and a mean pore size of 430 μm which encourages in-growth are realised [73, 75].

2.1.5 Magnesium and Magnesium-Based Alloys

Magnesium (Mg) has potential use as a biomaterial as it is non-toxic and stimulates bone regrowth, and has a lower yield strength and Young's modulus than most other metals [84, 85]. However early testing showed it to degrade quickly in physiological conditions and hence stainless steel attracted more interest for clinical situations [84–87]. This rapid degradation also causes the release of hydrogen gas that can become trapped and require surgical removal, although the other by-products are biocompatible [84, 86, 88].

To increase the corrosion resistance, enhance the mechanical properties or control the degradation rate, magnesium is used as an alloy [84, 86, 88], with aluminium, zinc [86,88] and rare earth metals [84,86,88] presently incorporated. However further investigations into the different alloys are needed as the biodegradation properties are not fully understood [86, 89–91].

2.2 Ceramics

Due to their biocompatibility and good compressive strength, ceramics are suitable for a range of tissue engineering purposes. The main drawback with using ceramics is that they are highly brittle, a characteristic exacerbated by processing difficulties leaving constructs susceptible to cracks and notches [3, 44, 92–94]. Bioceramics fall into three categories: inert (non-resorbable), semi-inert (bioactive) or bioresorbable [94], as shown in Figure 2.1.

2.2.1 Bioinert Ceramics

Bioinert ceramics are used in similar circumstances to metallic implants as they have high hardness, excellent wear resistance, low friction and elicit no adverse immune response [3, 92, 94]. The most commonly used bioinert ceramics are oxides

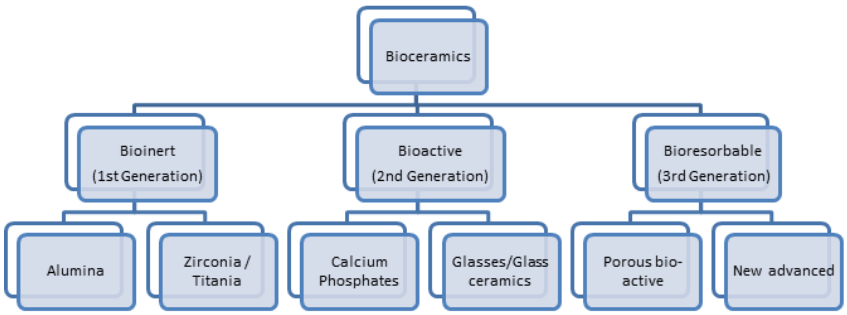

Figure 2.1: Classification of Bioceramics. They can be broken down into 3 types, with examples given for each (redrawn from [95])

of transition metals such as alumina, titania and zirconia, which are formed upon the reaction of the metal with oxygen. Incorporating porosity can generate semi-inert structures, with new growth at the implant-tissue interface [44, 92].

Aluminium oxide, alumina (Al_2O_3), is a very hard polycrystalline material which has low friction characteristics, high wear resistance and good biocompatibility [96]. It has a very high bulk compressive strength (2069-3861MPa, depending on grain size, distribution and intrinsic porosity [92]), although this has been reduced by incorporating porosity using a range of techniques [97–107], discussed further in Chapter 3. Furthermore, it is brittle in tension or flexure, requiring reinforcement via the use of polymeric [108] or composite [109] coatings. To initiate bone growth, naturally occurring ions can be incorporated, as can micro and nanoporosity [100, 101] or surface functionalization with organic products [108]. However, Andreiotelli et al [110] reported the long term (up to 10 year) survival rate of alumina implants to be lower than that of titanium implants, and that other ceramics, such as zirconia, may offer a more suitable alternative.

Zirconium oxide or zirconia (ZrO_2) has high mechanical strength and toughness [110–113], and good biocompatibility and chemical stability [110, 111, 114]. Osteoblasts have been grown directly onto zirconia surfaces [110, 112, 113] with porosity enhancing its properties with respect to biomedical applicationss [115–119]. The main concerns lie with the long term performance and cytotoxicity of zirconia powders [120]. Another consideration is that zirconia undergoes a phase change

at 1197 °C (monoclinic to tetragonal), a temperature regularly reached during processing, that can induce intrinsic stresses [111,114,119] due to the associated volume changes [121]. Whilst this can be used to toughen the structure, in a process known as transformation toughening [122,123], it can also cause imperfections in the structure that cause weakened mechanical properties. Metallic oxides can be used to stabilize cubic or tetragonal zirconia as partially-stabilized-zirconia (PSZ), which has enhanced flexural strength and fracture toughness [3,114,119]. Although oxides of calcium (Ca) [111], magnesium [92] or cerium [124] can be used, the most common stabilizer is yttria (yttrium oxide, Y_2O_3) as it generates lower amounts of intrinsic porosity and smaller grain sizes [124]. Not only should small amounts of yttria be incorporated as it is radioactive [3,92], but only concentrations below 3.5 mol.% are required to maintain the fracture strength of PSZ [92].

The biocompatibility of titanium is due to the formation of an oxide layer, titania (TiO_2), on its surface [125–128], which forms by an ionic exchange close to the surface of the implant. Therefore titania should be a suitable biomaterial. It is biocompatible [129], and has good mechanical, structural and chemical properties [127, 130]. It is available in three phases: rutile, which is the most stable in a physiological environment [126,131,132]; anatase, which elicits the strongest bodily reactions [131]; and brookite. The bioactivity is similar to that of titanium [128], with tissue bonding directly to implants [125, 133, 134]. This can be enhanced through coatings [126, 128, 130, 135–137], the inclusion of bioactive ions [138], nanotubular production [139,140] or variations to the hydroxide (OH) groups [141,142]. Furthermore, porous scaffolds are easily obtainable using such techniques as outlined in Chapter 3 [131,135,142–144], with microporous surfaces of particular research interest [136, 142].

2.2.2 Bioactive Ceramics

2.2.2.1 Calcium Phosphate

The many variants of calcium phosphate make up a bioactive family known as apatites. There are 8 main variations, Table 2.1, with hydroxyapatite (HA; Ca/P: 1.67) and tricalcium phosphate (TCP; Ca/P: 1.5) the most commonly investigated due to the crystallographic and chemical similarities to the mineral phase of bone [95]. Ionic exchange between the implant and surrounding bodily fluids generates bone growth [3, 44, 94, 95, 145].

Table 2.1: Main apatites used in biological applications (adapted from [3, 94, 146])

Name	Chemical Formula	Ca:P ratio
Monocalcium phosphate monohydrate (MCPM)	$Ca(H_2PO_4)_2 \cdot H_2O$	0.5
Monocalcium phosphate anhydrous (MCPA)	$Ca(H_2PO_4)_2$	0.5
Dicalcium phosphate dihydrate (Brushite) (DCPD)	$CaHPO_4 \cdot 2H_2O$	1
Dicalcium phosphate anhydrous (Monetite) (DCPA)	$CaHPO_4$	1
Octacalcium phosphate (OCP)	$Ca_8(HPO_4)_2(PO_4)_4 \cdot 5H_2O$	1.33
Tricalcium phosphate (TCP)	$Ca_3(PO_4)_2$	1.5
Hydroxyapatite (HA)	$Ca_{10}(PO_4)_6(OH)_2$	1.67
Tetracalcium phosphate monoxide (Hilgenstockite) (TCPM)	$Ca_4(PO_4)_2O$	2

HA resorbs slowly and encourages significant in-growth [94]. It has a Young's modulus of 80-110 GPa [3] which can be reduced using porosity. TCP resorbs more rapidly and is used as bone filler as total resorption can occur before complete regrowth [44, 92]. Biphasic combinations of TCP and HA with tailored resorption rates can also be used [3, 95].

Calcium phosphates can be combined with inorganic salts and injected as a gel to the fracture site where it cures [3, 95, 145, 147–150]. Although the biocompatibility, bioactivity and osteoconductivity are retained, there may be problems with the safety, mechanical toughness and curing time. Nevertheless, commercialisation of such biocements has been undertaken [44, 147, 148].

2.2.3 Glass and Glass Ceramics

The discovery of bone bonding by Hench et al [151] has led to the use of glasses and glass ceramics for bone regenerative applications. Of these silicon oxide based systems, Bioglass 45S5 ® has the optimal composition (42.1% SiO_2, 28% CaO, 26.3% Na_2O, 2.6% P_2O_5 [92] [92]) to instigate growth. Glass particles of 0.1-1 μm are formed via the nucleation and growth of uniform crystals through melt or sol-gel methods. Although melt techniques have been used to produce glasses for a range of applications, sol-gel techniques can produce scaffolds with a range of porosities and surface properties, or with biological agents [3, 95] and are discussed further in Section 3.1.7. As with all glasses, they are brittle and it is difficult to apply them, for example as coatings, to other materials [3, 44, 94, 95] due to mismatched thermal coefficients [92, 152], minimal chemical bonding [92] and chemical variations to the glass during sintering [92, 153],

2.3 Polymers

Although most polymers used in tissue engineering are suited to soft tissue regeneration, there are some that stimulate hard tissue regrowth. Polymers are long chain molecules, with covalent bonds along backbone chains that are linked by van-der-Waals forces or crosslinks. They are easy to manufacture, relatively cheap and the different types give rise to a diverse range of mechano-physical properties, depending on the degree of polymerisation of each chain [44].

Table 2.2 outlines the most commonly used biodegradable polymers, with poly-lactic acid (PLA), poly-glycolic acid (PGA), their copolymer poly-lactic-co-glycolic acid (PLGA) and polycaprolactone (PCL) the most important for orthopaedic applications. PGA degrades to glycolic acid and has excellent mechanical properties, although a short degradation time [154–164]; PLA degrades to lactic acid and has a longer degradation time, yet is not as mechanically similar to bone [157, 163–175]. PLGA degrades to a combination of lactic and glycolic acids, and can be tailored to provide suitable mechanical and degradation properties [176–185]. By modeling the degradation properties, the degradation rates of such copolymers can be optimized [5,6,92,93,186–188]. PCL degrades at an appropriate rate for regrowth, however it is weak and thus must be strengthened via co-polymerisation, incorporation in composites or resynthesizing [189–204].

In general, polymeric materials alone are not suitable for use as bone regenerative bioscaffolds due to their weak mechanical properties, however they can be used as coatings to enhance the bioactivity of scaffolds. Hence, porous polymeric scaffolds will not be produced in this work however their use as coatings will be considered.

2.4 Composites

A composite material has two or more constituent materials and/or phases when evaluated at a scale larger than atomic, allowing for control over the material properties. Bone is one of Nature's composites, and hence scaffolds made from composite materials could more closely mimic the properties of bone [3, 92, 145]. Further to the general scaffold requirements, all components of biocomposites must be biocompatible and the interface between them must not be weakened by the bodily environment [7, 44, 220].

Polymer-matrix composites (PMCs) are the most common biocomposites and consist of a ceramic construct within a polymer matrix [7, 44, 220]. They benefit from

Table 2.2: Some of the more important polymers used in bone regeneration, with the advantages and limitations, as well as the Young's modulus and examples for each class

Polymer Group	Examples	Advantages	Disadvantages	Modulus (GPa)	Ref.
Polyanhydride	Aliphatic polyanhydride Unsaturated polyanhydride Aromatic polyanhydride	Controllable degradation, Surface erode[a]	Hydrolytic and require variations to monomer for controllability, Storage instability	n/a	[44, 187, 189, 190, 205, 206]
Poly(amino acids)	Poly-L-lysine Poly-L-orthinine Poly-L-arganine	Low toxicity, Degrade to amino acids	Highly insoluble, Non-processability	n/a	[44, 190, 207]
Polycaprolactone	n/a	High solubility	Slow degradation rate, Mechanically weak, Hydrophobic	0.4 – 6.9	[44, 186, 190, 192, 195, 204, 208]
Poly(α-hydroxy acids)	Poly(glycolide)	Low solubility in organic solvents, High melting point Degrades to bio-monomer	Mechanically weak in-vivo, Possible problems with degradation products[b]	7 (reduced by 50% in-vivo)	[44, 186, 190, 206, 207, 209, 210]
	Poly(lactide)	High strength and toughness, Degrades to bio-monomer	Limited backbone hydrolysis, Hydrophobic. Possible problems with degradation products[c]	1.4-3.3	[44, 186, 190, 209, 211]
	Poly(lactide-co-glycolide)	Controllable chemo-physical properties, Degrades to natural monomers	Possible problems with degradation products, Proteins and peptides unsuitable	0.34-2	[44, 190, 209, 212–214]
Polycarbonates	Poly (trimethyl carbonate)	Surface erode	Low softening point, Mechanically weak	0.3	[187, 190, 215, 216]
	Poly (BPA-iminocarbonate)	Stable, Mechanically strong, Low toxicity	Virtually non-resorbable, Ultimate biocompatibility unknown	2.4-7.9	[187, 190, 217–219]

[a] erosion mechanism where the surface degrades first and is more controllable than bulk erosion, where the whole construct erodes at the same time
[b] The excess build up of glycolic acid can lead to problems if not removed
[c] The excess build up of lactic acid can lead to problems if not removed

the toughness of the polymer and the strength of the ceramic whilst incorporating bioresorbable polymers can aid bioactivity [3, 5, 7, 93]. Organic-inorganic hybrids can be formed using sol-gel techniques. One particularly exciting type of these are star gels, which have an organic core surrounded by flexible arms to enhance their mechano-physical properties [95, 145]. They are homogenous, have better mechanical properties than conventional glasses that are more closely matched to those of bone [95] and apatitic phases can grow on their surface [145],

Composite production is specific to the materials used. Although the methodology used in this work will not be specifically aimed at producing composite bioscaffolds, it may be suitable to incorporate polymeric coatings.

2.5 Summary

There is a wide range of materials that can be used to produce scaffolds suited to bone repair. Metallic scaffolds are the most prevalent clinically, with stainless steel and Co-Cr alloys being replaced by transition metals such as titanium, tantalam and zirconium, and their alloys, to overcome the issues with toxic ion leakage. Ceramics can be broken down into three groups: inert, semi-inert or resorbable. Inert ceramics are mainly based on oxides of transition metals and do not elicit any bodily reactions; semi-inert ceramics encourage bone growth at the implant-tissue interface and are CaP or glass based; and resorbable ceramics undergo resorption and instigate tissue regeneration. Although there are some polymers suited to bone regeneration, the majority are produced as soft tissue scaffolds due to the weak mechanical properties they have. Bone scaffolds can also be produced from composites with PMCs the most common. The wide range of matrices and cores that can be used enable enhanced performances over single phase structures. Whilst each material can be used to produce bone reparative structures, the generation of porosity is important in ensuring the complete cellular infiltration. Thus, the following chapter investigates the different techniques used to manufacture bioscaffolds.

Chapter 3

Scaffold Manufacturing Techniques

There are many techniques that can be used to produce porous scaffolds. These can be broken down into two major sets: conventional techniques and additive layer manufacturing (ALM). The most popular methods within each are outlined (Sections 3.1 and 3.2) and analysed (Section 3.3) to determine the optimal technique for use in this project.

3.1 Conventional Manufacturing Techniques

Conventional techniques use the reaction of materials to certain conditions such as heat or pressure to generate porous structures and are currently more prevalent than ALM due to the lower costs involved. Depending on the technique used, a wide range of porosities, pore sizes and strengths can be achieved.

3.1.1 Dry Methods

Dry methods are the simplest manufacturing technique used to generate porous structures and involve compressing powdered biomaterials with the pressure varied to make changes to the porosity [2, 93]. However scaffolds produced in this way are limited to simple geometries with little porosity [221], and the problems with

weak mechanical properties [222] and polymer springback, where structures expand after compression in an unpredictable manner, [223] have led to the exploration of hot isostatic pressing (HIP) and uni-axial hot pressing (HP). Such techniques involve sintering the sample under pressure to improve the strength and hardness [224, 225] by enhancing interparticular bridging whilst preventing the formation of nonhomogenous ceramics [224]. Highly porous constructs can only be obtained if porosity is incorporated before sintering with the highly pressurized gas preventing collapse of the pores [226]. For example, Zhao et al [224] implemented HIP as a second sintering step for bioscaffolds produced by foam reticulation (detailed in Section 3.1.5) to significantly improve the compressive strength.

For metallic implants, the production of scaffold using dry powders under compression is known as powder metallurgy (PM) or the space holder method [50, 227–231], which involves the incorporation of porogens. A porogen is any material included sacrificially such that the subsequent removal generates porosity.

3.1.2 Slip Casting

Most other production methods involve producing a slurry by mixing the powdered biomaterial with a liquid, a dispersant and a binder. Slip casting is the simplest of these whereby the slurry is poured into a porous mould, which is removed before sintering [7]. A hierarchical structure can be produced by including porogens into the slurry. The incorporation of porogens, for example polymethyl methacrylate (PMMA) beads [223], has led to the development of solvent casting/particulate leaching as outlined below in Section 3.1.3. However, slip casting is a highly wasteful procedure as the mould is generally discarded after use [7, 223, 232], and as such research is aimed at using the slurry in other ways such as those discussed in Sections 3.1.3 - 3.1.5 and 3.2.3.

3.1.3 Solvent Casting/Particulate Leaching

Solvent casting is one of the more popular techniques whereby pores are generated via the inclusion of porogens. For ceramic based biomaterials, a porogen-containing biomaterial slurry is produced and is cast into a mould which can be either porous or non porous. Once dry, the green body is removed from the mould and subjected to a controlled heating protocol during which removal of the porogen generates porosity and sintering ensures suitable densification.

It is a highly versatile technique and has been used to produce polymeric [2, 233], ceramic [12, 99, 105, 234–237] and metallic [46, 47, 50, 227–231] bioscaffolds. The level of porosity is controlled by the amount of porogen in the slurry, whilst the pore size is controlled by the size of the porogen.. The wide range of porogens include salt (NaCl) [2, 233], waxy hydrocarbons [233], organic particles [2], paraffin [12, 50, 237], napthalene [12, 227], starch [12, 105], flour [12], synthetic polymers [12,50,99,234], hydrogen peroxide [12] and sucrose [235,236], enabling variability and controllability over the final structure. The only constraint with the porogen is that it must either be biocompatible, or the complete removal must be ensured to avoid any issues with cytotoxicity. As such, it is only possible to produce thin (<3 mm) scaffolds, with relatively poor mechanical properties [2, 12, 233–240]. Shastri et al [241] overcame this by vacuum drying samples, however the drying procedure took several days. Finally, due to differences in the surface roughness of constructs depending on whether the surface is exposed to air or on the surface of the mould during leaching, the Mikos research group [233, 242, 243] have developed a method incorporating compression moulding to enable the production of structures with uniform surfaces. However this is only suitable for polymeric biomaterials.

3.1.4 Phase Separation/Freeze Casting

Upon the freezing of a liquid, it forms solid dendrites [244, 245]. Using a closely controlled combination of heat and pressure the liquid phase can then be bypassed,

and the solid ice sublimed directly to vapour. Freeze casting consists of three main steps, shown in Figure 3.1: these are freezing, primary drying and secondary drying [246–249]. When a slurry is frozen, freezing of the liquid components generates dendritic ice crystal growth [49, 106, 245, 250–259]. Freezing rates and temperatures are important in controlling the size and nature of the dendrites, and close control over these allows for some controllability over the final structure [250, 256–261]. Many commercial and laboratory driers are limited by the minimum temperatures obtainable generally being approximately -67 °C, although lower temperatures can be achieved.

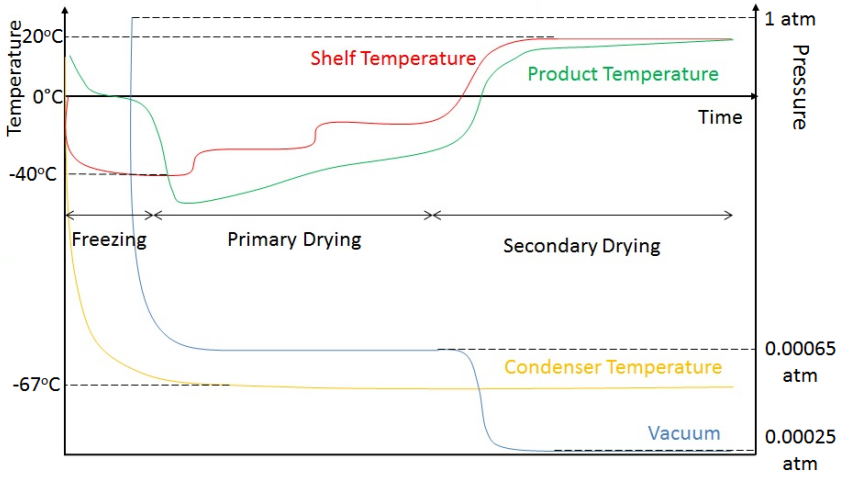

Figure 3.1: Simplified freeze-drying cycle chart using water as the porogen. There are three steps: freezing, primary drying and secondary drying leading to a porous structure (redrawn from [262])

Removal of the ice crystals generates the porosity in freeze cast scaffolds. Primary drying, or sublimation, is the process whereby ice is converted directly to vapour without melting, generating pores of the size and shape of the dendrites. The basic states of matter and their transformation are dependent on the temperature and pressure of the system within which they lie, as shown in phase diagrams such as Figure 3.2 for water. Sublimation is achieved by holding the product below the eutectic temperature of the ice and using controlled vacuum conditions to remove the vapour [256–258, 260]. Some heat input is required to maintain a constant

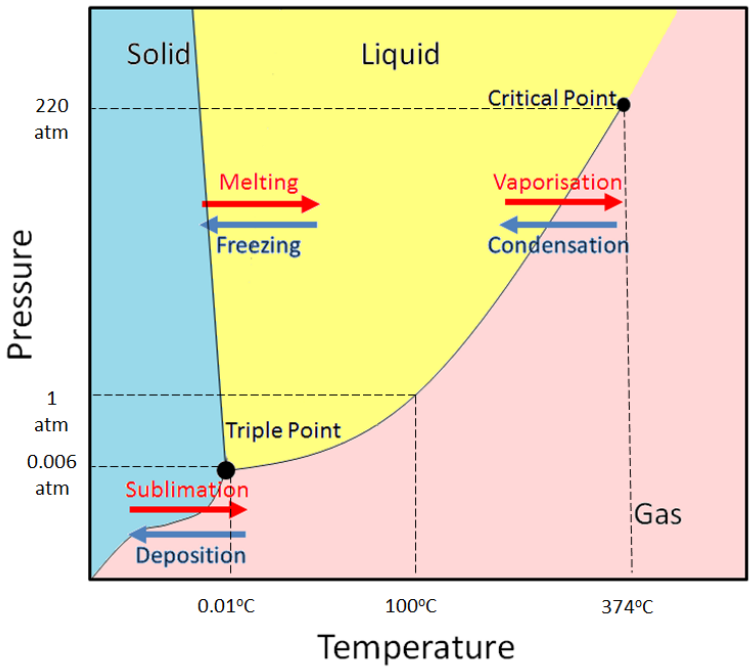

Figure 3.2: Phase diagram for water. The three basic states of matter, solid, liquid or gas, are dependent on the temperature and pressure (redrawn from [263])

temperature as sublimation cooling occurs which can affect the process, however too much heat can lead to the sample collapsing [250, 253, 257–260]. Secondary drying occurs when the only water that remains is that which is bound to other particles within the structure. This is particularly important in the case of drying substances used, for example, in long-life foodstuffs. It is a continuation of primary drying with reduced pressure and a raised temperature [246–249].

Production of freeze cast bioscaffolds involves the production of a porogen-containing biomaterial slurry which is frozen, dried and finally sintered, with the procedure outlined in Figure 3.3. Variations to the slurry concentration, freezing temperature and sublimation pressure can be readily achieved and enable variations to the final structure [2, 250, 253, 254, 264, 265]. HA structures predominantly have relatively limited porosity [250, 254, 260, 264] with mechanical strengths similar to that of cancellous bone (12 MPa at 52 % [250] to 36.4 MPa at 31 % [254]). However, Macchetta et al [254] have produced scaffolds with 72 % porosity, albeit with a low yield stress

of 2.3 MPa. Alternatively, Deville et al [260] have produced constructs with zones of different levels of porosity, ranging from dense, through cellular to lamellar depending on the proximity of the slurry to the cold surface during freezing, thus generating high mechanical properties of up to 65 MPa and 145 MPa at 56 and 47 % porosity respectively, within the range seen in cortical bone (131 MPa [1]). Finally, combinations of different porogens can generate multi-scale porosity for improved biological responses [5, 23]. In particular, Fu et al [264] combined dioxane and water to enhance the response of osteoblastic cells *in-vitro* compared to those produced with just water.

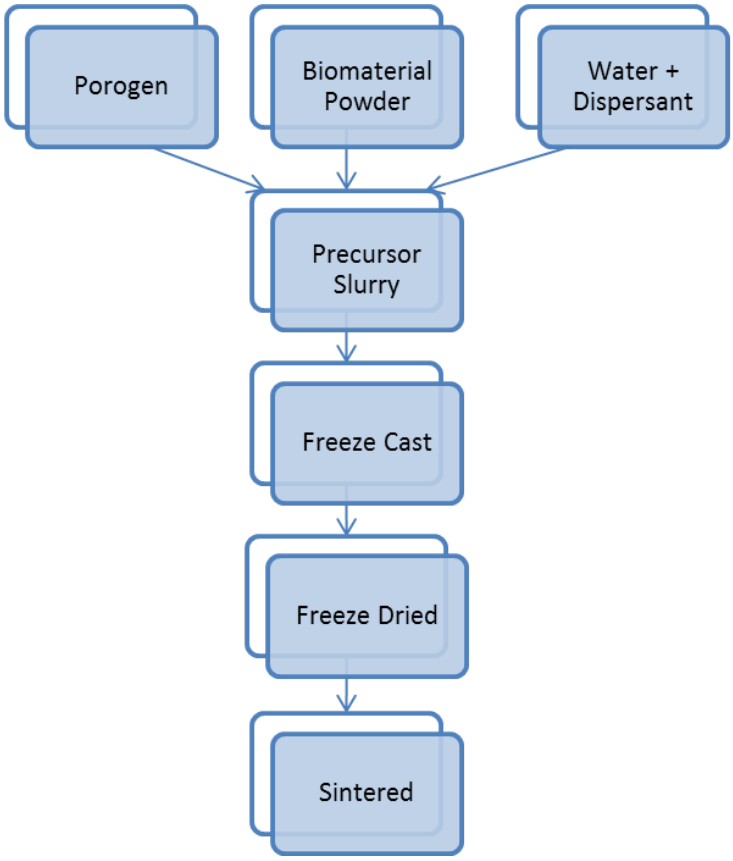

Figure 3.3: Outline of the stages of freeze casting technique used to produce scaffolds. A slurry is formed using the biomaterial and the slurry is freeze cast and dried before sintering the resultant green body

3.1.5 Replication Techniques

There are many natural and synthetic porous structures that have a range of porosities and pore sizes and from which it is possible to develop structures suited for tissue engineering applications. Foam reticulation aims to utilize such porous constructs as a template from which a scaffold is based [12, 266–275]. Briefly, the biomaterial is mixed into a slurry which is then coated onto the template. Once the slurry has dried, the sample is sintered using a protocol that also enables pyrolysis of the template [65, 230, 273–277], with the technique outlined in Figure 3.4.

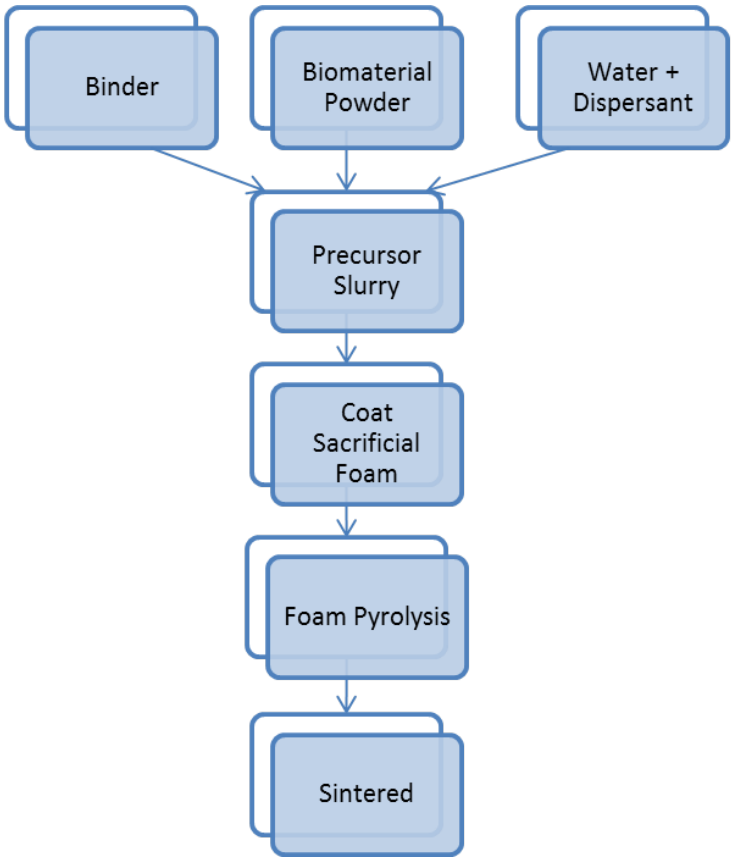

Figure 3.4: Outline of the stages of replication technique used to produce scaffolds. A slurry is produced that is coated onto a sacrificial foam, which is burnt out to leave a green body which is sintered

Material choice, of both the template and biomaterial, is important in producing suitable structures. The biomaterial must have a sufficiently high melting tem-

perature such that, upon template sublimation, the structure is not compromised. Meanwhile, the template must have a suitable melting temperature such that the structure has sufficiently consolidated before the onset of pyrolysis to maintain its shape. Furthermore, slurry characteristics are important, and the optimal components and rheology must be predetermined before scaffold fabrication [232].

The main limitation with the technique is the oxymoronic relationship between template strength and porosity; scaffolds with a higher level of porosity have an enhanced biological performance however they also have significantly compromised mechanical properties [273, 277]. Furthermore, the poor mechanical properties of scaffolds are exacerbated during removal of the template, when microcracks can be introduced into the construct [270, 274]. Increasing the number of coatings of the slurry on the template increases the strength of the component, but reduces the pore size [65,267,278,279]. Therefore a trade-off must be made to maximize strength and create pores of a suitable size. Sample strength can also be improved by increasing the sintering temperature as this causes increased densification [280]. However, this enhances shrinkage which must be considered for the production of appropriately sized pores. Finally, Cunningham et al have improved the strength of constructs [273,277] by varying the template, whist Jo et al [276] have added directionality by elongating the template prior to coating, such that the final structure more closely mimics that of natural bone.

Chang et al [15] have shown that foam reticulated HA scaffolds with open porosity of 100-500 μm encourage the formation of Haversian canals and facilitate remodeling *in vivo*. To further improve the biological activity, Mallick and Winnett [267,278], in previous work, and Lee et al [268,281] have separately introduced porogens into the precursor slurry to create structures with macro and microporosities, which has led to the development of the Adaptive Foam Reticulation (AFR) technique, discussed further in Section 3.1.5.1.

3.1.5.1 Adaptive Foam Reticulation

The limitations of the foam reticulation technique, described in Section 3.1.5, need to be overcome to enable its widespread use in producing bioscaffolds. One possible way to achieve this is to generate microporous struts that enhance the biological performance and hence significantly increase the regrowth rate of host tissue by providing cell attachment sites [2, 16]. Microporosity can be achieved by the incorporation of a porogen within the slurry as in solvent casting/particulate leaching [235, 236, 239] or freeze casting [256, 257]. The porogen is removed either during freeze drying or at the polymer burnout stage to leave a macroporous structure of microporous struts. The technique, outlined in Figure 3.5, follows that of foam reticulation with a freeze drying stage to generate micropores. Briefly, a template is coated with a porogen-containing biomaterial slurry. This is freeze dried to sublime the porogen, and the structure is then subjected to a controlled sintering protocol to enable complete polymer burnout and densification of the scaffold [267, 278].

As with freeze casting, control of the freeze drying parameters allows for the level of microporosity and micropore size to be varied [250, 253, 259, 260]. Meanwhile, template choice in replication techniques facilitates the production of a controllable macroporous structure [273, 276, 277]. Therefore combining these facilitates the generation of constructs of a predictable, hierarchical nature [267, 278].

3.1.6 Gelcasting

Gelcasting involves the foaming and direct consolidation into a gel of an aqueous solution consisting of a monomer, cross-linker, free radical initiator and catalyst. The gel is then cast into an appropriate mould and polymerised to form a water-polymer gel in which biomaterial particles are immobilised in the shape of the mould. Whilst still wet, the gelled part is removed from the mould and dried under controlled conditions to leave a mechanically stable green body [187, 282–287], with the technique outlined in Figure 3.6.

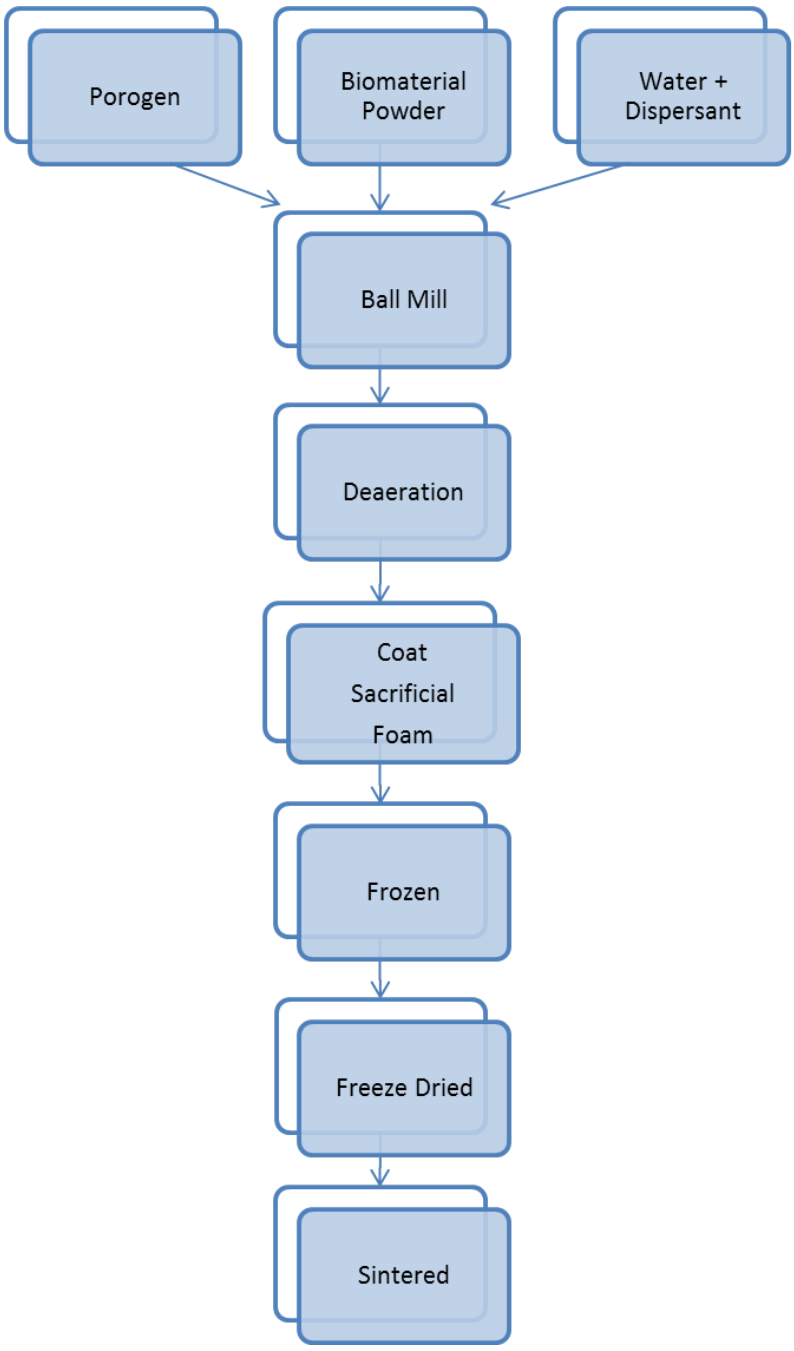

Figure 3.5: Outline of the AFR technique used to produce bioscaffolds. A polymeric template is coated with a slurry, freeze dried and subjected to a controlled sintering protocol

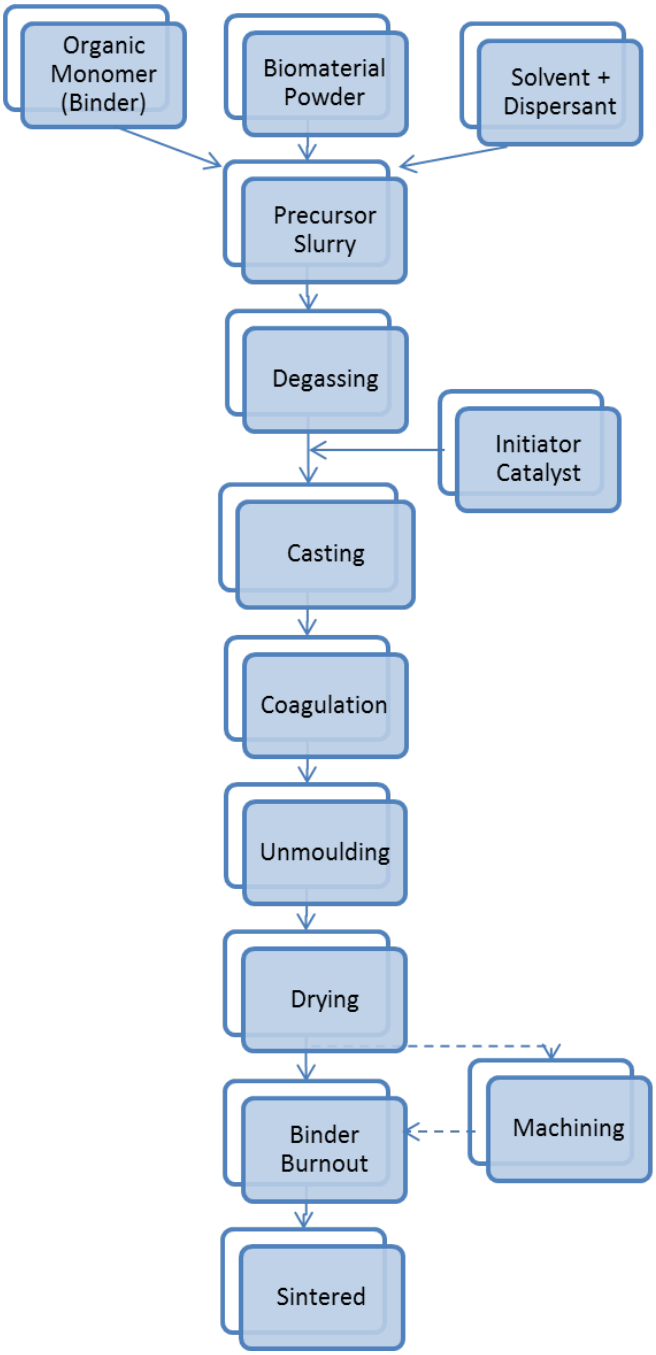

Figure 3.6: Outline of the stages of gelcasting technique used to produce scaffolds. An aqueous solution is consolidated into a gel, which is cast into a mould before drying and sintering

Of particular importance is the gelation speed, which must be fast enough that the foam does not collapse, yet not so fast as to inhibit complete penetration of the mould [7, 283, 288]. The physical properties of the green body can be affected by microcracks and inner stresses generated during gelation and drying [285, 286, 289], or by surface exfoliation, whereby free-radical polymerization is inhibited by oxygen in the natural atmosphere. This is a particular problem for acrylamide monomer systems [287, 290] and leads to powdery surfaces, although Ha [290] reported that surface exfoliation can be overcome by the use of oxygen free atmospheres. Furthermore, traditional components of the solution are toxic and thus gel system selection is important to ensure a biocompatible product [287] with research currently aimed at low toxicity (methylacrylamide [284, 287, 291]) or non-toxic (such as 2-hydroxyethyl methacrylate [292], agarose [288] or sodium alginate [289]) [287] systems.

3.1.7 Sol-Gel Techniques

Sol-gel techniques have been developed with the aim of producing structures with increased homogeneity, higher purity and at lower temperatures than with traditional techniques [293]. Sol-gel techniques revolve around the inorganic polymerization of a solvent [294, 295] to generate a gel, which is then cast and reduced to form stable scaffolds using controlled thermal processes [293, 296–299]. There are three main approaches, namely the gelation of colloidal powders, the hydrolysis and polycondensation of nitrate precursors with hypercritical drying of the gel, or the hydrolysis and polycondensation of alkoxide precursors with aging and drying under ambient conditions. In all cases, the precursor materials are mixed together to form a low viscosity liquid and cast into a mould. The colloidal particles and silica species link together in a process known as gelation to form a gel which is then aged. The structure is then dried under careful conditions to stop the formation of large capillary stresses before dehydration, and densification [125, 133, 293, 298, 300–302], with the technique outlined in Figure 3.7.

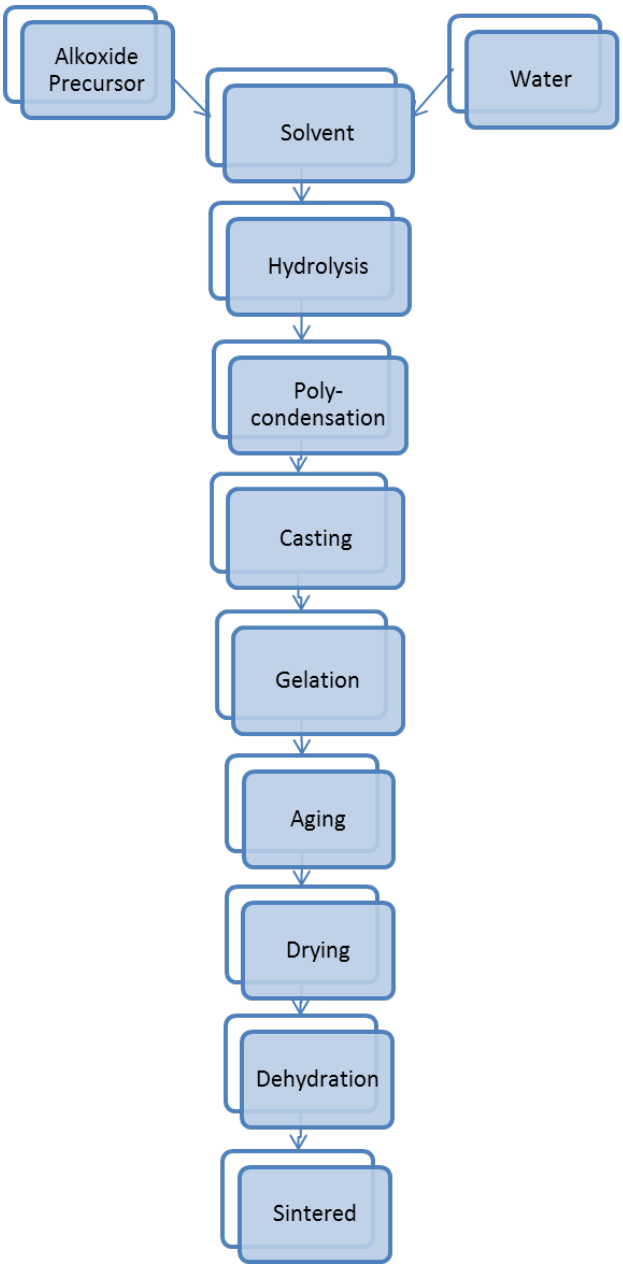

Figure 3.7: Outline of the stages of sol-gel technique used to produce scaffolds. Polymerization of a solvent via hydrolysis and polycondensation leads to a gel, which is made into a stable scaffold through thermal processes

Sol-gel technology is particularly useful in the production of glass structures (using silica based precursors [125, 293, 299, 303–305]) although it can be used to produce structures from a variety of materials based on inorganic metal salts or metal organic compounds, such as metal alkoxides [M(OR)n], where M is the network forming element (such as Ti, Zr, Al) and R is an alkyl group [72,119,125,133,141,298,300,302, 306]. Although generally used to produce bulk structures wih nanoporosity [141], macroporosity can be incorporated by foaming of the sol [295, 305], the inclusion of pore forming agents [295,306], by coating sacrificial structures with the sol [119, 295] or by sintering together sol-gel derived microspheres [307].

One of the major advantages is that it allows sol-derived materials to be dip-coated onto structures with control of the surface properties and layer thickness [72,133,300, 302]. Furthermore, extreme temperatures are not required, enabling bioactive agents (such as cells, enzymes, proteins or antibodies [295, 297, 302]) to be incorporated into the scaffold [297, 299, 303]. Even so, the processing conditions, such as the mild thermal and chemical conditions, can still be harmful to such agents [308, 309]. The precursors can be varied to tailor the porosity [233,294,297]. However, the constructs have poor mechanical properties and the technique is associated with higher costs and complexity than other conventional techniques limiting its commercial viability [288, 295, 297, 298].

3.2 Additive Layer Manufacturing

Additive layer manufacturing, also known as solid freeform fabrication or rapid prototyping, is a set of techniques based on the “bottom up” approach to manufacturing, whereby building units, in the form of powders, liquids or colloids, are arranged in a predetermined manner [310–312]. As production involves computer aided design and manufacture (CAD-CAM), the scaffold can be tailored to the host requirements.

3.2.1 Liquid-Based Techniques

Liquid-based techniques involve selectively drying a liquid. The most common is stereolithography (SLA) which requires materials with ultraviolet (UV) sensitivity to be used. Each layer of the scaffold is traced by a laser beam on the surface of a vat of the photopolymer, causing local solidification as shown in Figure 3.8a. Once complete, the structure is washed and cured in a UV oven. This is a highly accurate technique, however there is a lack of suitable photosensitive biomaterials which can be readily liquidized [313–317]. Although Chu et al [316] have reported some photosensitive ceramics and Sachlos and Czernuszka [310] have investigated producing ceramic constructs by dispersing ceramic powders in photosensitive monomers, liquid based methods are only readily suitable for polymeric biomaterials which will not be used in this work due to the weak mechanical properties as outlined in Section 2.3. As such, these techniques will not be discussed any further.

3.2.2 Powder-Based Techniques

Powder-based techniques are based upon the joining of thin layers of powdered (bio)material. A thin layer of powder is rolled onto the build table and selectively joined. This can be either by the localized spraying of an adhesive as in 3D printing (3DP) [318–324], Figure 3.8b, or the localized melting with a laser as in selective laser sintering (SLS) [325–330], Figure 3.8c. The build table is then lowered, and the procedure repeated.

A range of ceramics have been used with 3DP, including hydroxyapatite and other calcium phosphates [331], and bioactive glass [320]. The main considerations with respect to material choice are that the material must have suitable flowability to be easily transferred to the build table and for depowdering of the construct whilst enabling high resolution [313, 321], and that the powder can be bound by the binder, without the spraying forces creating large craters or binder-powder reactions [313, 321]. Although there are many reports confirming the biocompatibility

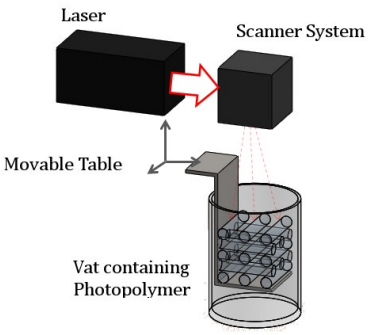

(a) SLA uses a laser system to selectively solidify a liquid

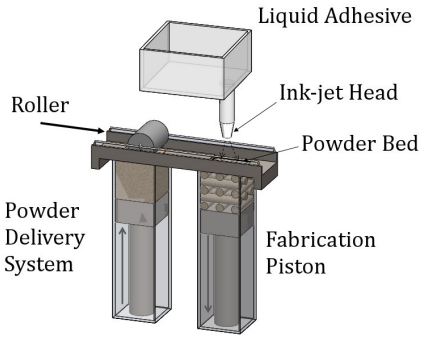

(b) 3DP uses a liquid adhesive to join particles of the material together

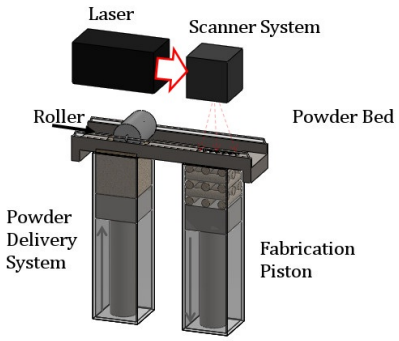

(c) SLS works on the same principle as 3DP, however uses a laser system

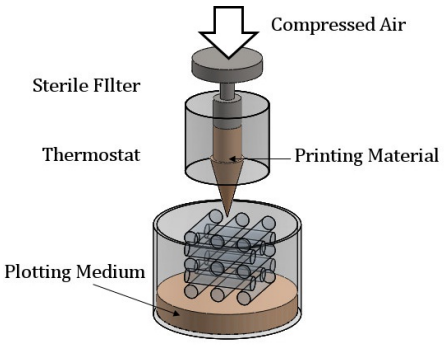

(d) 3D bioplotting drops a colloidal ink onto a liquid where it solidifies

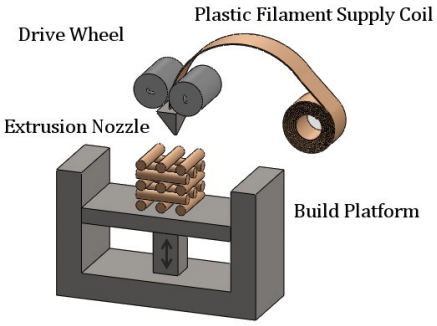

(e) FDM drops the colloid directly onto the build table

Figure 3.8: The various ALM based techniques work in different ways (redrawn from [311])

of structures [318, 319, 324], there are conflicting results regarding the bioactivity of the scaffolds. For example Shanjani et al [332] found the biological performance of 3DP fabricated scaffolds to be similar to that of sintered calcium polyphosphate, whilst Leukers et al [319] found that 3DP HA scaffolds only offer similar proliferative ability as plastic controls [318]. Furthermore, Will et al [324] found that there was no bone remodelling after 4 weeks *in-vivo*, whilst this has been reported for various conventionally produced bioscaffolds [15, 16, 235, 333, 334]. There are also problems due to powder entrapment [310] and the weak inter-particular strength of green bodies [313, 331, 332] which exacerbates the difficulties in depowdering [313], although Shanjani et al [331] improved the mechanical strength of constructs by orientating the layers in the direction of the load.

Research into the use of SLS for bone scaffold applications has predominantly involved mixing or coating HA with polymeric binders to form biocomposites [325, 328, 329], or by producing polymeric structures such as polyetheretherketone [328]. Constructs have been reported to be very fragile as a result of incomplete fusion between particles [325, 328, 329] and, as with 3DP scaffolds, Zhou et al [329] found difficulties in the complete depowdering of SLS fabrications. Finally, Chua et al [325] report the formation of a carbonated HA layer on the the surface of SLS fabricated HA/poly-vinyl-alcohol (PVA) composite scaffolds in simulated bodily fluid, inferring their biocompatibility.

3.2.3 Colloidal Ink-Based Techniques

A colloid is a biomaterial-based slurry, with three major techniques utilizing these: robocasting, ink-jet printing and the related 3D bioplotting, and fused deposition modelling (FDM). Robocast structures are deposited as a highly concentrated colloid able to support its own weight; the final structure is however limited by the mechanical strength [335–338]. Ceramic structures have been produced from PSZ [339], HA [335, 338] and other calcium phosphates [337], bioactive glass [338] and composites based on a ceramic interspersed with a polymer [335, 338], with a range of poros-

ities [335, 337–339]. One of the important features is the rheology of the precursor slurry, which affects the construct properties, in particular the green body strength and porosity of the sintered product [335, 338–340], with well dispersed suspensions increasing the density and homogeneity of the scaffold. Structures are biocompatible, with apatitic deposition reported by Russia et al [338] in simulated bodily fluid, whilst tailored degradation can be incorporated by including biodegradable polymers [335, 338]. Furthermore, Polak et al [341] and Woodard et al [333]incorporated sacrificial polymers into the colloid to produce heirarchical structures.

Ink-jet casting deposits the colloid as droplets, which can spread to give elongated pores with a high mechanical strength. However, the pore size of these is, in general, not suitable for bioscaffolds [340,342,343]. 3D bioplotting also deposits droplets, but into a liquid medium in which they solidify to limit the spreading as shown in Figure 3.8d. The major consideration with this is ensuring the complete removal of the liquid medium [310–312]. For both ink-jet printing and 3D bioplotting, the rheology of the ink is important in ensuring sufficient drop formation and solidification [340]. Furthermore, there must be a high level of dispersion of the biomaterial within the ink to stop the nozzle becoming clogged [340, 342], although suitable dispersion techniques can be used to avoid this [340]. Colloids are either solvent based, where solidification occurs by the drying of the solvent [340], or wax based, where the wax is frozen [340]. In a review by Lewis et al [340], it was reported that solvent based ink-jet printing is affected by the dwell time required for drying which causes bottlenecks in the process, although the solvent can induce microporosity. They also report that complete removal of the wax can take a long time and cause structural changes in the construct. Finally, Wu et al [320] observed rapid apatitic deposition *in-vitro* on glass-derived structures, which simultaneously released ions suitable for bone regeneration.

Finally, FDM, shown in Figure 3.8e, pumps a filament of the material through a head-heated liquifier. This generates structures with mechanical anisotropy, however a thermoplastic polymer must be used and there is a lack of these suitable for

hard tissue engineering applications [312, 343–346]. As the liquifier operates at temperatures exceeding 120 °C, biological molecules cannot be incorporated into the scaffold [310]. Seeding FDM-fabricated PCL/CaP structures with bone-derived cells has indicated biocompatibility [312, 344], with Schantz et al [344] reporting suitable proliferation and mineralization.

3.3 Comparison of Techniques for Scaffold Fabrication

The above techniques are some of the more prevalent methods suitable for fabricating porous structures. Table 3.1 summarises the advantages and limitations of these compared to the scaffold criteria outlined in Section 1.1.1, with the pore size, porosity, compressive yield strength and biological response analysed. All of the aforementioned methods can be used to produce structures with open pore fenestrations [12, 259, 268, 283, 305, 322, 329, 333, 335, 338] within the range detailed for cancellous bone growth (100-900 μm), although phase separation/freeze casting is at the lower limit of this. Furthermore, all can generate scaffolds with porosities similar to that of cancellous bone depending on the processing parameters. The mechanical properties of the scaffold are closely linked with the porosity, with structures from most techniques having a yield stress within the limits of 2-23 MPa known to be suitable for cancellous bone reparation [254, 274, 285, 322]. This is material dependant however, with the values above given for HA being the biomaterial, as it offers the greatest osteogenic potential. Similarly, the biological response reported herein is also for HA structures. Scaffolds produced from all conventional techniques apart from dry methods have an enhanced biological response [347], whilst ALM fabricated constructs exhibit conflicting responses. This is due to the smooth surface finish of colloidal ink-based techniques [312], entrapped powders [310, 329], which are cytotoxic, with powder-based techniques and the incomplete removal of toxic solvents/binders in colloidal ink-based techniques [310, 340] and 3DP [313].

The techniques outlined in this chapter have been ranked with the analysis given

Table 3.1: Analysis of manufacturing techniques against scaffold requirements. The biological response and compressive strength given is for HA structures.

Method	Pore Size (μm)	Porosity (%)	Compressive Strength (MPa)	Biological response[a]	Ref
Cancellous Bone	1 - 3500	10 - 90	2 - 23	n/a	[25, 32, 33]
Dry Methods	n/a	n/a	0.11 - 0.23	n/a	[93, 223, 224]
Phase Separation / Freeze casting	8 - 200	30 - 75	2 - 36	Enhanced MC3T3[b] and ALP[c]	[250, 253, 254, 264]
Replication Techniques	Foam dependent (10 - 1000)	<95	0.3 - 8.4	Enhanced MG63[d], ALP and other gene groups	[267, 274, 277, 348, 349]
Gelcasting	0.1 - 1000	<90	2 - 32.6	Enhanced ALP and osteoblast like cells	[283–285, 287, 350, 351]
Sol-gel Techniques	Graded (0.037 - 1000)	50 - 70	2 - 20	Increased osteogenic cell markers	[295, 298, 303, 352, 353]
Solvent Casting / Particulate Leaching	Particle dependant (5 - 600)	50 - 90	0.3 - 9.3	Enhanced osteoblast growth	[236, 237, 354]
3DP	Feature > 10 Layer > 20	Tailored 30 - 80	0.2 - 45	bMSC[e] decreased, ALP enhanced	[318–320]
SLS	Feature > 10 Layer > 76	Tailored 30 - 80	2 - 31	No change	[311, 327, 331, 332]
SLA	Feature: 1 - 100 Layer > 1	Tailored 30 - 80	1.3 - 56	Similar at best	[313, 314, 329]
Robocasting	Feature > 30 Layer > 30	Tailored 30 - 80	2 - 20	n/a	[335, 337, 338, 340, 342]
Ink-jet printing	Feature > 200 Layer > 0.4	Tailored 30 - 80	n/a	n/a	[340, 342, 343]
FDM	Feature > 100 Layer > 100	Tailored 30 - 80	0.16 - 15	Enhanced	[344–346]

[a]Compared to base level of non-porous surface
[b]Undifferentiated mouse cell type of pre-osteoblastic lineage
[c]Alkaline phosphatase, expressed during osteoblastic lineage
[d]Undifferentiated human cell type of pre-osteoblastic lineage
[e]Bone marrow stromal cells

in Table 3.2. Not only does this include the factors analysed in Table 3.1, it also incorporates an analysis of the more tangible factors discussed in the following paragraphs. Not included in the table is the AFR as it is in the early stages of development. This has been developed with the aim of minimising the relatively poor performances of the constituent techniques [267], as detailed in Section 3.3.1.

The pore size is of paramount importance to the tissue response to the scaffold. Macropores (>10 μm) and micropores (0.5-10 μm) enhance the biological activity in different ways, and so ideally both would be present. This is more achievable using conventional techniques due to the limitations with the resolution of rapid prototyping techniques. The few methods capable of producing scaffolds with both types of porosity have been developed using combinations of different techniques with macropores generated via foam reticulation and microporosity created through various routes, with Yang et al [355] incorporating freeze-gel casting, Mallick and Winnett [267,278], in work completed prior to this PhD, using freeze casting (AFR) and Lee et al [268] integrating solvent casting. In both cases, scaffolds consisted of microporous struts, with the size of the micropores approximately 2-10 μm. There are few reports investigating the influence of microporous struts on biological performance, although generating microporosity has been shown to have a more significant impact than including bone-specific growth factors [333, 341].

Controllability is important in functionally optimizing the scaffold. Both sets of techniques have some degree of controllability. This affects the scaffold in two main ways: the first is the production of suitable pore sizes. The porous network of ALM produced scaffolds is predetermined and CAD-CAM enables the desired structure to be easily realised with close control over the porosity, pore size and strut size [311, 312, 356]. The only limitation however is the resolution of the machinery, with most techniques unable to define features smaller than 10 μm and as such unable to introduce microporosity [311]. Although the orientation of pores is not controllable using most conventional techniques [310], the size and amount of porosity is. Secondly, tailoring of the external dimensions of the structure requires a high level of

Table 3.2: Ranking of the different techniques against key performance factors. ✓✓ denotes ranks best, ✓ denotes ranks good, ∘ denotes ranks average, ✗ denotes ranks poor, ✗✗ denotes ranks worst

Technique	Pore Size	Porosity	Compressive Strength	Biological Performance	Potential Materials	Control (pore size)	Repeatability	Cost	Adaptability
Dry Methods	n/a	n/a	✗✗	n/a	✓✓	✗✗	✗✗	✓✓	∘
Freeze casting	✗	✓	✓✓	✓	✓	✗	✗	✓	✓✓
Replication	✓	✓	✗	✓✓	✓	✓	✓	✓	✓✓
Gelcasting	✓	✓	✓✓	✓✓	∘	✗	∘	∘	✓
Sol-Gel	✓✓	✓	∘	✓	∘	✗	∘	∘	✗
Solvent Casting	✗	✓	✗	✓✓	✓	✗	✗	✓	✓
3DP	∘	✓	∘	✗	∘	✓	✓	✗✗	✗
SLS	∘	✓	✓✓	∘	∘	✓	✓	✗✗	✗
SLA	✓	✓	∘	∘	✗✗	✓	✓	✗✗	✗✗
Robocasting	✗	✓	✓✓	n/a	✗	✓	✓	✗✗	✗
Ink-Jet Printing	✗✗	✓	✗✗	n/a	✗	✓	✓	✗✗	✗
FDM	✗✗	✓	∘	✓	✗✗	✓	✓	✗✗	✗

control over the total structure. This can be readily achieved using ALM techniques, with Peltola et al [311] anticipating that patient specific scaffolds are possible using, for example, computed tomography (CT), magnetic resonance imaging (MRI) or X-ray scans. Achieving this with conventional techniques would involve the use of prefabricated moulds [310], which would involve an extra processing step.

Repeatability is the ability of a technique to consistently produce a similar structure. Due to the high level of controllability, this is readily achieved using ALM techniques [310–312]. Most conventional techniques only have control over the porosity and pore size whilst the location and orientation of the pores is more random [312], although if a suitable template is used, replication techniques are repeatable [65,267,277,347].

Cost must also be considered. ALM has a much higher initial cost which, despite having been been reduced recently, is still a limitation to these methodologies being commonplace [356–358]. As outlined in Section 3.1, many conventional techniques use sacrificial raw materials to generate porosity that cannot be reused, whilst some ALM based techniques use similarly sacrificial binders. Furthermore, after the machinery has been obtained, there are further costs associated with the labour required for the CAD design of the scaffold, with conventional techniques also involving highly skilled and experienced individuals. No evaluation of the individual scaffold cost has been undertaken, so it is not known which technique is more economically viable in the long term.

Finally, the adaptability of a technique to enable more functional optimization is important. Whilst ALM uses machinery that allows for some degree of variability [312, 356, 357], such as the materials that can be used and the pore structure, there are limitations to this. Conventional techniques have been varied to differ the pore size, pore orientation and porosity to generate more biologically and mechanically suitable scaffolds [267, 268, 355]. This is only possible using ALM techniques by producing moulds which are then used with conventional pore forming methods [359]. Furthermore, most relevant biomaterials can be utilised with many conventional techniques which is important for industrial applications; in contrast

Yeong et al [359] identify one of the challenges of ALM techniques being their limitation to specific material types.

3.3.1 Comparison of AFR to existing techniques

The main strength of AFR is the controllable production of micropores within the macroporous struts, which is expected to increase the biological activity of the sample by encouraging cells to adhere to the struts [2, 16] as was reported by Polak et al [341] who incorporated microporosity into robocast structures. It is also hypothesized that the mechanical properties could be increased by the inclusion of micropores, stopping the generation of microcracks during polymer burn out by providing routes for the template to be removed from within the scaffold [267]. However, this will be dependant on the size and amount of microporosity, as high levels of microporosity will be detrimental to the compressive strength by significantly increasing the overall porosity. The increase in the compressive strength of robocast scaffolds with microporosity, compared to those fabricated without, after implantation in pigs has been investigated by Woodard et al [333], who deduced this to be due to increased bone ingrowth, with similar effects expected with AFR produced scaffolds

There is significant control over the structure of the final construct. Not only is macroporosity controlled by template choice, but the microporosity is also controllable due to the incorporation of the freeze casting technique [256,257]. Furthermore the limitations of the freeze cast method associated with the maximum size of the construct and the small pore sizes [250, 253, 264] are overcome, as small micropores are desired and the thickness of the sample to be freeze cast is that of the coating on the strut.

For these reasons, it has been decided that enhancing the knowledge of this technique would be highly beneficial to the scientific community. To date, only HA [267, 278] and Bioglass ® [279] scaffolds have been produced, with some potential materials

summarized in Table 3.3. The range of freezing temperatures has been limited to room temperature and the porogen confined to camphene thus far [267, 278], although Yang et al [355] and Lee et al [268] have recently published similar work with tertiary-butyl alcohol (TBA) as the solvent.

As shown in Table 3.3, camphene has been used as the porogen in freeze cast structures from a variety of materials [49, 97, 106, 107, 117, 253, 254]. It is a bicyclic monoturpene that is insoluble in water, although soluble in a range of solvents including ether and alcohol [378]. One of the more interesting features is that it has a melting point of 51.5 °C [378]. Thus, it is highly useful in freeze casting: by heating the biomaterial containing slurry to approximately 60 °C the camphene is melted, and therefore freezes when cast at room temperature. The dendritic structure it produces during freezing has been well documented [97, 106, 107, 117, 254]. As such, this material allows for control over the microporosity which is a significant feature in terms of developing a method of controllably fabricating porous bioscaffolds.

3.4 Aims and Objectives

Optimized, multi-scale porosity is vital to enhancing the ability of cells to attach and grow on scaffolds [1, 6]. Not only does this enhance the bioactivity of scaffolds from bioactive materials [5], it also transforms bioinert materials into those that can initiate cell adhesion [5]. Although porous structures can be produced from any of a range of techniques, very few [267, 268, 278, 281, 333, 341] enable the realisation of structures with controllable macro and microporosity. It is expected that the biological activity of such structures with pore size optimization could facilitate significant advances in bone regenerative medicine.

Hence the aim of this PhD is to enhance the knowledge of the adaptive foam reticulation technique for producing bioscaffolds for bone tissue engineering applications. Varying the macroporosity to enable the optimization of the pore size with respect to

Table 3.3: Possible materials that could be used with the AFR technique, the porogens currently utilized with them when freeze cast and other manufacturing routes currently used to manufacture them into porous scaffolds.

Material	Foam Reticulation	Freeze Cast	AFR	Porogen	Other manufacturing routes	Ref.
Aluminium	Yes	n/a	n/a	n/a	Investment casting, foaming techniques, PM	[45–48, 360]
Titanium (and alloys)	Yes	Yes	n/a	Paraformaldehyde spheres, napthalene, camphene, salts, gaseous compounds	PM, sintering, rapid prototyping, investment casting, HIP, foaming techniques, gelcasting	[49–54, 67, 126, 128, 227–232, 252, 275, 361–367]
Tantalum	n/a	n/a	n/a	n/a	Deposition techniques, PM	[74–81]
Magnesium	n/a	n/a	n/a	n/a	PM, casting techniques	[84–88, 368]
Zirconium	Yes	Yes	n/a	Gaseous compounds, salts, methyl-cellulose	Foaming techniques, PM	[69, 71, 368]
Alumina	Yes	Yes	n/a	Camphene, sucrose, ethanol, gelatin, glycerol, sodium chloride	Gelcasting, rapid prototyping, electrospray	[96–98, 100, 102, 104–107, 109, 255, 281, 289, 369, 370]
Zirconia	Yes	Yes	n/a	Camphene, water, gaseous compounds	Colloidal processes, foaming techniques, HIP	[115–119, 251, 339, 371]
HA	Yes	Yes	Yes	Sucrose, gelatine, PMMA beads, camphene, napthalene	HIP, slip casting, gelcasting, sol-gel, rapid prototyping	[12,15,224,234, 235, 250, 253, 254, 260, 264, 268, 273, 274, 276, 277, 285, 318, 324, 333, 335, 355, 372]
TCP	Yes	Yes	n/a	Camphene, napthalene	Rapid prototyping	[223, 237, 266, 337, 373]
Other CaP	Yes	n/a	n/a	n/a	Rapid prototyping	[236, 288, 331, 332, 344, 373, 374]
Bioglass ®	Yes	Yes	Yes	Camphene, napthalene	Dry process with porogens, sol-gel, HIP	[253, 265, 303–305, 307, 320, 375–377]

the complete infiltration of cells throughout the structure whilst concurrently varying the microporosity to facilitate the achievement of optimally sized micropores facilitating cell attachment requires further investigation. Furthermore, a variety of currently used and potential biomaterials should be investigated to analyse the versatility of the technique, with the biological performance of fabricated scaffolds also requiring determination. Finally, although the long term (10+ years) performance cannot be evaluated in this thesis due to the time constraints of the PhD, these should be considered in ongoing and future research projects.

3.5 Summary

Porous scaffolds can be manufactured using a range of techniques, which can be broken down into conventional and ALM. Conventional techniques utilise the reaction of materials to different environments such as temperature and pressure to generate porosity, whilst ALM techniques involve the 'bottom-up' approach of arranging building units in a predetermined manner. Most conventional techniques involve mixing the biomaterial into a slurry. Porosity can then be incorporated using porogens which can also be frozen to increase the range of sizes. The slurry can be placed into moulds or coated onto templates to obtain different structures. ALM techniques are further broken down depending on the form with which the biomaterial takes during processing, such as colloidal, powder or liquid. There is a greater deal of control over the final structure of ALM fabrications due to the CAD-CAM procedure. The advantages and limitations of the techniques are discussed and as such the aim of the PhD is to enhance the knowledge of the AFR technique, a relatively new technique which has a wide scope for development.

Part II

Experimental

Chapter 4

Materials and Methodology

This chapter outlines the materials and methodologies used in this work to produce and characterise bioscaffolds. The theory behind the characterisation techniques is also detailed.

4.1 Scaffold Fabrication

The AFR technique is used to produce scaffolds in this work. As previously described in Section 3.1.5.1, this involves mixing the biomaterial into a slurry and coating it onto a template. This is then frozen, dried and subjected to a controlled heating protocol combining polymer pyrolysis and sintering of the construct. Each stage of the procedure is outlined in the following subsections.

4.1.1 Slurry Preparation

To enable the biomaterial to be coated onto the polymeric template, it needs to be mixed into a slightly viscous fluid or slurry. This is accomplished by combining the biomaterial with a binder, a dispersant and water, whilst a porogen is also included for AFR.

4.1.1.1 Hydroxyapatite

Slurries incorporating HA as the biomaterial consist of hydroxyapatite ($\geq$90%, Sigma Aldrich, UK), methylcellulose (average molecular weight 86000 g/mol, Sigma

Aldrich, UK) as the binder, Dolapix CE64 (average molecular weight 320 g/mol, Sigma Aldrich, UK) as the dispersant and water. As it is well documented as to how ice dendrites can be formed in a controllable manner, camphene (95%, Sigma Aldrich, UK) has been used as a porogen. Although solid at room temperature, it can be dissolved in dimethyl-carbonate (DMC) (≥99%, Sigma Aldrich, UK), with a minimum ratio of 40:60 camphene:DMC. Components of the slurries, given in Table 4.1, were ball milled (alumina balls, 3mm diameter, Fisher Scientific, UK) for 24 hrs to ensure homogenisation. The effect of camphene was evaluated by varying the camphene percentage.

Table 4.1: Slurry components (wt.%) for hydroxyapatite slurry. The column headers denote the ratio of camphene to hydroxyapatite

	Pure HA	5:95	10:90	20:80	25:75
HA	39	37	34	30	27
Camphene	0	2	4	8	10
DMC	0	3	6	12	20
Dolapix	2	2	2	2	2
Methylcellulose	1	1	1	1	1
Water	58	55	53	47	40

4.1.1.2 Titanium/Titanium-Aluminium-Vanadium

As above with HA-based slurries, Ti-based slurries use methylcellulose as the binder, Dolapix CE64 as the dispersant, water and camphene dissolved in DMC as the porogen. For Ti components, titanium hydride (TiH_2)(≥98%, Merck KGaA, UK) is used as the raw biomaterial as this can be handled with minimum risks to the user and when sintered to temperatures above 550 °C decomposes to Ti and H_2. Components of the slurries, given in Table 4.2, were ball milled for 24 hrs to ensure complete mixing. Ti-6Al-4V (≥98%, Phelly Materials U.S.A. Inc, USA) slurries were also produced, using the same conditions and proportions as for TiH_2. The Ti-6Al-4V powder was provided in three mesh sizes (500-,400- and 325- equating to average particle sizes of 15, 25, and 40 µm respectively), however only the 325-mesh fraction was used to produce scaffolds.

Table 4.2: Slurry components (wt.%) for titanium-based slurries. The column headers denote the ratio of camphene to TiH_2/Ti-6Al-4V

	Pure Ti or Ti-6Al-4V	5:95	10:90	20:80	25:75
TiH_2/Ti-6Al-4V	61	56	52	45	37
Camphene	0	3	6	11	12
DMC	0	4	9	16	27
Dolapix	2	2	2	1.5	1.5
Methylcellulose	1	1	1	0.5	0.5
Water	36	34	30	26	22

4.1.2 AFR

Two variations of the AFR technique were used in this work: conventional, and with freeze drying. These were standardised such that scaffolds can be manufactured from all biomaterials without varying the techniques.

4.1.2.1 Conventional AFR

The biomaterial slurry was prepared as above in Section 4.1.1. Polyurethane (PU) foam templates (Recticel, UK) of 15 mm diameter with 2 porosities (45 and 90 pores per inch (ppi)) were cut to 20 mm lengths and briefly immersed in the slurry before light manual squeezing to remove some of the excess. The template was then placed in an in-house manufactured Nylon sample holder designed to fit into the top opening of a Buchner flask and with a central, stepped hole that provides a location for the samples to sit on. This was placed in the top of a Buchner flask and light vacuum conditions (0.02 MPa) were generated to further remove the excess slurry. The equipment used is shown in Figure 4.1.

Impregnation was undertaken up to 5 times, with the slurry allowed to dry at room temperature (20 °C) for 30 mins between coatings. This allowed for partial drying such that upon manual squeezing of subsequent coats, as little of the previous

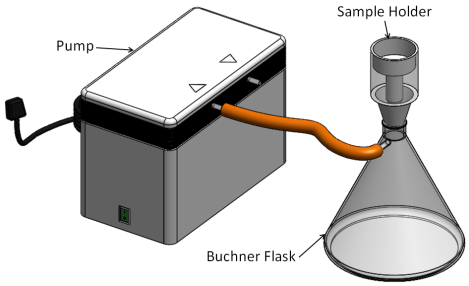

(a) CAD representation of the equipment used in the AFR technique

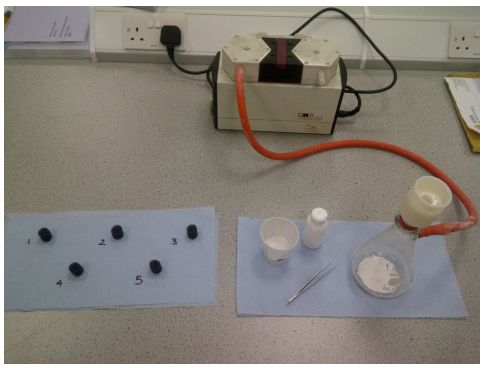

(b) Photograph of actual equipment used to produce scaffolds using AFR. The foam is dipped in the slurry, lightly squeezed by hand before being placed in the holder atop the buchner flask, where suction removes the remaining excess

Figure 4.1: The equipment used to produce bioscaffolds using AFR. The coated foam sits in the sample holder, which in turn sits in a Buchner flask connected to an air pump

coat was removed as possible. This was undertaken for all HA, Ti and Ti-6Al-4V slurries and for all sintering programmes, described below in Section 4.1.3, to enable the analysis of multiple variables: camphene percentage, sintering temperature and number of coats. Once all coats had been applied, the samples were allowed to completely dry at room temperature for 24 hrs before sintering.

4.1.2.2 AFR with Freeze Drying

The effect of the freeze drying temperature on micropore formation was investigated by coating the templates and placing them in a Labconco FreeZone 2.5 Liter Freeze Dry System (Labconco, USA) equipped with a Small Clear Drying Chamber. As with conventional AFR, the slurry was prepared and coated onto foam templates 20 mm in length using the equipment shown in Figure 4.1. Only 1 coating was used before freezing; once the excess slurry was removed, the samples were placed on the bottom shelf of the chamber or on the condensor and frozen for 4 hrs. To determine the final temperatures of the scaffolds after freezing, the temperature was measured

using k-type thermocouples (Omega Engineering Ltd., UK) attached to a datalogger (Model HH1384, Omega Engineering Ltd., UK). Once samples had been frozen, a controlled heating regime was implemented under pressure (0.133 mbar) to sublime the ice crystals. Conventional AFR incorporating camphene also provides a third freezing temperature as DMC evaporates at room temperature.

4.1.3 Sintering

To enable complete polymeric burnout, HA samples were heated at 0.5 °C/min to 500 °C. The green body was held at this temperature for 3 hrs before being heated at the same rate to the final sintering temperature. To determine the optimal final temperature, 50 °C intervals were chosen to which the samples were heated. Thus, maximum temperatures of 1100, 1150, 1200, 1250, 1300 and 1350 °C were used.

Sintering of TiH_2 must facilitate the decomposition of the hydride whilst ensuring that no oxide is produced. This is achieved by using a furnace through which inert gas has been flushed to remove as much of the natural atmosphere as possible. Flushing was carried out at room temperature for 30 mins prior to sintering and for the duration of the heating cycle using a 95:5 nitrogen:argon mix. TiH_2 decomposes above 600 °C [379, 380], hence the initial holding temperature was below this such that the Ti will not react with the polymer; for this work, this was 500 °C. Maximum temperatures for Ti sintering range from 1000 °C to 1300 °C [67,381], so 1000, 1100, 1200 and 1300 °C were used.

For Ti-6Al-4V samples, sintering must also be undertaken in an inert atmosphere to prevent the formation of any oxides (TiO_2, Al_2O_3 or vanadium oxide). The furnace and methodology used for TiH_2-slurry coated templates was used, although the final sintering temperatures differed. Briefly, the sample was heated to 500 °C to remove the foam before heating to final sintering temperatures of 1200, 1250 and 1300 °C, similar to that used by Li et al [275]. The sintering protocols for HA, TiH_2 and Ti-6Al-4V are given in Table 4.3.

Table 4.3: Sintering protocol for scaffolds produced from HA, Ti and Ti-6Al-4V

	HA	TiH_2	Ti-6Al-4V
Initial Heating Rate	0.5 °C/min	3 °C/min	3 °C/min
Holding time (at 500 °C)	3 hours	3 hours	3 hours
Secondary heating rate	0.5 °C/min	3 °C/min	3 °C/min
Holding time (at final sintering temperature)	3 hours	3 hours	3 hours
Cooling rate	1 °C/min	3 °C/min	3 °C/min

4.1.4 Summary of Processed Samples

A complete list of samples generated for this work is given in Tables 4.4, 4.5 and 4.6 for HA, Ti and Ti-6Al-4V respectively. Samples are labelled depending on the processing parameters used during fabrication: construct material (hydroxyapatite (HA), titanium (Ti) or Ti-6Al-4V (T64) is followed by the sintering temperature, which is followed by the number of coats, which is followed by the porogen content where included. The labels of structures frozen during production consist of: construct material, followed by position of sample within freeze drier (FCS as freeze cast on shelf; FCC as freeze cast on condenser) followed by porogen content where included. All samples were fabricated from both the 45 and 90 ppi templates.

4.2 Scaffold Characterisation

The methodology of the techniques used to analyse the precursor materials and bioscaffolds is given in this section, along with a brief theoretical review. As they enable a thorough examination of the precursor materials and final scaffolds and are standard for the field of scaffold manufacture, these are X-ray diffraction for chemical and crystallographic determination, simultaneous thermal analysis for investigating high temperature behaviour, scanning electron microscopy and micro-computed tomography for structural analyses, porosimetry for porosity measurements, com-

Table 4.4: Complete list of samples generated from HA using AFR technique. Label constructed as: material followed by sintering temperature followed by number of coats followed by porogen content where included. Structures frozen during production are labeled as: material followed by freeze cast on shelf (FCS) or on condenser (FCC) followed by porogen content where included.

		Number of Coats				
		1	2	3	4	5
Porogen Content (%)	0	HA11001c HA11501c HA12001c HA12501c HA13001c HA13501c HAFCS HAFCC	HA11002c HA11502c HA12002c HA12502c HA13002c HA13502c	HA11003c HA11503c HA12003c HA12503c HA13003c HA13503c	HA11004c HA11504c HA12004c HA12504c HA13004c HA13504c	HA11005c HA11505c HA12005c HA12505c HA13005c HA13505c
	5	HA12501c5 HA13001c5 HA13501c5 HAFCS5 HAFCC5	HA12502c5 HA13002c5 HA13502c5	HA12503c5 HA13003c5 HA13503c5	HA12504c5 HA13004c5 HA13504c5	HA12505c5 HA13005c5 HA13505c5
	10	HA12501c10 HA13001c10 HA13501c10 HAFCS10 HAFCC10	HA12502c10 HA13002c10 HA13502c10	HA12503c10 HA13003c10 HA13503c10	HA12504c10 HA13004c10 HA13504c10	HA12505c10 HA13005c10 HA13505c10
	20	HA12501c20 HA13001c20 HA13501c20 HAFCS20 HAFCC20	HA12502c20 HA13002c20 HA13502c20	HA12503c20 HA13003c20 HA13503c20	HA12504c20 HA13004c20 HA13504c20	HA12505c20 HA13005c20 HA13505c20
	25	HA12501c25 HA13001c25 HA13501c25 HAFCS25 HAFCC25	HA12502c25 HA13002c25 HA13502c25	HA12503c25 HA13003c25 HA13503c25	HA12504c25 HA13004c25 HA13504c25	HA12505c25 HA13005c25 HA13505c25

Table 4.5: Complete list of samples generated from Ti using AFR technique. Label constructed as: material followed by sintering temperature followed by number of coats followed by porogen content where included.

		Number of Coats				
		1	2	3	4	5
Porogen Content (%)	0	Ti10001c Ti11001c Ti12001c Ti13001c	Ti10002c Ti11002c Ti12002c Ti13002c	Ti10003c Ti11003c Ti12003c Ti13003c	Ti10004c Ti11004c Ti12004c Ti13004c	Ti10005c Ti11005c Ti12005c Ti13005c
	5	Ti10001c5 Ti11001c5 Ti12001c5 Ti13001c5	Ti10002c5 Ti11002c5 Ti12002c5 Ti13002c5	Ti10003c5 Ti11003c5 Ti12003c5 Ti13003c5	Ti10004c5 Ti11004c5 Ti12004c5 Ti13004c5	Ti10005c5 Ti11005c5 Ti12005c5 Ti13005c5
	10	Ti10001c10 Ti11001c10 Ti12001c10 Ti13001c10	Ti10002c10 Ti11002c10 Ti12002c10 Ti13002c10	Ti10003c10 Ti11003c10 Ti12003c10 Ti13003c10	Ti10004c10 Ti11004c10 Ti12004c10 Ti13004c10	Ti10005c10 Ti11005c10 Ti12005c10 Ti13005c10
	20	Ti10001c20 Ti11001c20 Ti12001c20 Ti13001c20	Ti10002c20 Ti11002c20 Ti12002c20 Ti13002c20	Ti10003c20 Ti11003c20 Ti12003c20 Ti13003c20	Ti10004c20 Ti11004c20 Ti12004c20 Ti13004c20	Ti10005c20 Ti11005c20 Ti12005c20 Ti13005c20
	25	Ti10001c25 Ti11001c25 Ti12001c25 Ti13001c25	Ti10002c25 Ti11002c25 Ti12002c25 Ti13002c25	Ti10003c25 Ti11003c25 Ti12003c25 Ti13003c25	Ti10004c25 Ti11004c25 Ti12004c25 Ti13004c25	Ti10005c25 Ti11005c25 Ti12005c25 Ti13005c25

Table 4.6: Complete list of samples generated from Ti-6Al-4V using AFR technique. Label constructed as: material followed by sintering temperature followed by number of coats followed by porogen content where included.

		Number of Coats				
		1	2	3	4	5
Porogen Content (%)	0	T6412001c T6412501c T6413001c	T6412002c T6412502c T6413002c	T6412003c T6412503c T6413003c	T6412004c T6412504c T6413004c	T6412005c T6412505c T6413005c
	5	T6412001c5 T6412501c5 T6413001c5	T6412002c5 T6412502c5 T6413002c5	T6412003c5 T6412503c5 T6413003c5	T6412004c5 T6412504c5 T6413004c5	T6412005c5 T6412505c5 T6413005c5
	10	T6412001c10 T6412501c10 T6413001c10	T6412002c10 T6412502c10 T6413002c10	T6412003c10 T6412503c10 T6413003c10	T6412004c10 T6412504c10 T6413004c10	T6412005c10 T6412505c10 T6413005c10
	20	T6412001c20 T6412501c20 T6413001c20	T6412002c20 T6412502c20 T6413002c20	T6412003c20 T6412503c20 T6413003c20	T6412004c20 T6412504c20 T6413004c20	T6412005c20 T6412505c20 T6413005c20
	25	T6412001c25 T6412501c25 T6413001c25	T6412002c25 T6412502c25 T6413002c25	T6412003c25 T6412503c25 T6413003c25	T6412004c25 T6412504c25 T6413004c25	T6412005c25 T6412505c25 T6413005c25

pression testing for analysis against cancellous and cortical bone compressive yield stresses, and *in-vitro* cell viability for biological behaviour of the scaffolds.

4.2.1 Diffraction

4.2.1.1 X-Ray Diffraction

X-ray diffraction (XRD) is used to establish the chemical and crystallographic composition and yield information about the structure of a material [382–384]. Any 3D, non-amorphous material is made of regular, repeating planes of atoms that form a crystal lattice. X-rays are diffracted by a sample of the material [382] according to Bragg's Law:

$$2dsin\theta = n\lambda \tag{4.1}$$

where d is the atomic spacing, θ is the angle of incidence, n is a whole integer representing the order of the number of planes of atoms, and λ is the wavelength.

For most angles the superposition of waves reflected from neighboring planes causes near annihilation. However, at some angles the amplitudes superimpose, with a maximum intensity when the phase difference is zero, which occurs at a certain angle, the Bragg angle [383, 384]. This can be compared to standard graphs (such as Joint Committee on Powder Diffraction Standards (JCPDS) Powder Diffraction Files) for each constituent phase to evaluate the composition of the material.

Powder diffraction, with the method of Debye and Scherrer the most popular, is used in this work. Further information on the technique can be found in Cullity and Stock [383]. Briefly, a beam of monochromatic X-rays, with a fixed value of λ, is generated and ϑ varied. Finer powders produce smoother, more continuous lines and are therefore preferable, hence samples are usually ground prior to analysis [383].

4.2.1.2 Laser Diffraction

Laser diffraction uses the diffraction of light to determine the size of particles. A laser beam is collimated and passed through the sample cell, containing a movind suspension. The diffracted light is focused to the detector and the angular distribution, I(ϑ) given by:

$$I(\theta) = \frac{1}{\theta^2} \int_0^\infty R^2 n(r) J_i^2(\theta k R) dR \tag{4.2}$$

where ϑ is the scattering angle, R is the particle radius, m(R) is the size distribution function, $k = \frac{2\pi}{\lambda}$ and J is the Bessel function of the first kind [385].

The suspension fluid is generally filtered water, which must be degassed of dissolved air. Generally, between 0.1 and 2 g of sample is reqired, which is dissolved in approximately 10ml of deionized water. Results are reproducible, and if correctly calibrated, highly accurate [385–387].

4.2.1.3 Methodology

Phase analysis of the precursor biomaterial powders and powdered scaffolds treated at various sintering temperatures were analysed using powder XRD with an incident angle of 2ϑ = 5-90 °, with a step size of 0.02 ° and a step duration of 0.5 s on a Fe-filtered diffractometer (Model Empryean, PANalytical, UK). Sample preparation involved grinding with a mortar and pestle, placing in a holder, pressing slightly and leveling off in line with the uppermost surface of the holder. To ensure the diffractometer was correctly calibrated, silicon (99%, Sigma Aldrich, UK) was added (10 wt.%) to selected samples. For all scans, Cobalt $K\alpha$ radiation was used and peak analysis was conducted using HighScore (PANalytical, UK), preloaded with standard Crystallography Open Database (COD) diffraction files.

For analysis, the area of the peak is considered, which is fitted in HighScore using the Pseudo-Voigt function [388–390]:

$$G_{jk} = \gamma \frac{C_0^{1/2}}{H_k \pi} [1 + C_0 x_{jk}^2]^{-1} + (1 - \gamma) \frac{C_1^{1/2}}{H_k \pi^{1/2}} exp[-C_1 x_{jk}^2] \tag{4.3}$$

where C_0 and C_1 are constants, of 4 and 4ln2 respectively, γ is a refinable 'mixing' parameter, $x_{jk} = (2\theta_j - 2\theta_k)/H_k$, and H_k is the full-width at half-maximum (FWHM) which is defined from the function using using:

$$H_k = (A \tan^2 \theta + B \tan \theta + C)^{1/2} \tag{4.4}$$

where A, B, and C are refinable variables.

Furthermore, for semi-quantitative analysis of the estimated mass fractions of identified phases, the inbuilt function of HighScore is used, which is based on the reference intensity ratio (RIR) [388–390]. The concentration, X, of phase a is calculated using:

$$X_a = \frac{I_{(hkl)a}}{RIR_a I^{rel}_{(hkl)a}} \left[\frac{1}{\sum_{j=1}^{n} (I_{(hkl)'j} / RIR_j I^{rel}_{(hkl'j)})} \right] \tag{4.5}$$

where I^{rel} is the net peak of the strongest line of the phase.

Particle size analysis was carried out using a LS 13 320 Particle Size Analyzer (Beckman Coulter, UK) equipped with a Universal Liquid Module. Briefly, powdered biomaterials were placed in suspension with water and added dropwise to the diffractometer. Once an appropriate amount was added, the diffractometer ran a set programme to analyse the particle size.

4.2.2 Simultaneous Thermal Analysis

4.2.2.1 Theory

Thermogravimetric analysis (TGA) measures the change in mass of a substance as it undergoes a predetermined temperature program using an electronic microbalance, enabling the active and stable components to be determined, as well as the decompositional, oxidation and dehydration behaviour. [391–393].

Differential thermal analysis (DTA) measures the change to the heat flow rate of the sample compared to a reference material whilst both follow a predetermined temperature program to determine whether materials undergo endothermic dehydration (when the sample exhibits an isothermal change as the reference temperature increases) or exothermic reactions (when the sample temperature changes during isothermal changes to the reference) [392, 394–398].

Simultaneous thermal analysis (STA) undertakes both DTA and TG simultaneously to obtain a complete mass spectrum of the sample. Running both techniques concurrently also allows for the more rapid generation of results whilst using less of the

material. Furthermore, as only one thermocouple is required, the accuracy of the result is increased [399].

4.2.2.2 Methodology

The isothermal behaviour, thermal stability and composition of the precursor HA, Ti and Ti-6Al-4V slurries, and the pyrolysis behaviour of the polyurethane foam was studied using simultaneous differential thermal analysis and thermogravimetric analysis using an STA1500 (TA Instruments, UK). 20mg of sample was placed in a precalibrated platinum pan and heated up to 1400 °C (HA, Ti, Ti-6Al-4V) or 500 °C (PU foam) at a ramp rate of 10 °C/min in flowing air (HA, PU foam) or nitrogen (Ti, Ti-6Al-4V).

4.2.3 Scanning Electron Microscopy

4.2.3.1 Theory

Scanning electron microscopy (SEM) permits the observation and characterisation of organic and inorganic materials on a micro to nanometer scale, thus allowing the surface properties of many materials to be analysed. The limits of magnification enable both the macro and microscopic features of bioscaffolds to be viewed [400, 401], with a good depth of focus and reasonable resolution [400]. To avoid charging of non-conducting surfaces, sample preparation usually requires gold or carbon coating of the sample [384, 400].

During SEM using the instrument available for this work, the samples must be held under a vacuum to ensure no air particles are present that may obstruct the electrons. This is also true for many other systems and thus a large portion of research has been given to the development of suitable vacuum systems [384]. A computer controls the microscope with six main categories of usage: instrument

control, instruction, data acquisition, data storage, data processing and image quantification [384, 400, 401]. Further information on SEM can be found in Wells [401] or Hearle, Sparrow and Cross [400].

4.2.3.2 Methodology

Samples were attached to SEM stubs using Acheson Silver DAG 1415M (AgarScientific, UK). Briefly, some DAG was applied onto the stub and the sample placed onto this, where the DAG acted as an adhesive as it dried. Some extra silver DAG was added to the sides of the sample to aid electron conduction away from the top surface. The samples then underwent gold coating using an automatic sputter coater (Agar Auto Sputter Coater, AgarScientific, UK).

SEM was undertaken on a Zeiss Sigma Aldrich E-SEM (Zeiss, Germany). Standard magnifications were used such that consistency was achieved and for suitable comparison of samples. For secondary electron micrographs, standard conditions were used, with details of the voltage, working distance and magnification used provided in figures in Part III. The software used to control the SEM, SmartSEM (Zeiss, Germany), enables the real time measurement of points within the image and as such was used to measure the particle sizes of raw materials and the pore and strut sizes of scaffolds. Average particle sizes were obtained by averaging the length and width of individual particles. This was confirmed using particle size analysis, detailed above in Section 4.2.1.2. Where possible, 10 measurements of each pore and strut size were taken from a variety of locations across the scaffold surface. The pore dimension was calculated by determining the equivalent circle diameter, whilst strut sizes were measured at the central point of the strut.

4.2.4 Micro-Computed Tomography

Micro-computed tomography (micro-CT) is a non destructive technique that provides 3D images of an object. Micro-CT is a high resolution adaptation of computed

tomography, which is based on the interaction of ionizing radiation, such as X-ray or synchrotron, with matter. As an X-ray beam penetrates an object, it is exponentially attenuated according to the material. Thus, an X-ray image is a representation of the sum of all the local attenuations along the beam, with 3D images being the collation of a set of 2-dimensional (2D) projections [402–405].

Micro-CT images are usually obtained using a fixed source and detector, whilst the object is rotated, as shown in Figure 4.2. The source can be a microfocus X-ray tube or the insertion device of a synchrotron radiation facility; the detector is usually based on a charge-coupled device (CCD) camera. The beam is collimated and filtered to narrow the energy spectrum before it is passed through the sample [402, 404].

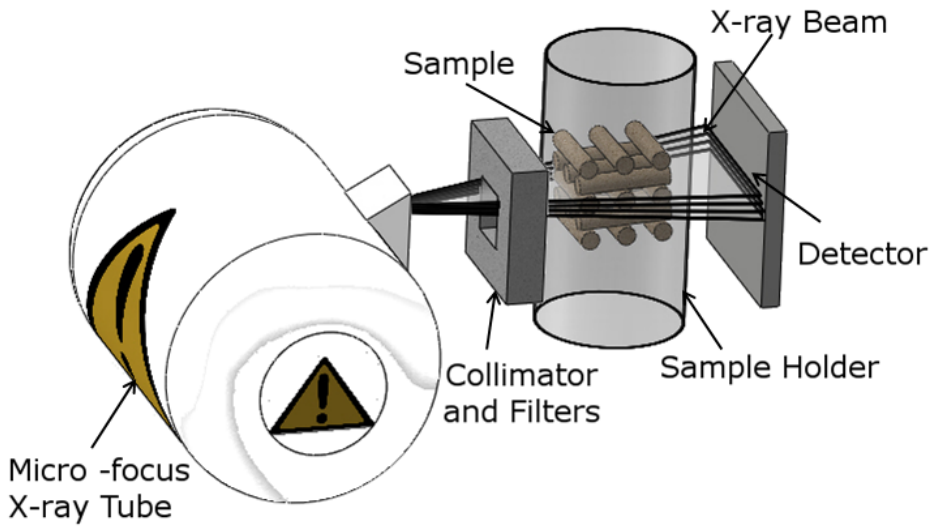

Figure 4.2: Main components of a micro-CT scanner. The tube and detector are fixed in this case, whilst the sample is rotated.

High resolution is achieved via cone beams, optical magnification or Bragg diffraction [404]. The projections are recorded as discrete points in 2D images which are reconstructed to produce a 3D image [402–405]. Post processing software allows for the determination of a variety of features of the sample, including porosity, surface area and pore size [403–405].

4.2.4.1 Methodology

MicroCT scanning was undertaken using a Zeiss Xradia 520Versa (Zeiss, Germany) equipped with an X-ray sealed source (40kV, 3W), a CCD detector, quartz filter and lens optic magnification, which enables scans with resolution of between 50 nm and 25 μm depending on the conditions used. For low resolution scans (resolution = 5 μm), 0.4x optical magnification was used; for high resolution scans (resolution = 0.8 μm), 4x optical magnification was used. The low resolution scans were obtained using 3201 projections with an exposure time of 15 s. The high resolution scans were internal scans, where different sections of the scaffold came in and out of view during rotation. Hence a higher number of projections (4500) was used with an increased exposure time of 38 s.

Analysis was undertaken using Avizo 8.1 (Visualizations Sciences Group, FEI, USA). To determine the parts of the greyscale image that were material, the Iso-50% value was used. This is obtained by attributing a numerical value (between 0 and 65536) and plotting all values as a histogram, with the Iso-50% the number halfway between the peaks for background noise and material (for one material). Furthermore, only connected components were incorporated to remove any noise.

The low resolution scans were treated as having no microporosity. Hence, for each orthoslice the material was selected and a `fill holes´ treatment applied to make all the struts solid. Hence, the strut volume was determined which was inverted to determine the porosity. Segmenting was undertaken using a `separate objects´ treatment, which uses Voroni volumes to identify individual components.

High resolutions scans were subjected to similar treatments, however before the `fill holes´ treatment, the orthoslices underwent `closing´ to close off strut pores. The holes were filled and the new image compared to the original orthoslice. An exclusive or (XOR) treatment then allowed for the selective segmenting of strut pores and thus determination of the strut volume. Inverting this enabled the calculation of the pore volume.

4.2.5 Porosimetry

Porosimetry is the measurement of the amount of porosity of a structure. This can be undertaken using the Archimedes' method, gas adsorption pyconometry or mercury porosimetry. Due to the expected size and nature of the porosity that will be present in AFR fabricated scaffolds and as other non-porosimetric techniques can be used to estimate the pore size, it is only suitable to use the Archimedes' method in this work.

4.2.5.1 Archimedes' Principle

Archimedes' principle states that a structure that is partially or completely submerged in a fluid, which can be gaseous or liquid, will, whilst at rest, be acted upon by a buoyant force. In turn, this force equates to the weight of the fluid displaced by the volume of the object that is submerged below the surface of the liquid [406]. It is a well-known technique and has been used to calculate bone density [407–409] cementing the importance it has in tissue engineering. Although water is the standard material, any liquid can be used and the presence of mesopores (2-50 nm) led to other substances being preferable and the development of pyconometry [410]. It is only capable of determining the overall porosity of the structure and cannot determine exact pore sizes or their distribution. To enable calculation of the porosity, P_o, the density of a sample, $\rho_{scaffold}$, must first be measured using:

$$\rho_{scaffold} = \rho_{water} \cdot \frac{W_d}{W_w - W_{su}} \tag{4.6}$$

where ρ_{water} is the absolute density of water, and W_d, W_w and W_{su} are the dry, wet and submerged masses of the scaffold respectively. The temperature of the water in which the sample is submerged should also be measured so that any variances could be accounted for with respect to the absolute density of water [406, 408, 409]. Thus, porosity is calculated using:

$$P_o = 1 - \frac{\rho_{scaffold}}{\rho_{solid}} \tag{4.7}$$

where ρ_{solid} is the bulk density of the material [406–409].

4.2.5.2 Methodology

Bulk density and porosity of the scaffolds was determined using the Archimedes method on a Mettler Toledo MS204 balance equipped with MS-DNY-4 density kit (Mettler Toledo, UK). The dry, wet and submerged masses of the scaffolds were measured, whilst recordings of the water temperature were also made between each reading. These values were then used with Equation 4.6 to obtain the density of the scaffold, which was used in Equation 4.7 to obtain the scaffold porosity. The bulk densities of HA, Ti and Ti-6Al-4V used were 3156 [44], 4507 [411] and 4428 [411] $^{kg}/_{m^3}$ respectively.

4.2.6 Compression Testing

The strength of a material under compression is usually given as either the yield stress or the Young's modulus. It is readily possible to test a sample and obtain the force required to cause failure [269, 271, 272, 277, 337, 412]. Knowledge of the dimensions of the sample allows for the yield stress to be calculated using:

$$\sigma = \frac{F}{A} \tag{4.8}$$

where σ is the yield stress, F is the applied force at failure and A is the cross-sectional area of the sample being tested. The Young's modulus, E, is calculated using:

$$E = \frac{\sigma}{\varepsilon} = \frac{^F/_A}{^{\Delta L}/_L} \tag{4.9}$$

where ε is the strain of the material, which is calculated by dividing the change in length of a sample, ΔL, by the original length L.

Experimental evaluation requires destructive testing of the sample, which can be expensive depending on the cost and time required to produce and test the structures. Thus determination of the yield stress using non-destructive methods is important. This can be undertaken using FEA of CT scans of the final structure [413–417], FEA of the model used to fabricate ALM produced structures [418–420], or theoretical calculations based on the porosity, pore size and strut size of the scaffolds [421,422]. Due to the expected presence of microporosity, microCT scanning of the samples would be necessary and as some of the finer features can be beyond the maximum resolution [270,274], FEA may not yield representative values.

The theoretical yield stress of a cellular solid under compression can be calculated using the following equation:

$$\frac{\sigma_{theo}}{\sigma} = 0.2 \cdot (\frac{\rho_{scaffold}}{\rho_{solid}})^3 \frac{1 + (t_p/t_s)^{\frac{3}{2}}}{\sqrt{1 - (t_p/t_s)^{\frac{3}{2}}}} \tag{4.10}$$

where σ_{theo} is the theoretical compressive strength, $\rho_{scaffold}/\rho_{solid}$ is the relative density, t_p/t_s is the ratio of the pore to strut size and σ the yield stress of the bulk material [421,423]. One major assumption with this however is that the structure is stress and defect free prior to testing and as such does not allow for microporosity. The strength of macroporous structures with microporosity has not been previously evaluated, however the incorporation of a shape factor, μ_0, into Equation 4.10 that allows for such microstructure is expected to provide a suitable estimate. This is calculated using the following equation:

$$\mu_0 = \frac{\frac{\pi}{4}(1 - \frac{t_m}{t_p})^3}{1 - \frac{\pi}{4}(1 - \frac{t_m}{t_p})^3} \tag{4.11}$$

where t_m/t_p is the ratio of micropore to macropore size [424,425].

4.2.6.1 Methodology

Compression tests were performed on cylindrical samples of 15 mm height with 10 mm diameter. To ensure that the surfaces were parallel, the scaffolds were cast in machining wax, the structure cut to size and the wax removed using a low heat (100 °C). The final height and diameter of the samples was measured using callipers prior to testing. As the yield stress of the structure as a whole is of importance, no allowance was made for the porous nature of the surface in contact with the test rig.

The structures were loaded into a custom, in-house manufactured stainless steel holder, designed to keep the scaffold in place during the test, on an Instron 5800R machine (Instron, UK) equipped with a 1 kN load cell. In agreement with the literature REFS, testing (n=5) was undertaken with a cross head speed of 2 mm/min on HA scaffolds produced from both templates with 5 coats and sintered to 1350 °C, with two different porogen contents (0 and 25 %) analysed. The results were then correlated with the theoretical values calculated using Equation 4.10 to determine the efficacy of using a non-destructive technique to analyse the compressive strength of these scaffolds. For theoretical calculations, the yield stress of bulk HA, Ti and Ti-6Al-4V was taken as 1.12 times the tensile strengths [426] of 40 [44], 328 [411] and 795 [411] MPa respectively.

4.2.7 Error Calculation

Due to the relatively low number of samples (n=10 for pore/strut size measurements, n=3 for porosity measurements), it was not appropriate to approximate the error using the standard deviation of the measurements alone. Instead, it is more applicable to calculate the standard error of the mean. For a set of n samples, $x = x_1,\ x_2,\ ...\ x_n$, the mean value, $\bar{x}$ can be calculated using:

$$\bar{x} = \frac{1}{n} \sum x_n \tag{4.12}$$

Furthermore, the standard deviation can be calculated using the sum of all the errors squared. Theoretically, this involves subtracting the values from the true value, X, however this is not known and as such it is appropriate to use the mean value as a close approximation. Thus, the difference between the measured value and the mean value is calculated:

$$d_i = x_i - \bar{x} \tag{4.13}$$

from which the standard deviation, SD, is calculated:

$$SD^2 = \frac{1}{n} \sum d_i^2 \tag{4.14}$$

The standard error, σ_e, is then calculated using:

$$\sigma_e = \left(\frac{n}{n-1} \right)^{1/2} SD \tag{4.15}$$

which enables the standard error of the mean, σ_{er}, to be calculated:

$$\sigma_{er} = \frac{\sigma_e}{\sqrt{n}} \tag{4.16}$$

Calculations of the compressive strength involve multiplication, division and power raising of variables with errors in them. The variables have been calculated independantly, and as such the errors within each need to be treated as independant errors. For calculation of a final quantity, Z, using independant variables, A, B, C, ..., the error within Z, ΔZ, can be calculated depending on the relationships between the variables:

$$\left.\begin{array}{l} Z = AB \\ Z = A/B \end{array}\right\} \qquad \left(\frac{\Delta Z}{Z} \right)^2 = \left(\frac{\Delta A}{A} \right)^2 + \left(\frac{\Delta B}{B} \right)^2 \tag{4.17}$$

$$Z = A^n\} \qquad \frac{\Delta Z}{Z} = n\frac{\Delta A}{A} \tag{4.18}$$

where ΔA and ΔB are the standard errors of the mean of A and B respectively [427].

4.2.7.1 Methodology

For pore and strut size measurements as well as for porosity calculations, the mean and standard error of the mean is calculated using Equations 4.12 and 4.16 respectively. For the compressive yield stress, the maximum values were calculated using the maximum strut size with the minimum porosity and pore size; the minimum with minimum strut sizes and maximum porosity and strut sizes; and the average using the average of each. Thus, Equation 4.12 was used to calculate the mean from these three values. Calculation of the error however involves breaking Equation 4.10 into respective parts to incorporate the error within each variable. If the porosity is denoted as A, the pore size as B and the strut size as C, ignoring all constants and assuming the micropore size remains constant within each sample, then the compressive yield stress, denoted by Z, can be expressed in terms of variables as:

$$Z = A^3 \cdot \frac{B^{-3}}{B^{-3}} \cdot \frac{\left(B/C\right)^{3/2}}{\left[\left(B/C\right)^{3/2}\right]^{1/2}} \tag{4.19}$$

Thus the error can be calculated using:

$$\begin{aligned}\left(\frac{\Delta Z}{Z}\right)^2 &= \left(3\frac{\Delta A}{A}\right)^2 + \left[\left(-3\frac{\Delta B}{B}\right)^2 + \left(-3\frac{\Delta B}{B}\right)^2\right] + \left[\left(\frac{3}{2}\left[\left(\frac{\Delta B}{B}\right)^2 + \left(\frac{\Delta C}{C}\right)^2\right]\right) + \right. \\ &\left. \left(\frac{3}{4}\left[\left(\frac{\Delta B}{B}\right)^2 + \left(\frac{\Delta C}{C}\right)^2\right]\right)\right]\end{aligned} \tag{4.20}$$

4.2.8 Graphical Representations

For comparison of data between samples produced using different processing parameters, it is sometimes more appropriate to use graphical representation as opposed to tables of data. This is particularly the case where there are trends within the data. In such cases, the data is plotted as a scatter graph, with lines of best fit included to show the trends between the data.

4.2.8.1 Line of Best Fit

If it can be assumed that one quantity, y, is a function of another, x, then

$$y = mx + c \tag{4.21}$$

The calculation of the slope of the line and the constant can be calculated using the method of least squares. For a set of n measurements, $(x_1, y_1), (x_2, y_2), \ldots (x_n, y_n)$, the deviation of the ith reading is

$$y_i - mx_i - c \tag{4.22}$$

The best values for m and c are thus obtained by calculating the minimum value of

$$\mathbf{S} = \sum (y_i - mx_i - c)^2 \tag{4.23}$$

From this, it is possible to generate a set of simultaneous equations which solve to show the line must pass through the point:

$$\bar{x} = \frac{1}{n} \sum x_i \qquad \bar{y} = \frac{1}{n} \sum y_i \tag{4.24}$$

and that

$$m = \frac{\sum(x_i - \bar{x})y_i}{\sum(x_i - \bar{x})^2} \tag{4.25}$$

$$c = \bar{y} = m\bar{x} \tag{4.26}$$

Thus, the line of best fit can be plotted [427].

4.2.8.2 Methodology

Analysis was undertaken using Microsoft Excel 2010 (Microsoft, USA) with graphs produced using OriginPro 8.5 (OriginLab Corporation, USA). The mean and standard error of the mean for each dataset was calculated using Equations 4.12 and 4.16. Scatter graphs were plotted using the calculated values and lines of best fit calculated using the inbuilt function of OriginPro 8.5, which works in accordance with theory outlined in Section 4.2.8.1. Graphs of data from scaffolds from the same template and material are plotted on similar y-axis scales to observe the effects due to varying specific parameters. It should be noted that, due to the samples being coated multiple times prior to sintering, each dataset was taken from different samples, i.e. the pore and strut sizes of the sample produced with one coat was obtained using one sample and the pore and strut sizes of the sample produced with two coats from another, etc.. As such the line of best fit is used as a visual aid to show relative trends and is not a direct correlation between variables.

4.2.9 Biological Testing

The biological suitability of a bioscaffold must be tested as part of FDA guidelines and as a measure against other similar products. There are two main test areas:

in-vivo and *in-vitro*. *In-vitro* tests are used as initial testing protocols that assess the inherent nature of scaffolds to facilitate cell growth by testing the response of cells when outside of their normal biological environment. Nevertheless, a scaffold that seems suitable after such tests must still undergo a rigorous *in-vivo* procedure to test the cell response within a normal biological environment by implantation in a suitable host, such as mice or rabbits. As *in-vivo* testing will not be carried out within this work, it will not be discussed here.

4.2.9.1 Cell Viability

Cells can be seeded onto scaffolds and their viability with time analysed. The appropriate cells are isolated and placed into a suspension which is seeded onto the scaffold. A wide range of cells are suitable for use in bone scaffold analyses, with human osteoblasts, human embryonic mesenchymal cells, and pre-fibroblastic or pre-osteoblastic cells the most popular. Measurements of the performance are then taken according to a predetermined timescale.

There are many measures of cell viability used to analyse the cytotoxicity, cell viability, attachment and proliferation characteristics, and protein expression of seeded cells, with the most appropriate for bone scaffold analyses outlined below. Once completed, statistical analysis of variance (ANOVA), outlined in Section 4.2.9.4, of the results is undertaken with student's T-test, Tukey's Pairwise correlation or Kolmogorov-Smirnov being the more commonly used methods.

Tetrazolium Salt Assays There are two types of tetrazolium salt assays commonly used: MTT and MTS assays. The 3-(4,5-dimethylthiazol-2-yl)-2,5-diphenyl tetrazolium bromide (MTT) assay is a live/dead test used to determine the cytotoxicity of scaffolds immersed in SBF or seeded with cells. In the presence of live cells, the yellow solution turns blue/purple due to the mitochondria of metabolically active cells secreting dehydrogenase enzymes that cleave the tetrazolium ring and

convert the MTT to a formazan. As the intensity of the colour is directly related to the number of live cells, it is measured spectrophotometrically using a spectrophotometer [428]. It has been tested on a variety of cell types and provides rapid, precise results without the need for radioisotopes which were previously used [428–432].

The main limitation with MTT assays is that the formazan solution must be dissolved in isopropanol for spectroscopy. This halts any further readings being taken and thus the time frame for reduction must be carefully predetermined. This led to two other tetrazolium salt reduction assays being developed: 2,3-bis(2-methoxy-4-nitro-5-sulfophenyl)-5-[(phenlyamino)carbonyl]-2H-tetrazolium hydroxide (XTT) and 3-(4,5-dimethylthiazol-2-yl)-5-(3-carboxymethoxyphenyl)-2-(4-sulfophenyl)-2H-tetrazolium, inert salt (MTS). Compared to MTS, XTT is limited by the instability of the reagent and the speed of formazan production [433] and so is not discussed further.

The MTS assay is based on the reduction of a tetrazolium salt to a formazan. Specimens are placed in a medium containing the assay and an intermediate electron acceptor, such as phenazine methosulphate (PMS). As with MTT, the coloured formazan is proportional to the number of living cells; however the MTS formazan is water soluble [433–435]. Problems have been observed with the evaporation of the solution, yet this can be overcome through variations to the set-up time or time of introduction of the assay [436].

Although the MTS assay can be used over the duration of a study, the MTT assay is more commonly used as it is easier to perform and considerably (up to 50 times) cheaper than either the XTT or MTS assays [437].

alamarBlue Assay The alamarBlue assay is a non-destructive test used to assess the cytotoxicity of a sample. Upon introduction of the assay to live cells, the dye undergoes a reaction to resorufin. This is correlated to the number of viable cells using an oxidation-reduction indicator. The reduction of the dye causes a colour

change from a non-fluorescent blue to a fluorescent red, therefore spectophotometric or fluorescence readings of the colour are taken at various time intervals [438–442].

As with MTS, the product is water soluble allowing daily monitoring of proliferation. Furthermore, it does not affect the sterility of the culture, and alternative analytical methods can be incorporated simultaneously. It is reliable, simple, non-radioactive and compares well with other cytotoxicity assays for many cell types [440–444]. However, once the colour change has taken place, the dye is stable even upon removal of cells, high levels may be cytotoxic and extracellular forms of alamarBlue may underestimate the reduction [441, 442].

Alizarin Red-S Assay The alizarin red-S assay is used to examine bone nodule formation due to its reactivity with calcium and other cations. The seeding medium is replaced with an alizarin red-S containing solution, with the amount of calcium formed quantified spectrophotometrically after destaining [445–449]. It is generally used in conjunction with other tests as it is not possible to determine the exact cation causing the colour change. Furthermore, calcium based scaffolds can react causing false readings [445].

Alkaline Phosphatase Assay Alkaline phosphatase (ALP) was one of the earliest enzyme determination assays to gain widespread approval and is still regularly used [450]. The release of ALP is a marker for early osteoblast differentiation and thus highly useful in bone scaffold analysis. Seeded scaffolds are evaluated via the introduction of a substrate, *p*-nitrophenyl phosphate (pNPP), that reacts with the enzyme. Colourless in alkaline solution, this reacts with ALP to form a yellow product, *p*-nitrophenyl, which is directly related to the amount of ALP present and can be measured spectrophotometrically. It is a rapid, accurate technique and has been developed to cope with large workload requirements for a range of cell types [450–459].

Ethidium-Bromide Assay Ethidium-bromide is a cytotoxicity assay that estimates the levels of DNA and RNA. Ethidium bromide fluoresces due to the complex formation of native nucleic acids, with the solution examined on an inverted fluorescent microscope [460–463]. The major advantage with this assay is that live and dead cells can be examined, as live cells fluoresce green, whilst non-viable cells become red.

4.2.9.2 Dissolution Analysis

The effect of calcium (Ca^{2+}) and phosphate (PO_4^{3-}) ions on bony growth has been extensively studied *in-vitro* [464–468] and *in-vivo* [465, 469, 470]. Increased solubility of apatitic implants leads to more pronounced *de-novo* growth [466] due to the mechanisms behind regeneration. Firstly, there is dissolution of Ca^{2+} and PO_4^{3-}, followed by reprecipitation onto the implant of either the dissolved ions or cells summoned to the area due to the dissolution. The interface then undergoes a period of ion exchange and structural rearrangement before interdiffusion between the surface boundary layer and the implant. The local environment then causes the deposition of either a mineral or organic phase onto the surface which slowly becomes integrated [464, 469, 471, 472].

The rate of dissolution is affected by many factors [465]. Firstly, the calcium:phosphate ratio of the apatite leads to different dissolution rates [465, 466], with, for example, HA being more stable than TCP, which is more stable than OCP [465, 466, 470]. Secondly, increased crystallinity decreases the solubility due to a reduction in the presence of defects [465, 467, 470]. Thirdly, additives affect the crystal structure, causing an increase (carbonate, silicate or strontium in HA) or decrease (fluoride in HA; magnesium or zinc in TCP) in the solubility [465, 472]. Finally, macro and microporosity affect dissolution as structures with a higher surface area have a greater number of localities at which ionic exchanges can take place [465, 470].

The main role of Ca^{2+} in bone formation is to stimulate osteoblast proliferation and

inhibit osteoclast resorption [467, 473]; PO_4^{3-} induces preprogrammed cell death (apoptosis) in osteoclasts and osteoblasts, causing the amalgamation of new bone cells [474]. The level of apoptosis enhanced when both ions are present. As osteoblasts mature, osteoclast formation decreases and ALP activity increases; during ALP synthesis, PO_4^{3-} ions are cleaved from β-glycerol phosphate and thus PO_4^{3-} is also related to bone mineralization [468, 475–478]. Finally, PO_4^{3-} plays a role in regulating osteopontin [467, 468, 476–478], a non-collagenic protein found in bone as well as non-osteoblastic cell types, including smooth muscle cells, murine kidney cells and pre-fibroblasts [476, 478]. In such cases, increased osteopontin has been linked with calcification diseases such as arterial plaque and kidney stone formation [478].

There are various routes for determining the level of Ca^{2+} in solution, including atomic absorption spectroscopy [479, 480], the use of calcium electrodes [470] or colorimetric assays. Of the spectophotometric assays, the *o*-cresolphthalein complexone, a metal complexing dye, is the most sensitive and specific [481, 482]. The molybdenum blue assay is used for PO_4^{3-} determination. This is based on the formation of molybdophosphoric acid from molybdate and phosphate in an acidic solution and the subsequent reduction to a blue heteropoly compound [481, 483–487].

4.2.9.3 Assay Evaluation

Once seeded and subjected to one of the aformentioned assays, analysis involves either viewing the cells fluorescence or confocal microscopy, or taking quantitative measurements using spectophotometry.

Fluorescence Microscopy Objects that emit light shortly after absorbing light, which is typically of a shorter wavelength, are said to fluoresce [488, 489]. Filtering to remove the exciting light enables the observation of only the fluorescing objects. Hence, fluorescence microscopes are used to observe objects that fluoresce. The specimen is illuminated with one wavelength and the returning light is filtered to only

allow the emitted light to be observed [488]. Single-photon or two-photon excitation can be used, with one-photon techniques using UV or visible light and two-photon processes using less energetic photons that are simultaneously absorbed [489].

Confocal Microscopy Confocal microscopy combines light or fluorescence microscopy and confocal imaging and is used to determine the location of cellular components within cells or tissues [490]. It offers greater focus than is obtainable via light microscopy by replacing the microscope condensor with a lens identical to the objective lens, and limiting the field of illumination with a pinhole. The specimen is scanned with a point of light, with variations captured using photoelectric cells. Increased resolution is obtained as the use of a pinhole means the image is free from out of focus fluorescence [490–492].

Multiple structures can observed using multiple labeling imaging. Each fluorochrome is illuminated by appropriate laser lines, with different filters used to prevent bleeding of the colour between the different chanels. These can be merged onto a single image to observe the relationships between the different structures [491, 492].

Spectophotometry Spectroscopy measures the interaction of molecules with electromagnetic radiation, generally in the UV or visible range of light [493, 494]. Spectophotometers emit light that is optically filtered and directed at the sample, with the amount of light that passes through detected. It is very sensitive, non-destructive and only a small amount of material is required [493, 494]. The most suited spectroscopic method for the aforementioned assays is adsorption spectroscopy, which enables quantitative measurements to be obtained as the absorbance of a solute depends linearly on its concentration [493].

4.2.9.4 Statistical Analyses

The determination of whether what is being analysed has statistical significance and thus can be taken as a reliable result is important in many characterisations.

There are numerous techniques that enable this, however only those used regularly in biological assays for bone scaffolds are analysed here.

Analysis of Variance (ANOVA) ANalysis Of VAriance (ANOVA) groups parameters into populations to evaluate the variance of each component [495, 496]. In the most basic form, this is achieved by subtracting the sum of squares (SS) from each of the populations from the total sum of squares, leaving the residual sum of squares [496–498]. Finally, the mean sum of squares (MS) is calculated by dividing the sum of squares by the degrees of freedom.

For a model of sample size, n, with k parameters which can be described as:

$$X_{ij} = \mu_i + e_{ij} \qquad (1 \leq i \leq n,\, 1 \leq j \leq k) \tag{4.27}$$

where the e_{ij} are independently distributed random variables $n(0, \sigma^2)$ and μ_i is the mean of the ith treatment, the mean squares for error (MS(E)) can be expressed as

$$MS(E) = \sigma^2 = \frac{1}{n-I}\sum_{i=1}^{n}\sum_{j=1}^{k}(X_{ij} - \bar{X_{ij}})^2 \tag{4.28}$$

where $\bar{X}$ is the mean of the variables. This forms the basis from which other, more complex analysis techniques are derived, that are discussed below.

Student's T-Test The Student's T-test is one of the most common statistical methodologies used to construct the confidence interval or for hypothesis testing. The method assumes that the sample is from a normal distribution [499] and where $X_1, X_{2,} \ldots, X_{n,}$are independent and identically distributed random variables with mean μ and variance σ^2. The following variables are calculated:

$$\bar{X} = \frac{1}{n}\sum_{i=1}^{n} X_i \tag{4.29}$$

$$s_n^2 = \frac{1}{n-1}\sum_{i=1}^{n}(X_i - \bar{X})^2 \tag{4.30}$$

$$v = \sum_{i=1}^{n} X_n - n \tag{4.31}$$

where s_n is the pooled variance and v is the number of degrees of freedom of the sample. The Student's T-statistic, t_n is calculated [499–501] using:

$$t_n = \sqrt{n}\frac{\bar{X} - \mu}{s_n} \tag{4.32}$$

Once the T-statistic and the number of degrees of freedom are known, the probability ($\mathrm{P_r}$) value can be calculated using the Gayen method [502–504]. Although not detailed here, this method has resulted in the publication of tables that enable the simple calculation of $\mathrm{P_r}$, such as in [502]. The resulting probability is the likelihood of a sample being within the variance for other samples from the same variable set [499, 502].

Tukey's Pairwise Comparison For a standard ANOVA model, Equation 4.27, Tukey [505] proposed a procedure to determine the confidence interval $(1 - a)$ provided all the sample sizes, n_i are equal, n:

$$1 - a = P_r\left\{\mu_i - \mu_j \in \left[\overline{X}_i - \overline{X}_j \pm q_{k,v}^{(n)}\frac{S}{\sqrt{n}}\right];\ 1 \leq i,\ j \leq k\right\} \tag{4.33}$$

where $q_{k,v}^{(n)}$ is the upper point of the studentized range distribution with parameter k and v degrees of freedom, and S is the pooled estimate of the common variance. Furthermore, this can be modified for unequal sample sizes by replacing $1/\sqrt{n}$ with $[(1/n_i + 1/n_j)/2]^{1/2}$ [505–510].

It is a test enabling comparisons to be made between treatments in a k-treatment experiment [505, 507, 508, 510]. Normality of the parent population is assumed and

differences between the pairs of the means must have the same population variance [511]. However, in cases where pooling of the sample variance is inappropriate, S can be replaced by $\left(s_i^2 + s_j^2\right)$ [508, 512].

Kolmogorov-Smirnov The Kolmogorov-Smirnov test is used to analyse whether observations are from a completely specified continuous distribution by analysing the agreement of a distribution of a set of sample values and theoretical distributions in a goodness of fit test. For a sample of n observations,

$$D = max_x \mid F(X) - S_n(X) \mid \tag{4.34}$$

where $S_n(X)$ is the sample cumulative distribution function and $F(X)$ is the cumulative normal distribution function [513–519]. If the value of D exceeds the critical value, as can be obtained from tables such as in [513–516, 520], the hypothesis that the observations are from a normal population is rejected.

4.2.9.5 Methodology

The biological testing and analysis was undertaken in two sections. Preliminary tests were undertaken by colleagues at the University of Sheffield (Department of Materials Science and Engineering) on scaffolds produced without any porogen inclusion during manufacture to assess their viability against a commercially available scaffold. Once this had been undertaken, further tests were carried out by the author at the University of Birmingham (TRAILab, Department of Chemical Engineering) to compare the biological performance between scaffolds with and without porogen.

Preliminary Tests Hydroxyapatite scaffolds produced without porogen using the 45 and 90 ppi templates, and sintered to 1350 °C were cut into fragments of 10 mg and sterilized in 70 vol.% ethanol (Fisher, UK). Cells from the MG-63 cell line (ATTC-LGC standards, UK) were cultured in monolayer up to passage 65 in Dulbecco's

Table 4.7: Data of CellSupports porous HA discs as provided by manufacturer

Composition	100% HA
Macroporosity	50-65%
Pore Size	200-300 µm
Strut Size	30-120 µm
Pore Interconnectivity	>95%

Modified Eagle's Medium (DMEM)(Lonza, Belgium) supplemented with 10 vol.% foetal bovine serum (FBS)(Labtech, UK), 1 vol.% Penicillin (10^5 U / L) / Streptomycin solution (0.1 g / L) (Pen/Strep)(Sigma Aldrich, UK), 1 vol.% L-glutamine ($2 \text{ X } 10^{-3}$ M, Sigma Aldrich, UK) and 0.25 vol.% fungizone (0.25 g / L, Sigma Aldrich, UK). Scaffolds were seeded with $1 \text{ X } 10^6$ cells and completely submerged in medium. Controls were created by following the same procedure with commercially available porous HA discs (CellSupports, UK), detailed in Table 4.7 and by seeding cells directly onto tissue culture plastic to act as the 100% marker.

Cell viability was measured after 1, 4 and 7 days using resazurin which increases in fluorescence during metabolism of cells. Briefly, the seeding medium was removed and replaced with 1 mL of medium containing $1 \text{ X } 10^{-4}$ M resazurin powder (Sigma Aldrich, UK). This was incubated for 3 hrs and the resazurin containing medium changed back to supplemented DMEM, with the fluorescence of the retrieved medium from all samples determined spectrofluorometrically (excitation = 540 nm; emission = 635 nm). Fluorescence was expressed relative to cells seeded on tissue culture plastic measured at day 1.

For examination with confocal microscopy, samples were fixed after 1 day using a 3.7 wt.% solution of formalin (Sigma Aldrich, UK). Cell membranes were permeabilized by incubation in a 1:100 dilution of Triton-X (VWR, UK) for 15 mins, washed and stained with a solution containing 1 µg/mL 4',6-diamidino-2-phenylindole (DAPI) (Invitrogen, UK), staining cell nuclei blue, and 0.5 µg/mL Phalloidin, Tetramethylrhodamine B isothiocyanate (Phalloidin-TRITC) (Sigma Aldrich, UK), which stains the actin component of the cell cytoskeleton red. Constructs were imaged at the Kroto Research Institute Confocal Imaging Facility, using a LSM510 Meta upright

confocal microscope (Zeiss, Germany), with DAPI visualized using two-photon excitation at 800 nm using a Ti:sapphire laser and Phalloidin-TRITC visualized using single-photon excitation at 543 nm.

Further Analysis Due to the large number of scaffolds produced, it was not deemed economically or temporally feasible to analyse all scaffolds. To test the hypothesis that the inclusion of a porogen impacts upon the cell growth on the scaffolds, the HA scaffolds that could be most readily handled were analysed. Thus, those produced with 5 coats of the slurry and sintered to 1350 °C were chosen, with both the 45 and 90 ppi foams analysed.

Cell Culture To further assess the biocompatibility of the ceramics, cell viability over a period of time was measured using a live/dead assay; a tetrazolium salt (MTT) assay; a measure of the metabolic activity of ALP; and of the dissolution of calcium ions from the scaffold into the surrounding culture medium. HA scaffolds produced using AFR were cut to 10 mm diameter with 3 mm height and sterilized in 70 vol.% ethanol (Fisher, UK). 3T3 cells (NIH, Sigma Aldrich, UK) were cultured in monolayer up to the 23rd passage in DMEM (Sigma Aldrich, UK), supplemented with 10 vol.% bovine serum (Sigma Aldrich, UK), 2 vol.% L-glutamine, 1 vol.% Pen/Strep and 2.4 vol.% 4-(2-hydroxyethyl)-1-piperazine-1-ethanesulfonic acid) (HEPES) buffering solution (Fluka, UK) whilst MC3T3 (European Collection of Cell Culture (ECACC), Sigma Aldrich, UK) cells were cultured in monolayer up to the 18th passage in similarly supplemented media. Cells were diluted at 1:1 with Trypan Blue (Sigma Aldrich, UK) for counting using a Countess® Automated Cell Counter (Invitrogen, UK), using disposable Countess® cell counting chamber slides.

Due to the relative versatility of 3T3 cells, a more complete analysis was undertaken on scaffolds seeded with these cells, however as they are of fibroblastic lineage it was also important to analyse some scaffolds seeded with cells from the osteoblastic MC3T3 line. The scaffolds selected for this analysis were those produced from 45

and 90 ppi templates, with 5 coats, sintered to 1350 °C and with 2 camphene contents (0 and 25%).

Live/Dead Cell Viability Cell viability was analysed using a live/dead assay using Calcein AM (Invitrogen, UK) and propidium iodide (PI)(Invitrogen, UK), similar to the ethidium bromide assay outlined in Section 4.2.9. Calcein AM is converted to the fluorescent calcein dye by intracellular esterases in live cells. However, PI can not permeate the membranes of live cells and instead fluoresces in the presence of nucleic acids and is used to identify dead cells. Briefly, $2.5\,\mathrm{X}\,10^5$ 3T3 cells were seeded onto each scaffold in 24-well tissue culture treated plates and incubated for 1 and 3 days. To assess the viability, the media was removed and the scaffolds washed with posphate buffered solution (PBS)(Sigma Aldrich, UK), before 3 mL of PBS containing 10 µg/ml calcein AM and 10 µg/ml PI was added and incubated for 30 mins. Analysis was undertaken using an Axiolab microscope (Zeiss, Germany), connected to an Axiocam ICM-1 camera (Zeiss, Germany) with excitation/emission at 488 nm/525 nm for calcein AM and 525 nm/620 nm for PI. Analysis was undertaken using Zen software (Zeiss, Germany).

MTT Assay The number of viable 3T3 and MC3T3 cells was quantified using the MTT assay after 1, 4 and 7 days. Scaffolds (n=9) were seeded with $2.5\,\mathrm{X}\,10^5$ cells in 24-well tissue culture treated plates, with 5 mL supplemented media added to completely submerge the scaffold. MTT reagent (Sigma Aldrich, UK) was added at 10 vol.% (0.5 mL) of the culture media, and incubated at 37 °C for 4 hrs. The formazan crystals were dissolved via the addition of 5 mL 0.1 N acidic isopropanol (isopropanol (≥99.5%, Sigma Aldrich, UK) /hydrochloric acid (HCL)(37%, Sigma Aldrich, UK)) for 45 mins, with gentle agitation every 15 mins. Samples of the solution were then transferred to a 96-well plate where they were diluted appropriately for accurate measurements at 570 nm using a Glomax® -Multi Detection System spectrofluorometer (Promega, UK).

ALP Assay To determine the level of osteogenic differentiation, $2.5\,\mathrm{X}\,10^5$ cells were seeded onto each scaffold in 24-well tissue culture treated plates and additional media added to completely submerge the scaffolds. Media was changed every 3 days, with ALP activity measured at 1, 4 and 7 days following the manufacturer's protocol provided with a SensoLyte ® pNPP Alkaline Phosphatase Assay Kit *Colorimetric* assay kit (Anaspec, Cambridge Bioscience, UK).

The optimal route for removal of cells from the scaffolds was analysed using three techniques. The first involved removing the scaffolds (n=9) from the media, washing them in PBS and submerging them in TrypLE$^{\mathrm{TM}}$ Express (1X) dissociation agent (Gibco, UK). After incubation for 5 mins, the TrypLE was mixed with an equivalent amount of media and centrifuged at 1000 rpm for 3 mins. The supernatant was removed, and the cell pellet homogenised using the lysis buffer provided in the kit, incubated for 10 mins under agitation at 4 °C and centrifuged at 2500 G for 10 mins at 4 °C. The second method was identical to the first except that rather than adding the lysis buffer directly to the cell pellet, the cells were resuspended in a small amount of media prior to homogenisation. In the final method, the scaffolds were washed with and then submerged in the lysis buffer. The cell suspension was then collected, incubated under agitation for 10 mins at 4 °C and centrifuged at 2500 G for 15 mins at 4 °C.

Once the optimal technique for removing the cells from the scaffolds had been determined, this was used for all subsequent analyses. After centrifugation the supernatant was collected for the assay; 50 µL was transferred to a 96-well plate, to which 50 µL alkaline phosphatase dilution buffer was added and incubated for 45 mins. Finally, 50 µL of the stop solution was added, the plate shaken on a plate shaker for 1 min and the absorbance measured at 410 nm on the Globax® -Multi Detection System.

Dissolution Assay To determine the level of calcium dissolution, the calcium content of the culture solution was measured after 1, 4 and 7 days following the manufac-

turer's protocol provided with a Cayman Chemical Calcium Assay kit (Cambridge Bioscience, UK). Briefly, scaffolds were sterilised in 70 vol.% ethanol and submerged in 2 mL PBS (n=9) or DMEM (n=9). For analysis, the scaffold was removed, the solution mixed and 10 µL PBS or 5 µL DMEM was placed in a 96 well plate. The scaffold was then returned to the solution from which it had been removed. The DMEM solution was diluted using 5 µL of the buffer solution included in the kit. Finally, 100 µL of the reagant was added to the solutions, the plate shaken for 30 s on a plate shaker and incubated for 5 min at room temperature before reading at 570 nm on the Globax® -Multi Detection System.

Statistical Analysis All statistical analyses were carried out using Students T-test (Equation 4.32) and Tukey's Pairwise Correlation (Equation 4.33) as outlined in Section 4.2.9.4.

4.2.10 Summary of Characterised Samples

A complete list of which samples were subjected to the different characterisation techniques is shown in Table 4.8, with samples described using the same annotation as used in Section 4.1.4. All scaffolds were evaluated using SEM and porosimetry and the yield stress was calculated theoretically. Selected samples at each temperature were evaluated using XRD to determine the effect of the sintering temperature on material composition. Furthermore, the viability assays were undertaken on selected samples, with microCT only undertaken on samples manufactured under the same conditions. In all cases, scaffolds produced from both templates were evaluated. Furthermore, raw powders for each biomaterial were subjected to XRD and SEM, whilst samples of each of the slurries with the different biomaterials and different porogen contents were evaluated using STA.

Table 4.8: List of which samples were subjected to the different characterisation techniques

XRD	SEM	microCT	Porosity	Theoretical Yield Stress	Mechanical Testing	Biological Evaluation
HA12503c	All	HA13505c	All	All	HA13505c	HA13505c
HA12504c10		HA13505c5			HA135025c	HA13505c5
HA13003c		HA13505c10				HA13505c10
HA13002c25		HA13505c20				HA13505c20
HA13503c		HA13505c25				HA13505c25
HA13501c20						
Ti10003c						
Ti10001c25						
Ti11003c						
Ti11003c25						
Ti12003c						
Ti12004c10						
Ti13003c						
To13005c5						
T6412003c						
T6412004c10						
T6412503c						
T6412503c25						
T6413003c						
T6413003c20						

4.3 Summary

This chapter provides a brief summary of the methodologies implemented in this PhD. Processing of the scaffold using AFR is detailed, with a particular emphasis on the paramaters varied. The theory behind relevant techniques used to characterise the raw materials and as-produced scaffolds is described as well as the methodology implemented. STA is used to analyse the thermodynamic properties of precursor materials; optical microscopy, SEM, microCT and XRD and can be used on both the precursors and final scaffolds to determine the structure, in terms of nature of pores and material; porosimetry provides information on the porous nature of the sample; compression testing evaluates the mechanical suitability of the scaffold; and biological testing is used to determine how the structure will react to the bodily environment.

Part III

Results and Discussion

Chapter 5

Precursor Characterisation

5.1 Foam Characterisation

5.1.1 Foam Sizes

The manufacturers information stated that the foams provided for use in this work have an average number of pores per inch (ppi) of 20, 45 or 90. From this the theoretical value of the pore size can be determined using:

$$Pore\,size\,(\mu m) = \frac{25.4}{ppi} \times 1000 \tag{5.1}$$

This relates to pore sizes of 1270, 564 and 282 µm for the 20, 45 and 90 ppi foams respectively. To verify this, samples of the foam were analysed using SEM, with examples shown in Figure 5.1. The as measured pore sizes for the 20, 45 and 90 ppi foams are 1221± 59, 622± 28 and 235± 7 µm, with struts of 223± 7, 95± 3 and 39± 0.9 µm respectively. The average and standard error of the mean of the measured values is given in Table 5.1, along with their predicted size. The 20 ppi foam will not be used further as the pore and strut sizes are outside of the accepted range required for regrowth.

5.1.2 Foam Thermal Properties

The thermal properties of the foam were measured using STA. As shown in Figure 5.2, the foam begins crystallisation at 50 °C, followed by the onset of melting at

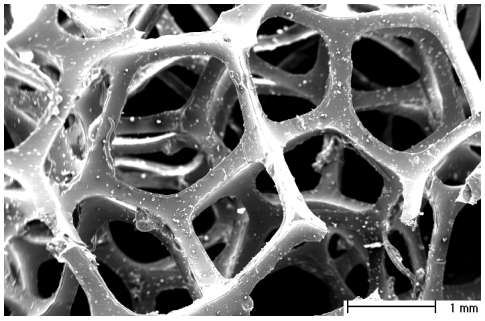

(a) SEM micrograph of the 20ppi foam (V = 15kV; WD = 12.7mm; mag = 25x)

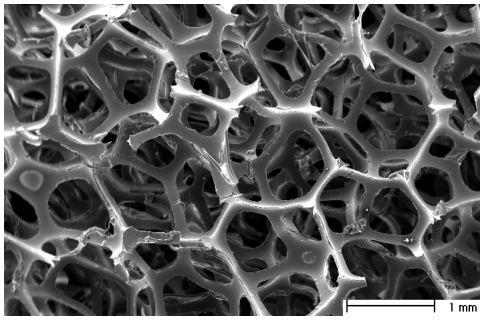

(b) SEM micrograph of the 45ppi foam (V = 15kV; WD = 18.8mm; mag = 25x)

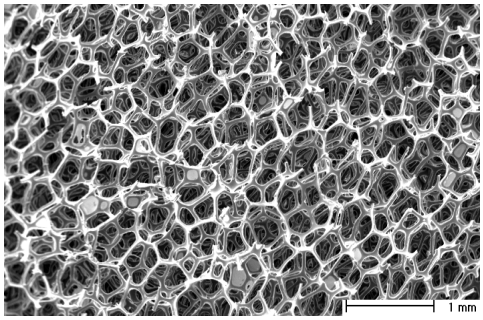

(c) SEM micrograph of the 90ppi foam (V = 15kV; WD = 16.8mm; mag = 25x)

Figure 5.1: SEM micrographs of the as-received foam templates

Table 5.1: Average $\pm\sigma_{er}$ (n=10) pore and strut sizes of the foams, along with their predicted pore size

	20 ppi		45 ppi		90 ppi	
(μm)	Pore Size	Strut Size	Pore Size	Strut Size	Pore Size	Strut Size
Average	1221 ± 59	223 ± 7	622 ± 28	95 ± 3	253 ± 7	39 ± 0.9
Predicted Pore Size	1270		564		282	

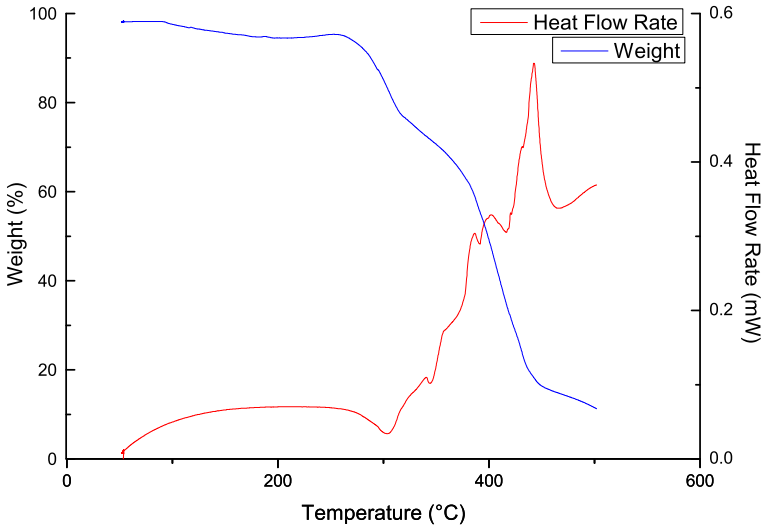

Figure 5.2: STA thermogram of PU foam, heated to 500 °C at 10 °C/min shows a phase change at 50 °C, followed by a further change at 300 °C, whilst most of the weight is removed. The red line indicates the DTA reading, whilst the blue line shows the TG data.

300 °C. The peak assoicated with this, at 450 °C, coupled with the dramatic weight loss, indicates that when held at the prescribed holding temperature of 500 °C, as outlined in Section 4.1.3, all foam will be pyrolised.

5.2 Precursor Crystallography

The indexed XRD of the raw HA powder matched the standard HA COD reference pattern (96-230-0274) and thus the raw material is predominantly phase pure hydroxyapatite, although there is also some monetite present. The indexed XRD of the as-recieved TiH_2 powder strongly matched the reference pattern (04-001-6850) for TiH_2 on the Powder Diffraction File (PDF) 4+ (International Centre for Diffraction Data (ICDD), USA), confirming the phase purity of the raw material. The pattern of the raw Ti-6Al-4V powder matched the standard reference for α-Ti (96-900-8518), with peaks also matching those of β-Ti (96-901-1601) indicating that this was also

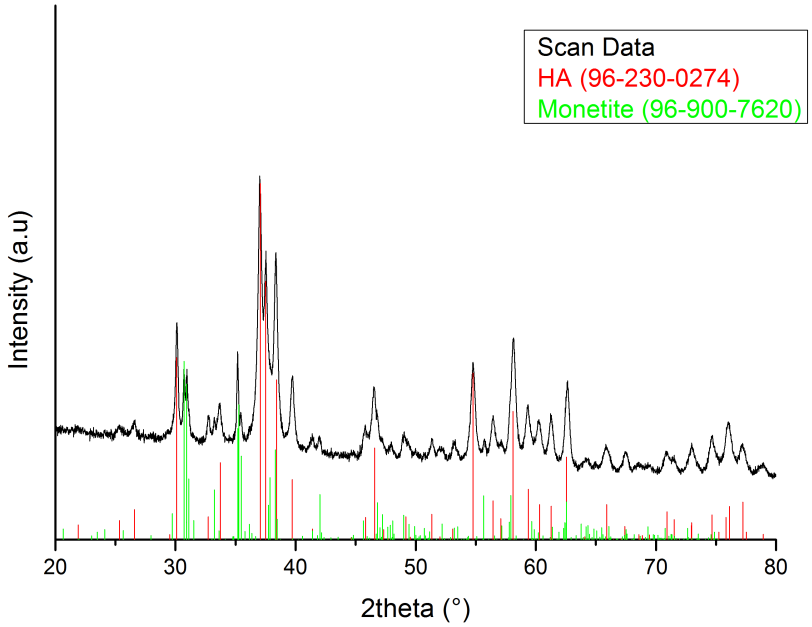

Figure 5.3: XRD plot of raw HA powder with COD standard reference patterns for HA (96-230-0274) and Monetite (96-900-7620)

pure. Plots of HA, TiH_2 and Ti-6Al-4V are given in Figures 5.3, 5.4, and 5.5 respectively, with estimates of the composition as obtained using peak intensity, peak area and semi-quantitative analyses shown in Table 5.2.

Compositional analysis was undertaken using the three methodologies. The analysis performed using the HighScore program theoretically gives perfect results [521] and hence allows for the exact composition of the material to be determined [388,389,521, 522]. In practice, this is not realised due to two main reasons. Firstly, the analysis is based on the relative intensity of the peak heights, and assumes that all peaks have the same FWHM [521]. This is not always the case, and as such a more accurate determination of the phase composition is carried out using analysis of the peak area [522]. Secondly, the relative intensity of each phase is given by a 'scale factor'. To counteract any affects caused by the texture of the material, HighScore determines the scale factor with a least squares fit through all matching reference pattern lines

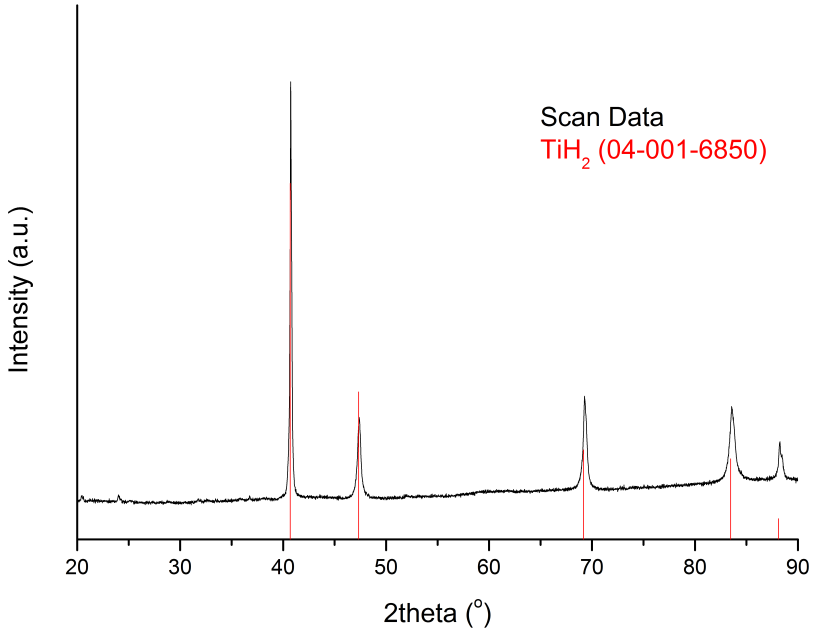

Figure 5.4: XRD plot of raw TiH_2 powder, with ICDD standard reference pattern for TiH_2 (04-001-6850)

Table 5.2: Compositional estimation of raw HA and Ti-6Al-4V as evaluated using peak intensity, peak area and HighScore semi-quantitative analyses. TiH_2 has not been included as there is no COD reference pattern against which to match it

Raw Material	Analysis Method	HA (%)	Monetite (%)	α-Ti (%)	β-Ti (%)
HA	Peak Intensity	67	33	-	-
	Peak Area	89	11	-	-
	Semi-Quantitative	64	36	-	-
Ti-6Al-4V	Peak Intensity	-	-	94	4
	Peak Area	-	-	60	40
	Semi-Quantitative	-	-	72	28

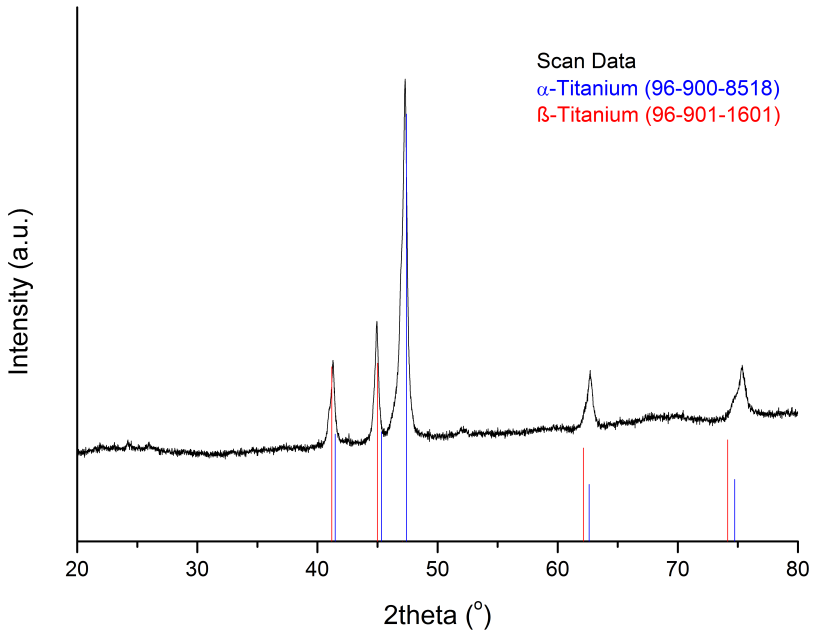

Figure 5.5: XRD plot of raw Ti-6Al-4V powder, with COD standard reference patterns for α-Ti (96-900-8518) and β-Ti (96-901-1601)

as opposed to considering solely the measured intensity of the strongest line [521]. As seen in Table 5.2, there are some discrepancies between the values obtained using the different methods. For example, the peak intensity and semi-quantitative analyses provide similar values for the composition of the raw HA powder, of 67 and 64% HA and 33 and 36% monetite respectively, however the peak area analysis suggests the proportion of HA is much higher, at 89%. This corresponds more closely with the manufacturers information, stating the raw powder is approximately 90% pure HA, suggesting that it is more appropriate to use the peak area analysis for compositional calculation, as has been described by others [522]. Thus, sample composition is estimated using peak area analysis in all further analyses.

5.3 Precursor Particle Sizes

The initial particle size of biomaterial components is of interest as smaller particles can be more closely packed and hence can enable smaller pores. They are also of interest with respect to freeze cast slurries as larger particles can sediment within the processing time scale. The as measured, and where available manufacturers' information, is given in Table 5.3, with micrographs shown in Figure 5.6. Due to the number of particles measured, the standard deviation was calculated, using Equation 4.14, as opposed to the standard error of the mean. HA particles were the smallest at 1.0 $\pm$0.4 µm, whilst TiH_2 particles were the next size, at 14 $\pm$3 µm, although this was not significantly different from the 500- mesh Ti-6Al-4V particles, 15 $\pm$5 µm. The range observed for all Ti-6Al-4V powders was within the size specified by the manufacturer, however there was no real difference between the average sizes of the 325- and 400- mesh, of 33 $\pm$11 and 32$\pm$5 µm respectively. Furthermore, the particle size was confirmed using a laser diffraction particle sizer, with close correlation to the analysis undertaken using SEM measurements for titanium based materials: the slight overestimation observed is likely to have been caused by the laser analysis using the volume measurements taken to generate an equivalent particle size diameter. As the particles are not spherical, this is likely to

have led to the minor variations observed. There was some difference however with the measurements for HA; this is due to the bimodal particle size distribution, as shown in Figure 5.7.

Table 5.3: Mean and standard deviation of particle sizes for the as recieved biomaterial powders. For the Ti-6Al-4V powders, the manufacturers information is also stated

		HA	TiH_2	Ti-6Al-4V		
	(μm)			325-mesh	400-mesh	500-mesh
SEM	n	30	30	20	20	20
	Mean	1.0	14	33	32	15
	Standard Deviation	0.4	3	11	5	5
Laser Diffraction	Mean	16	15	49	29	19
	Standard Deviation	18	9	18	14	8
	Manufacturers Information	n/a	n/a	40.3	25.6	15.5

5.4 Slurry Thermal Characteristics

STA was undertaken on HA slurries up to 1450 °C as this is the temperature at which it is expected to have started undergoing a phase transformation from HA to β-TCP or biphasic calcium phosphate [280, 523]. As shown in Figure 5.8, there is an initial endothermic reaction as the water is removed from the slurry, with an associated decrease in weight. Furthermore, all components of the slurry other than HA are removed by around 300 °C, as seen by the lack of any changes on the TGA thermogram. The sample then consolidates above 800 °C, until a further exothermic peak at 1200 °C due to crystallisation. The samples run for this work exhibited no phase transformations within the range given, hence sintering temperatures within this range are suitable.

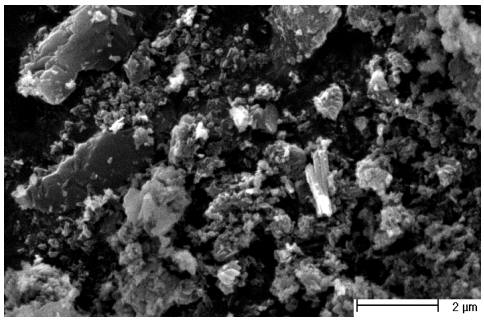

(a) SEM micrograph of HA particles (V = 25kV; WD = 10.7mm; mag = 10000x)

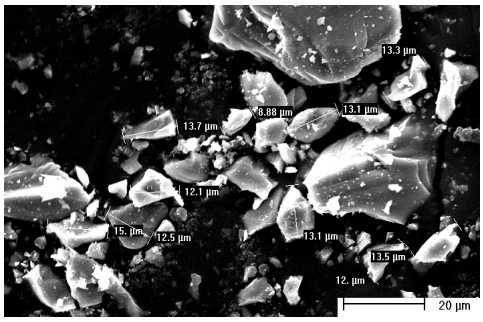

(b) SEM micrograph of TiH_2 particles (V = 25kV; WD = 10.6mm; mag = 1000x)

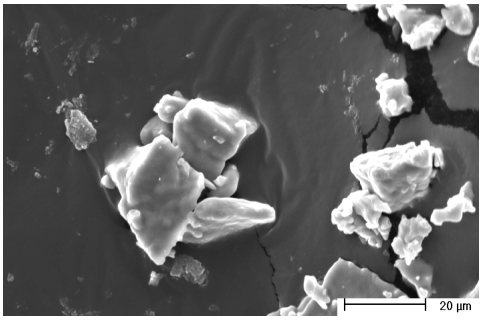

(c) SEM micrograph of Ti-6Al-4V (325 mesh) particles (V = 25kV; WD = 19.4mm; mag = 1000x)

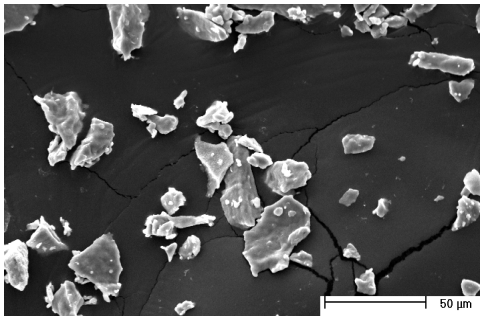

(d) SEM micrograph of Ti-6Al-4V (400 mesh) particles (V = 25kV; WD = 19.5mm; mag = 500x)

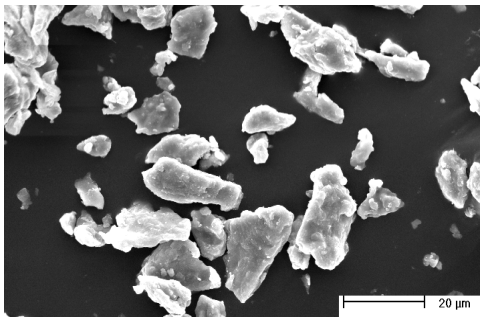

(e) SEM micrograph of Ti-6Al-4V (600 mesh) particles(V = 25kV; WD = 19.5mm; mag = 1000x)

Figure 5.6: SEM micrographs of as-received precursor biomaterial powders

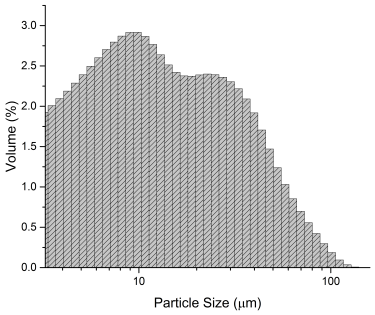

(a) Particle size analysis of HA powder

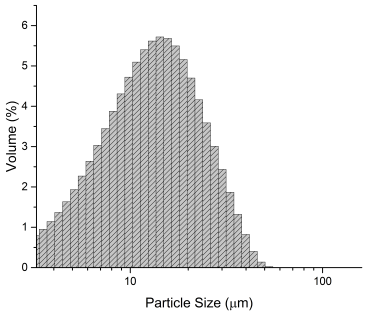

(b) Particle size analysis of TiH_2 powder

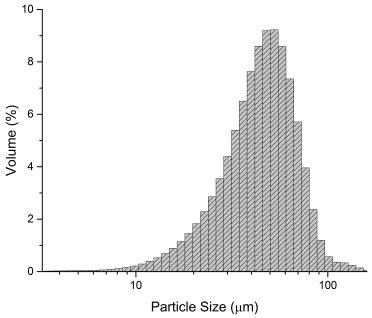

(c) Particle size analysis of 325- mesh Ti-6Al-4V powder

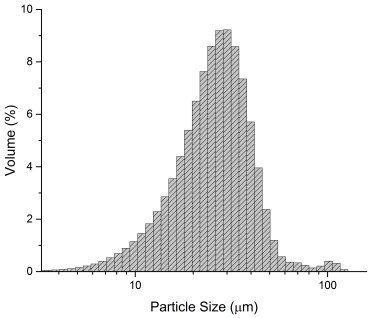

(d) Particle size analysis of 400- mesh Ti-6Al-4V powder

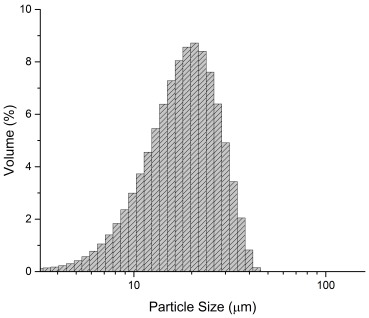

(e) Particle size analysis of 500- mesh Ti-6Al-4V powder

Figure 5.7: Particle size analysis of as-received precursor biomaterial powders

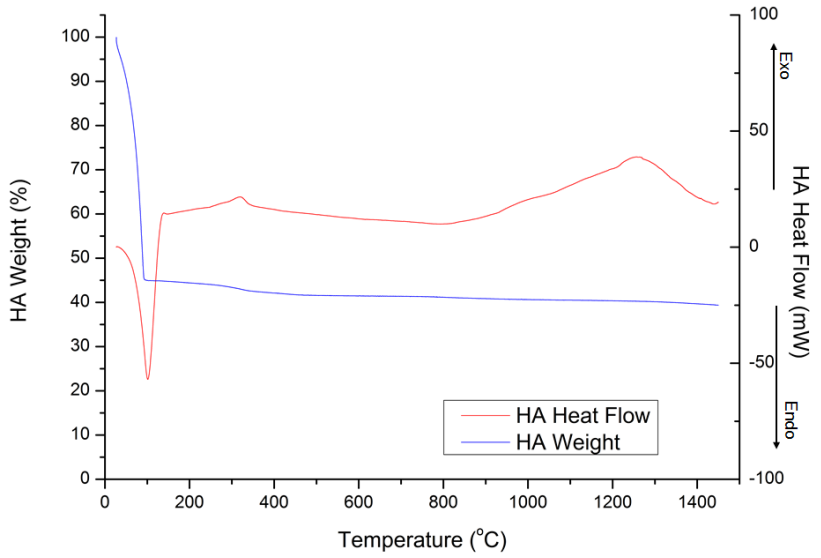

Figure 5.8: STA thermogram for the hydroxyapatite slurry containing no porogen, heated to 1450 °C at 10 °C/min. The red line indicates the DTA reading, whilst the blue line shows the TG data.

As for the DTA-TG thermogram of HA slurries, the thermograms of the TiH_2 and Ti-6Al-4V, shown in Figures 5.9 and 5.10 respectively, slurries also indicated camphene melting and all components of the slurry except the biomaterial burning off by 300 °C. This was indicated by an inital endothermic reaction that was accompanied by an associated weight loss. Both slurries were heated up to 1450 °C and whilst no further changes were observed in the Ti-6Al-4V slurry, the TiH_2 thermogram exhibited a further exothermic peak just above 550 °C indicating the onset of hydride decomposition.

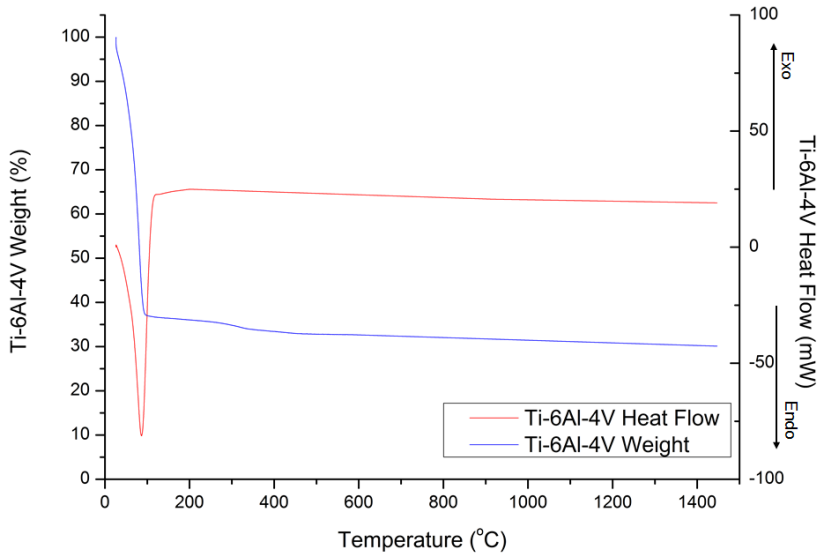

Figure 5.10: STA graph for the titanium-aluminium-vanadium slurry containing no porogen, heated to 1450 °C at 10 °C/min. The red line indicates the DTA reading, whilst the blue line shows the TG data.

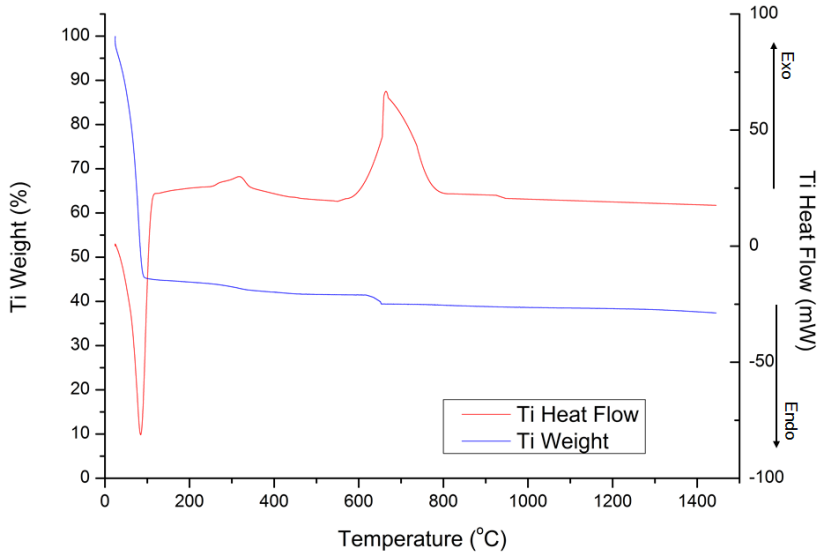

Figure 5.9: STA graph for the titanium hydride slurry containing no porogen, heated to 1450 °C at 10 °C/min. The red line indicates the DTA reading, whilst the blue line shows the TG data

5.5 Summary

The biomaterials that will be used throughout this work have been investigated to determine the most appropriate parameters for scaffold fabrication. Foam templates were obtained with three pore sizes, however only the 45 and 90 ppi templates will be used as the 20 ppi template has pore sizes outside of the predetermined range. Furthermore, the thermal properties have been investigated to confirm whether the holding temperature previously hypothesised is suitable to fully remove the template. The particle size of the raw biomaterials has been investigated, with increasing particle sizes through HA, Ti, Ti-6Al-4V 500-, 400-, and 325- mesh. The crystallographic composition of these materials has been investigated, with HA containing some monetite, whilst TiH_2 and Ti-6Al-4V were found to have no impurities. Finally, the effects of heating the biomaterial slurries was investigated by STA, which showed all components of the slurry being removed, followed by the crystallisation of HA-based slurries and the decomposition of TiH_2-based slurries.

Chapter 6

Hydroxyapatite

The results of analysing the different processing parameters as described above are given here. This chapter explicitly deals with the results obtained when hydroxyapatite was used as the biomaterial. Furthermore, the discussions in this chapter solely relate to HA structures, with a discussion of the technique in general given in Chapter 8.

Where graphical representation of results is shown, tables of the raw data are given in Appendix A. As previously mentioned in Section 4.2.8, datasets are obtained from different samples and as such trend lines are used as a visual aid and not as interpretation of the data.

6.1 Crystallography of Sintered Constructs

The indexed raw material, Section 5.2, is predominantly hydroxyapatite with some monetite. The indexed XRD of the powdered scaffolds sintered to 1250 and 1300 °C matched the COD reference pattern of whitlockite ($Ca_9Mg_{0.7}Fe^{2+}_{0.5}(PO_4)_6(PO_3OH)$) (96-901-2137), a calcium deficient form of hydroxyapatite. The samples sintered to 1350 °C strongly matched the standard of HA, with further peaks matching those of whitlockite. Furthermore, the significantly sharper nature of the peaks after sintering compared to those of the raw powder indicated that the material became more crystalline, with the results shown in Figure 6.1. The samples sintered to 1250 and 1300 °C were found to be 100% whitlockite, whilst that sintered to 1350 °C was

estimated to be 91% HA and 9% whitlockite. All compositional estimates are given in Table 6.1.

Table 6.1: Composition of raw powder and samples sintered to 1200, 1250 and 1350 °C as estimated using peak area analysis

Analysis	Specimen	HA (%)	Monetite (%)	Whitlockite (%)
Peak Area	Raw powder	89	11	-
	1250 °C	-	-	100
	1300 °C	-	-	100
	1350 °C	91	-	9

6.1.1 Discussion

The results of the slurry thermal characteristics, Section 5.4, indicated that all components of the slurry except for HA were burnt off by around 300 °C and that further heating up to 1400 °C did not elicit any phase transformations. However, XRD of powdered sintered scaffolds indicated at least a partial phase change at all sintering temperatures used to whitlockite [524, 525]. Whereas HA has a calcium:phosphate ratio of 1.67, that of whitlockite is 1.5, similar to TCP. The reduction in calcium content is due to the partial replacement of calcium ions by magnesium and iron [524–526], with any structural changes exacerbated at high temperatures [526]. Although the more common phase change observed [527,528] is from HA to a combination of HA and TCP (biphasic calcium phosphate (BCP)), it is thought that the use of water that has been filtered but not deionized introduced the impurites and caused the observed changes to the structure. Whitlockite is more similar to the natural apatitic phase of bone due to the presence of metal ions found naturally within the human body and thus is not expected to have a detrimental effect on the biological functionality of the scaffolds.

HA becomes unstable above 1000 °C due to the partial loss of hydroxide groups [225, 523, 529]. At this temperature, it begins decomposing, firstly to oxyhydroxyapatite

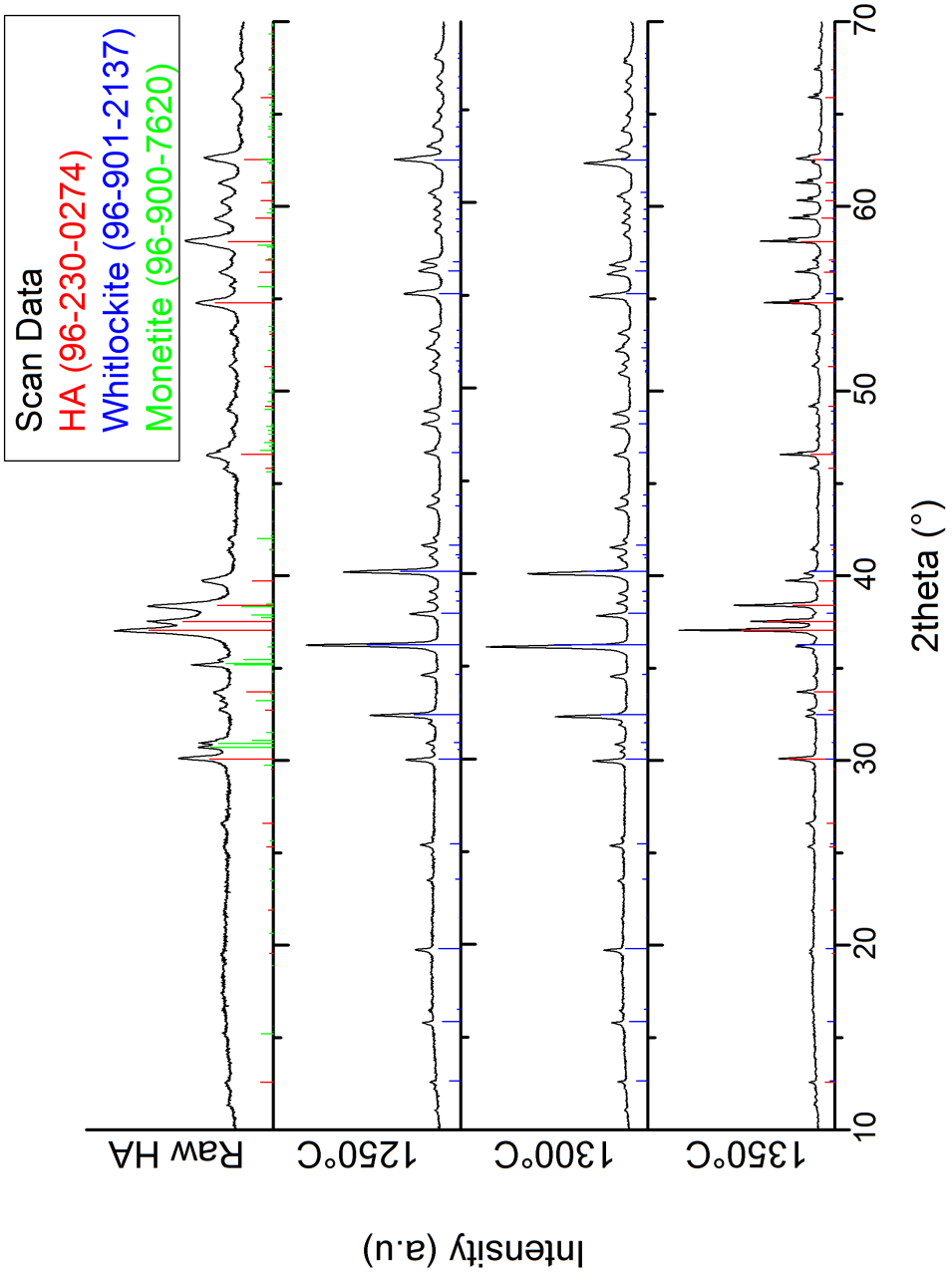

Figure 6.1: Indexed XRD of powdered scaffolds sintered to 1250, 1300 and 1350 °C, plotted on the same axis as the COD reference pattern for whitlockite (96-901-2137) (1250, 1300 °C) and whitlockite and hydroxyapatite (96-230-0274) (1350 °C). For reference, the scan of the raw HA powder, with COD reference for HA and monetite (96-900-7620) is also included.

(OHAP) and then, at temperatures above 1360 °C, OHAP decomposes to TCPM or TCP, [280, 523], with the phase diagram for a selected range of calcium phosphate systems sintered to high temperatures shown in Figure 6.2. OHAP is gradually rehydrated as the temperature cools to reform HA and TCP [523], however the ion replacement observed in this work means that whitlockite is formed instead of TCP.

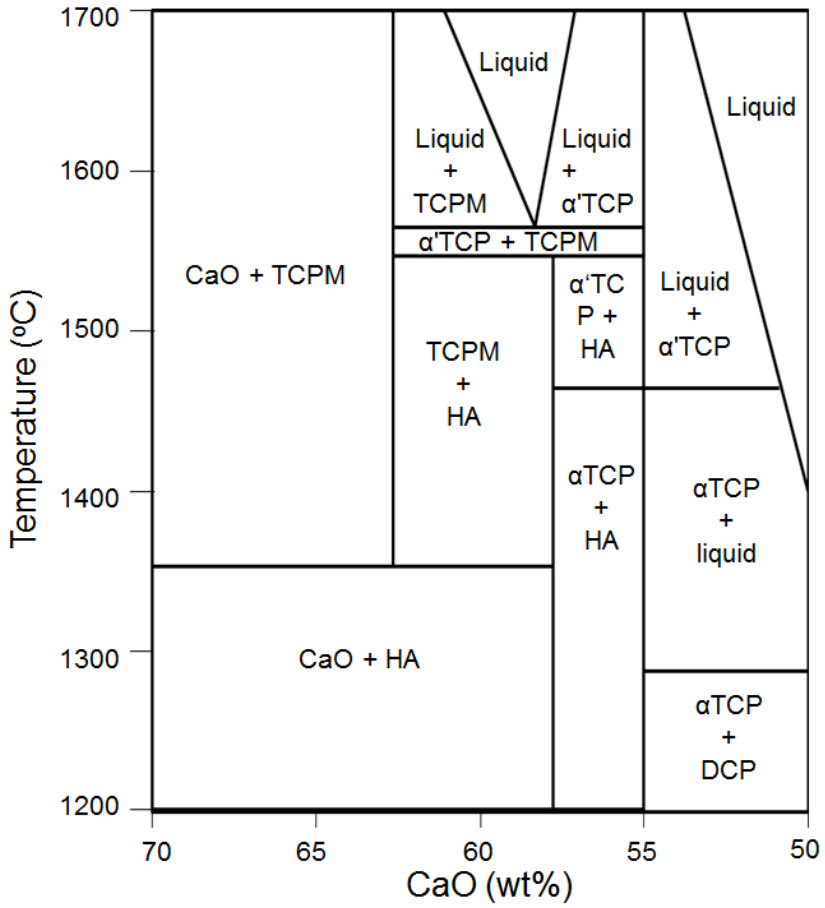

Figure 6.2: High temperature phase diagram for selected calcium phosphate systems. CaO - calcium oxide; TCPM - tetracalcium phosphate; HA - hydroxyapatite; TCP - tricalcium phosphate; DCP - dicalcium phosphate (redrawn from [528, 530])

6.2 3-D Interconnected Porous Network

6.2.1 Macrostructure

The AFR technique has been successfully implemented to produce constructs from both the 45 and 90 ppi template. The structure of the scaffolds closely replicated that of the template, regardless of which was used during manufacture to such an extent that it is expected that templates of different pore sizes could be used and the final porous network would also closely mimic their structure. This section is used to deal solely with the results surrounding the macroporosity of the as-fabricated scaffolds, with the microporous nature discussed below in Section 6.2.2. For all scaffolds, pore and strut size measurements (n=10) were taken during SEM analysis.

6.2.1.1 Effect of Variation of Sintering Temperature

The initial sintering temperature of 1100 °C was unsuitable as samples from both templates crumbled upon removal from the furnace. Samples sintered to 1150 °C were very fragile, and even those sintered to 1200 °C were unsuitable as the strength was too weak for the structures to be readily handled. Although some samples were suitable for SEM analysis, only structures coated 5 times were handleable. It is thought that the high level of porosity observed led to insufficient densification at these temperatures. As samples sintered to 1200 °C were produced with up to 5 coatings and containing no porogen, the results for these have been included. However, for all further experimental work, the minimum sintering temperature used is 1250 °C.

Samples produced using the 45 ppi foam and sintered to 1250 °C could be handled, however were still fragile and special care was required for movement. Some surface roughness was visible on the struts of the ceramics in higher magnification SEM

micrographs, shown in Section 6.2.2. The increased adherence to neighbouring particles indicated there was increased consolidation compared to samples sintered to lower temperatures as shown in Figure 6.3. The trends observed as the sintering temperature was increased from 1200-1250 °C were similar to those seen with further increases to 1300 °C and 1350 °C. Increasing the temperature led to an increase in the amount of shrinkage and hence smaller pore and strut sizes, with enhanced ease of handling of the scaffold. As such, pore sizes for scaffolds coated 5 times decreased from 507 ± 64 µm when sintered at 1200 °C to 266 ± 20 °C at 1350 °C. The strut size exhibited a slight increase between 1200 °C and 1250 °C from 91 ± 4 µm to 108 ± 7 µm, however all further increases to the sintering temperature caused decreases down to a minimum of 89 ± 8 µm at 1350 °C. The increase in strut size between these temperatures is likely to have been caused by slight variations to the pressure applied during manual squeezing as the decrease in total pore and strut size indicates increased shrinkage of the overall structure. The variation in pore and strut size over the different sintering temperatures is given in Table 6.2.

Table 6.2: Mean $\pm\sigma_{er}$ (n=10) pore and strut sizes (µm) for HA samples produced using the 45 ppi template, with 5 coats and sintered to 1200, 1250, 1300 and 1350 °C

	Template	1200 °C	1250 °C	1300 °C	1350 °C
Pore size	622 ± 28	507 ± 64	329 ± 21	302 ± 26	267 ± 20
Strut Size	95 ± 3	91 ± 4	108 ± 7	95 ± 5	89 ± 8

As with samples produced from 45 ppi templates, increasing the sintering temperature of those produced using the 90 ppi foam led to an increase in the shrinkage of the scaffolds with pore sizes decreasing from 133 ± 12 µm at 1200 °C to 100 ± 5 µm at 1350 °C. In all cases, scaffolds produced using the 90 ppi template were more stable than those produced with the more porous 45 ppi template. Samples sintered to 1200 °C could be handled, yet were fragile, while ceramics sintered to 1250 °C had greater strength and were more readily handleable. An increase to 1300 °C led to further increased mechanical properties, and elevated shrinkage, although there was no significant difference between the strut sizes of 52 ± 7 or 55 ± 3 µm. Structures

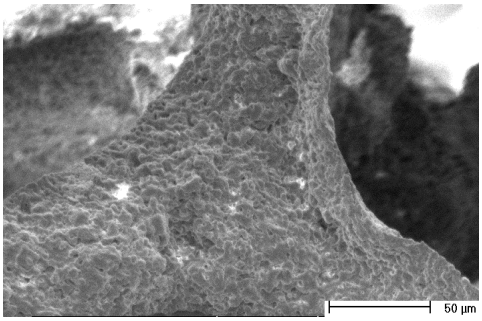

(a) SEM micrograph of scaffold sintered to 1250 °C (V = 10kV; WD = 11.1mm; mag = 500x)

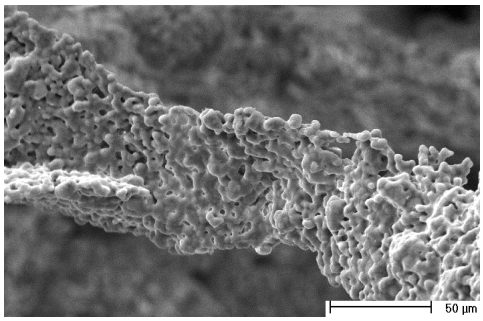

(b) SEM micrograph of scaffold sintered to 1300 °C (V = 20kV; WD = 10.1mm; mag = 500x)

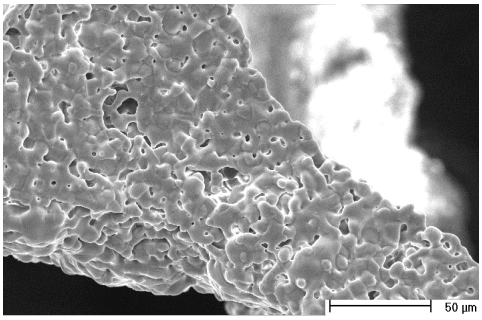

(c) SEM micrograph of scaffold sintered to 1350 °C (V = 16kV; WD = 18.0mm; mag = 500x)

Figure 6.3: SEM micrographs showing the effect of increasing the sintering temperature on the structure of HA scaffolds produced using the 45 ppi template

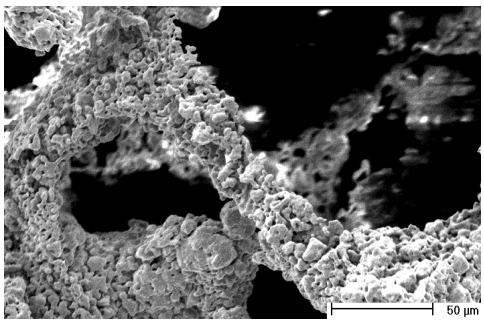

(a) SEM micrograph of scaffold sintered to 1250 °C (V = 10kV; WD = 12.8mm; mag = 500x)

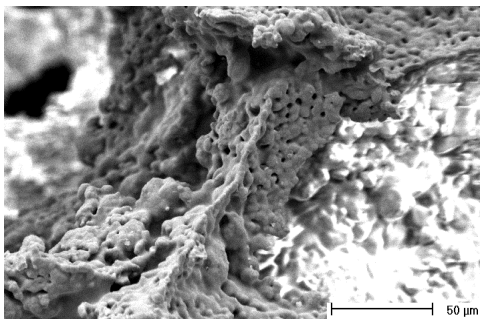

(b) SEM micrograph of scaffold sintered to 1300 °C (V = 10kV; WD = 11.4mm; mag = 500x)

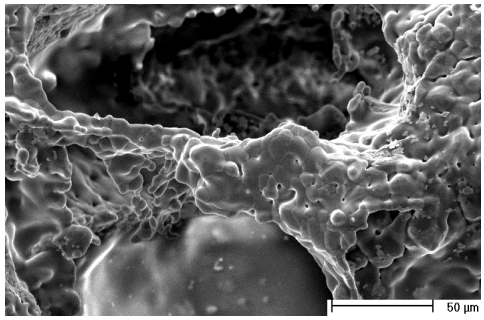

(c) SEM micrograph of scaffold sintered to 1350 °C (V = 16kV; WD = 17.1mm; mag = 500x)

Figure 6.4: SEM micrographs showing the effect of increasing the sintering temperature of HA structures produced using the 90 ppi template

sintered to 1350 °C exhibited the smallest pore and strut sizes, of 100 ± 5 µm and 46 ± 3 µm respectively. The different pore and strut sizes obtained are given in Table 6.3, with representative SEM micrographs showing increased densification of the structures in Figure 6.4.

Table 6.3: Mean $\pm\sigma_{er}$ (n=10) pore and strut sizes (µm) for HA samples produced using the 90 ppi template, with 5 coats and sintered to 1200, 1250, 1300 and 1350 °C

	Template	1200 °C	1250 °C	1300 °C	1350 °C
Pore size	253 ± 7	133 ± 12	129 ± 10	108 ± 6	100 ± 5
Strut Size	39 ± 0.9	50 ± 3	52 ± 7	55 ± 3	46 ± 3

6.2.1.2 Number of Coats

For all sintering temperatures, an increase in the number of coats led to an increased strut size and a decreased pore size. There was also greater uniformity to the strut and pore sizes as the number of coats increased as well as an elevated susceptibility to pore occlusion. The increase in pore occlusion with increasing number of coats was more noticable on samples produced using the 90 ppi template. Although this was not desired, in no case has the 3-dimensional interconnectivity been compromised and so this is not expected to have any detrimental effects on the ability of cells to fully infiltrate the structure. Representative micrographs showing the effect of the number of coatings is given in Figure 6.5 for the 45 ppi foam and Figure 6.6 for the 90 ppi foam. Finally, the number of coats did not affect the trends observed with varying the sintering temperature, as described in Section 6.2.1.1, indicating these variables act independantly when controlling the macroporous network. The relationships between sintering temperature, number of coats and pore or strut size is shown in Figures 6.7 and 6.8 for samples produced using the 45 and 90 ppi foams respectively.

6.2.1.3 Porogen Inclusion

The macrostructure of scaffolds fabricated with varying amounts of porogen was evaluated using SEM. From the representative micrographs shown in Figure 6.9, it is possible to see that, microstructural characteristics aside, the struts have not been significantly impacted by the inclusion of the porogen. In most cases, the pore and strut sizes are within the typically accepted experimental variation of 10 %. Furthermore, the trends observed when varying the sintering temperature and number of coats, as discussed above in Sections 6.2.1.1 and 6.2.1.2 are not affected, with graphical representation of the relationships between the amount of porogen in the slurry, number of coats of the slurry on the template and pore and strut size of the scaffold shown in Figures 6.10, 6.11 and 6.12 for constructs fabricated using the

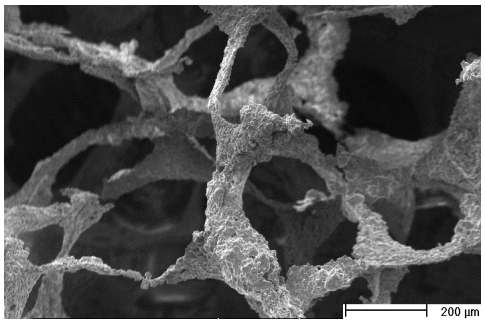

(a) SEM micrograph of scaffold sintered to 1350 °C with 1 coat (V = 16kV; WD = 18.1mm; mag = 100x)

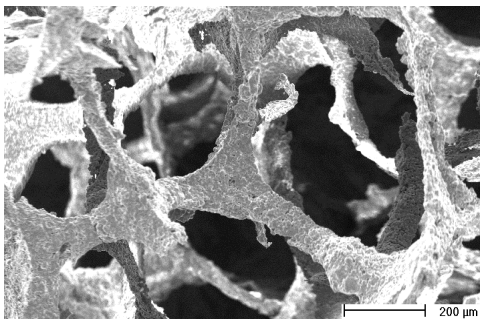

(b) SEM micrograph of scaffold sintered to 1350 °C with 2 coats (V = 16kV; WD = 18.4mm; mag = 100x)

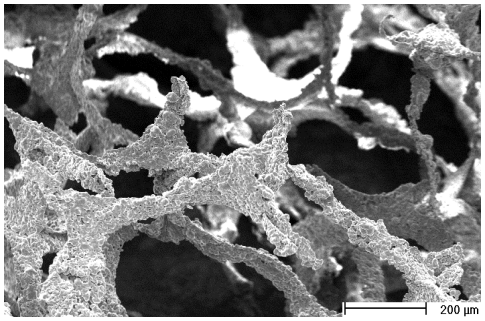

(c) SEM micrograph of scaffold sintered to 1350 °C with 3 coats (V = 16kV; WD = 17.2mm; mag = 100x)

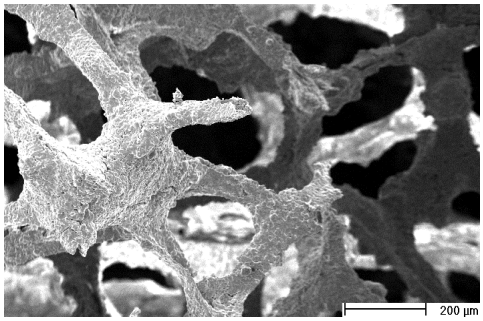

(d) SEM micrograph of scaffold sintered to 1350 °C with 4 coats (V = 16kV; WD = 16.9mm; mag = 100x)

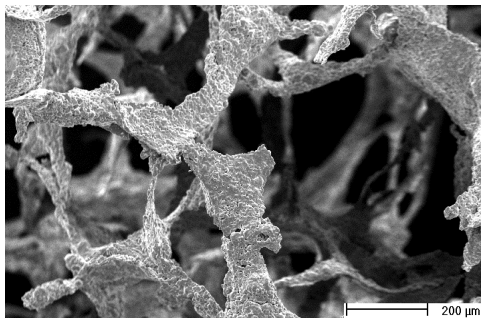

(e) SEM micrograph of scaffold sintered to 1350 °C with 5 coats (V = 16kV; WD = 16.9mm; mag = 100x)

Figure 6.5: SEM micrographs showing the effect of increasing the number of coats on the structure of HA scaffolds produced using the 45 ppi template

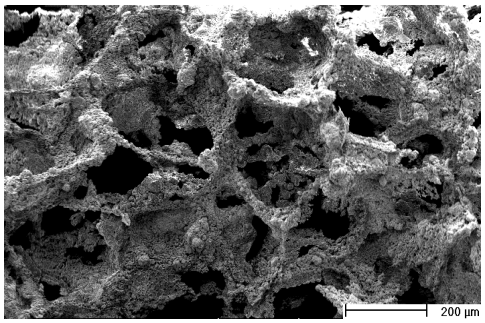

(a) SEM micrograph of scaffold sintered to 1250 °C with 1 coat (V = 10kV; WD = 13.0mm; mag = 100x)

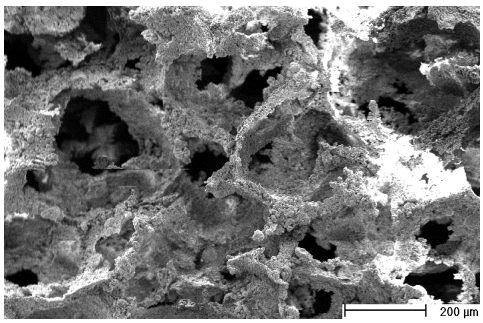

(b) SEM micrograph of scaffold sintered to 1250 °C with 2 coats (V = 10kV; WD = 10.7mm; mag = 100x)

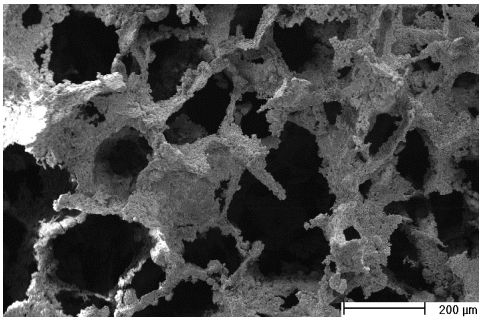

(c) SEM micrograph of scaffold sintered to 1250 °C with 3 coats (V = 10kV; WD = 12.0mm; mag = 100x)

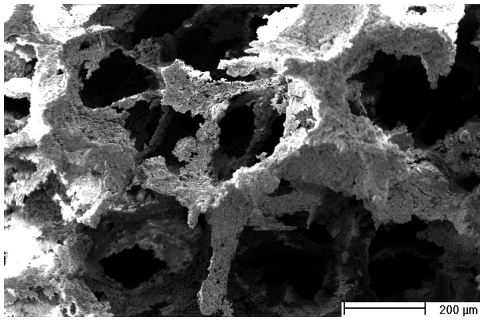

(d) SEM micrograph of scaffold sintered to 1250 °C with 4 coats (V = 10kV; WD = 11.4mm; mag = 100x)

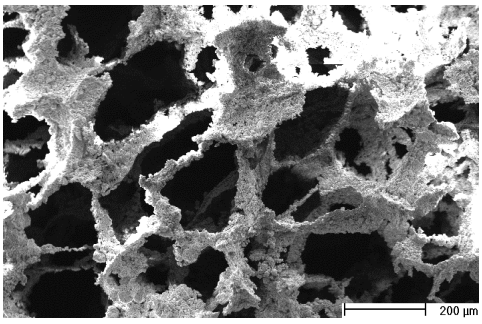

(e) SEM micrograph of scaffold sintered to 1250 °C with 5 coats (V = 10kV; WD = 10.9mm; mag = 100x)

Figure 6.6: SEM micrographs showing the effect of increasing the number of coats of HA structures produced using the 90 ppi template

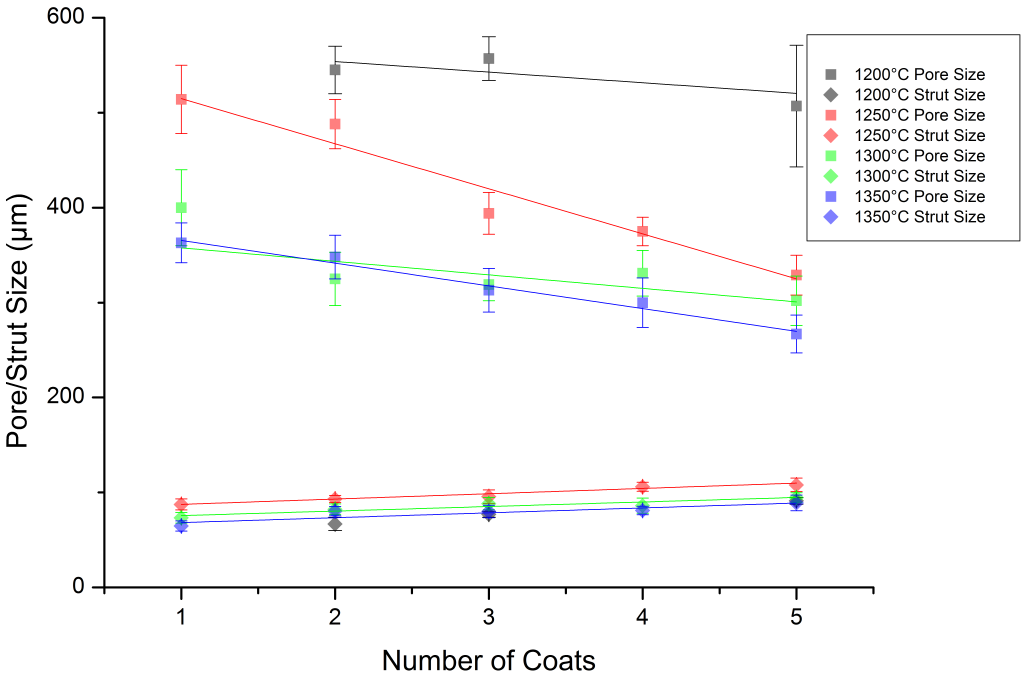

Figure 6.7: Graph showing how the pore and strut size varies with the number of coats and sintering temperature on HA samples produced using the 45 ppi template

45 ppi template and sintered to 1250, 1300 and 1350 °C respectively, and in Figures 6.13, 6.14 and 6.15 for those from the 90 ppi template.

6.2.1.4 Freezing Temperature

The freezing temperature of the scaffolds could be varied by changing their location within the freeze dryer. Scaffolds placed on the bottom shelf had internal surface temperatures of 10 °C after freezing for 4 hrs, whilst those placed directly on the condenser were -20 °C. Variations to the freezing temperature during production had little effect on the macrostructure of the scaffolds, with the pore and strut sizes shown graphically in Figures 6.16 and 6.17. Representative micrographs are shown in Figures 6.18 and 6.20 for structures produced from the 45 and 90 ppi foams respectively when the constructs were frozen to 10 °C, and in Figures 6.19 and 6.21 when the structures were frozen to -20 °C. Particularly with the lower temperature,

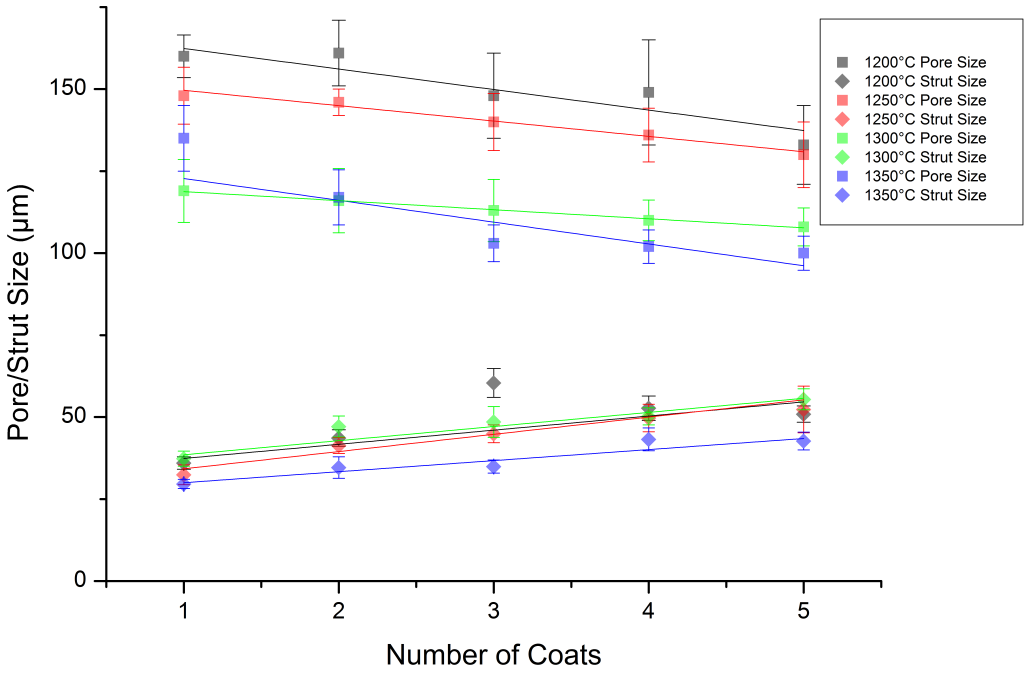

Figure 6.8: Graph showing how the pore and strut size varies with the number of coats and sintering temperature on HA samples produced using the 90ppi template

there is a more obvious effect on the microstructure, as discussed below, however from the micrographs it is clear that there is no effect on the structure of the macroporous network. Furthermore, the graphs show the strut sizes in particular are very similar regardless of the freezing temperature. There is some variation to the pore size between structures frozen to different temperatures with similar porogen contents, however this is not consistent.

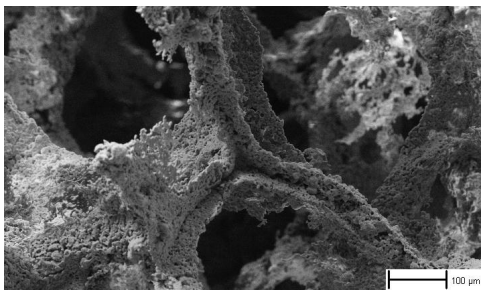

(a) SEM micrograph showing macrostructure of sample produced without camphene (V = 20kV; WD = 5.5mm; mag = 250x)

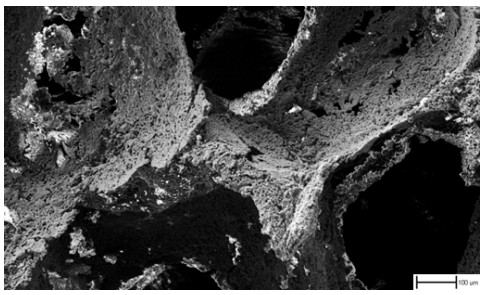

(b) SEM micrograph showing macrostructure of sample produced with 5% camphene (V = 15kV; WD = 8.2mm; mag = 250x)

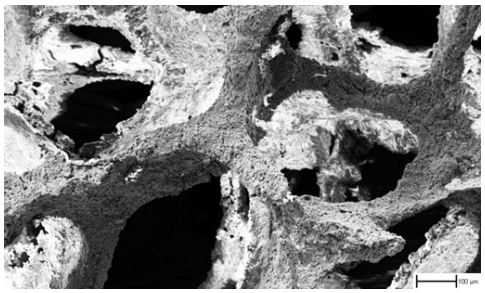

(c) SEM micrograph showing macrostructure of sample produced with 10% camphene (V = 15kV; WD = 8.0mm; mag = 250x)

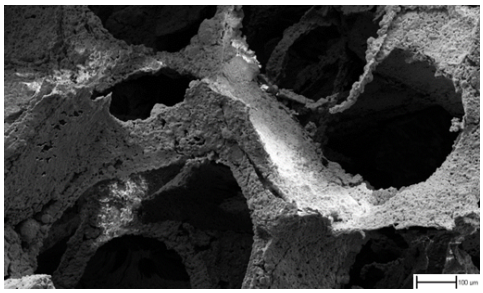

(d) SEM micrograph showing macrostructure of sample produced with 20% camphene (V = 10kV; WD = 10.5mm; mag = 250x)

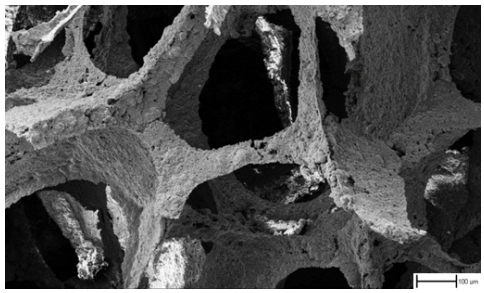

(e) SEM micrograph showing macrostructure of sample produced with 25% camphene (V = 10kV; WD = 12.0mm; mag = 250x)

Figure 6.9: Representative SEM micrographs showing the macrostructure of HA scaffolds produced via AFR using the 45 ppi template, with increasing camphene content through 0, 5, 10, 20 and 25 wt.%

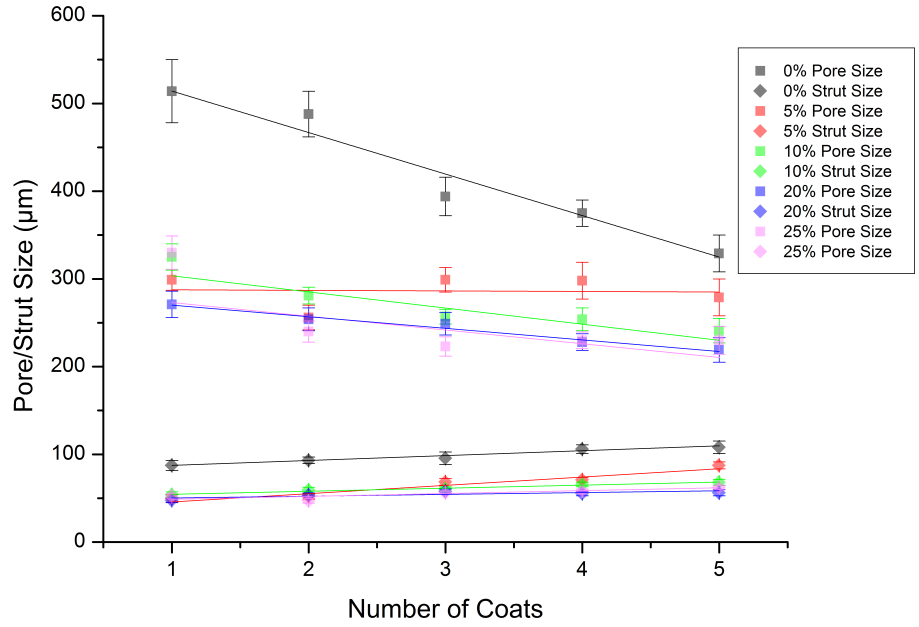

Figure 6.10: Graph showing the relationships between number of coats, porogen content and pore/strut size of scaffolds fabricated using the 45 ppi template and sintered to 1250 °C

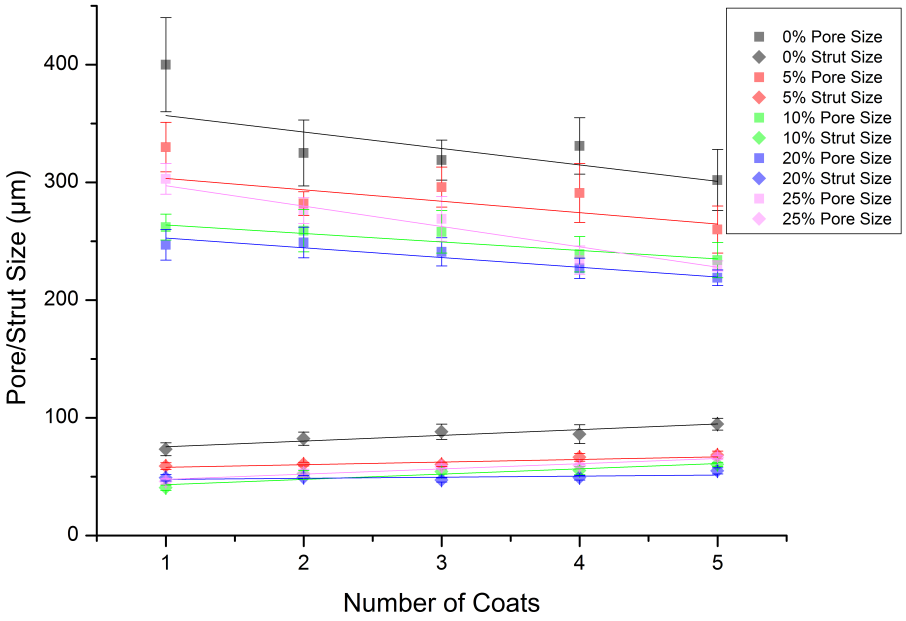

Figure 6.11: Graph showing the relationships between number of coats, porogen content and pore/strut size of scaffolds fabricated using 45 ppi template and sintered to 1300 °C

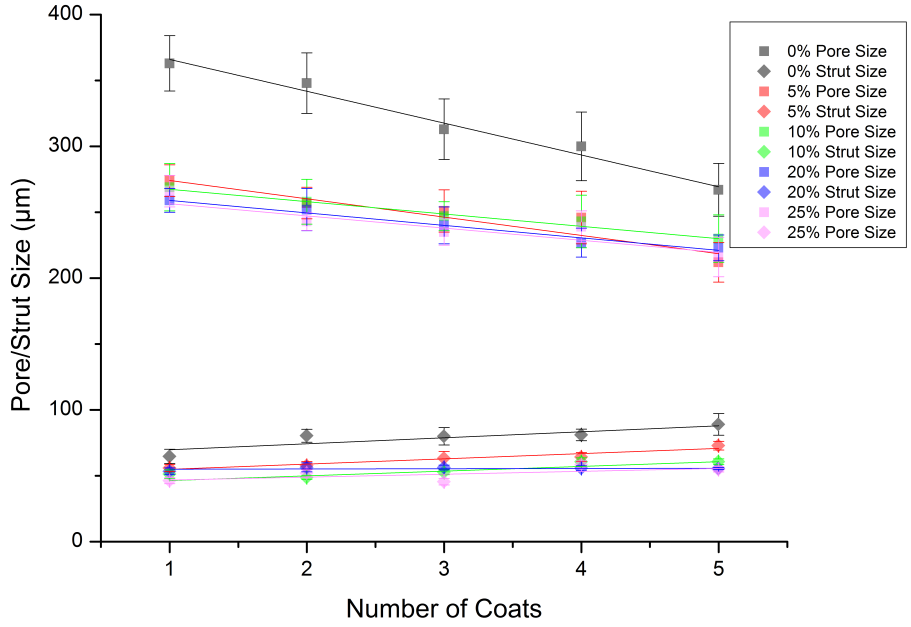

Figure 6.12: Graph showing the relationships between number of coats, porogen content and pore/strut size of scaffolds fabricated using the 45 ppi template and sintered to 1350 °C

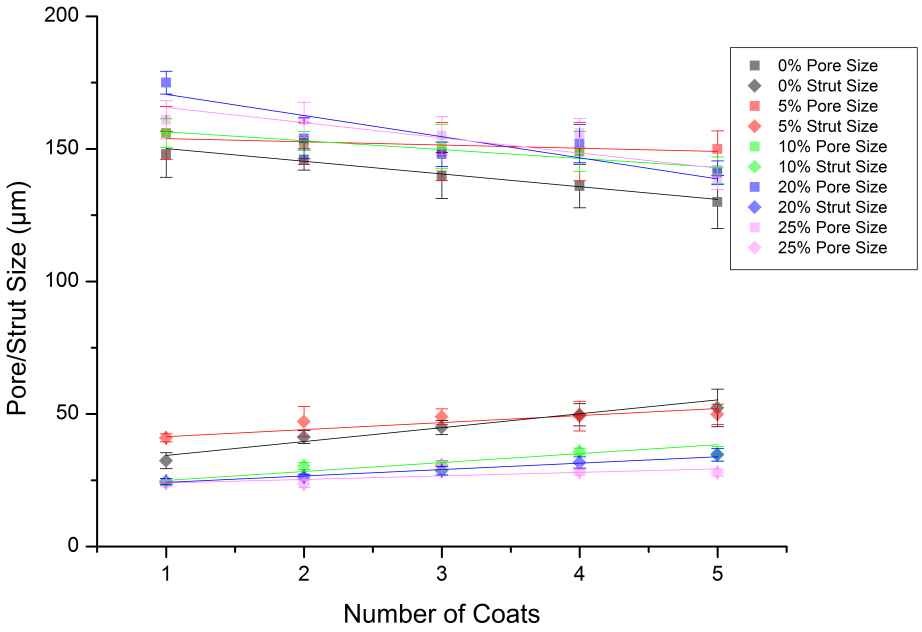

Figure 6.13: Graph showing the relationships between number of coats, porogen content and pore/strut size of scaffolds fabricated using the 90 ppi template and sintered to 1250 °C

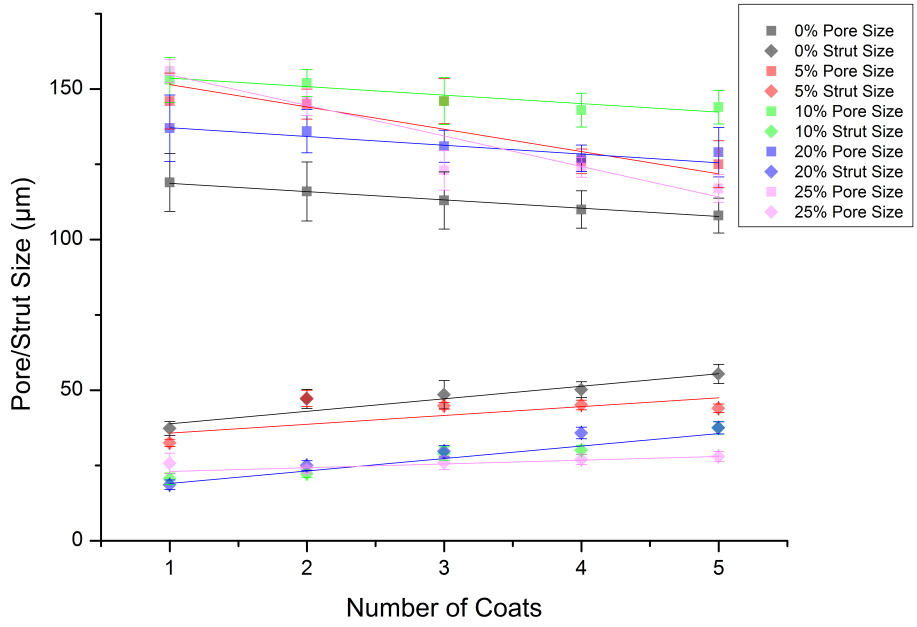

Figure 6.14: Graph showing the relationships between number of coats, porogen content and pore/strut size of scaffolds fabricated using the 90 ppi template and sintered to 1300 °C

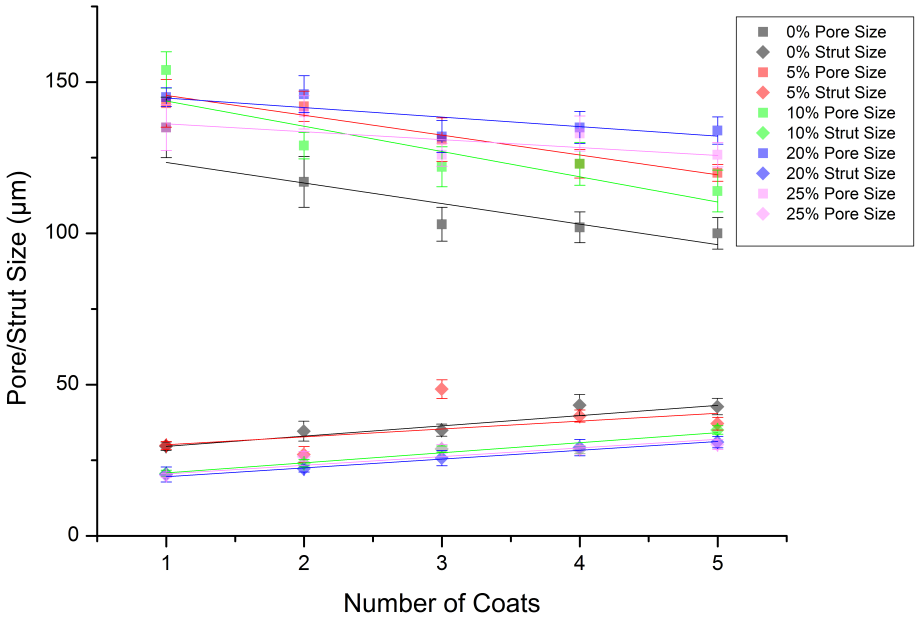

Figure 6.15: Graph showing the relationships between number of coats, porogen content and pore/strut size of scaffolds fabricated using the 90 ppi template and sintered to 1350 °C

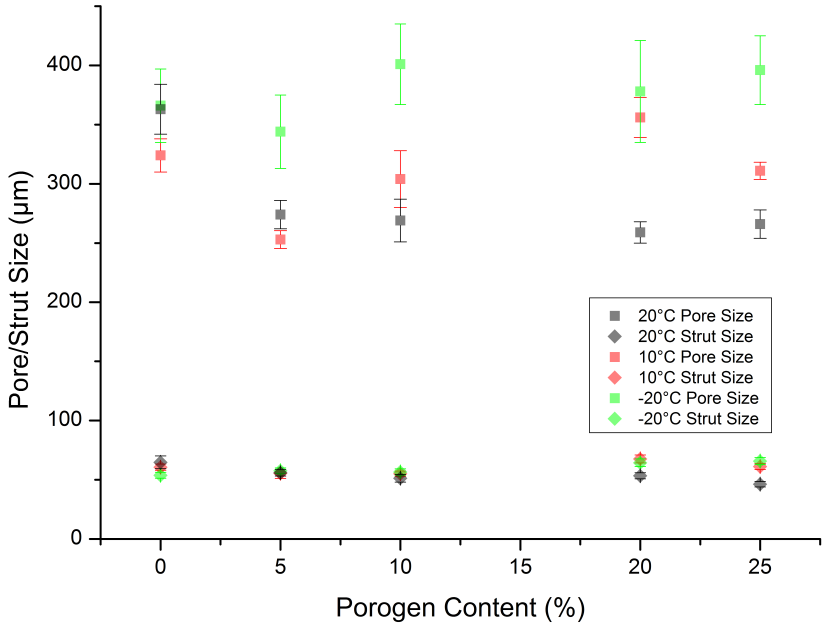

Figure 6.16: Graph showing relationship between porogen content, freezing temperature and pore/strut size of scaffolds fabricated using 45 ppi template and sintered to 1300 °C

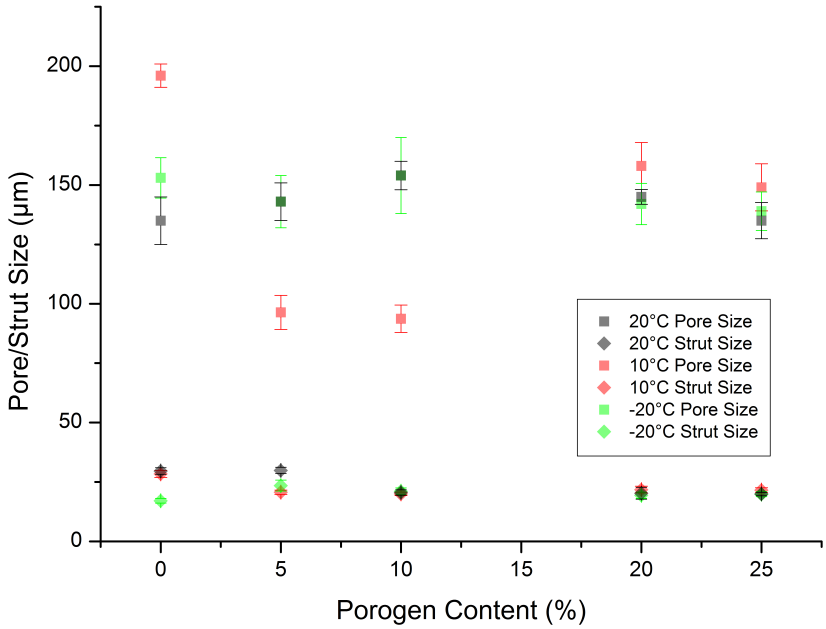

Figure 6.17: Graph showing relationship between porogen content, freezing temperature and pore/strut size of scaffolds fabricated using 90 ppi template and sintered to 1300 °C

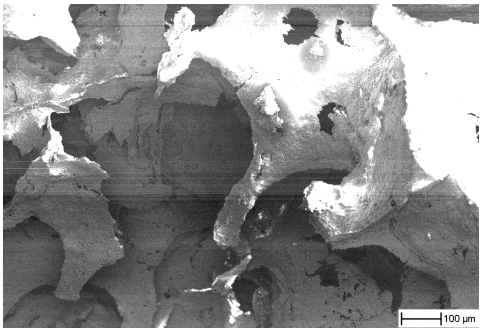

(a) SEM micrograph showing macrostructure of sample produced without camphene (V = 20kV; WD = 8.9mm; mag = 250x)

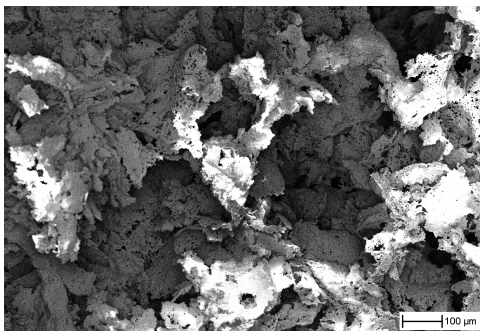

(b) SEM micrograph showing macrostructure of sample produced with 5% camphene (V = 15kV; WD = 9.7mm; mag = 250x)

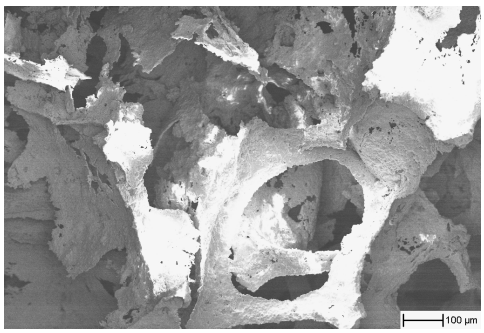

(c) SEM micrograph showing macrostructure of sample produced with 10% camphene (V = 15kV; WD = 8.4mm; mag = 250x)

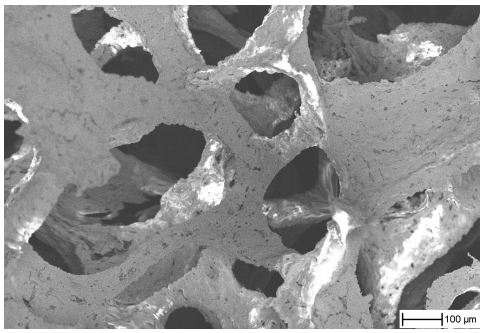

(d) SEM micrograph showing macrostructure of sample produced with 20% camphene (V = 15kV; WD = 9.2mm; mag = 250x)

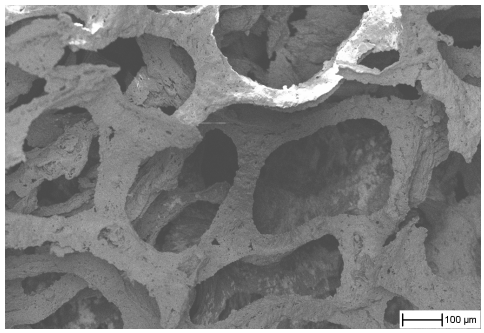

(e) SEM micrograph showing macrostructure of sample produced with 25% camphene (V = 15kV; WD = 10.3mm; mag = 250x)

Figure 6.18: Representative SEM micrographs showing the macrostructure of HA scaffolds produced via AFR using the 45 ppi template, with increasing camphene content through 0, 5, 10, 20 and 25 wt.% when the surface of the scaffold was frozen to 10 °C during production

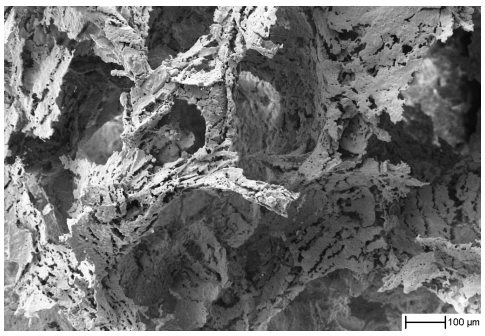

(a) SEM micrograph showing macrostructure of sample produced without camphene (V = 20kV; WD = 8.9mm; mag = 250x)

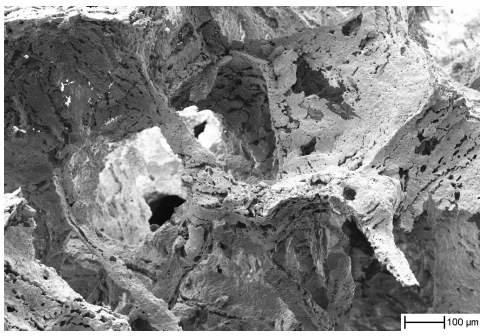

(b) SEM micrograph showing macrostructure of sample produced with 5% camphene (V = 15kV; WD = 9.7mm; mag = 250x)

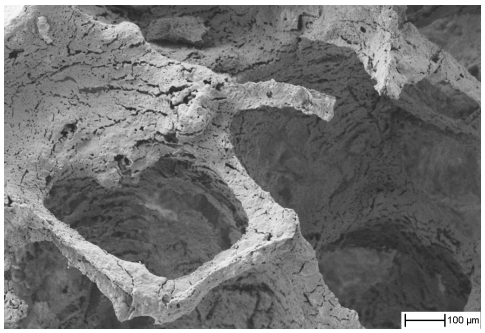

(c) SEM micrograph showing macrostructure of sample produced with 10% camphene (V = 15kV; WD = 8.4mm; mag = 250x)

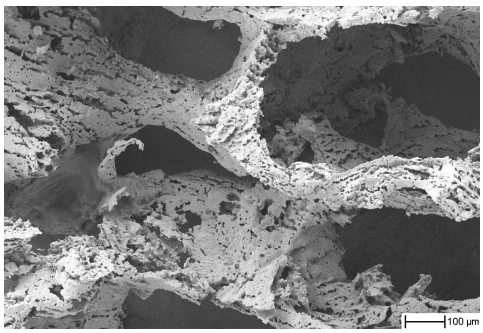

(d) SEM micrograph showing macrostructure of sample produced with 20% camphene (V = 15kV; WD = 9.2mm; mag = 250x)

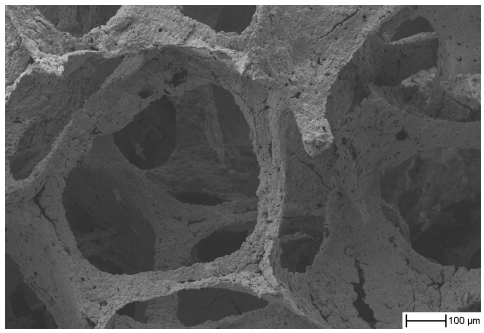

(e) SEM micrograph showing macrostructure of sample produced with 25% camphene (V = 15kV; WD = 10.3mm; mag = 250x)

Figure 6.19: Representative SEM micrographs showing the macrostructure of HA scaffolds produced via AFR using the 45 ppi template, with increasing camphene content through 0, 5, 10, 20 and 25 wt.% when the surface of the scaffold was frozen to -20 °C during production

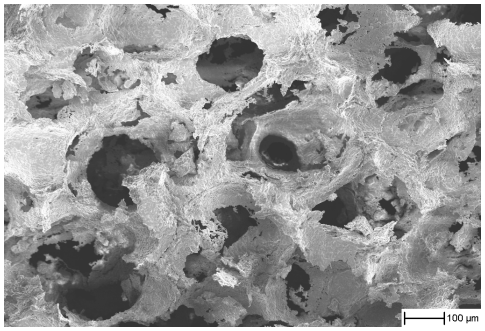

(a) SEM micrograph showing macrostructure of sample produced without camphene (V = 5kV; WD = 9.3mm; mag = 250x)

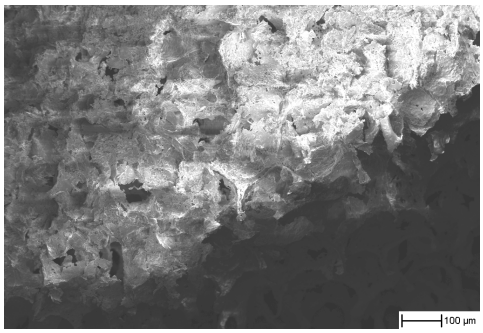

(b) SEM micrograph showing macrostructure of sample produced with 5% camphene (V = 5kV; WD = 8.4mm; mag = 250x)

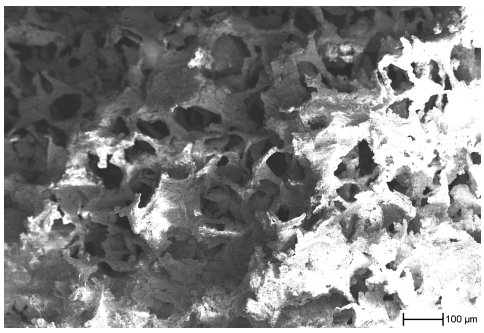

(c) SEM micrograph showing macrostructure of sample produced with 10% camphene (V = 5kV; WD = 8.5mm; mag = 250x)

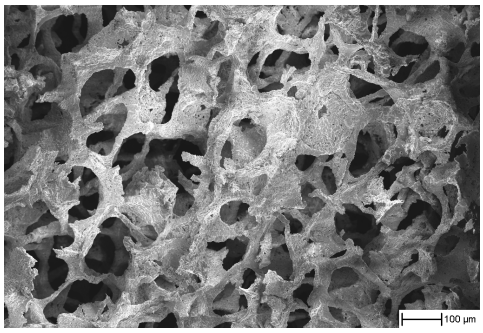

(d) SEM micrograph showing macrostructure of sample produced with 20% camphene (V = 5kV; WD = 9.2mm; mag = 250x)

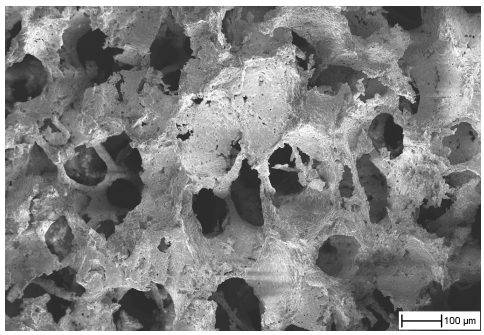

(e) SEM micrograph showing macrostructure of sample produced with 25% camphene (V = 5kV; WD = 10.7mm; mag = 250x)

Figure 6.20: Representative SEM micrographs showing the macrostructure of HA scaffolds produced via AFR using the 90 ppi template, with increasing camphene content through 0, 5, 10, 20 and 25 wt.% when the surface of the scaffold was frozen to 10 °C during production

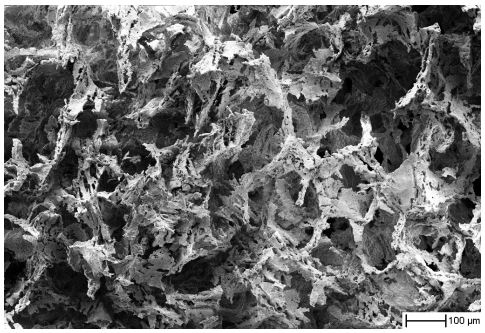

(a) SEM micrograph showing macrostructure of sample produced without camphene (V = 5kV; WD = 9.3mm; mag = 250x)

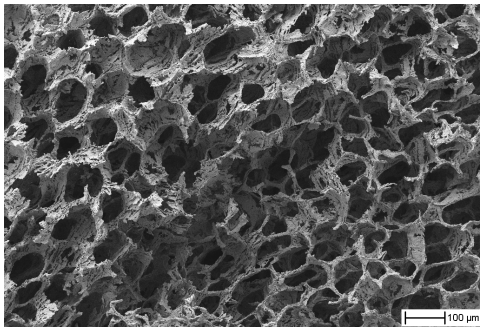

(b) SEM micrograph showing macrostructure of sample produced with 5% camphene (V = 5kV; WD = 8.4mm; mag = 250x)

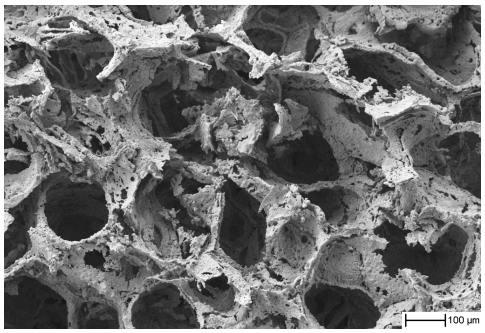

(c) SEM micrograph showing macrostructure of sample produced with 10% camphene (V = 5kV; WD = 8.5mm; mag = 250x)

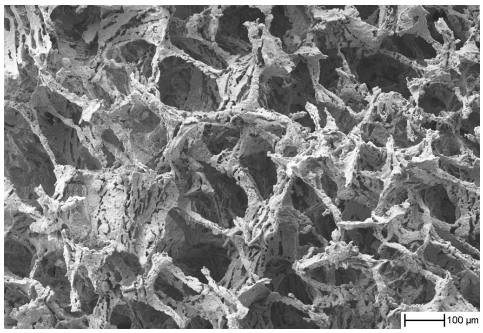

(d) SEM micrograph showing macrostructure of sample produced with 20% camphene (V = 5kV; WD = 9.2mm; mag = 250x)

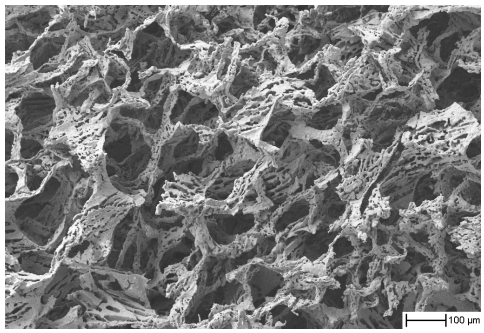

(e) SEM micrograph showing macrostructure of sample produced with 25% camphene (V = 5kV; WD = 10.7mm; mag = 250x)

Figure 6.21: Representative SEM micrographs showing the macrostructure of HA scaffolds produced via AFR using the 90 ppi template, with increasing camphene content through 0, 5, 10, 20 and 25 wt.% when the surface of the scaffold was frozen to -20 °C during production

6.2.2 Microstructure

6.2.2.1 Porogen Inclusion

Inclusion of a porogen into the slurry led to the generation of micropores. Camphene is a solid at room temperature, hence drying at this temperature led to microporous struts. The size of individual micropores was between 1-5 μm, regardless of the level of porogen included. As the camphene content was increased, the amount and density of these micropores also increased for structures from both templates, as shown in Figures 6.22 and 6.23 for those from the 45 and 90 ppi foams respectively. Particularly at the highest levels of porgen, this led to some coalescence, causing larger micropores of up to 20-30 μm. However, the level and amount of coalescence was not controllable despite mixing of the slurries for 24 h before casting.

6.2.2.2 Freezing temperature

Freezing of the scaffolds on the bottom shelf of the freeze dryer (10 °C) led to the production of larger micropores than when the equivalent amount of porogen was frozen at room temperature, as shown in Figures 6.24 and 6.25 for structures from the 45 and 90 ppi templates respectively. This is due to the evaporation of DMC leading to solidification of camphene at this temperature. Further increases to the micropore size were seen when coated templates were placed on the condenser (-20 °C), as shown in Figures 6.26 and 6.27. The base size was increased to 5-12 μm at 10 °C with this again unaffected by the amount of porogen in the slurry, although the number and density of the micropores increased with the camphene content. Structures frozen to -20 °C exhibited an elongated microporosity, with the width of the pores 5-12 μm and lengths up to 20-30 μm. As the size of the microporosity after freezing remained constant, the decreased size of structures produced from the 90 ppi template resulted in the increased effect on the overall structure.

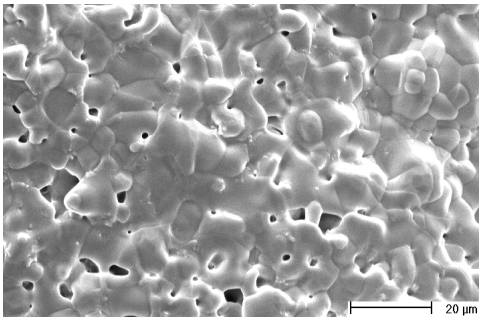

(a) SEM micrograph showing surface roughness/microporosity of scaffolds produced without camphene(V = 16kV; WD = 16.8mm; mag = 1000x)

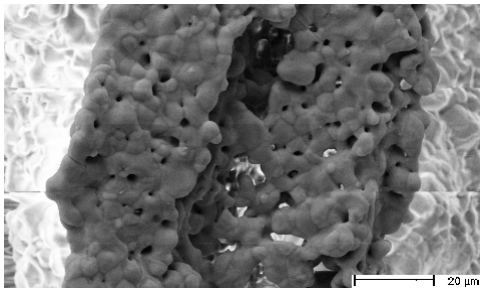

(b) SEM micrograph showing surface roughness/microporosity of scaffolds produced with 5% camphene (V = 15kV; WD = 11.1mm; mag = 1000x)

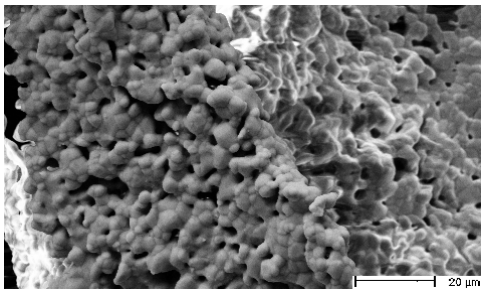

(c) SEM micrograph showing surface roughness/microporosity of scaffolds produced with 10% camphene (V = 15kV; WD = 11.8mm; mag = 1000x)

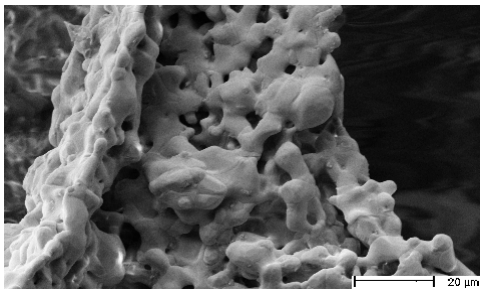

(d) SEM micrograph showing surface roughness/microporosity of scaffolds produced with 20% camphene (V = 10kV; WD = 11.5mm; mag = 1000x)

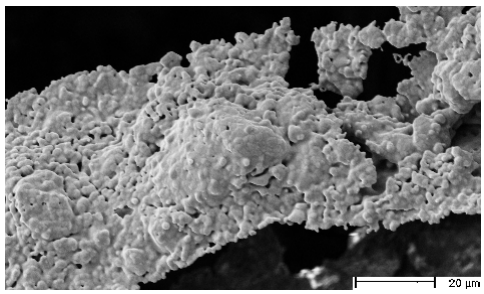

(e) SEM micrograph showing surface roughness/microporosity of scaffolds produced with 25% camphene (V = 10kV; WD = 11.2mm; mag = 1000x)

Figure 6.22: SEM micrographs showing surface roughness/microporosity on HA scaffolds produced using the AFR with the 45 ppi template, with increasing camphene content through 0, 5, 10, 20 and 25 wt.%

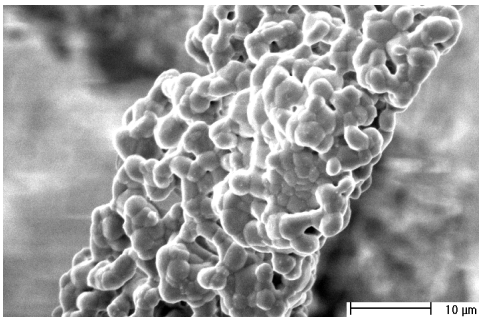

(a) SEM micrograph showing surface roughness/microporosity of scaffolds produced without camphene(V = 10kV; WD = 12.3mm; mag = 2000x)

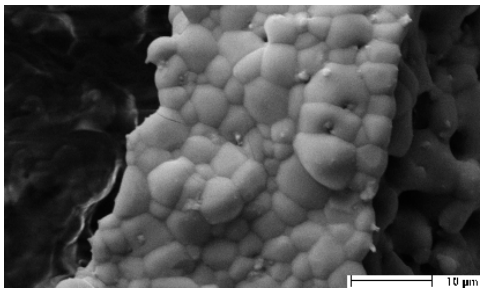

(b) SEM micrograph showing surface roughness/microporosity of scaffolds produced with 5% camphene (V = 15kV; WD = 10.0mm; mag = 2000x)

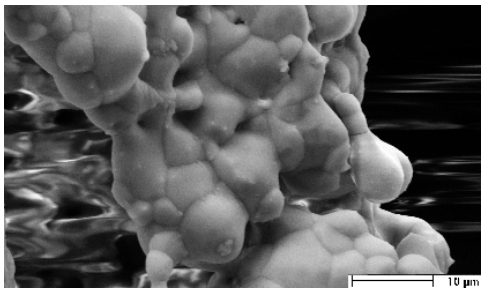

(c) SEM micrograph showing surface roughness/microporosity of scaffolds produced with 10% camphene (V = 15kV; WD = 10.3mm; mag = 2000x)

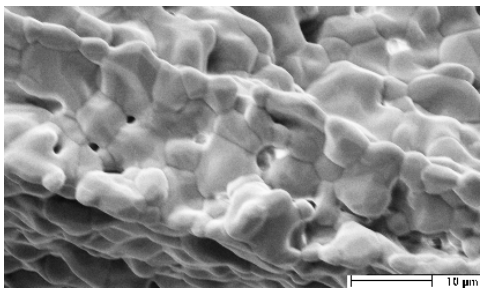

(d) SEM micrograph showing surface roughness/microporosity of scaffolds produced with 20% camphene (V = 10kV; WD = 12.0mm; mag = 2000x)

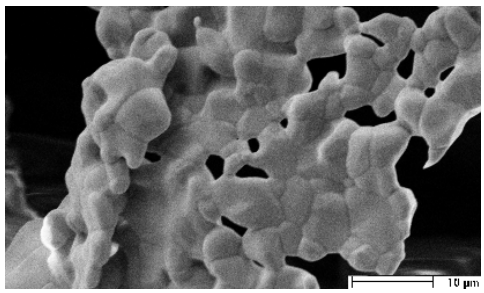

(e) SEM micrograph showing surface roughness/microporosity of scaffolds produced with 25% camphene (V = 10kV; WD = 11.5mm; mag = 2000x)

Figure 6.23: SEM micrographs showing surface roughness/microporosity on HA scaffolds produced using the AFR with the 90 ppi template, with increasing camphene content through 0, 5, 10, 20 and 25 wt.%

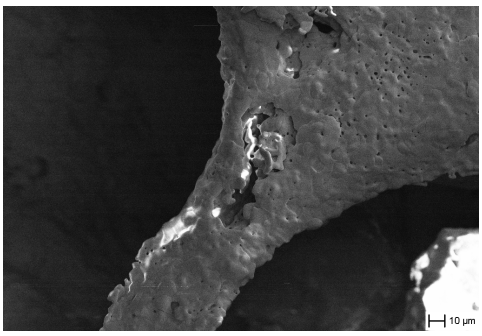

(a) SEM micrograph showing microstructure of sample produced without camphene (V = 15kV; WD = 9.0mm; mag = 1000x)

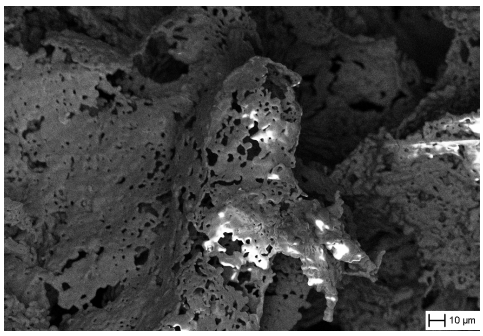

(b) SEM micrograph showing macrostructure of sample produced with 5% camphene (V = 15kV; WD = 9.4mm; mag = 1000x)

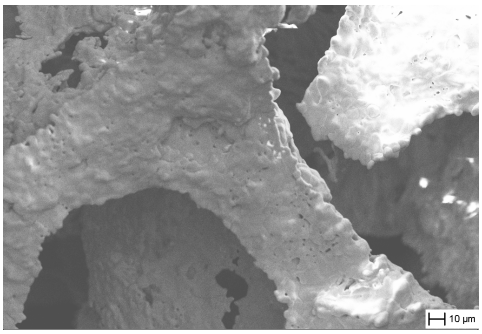

(c) SEM micrograph showing macrostructure of sample produced with 10% camphene (V = 15kV; WD = 8.4mm; mag = 1000x)

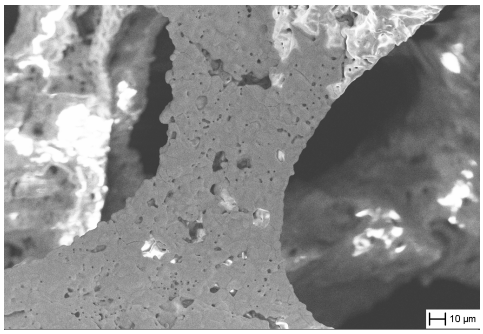

(d) SEM micrograph showing macrostructure of sample produced with 20% camphene (V = 15kV; WD = 9.2mm; mag = 1000x)

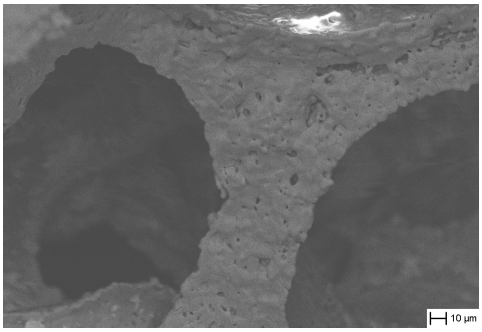

(e) SEM micrograph showing macrostructure of sample produced with 25% camphene (V = 15kV; WD = 10.3mm; mag = 1000x)

Figure 6.24: Representative SEM micrographs showing the microstructure of HA scaffolds produced via AFR using the 45 ppi template, with increasing camphene content through 0, 5, 10, 20 and 25 wt.% when frozen to 10 °C during production

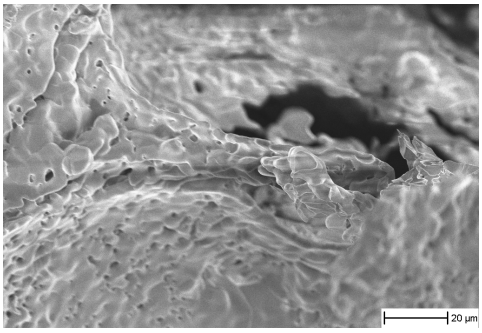

(a) SEM micrograph showing microstructure of sample produced without camphene (V = 5kV; WD = 9.2mm; mag = 2000x)

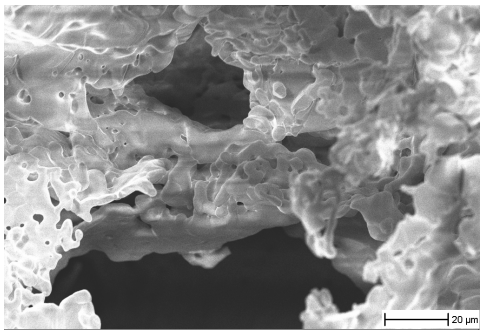

(b) SEM micrograph showing macrostructure of sample produced with 5% camphene (V = 5kV; WD = 8.5mm; mag = 2000x)

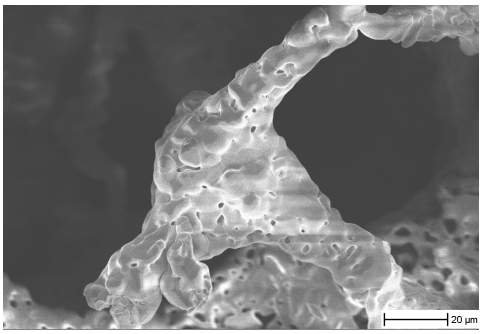

(c) SEM micrograph showing macrostructure of sample produced with 10% camphene (V = 5kV; WD = 8.6mm; mag = 2000x)

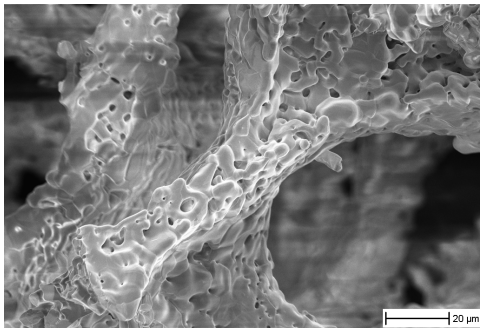

(d) SEM micrograph showing macrostructure of sample produced with 20% camphene (V = 5kV; WD = 9.1mm; mag = 2000x)

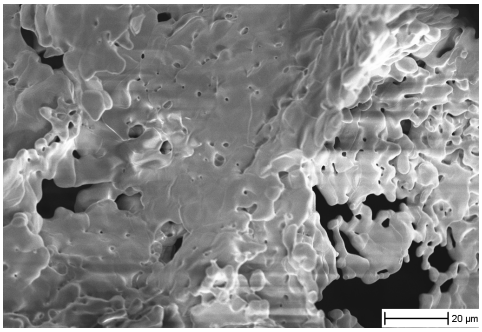

(e) SEM micrograph showing macrostructure of sample produced with 25% camphene (V = 5kV; WD = 10.0mm; mag = 2000x)

Figure 6.25: Representative SEM micrographs showing the microstructure of HA scaffolds produced via AFR using the 90 ppi template, with increasing camphene content through 0, 5, 10, 20 and 25 wt.% when frozen to 10 °C during production

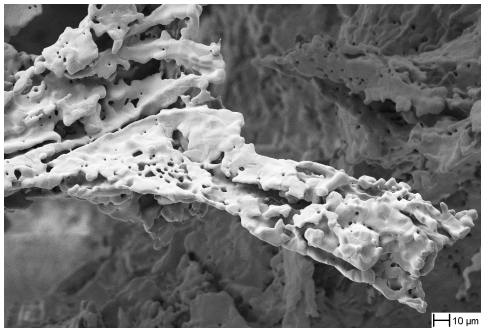

(a) SEM micrograph showing microstructure of sample produced without camphene (V = 15kV; WD = 9.0mm; mag = 1000x)

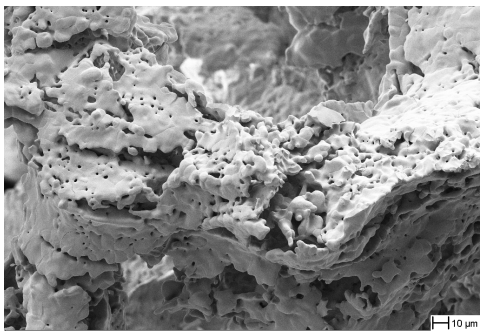

(b) SEM micrograph showing macrostructure of sample produced with 5% camphene (V = 15kV; WD = 9.4mm; mag = 1000x)

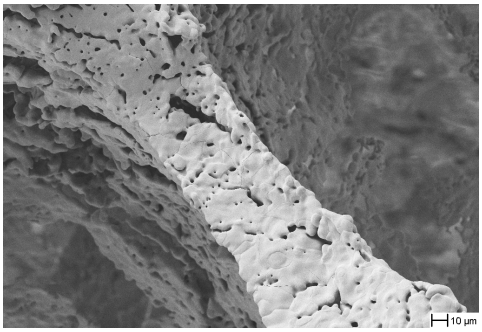

(c) SEM micrograph showing macrostructure of sample produced with 10% camphene (V = 15kV; WD = 8.4mm; mag = 1000x)

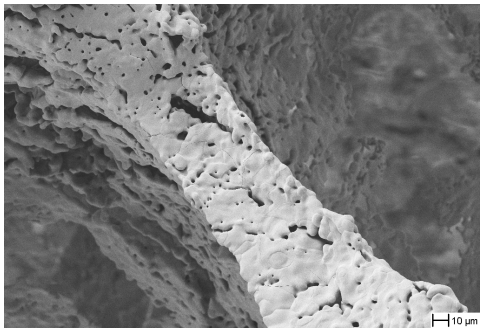

(d) SEM micrograph showing macrostructure of sample produced with 20% camphene (V = 15kV; WD = 9.2mm; mag = 1000x)

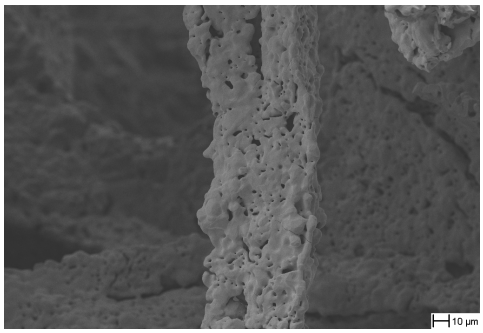

(e) SEM micrograph showing macrostructure of sample produced with 25% camphene (V = 15kV; WD = 10.3mm; mag = 1000x)

Figure 6.26: Representative SEM micrographs showing the microstructure of HA scaffolds produced via AFR using the 45 ppi template, with increasing camphene content through 0, 5, 10, 20 and 25 wt.% when frozen to -20 °C during production

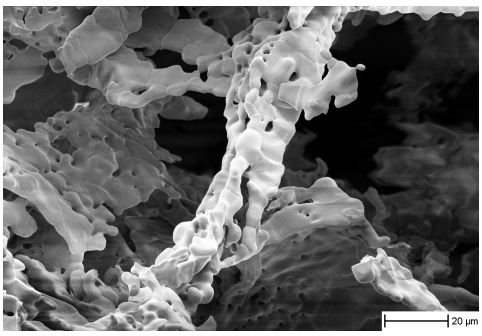

(a) SEM micrograph showing microstructure of sample produced without camphene (V = 5kV; WD = 9.2mm; mag = 2000x)

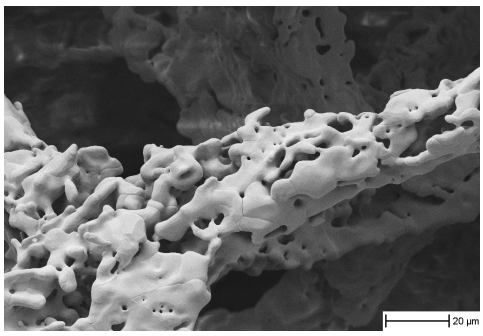

(b) SEM micrograph showing macrostructure of sample produced with 5% camphene (V = 5kV; WD = 8.5mm; mag = 2000x)

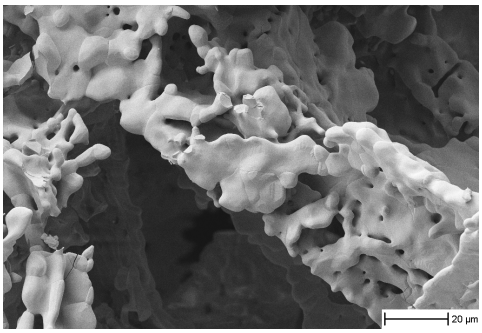

(c) SEM micrograph showing macrostructure of sample produced with 10% camphene (V = 5kV; WD = 8.6mm; mag = 2000x)

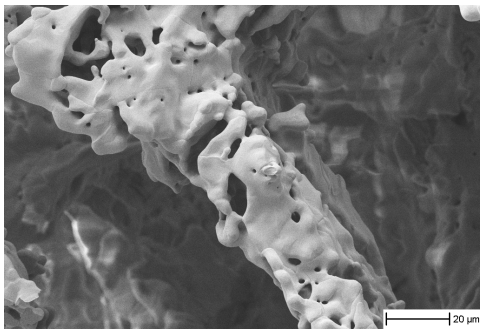

(d) SEM micrograph showing macrostructure of sample produced with 20% camphene (V = 5kV; WD = 9.1mm; mag = 2000x)

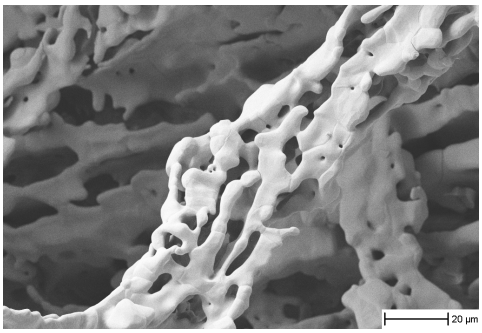

(e) SEM micrograph showing macrostructure of sample produced with 25% camphene (V = 5kV; WD = 10.0mm; mag = 2000x)

Figure 6.27: Representative SEM micrographs showing the microstructure of HA scaffolds produced via AFR using the 90 ppi template, with increasing camphene content through 0, 5, 10, 20 and 25 wt.% when frozen to -20 °C during production

6.2.3 Porosity

Porosity measurements were taken using the Archimedes method, with selected samples also analysed using microCT. The Archimedes method was used as it provides porosity values for the whole structure undergoing analysis and is able to account for both macro and microporosity. This overcomes the limitations of both image analysis, relating to the fact that only the selected area is analysed, and of microCT, due to reports that the porosity is underestimated due to resolution limits. Although a higher resolution machine has been used in this work, the accuracy needs verification, hence Archimedes method has also been used. The dry, submerged and wet masses of each sample were measured and used to calculate the relative density, using Equation 4.6, and hence the porosity, using Equation 4.7, with graphical representations of the results shown in Figures 6.28 - 6.30 and 6.31 - 6.33 for structures from the 45 ppi and 90 ppi templates respectively and in Figures 6.34 and 6.35 for scaffolds frozen during production.

For most scaffolds, increasing the number of coats led to a decrease in the level of porosity. As the pore size was decreased and the strut size was increased, this was expected. Furthermore, it followed other reports in the literature [270]. It was not always the case however, as described in the following paragraphs, and it is thought that variations were caused by slight variations during processing that were exacerbated by significant shrinkage during sintering. Additionally, scaffolds produced with more camphene inclusion were expected to have higher porosities, however this was not consistently observed. This is again thought to have been a result of processing variations being exagarated dufing template removal and sintering.

Structures fabricated from the 45 ppi template had porosities ranging from 82 - 96%, whilst those from the 90 ppi template were between 85 and 96%. Varying the number of coats, the sintering temperature, shown in Figure 6.36, or the porogen content in the slurry had little effect on the porosity of scaffolds produced using the 45 ppi template. Although there was a slight decrease, the porosity of structures from the

90 ppi template did not vary significantly with increases to the sintering temperture as shown in Figure 6.37. Additionally, there was little change with variations to the porogen content on structures from the 90 ppi template. However, increasing the number of coats from one to five led to an average decrease in the porosity of $3.6 \pm 1.0\%$. The only scaffolds which increased in porosity were those sintered to 1350 °C and with 10% porogen (which stayed the same) and 20% porogen (which increased by 2%).

Variations to the freezing temperature had no consistent effect on the porosity of scaffolds from either template. However, scaffolds frozen to -20 °C during production exhibited a decrease in porosity of approximately 5% between 10 and 20% porogen inclusion compared to those frozen to 10 and 20 °C. It is thought that this may be due to the greater number of larger ice dendrites facilitating a more complete removal of the polymeric template at a slightly lower temperature. Thus, the level of densification during sintering is slightly higher. Alternatively, slight variations to the degree of coating on the template may have occurred during processing. Thus, there may have been a slight increase in the amount of material coated onto the template or to level of pore occlusion that would increase the overall porosity.

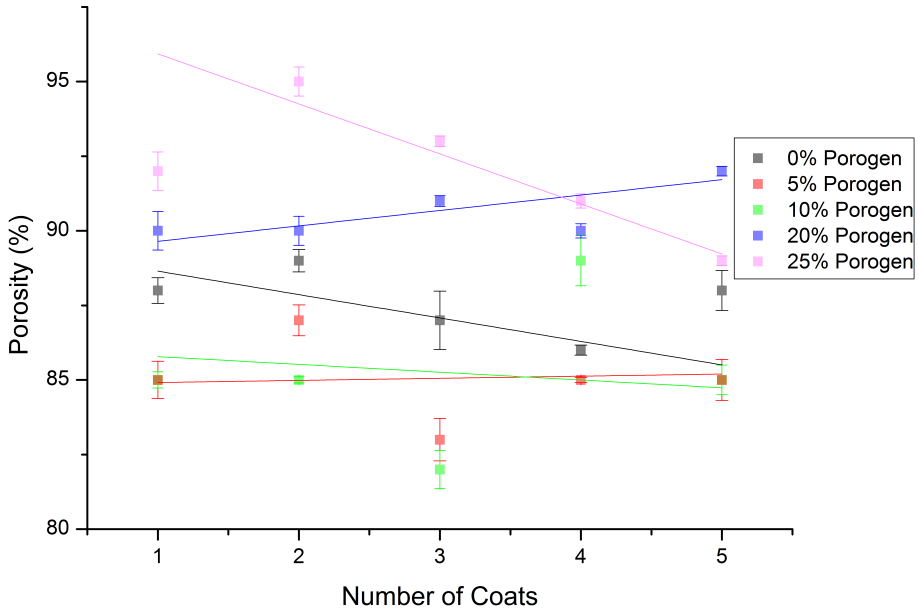

Figure 6.29: Porosity (%) of scaffolds fabricated using the 45 ppi template and sintered to 1300°C, with varying porogen content and number of coats of the slurry

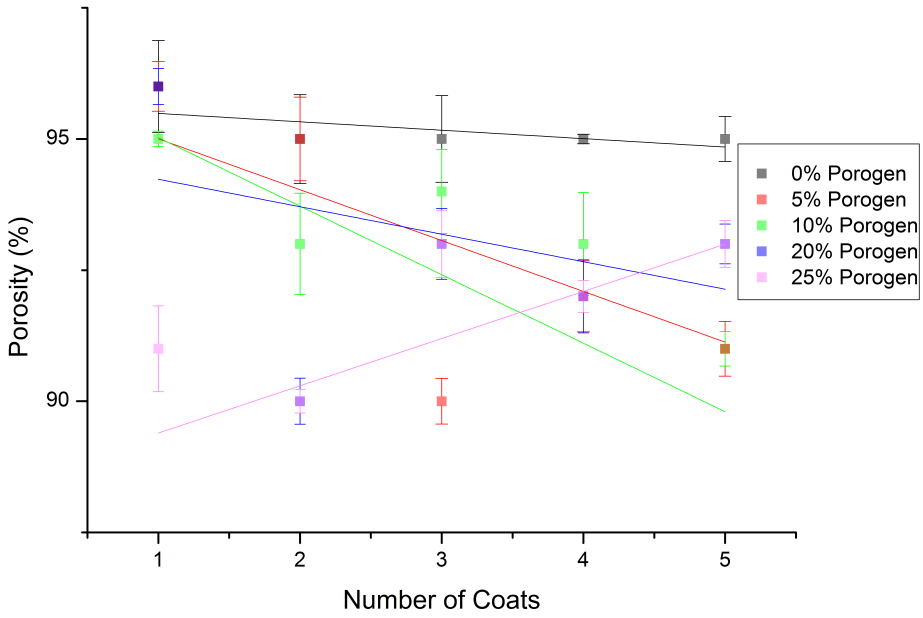

Figure 6.28: Porosity (%) of scaffolds fabricated using the 45 ppi template and sintered to 1250°C, with varying porogen content and number of coats of the slurry

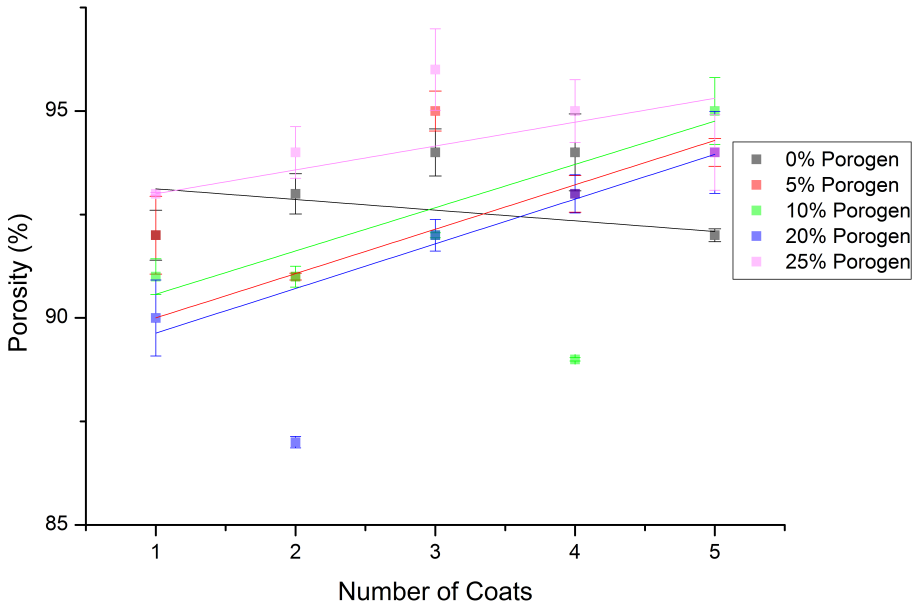

Figure 6.30: Porosity (%) of scaffolds fabricated using the 45 ppi template and sintered to 1350°C, with varying porogen content and number of coats of the slurry

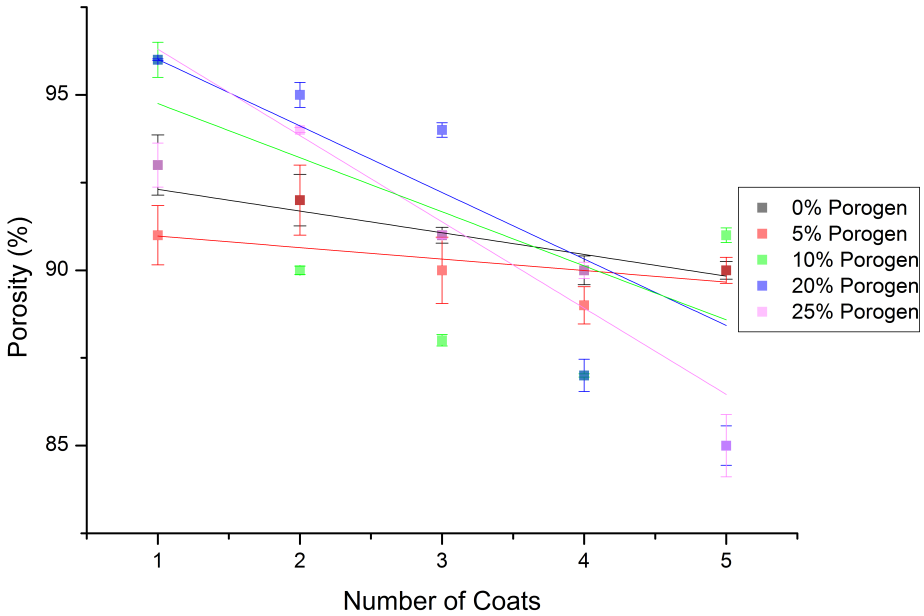

Figure 6.31: Porosity (%) of scaffolds fabricated using the 90 ppi templateand sintered to 1250°C, with varying porogen content and number of coats of the slurry

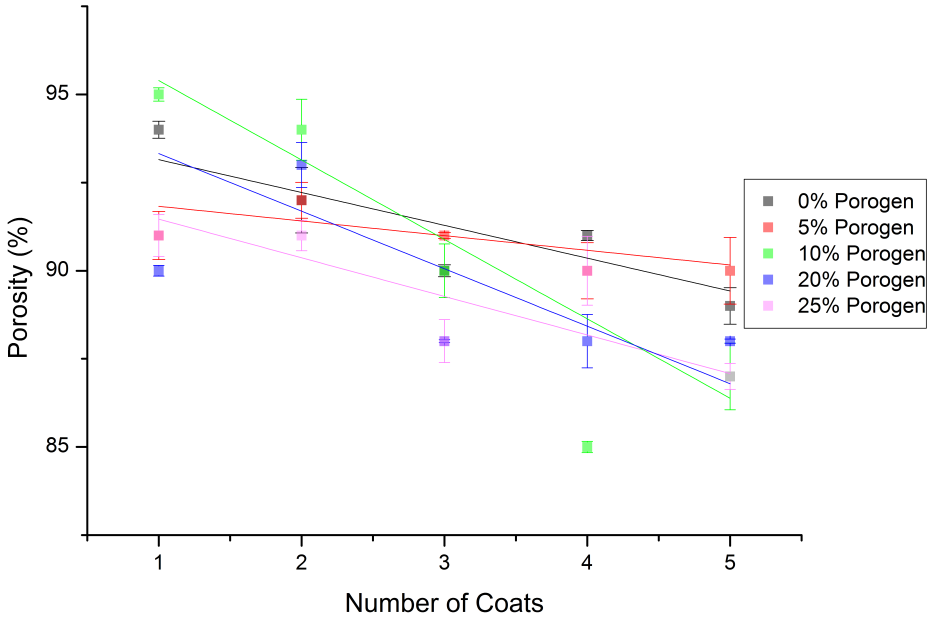

Figure 6.32: Porosity (%) of scaffolds fabricated using the 90 ppi templateand sintered to 1300°C, with varying porogen content and number of coats of the slurry

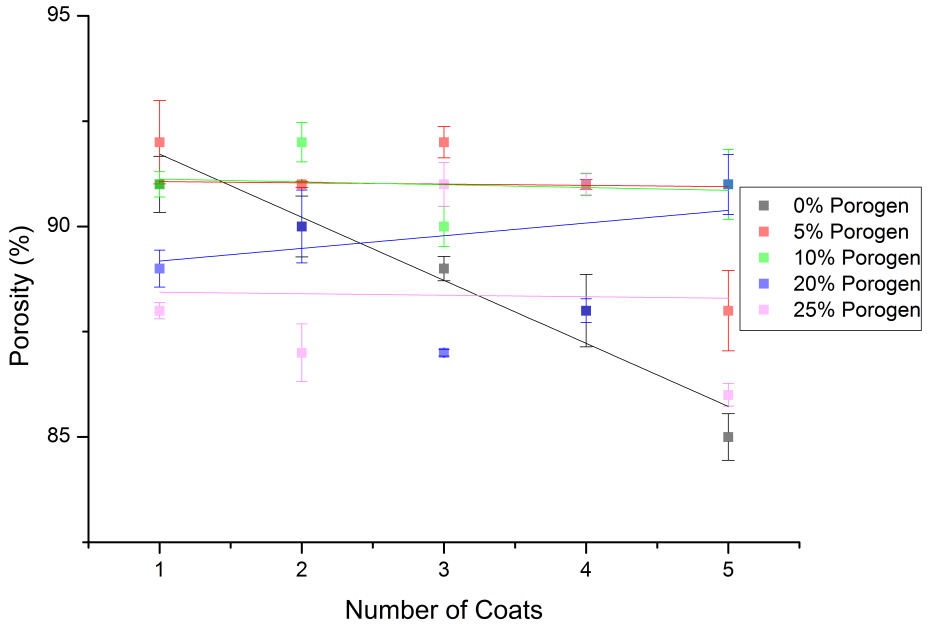

Figure 6.33: Porosity (%) of scaffolds fabricated using the 90 ppi templateand sintered to 1350°C, with varying porogen content and number of coats of the slurry

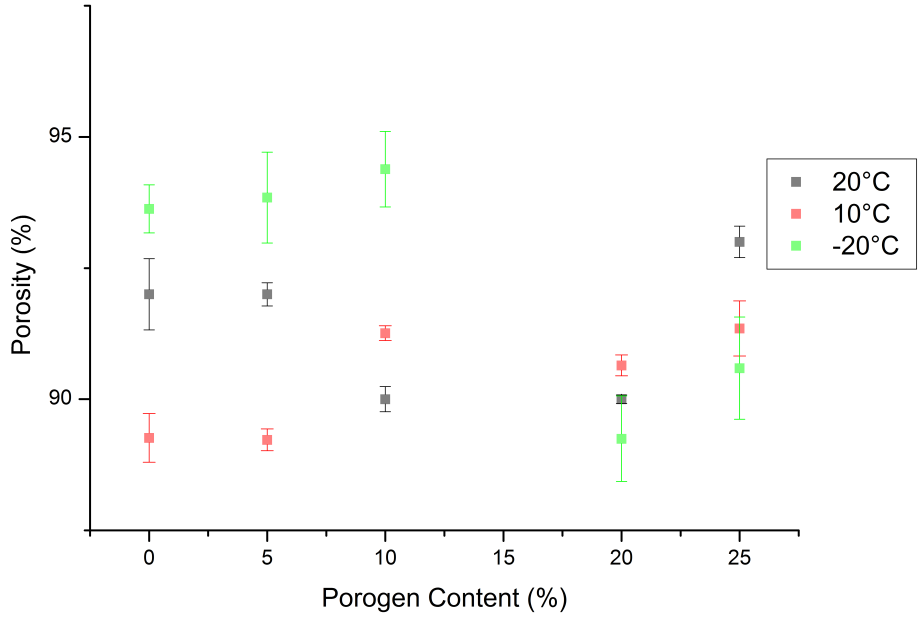

Figure 6.34: Porosity (%) of samples produced using different freezing temperatures, with 1 coat of the slurry on the 45 ppi template, varying porogen contents and sintered to 1350 °C

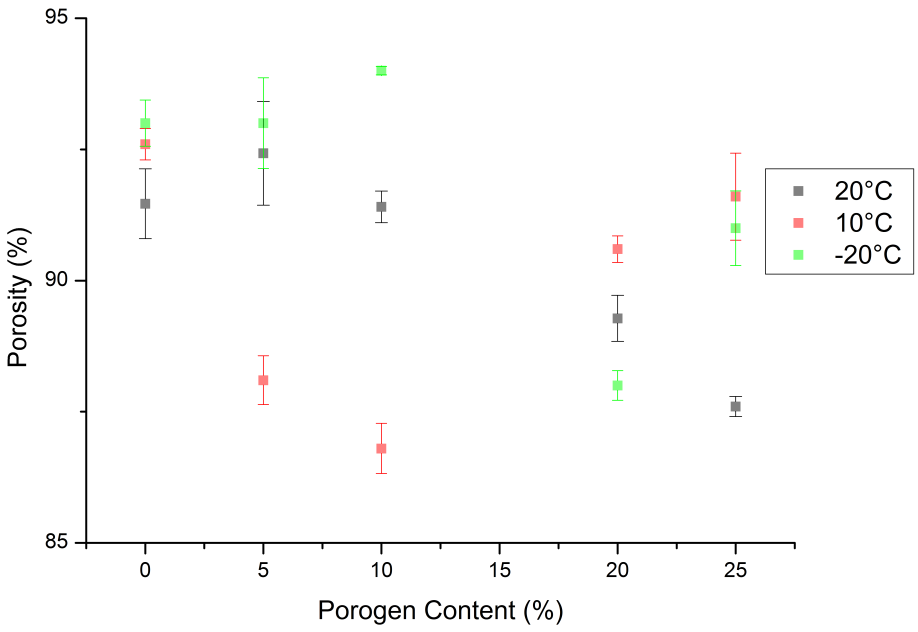

Figure 6.35: Porosity (%) of samples produced using different freezing temperatures, with 1 coat of the slurry on the 90 ppi template, varying porogen contents and sintered to 1350 °C

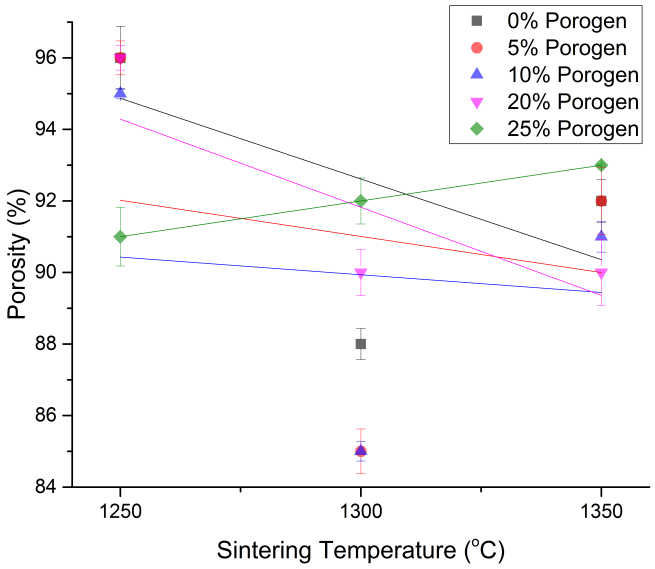

Figure 6.36: Effect of varying the sintering temperature on the porosity (%) of samples produced with 1 coat of the slurry on the 45 ppi template, varying porogen contents and sintered to 1350 °C

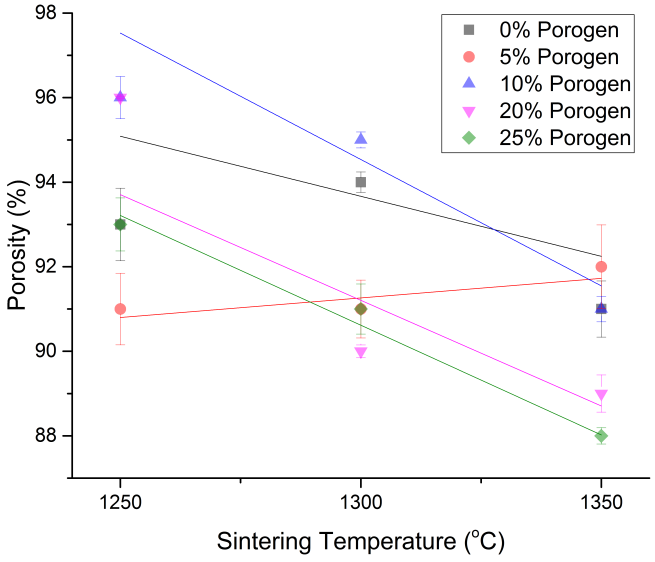

Figure 6.37: Effect of varying the sintering temperature on the porosity (%) of samples produced with 1 coat of the slurry on the 90 ppi template, varying porogen contents and sintered to 1350 °C

6.2.4 MicroCT

MicroCT was also used to measure the porosity of the samples, as well as determine their surface area and obtain qualitative information regarding the nature of the size, interconnectivity and shape of the pores. Images of the the macrostructure of scaffolds produced using the 45 ppi and 90 ppi templates with varying camphene contents included in the slurry are shown in Figures 6.38 and 6.39 respectively, whilst the microstructure is shown in Figures 6.40 and 6.41 and the porosity and surface area measurements given in Table 6.4.

The images corroborate the observations made during SEM: namely that the macropores are open and interconnected, albeit with some occlusion randomly distributed throughout the analysed structures; and that the struts generating the macroporous network contain micropores. Furthermore, microCT has enabled the complete structure to be viewed, and thus the hollow nature of some of the struts. Finally, the total porosity has been measured which is similar to that obtained using the Archimedes principle method. Furthermore, the strut microporosity has also been measured, which generally increases with increasing porogen contents. For example, the strut porosity of structures from the 45 ppi template increases from 36.8 to 51.1% as the porogen content increased from 0 to 25%, with increases from 28.5 to 37.2% observed in structures from the 90 ppi template. There was some microporosity noticable in the centre of struts, particularly those fabricated using the 45 ppi template. This is thought to be caused by the pyrolysis of the foam, as has been observed by others [273, 277].

6.2.5 Discussion

The first requirement given in Section 1.1.1 is that the porosity of bone regenerative scaffolds must be open and interconnected to avoid regions where growth cannot occur [233, 310, 312, 347]. As such, the porosity of all scaffolds was measured using the Archimedes method which is simple and allows accurate density measurements

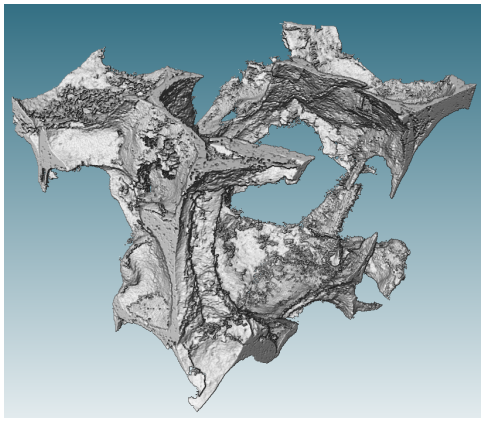

(a) MicroCT image of scaffold produced without camphene

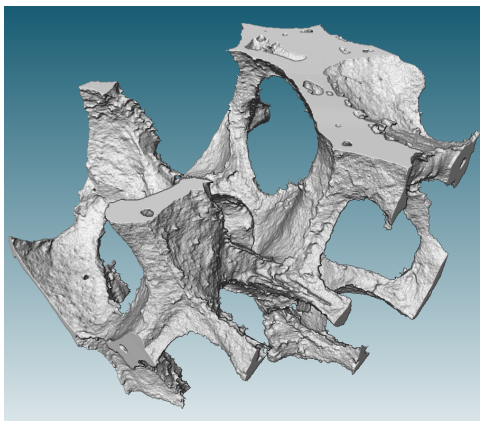

(b) MicroCT image of scaffold produced with 5% camphene included in the slurry

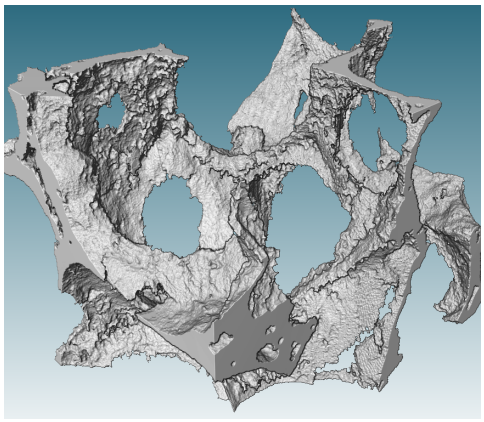

(c) MicroCT image of scaffold produced with 10% camphene included in the slurry

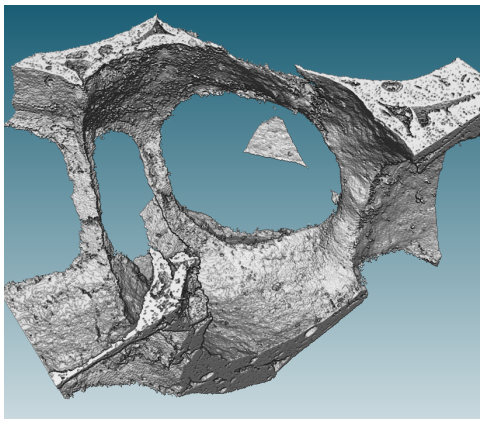

(d) MicroCT image of scaffold produced with 20% camphene included in the slurry

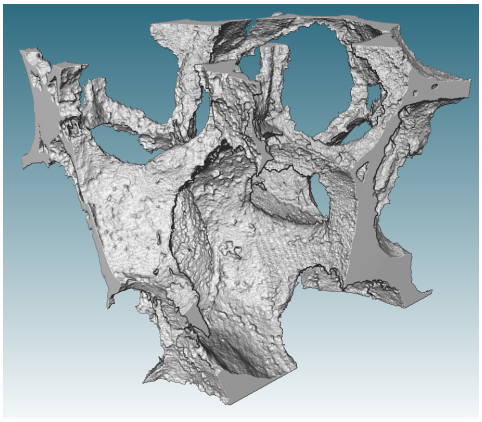

(e) MicroCT image of scaffold produced with 25% camphene included in the slurry

Figure 6.38: 3D microCT images of macrostructure of scaffolds produced using the 45 ppi template, with 5 coats of the slurry, sintered to 1350 °C and with varying amounts of camphene included in the slurry

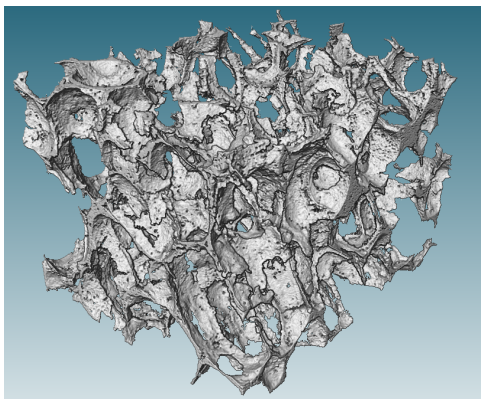

(a) MicroCT image of scaffold produced without camphene

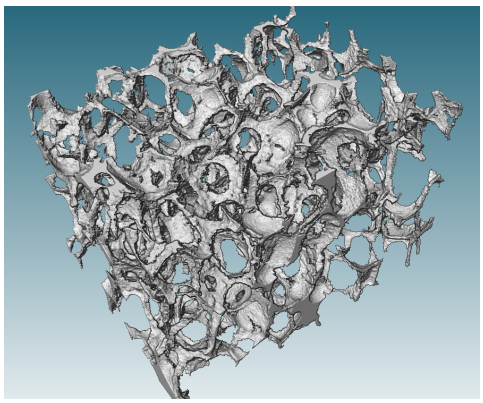

(b) MicroCT image of scaffold produced with 5% camphene included in the slurry

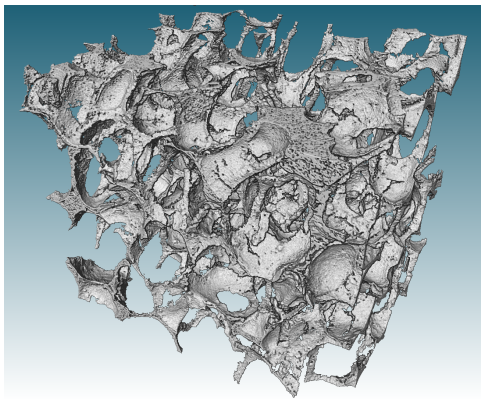

(c) MicroCT image of scaffold produced with 10% camphene included in the slurry

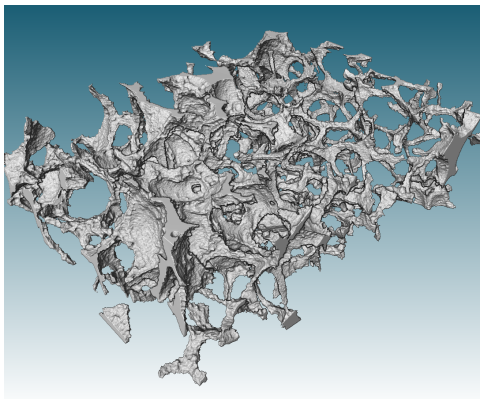

(d) MicroCT image of scaffold produced with 20% camphene included in the slurry

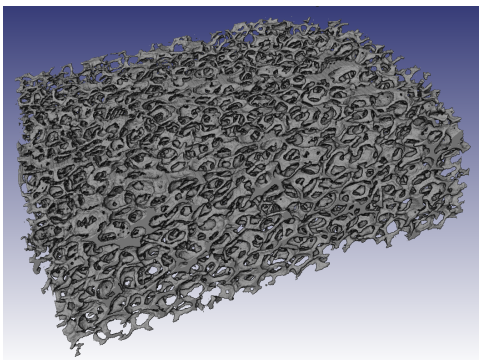

(e) MicroCT image of scaffold produced with 25% camphene included in the slurry

Figure 6.39: 3D microCT images of macrostructure of scaffolds produced using the 90 ppi template, with 5 coats of the slurry, sintered to 1350 °C and with varying amounts of camphene included in the slurry

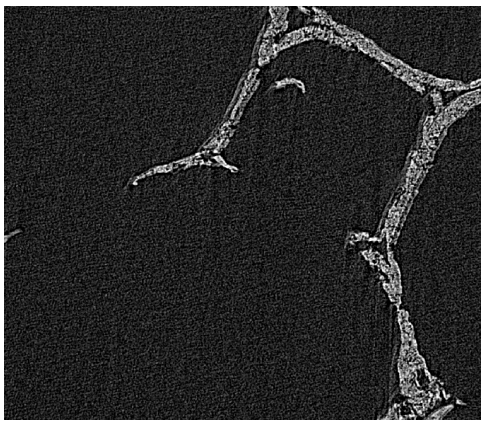

(a) Orthoslice image of scaffold produced without camphene

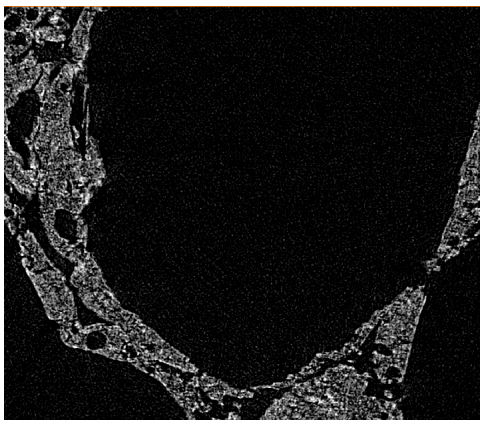

(b) Orthoslice image of scaffold produced with 5% camphene included in the slurry

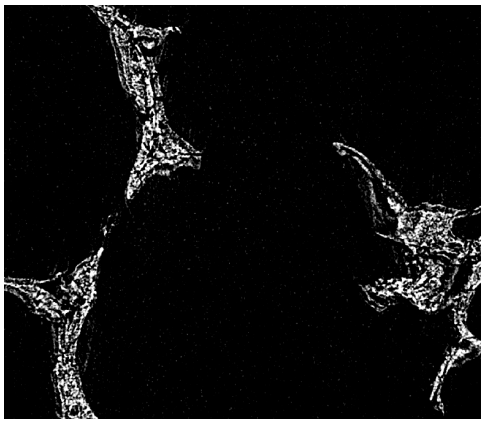

(c) Orthoslice image of scaffold produced with 10% camphene included in the slurry

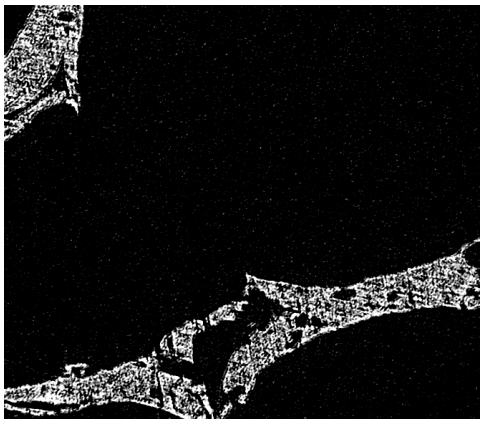

(d) Orthoslice image of scaffold produced with 20% camphene included in the slurry

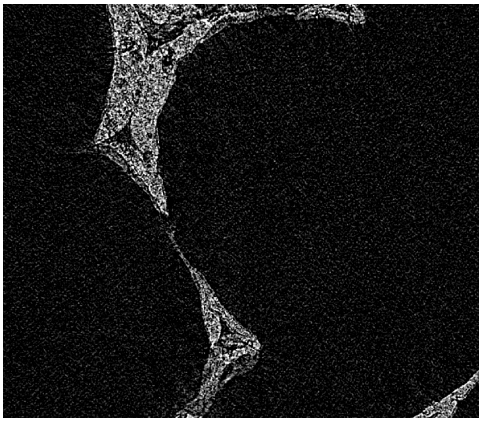

(e) Orthoslice image of scaffold produced with 25% camphene included in the slurry

Figure 6.40: 2D orthoslice of microCT images showing microporosity of scaffolds produced using the 45 ppi template, with 5 coats of the slurry, sintered to 1350 °C and with varying amounts of camphene included in the slurry

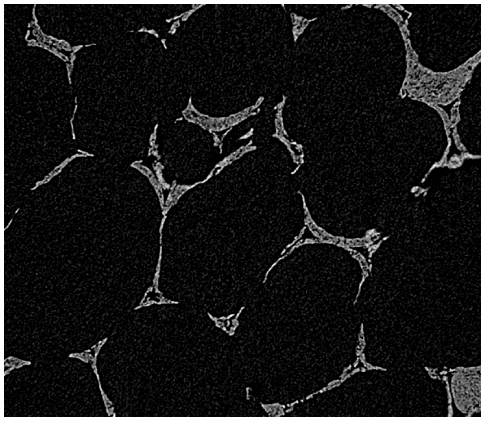

(a) Orthoslice of scaffold produced without camphene

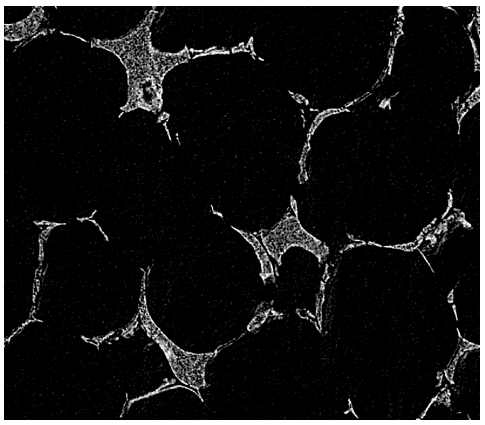

(b) Orthoslice of scaffold produced with 5% camphene included in the slurry

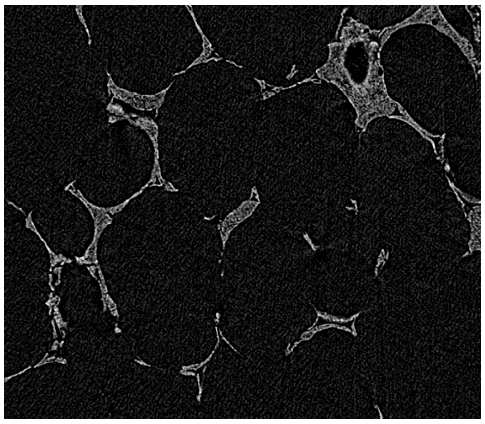

(c) Orthoslice of scaffold produced with 10% camphene included in the slurry

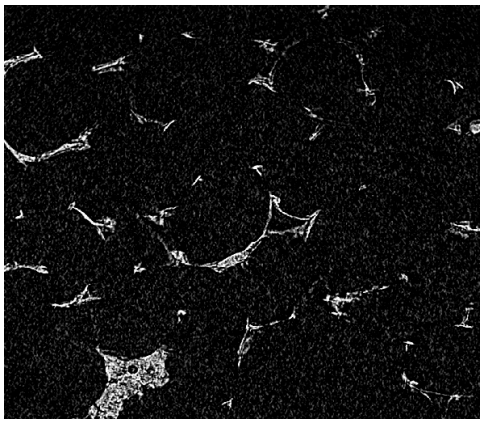

(d) Orthoslice of scaffold produced with 20% camphene included in the slurry

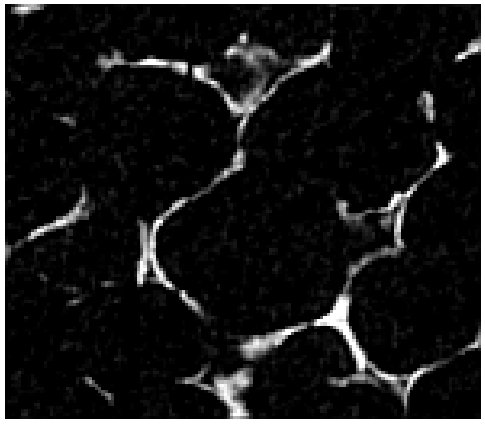

(e) Orthoslice of scaffold produced with 25% camphene included in the slurry

Figure 6.41: 2D orthoslice of microCT images showing microporosity scaffolds produced using the 90 ppi template, with 5 coats of the slurry, sintered to 1350 °C and with varying amounts of camphene included in the slurry

Table 6.4: Porosity and surface area measurements obtained using microCT for scaffolds produced using both templates, with 5 coats of the slurry, sintered to 1350 °C and with varying amounts of camphene included in the slurry

Template	Porogen Content	Total porosity (%)	Strut Porosity (%)	Specific Surface Area (mm^2 / mm^3)
45 ppi	0% camphene	89.8	36.8	55.1
	5% camphene	87.0	39.6	36.1
	10% camphene	91.5	43.6	67.3
	20% camphene	87.5	29.5	38.4
	25% camphene	87.6	51.1	37.9
90 ppi	0% camphene	91.6	28.5	122.7
	5% camphene	94.0	23.0	200.0
	10% camphene	92.5	34.4	139.7
	20% camphene	93.2	38.1	134.1
	25% camphene	89.5	37.2	56.6

to be taken rapidly [406–409]. Although quicker, cheaper and easier to perform than any other method of measuring the density, it does not allow for the determination of other features defining the porous network [531, 532] and thus microCT was also used on selected samples. MicroCT scans provide qualitative information about the pore shape, size and interconnectivity which, due to the 3-dimensionality of microCT scans, can be more informative than OM or SEM micrographs. However, Kim et al [274] and Kwon et al [270] reported that microCT porosimetry provides estimates that are 12-15% lower than those measured using other techniques due to the presence of features smaller than the maximum resolution of microCT. However these observations were made on older machines, and as a high resolution scanner able to observe nanoscale features was used in this work, there was not a significant difference between the porosity values obtained using the different methods.

Foam reticulation techniques have been used to produce highly porous samples [51, 54, 100, 103, 116, 266, 268, 269, 275, 276, 372, 375, 376]. The AFR also produces highly porous scaffolds, with porosity of 75 to 95%. The high level of porosity indicates that it is open, a fact corroborated by SEM and microCT images. Furthermore, the porosity could be controlled by varying the processing parameters. It was thought

that the inclusion of the porogen and the subsequent production of microporosity would increase the porosity. However due to the open nature of the porosity of the scaffolds, a high sintering temperature was required to ensure there was suitable densification and this is likely to have caused some shrinkage [280,347,529], affecting the microporosity and leading to the relatively small impact observed. Furthermore, the macroporosity of the samples dominates the porosity in AFR fabricated scaffolds and as such the microporosity does not have a major effect on the overall porosity.

Scaffolds from the 45 ppi template generally exhibited higher porosity than those from the 90 ppi template due to the relatively larger pore sizes with respect to the strut diameter. Additionally, there was less of an impact on the porosity of structures fabricated using the 45 ppi template when varying the processing parameters. This is because the ratio of pore to strut size is affected less when coating the 45 ppi template multiple times. The changes to the pore and strut size for all structures is relatively small implying that each additional coating only adds a thin layer of material. Thus the ratio between pore and strut size is impacted less where there are larger pore and strut sizes, leading to a relatively small effect on the porosity

The porosity consists of pores within different ranges. As described in Section 3.1.5, the foam reticulation technique enables the controllable production of macropores which closely replicate the structure of the template [274, 277, 533], whilst the freeze drying facilitates the production of micropores in the macroporous struts. Many of the parameters affecting foam reticulated structures have previously been investigated [266–269, 273–277]. Increasing the sintering temperature has been reported [529, 533] to lead to shrinkage of the scaffolds due to increased densification. Increasing the number of coats of the slurry leads to larger strut sizes and smaller pore sizes [270], as the only place that material can attach to the template is on the struts, and hence as more biomaterial is added it must increase their size. As the template is of a fixed size, increasing the strut size must decrease the pore size. These effects were all seen with AFR produced structures. Hence, with allowances made for the shrinkage expected at high sintering temperatures [347] and through

variations to the pore and strut sizes by varying the number of coats, it is possible to produce structures with tailored macroporosity. This is of particular importance as although the size of the macropores is known to have some effect on the biological performance of cells [15, 16], this is not fully understood and hence the optimal macropore size has not yet been determined. Nevertheless, it enables the realisation of pores within the range specified in Section 1.1.1 (100-900 μm) [12, 13, 15] as suitable for bone regeneration.

The macropore size was unaffected by the incorporation of a porogen into the precursor slurry, regardless of the level of inclusion. As the interconnecting struts provide the construct with its strength and stability, it was undesirable for the generation of microporosity to have any detrimental effects on the macrostructure. The freeze casting technique has been used to produce scaffolds with pore sizes up to 300 μm [97, 254, 255, 260], although such large pores were not necessary in this work. When implemented here, even at the freezing temperature facilitating the growth of the largest ice crystals, there was no detrimental effect to the macropores.

Whether the porogen was included or not, all scaffolds exhibited surface roughness. This has a positive effect on the biological functionality of scaffold structures [18, 19, 21, 22], however introducing micropores may enhance this by not only providing the cells with surfaces onto which they can attach, but by also facilitating vascularization and capillary growth. Surface roughness has been observed by others using foam reticulation [51, 269, 270, 275, 276, 372], with the incorporation of micropores being the subject of current research attention [268, 281].

At all levels of porogen inclusion, some microporosity was observed. The level of porogen inclusion had little effect on the size of individual micropores (1-5 μm) as the pore size is dictated by the freezing rate as opposed to the level of porogen [254, 260]. Instead, increasing the amount of porogen resulted in the number and density of the micropores increasing, to the point where there was some micropore agglomeration and thus the production of larger micropores of up to 20-30 μm. The size of the micropores, particularly those that were agglomerated, is expected to

benefit the biological activity of cells seeded onto the scaffolds as it is suitable for the attachment of cells [2, 16–18] and the formation of extracellular matrices [2] without being so small that cells will grow over them [21,22]. Previous investigations regarding the freezing parameters have mainly been aimed at increasing the pore size [97,104,254,255,259,260,534]. This is not the case with the AFR as the majority of the porosity is caused by the template and the freeze casting is only used to add microporosity to the struts of the scaffolds. However, the investigations show that the microporosity and micropore size is highly controllable.

6.3 Mechanical Properties

6.3.1 Experimental Yield Stress

Due to the large number of samples fabricated during the course of this work, selected samples were tested to failure to determine the actual strength, with the results shown in Table 6.5. As the structure collapses, the porosity is compromised and as such a representative value of the strength is no longer observed. Hence, the value for the load at the point at which the structure begins to break has been used. This is the first peak on the load-displacement graph with a representative example shown in Figure 6.43. These have been compared with the theoretical values, as shown graphically in Figure 6.42 to determine whether the theoretical predictions were a suitable alternative to experimental calculations. In most cases, there was a close correlation between the theoretical and experimental values, within a reasonable experimental variation (within 12%). However, the theoretical strength did not match the measured yield stress for the samples produced using the 90 ppi template with 25% porogen in the slurry.

For most scaffolds, theoretical calculations underpredicted the strength compared to experimentally obtained values. This could have been caused by the average micropore size being used as opposed to a weighted average. Similarly a weighted

average of macropore and strut size could have led to increased theoretical predictions. Alternatively, in all load-displacement graphs, there are fluctuations below the first major peak. Thus, the experimentally obtained values of the strength may be lower than that reported. Whilst using the graph may not enable the precise calculation of compressive strength, it enables a realistic estimation and as such is highly useful in analysing the mechanical properties of scaffolds.

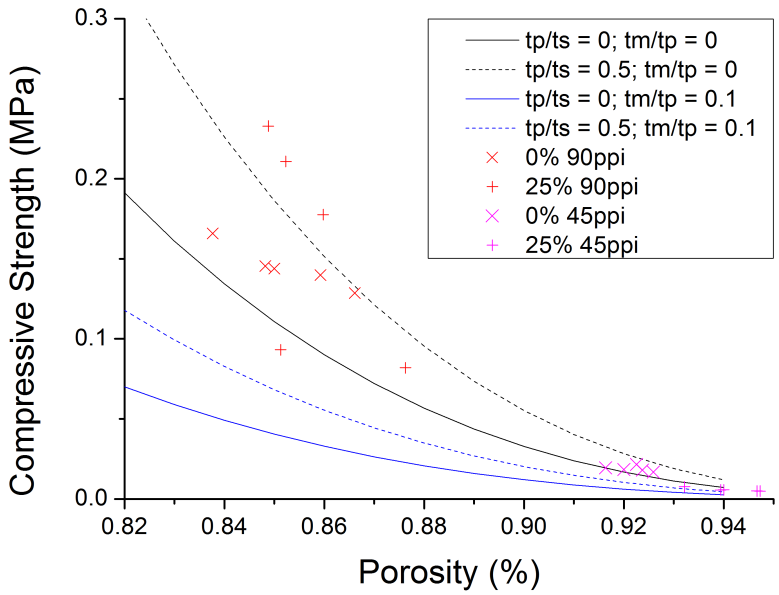

Figure 6.42: Graphical representation showing theoretical mechanical strengths calculated with varying parameters and results of the experimental tests to failure. Data from experimental tests plotted as scatter; theoretical calculations plotted as lines, calculated using Equation 4.10, with the shape factor from Equation 4.11. (tp/ts - ratio of pore to strut size; tm/tp - ratio of micropore to macropore size)

6.3.2 Theoretical Yield Stress

The yield stress of all scaffolds was calculated theoretically using Equation 4.10, with the shape factor calculated using Equation 4.11 and the bulk modulus of HA taken as 44.8 MPa (1.12 x tensile strength (40MPa [44]) [426]). Graphical representation of the compressive strength of the scaffolds sintered to 1250 °C - 1350 °C are shown

Table 6.5: Comparison of mean $\pm\sigma_{er}$ theoretical values of yield stress against the mean $\pm\sigma_{er}$ (n=5) values obtained through the testing of selected samples to failure

	Diameter (mm)	Load (N)	Porosity (%)	Theoretical Stress (kPa)	Yield Stress (kPa)
0%: 90ppi	12.56	19.02	85	134 ± 22	144 ± 12
0%: 45ppi	13.00	4.74	92	16.5 ± 4.5	18.4 ± 1.9
25%: 90ppi	12.41	22.03	86	16.5 ± 1.7	159 ± 61
25%: 45ppi	11.43	0.64	94	3.71 ± 0.8	5.70 ± 1.0

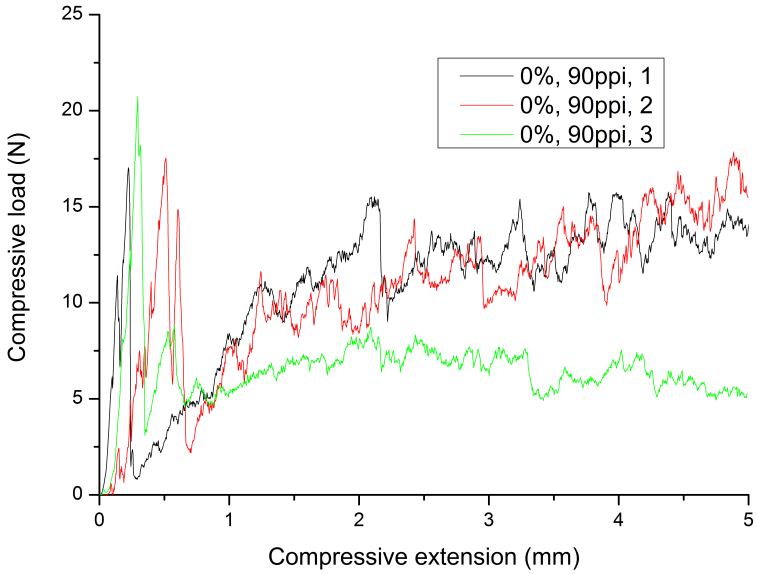

(a) Load-displacement graph evaluating compressive load against compressive extension for complete test for 3 samples produced using identical conditions: 5 coats of the slurry, with 0% porogen and sintered to 1350 °C

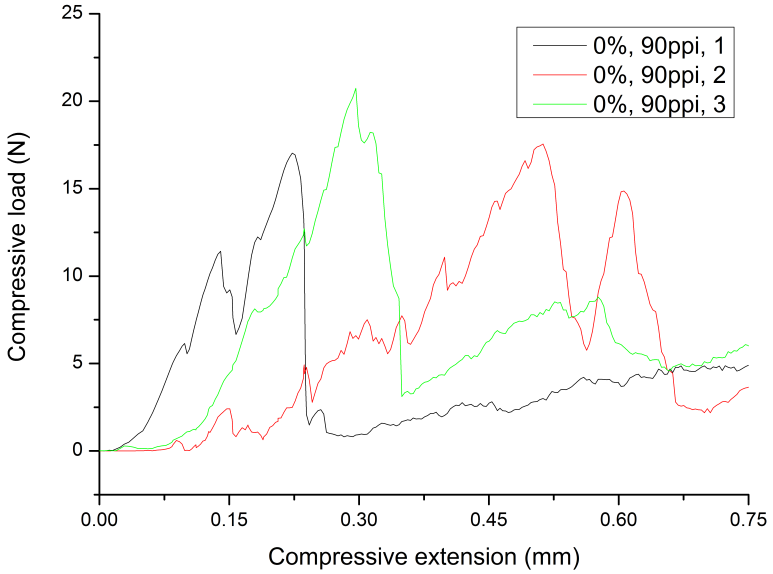

(b) Load-displacement graph showing evaluation of the same samples as in 6.43a. The initial peak is examined to determine the fracture point

Figure 6.43: Typical load-displacement graph obtained during mechanical testing. All have a sharp initial peak denoting fracture of the weakest struts, followed by a general increase with peaks denoting stronger strut breakage

in Figures 6.44 - 6.46 and 6.49 - 6.51 for structures produced from the 45 and 90 ppi foam respectively, with the yield stress of structures produced when the freezing temperature was varied shown in 6.47 and 6.52.

Scaffolds produced using the 45 ppi template were relatively unaffected by the number of coats on the template. When sintered to 1300 °C, scaffolds exhibited a significantly increased yield stress (11 ± 3 to 180 ± 29 kPa), compared to samples sintered to 1250 and 1350 °C, which had similar yield stress ranges of 1.7 ± 0.3 to 41 ± 6 kPa and 1.7 ± 0.2 to 42 ± 10 kPa respectively, with a representative example shown in Figure 6.48. In most cases, increasing the amount of porogen in the slurry led to a slight insignificant decrease in the yield stress, however this was not consistent across all scaffolds evaluated. Varying the freezing temperature also had a limited effect, although structures with a low camphene content that were frozen to -20 °C were much weaker than those frozen to 20 °C and 10 °C. At higher camphene contents, this effect was not observed. As the theoretical values are calculated using measured values for the pore size, strut size and density, any variations to these parameters during processing has a significant effect on the final values. As such, some abnormal values have been obtained.

When the 90 ppi template was replicated, the trends observed differed greatly from the 45 ppi template. The strength of the scaffold was increased with an increasing number of coats in all cases apart from that produced with 25% porogen and sintered to 1350 °C. Variations to the sintering temperature had little effect on the compressive stress in general, with a representative example given in Figure 6.53, however the strongest scaffold, 134 ± 22 kPa, was obtained at the maximum sintering temperature. Variations to the camphene content did not significantly affect the mechanical strength of most scaffolds. Finally, decreasing the freezing temperature led to a general decrease in the mechanical properties. There was a significantly decreased amount of outliers compared to the values obtained when calculating the theoretical compressive stress using scaffolds fabricated using the 45 ppi template. This is due to the smaller variations observed in the variables used in the calculation.

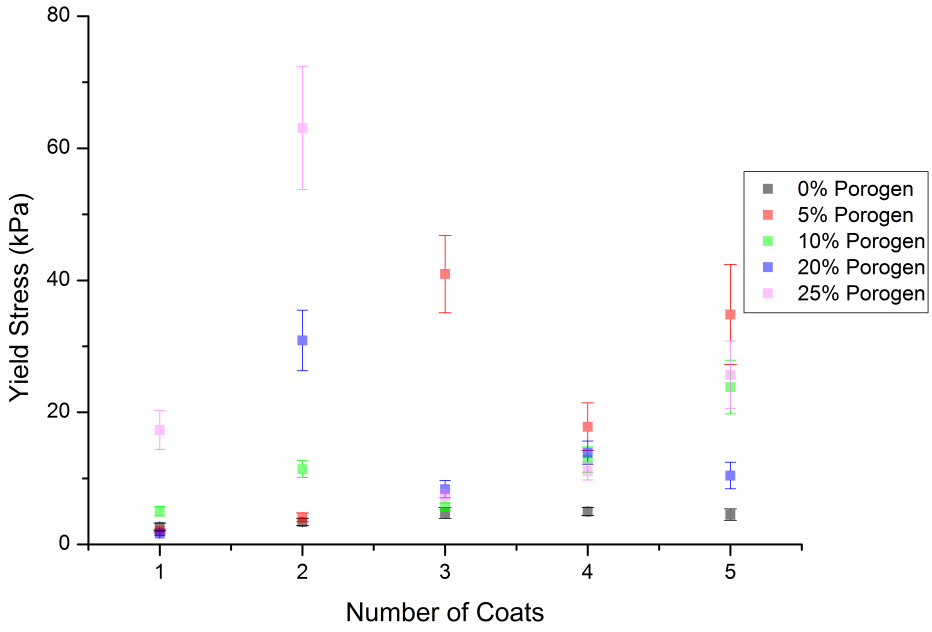

Figure 6.44: Theoretical compressive yield stress (kPa) of scaffolds fabricated using the 45 ppi template and sintered to 1250°C, with varying porogen content and number of coats of the slurry

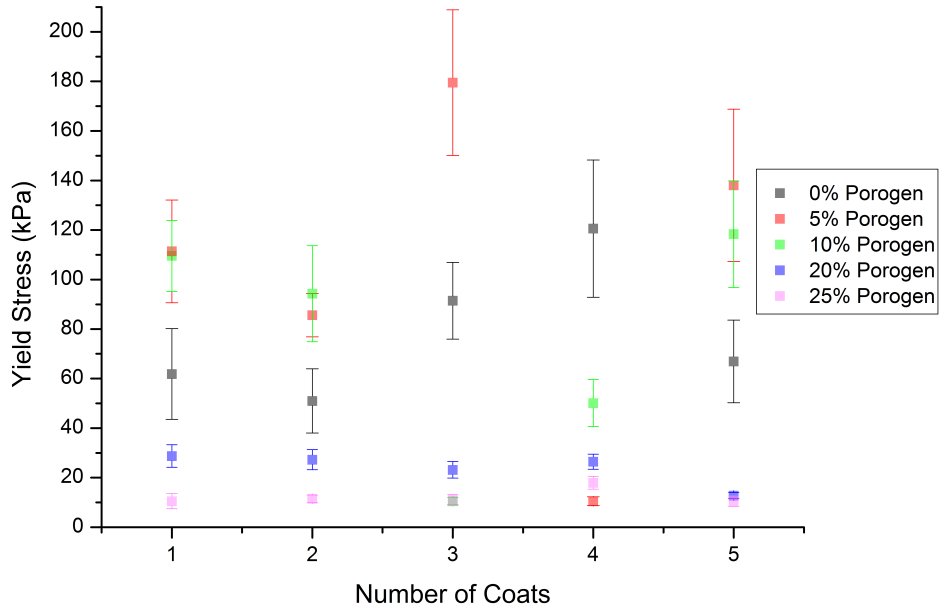

Figure 6.45: Theoretical compressive yield stress (kPa)of scaffolds fabricated using the 45 ppi template and sintered to 1300°C, with varying porogen content and number of coats of the slurry, plotted on the same y-scale as Figure 6.44

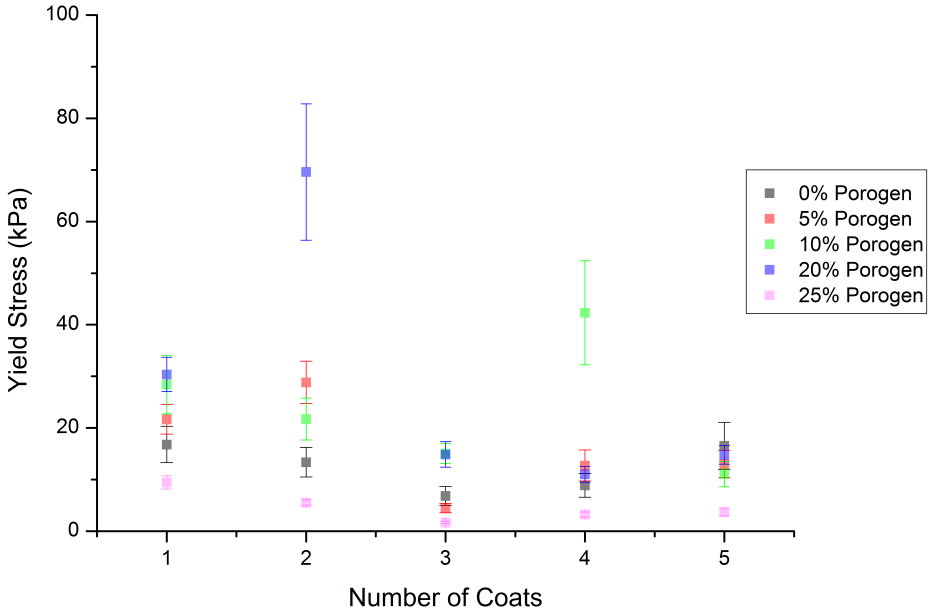

Figure 6.46: Theoretical compressive yield stress (kPa)of scaffolds fabricated using the 45 ppi template and sintered to 1350°C, with varying porogen content and number of coats of the slurry, plotted on the same y-scale as Figure 6.44

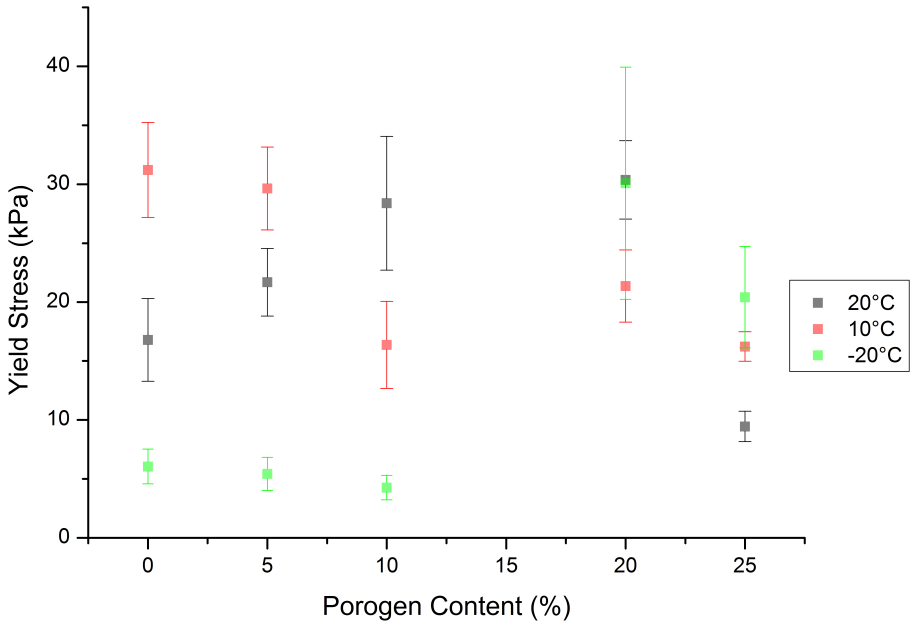

Figure 6.47: Theoretical compressive yield stress (kPa) of samples produced using different freezing temperatures, with 1 coat of the slurry on the 45 ppi template, varying porogen contents and sintered to 1350 °C

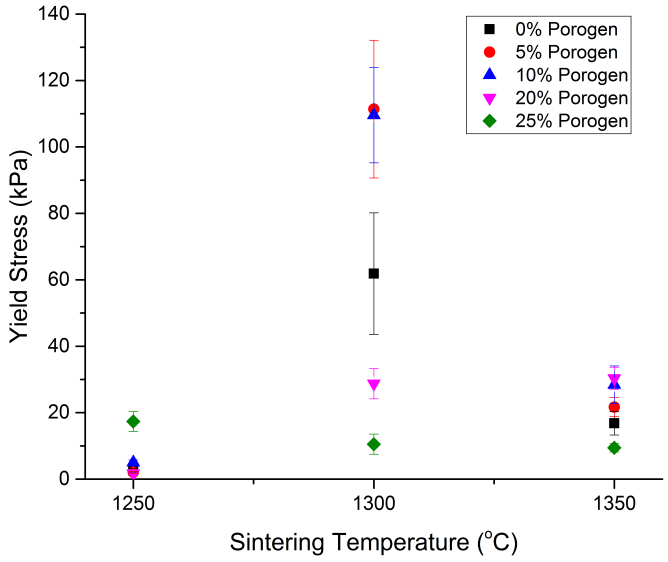

Figure 6.48: Theoretical compressive yield stress (kPa) of samples produced using different sintering temperatures, with 1 coat of the slurry on the 45 ppi template and varying porogen contents

6.3.3 Discussion

The mechanical properties of the scaffold need to be harmonized with those of bone, outlined in Table 1.1. Density measurements taken using the Archimedes method, or any other method, can be used to determine the theoretical mechanical strength [421, 423], with the equations used in this work correlating well with the yield stress obtained experimentally. There is a range of literature on those who have examined and investigated the mechanical strength of HA foams [224, 269, 271, 272, 276, 277, 283, 372] with similar values obtained for structures of equally high porosity as shown in Table 6.6, although in all cases this is much less than that of natural cancellous bone, 2-23MPa [43].

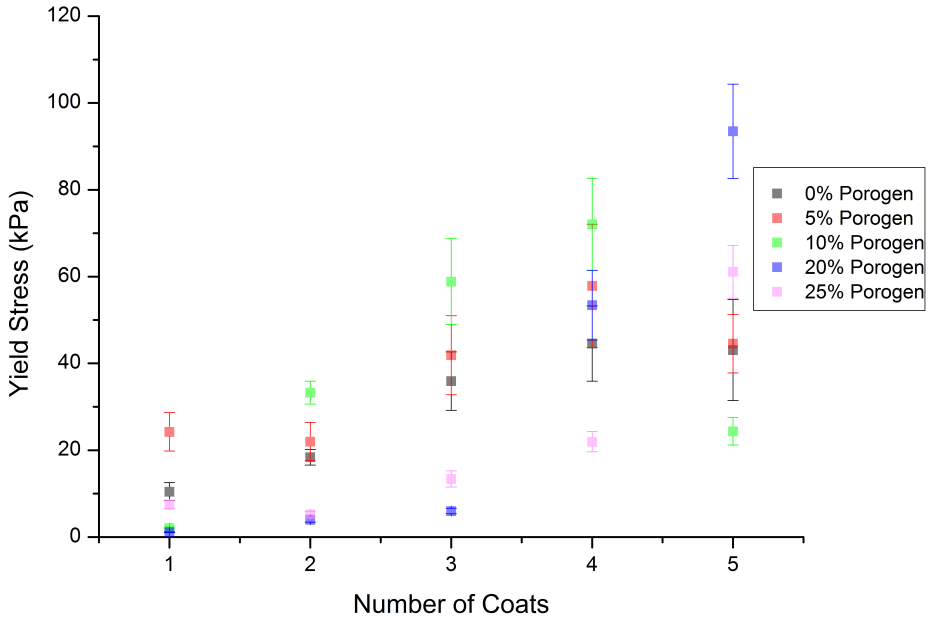

Figure 6.49: Theoretical compressive yield stress (kPa) of scaffolds fabricated using the 90 ppi template and sintered to 1250°C, with varying porogen content and number of coats of the slurry

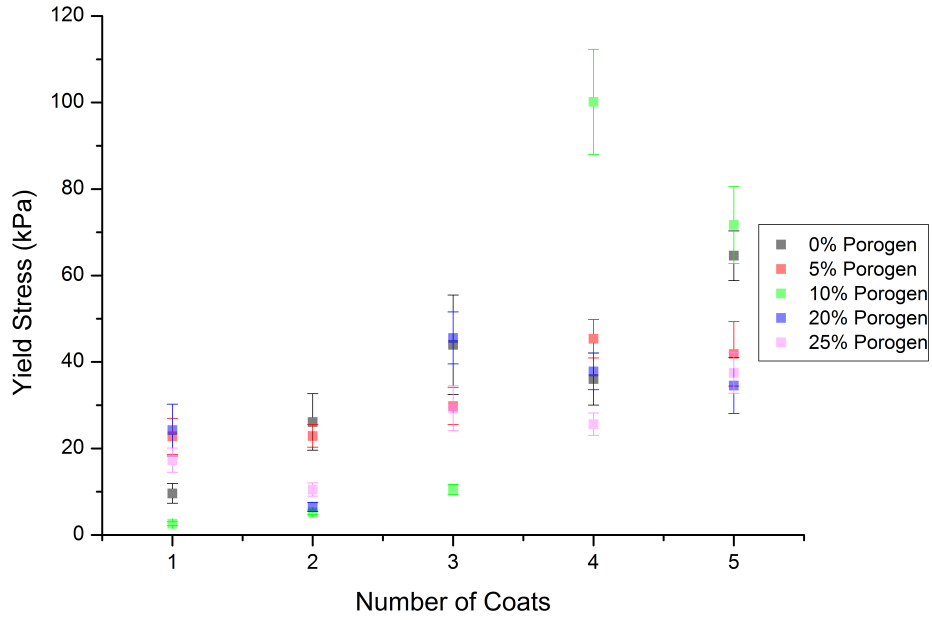

Figure 6.50: Theoretical compressive yield stress (kPa) of scaffolds fabricated using the 90 ppi template and sintered to 1300°C, with varying porogen content and number of coats of the slurry, plotted on the same y-scale as Figure 6.49

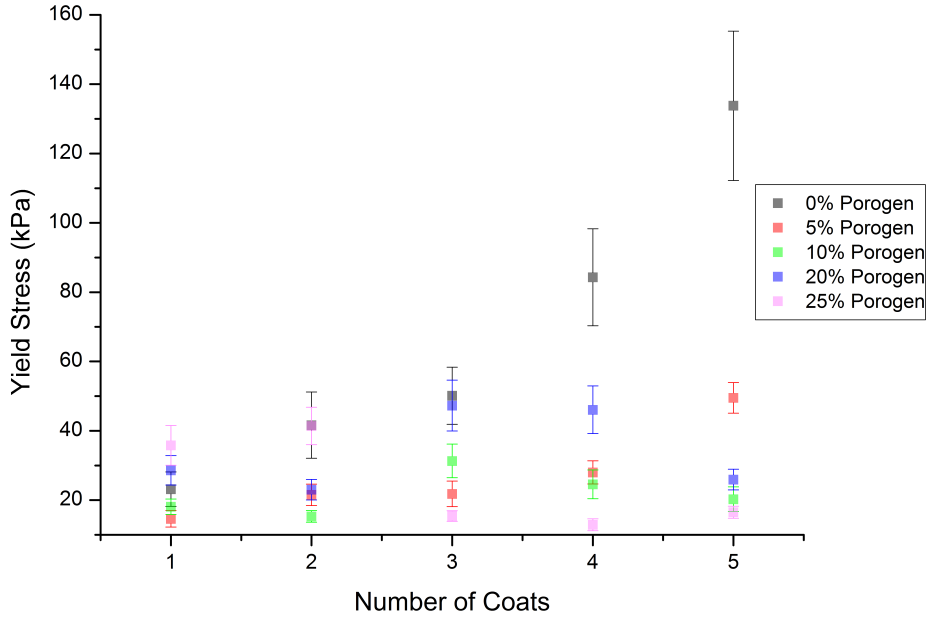

Figure 6.51: Theoretical compressive yield stress (kPa) of scaffolds fabricated using the 90 ppi template and sintered to 1350 °C, with varying porogen content and number of coats of the slurry, plotted on the same y-scale as Figure 6.49

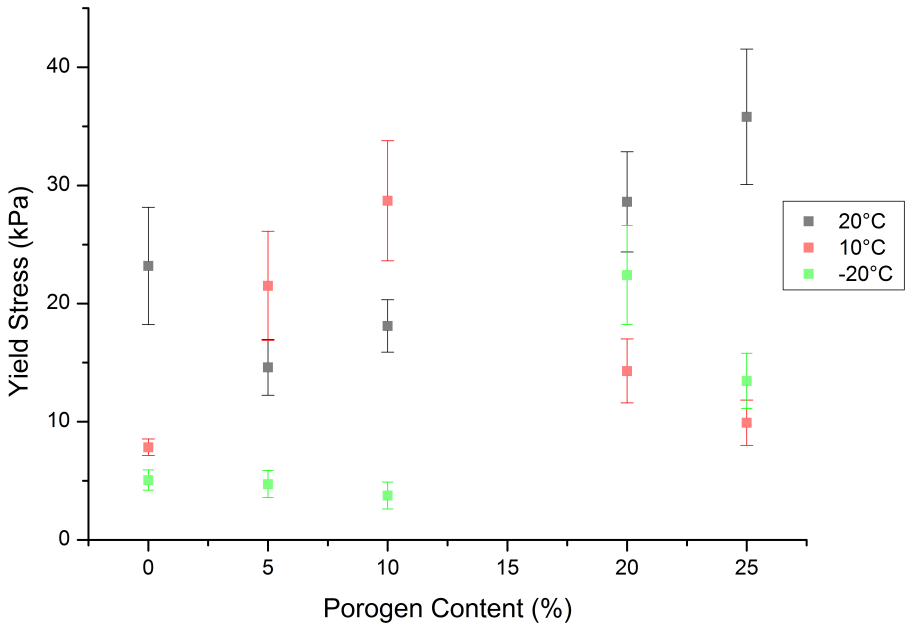

Figure 6.52: Theoretical compressive yield stress (kPa) of samples produced using different freezing temperatures, with 1 coat of the slurry on the 90 ppi template, varying porogen contents and sintered to 1350 °C

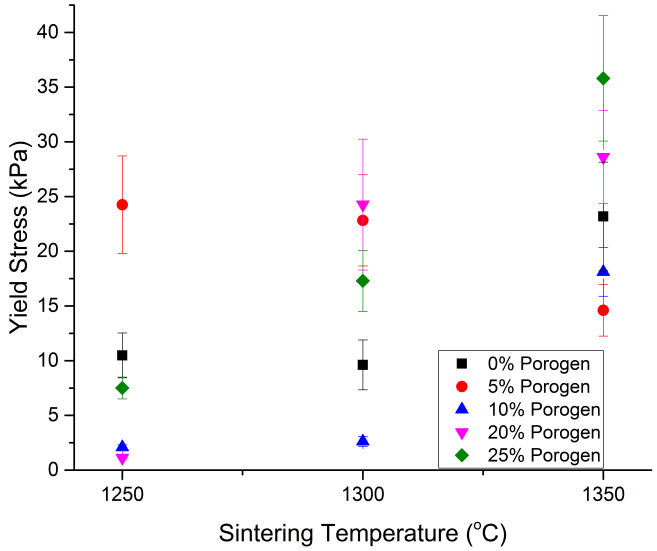

Figure 6.53: Theoretical compressive yield stress (kPa) of samples produced using different sintering temperatures, with 1 coat of the slurry on the 90 ppi template and varying porogen contents

Table 6.6: Compressive yield stress of scaffolds fabricated using foam reticulation, with values obtained experimentally in this work compared to those available in the literature for similarly highly porous structures

Porosity	Yield Stress (kPa)	Ref
85-94	5.7-159	This Work
95	7	[271]
83	110-230	[224]
80-90	<0.5	[269]
70	950	[277]

The theoretical mechanical strength was more dependant on the processing parameters when structures were fabricated from the 90 ppi template as opposed to the 45 ppi template, as outlined in Section 6.3. The ratio of pore to strut size, the porosity and the ratio of macro to micro pore size are important in the theoretical yield stress calculations. The ratio of pore to strut size is affected less by coating the 45 ppi template multiple times. The changes to the pore and strut size for all structures is relatively small, hence, for structures with larger pore and strut sizes,

the ratio between these is not as affected as for those with smaller pore and strut sizes. Increasing the sintering temperature leads to increased densification and as such should result in greater mechanical properties [225,529], a phenomenom not observed consistently in this work. It is likely that the significant porosity of the structures adversely affected the densification process. Freezing the structures to different temperatures during processing causes the micropore size to increase [257,259], particularly when frozen to -20°C. This affects structures produced with low camphene contents, but has less of an effect when higher porogen percentages are incorporated. This is most probably due to the shape factor being based on the individual micropore size, Equation 4.11. The agglomeration of these micropores at higher camphene percentages means that the microporosity at, for example, 25% camphene is of a similar size to that observed in freeze dried structures.

Using Equation 4.20 to calculate the error, the σ_{er} for most samples was witin 10-20% of the mean. There were some cases outside of this range, with the maximum error of 33% on the sample with 20% porogen and frozen to -20 °C during production. This is due to the relatively high error in the pore size, of 11%. Furthermore, in all cases where the error in the pore size was over 7% of the mean, σ_{er} of the mechanical strength was over 20%. Thus, to be able to state a value for the theoretical yield stress within a suitable range, it is necessary for scaffolds to be produced with a high degree of control over the pore size, and for that pore size to be within a relatively small range.

A final point of note regarding the theoretical compressive yield stress calculations is that the values have been obtained in this work using the bulk yield stress of HA. There has been at least a partial phase change to whitlockite, which has a slightly higher bulk yield stress (47.0 MPa for whitlockite as opposed to 44.8 MPa for HA [44]). The bulk yield stress is 5% greater for whitlockite than for HA, which is within the error obtained for all scaffold strengths calculated theoretically. As such this is only likely to have had a small impact on the calculated values.

The load-displacement graph for HA scaffolds when tested under compression, as

shown in Figure 6.43a, can be used to determine the yield stress, strain, toughness and compressive modulus [337, 412], although in this case it has only been used to determine the yield stress. There is a sharp incline in the graph due to the brittle nature of the ceramic that peaks at the failure of the weakest struts [271, 272, 337]. This is followed by a general rise, as the initial layer of pores becomes compressed and covers the pores of the next layer, increasing the relative density of the structure [271, 272]. The initial peak, Figure 6.43b, is generally taken as the yield strength [271, 272, 337, 412], as it is at this point that the structure has failed, however this is not necessarily at the maximum load that the scaffold could withstand, particularly after implantation [12, 15].

The theoretical values closely matched those obtained using destructive testing for most samples. As there are no cases in the literature comparing the theoretical mechanical strengh to the observed strength for structures combining macro and microporosity, the suitability of incorporating a shape factor as used for microporous structures had not been verified. From this work, it can be deduced that the incorporation of a shape factor, Equation 4.11 [424, 425], into Equation 4.10 [421–423] enables a reasonable estimation of the yield strength of macroporous structures with microporous struts. However it cannot be taken *verbatim* that the calculated value will be the true strength of the structure. As seen with the scaffold produced from the 90 ppi template with 25% porogen, there is a significant reduction in the theoretical calculation due to the increased porosity which was not observed during testing. It should also be noted that the minimum strength measured during testing was greater than the values obtained theoretically. Furthermore, there was wide inter-sample range to the yield strengths of the sample produced using these conditions when tested to failure which must also be considered with such scaffolds. As such, further work, as detailed in Section 9.1 is required for a proper evaluation of the inclusion of a shape factor into theoretical mechanical properties of macro and microporous structures.

6.4 Cell Viability

6.4.1 Preliminary Analysis

Initial testing was undertaken to compare the performance of scaffolds fabricated via AFR without any porogen to a commercially available HA control.

Cells were successfully seeded onto both ceramics and controls. The cell metabolic activity was higher on the ceramics than that of the tissue culture plastic marker at day 1, indicating good cell attachment. This viability was maintained over 7 days, as shown in Figure 6.54, although there was no significant increase in the cell number over time on the scaffolds. By day 4, scaffolds of both pore sizes contained more metabolically active cells than the commercial HA control ($P_r < 0.05$), with this trend continuing at day 7 even though only the 45 ppi ceramic showed a significant difference. Confocal microscopy after 24 h, shown in Figure 6.55, confirmed cell attachment. The outer pores of the scaffolds contained cells with an elongated morphology, indicating they were attached to the struts of the pores.

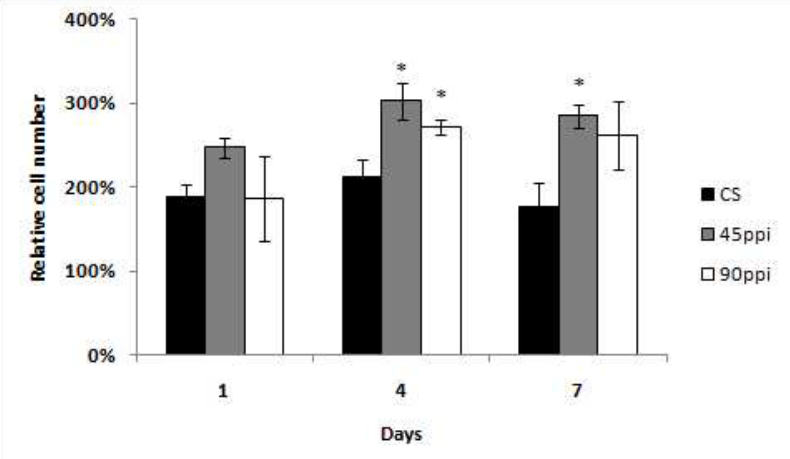

Figure 6.54: Metabolic activity of MG63 cells as measured using the resazarin assay relative to cells seeded in monolayer on tissue culture plastic at day 1. Mean ±S.D (n = 3); CS = 'CellSupports'; * significantly different from CS scaffolds at the same time point, Tukey's pair-wise comparison $p < 0.05$

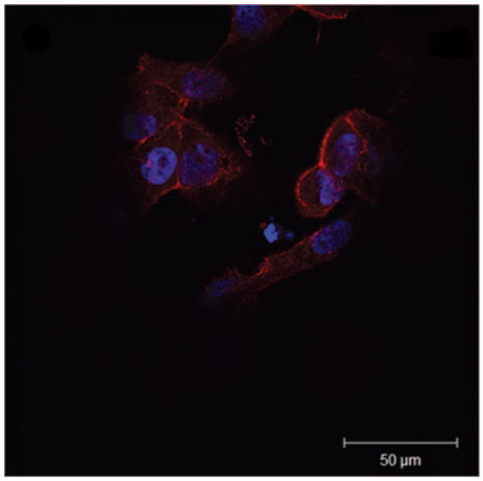

(a) Confocal microscopy of CS

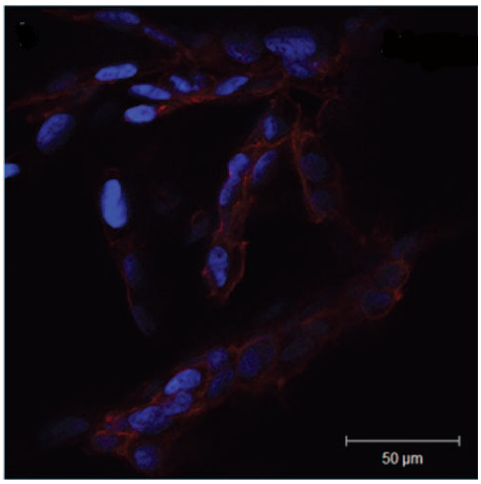

(b) Confocal microscopy of scaffold produced using 45 ppi template

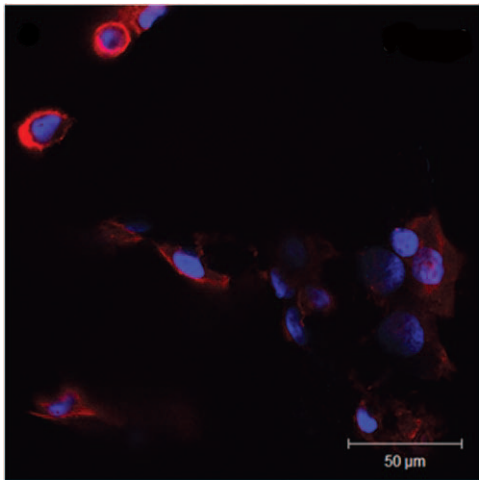

(c) Confocal microscopy of scaffold produced using 90 ppi template

Figure 6.55: Confocal microscopy images of HA scaffold seeded with MG-63 cells and stained with DAPI (nuclei – blue) and Phalloidin- TRITC (cytoskeleton = red) after 24 h of seeding on (a) CS, (b) 45 ppi scaffold and (c) 90 ppi scaffold. (scale bar = 50 µm).

6.4.2 Live/Dead Assay

The live/dead assay was used to determine whether cells could survive on the structures. There was a high number of live cells after both 1 and 3 days, Figure 6.56 and Figure 6.57 respectively, on scaffolds produced with and without any porogen. It is possible to see a large number of live, green, cells with a small number of dead, red, cells, with a viability of approximately 95%. Cells seeded on both 90 and 45 ppi scaffolds produced with and without porogen at both 1 and 3 days could be seen to have become elongated in morphology, indicating that they were not only surviving on the scaffolds, but were also attaching to them.

6.4.3 MTT Assay

6.4.3.1 3T3 Cell Line

The cell number was quantified using the MTT assay after 1, 4 and 7 days as shown in Figure 6.58. After 1 day, the number of cells had reduced significantly compared to the number seeded. Although this decrease was seen across all scaffolds, the decrease was smaller on scaffolds that were produced with some porogen included. At all timepoints, the highest cell number was seen on the scaffold produced with 25% porogen on the 45 ppi template. After 4 days the number of cells on the scaffold from the 90 ppi template without porogen has more cells than any from that template with porogen inclusion.

Although incorporating 25% porogen into the precursor slurry had a positive effect on the number of viable cells after 4 and 7 days, this was not observed for the other camphene contents. All remaining scaffolds except the one produced with 5% camphene on the 45 ppi template exhibited a lower number of cells than those produced without porogen. Including 25% porogen had a much more statistically significant effect on the number of cells that were able to survive on 90 ppi scaffolds ($P_r = 0.0005$) compared to those produced on the 45 ppi template ($P_r = 0.17$) after

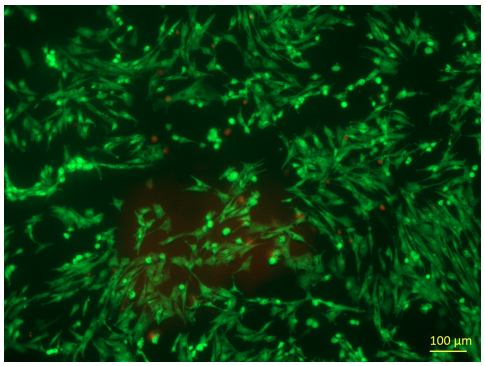

(a) Live/dead assay performed on scaffold produced from 45 ppi template with 0% camphene

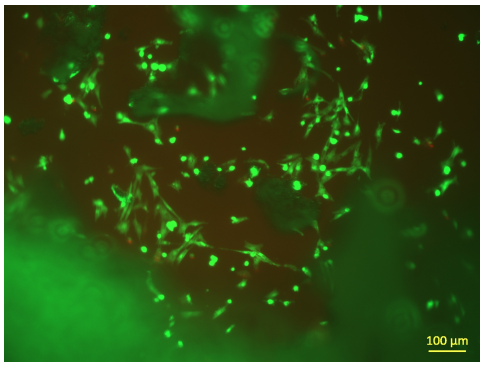

(b) Live/dead assay performed on scaffold produced from 90 ppi template with 0% camphene

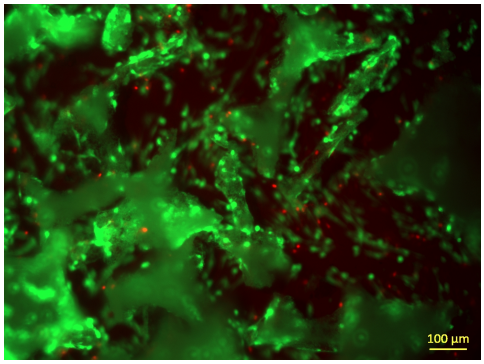

(c) Live/dead assay performed on scaffold produced from 45 ppi template with 25% camphene

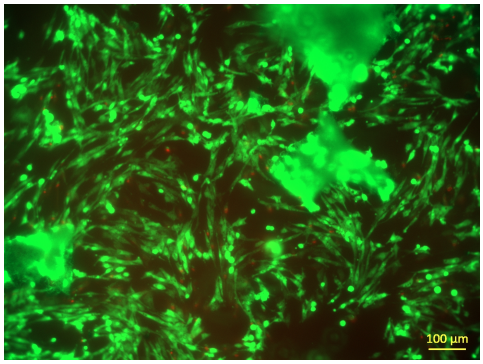

(d) Live/dead assay performed on scaffold produced from 90 ppi template with 25% camphene

Figure 6.56: Microscopy images of scaffolds seeded with 3T3 cells and stained with CalceinAM and PI after 24 h. Live cells individually fluoresce green and dead cells individually fluoresce red, with analysed scaffolds fabricated using 0% porogen on the 45 (a) and 90 ppi (b) templates and 25% on the 45 (c) and 90 ppi (d) templates

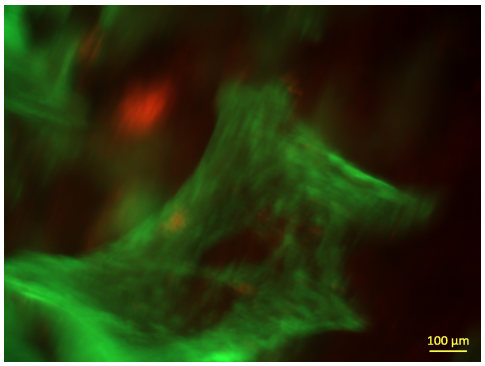

(a) Live/dead assay performed on scaffold produced from 45 ppi template with 0% camphene

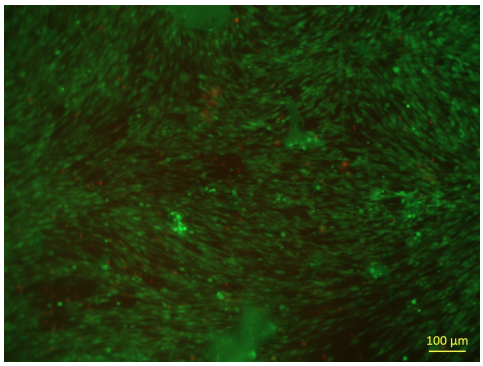

(b) Live/dead assay performed on scaffold produced from 90 ppi template with 0% camphene

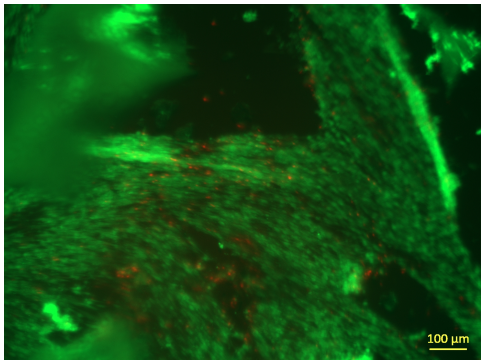

(c) Live/dead assay performed on scaffold produced from 45 ppi template with 25% camphene

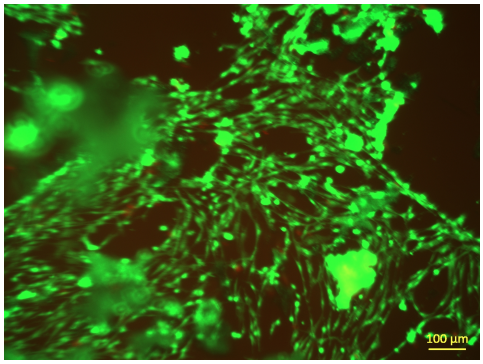

(d) Live/dead assay performed on scaffold produced from 90 ppi template with 25% camphene

Figure 6.57: Microscopy images of scaffolds seeded with 3T3 cells and stained with CalceinAM and PI after 72 h. Live cells individually fluoresce green and dead cells individually fluoresce red, with analysed scaffolds fabricated using 0% porogen on the 45 (a) and 90 ppi (b) templates and 25% on the 45 (c) and 90 ppi (d) templates

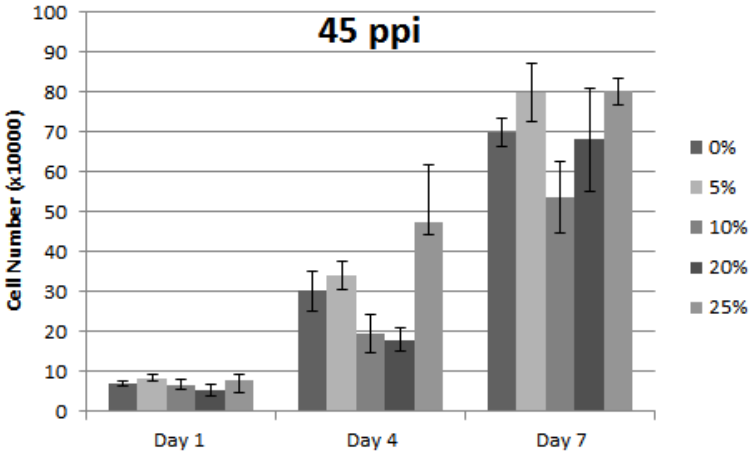

(a) Results of the MTT assay for scaffolds produced using scaffolds produced using the 45 ppi foam as template

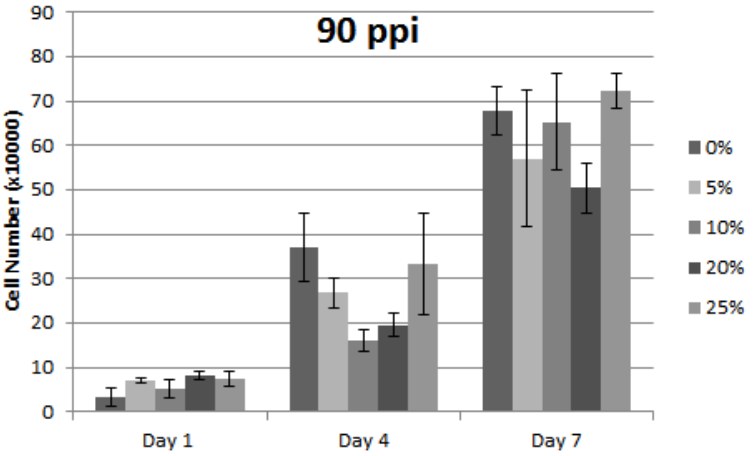

(b) Results of the MTT assay for scaffolds produced using scaffolds produced using the 90 ppi foam as template

Figure 6.58: Mean ±SD (n=9) cell number as quantified by MTT assay for scaffolds produced using the AFR with varying amounts of camphene included in the slurry and seeded with 3T3 cells. Scaffolds have been coated 5 times with the slurry and sintered to 1350 °C

1 day. After 4 days, scaffolds from the 45 ppi template were affected by the amount of porogen ($P_r = 0.004$) whilst there was no statistical difference ($P_r = 0.44$) seen on scaffolds produced with and without porogen on the 90 ppi template. Table 6.7 gives the P_r values for the cell numbers on all scaffolds compared to that produced without porogen. It is thought that incorporating 25% porogen during production led to micropores which cells could infiltrate and hence attach to. Meanwhile, the cells were unable to infiltrate smaller micropores fabricated with lower porogen inclusions. Furthermore, the surface topography of such pores may have been less conducive to cell adhesion due to the lack of material onto which they could attach.

Table 6.7: P_r values obtained using Student's T-Test and Tukey's Pairwise Comparison between scaffolds produced with and without porogen at the same time point. [a] denotes those values where the scaffold without camphene had a higher number of viable cells than that specified.

		45 ppi	90 ppi
5%	1 day	0.0034	<0.0001
	4 day	0.0737	[a]0.0023
	7 day	0.0071	[a]0.0644
10%	1 day	[a]0.4733	0.1194
	4 day	[a]0.0003	[a]<0.0001
	7 day	[a]<0.0001	[a]0.5328
20%	1 day	0.0082	<0.0001
	4 day	[a]<0.0001	[a]<0.0001
	7 day	[a]0.4189	[a]<0.0001
25%	1 day	0.17	0.0005
	4 day	0.004	0.4353
	7 day	<0.0001	0.066

6.4.3.2 MC3T3 Cell Line

Scaffolds produced with 0 and 25 % camphene were seeded with MC3T3 cells, with the cell number shown in Figure 6.59. MC3T3 cells were seeded more successfully than 3T3 cells, with a significant improvement in the number seen one day after seeding. There was a slight improvement in viability using the 45 ppi template compared to the 90 ppi template after 4 and 7 days. Furthermore, incorporating 25%

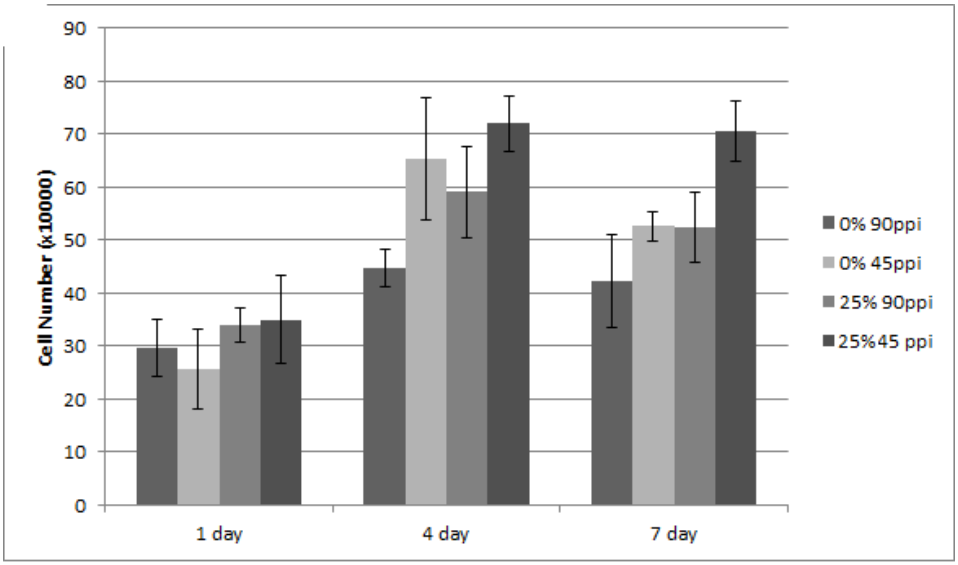

Figure 6.59: Mean ±SD (n=9) cell number as quantified by MTT assay for scaffolds produced using the AFR with 0 and 25 % camphene included in the slurry and seeded with MC3T3 cells. Scaffolds have been coated 5 times with the slurry and sintered to 1350 °C

porogen in the slurry during scaffold manufacture led to a statistically significant increase in the number of cells in all cases except for the 45 ppi scaffold at day 4 as shown in Table 6.8. The maximum number of cells is similar to the maximum number seen on the scaffolds seeded with 3T3 cells, indicating that the scaffolds are fully confluent and can not support any more cells.

Table 6.8: P_r values obtained using Student's T-Test and Tukey's Pairwise Comparison between scaffolds produced with and without porogen at the same time point

	45 ppi	90 ppi
1 day	0.0618	0.0241
4 day	0.0002	0.1384
7 day	0.0136	<0.0001

6.4.4 ALP Assay

6.4.4.1 Optimal Route for Removal of Cells

The ALP activity was measured for 4 sets of samples sintered to 1350 °C (produced using slurries incorporating 10 and 20% porogen, using the 45 and 90 ppi foams), with the results shown in Table 6.9. For each technique, the average and standard deviation was calculated as was the standard deviation as a percentage of the mean ALP measurement for each sample. The results are shown in Table 6.10, where it can be seen that method 1 is the result with the most repeatability as it has the lowest standard deviation as a percentage of the mean reading. Therefore this method is used hereafter to remove cells from the scaffolds when measuring the ALP release.

Table 6.9: Mean ±SD (n=9) as quantified by ALP (ng/mL) on structures produced using the processing parameters given and sintered to 1350 °C obtained when cells had been removed from the scaffolds using the different methods

		10% camphene; 45 ppi template	10% camphene; 90 ppi template	20% camphene; 45 ppi template	20% camphene; 90 ppi template
Method 1	1 day	0.62 ± 0.09	0.39 ± 0.02	0.32 ± 0.01	0.67 ± 0.13
	7 day	1.16± 0.08	1.11± 0.05	0.97± 0.03	0.87± 0.14
Method 2	1 day	0.84 ± 0.12	0.41 ± 0.06	0.36 ± 0.04	0.82 ± 0.17
	7 day	1.02± 0.09	0.94± 0.10	0.90± 0.03	0.88± 0.05
Method 3	1 day	0.78 ± 0.02	0.55 ± 0.11	0.27 ± 0.04	0.84 ± 0.25
	7 day	0.58± 0.02	0.53± 0.04	0.48± 0.04	0.68± 0.07

Table 6.10: Average standard deviation and average standard deviation as a percentage of the mean ALP using the different techniques to remove the cells from the scaffolds

		Standard Deviation (±)	Standard Deviation as percentage of mean (%)
Method 1	1 day	0.064	11
	7 day	0.043	4.0
Method 2	1 day	0.099	15
	7 day	0.070	7.3
Method 3	1 day	0.11	17
	7 day	0.036	6.2

6.4.4.2 3T3 ALP release

The ALP activity was quantified after 1, 4 and 7 days as shown in Figure 6.60. After culture for 1 day, the scaffolds without porogen generally released the highest level of ALP, however this was with little statistical significance. There was little change to the amount of ALP released from cells on these scaffolds after 4 days, however all scaffolds produced using porogen demonstrated a significant improvement compared to day 1. The scaffold with 10% porogen had the largest average amount of ALP release at this timepoint, however this was not statistically significant compared to the other scaffolds. After 7 days, the scaffolds produced without porogen again released the largest amounts of ALP on both templates. While those produced with 10, 20 and 25% porogen incorporation released similar amounts to that at day 4, the scaffold produced using 5% porogen exhibited a decrease in the average amount of ALP released, although this was not statistically significant.

There was little effect with using different templates for producing scaffolds, with similar amounts of ALP released regardless of whether the 45 or 90 ppi foam was used. There was quite a large range to the results, causing the statistical significance to be small in most cases, with the P_r values for the ALP release on all scaffolds compared to that produced without porogen given in Table 6.11.

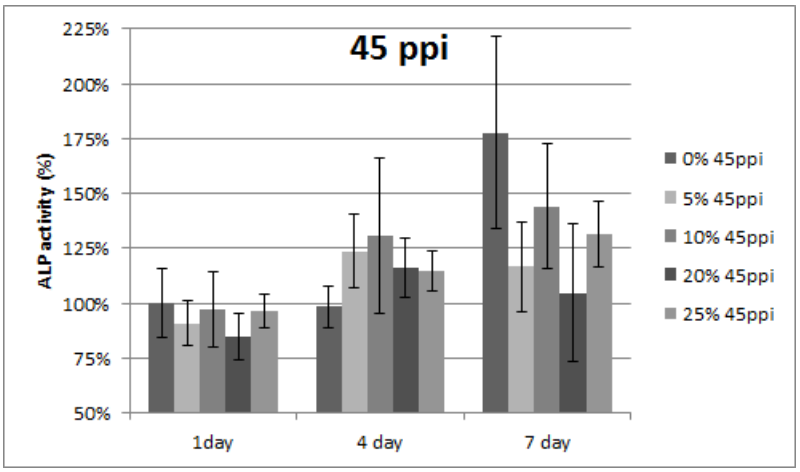

(a) Results of the ALP assay for scaffolds produced using scaffolds produced using the 45 ppi foam as template

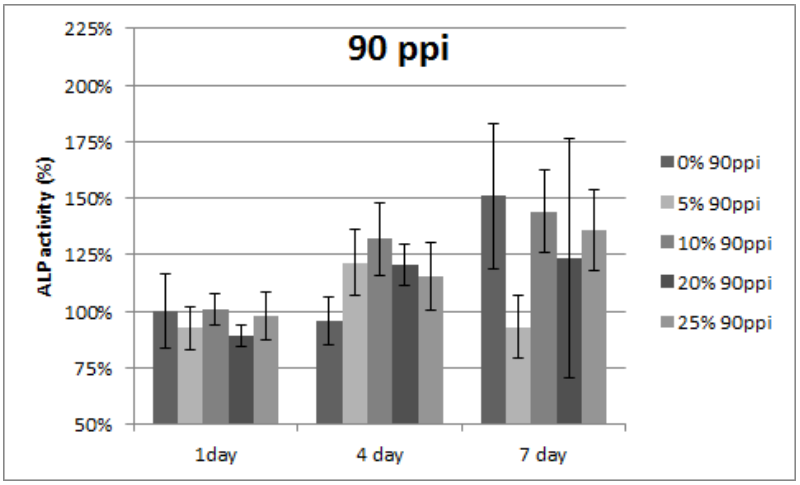

(b) Results of the ALP assay for scaffolds produced using scaffolds produced using the 90 ppi foam as template

Figure 6.60: Mean ±SD (n=9) ALP released by scaffolds produced using the AFR with varying amounts of camphene included in the slurry and seeded with 3T3 cells. Scaffolds have been coated 5 times with the slurry and sintered to 1350 °C

Table 6.11: P_r values obtained using Student's T-Test and Tukey's Pairwise Comparison for scaffolds that underwent ALP assay with release compared to that on the scaffold produced without porogen when seeded with 3T3 cells. [a] denotes those values where the scaffold without camphene expressed a greater amount of ALP that that specified

		45 ppi	90 ppi
5 %	1 day	[a]0.12	[a]0.23
	4 day	<0.0001	<0.0001
	7 day	[a]0.81	[a]0.81
10 %	1 day	[a]0.67	0.89
	4 day	0.008	0.02
	7 day	[a]0.12	[a]0.11
20 %	1 day	[a]0.015	[a]0.065
	4 day	0.003	<0.0001
	7 day	[a]0.10	[a]0.18
25 %	1 day	[a]0.51	[a]0.76
	4 day	<0.0001	0.35
	7 day	[a]0.77	[a]0.87

6.4.4.3 MC3T3 ALP release

As with scaffolds seeded with 3T3 cells, the ALP activity on scaffolds seeded with MC3T3 cells was quantified after 1, 4 and 7 days, as shown in Figure 6.61. After 1 and 7 days, the level measured on scaffolds produced with porogen was slightly lower than that on those produced without. However at 4 days, there was a greater increase in ALP expression on those produced with the porogen. All scaffolds except that produced without camphene on the 90 ppi template exhibited a decrease in the level of ALP at day 7 compared to day 4, causing the level to be similar to that observed at day 1. With respect to the inclusion of camphene within the manufacturing process, the only times any significant statistical significance was observed was at day 4 where the structure from the 90 ppi template with porogen exhibited signicantly enhanced ALP expression (P_r<0.0001), and at day 7, where the structure from the 45 ppi template without camphene exhibited greater ALP expression than that with (P_r=0.0209), with all P_r values given in in Table 6.12. It is also important to note that the levels of ALP expressed with the MC3T3 cells on

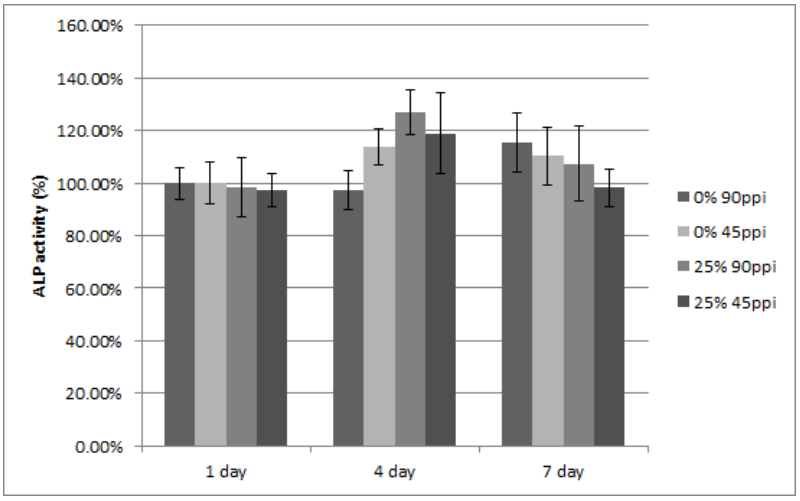

Figure 6.61: Mean ±SD (n=9) ALP released by scaffolds produced using the AFR with 0 and 25 % camphene included in the slurry and seeded with MC3T3 cells. Scaffolds have been coated 5 times with the slurry and sintered to 1350 °C

the scaffolds produced without porogen after 1 day was double the number expressed when 3T3 cells were seeded, and there was a significant reduction to the range of the results.

Table 6.12: P_r values obtained using Student's T-Test and Tukey's Pairwise Comparison between scaffolds produced with 25 % and without porogen at the same time point when seeded with MC3T3 cells. [a] denotes those values where the scaffold without camphene expressed a greater amount of ALP than that specified.

	45 ppi	90 ppi
1 day	[a]0.4036	[a]0.6765
4 day	0.4375	<0.0001
7 day	[a]0.0209	[a]0.2420

6.4.5 Dissolution Assay

The amount of calcium in the culture solution was measured after 1, 4 and 7 days as shown in Figure 6.62 for PBS and Figure 6.63 for DMEM. There was an increase in the amount of dissolved calcium with time for all scaffolds, with little significant difference between structures fabricated using different templates. The amount of porogen in the slurry did not have a great impact on the amount of dissolution,

Table 6.13: P_r values obtained using Student's T-Test and Tukey's Pairwise Comparison for calcium dissolution of scaffolds compared to that on the scaffold produced without porogen. [a] denotes those values where the scaffold without camphene exhibited greater levels of calcium dissolution that that specified

		PBS		DMEM	
		45 ppi	90 ppi	45 ppi	90 ppi
5 %	1 day	[a]<0.0001	<0.0001	<0.0001	[a]<0.0001
	4 day	[a]<0.0001	[a]0.037	<0.0001	[a]<0.0001
	7 day	[a]<0.0001	0.665	<0.0001	[a]<0.0001
10 %	1 day	[a]<0.0001	<0.0001	<0.0001	0.0008
	4 day	[a]<0.0001	[a]0.0007	<0.0001	[a]<0.0001
	7 day	[a]<0.0001	[a]<0.0001	<0.0001	<0.0001
20 %	1 day	[a]<0.0001	<0.0001	<0.0001	0.318
	4 day	0.078	[a]0.004	<0.0001	[a]0.017
	7 day	[a]0.001	<0.0001	<0.0001	<0.0001
25 %	1 day	[a]<0.0001	<0.0001	<0.0001	<0.0001
	4 day	<0.0001	0.7279	<0.0001	[a]<0.0001
	7 day	[a]0.977	<0.0001	<0.0001	<0.0001

with the statistical significances against the structure without porogen in the slurry given in Table 6.13. Finally, there was a difference of 7.7 ± 0.97 mg/dl between equivalent scaffolds submerged in PBS and DMEM. This is due to the calcium salts in DMEM which give a calcium content of approximately 10 mg/dl when diluted 1:1 with the buffer. This corresponds with the measured calcium contents of the DMEM (9.3 ± 0.18 mg/dl).

6.4.6 Discussion

Scaffolds fabricated using the adaptive foam reticulation technique have shown good cell attachment of MG63 bone cells, maintaining good cell viability throughout the culture period of 7 days. This was slightly better than the viability of cells on a commercially available porous HA disc. Over time, the cell number increased only slightly and without statistical significance, indicating limited proliferation. The most probable cause of this is that the high number of cells seeded led to their confluence in the scaffold. The maintenance of the cell viability indicates that the

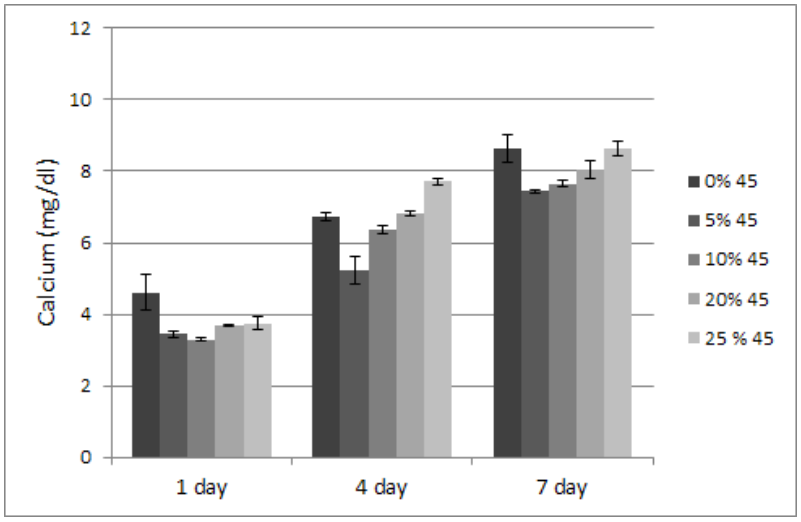

(a) Amount of calcium dissolved in PBS for scaffolds produced using the 45 ppi template

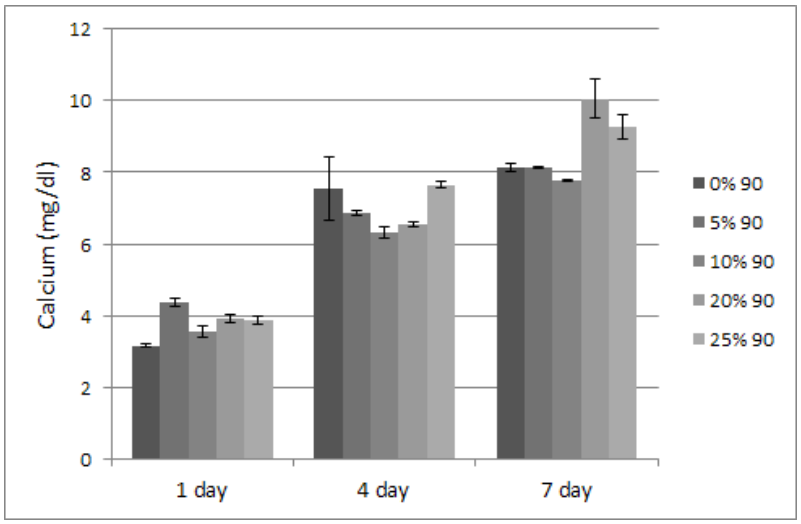

(b) Amount of calcium dissolved in PBS for scaffolds produced using the 90 ppi template

Figure 6.62: Mean ±SD (n=9) amount of calcium in solution when scaffolds produced with varying amounts of camphene included in the slurry were cultured in PBS. Scaffolds have been coated 5 times with the slurry and sintered to 1350 °C

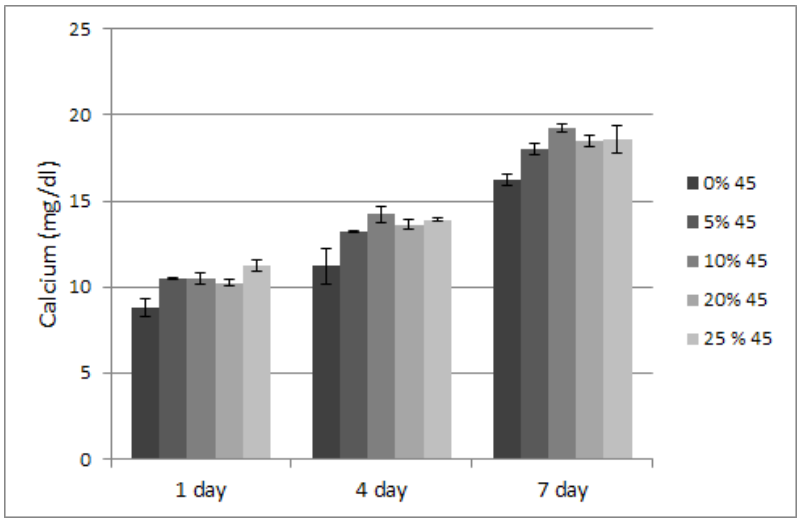

(a) Amount of calcium dissolved in DMEM for scaffolds produced using the 45 ppi template

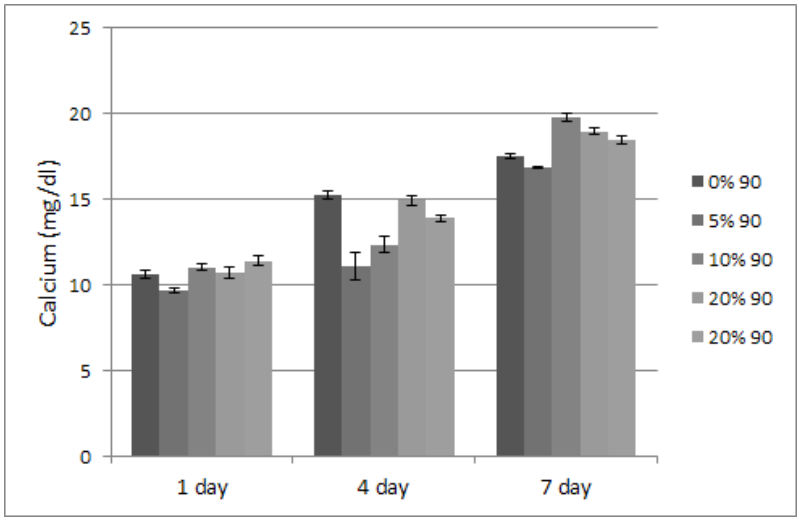

(b) Amount of calcium dissolved in DMEM for scaffolds produced using the 90 ppi template

Figure 6.63: Mean ±SD (n=9) amount of calcium in solution when scaffolds produced with varying amounts of camphene included in the slurry were cultured in DMEM. Scaffolds have been coated 5 times with the slurry and sintered to 1350 °C

scaffolds exhibit no toxicity and are sufficiently porous to enable good nutrient access.

To determine whether incorporating a porogen has a positive effect on the biological performance, further analyses was undertaken using scaffolds fabricated without any porogen as the base against which their performance was analysed. Although visualisation of the cells was undertaken using different assays, the live/dead assays from both the preliminary tests and the further analyses showed that cells seeded on the scaffolds were able to survive on the structures. Furthermore, 24 hours after seeding the cells exhibited an elongated morphology suggesting that they had attached to the struts of the scaffolds. There were some dead cells, however the viability was approximately 95% which is similar to that observed when the cells were counted prior to seeding. Thus it can be deduced that the structures offer a suitable surface onto which cells can grow and the biocompatibility correlates well with other conventional techniques [12, 51, 264, 277, 283] as outlined in Table 3.1.

All scaffolds seeded with 3T3 cells underwent a large reduction in the number of cells after 1 day compared to the amount seeded, indicating low viability. There are a number of factors that could have caused this [1, 6, 16–19, 37], and although any one of these could have had an impact, the most probable cause is related to cell attachment. The scaffolds were seeded by applying the cells directly to the top of the scaffolds, followed by surrounding the cells in media. In many cases, there were regions of the scaffolds which exhibited little or no activity when observing the formazan production before its dissolution for analyses, as shown in Figure 6.64, and thus it may have been necessary to apply the cells more evenly over the structure. Alternatively, although the cells were submerged in media, the lack of any movement may have inhibited the migration of cells throughout the structures. Finally, the scaffolds were dried for 1 hour after sterilisation, yet the highly porous nature of the scaffolds may have led to some residual ethanol within the structure that could kill the cells.

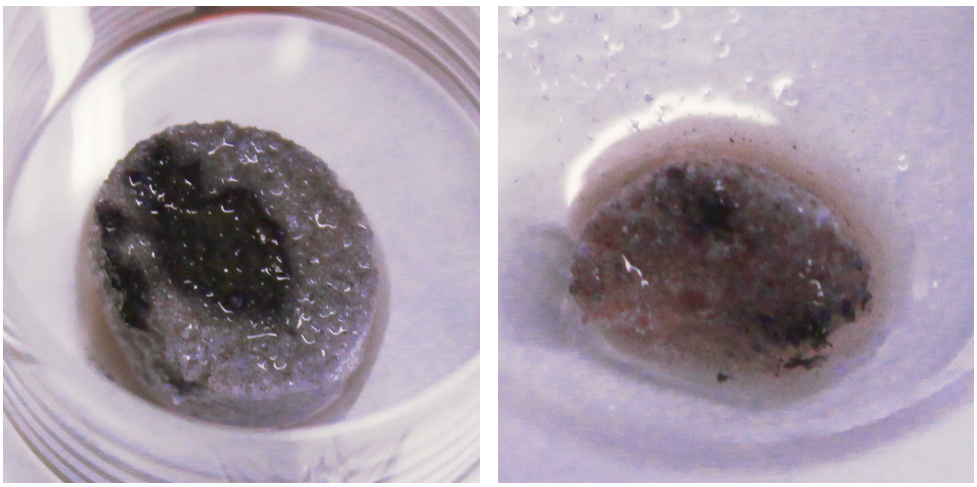

(a) Photograph of formazan crystals on scaffold produced from 90 ppi template

(b) Photograph of formazan crystals on scaffold produced from 45 ppi template

Figure 6.64: Representative photographs showing the distribution of formazan crystals during MTT assay on scaffolds produced with 5 coats of the slurry and sintered to 1350 °C after 1 day in culture

Both templates produced scaffolds with pore sizes within the range outlined as suitable for cell adhesion and proliferation [5, 12, 14]. The macropores generated allow for the complete infiltration of cells, nutrients and metabolites which was enhanced by the open nature of the porosity. Although in most cases the template used to produce the scaffold did not have a significant effect on the number of cells, those produced with 25% camphene led to a significantly higher number of cells on the 45 ppi template than on the 90 ppi template. This suggests that the larger pore size produced is more suited to bone regenerative medicine, however further analyses on the exact pore size required is necessary before this can be stated definitively.

Possibly the more interesting feature of the analysis using 3T3 cells was that any ALP expression was measured. They are fibroblastic with little scope for changing their phenotype [535, 536] and as such there was expected to be little more than a background reading. Nevertheless, they are taken from mouse embryo tissue and as such there may still be some residual ability for the cells to differentiate down other lineages. Not only could this give a further possibility for the significant reduction

in cell number after seeding - the microstructure of the surface could have caused cell signalling [17, 18, 20, 21, 537] that selected only for the attachment of cells with the potential to become osteoblastic - but it also could explain why such cells were able to express ALP. However, Huschtscha et al [538] developed a cell quantification assay based on ALP expression suitable for use with 3T3 cells. As such, the assay may have been sensitive enough to show the base levels of ALP expressed by the cells, with the increase solely due to the increase in cell number.

The scaffolds dissolved in media with the amount of Ca^{2+} measured. Although not analysed, there must also have been dissolution of PO_4^{3-} ions as they are bound to the calcium in HA. Beck et al have shown that PO_4^{3-} regulates the release of osteopontin [476] and can alter gene expression [478]. Hence, the dissolution of the construct could cause subtle changes in cell morphology that ultimately led to the expression of ALP.

The scaffolds with 25% camphene inclusion exhibited a statistically significant increase in the number of cells counted, particularly 7 days after seeding. This indicates that the inclusion of a porogen into the precursor slurry does have an impact on the ability of the cells to attach, differentiate and proliferate on the structures. However, along with the scaffolds produced with 5% camphene on the 45 ppi template, this is the only level at which scaffolds with porogen of any amount exceeded the performance of the scaffolds fabricated without camphene. The micropores generated are 2-3 μm, which is large enough to affect cell signalling and the subsequent differentiation, but not to allow for capillary growth [21, 537]. The larger micropores observed due to the coalescence of the smaller micropores however may aid growth as cells cannot infiltrate individual micropores which are smaller than the cells [17, 18].

The number of viable MC3T3 cells was greater at all time points on scaffolds produced with 25 % porogen in the slurry than those fabricated without porogen. This corroborates the observations made when 3T3 cells were seeded onto the structures, suggesting that incorporating this level of porogen enhances viability compared to

scaffolds fabricated without any porogen at all. The viability of the MC3T3 cells is perhaps more important as although these are fibroblastic in nature [539–542], they can differentiate down osteoblastic lineages depending on the environment in which they are being cultured [539–545].

Although the exact interaction is unknown, it is possible that either the strut surface roughness, for reasons detailed in Section 1.1.1 or the scaffold dissolution leading to free Ca^{2+} and PO_4^{3-} ions, detailed in Section 4.2.9.2, encouraged osteoblastic differentiation with the cells undergoing the necessary changes between days 4 and 7. Thus there are two possible causes for the decrease in cell number between these time points: firstly, the scaffolds could have become fully confluent, and hence there would be no more space for cells to grow onto; or secondly some cells could have changed to become more osteoblastic in nature, a possibility which could be investigated by determining whether any osteoblastic markers, such as osteocalcin, are present. The ALP expression between days 4 and 7 dropped on scaffolds seeded with MC3T3 cells, yet due to the reduction in the cell number, there was more ALP produced per cell. This could also represent the cells becoming more osteoblastic than fibroblastic.

As Chang et al [15] have shown that foam reticulated structures facilitate enhanced bony growth compared to autografts *in vivo*, the enhanced cell viability of structures fabricated with a porogen in the slurry to produce controllable microporosity could offer a suitable alternative to grafting procedures. This cannot be stated with any certainty however until *in vivo* analyses has been undertaken.

6.5 Summary

The AFR has been implemented to fabricate HA structures suitable for use as bone replacement bioscaffolds. Crystallographic evaluation has shown there has been at least a partial phase change at all sintering temperatures to whitlockite, a calcium

deficient form of HA that is more chemically similar to the natural mineral phase of bone. As such, although not desired this phase change is not expected to detrimentally affect the biological viability of the scaffolds. SEM and microCT analysis demonstrated constructs have a highly interconnected 3D structure, with macropore sizes within the range specified for bone regenerative scaffolds. The macroporosity, and macropore and strut size can be adjusted by varying the processing parameters, namely the sintering temperature, template and number of coats of the slurry on the template. Furthermore, inclusion of a porogen, camphene, has led to the introduction of micropores within the macroporous struts. The number and density of the micropores can be controlled by the amount of porogen, while the size is varied with alterations to the freezing temperature.

The porosity of the scaffolds has been measured using the Archimedes method, with the structures fabricated from the 90 ppi template more susceptible to changes to the processing parameters. The porosity has been used to calculate the theoretical compressive yield stress using the novel incorporation of a shape factor to allow for the microporosity. This correlates well with experimental data for certain samples, however a more indepth analysis is required as there was some differences between one set of samples. The strength of the samples is weak compared to that of natural bone, and as such further work is required to sufficiently improve this. Finally, there is enhanced biological viability of AFR fabrications (produced without microporosity) compared to a commercially available porous HA disc. Furthermore, the viability was similar for all samples with porogen compared to those without except for those with the maximum inclusion, which performed better in most analyses. Further *in-vivo* analyses are required, however, to state whether the samples offer a suitable alternative to existing grafting procedures.

Chapter 7

Titanium/Titanium-Aluminium-Vanadium

The previous chapter, Chapter 6, dealt exclusively with the results obtained when HA was used as the biomaterial. To ascertain whether the methodology implemented could be suitable for use with other biomaterials, structures were fabricated from Ti and Ti-6Al-4V. Thus this chapter deals solely with whether the AFR technique can be used for controllably manufacturing bioscaffolds from these materials, with an overall discussion of the technique and the suitability of it to produce scaffolds suited to bone reparation given in Chapter 8.

As with results from HA scaffolds, raw data is available in Appendix A where a graphical representation of results is given. Furthermore, as previously outlined in Section 4.2.8, trend lines on graphs are used as visual aids due to the datasets for each scaffold coming from different samples.

7.1 Crystallography

7.1.1 Titanium

The indexed XRD of the raw material has been shown to be titanium hydride, Section 5.2. The indexed XRD of powdered scaffolds, Figure 7.1 matched the COD reference patterns of α-titanium (Ti_2) 96-900-8518), β-titanium (Ti_4) (96-901-1601), titanium-carbide (TiC) (96-591-0092), and titanium-carbide-nitride (Ti-C-N)

(Ti_5CN_4) (96-101-0872). As the sintering temperature was increased, a higher proportion of the sample underwent carbide formation, with 100% of the material being either Ti_2 or Ti_4 at 1000 °C, whilst at 1300 °C this had decreased significantly. As such, at 1200 °C and 1300 °C, only 37 and 48% of the material was estimated to have remained as Ti, with estimated compositions shown in Table 7.1.

Table 7.1: Composition of Ti samples sintered to 1000, 1100, 1200 and 1300 °C as estimated using peak area analysis

Analysis	Specimen	Ti_2 (%)	Ti_4 (%)	Ti-C (%)	Ti-C-N (%)
Peak Area	1000 °C	77	23	-	-
	1100 °C	69	21	6	4
	1200 °C	37	-	39	24
	1300 °C	48	-	29	23

Due to the high susceptibility of titanium to react with oxygen, the complete lack of any oxide formation was not expected, and it is thought that the use of a cobalt tube for X-ray diffraction may have contributed to errors in the minority phases identified. Hence, scans were also undertaken on the same samples using an Fe-filtered diffractometer (Model Empryean, PANalytical, UK) equipped with a copper tube and with an increased step time of 1 s, whilst all other parameters remained identical: step size of 0.02°, incident angle 2ϑ of 5-90°. Whilst there was a similar shape to the peak profile, this led to a significant shift in the profile, as shown in Figure 7.2. Additionally, compared to samples analysed using the cobalt source diffractometer, the major difference observed for samples sintered to 1200 and 1300 °C is that the presence of Ti_2 or Ti_4 is no longer evident. Furthermore, due to the slower scan speed, for all scans the peaks were sharper and it was possible to observe more features that were thought to be the background reading during analysis using a cobalt tube. Table 7.2 gives the material composition obtained using XRD with a copper tube. The samples sintered to 1200 and 1300 °C underwent complete transformation to a combination of Ti-C or Ti_2-C-N and Ti-N, whilst those sintered to 1000 and 1100 °C underwent some oxide formation as well as transformation to Ti-N and Ti-C.

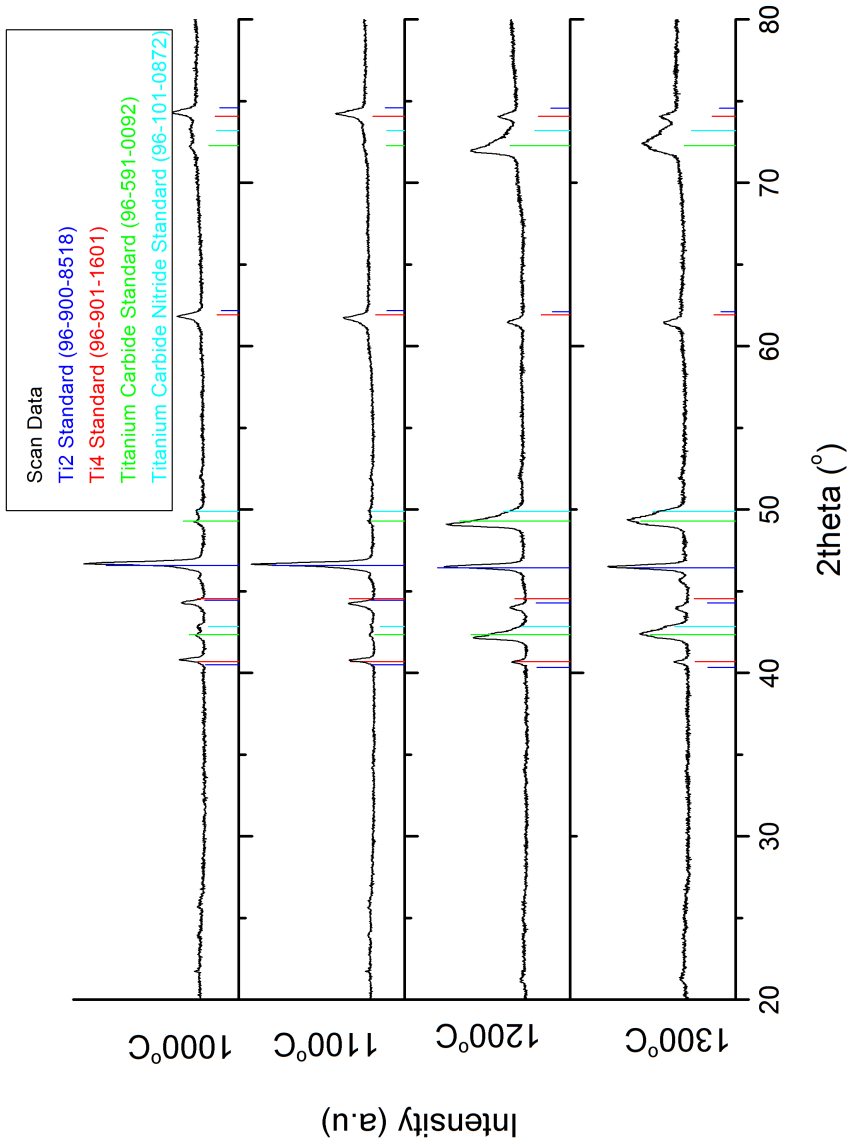

Figure 7.1: Indexed XRD of powdered Ti scaffolds sintered to 1000, 1100, 1200 and 1300 °C, plotted on the same axis as the COD reference pattern for Ti_2 (96-900-8518), Ti_4 (96-901-1601), titanium-carbide (96-591-0092), and titanium-carbide-nitride (96-101-0872)

Table 7.2: Composition of Ti samples sintered 1000, 1100, 1200 and 1300 °C as estimated using peak area analysis after XRD undertaken with a copper tube

Specimen	Ti_2 (%)	Ti^4 (%)	Ti-C (%)	Ti-C-N (%)	Ti_2-C-N (%)	Ti-N (%)	Ti_2-N (%)	Ti_2-O (%)	Ti_3-O (%)	Ti_6-O (%)
1000 °C	19	-	3	-	-	5	2	31	41	-
1100 °C	1	1	6	-	-	9	5	-	19	59
1200 °C	-	-	-	-	60	40	-	-	-	-
1300 °C	-	-	54	-	-	46	-	-	-	-

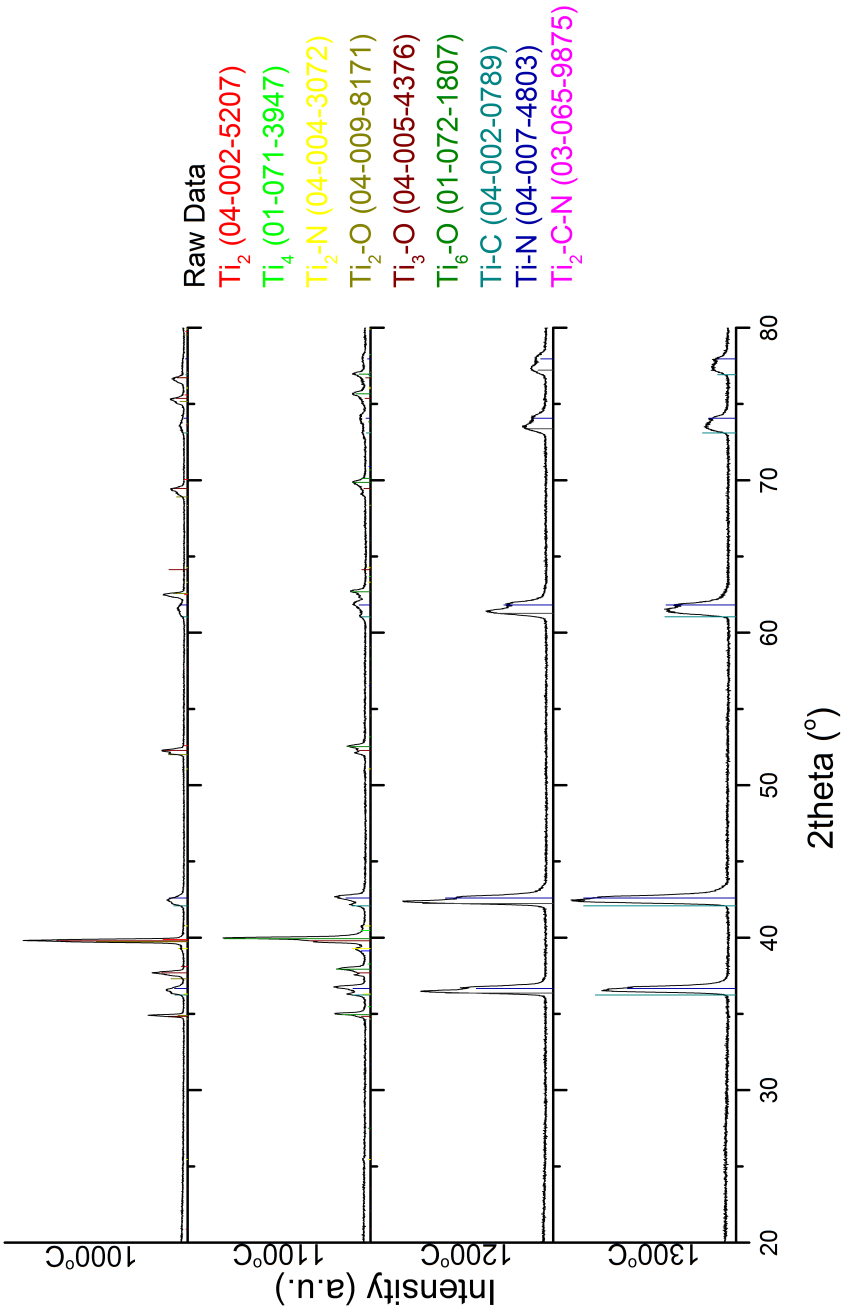

Figure 7.2: Indexed XRD of powdered Ti scaffolds sintered to 1000, 1100, 1200 and 1300 °C, plotted on the same axis as the ICDD reference pattern for Ti_2 (04-002-5207), Ti_4 (01-071-3947), titanium$_2$-nitride (04-004-3072), titainum$_2$-oxide (04-009-8171), titanium$_3$-oxide (04-005-4376), titanium$_6$-oxide (01-072-1807) titanium-carbide (04-002-0789), titanium-nitride (04-007-4803) and titanium-carbide-nitride (03-065-9875)

Table 7.3: Composition of Ti-6Al-4V samples sintered to 1200, 1300 and 1350 °C as estimated using peak area analysis

Analysis	Specimen	Ti_2 (%)	Ti_4 (%)	Ti-C (%)	Ti-C-N (%)
Peak Area	Raw	60	40	-	-
	1200 °C	27	-	41	32
	1250 °C	51	-	28	21
	1300 °C	17	-	46	37

7.1.2 Titanium-Aluminium-Vanadium

The as-received material, Section 5.2, exhibited the characteristic peaks of α-Ti and β-Ti, suggesting that it is Ti-6Al-4V. Structures sintered to 1200, 1250 and 1300 °C were found to show strong peaks for Ti_2. Furthermore, there were significant peaks for Ti-C and Ti-C-N. The indexed XRD peaks are shown in Figure 7.3, with estimates of the sample composition given in Table 7.3. Samples sintered to 1250 and 1300 °C were evaluated after silicon inclusion. Furthermore, there were some small peaks between 20 and 30 ° that have not been identified. The small values these account for are not expected to have a significant impact on the material as the peak areas are less than 5%. All sintered constructs underwent a significant amount of carbide formation with approximately 73, 49 and 83% of the material becoming TiC or Ti-C-N at 1200, 1250 and 1300 °C respectively.

The differences observed when a copper tube was used in the analysis for Ti samples led to the additional scanning of Ti-6Al-4V samples using the same procedure as described above for Ti. In general, the same features were observed: there was a significant shift and increase in sharpness of the peaks, there was less background noise and there was no increase to the background at high angles, as shown in Figure 7.4. The increased resolution led to some differences in the compositional analysis, as detailed in Table 7.4. In particular, there were increased levels of titanium carbo-nitride as well as some titanium-aluminium phases. The only structure that underwent some limited oxide formation was that sintered to 1250 °C, which exhibited some peaks for vanadium oxide.

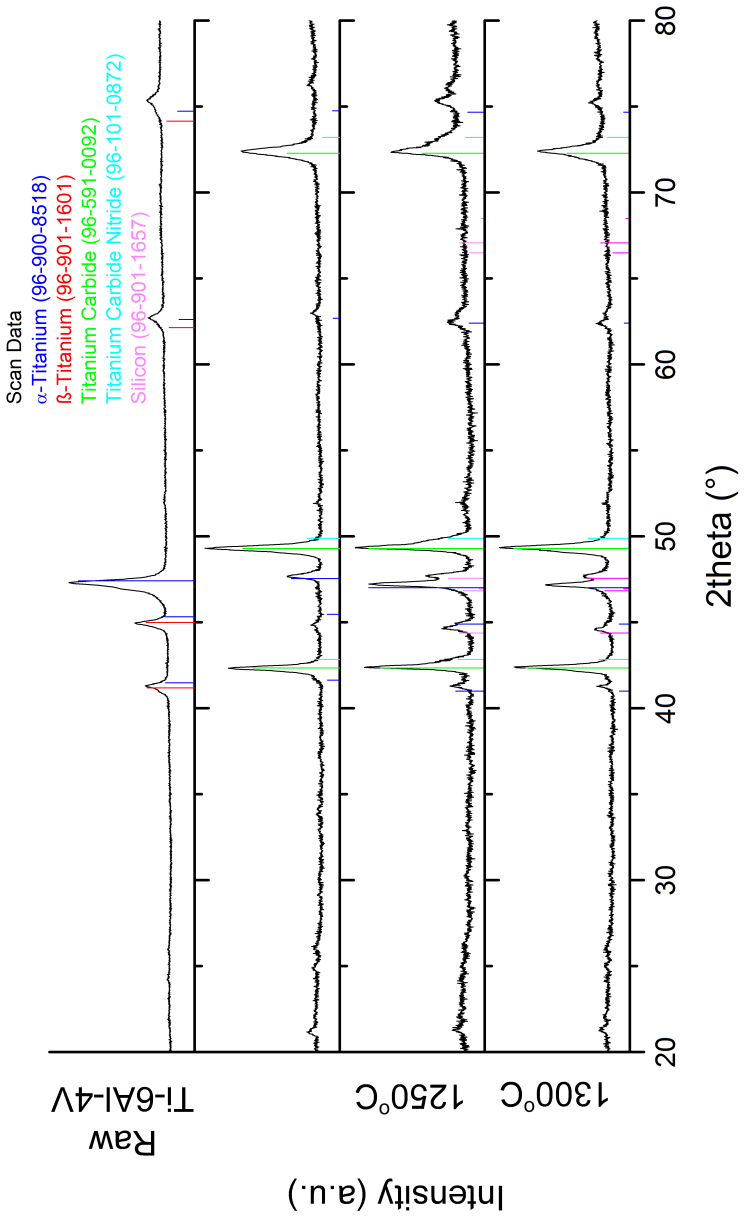

Figure 7.3: Indexed XRD of powdered Ti-6Al-4V scaffolds sintered to 1200, 1250 and 1300 °C, plotted on the same axis as the COD reference pattern for Ti_2 (96-900-8518), Ti_4 (96-901-1601), titanium-carbide (96-591-0092) and silicon (96-901-1657).

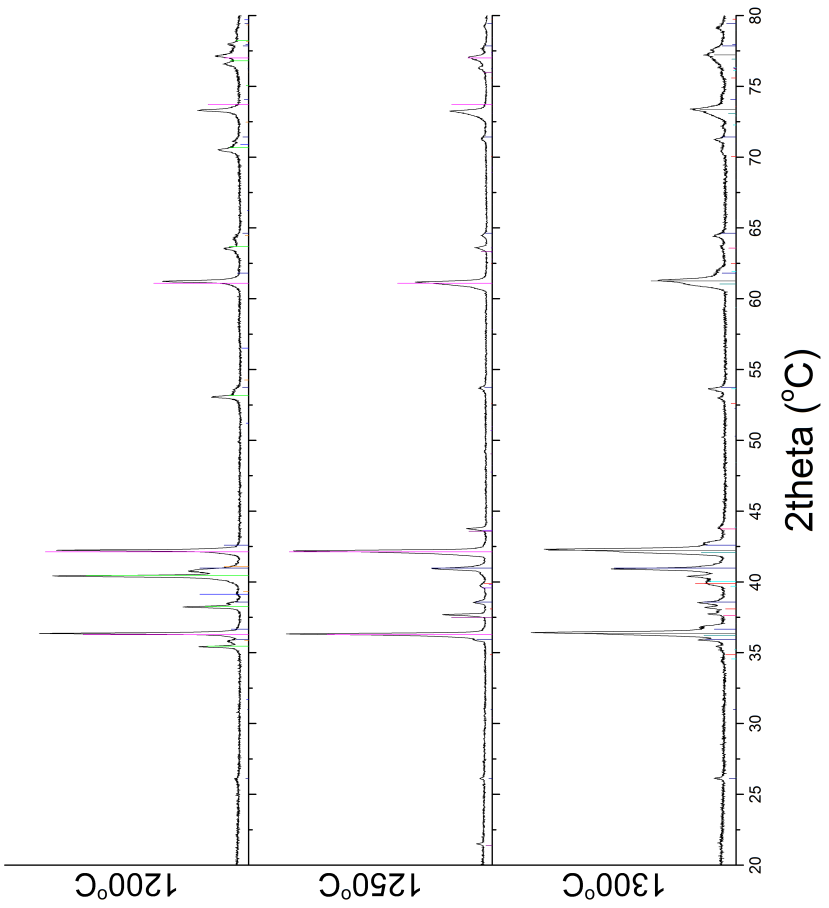

Figure 7.4: Indexed XRD of powdered Ti-6Al-4V scaffolds sintered to 1200, 1250 and 1300 °C, plotted on the same axis as the COD reference pattern for Ti_2 (04-002-5207), Ti_4 (07-071-3947), titanium$_2$-carbide (03-065-9875), titanium$_2$-aluminium-nitride (04-001-6325), titanium$_3$-aluminium (04-015-7850), titanium$_3$-aluminium-carbide (04-001-6068), titanium-nitride (04-007-4803), vanadium$_2$-carbide (04-077-7210), vanadium$_7$-oxide$_3$ (04-007-0520) and vanadium-nitride (04-008-7244).

Table 7.4: Composition of Ti-6Al-4V samples sintered 1200, 1250 and 1300 °C as estimated using peak area analysis after XRD undertaken with a copper tube

Specimen	Ti_2 (%)	Ti_4 (%)	Ti-C (%)	Ti_2-C-N (%)	Ti_2-Al-N (%)	T_3-Al (%)	Ti_3-Al-C (%)	Ti-N (%)	V_2-C (%)	V_7-O_3 (%)	V-N (%)
1200 °C	27	8	-	50	-	8	-	5	3	-	-
1250 °C	1	-	-	69	-	14	11	-	-	5	-
1300 °C	2	-	10	53	2	7	-	23	-	-	3

7.1.3 Discussion

At temperatures above approximately 600 °C, TiH_2 decomposes to titanium and hydrogen gas [380], although slower heating rates have been reported [379] to reduce the onset temperature to lower than 550 °C. The desorption of hydrogen in hydride-containing materials consists of several steps including the thermal decomposition at the hydride-metal interface, diffusion of hydrogen through the metal phase, surface penetration of hydrogen atoms, recombination of absorbed atoms and hydrogen degassing [379].

Ti-H systems undergo phase changes depending on the amount of hydrogen in the atmosphere at elevated temperatures, with the phase diagram for Ti-H in environments of varying hydrogen contents up to 5 wt.% at 1 atm shown in Figure 7.5. At temperatures as low as 400 °C, with low concentrations of hydrogen (0-10 at.%), $TiH_{0.1}$ (α-phase, hexagonal close-packed (HCP)) forms, which becomes $TiH_{0.3}$ (β-phase, body-centered cubic (BCC)) at 10-44 at.%. This becomes TiH (γ-phase, face-centered tetragonal (FCT)) at 44-50 at.%, $TiH_{1.5}$ (δ-phase, face-centered cubic (FCC)) at 50-66 at.% and TiH_2 (ε-phase, FCT) at 66-67 at.% [380]. Conversely, with decreasing hydrogen content, TiH_2 transforms through the various phases to Ti. The use of flowing gas to generate an inert atmosphere in this work led to the removal of the H_2 gas as the TiH_2 decomposed, essentially creating a hydrogen free atmosphere. Thus, as is shown in Figure 7.1, none of the starting material (TiH_2), Figure 5.4, was present in the final structure. From the phase diagram, it can be seen that at temperatures and in environments enabling the decomposition of the hydride, the process is from the ε-phase to a combination of δ- and ε-phases, then to the β-phase and finally, during cooling to the α-phase [379, 380].

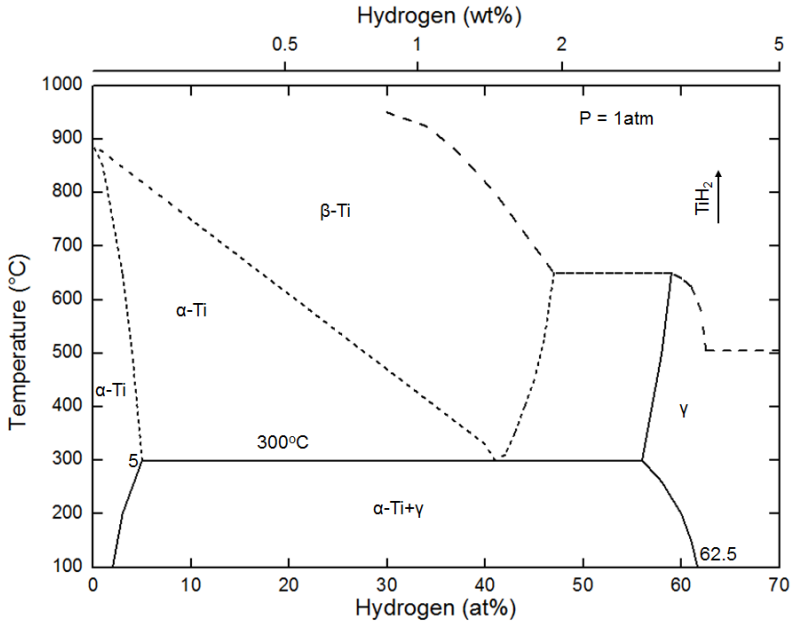

Figure 7.5: Phase diagram for TiH_2 at P=1atm. α-Ti - Ti_2; β-Ti - Ti_4; γ - phase of TiH (redrawn from [379, 380])

Ti is highly susceptible to oxidation [44, 230]. Hence, processing was undertaken in an inert atmosphere to minimise this risk. No oxide was seen in structures fabricated using TiH_2 in the biomaterial slurry indicating that all oxygen was succesfully removed from the local atmosphere prior to sintering during analysis of the XRD undertaken with a cobalt tube. However, there were XRD peaks matching the reference for titanium-carbide and titanium-carbide-nitride. This is believed to be due to incomplete polymer burnout resulting in the subsequent reaction of titanium with some of the carbon atoms, a theory strengthened by the build up of polymer within the tube of the furnace. This phenomenom is not uncommon with foam reticulation based techniques for titanium bioscaffolds with carbide formation also having been reported by others [53, 67, 275]. The inert atmosphere was created by passing a mix of 95:5 Nitrogen:Argon through the tube during sintering, and it is believed that the flow rate (0.016 L/min) was not high enough to fully remove the carbon atoms leading to their reaction with the surface of the scaffold. Thus the carbide has been generated, with the carbide-nitride most probably generated at

the same time. Alternatively, decomposition of the hydride may have commenced below the burnout temperature of the polymer due to the relatively slow heating rate (3 °C/min) used [379]. As such, pyrolysis of the polymer would facilitate the reaction of the C atoms with the highly reactive titanium.

At the lower sintering temperatures, the structures were much less susceptible to the formation of the carbide and the carbide-nitride, as seen in Table 7.1. At 1000 °C, all analyses used found no TiC or Ti-C-N, whilst at 1100 °C very small amounts were found. However, the values increased substantially such that at 1200 °C at least 49% of the material had formed a carbide or carbide-nitride, with similar values at 1300 °C. It is thought that this is due to the extra time at which the highly reactive titanium was at heightened temperatures [379]. The titanium-carbon phase diagram is shown in Figure 7.6 from which it can be seen that at all sintering temperatures used the incomplete polymeric burnout should cause a mixture of β-Ti and TiC [546]. However, the primary titanium phase observed was α-Ti, suggesting that the cooling rate (3 °C/min) was slow enough to enable the reformation of α-Ti during cooling.

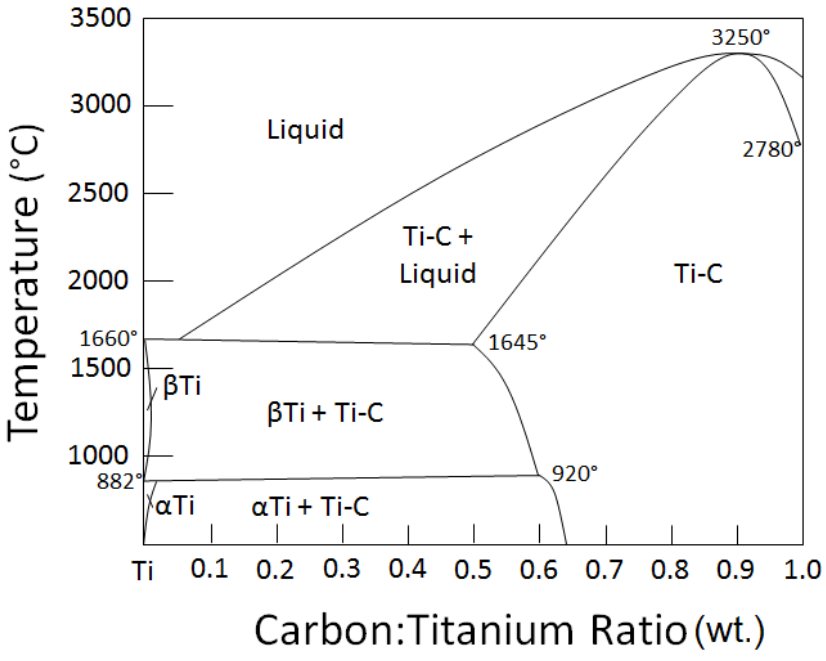

Figure 7.6: Titanium-carbon phase diagram (α-Ti - Ti_2; β-Ti - Ti_4; Ti-C - titanium carbide) (redrawn from [546])

Structures fabricated from Ti-6Al-4V also experienced carbide formation. This supports the theory put forward earlier for Ti constructs that the flow rate of the inert gas was insufficient to fully remove the carbon atoms. Oxidation can occur on titanium based materials from temperatures below 300 °C [547]. As there was no oxide formation, all oxygen must have been removed from the local environment in which the samples were sintered. Interestingly, α-phase Ti was the predominant form of Ti-6Al-4V observed. The phase diagram for Ti-Al-4V systems, shown in Figure 7.7, indicates that the sintering temperatures used should lead to a partial formation of the β-phase [44]. However, Wendler and Jakubowski [548] investigated the high temperature behaviour of Ti and TiC layers and found that below 1100 °C, there was no change to the crystal structures within a two-phase material, whereas above this, both Ti and TiC transformed into a single phase TiC. This may also account for the higher levels of TiC found when both Ti and Ti-6Al-4V structures were sintered above 1100 °C.

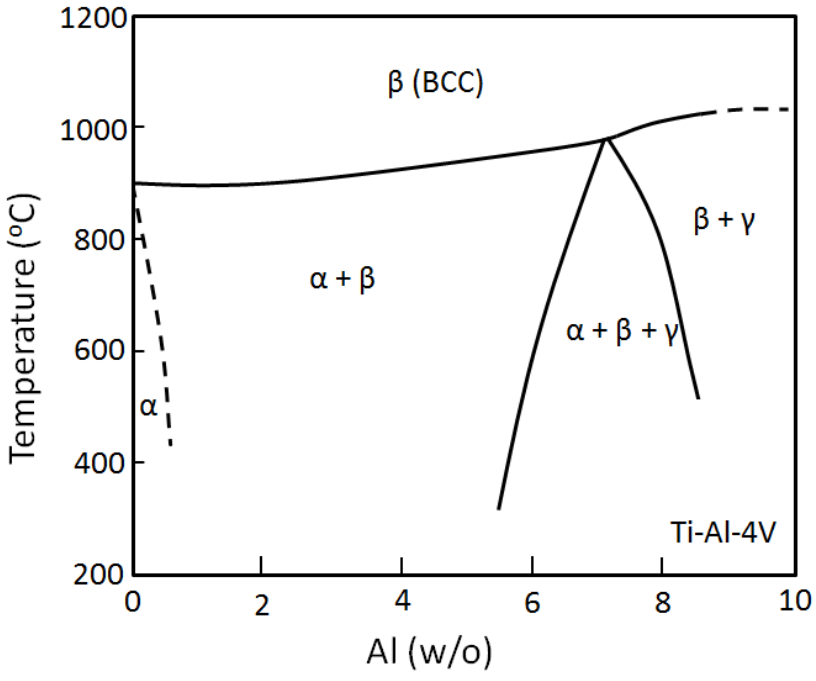

Figure 7.7: Part of phase diagram for titanium-aluminium-vanadium systems with varying Al at 4 wt.% V (redrawn from [44])

The removal of unwanted impurity compounds from the surface of titanium structures involves the use of extremely corrosive materials, such as acidic mixes of sulphuric acid, hydrochloric acid and water for carbides [54]. The use of these could affect the surface roughness or microporosity hence a highly controlled protocol would need to be developed to maintain the structure generated via AFR. One possible method of avoiding the generation of the carbide would be to use a vacuum furnace rather than an inert atmosphere as there would be a more complete removal of the carbon during sintering. Furthermore, this would prevent nitride formation, which must have been caused by passing nitrogen over the structure. However, TiC is known to be biocompatible [137,366,549] with Jorgensen et al [366] and Brama et al [137] having independantly shown that the presence of TiC layers does not affect the biocompatibility of scaffolds. In consequence, the coating has not been removed in this work and instead the macrostructural and microstructural characteristics have been investigated without potentially damaging the Ti.

The increase in the background intensity of the cobalt-tube diffractometer scan data at high angles is suggestive of fluorescence of some of the ions under the X-rays [384]. Additionally, it was not expected that the use of an inert atmosphere during sintering would lead to a complete lack of oxidation. As such, analysis was also undertaken using a copper tube as the X-ray source as titanium-based materials are much less likely to fluoresce under these conditions than when a cobalt tube is used. There were some differences in the observed results. In particular, oeaks which could be attributed to oxide phases were observed in the spectra taken from structures fabricated from TiH_2 and sintered to 1000 and 1100 °C. There are possible explanations for the differences in the scan data. The samples underwent cobalt-source XRD prior to density measurements using Archimedes Method, whereby samples are submerged in water. To ensure complete drying prior for copper-source XRD, the samples were heated to 100 °C and held at that temperature overnight. This could have led to some oxidation of the pure titanium in these samples. Furthermore, the samples were stored in air for approximately one year between the cobalt and copper-source XRD analyses, during which time there could have been some atmospheric reaction.

Alternatively, there is an algorithm within HighScore that compensates for the use of different source tubes. There is a significant amount of overlap in the peaks of the scan data, as well as the peaks of titanium and titanium oxide. The shift thus may have introduced some errors, to the analysis on samples analysed using either source tube. Additionally, the scanning with the copper tube was undertaken with a longer timestep, 1 s, enabling the determination of smaller peaks not observed in the initial scan with the cobalt tube as well as features such as 'shoulders' on other peaks. Thus, structures with overlapping peaks could be defined more accurately: in particular, titanium-oxides have a number of smaller peaks that were not definable in the initial scan. Although it cannot be definitively stated at the location and level within the porous structure, some titanium oxide is likely to be present on the surface of scaffolds. This cannot be accurateley determined however, as suitable surface analysis techniques, such as glancing angle XRD, cannot be accurately undertaken due to the porous nature of the scaffolds. Finally, the samples fabricated from Ti-6Al-4V exhibited the presence of titanium-aluminium based materials, as well as some vanadium based compounds. The relatively small proportion of these, coupled with the peak overlapping of the more significant peaks suggests that these materials are likely to have been present in the cobalt-source tube, but this has only been determined with the higher resolution and peak intensity obtainable with the copper-source measurement.

Possibly the most interesting feature of the copper-source XRD analysis is that the level of oxide in the scans run with a copper-source diffractometer was related to the amount of pure titanium measured using a cobalt-source diffractometer. This indicates that the most plausible explanation is that some transformation has occurred during either storage of the samples or density measurements and the subsequent drying of samples. As such, all further analyses will consider the assumption that the scans undertaken with a cobalt-source provide a more accurate approximation of the material composition.

7.2 Structure

7.2.1 Macrostructure

As has been shown with the use of HA as the biomaterial, Section 6.2.1, it is possible to use the AFR to produce macroporous HA structures with a high degree of controllability. This section investigates whether this can be extended to Ti and Ti-6Al-4V scaffolds. As for the analysis undertaken on HA scaffolds, all macropore, strut and micropore sizes (n=10) have been measured during SEM analyses.

7.2.1.1 Sintering Temperature

Varying the sintering temperature had little effect on the pore or strut size of Ti scaffolds from the 45 ppi template, with values given in Table 7.5 and representative micrographs shown in Figure 7.8. The strut size was within a relatively small range of 79± 5 to 90± 6 µm when coated 5 times with the slurry and sintered at 1000 to 1300 °C. There was a greater range for the pore size of 322± 27 to 439± 26 µm, however treating the sintering temperature of 1100 °C as an outlier greatly reduces this to 322± 27 to 371± 12 µm. Furthermore, the integrity of the structures was improved with an increase in the sintering temperature.

Table 7.5: Average $\pm\sigma_{er}$ pore and strut sizes (µm) for Ti samples produced using the 45 ppi template, with 5 coats and sintered to 1000, 1100, 1200 and 1300 °C

	Template	1000 °C	1100 °C	1200 °C	1300 °C
Pore size	622 ± 28	322 ± 27	439 ± 26	371 ± 12	347 ± 14
Strut Size	95 ± 3	79 ± 5	90 ± 6	84 ± 8	79 ± 3

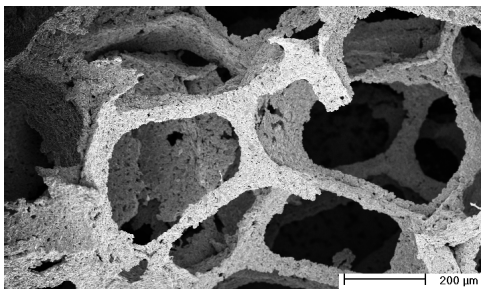

(a) SEM micrograph of Ti scaffold sintered to 1000 °C (V = 20kV; WD = 10.1mm; mag = 100x)

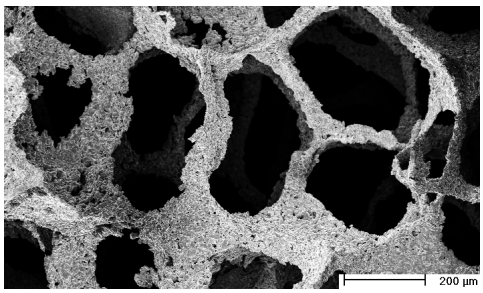

(b) SEM micrograph of Ti scaffold sintered to 1100 °C (V = 20kV; WD = 12.5mm; mag = 100x)

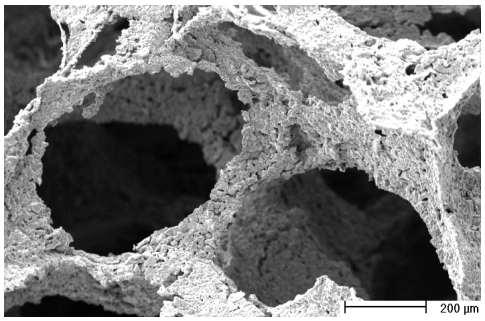

(c) SEM micrograph of Ti scaffold sintered to 1200 °C (V = 20kV; WD = 12.2mm; mag = 100x)

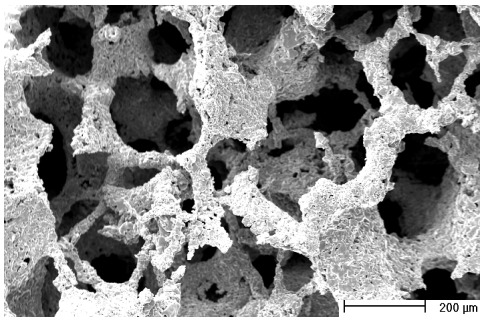

(d) SEM micrograph of Ti scaffold sintered to 1300 °C (V = 20kV; WD = 12.8mm; mag = 100x)

Figure 7.8: SEM micrographs showing the effect of the sintering temperature on Ti scaffolds produced using the 45 ppi template

As with titanium scaffolds produced using the 45 ppi template, those produced using the 90 ppi foam exhibited enhanced stability with no significant variations to the pore or strut sizes as the sintering temperature was increased, as shown in Figure 7.9 with values given in Table 7.6. There was a slight decrease in the pore size, from 187 ± 9 to $158 \pm 7\,\mu m$, however the range is within a reasonable experimental error (15%). There was a slightly greater relative range (36 ± 2 to $51 \pm 3\,\mu m$) to the strut size, however this is likely to have been caused by user sensitivity.

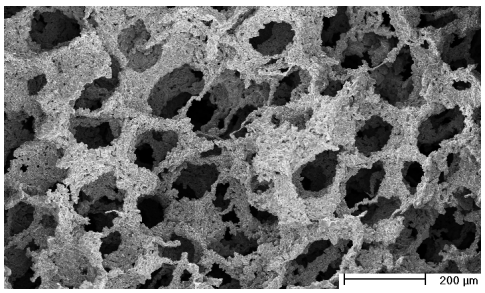

(a) SEM micrograph of Ti scaffold sintered to 1000 °C (V = 20kV; WD = 9.0mm; mag = 100x)

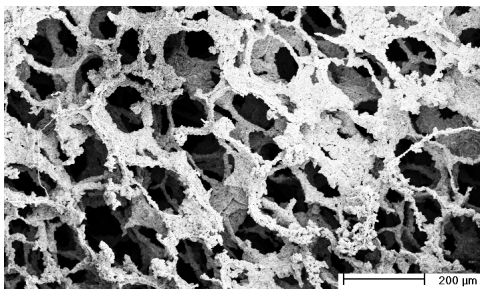

(b) SEM micrograph of Ti scaffold sintered to 1100 °C (V = 20kV; WD = 13.2mm; mag = 100x)

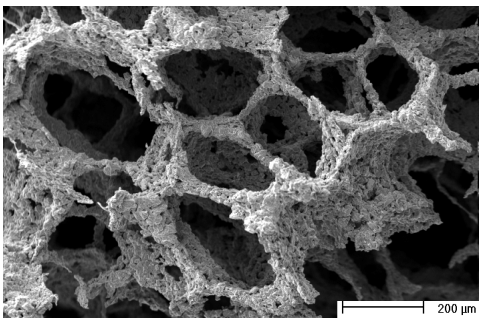

(c) SEM micrograph of Ti scaffold sintered to 1200 °C (V = 20kV; WD = 11.2mm; mag = 100x)

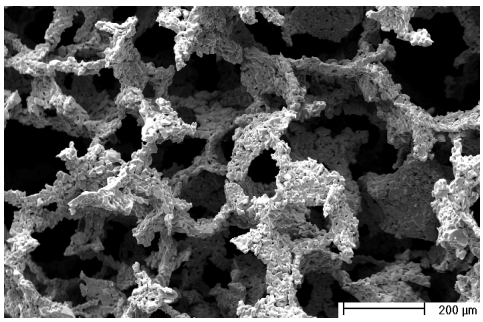

(d) SEM micrograph of Ti scaffold sintered to 1300 °C (V = 20kV; WD = 13.5mm; mag = 100x)

Figure 7.9: SEM micrographs showing the effect of the sintering temperature on Ti scaffolds produced using the 90 ppi template

Table 7.6: Average $\pm\sigma_{er}$ pore and strut sizes (µm) for Ti samples produced using the 90 ppi template, with 5 coats and sintered to 1000, 1100, 1200 and 1300 °C

	Template	1000 °C	1100 °C	1200 °C	1300 °C
Pore size	253 ± 7	187 ± 9	167 ± 5	155 ± 5	158 ± 7
Strut Size	39 ± 0.9	45 ± 4	51 ± 3	41 ± 3	36 ± 2

Similarly, the sintering temperature did not have a great affect on the size of Ti-6Al-4V scaffolds, although the ease of handling of the sintered constructs improved at higher temperatures. SEM micrographs of the scaffolds fabricated from Ti-6Al-4V using the 45 ppi template are shown in Figure 7.10, with values of the pore and strut sizes given in Table 7.7. The strut size is not significantly affected, with

values obtained between 90± 6 to 104± 10 µm, although the pore size decreased from 374± 22 to 277± 16 µm as the sintering temperature was increased from 1200 to 1300 °C. Some samples coated fewer than 3 times underwent partial collapse, however this was not observed in all cases. This will be discussed further in Section 7.2.1.2.

Table 7.7: Average $\pm\sigma_{er}$ pore and strut sizes (µm) for Ti-6Al-4V samples produced using the 45 ppi template, with 5 coats and sintered to 1200, 1250 and 1300 °C

	Template	1200 °C	1250 °C	1300 °C
Pore size	622 ± 28	374 ± 22	357 ± 23	277 ± 16
Strut Size	95 ± 3	104 ± 10	92 ± 6	90 ± 6

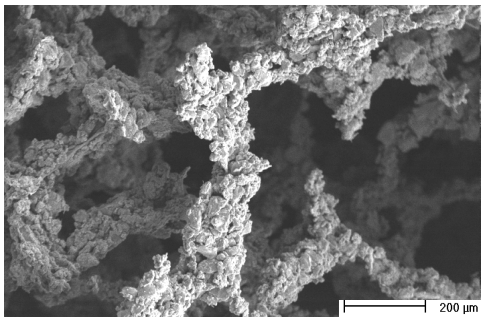

(a) SEM micrograph of Ti-6Al-4V scaffold sintered to 1200 °C (V = 20kV; WD = 17.5mm; mag = 100x)

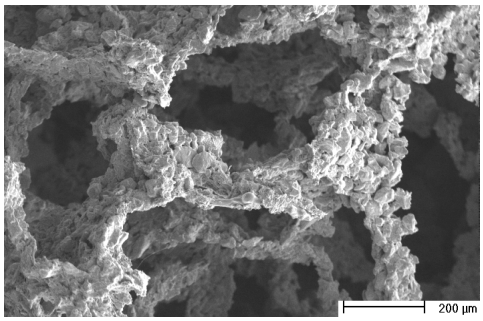

(b) SEM micrograph of Ti-6Al-4V scaffold sintered to 1250 °C (V = 20kV; WD = 17.6mm; mag = 100x)

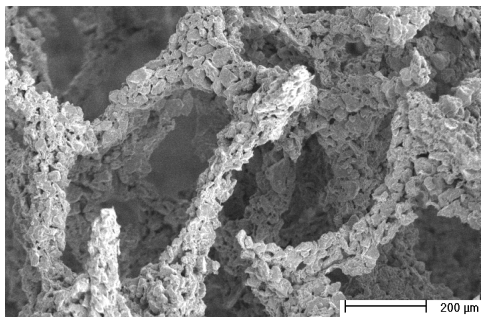

(c) SEM micrograph of Ti-6Al-4V scaffold sintered to 1300 °C (V = 20kV; WD = 17.1mm; mag = 100x)

Figure 7.10: SEM micrographs showing the effect of the sintering temperature on Ti-6Al-4V scaffolds produced using the 45 ppi template

As with Ti-6Al-4V scaffolds fabricated from the 45 ppi template, those produced using the 90 ppi template predominantly exhibited few noticeable changes when the sintering temperature was raised, as shown in Figure 7.11 and with values in Table 7.8. The pore and strut size both increased with maximum values occuring at the highest sintering temperature suggesting that this structure was fabricated with optimal coatings of the template and underwent minimal shrinkage. There was also collapse to some scaffolds with fewer than 3 coats at all temperatures as for those produced using the 45 ppi template, a phenomenom discussed further in Section 7.2.1.2.

Table 7.8: Average $\pm\sigma_{er}$ pore and strut sizes (μm) for Ti-6Al-4V samples produced using the 90 ppi templates, with 5 coats and sintered to 1200, 1250 and 1300 °C

	Template	1200 °C	1250 °C	1300 °C
Pore size	253 ± 7	142 ± 3	138 ± 6	190 ± 12
Strut Size	39 ± 0.9	73 ± 3	72 ± 3	83 ± 5

7.2.1.2 Number of Coats

Increasing the number of coats of the TiH_2 slurry on the template had similar effects as when the foams were coated in a HA-based slurry, outlined in Section 6.2.1.2. For example, when comparing samples coated five times to those coated once on the 45 ppi template, the strut size increased by up to 34%, which was accompanied by a decrease of up to 39% in the pore size. Coating the 90 ppi template 5 times led to increases of up to 57% in the strut and decreases of up to 22% in the pore size compared to applying one coating. Although the relative change to the strut size was greater for structures from the 90 ppi template, the actual change in size was similar regardless (20 ±9 μm for 45 ppi, 17 ±9 μm for 90 ppi). Furthermore, the uniformity of both the strut and pore sizes was increased as shown in representative SEM micrographs in Figures 7.12 and 7.13 and with a reduction to the relative stan-

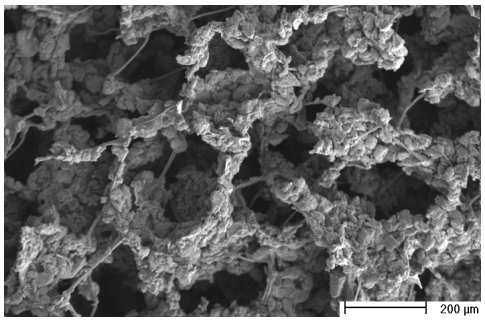

(a) SEM micrograph of Ti-6Al-4V scaffold sintered to 1200 °C (V = 20kV; WD = 20.0mm; mag = 100x)

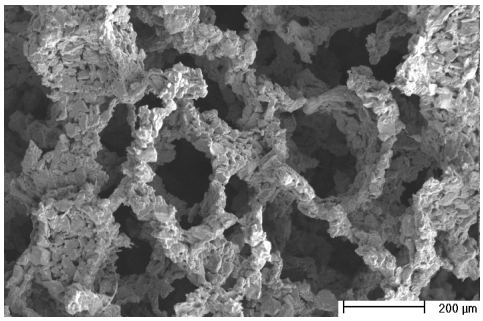

(b) SEM micrograph of Ti-6Al-4V scaffold sintered to 1250 °C (V = 20kV; WD = 17.2mm; mag = 100x)

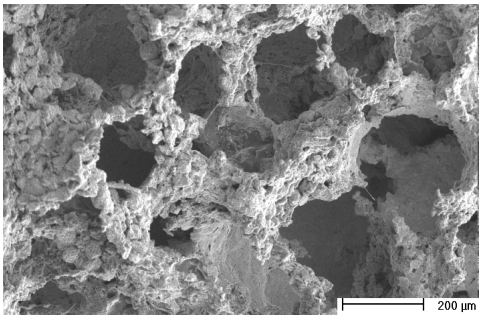

(c) SEM micrograph of Ti-6Al-4V scaffold sintered to 1300 °C (V = 20kV; WD = 20.2mm; mag = 100x)

Figure 7.11: SEM micrographs showing the effect of the sintering temperature on Ti-6Al-4V scaffolds produced using the 90 ppi template

dard deviation of the average pore and strut sizes. There was also an increase in the amount of pore occlusion, which, although not significant, combined with the other factors to increase the stability of the structures. As with HA structures, varying the number of coats changed the final structure independently from adjusting the sintering temperature. The average pore and strut sizes of titanium scaffolds produced using the 45 ppi and 90 ppi template are shown graphically in Figures 7.14 and 7.15.

Ti-6Al-4V scaffolds exhibited some degree of collapse at all sintering temperatures when there was a low number of coats of the slurry on the template. This collapse was only seen for scaffolds produced with less than 3 coats and affected structures from the 45 ppi template to a greater extent than those from the 90 ppi template, although it was not limited to one template alone. Where structures did not collapse, varying the number of coats had similar effects on Ti-6Al-4V scaffolds as to those produced from HA and Ti. Briefly, increasing the number of coats of the slurry from one to five on the template led to an increase in the strut size, of up to 14% and 43% when coating the 45 and 90 ppi template respectively, and a decrease in the pore size, of up to 42% and 52%. The actual increase in strut size was similar to that seen with the Ti scaffolds and was again irrespective of the template ($15 \pm 9\,\mu m$ for 45 ppi, $16 \pm 9\,\mu m$ for 90 ppi). Representative SEM micrographs for scaffolds from the 45 and 90 ppi templates, Figures 7.16 and 7.17, show the decrease in pore size and increase in the strut size, as well as the greater uniformity of pore and strut sizes and the increased pore occlusion. The sintering temperature again had a slight effect on the final structure, although this was independant from the number of coats. Graphical representations of the average pore and strut sizes for scaffolds from Ti-6Al-4V using the 45 and 90 ppi templates are shown in Figures 7.18 and 7.19.

For constructs from both materials, the strut thickness was expected to undergo a linear increase, as the methodology enables a thin layer of material to be coated onto the template with each additional dip-coating. However, the slight variations

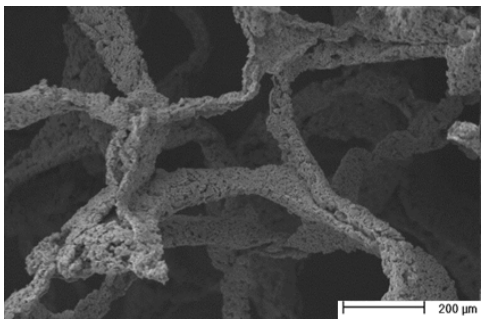

(a) SEM micrograph of scaffold sintered to 1000 °C with 1 coat (V = 20kV; WD = 13.2mm; mag = 100x)

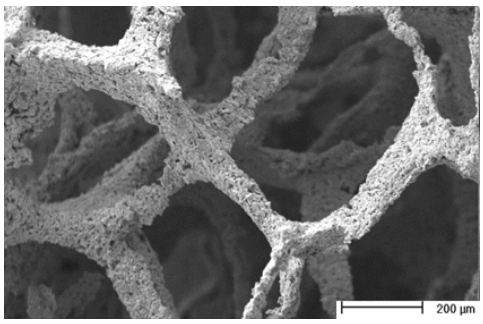

(b) SEM micrograph of scaffold sintered to 1000 °C with 2 coats (V = 20kV; WD = 12.7mm; mag = 100x)

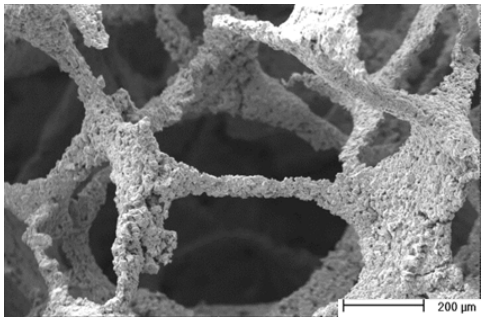

(c) SEM micrograph of scaffold sintered to 1000 °C with 3 coats (V = 20kV; WD = 12.3mm; mag = 100x)

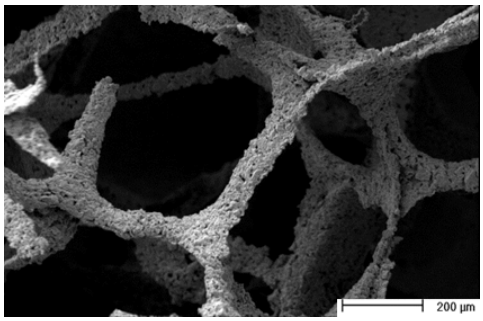

(d) SEM micrograph of scaffold sintered to 1000 °C with 4 coats (V = 20kV; WD = 13.8mm; mag = 100x)

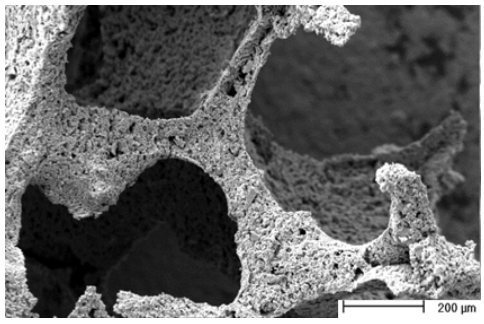

(e) SEM micrograph of scaffold sintered to 1000 °C with 5 coats (V = 20kV; WD = 13.9mm; mag = 100x)

Figure 7.12: SEM micrographs showing the effect of the number of coats of the slurry on the structure of titanium scaffolds produced using the 45 ppi template

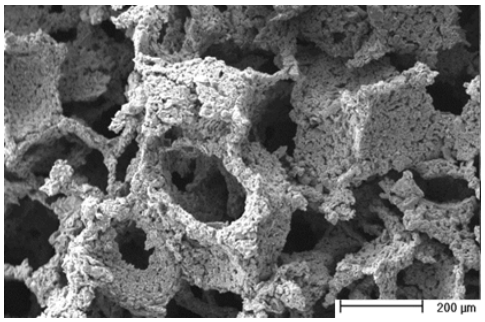

(a) SEM micrograph of scaffold sintered to 1000 °C with 1 coat (V = 120V; WD = 12.1mm; mag = 100x)

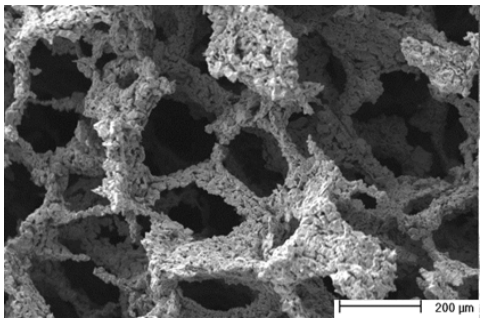

(b) SEM micrograph of scaffold sintered to 1000 °C with 2 coats (V = 20kV; WD = 11.7mm; mag = 100x)

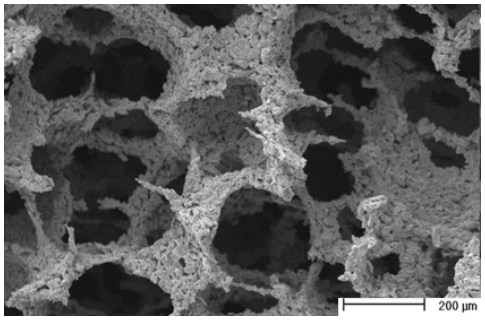

(c) SEM micrograph of scaffold sintered to 1000 °C with 3 coats (V = 20kV; WD = 11.1mm; mag = 100x)

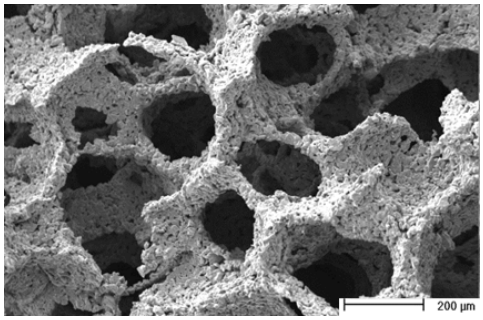

(d) SEM micrograph of scaffold sintered to 1000 °C with 4 coats (V = 20kV; WD = 13.3mm; mag = 100x)

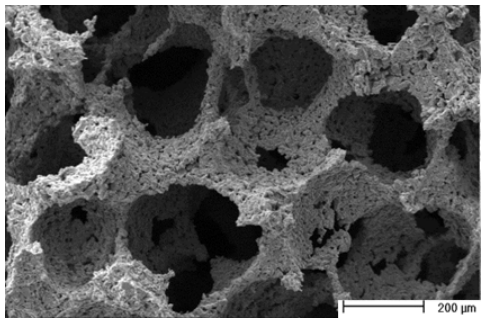

(e) SEM micrograph of scaffold sintered to 1000 °C with 5 coats (V = 20kV; WD = 11.8mm; mag = 100x)

Figure 7.13: SEM micrographs showing the effect of the number of coats of the slurry on the structure of titanium scaffolds produced using the 90 ppi template

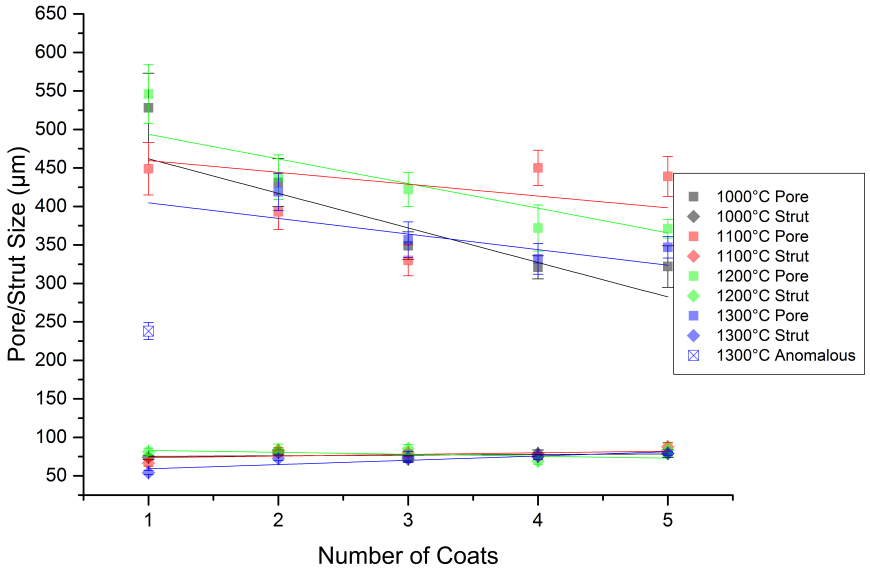

Figure 7.14: Graph showing how the pore and strut size of Ti structures varies with the number of coats and sintering temperature on samples produced using the 45ppi template

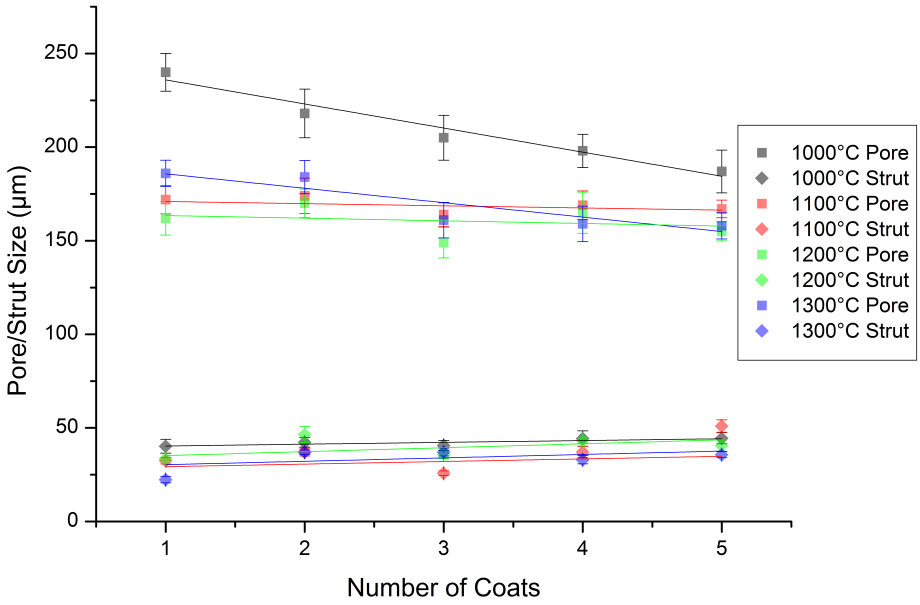

Figure 7.15: Graph showing how the pore and strut size of Ti structures varies with the number of coats and sintering temperature on Ti samples produced using the 90ppi template

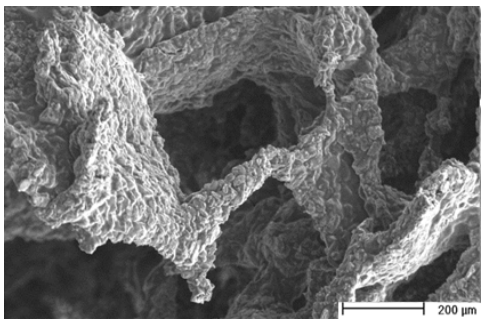

(a) SEM micrograph of scaffold sintered to 1300 °C with 1 coat (V = 20kV; WD = 13.6mm; mag = 100x)

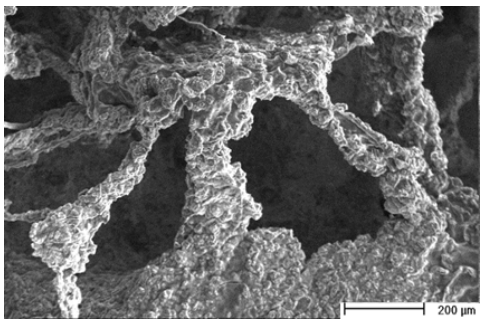

(b) SEM micrograph of scaffold sintered to 1300 °C with 2 coats (V = 20kV; WD = 15.9mm; mag = 100x)

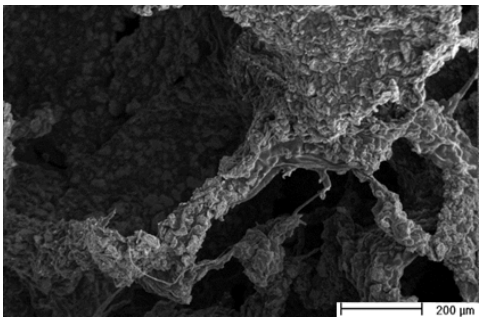

(c) SEM micrograph of scaffold sintered to 1300 °C with 3 coats (V = 20kV; WD = 16.4mm; mag = 100x)

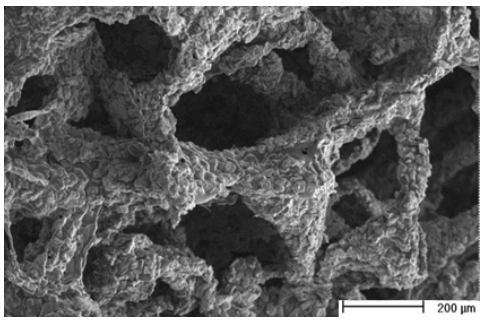

(d) SEM micrograph of scaffold sintered to 1300 °C with 4 coats (V = 20kV; WD = 16.0mm; mag = 100x)

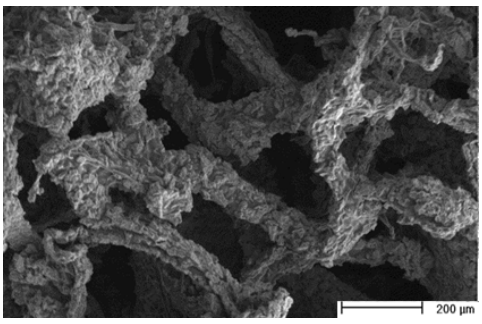

(e) SEM micrograph of scaffold sintered to 1300 °C with 5 coats (V = 20kV; WD = 16.9mm; mag = 100x)

Figure 7.16: SEM micrographs showing the effect of the number of coats of the slurry on the structure of Ti-6Al-4V scaffolds produced using the 45 ppi template

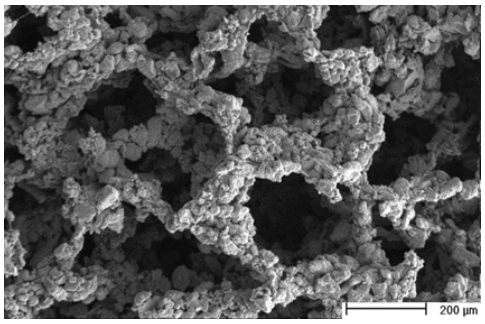

(a) SEM micrograph of scaffold sintered to 1300 °C with 1 coat (V = 20kV; WD = 16.6mm; mag = 100x)

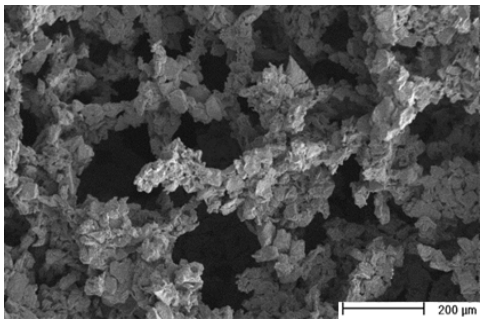

(b) SEM micrograph of scaffold sintered to 1300 °C with 2 coats (V = 20kV; WD = 16.7mm; mag = 100x)

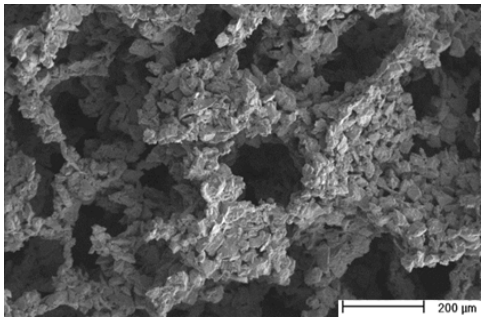

(c) SEM micrograph of scaffold sintered to 1300 °C with 3 coats (V = 20kV; WD = 16.5mm; mag = 100x)

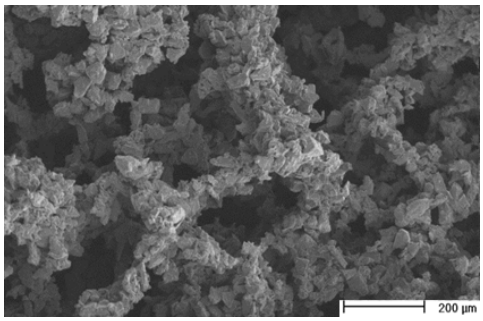

(d) SEM micrograph of scaffold sintered to 1300 °C with 4 coats (V = 20kV; WD = 16.5mm; mag = 100x)

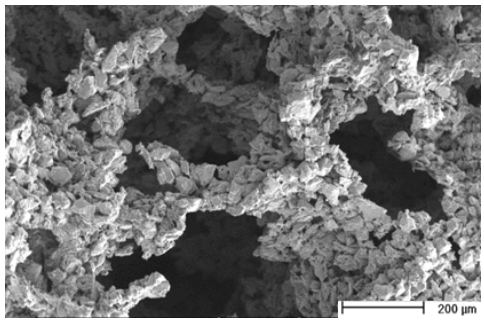

(e) SEM micrograph of scaffold sintered to 1300 °C with 5 coats (V = 20kV; WD = 17.1mm; mag = 100x)

Figure 7.17: SEM micrographs showing the effect of the number of coats of the slurry on the structure of Ti-6Al-4V scaffolds produced using the 90 ppi template

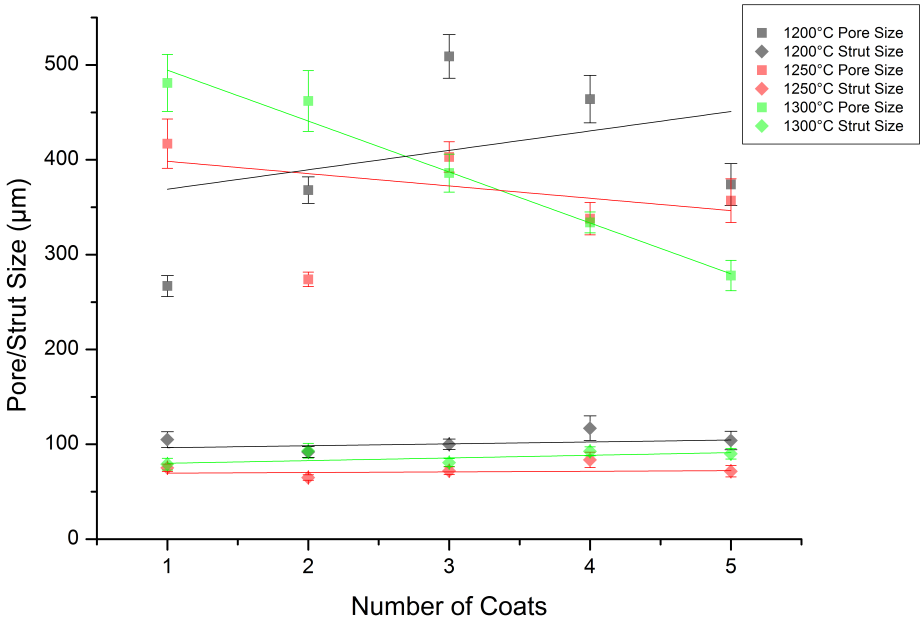

Figure 7.18: Graph showing how the pore and strut size of Ti-6Al-4V structures varies with the number of coats and sintering temperature on scaffolds produced using the 45 ppi template

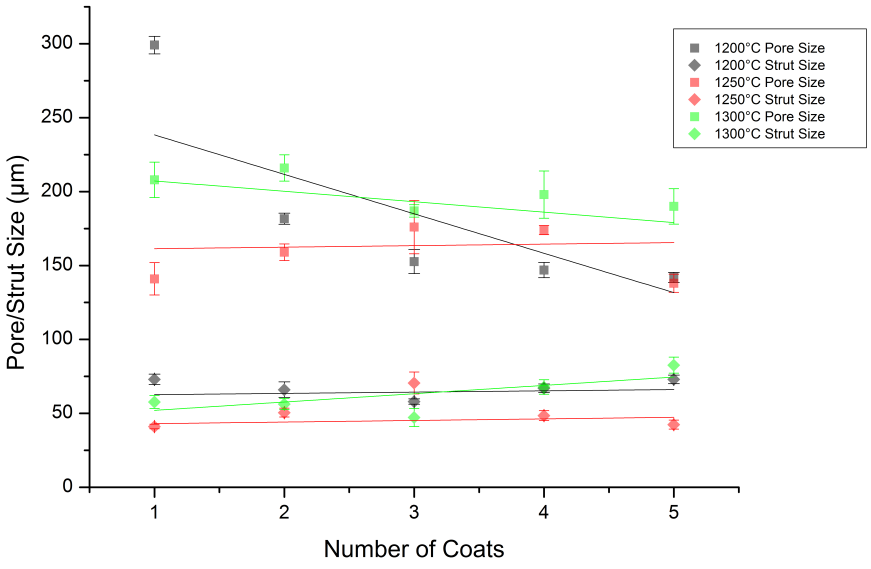

Figure 7.19: Graph showing how the pore and strut size of Ti-6Al-4V structures varies with the number of coats and sintering temperature on scaffolds produced using the 90 ppi template

observed, most probably due to the pressure applied during squeezing, led to some variation to the evenness of coating between samples. Furthermore, this is exacerbated by the fact that each measurement was taken from a different sample as the method does not allow for structures to be sintered, an additional coating added and re-sintering.

7.2.1.3 Porogen Inclusion

As the level of camphene included in the precursor slurry was increased, there was little noticable change to the macrostructure of Ti scaffolds produced from either template. At all sintering temperatures, with a low number of coats of the slurry on the 45 ppi template, there was some variation. However, there was no consistency to the variations. For example, when coated once and sintered to 1000 and 1200 °C the samples with 25% porogen exhibited the smallest pore sizes, however at 1100 °C this was the sample with 20% camphene and at 1300 °C, the sample with 0% porogen. As the number of coats increased, the differences between the pore sizes measured from scaffolds with different porogen contents decreased. In all cases, the samples coated 5 times and with 25% porogen in the slurry had the smallest pore sizes, however in most cases this was not significantly different from those produced using less camphene. As detailed further in Section 7.2.2, the struts exhibited microstructural variations depending on the porogen content, however there were no significant differences when considering the macrostructure. The relationships between the pore and strut sizes, level of camphene incorporation and number of coats of the slurry on the template of Ti constructs fabricated using the 45 ppi template are shown in Figures 7.21, 7.22, 7.23 and 7.24 when sintered to 1000, 1100, 1200 and 1300 °C respectively.

The effect of coating the 90 ppi template with TiH_2 slurries containing varying amounts of porogen was similar as when coating the 45 ppi template. In particular, the range of measurements obtained for the pore size of structures fabricated with one coating was decreased by increasing the number of coats, with the amount

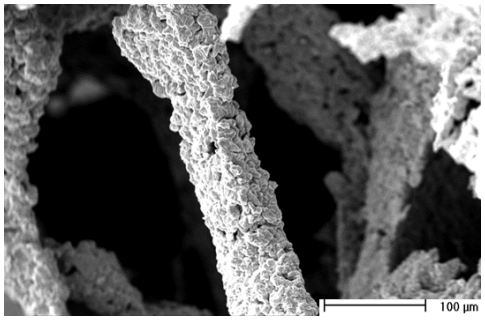

(a) SEM micrograph showing macrostructure of sample produced without camphene (V = 20kV; WD = 12.5mm; mag = 250x)

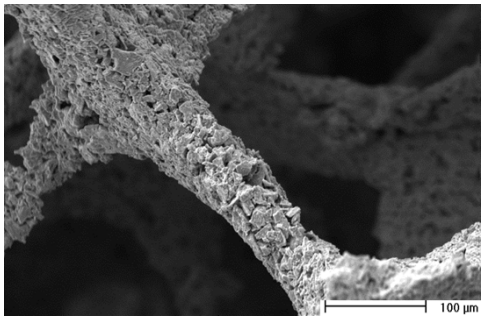

(b) SEM micrograph showing macrostructure of sample produced with 5% camphene (V = 20kV; WD = 12.7mm; mag = 250x)

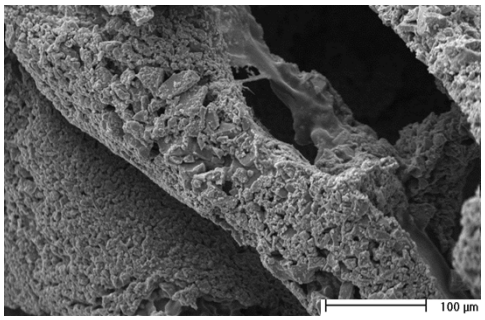

(c) SEM micrograph showing macrostructure of sample produced with 10% camphene (V = 20kV; WD = 14.7mm; mag = 250x)

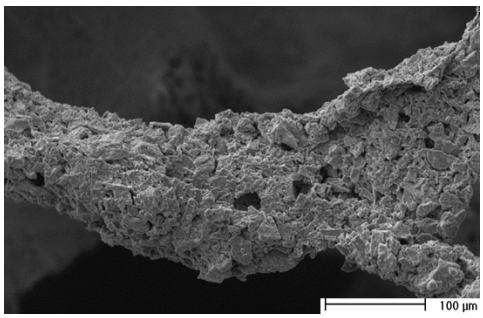

(d) SEM micrograph showing macrostructure of sample produced with 20% camphene (V = 20kV; WD = 12.3mm; mag = 250x)

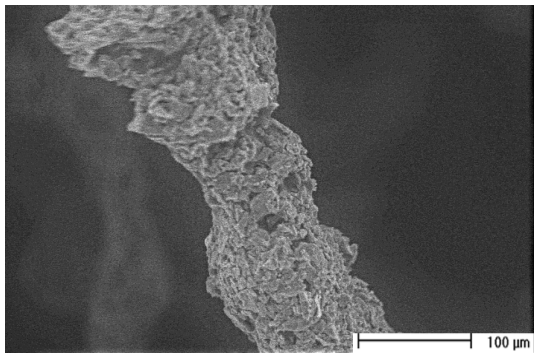

(e) SEM micrograph showing macrostructure of sample produced with 25% camphene (V = 25kV; WD = 10.3mm; mag = 250x)

Figure 7.20: SEM micrographs showing the macrostructure of Ti samples produced using the 45 ppi template, with increasing camphene content through 0, 5, 10, 20 and 25 wt.%

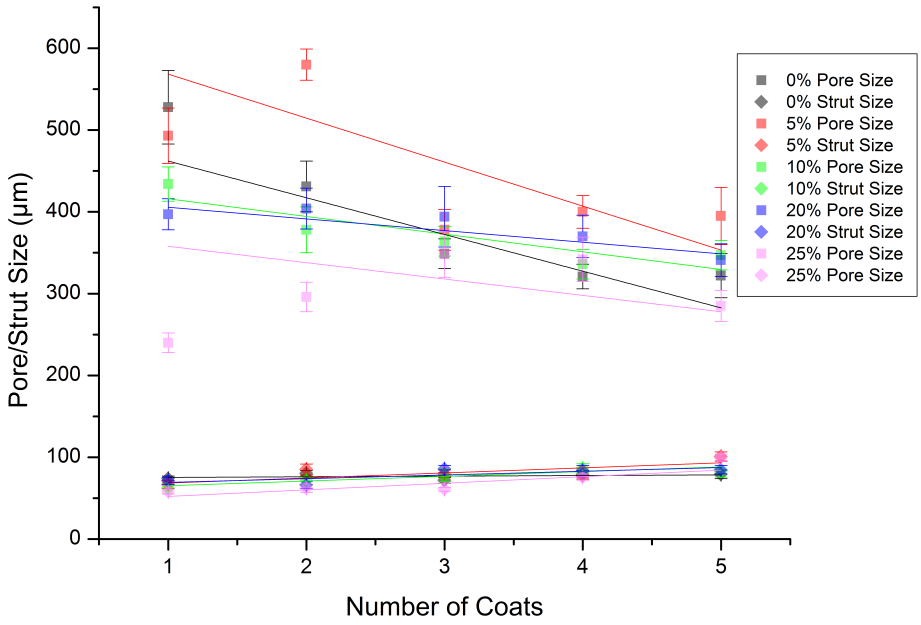

Figure 7.21: Graph showing the relationships between number of coats, porogen content and pore/strut size of Ti scaffolds fabricated using the 45 ppi template and sintered to 1000 °C

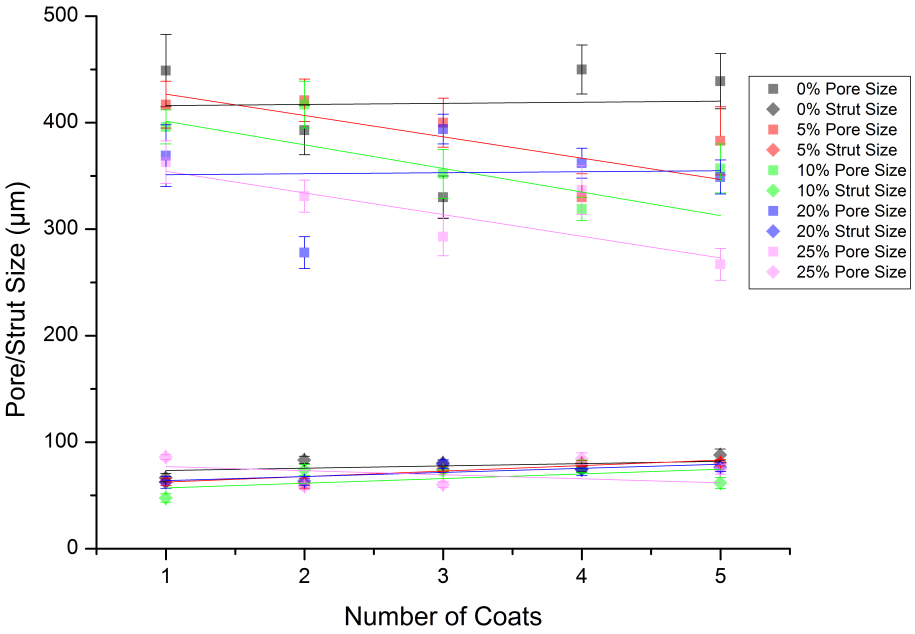

Figure 7.22: Graph showing the relationships between number of coats, porogen content and pore/strut size of Ti scaffolds fabricated using the 45 ppi template and sintered to 1100 °C

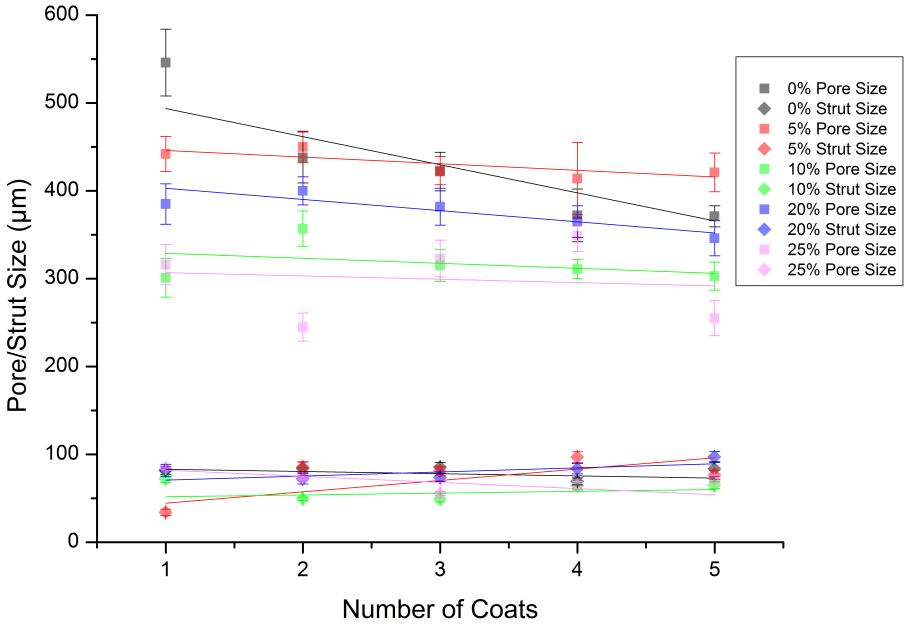

Figure 7.23: Graph showing the relationships between number of coats, porogen content and pore/strut size of Ti scaffolds fabricated using the 45 ppi template and sintered to 1200 °C

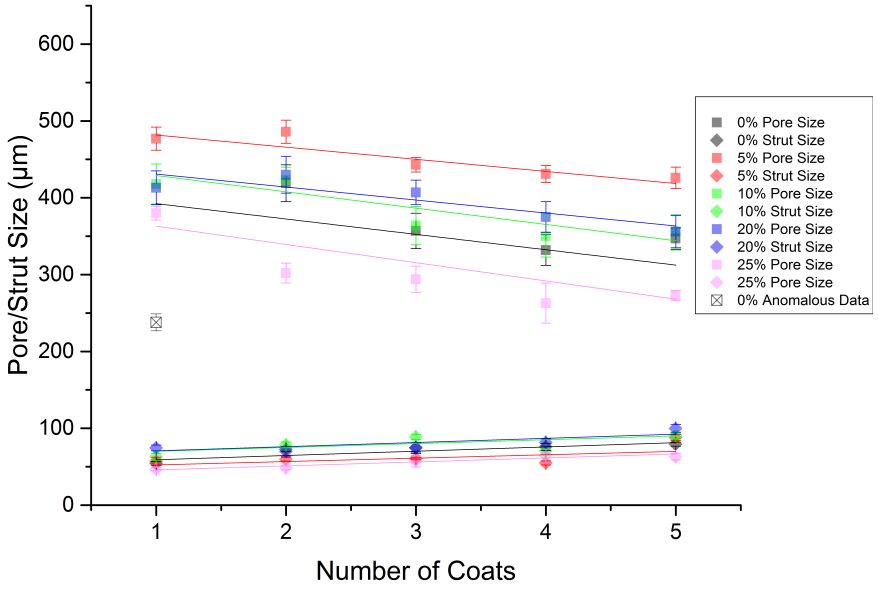

Figure 7.24: Graph showing the relationships between number of coats, porogen content and pore/strut size of Ti scaffolds fabricated using the 45 ppi template and sintered to 1300 °C

of porogen having no consistent effect on the final size. The samples fabricated with 5 coats with 0% porogen were towards the upper size limits at each temperature, however there was no trend as to which exhibited the smallest pore sizes. As such, the smallest pore sizes for samples sintered to 1000, 1100, 1200, and 1300 °C were measured on the samples fabricated with 10, 25, 25 and 5% porogen inclusion respectively. Furthermore, the level of camphene inclusion had little significance on the strut size, with graphs showing the relationships between the porogen content, number of coats and pore/strut size for the structures fabricated using the 90 ppi template and sintered to the different temperatures shown in Figures 7.25, 7.26, 7.27 and 7.28.

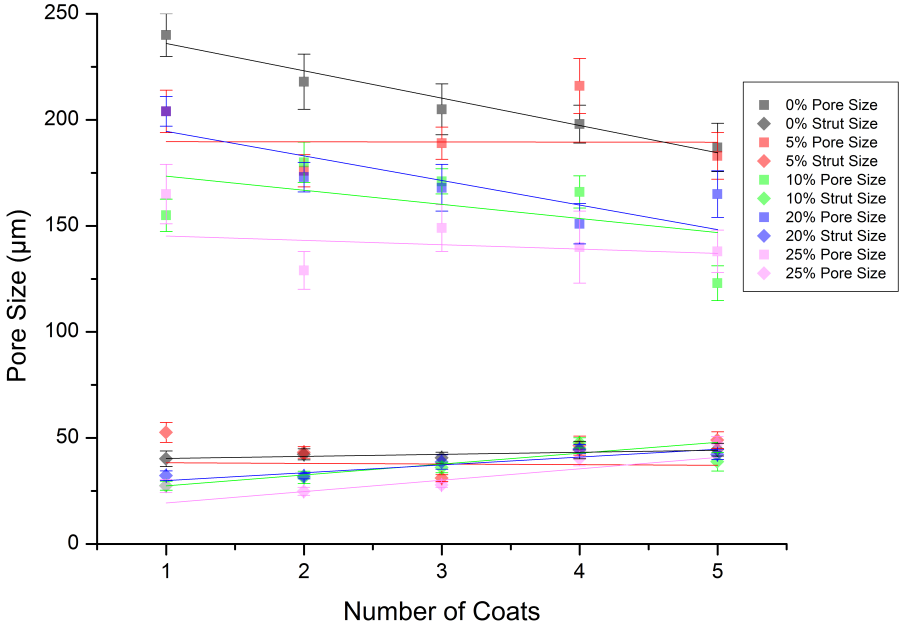

Figure 7.25: Graph showing the relationships between number of coats, porogen content and pore/strut size of Ti scaffolds fabricated using the 90 ppi template and sintered to 1000 °C

As discussed above, at least three coats of the slurry were required on the template to ensure the stability of the sample during sintering when Ti-6Al-4V structures were fabricated without any porogen inclusion. Collapse to some of the structure was also observed for some scaffolds produced with camphene present in the slurry.

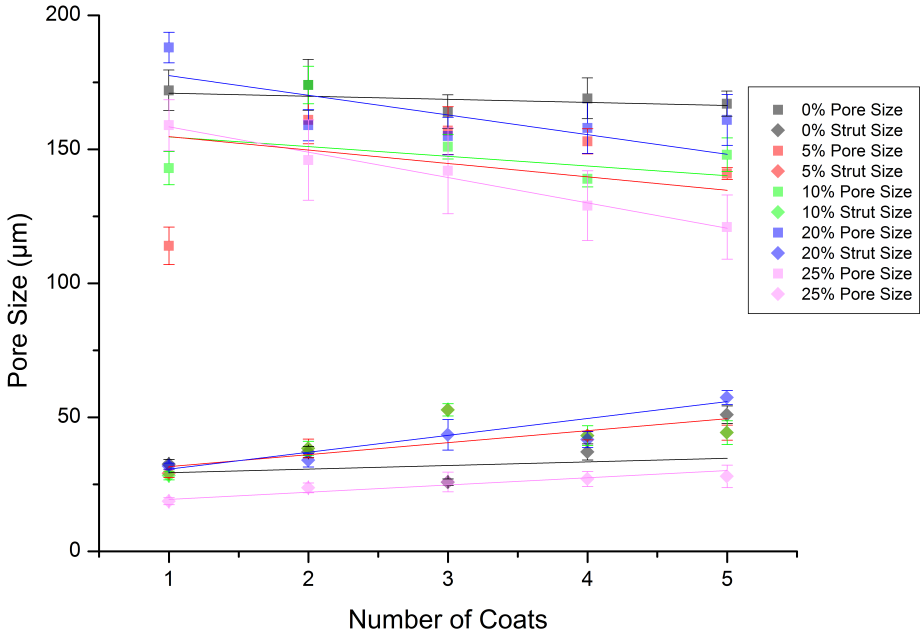

Figure 7.26: Graph showing the relationships between number of coats, porogen content and pore/strut size of Ti scaffolds fabricated using the 90 ppi template and sintered to 1100 °C

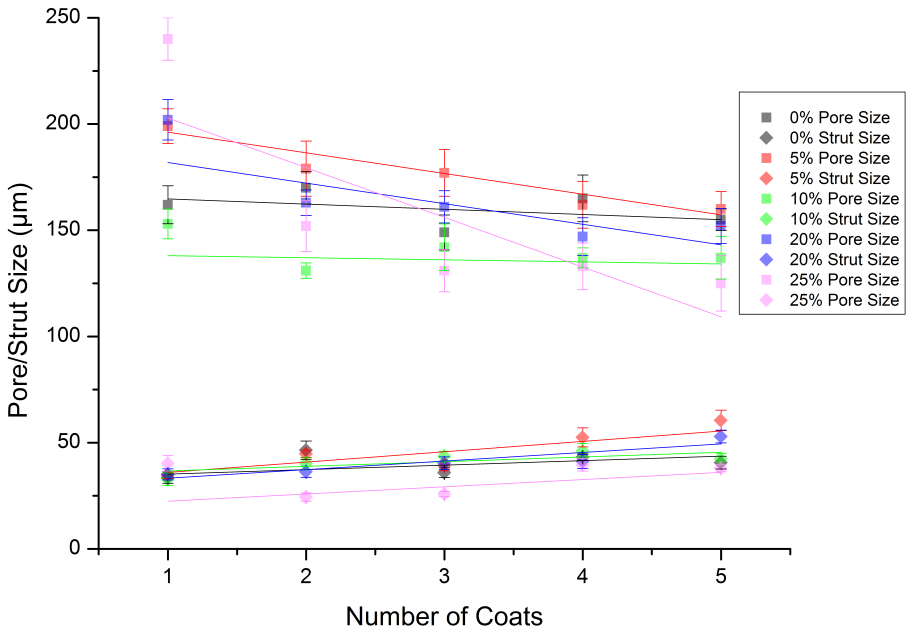

Figure 7.27: Graph showing the relationships between number of coats, porogen content and pore/strut size of Ti scaffolds fabricated using the 90 ppi template and sintered to 1200 °C

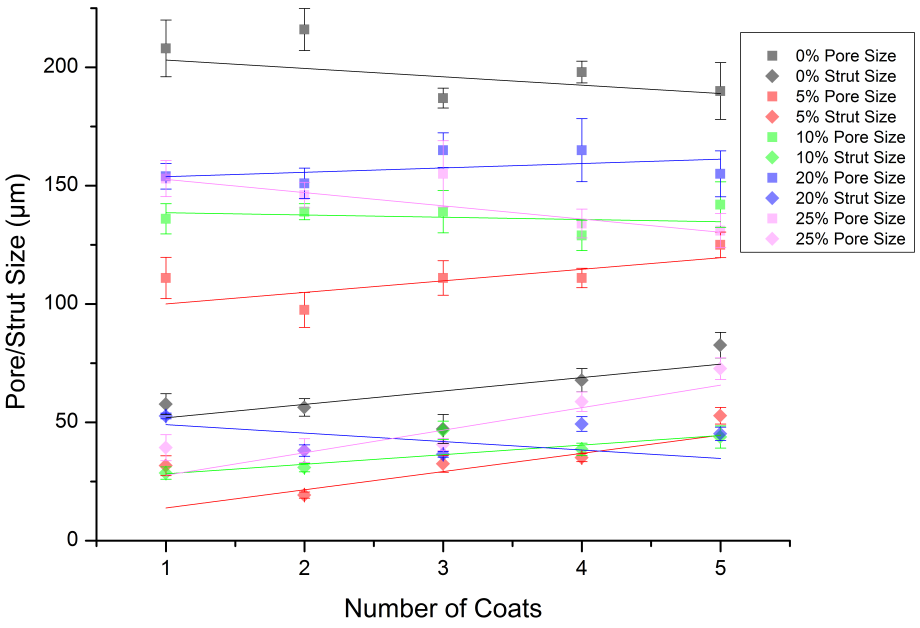

Figure 7.28: Graph showing the relationships between number of coats, porogen content and pore/strut size of Ti scaffolds fabricated using the 90 ppi template and sintered to 1300 °C

Again, this impacted scaffolds produced using the 45 ppi template more than those from the 90 ppi template, however any sample produced with less than three coats of the slurry could have been affected.

In general, the trends observed when varying the camphene content of Ti-6Al-4V scaffolds were similar to those seen with Ti constructs. The inter sample range of the pore size of constructs from both the 45 and 90 ppi templates decreased with an increasing number of coats. Furthermore, there were no trends with respect to the porogen content affecting which structures had the largest and smallest pore sizes. For example, the pore size was smallest when coating the 45 ppi template 5 times, and with 10, 25 and 5% porogen when sintered to 1200, 1250 and 1300 °C whilst the smallest sizes were measured on samples fabricated with 20, 0 and 5% porogen on structures from the 90 ppi template. The strut size, with representative SEM micrographs shown in Figure 7.29 for scaffolds fabricated using the 45 ppi template, also exhibited no significant differences between constructs fabricated with different

porogen contents when all other processing parameters were the same. Graphical representations of the relationships between the level of porogen, number of coats and pore/strut size are shown in Figures 7.30, 7.31 and 7.32 and Figures 7.33, 7.34 and 7.35 for samples produced using the 45 and 90 ppi template respectively and sintered to 1200, 1250 and 1300 °C.

7.2.2 Microstructure

The particles retained their features for all Ti structures, whilst micropores successfully generated on the macroporous struts through the introduction of the porogen into the slurry. These were of a standard size of between 2-5 μm, regardless of the level of porogen included. An increase to the camphene content led to an increase in the amount and density of these micropores, as shown in Figure 7.36. Particularly at the highest levels of porogen, this led to some coalescence, causing larger micropores of up to 20-30 μm.

Struts of the scaffolds fabricated from Ti-6Al-4V also exhibited surface roughness, or topology, regardless of the camphene content. Micropores of 2-5 μm were generated on the struts of all samples incorporating camphene as a porogen. As the level of porogen was increased, there was no change to the basic individual size of the micropores obtained, however the number and density of these increased, as seen in Figure 7.37, corroborating the results obtained using other materials. At the highest levels, there was also some coalescence as seen with both Ti and HA.

7.2.3 Discussion

Porous Ti and Ti-6Al-4V scaffolds have been successfully fabricated with pore sizes within the prescribed limit [12,13,15] of 100 - 900 μm for bone regenerative structures. The results confirm that AFR can be used to produce macroporous structures with a high degree of controllability, enabling the optimization of the pore and strut sizes.

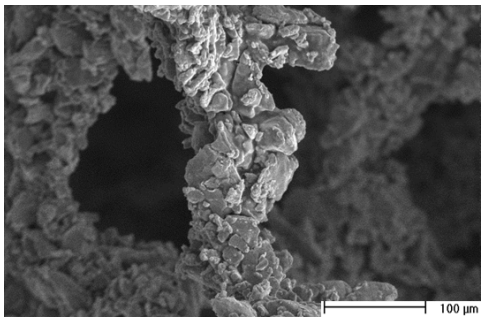

(a) SEM micrograph showing the macrostructure of sample produced without camphene (V = 20kV; WD = 19.2mm; mag = 250x)

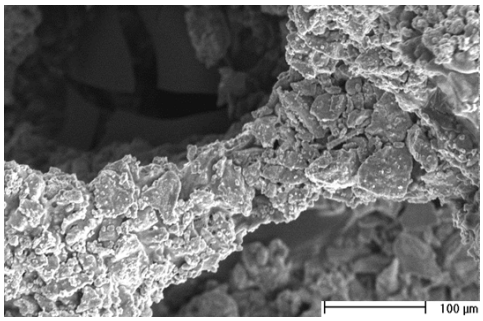

(b) SEM micrograph showing the macrostructure of sample produced with 5% camphene (V = 20kV; WD = 15.9mm; mag = 250x)

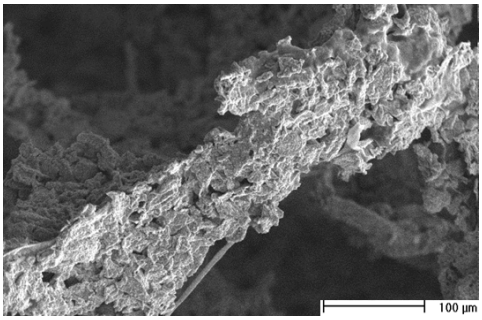

(c) SEM micrograph showing the macrostructure of samples produced with 10% camphene (V = 20kV; WD = 16.1mm; mag = 250x)

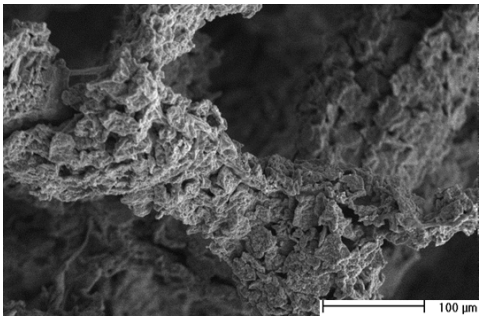

(d) SEM micrograph showing the macrostructure of sample produced with 20% camphene (V = 20kV; WD = 16.1mm; mag = 250x)

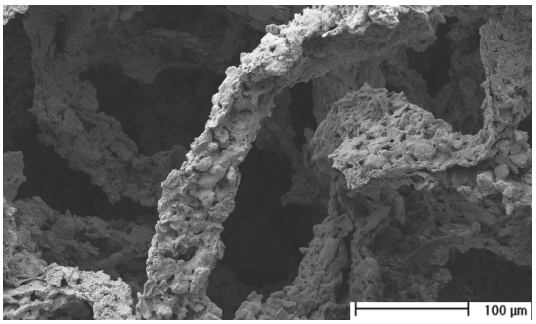

(e) SEM micrograph showing macrostructure of sample produced with 25% camphene (V = 10kV; WD = 8.0mm; mag = 250x)

Figure 7.29: SEM micrographs showing the macrostructure of Ti-6Al-4V scaffolds produced using the 45 ppi template, with increasing camphene content through 0, 5, 10, 20 and 25 wt.%

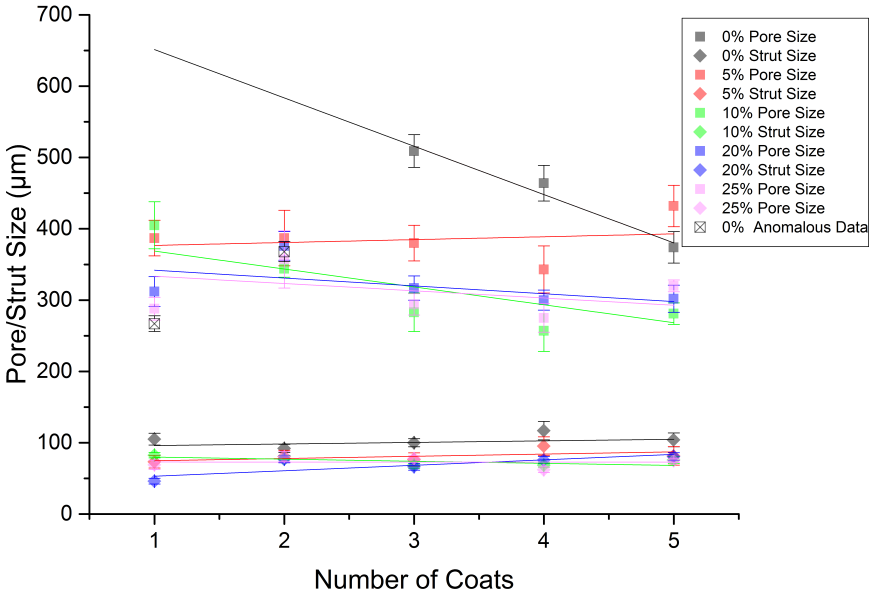

Figure 7.30: Graph showing the relationships between number of coats, porogen content and pore/strut size of Ti-6Al-4V scaffolds fabricated using the 45 ppi template and sintered to 1200 °C

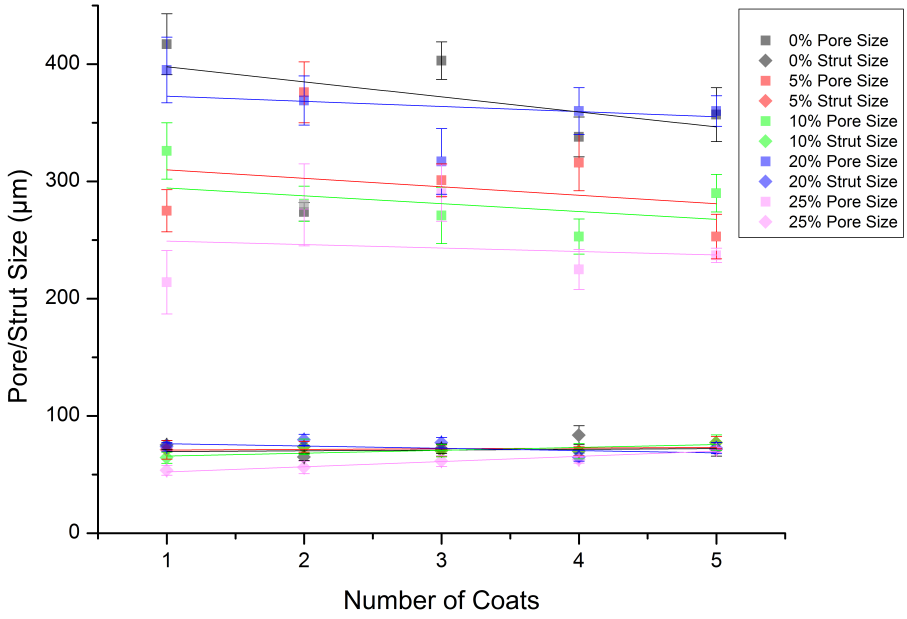

Figure 7.31: Graph showing the relationships between number of coats, porogen content and pore/strut size of Ti-6Al-4V scaffolds fabricated using the 45 ppi template and sintered to 1250 °C

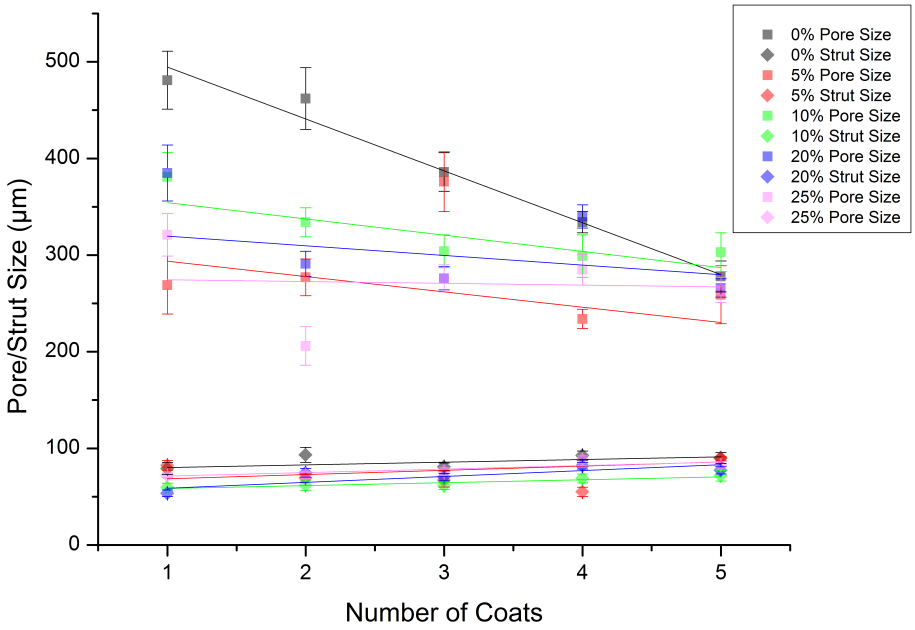

Figure 7.32: Graph showing the relationships between number of coats, porogen content and pore/strut size of Ti-6Al-4V scaffolds fabricated using the 45 ppi template and sintered to 1300 °C

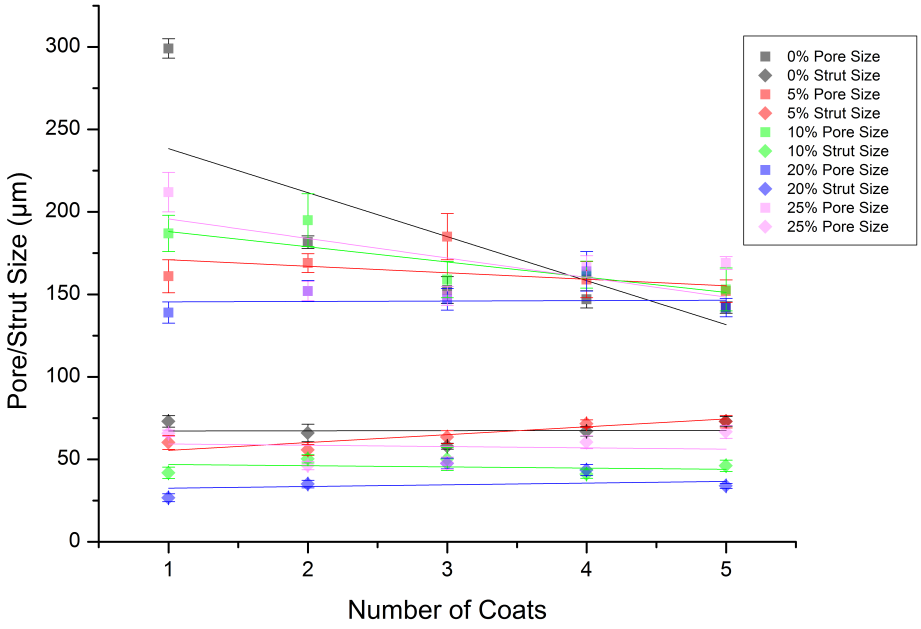

Figure 7.33: Graph showing the relationships between number of coats, porogen content and pore/strut size of Ti-6Al-4V scaffolds fabricated using the 45 ppi template and sintered to 1200 °C

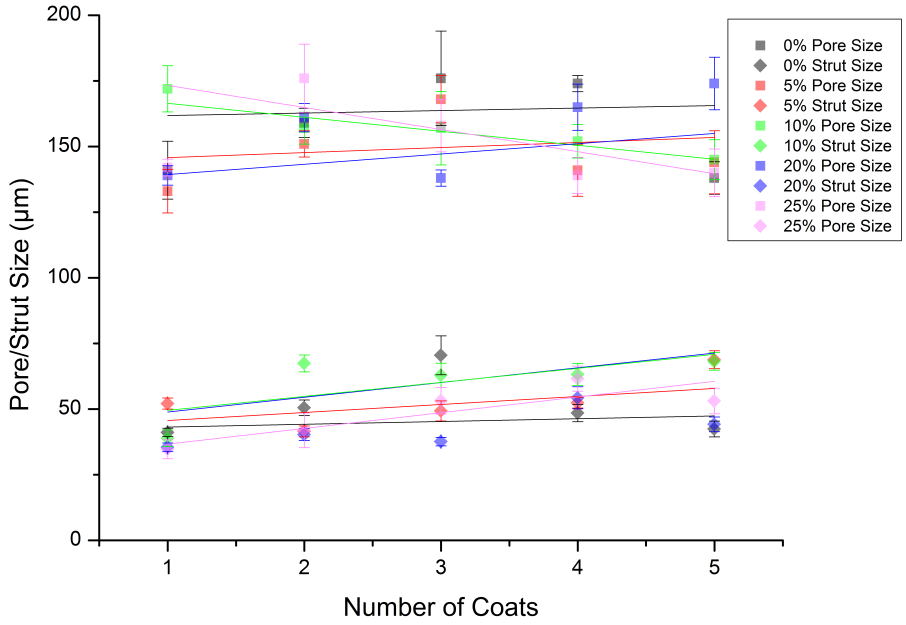

Figure 7.34: Graph showing the relationships between number of coats, porogen content and pore/strut size of Ti-6Al-4V scaffolds fabricated using the 45 ppi template and sintered to 1250 °C

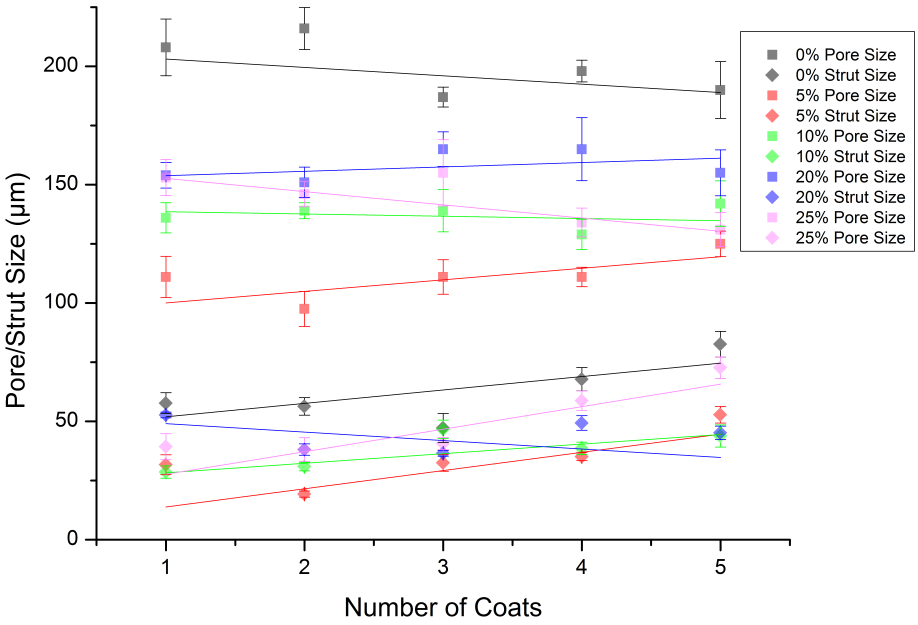

Figure 7.35: Graph showing the relationships between number of coats, porogen content and pore/strut size of Ti-6Al-4V scaffolds fabricated using the 45 ppi template and sintered to 1300 °C

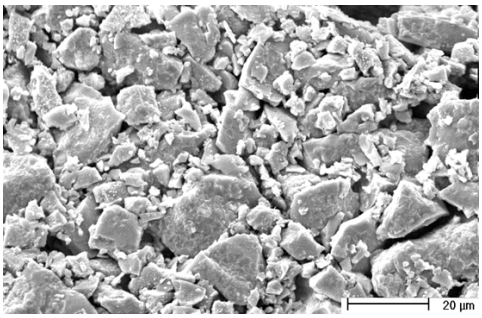

(a) SEM micrograph showing surface roughness/microporosity of scaffolds produced without camphene (V = 20kV; WD = 12.6mm; mag = 1000x)

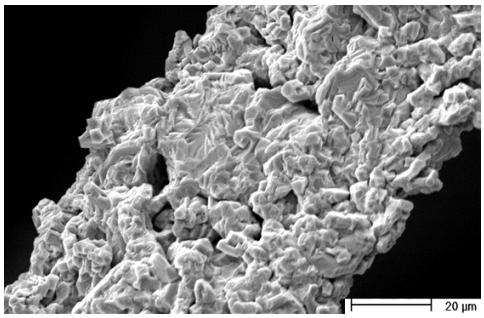

(b) SEM micrograph showing surface roughness/microporosity of scaffolds produced with 5% camphene (V = 20kV; WD = 13.6mm; mag = 1000x)

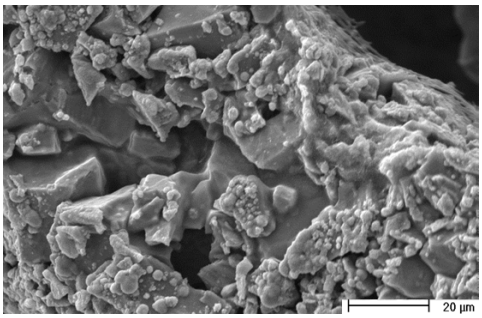

(c) SEM micrograph showing surface roughness/microporosity of scaffolds produced with 10% camphene (V = 20kV; WD = 14.6mm; mag = 1000x)

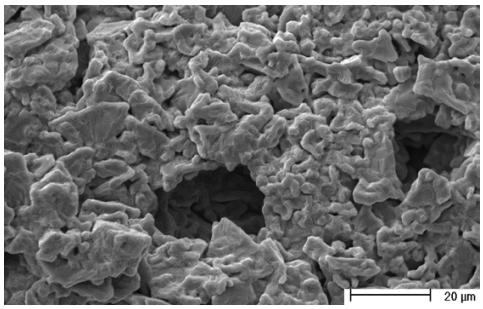

(d) SEM micrograph showing surface roughness/microporosity of scaffolds produced with 20% camphene (V = 20kV; WD = 12.4mm; mag = 1000x)

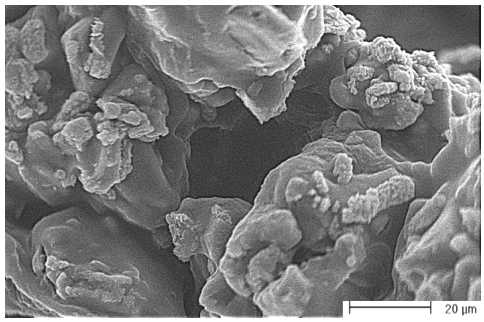

(e) SEM micrograph showing surface roughness/microporosity of scaffolds produced with 25% camphene (V = 25kV; WD = 8.1mm; mag = 1000x)

Figure 7.36: SEM micrographs showing surface roughness/microporosity on Ti samples produced using the 45 ppi template, with increasing camphene content through 0, 5, 10, 20 and 25 wt.%

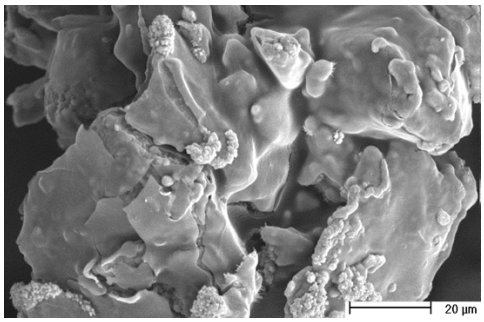

(a) SEM micrograph showing surface roughness/microporosity of sample produced without camphene (V = 20kV; WD = 19.3mm; mag = 1000x)

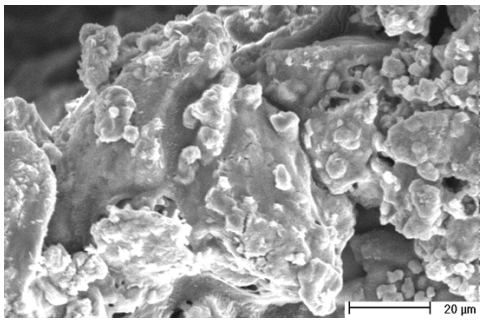

(b) SEM micrograph showing surface roughness/microporosity of sample produced with 5% camphene (V = 20kV; WD = 16.0mm; mag = 1000x)

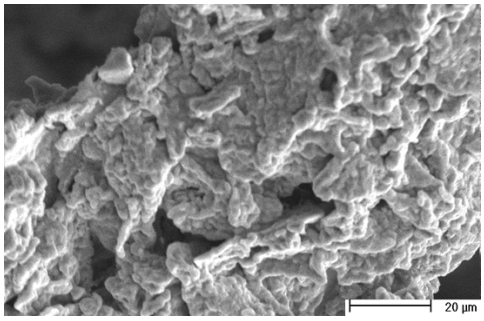

(c) SEM micrograph showing surface roughness/microporosity of sample produced with 10% camphene (V = 20kV; WD = 16.2mm; mag = 1000x)

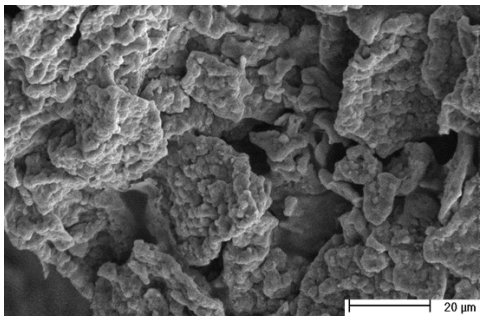

(d) SEM micrograph showing surface roughness/microporosity of sample produced with 20% camphene (V = 20kV; WD = 16.1mm; mag = 1000x)

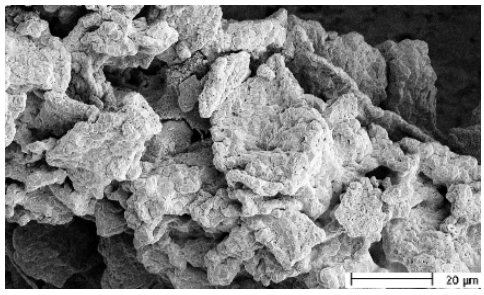

(e) SEM micrograph showing surface roughness/microporosity of sample produced with 25% camphene (V = 10kV; WD = 10.3mm; mag = 1000x)

Figure 7.37: SEM micrographs showing surface roughness/microporosity of Ti-6Al-4V scaffolds produced using the AFR with the 45 ppi template with increasing content through 0, 5, 10, 20 and 25 wt.%

It is known [549–551] that varying the sintering temperature has no significant impact on the shrinkage of Ti structures. However, as titanium undergoes a phase change from α to β at around 890 °C [44] which induces volumetric changes [551]of 2% in the unit cell, a range of sintering temperatures have been used. Furthermore, the slow cooling rate may facilitate the formation of a state such as that seen by Swarnakar et al [551], which has improved structural stability due to a reduction in the amount of dislocations [552, 553]. Furthermore, as outlined in Section 7.2.1.1, neither the pore nor strut size was significantly affected by changes to the sintering temperature, although there was improved structural stability. This is likely to be due to the general shrinkage from the template of up to 50%.

There was a decrease in the strut size, of up to 14% and 20% for structures from the 45 and 90 ppi template, when the sintering temperature was increased above 1100 °C accompanied by a transformation from Ti to TiC and Ti-C-N of approximately 30%. An increase in the density should lead to a comparable volume reduction for any affected material. The density of the Ti-C ($5040\,^{kg}/_{m^3}$) [554–556] and Ti-C-N ($5350\,^{kg}/_{m^3}$) [554–556] phases which formed are both greater than that of the α-Ti ($4540\,^{kg}/_{m^3}$) [554–556]. Therefore material that becomes TiC should occupy approximately 12% less volume whilst material that becomes Ti-C-N should reduce in volume by approximately 19%. The amount of material that undergoes phase changes cannot be accurately predicted, and as such this generates some degree of uncontrollable variability within the final structure. However, if precautionary measures to restrict carbide formation were used, the pore and strut size of titanium scaffolds would be highly controllable, as even with the shrinkage observed, the final structure closely mimics that of the template.

Similar to the trends observed for Ti scaffolds, varying the sintering temperature had little effect on the macrostructure of Ti-6Al-4V based constructs as was expected [549–551, 557]. The pore and strut size of structures fabricated from the 45 ppi and 90 ppi template, detailed in Section 7.2.1.1 were within normal experimental range regardless of the final sintering temperature.

Some Ti-6Al-4V structures exhibited collapse at all sintering temperatures, as outlined in Section 7.2.1.2. Multiple coats on the template enabled the body to maintain its structure during sintering as any collapse was only observed if the template was coated fewer than 3 times. Furthermore, this was significantly more noticable when the 45 ppi template was replicated, however it was also observed when the 90 ppi template was used. It is suggested that sample collapse is due to the polymer burning out before the particles have had sufficient time at an elvevated temperature to consolidate, which in this work consisted of holding the structures for 3 hrs at 500 °C. However, Dewider and Kim [558] suggest that the polymer burnout temperature should not be lower than 850 °C to ensure complete Ti-6Al-4V consolidation, although sintering of titanium based materials fabricated via reticulation techniques rarely involves holding at this temperature to facilitate the removal of the template. For example, Lee et al [52, 53] hold at 800 °C for 3 hrs, Ahmad et al [67] and Zhao et al [54] hold at 600 °C for 1 hr and an unspecified time respectively, and Cachinho and Correira [51, 232] and Li et al [275] hold at 500 °C, both for 2 hrs. In no case are there any reports of any sample distortion compared to the template. Interestingly both Ahmad et al [67] and Li et al [275] report an increase in the amount of carbon in the final material after sintering titanium alloys (Al_3Ti and Ti-6Al-4V respectively), whilst Lee et al [53] observed increased carbon content in Ti structures. Finally, in all cases where specified [51, 67, 232, 275], the heating rate used was 1 °C/min although in this work it was 3 °C/min. This increase may have led to the quicker removal of the polymer and thus caused the collapse.

As previously discussed in Section 6.2.5, it is undesirable for any microporosity to detrimentallly affect the macrostructure. The integrity of Ti and Ti-6Al-4V structures is not affected by the inclusion of a porogen and thus these structures could be suitable for enhancing the biological functionality of the scaffolds, provided the microporosity has the desired effect on cell attachment and proliferation as has been previously shown in thie work for HA fabrications from AFR in Section 6.4. It was expected that increasing the level of porogen would have decreased the amount of collapse of Ti-6Al-4V samples due to the production of routes for the polymer to

be removed from the structure [267, 268, 355]. However, as this is not the case, it is more likely that the greater ease with which the polymer can be removed could exacerbate the problem as the stability provided by the template is prematurely destroyed. Thus, provided there are a sufficient number of coats of the slurry on the scaffold for it to maintain its integrity, the inclusion of a porogen does not have any effect on the structure.

As with structures fabricated from HA, Section 6.2.2.1, the level of porogen had no impact upon the base size of the micropores, as shown in Figures 7.36 and 7.37 for Ti and Ti-6Al-4V fabrications. Instead, increasing the amount of camphene in the slurry caused an increase in the number and density of the micropores, to the point where there was coalescence. The pore size in freeze cast structures is related to the freezing temperature as opposed to the amount of porogen present [250, 254, 255, 257, 258] and thus no effect on the micropore size was expected. As freeze casting Ti and Ti-6Al-4V structures to different temperatures should affect the microporosity in the same way as seen when the temperature was varied for HA constucts, this has not been investigated here.

7.3 Porosity

7.3.1 Porosity Measurements

In general, varying the processing parameters had similar effects on the porosity of the final structure, regardless of which template or material the scaffold was produced from. The porosity of titanium samples from the 45 ppi template was largely unaffected by the sintering temperature, as shown in Figure 7.38, with values ranging from 85 to 94% at 1000 °C, 85 to 92% at 1100 °C, 85 to 94% at 1200 °C and 85 to 91% at 1300 °C. Varying the porogen content also had no consistent effect on the porosity; although there were some differences in the values obtained with the other processing parameters remaining equal, there was no trend as to which sample

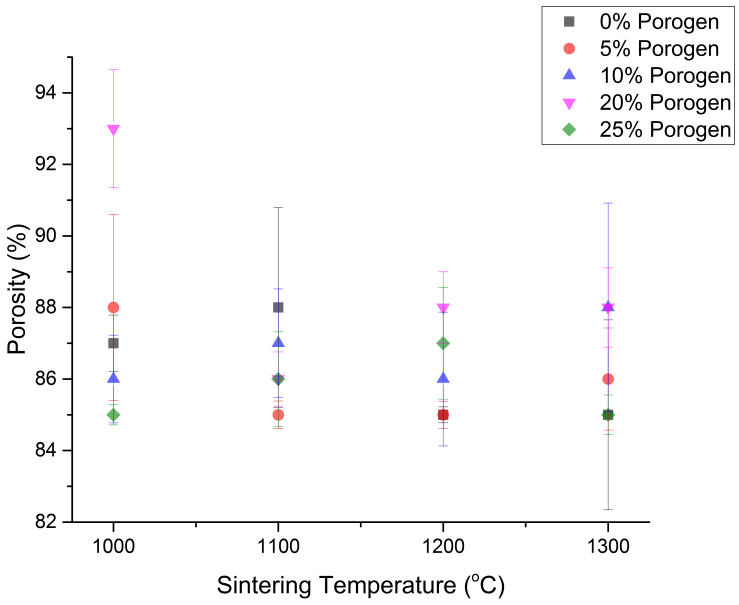

Figure 7.38: Porosity (%) of Ti scaffolds fabricated using the 45 ppi template, with 5 coats of the slurry on the template, with varying porogen content and sintering temperature

exhibited the least or most porosity. The only variable that had a significant effect was the number of coats of the slurry on the template. Particularly when comparing samples coated once to those with 5 coats, there was a decrease in porosity in all cases except for those produced with 20% porogen and sintered to 1000°C (which increased by 2%), and with 10 and 25% porogen when sintered to 1300°C (which increased by 1 and 4 %). The relationships between the number of coats, sintering temperature and porosity of samples from the 45 ppi template and sintered to 1000, 1100, 1200 and 1300 °C are shown in Figures 7.39 - 7.42.

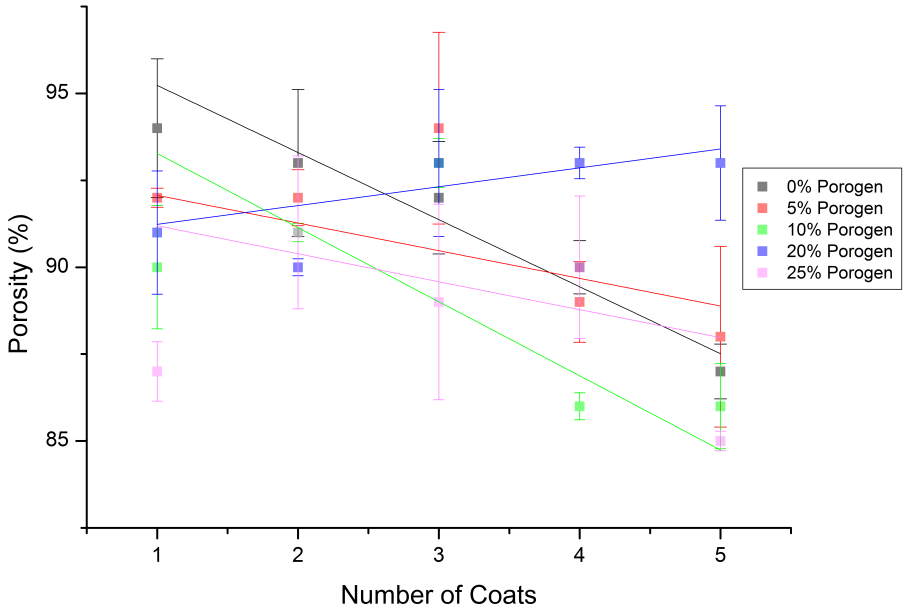

Figure 7.39: Porosity (%) of Ti scaffolds fabricated using the 45 ppi template and sintered to 1000 °C, with varying porogen content and number of coats of the slurry

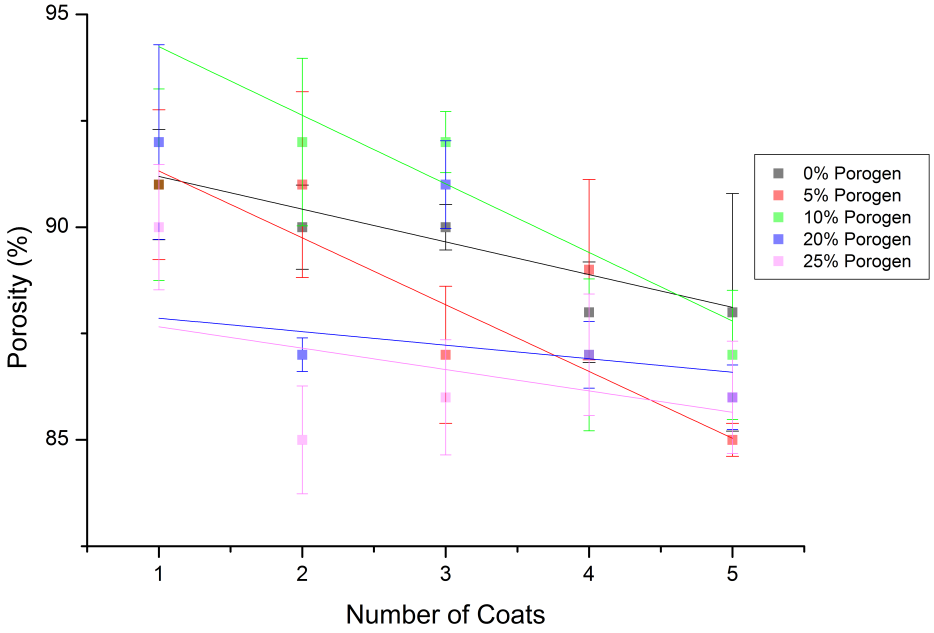

Figure 7.40: Porosity (%) of Ti scaffolds fabricated using the 45 ppi template and sintered to 1100 °C, with varying porogen content and number of coats of the slurry

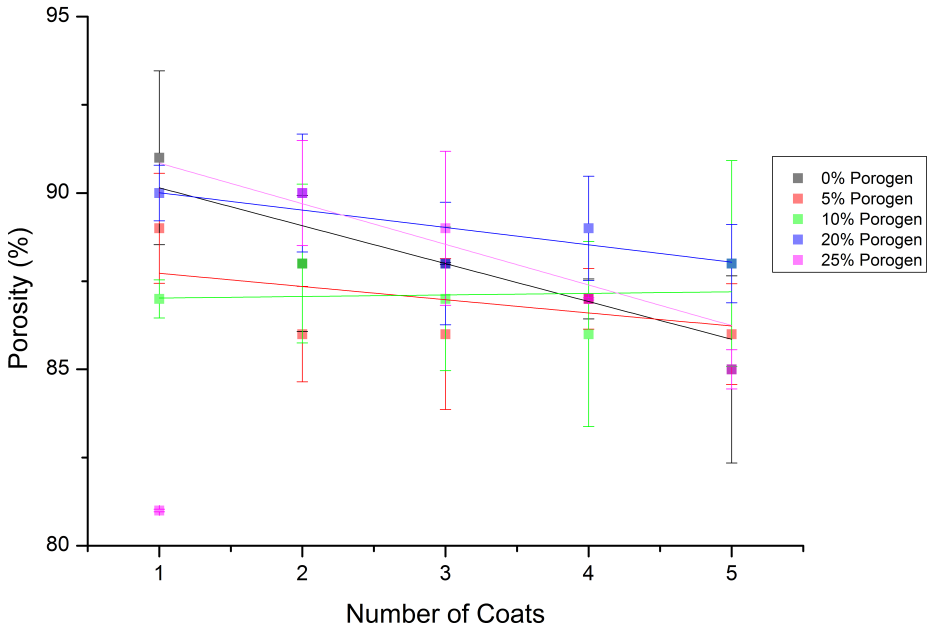

Figure 7.42: Porosity (%) of Ti scaffolds fabricated using the 45 ppi template and sintered to 1300 °C, with varying porogen content and number of coats of the slurry

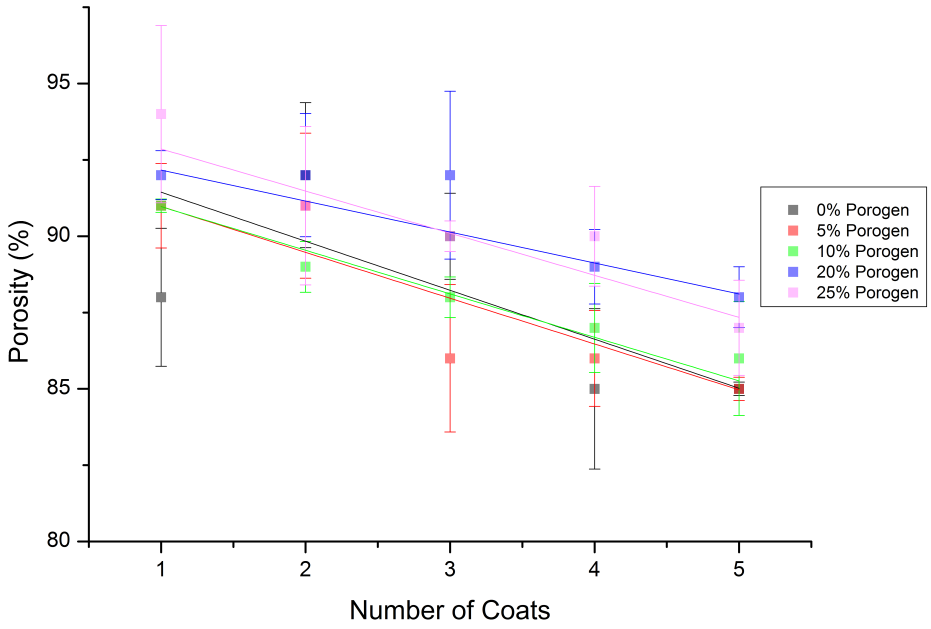

Figure 7.41: Porosity (%) of Ti scaffolds fabricated using the 45 ppi template and sintered to 1200 °C, with varying porogen content and number of coats of the slurry

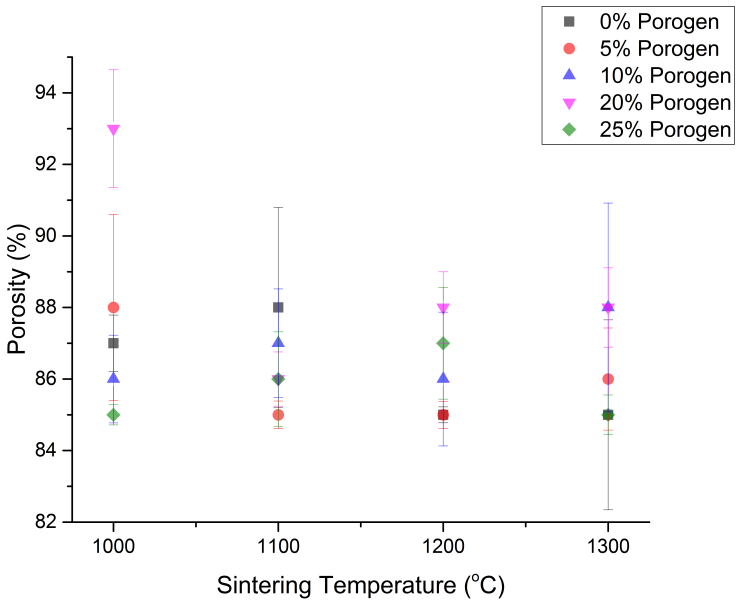

Figure 7.43: Porosity (%) of Ti scaffolds fabricated using the 90 ppi template, with 5 coats of the slurry on the template, with varying porogen content and sintering temperature

Titanium structures fabricated from the 90 ppi template exhibited very similar characteristics to those obtained using the 45 ppi template. The sintering temperature had little noticable effect on the porosity, as shown in Figure 7.43, with values from 81 to 93, 84 to 94, 87 to 92, and 85 to 91% at 1000, 1100, 1200 and 1300 °C respectively. The porogen content also did not cause significant changes to the porosity, with values generally within a small range when the other processing parameters remained constant. Finally, as with samples from the 45 ppi template, an increase to the number of coats from one to five caused a decrease in the final porosity in all samples except those produced with 25% porogen and sintered to 1000 °C (which increased by 1%), and with 5% porogen when sintered to 1100 °C (which remained the same). The relationships between the processing parameters and porosity of Ti samples fabricated using the 90 ppi template when sintered to the different temperatures are shown in Figures 7.44 - 7.47.

Structures fabricated from Ti-6Al-4V exhibited similar trends as those from Ti.

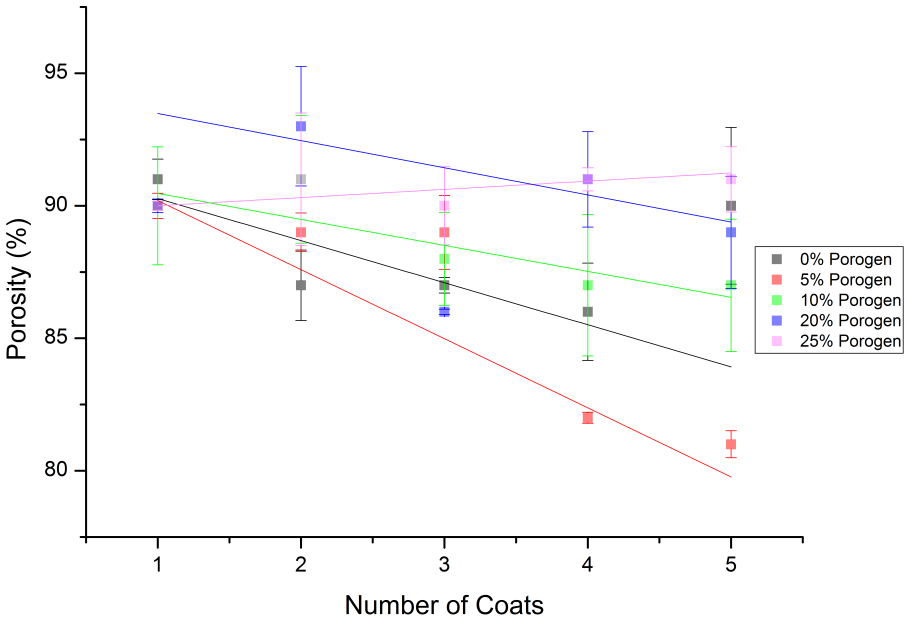

Figure 7.44: Porosity (%) of Ti scaffolds fabricated using the 90 ppi template and sintered to 1000 °C, with varying porogen content and number of coats of the slurry

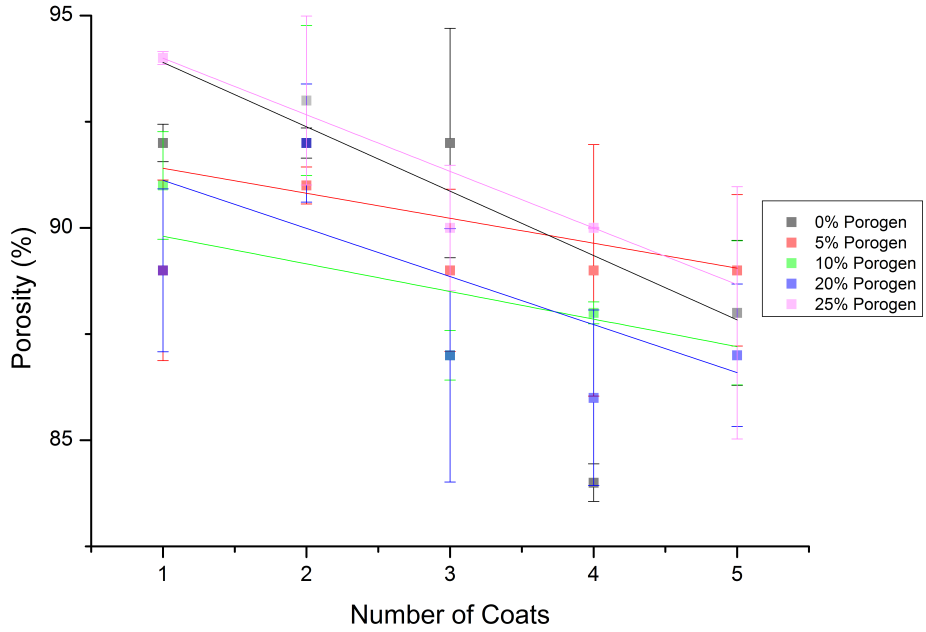

Figure 7.45: Porosity (%) of Ti scaffolds fabricated using the 90 ppi template and sintered to 1100 °C, with varying porogen content and number of coats of the slurry

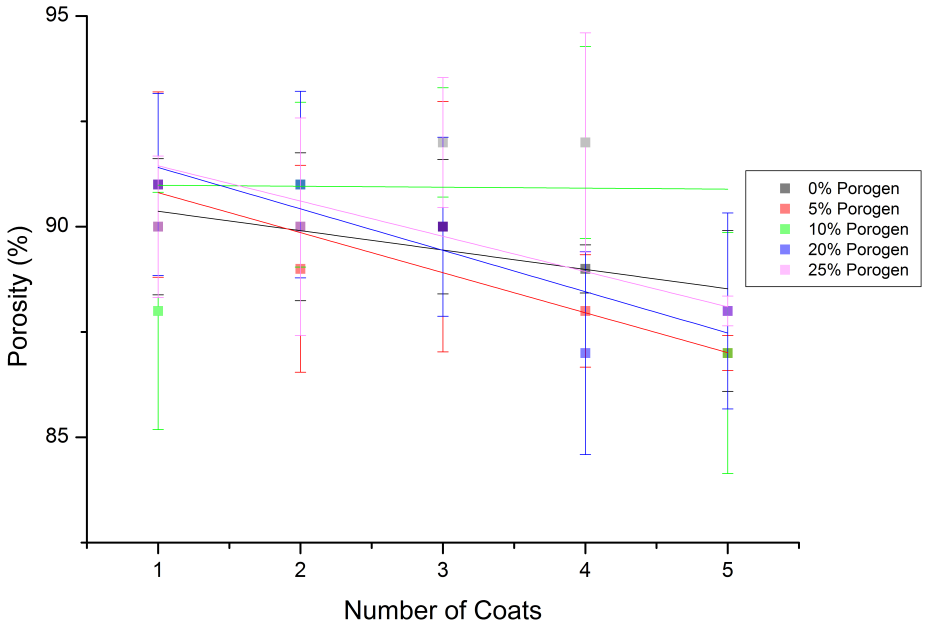

Figure 7.46: Porosity (%) of Ti scaffolds fabricated using the 90 ppi template and sintered to 1200 °C, with varying porogen content and number of coats of the slurry

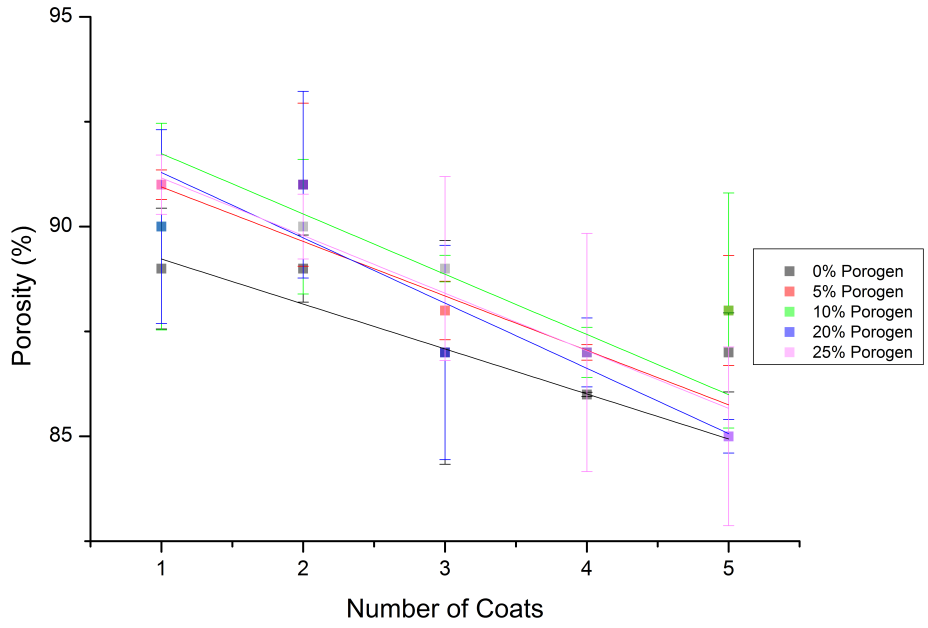

Figure 7.47: Porosity (%) of Ti scaffolds fabricated using the 90 ppi template and sintered to 1300 °C, with varying porogen content and number of coats of the slurry

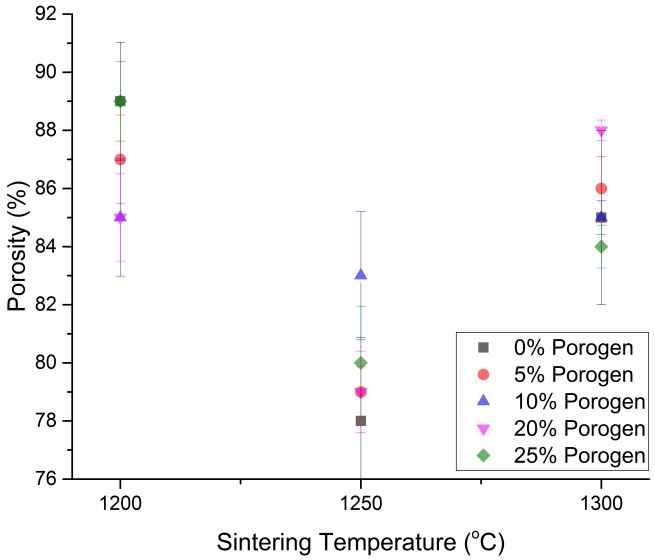

Figure 7.48: Porosity (%) of Ti-6Al-4V scaffolds fabricated using the 45 ppi template, with 5 coats of the slurry on the template, with varying porogen content and sintering temperature

The samples produced from the 45 ppi template were relatively unaffected by the amount of porogen in the slurry, with some variation that was not systematic. The samples sintered to 1200 and 1300 °C exhibited similar porosities, however those sintered to 1250 °C were approximately 5% lower on average, as shown in Figure 7.48. The number of coats of the slurry on the template affected the porosity, with samples coated multiple times generally exhibiting lower porosities than those coated once. There were only two instances of the sample with five coats exhibiting higher porosities than those with one coat - those with 25% porogen inclusion at 1200 °C (which increased by 1%) and with 20% at 1300 °C (which stayed the same). It is thought that this may have been due to the sample with fewer coats collapsing during sintering. The effect of varying the number of coats and sintering temperature on the porosity of samples sintered to 1200, 1250 and 1300 °C is shown in Figures 7.49, 7.50 and 7.51 respectively.

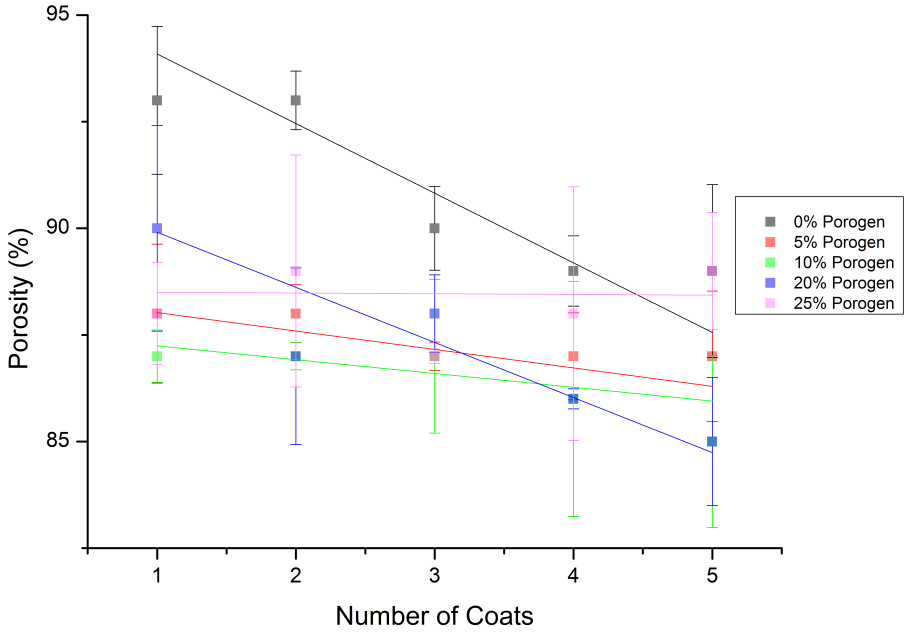

Figure 7.49: Porosity (%) of Ti-6Al-4V scaffolds fabricated using the 45 ppi template and sintered to 1200 °C, with varying porogen content and number of coats of the slurry

Varying the sintering temperature of Ti-6Al-4V samples fabricated using the 90 ppi template only had a small effect on the porosity. Sintering to 1250 °C led to structures to have a more consistent porosity, with values between 77 and 89%, regardless of the other processing parameters, whilst those sintered to 1200 and 1300 °C had larger ranges of 76 to 91 and 74 to 91%, as shown in Figure 7.52. In general, varying the porogen content did not have an impact on the porosity. However, when samples were sintered to 1300 °C, there was a much larger range when the samples were coated 3 times, of 76 to 89%, than observed in any other case. However, this does not necessarily seem to be caused by the porogen inclusion as there is no trend as to which have greater, or lesser, porosities. It is thought that the random nature of sample collapse affected structures most at this point. Finally, in all cases, increasing the number of coats from one to five led to an approximately linear decrease in the porosity in all cases. This affected structures sintered to 1200 and 1300 °C slightly more than those sintered to 1250 °C, with average decreases of 12, 13 and 9%

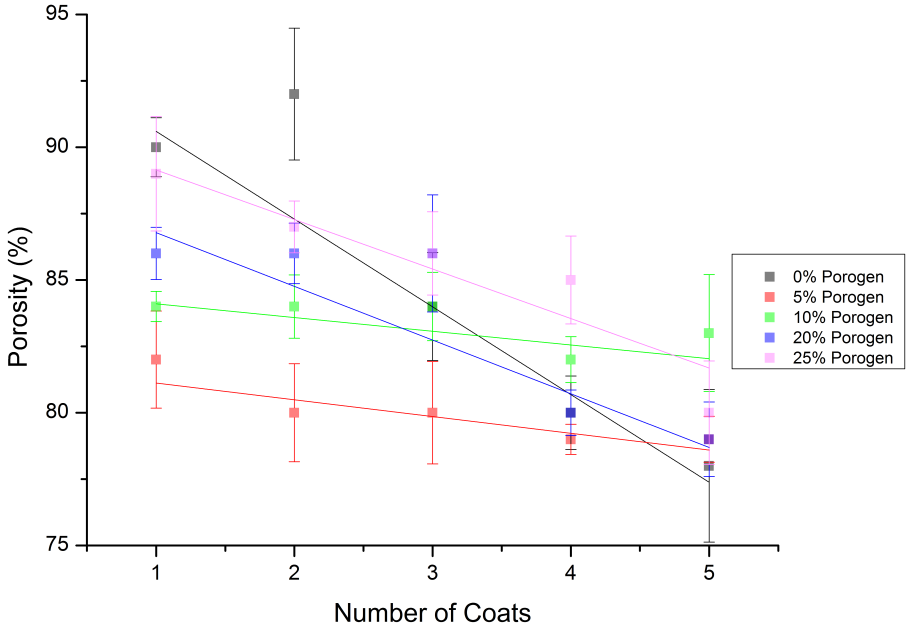

Figure 7.50: Porosity (%) of Ti-6Al-4V scaffolds fabricated using the 45 ppi template and sintered to 1250 °C, with varying porogen content and number of coats of the slurry

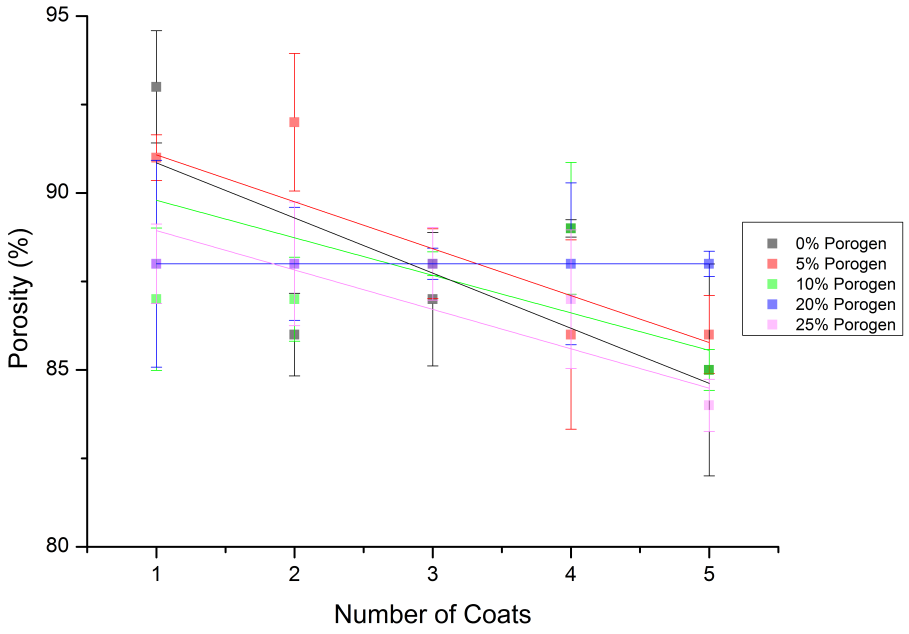

Figure 7.51: Porosity (%) of Ti-6Al-4V scaffolds fabricated using the 45 ppi template and sintered to 1300 °C, with varying porogen content and number of coats of the slurry

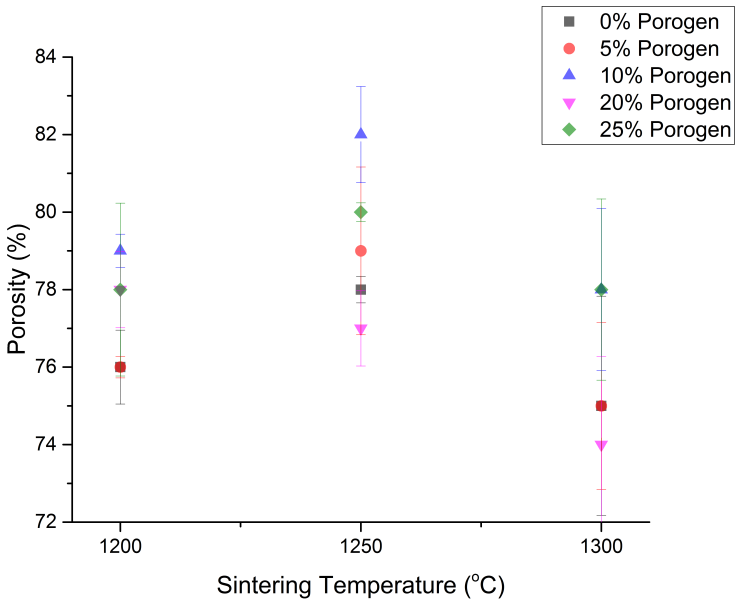

Figure 7.52: Porosity (%) of Ti-6Al-4V scaffolds fabricated using the 90 ppi template, with 5 coats of the slurry on the template, with varying porogen content and sintering temperature

respectively. The relationships between the porosity, number of coats and porogen content at the various sintering temperatures are shown in Figures 7.53 - 7.55.

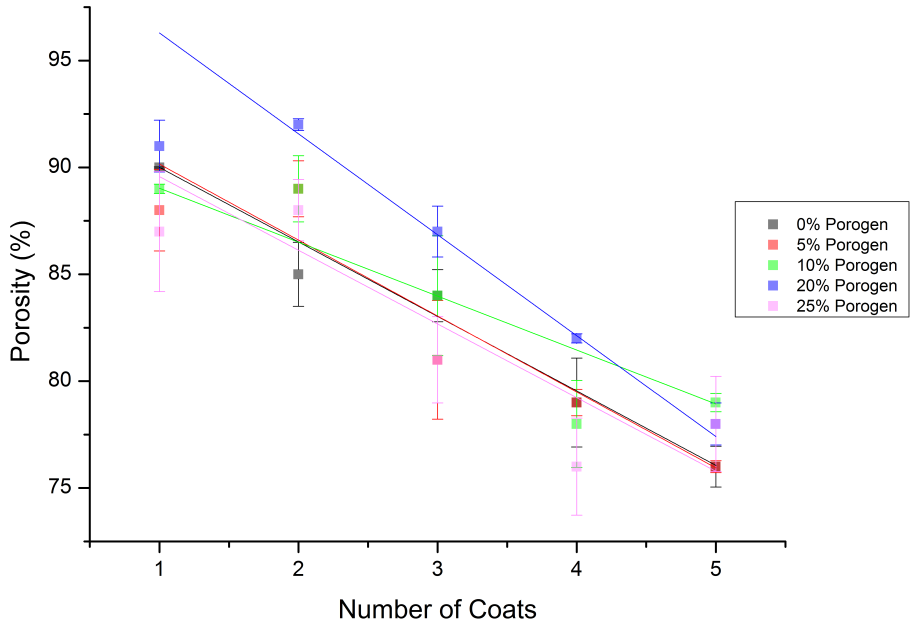

Figure 7.53: Porosity (%) of Ti-6Al-4V scaffolds fabricated using the 90 ppi template and sintered to 1200 °C, with varying porogen content and number of coats of the slurry

7.3.2 Discussion

The porosity of Ti samples, 81 to 94%, produced from both templates decreased with the number of coats, with a slight decrease with increasing sintering temperature. Additionally, the porosity for structures produced from the 45 ppi template was approximately 5% greater than for those from the 90 ppi template whilst the level of porogen had little impact upon the porosity.

As discussed above, in Section 7.2.3, the sintering temperature does not significantly affect the densification or shrinkage of Ti scaffolds [549–551]. Thus, it was not expected that this would have a large impact upon the level of porosity of the final scaffolds. Scaffolds with similar levels of porogen had porosity values within normal experimental ranges regardless of the sintering temperature. Lee et al [53] increased the number of coats of foam reticulation produced Ti scaffolds to reduce

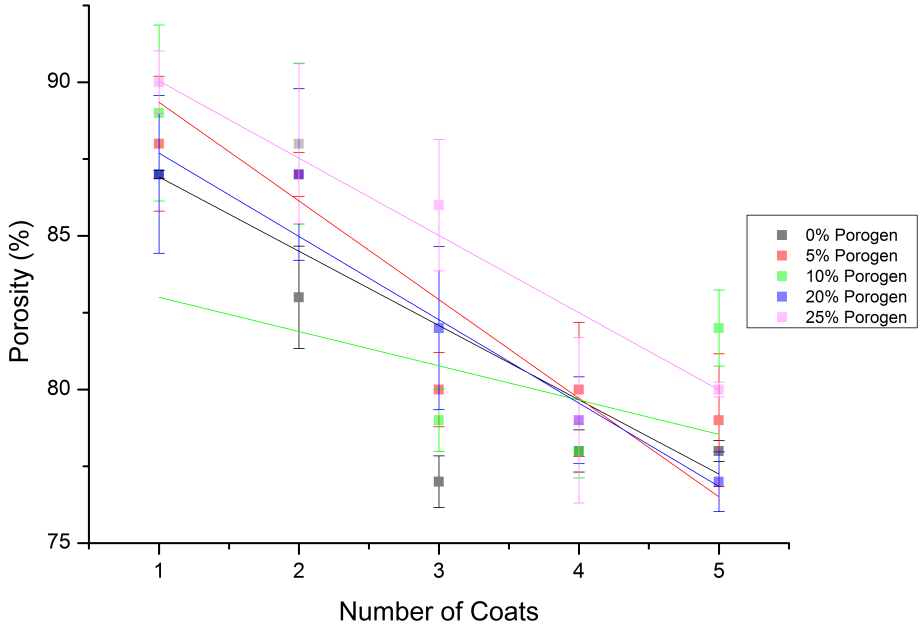

Figure 7.54: Porosity (%) of Ti-6Al-4V scaffolds fabricated using the 90 ppi template and sintered to 1250 °C, with varying porogen content and number of coats of the slurry

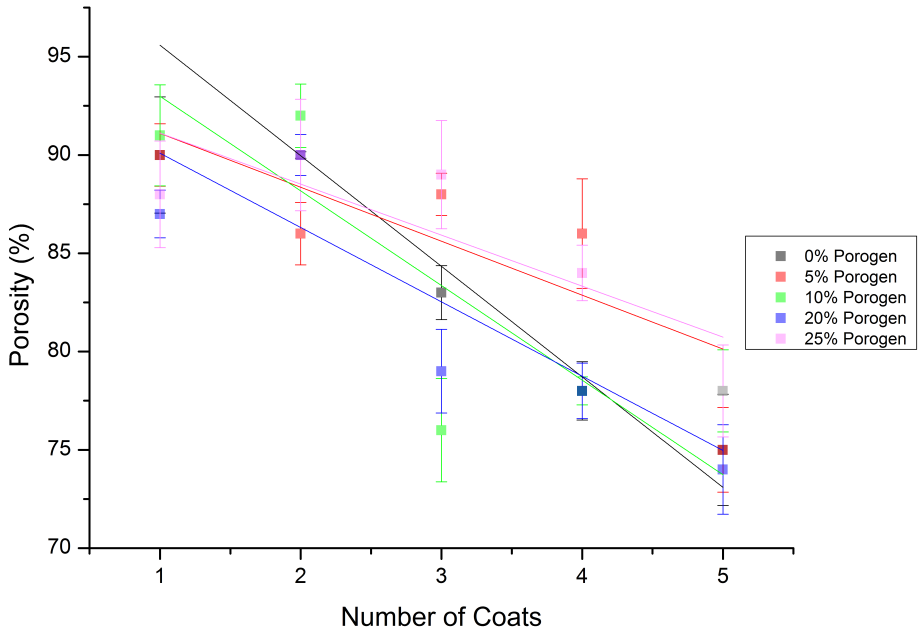

Figure 7.55: Porosity (%) of Ti-6Al-4V scaffolds fabricated using the 90 ppi template and sintered to 1300 °C, with varying porogen content and number of coats of the slurry

the porosity and increase the mechanical strength. Furthermore, similar effects have been found with calcium phosphate based constructs [267, 270]. AFR fabricated structures exhibited similar characteristics when increasing the number of coats as porosity is predominantly generated via foam reticulation.

The level of porogen had no significant effect on the total porosity even though it is included with the aim of producing microporosity on the struts. As high sintering temperatures were required to ensure the complete removal of the template and degassing of the structure [558], there was increased densification and hence shrinkage of the final scaffold compared to the green bodies before sintering. This led to smaller macro and micropores and thus the impact upon the total porosity was relatively limited.

Scaffolds fabricated from Ti-6Al-4V exhibited similar trends with respect to the level of porosity as those observed with Ti and HA scaffolds, although over a slightly larger range of between 74 and 94 %. Increasing the sintering temperature of Ti-6Al-4V does not effect densification [549–551, 557], as is also seen in this work with the negligible effect on porosity. The porogen content also had a limited effect due to the high levels of shrinkage compared with the template and the predominance of the macroporosity on the total porosity as previously mentioned. However, increasing the number of coats of the slurry reduced the porosity and increased the mechanical strength [53, 267, 270] similar to HA and Ti constructs.

Interestingly, scaffolds that underwent some collapse during sintering had no discernible differences in the level of porosity as to what would have been expected from complete scaffolds. There are two possible explanations for this. Firstly, collapsed constructs may have undergone increased TiC formation, which has an increased density compared to Ti-6Al-4V. XRD was only undertaken on selected samples and as such the exact amount of carbide formation for every fabrication is not known. As porosity calculations were made assuming no carbide formation, the relative normality in the porosity may have been caused by differences in the amount of carbide in collapsed samples. Secondly, during polymer pyrolysis, some

of the slurry may have been removed from the construct. The ratio of pore to strut sizes did not differ greatly between samples that collapsed and those that did not which would only be possible if the volume of titanium decreased in collapsed samples. The weights of complete dry samples prior to submerging in water, given in Table 7.9, further corroborates this. There have been no other reports of scaffolds affected in this way and as such further investigations into this are necessary to determine the exact reasons behind the observed phenomenom.

		1 coat	2 coat	3 coat	4 coat	5 coat
45 ppi	1250 °C	0.056 ± 0.02	0.12 ± 0.08	0.090 ± 0.05	0.046 ± 0.02	0.093 ± 0.02
	1300 °C	0.091 ± 0.04	0.077 ± 0.02	0.044 ± 0.01	0.058 ± 0.01	0.10 ± 0.03
	1350 °C	0.058 ± 0.02	0.034 ± 0.01	0.054 ± 0.02	0.073 ± 0.02	0.11 ± 0.03
90 ppi	1250 °C	0.088 ± 0.04	0.36 ± 0.09	0.57 ± 0.07	0.38 ± 0.08	0.53 ± 0.10
	1300 °C	0.16 ± 0.05	0.54 ± 0.11	0.52 ± 0.11	0.58 ± 0.04	0.60 ± 0.11
	1350 °C	0.13 ± 0.03	0.32 ± 0.09	0.27 ± 0.07	0.38 ± 0.06	0.44 ± 0.03

Table 7.9: Average dry weights (g) for samples sintered to different final temperatures with different numbers of coatings of the slurry on the template. Weights of scaffolds with varying porogen contents have been averaged for each temperature and coating number

The porosity values for Ti-6Al-4V scaffolds were slightly lower than those observed for Ti scaffolds. As the material becomes cubic (TiC) [546, 554–556] as opposed to HCP (α-Ti, β-Ti or Ti-6Al-4V) [554–556] the density increases which is associated with a reduction in the volume of the material or an increase in weight of the scaffold. Although in bulk constructs volumetric changes generate internal stresses [559–562], the porosity in scaffolds structures allows for volumetric changes [562, 563]. Changes to the weight of the scaffold are more likely in this case as the material has undergone a phase change to TiC or Ti-C-N and has thus incorporated C or N atoms. A greater proportion of the material underwent a phase change to TiC for structures fabricated

from Ti-6Al-4V, up to 93% as detailed in Table 7.3, as opposed to from Ti, up to 81% detailed in Table 7.1, which is believed to be the reason that a greater amount of shrinkage when compared to the template (up to 56 or 42% for Ti-6Al-4V scaffolds from the 45 or 90 ppi templates compared to up to 44 or 33% for Ti constructs) was observed.

7.4 Mechanical Properties

7.4.1 Yield Stress Calculations

As the experimentally obtained mechanical properties of as-fabricated HA scaffolds matched the theoretical values, Section 6.3, the mechanical strengths of Ti and Ti-6Al-4V scaffolds were calculated using Equation 4.10, with the shape factor calculated using Equation 4.11.

The compressive yield stress of structures fabricated from Ti using the 45 ppi template was relatively independant of the sintering temperature, with structures generally exhibiting a similar range of strengths when the other variables remained constant, as shown in Figure 7.56. There was a slight general increase, although the highest value was obtained with a sintering temperature of 1200 °C (942 $\pm$ 132kPa) with any variation more noticable when structures were coated multiple times. Including the porogen in the precursor slurry did not have a detrimental effect on the mechanical strength in most cases, however when sintered to 1200 and 1300 °C those without porogen exhibited the greatest strength. Increases to the mechanical strength could be obtained by increasing the number of coats of the slurry on the template, with only one instance of a decrease, from 166 $\pm$ 25 to 82 $\pm$ 15 kPa, when increasing the number of coats from one to five for the sample with 20% porogen and sintered to 1000 °C. In general, there was a reasonably linear increase however, particularly with samples sintered to 1000 °C the relationship was more exponential. The relationships between the processing parameters and the strength for Ti scaffolds from the 45 ppi template are shown in Figures 7.57 - 7.60.

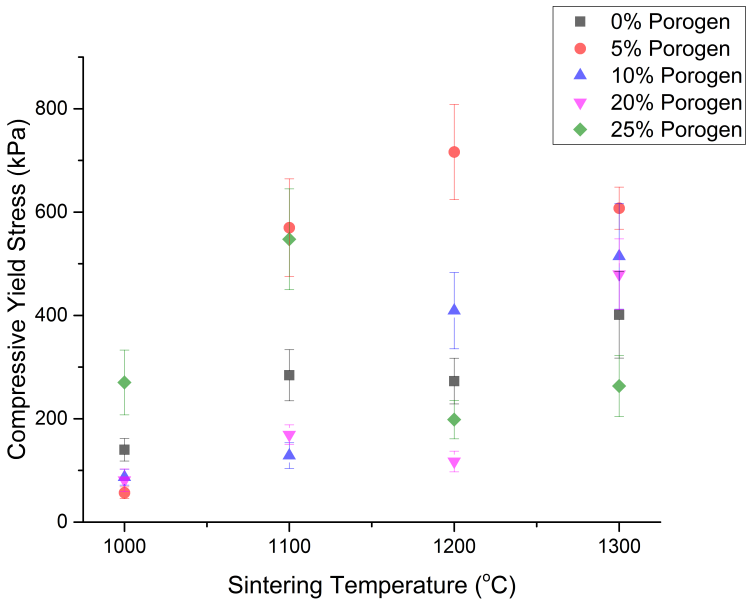

Figure 7.56: Theoretical compressive yield strength (kPa) of Ti scaffolds fabricated using 3 coats of the slurry on the 45 ppi template, with varying porogen content and sintering temperature

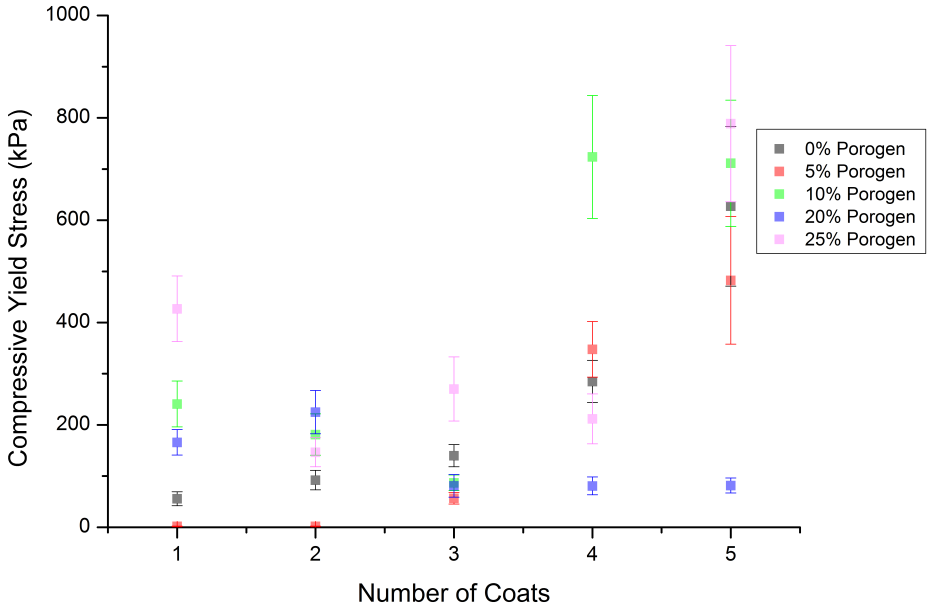

Figure 7.57: Theoretical compressive yield strength (kPa) of Ti scaffolds fabricated using the 45 ppi template and sintered to 1000 °C, with varying porogen content and number of coats of the slurry

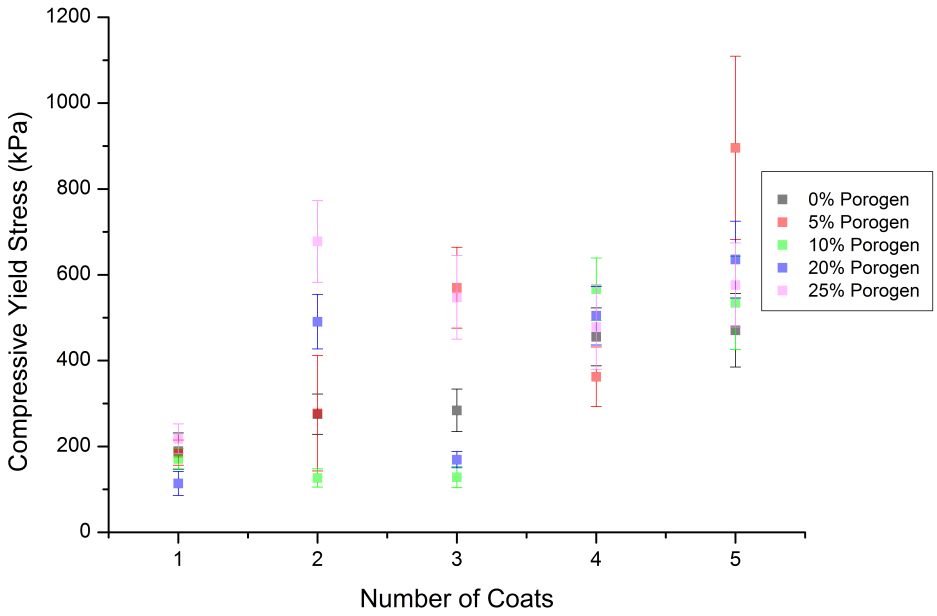

Figure 7.58: Theoretical compressive yield strength (kPa) of Ti scaffolds fabricated using the 45 ppi template and sintered to 1100 °C, with varying porogen content and number of coats of the slurry, plotted on same y-scale as Figure 7.57

Titanium structures produced using the 90 ppi template generally exhibited similar characteristics to those from the 45 ppi template. Furthermore, there were no significant differences in using the less porous template with respect to the theoretical compressive strength apart from the structure produced with 5% camphene included in the slurry and sintered to 1000 °C. The samples exhibited significantly higher strengths when coated 4 and 5 times (1.5 $\pm$0.3 and 1.8 $\pm$0.3 MPa respectively) than any other Ti sample. Disregarding this sample however, varying the sintering temperature, as shown in Figure 7.61 and porogen content had little impact on the strength of the scaffold, with values ranging from 65 $\pm$8 to 759 $\pm$124, 32 $\pm$6 to 1088 $\pm$178, 72 $\pm$16 to 671 $\pm$113 and 109 $\pm$25 to 655 $\pm$138 kPa at 1000, 1100, 1200 and 1300 °C respectively. The only parameter that had a consistent effect on the strength was the number of coats. As this was increased there was an associated increase in the average yield stress, with only the sample produced with 25% porogen and sintered to 1000 °C exhibiting a decrease as the number of coats was increased from one to five from 155 $\pm$42 kPa to 125 $\pm$27 kPa. The effects of

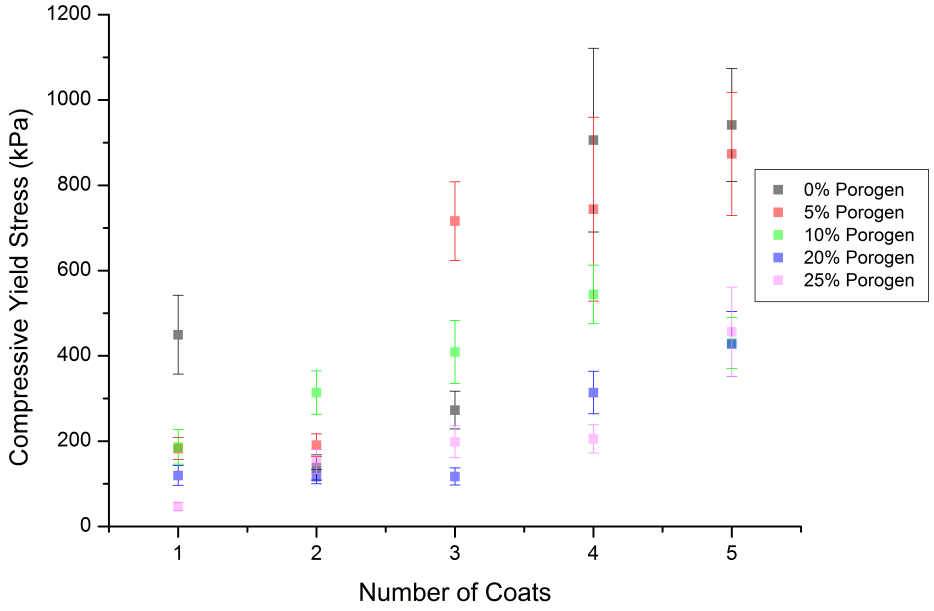

Figure 7.59: Theoretical compressive yield strength (kPa) of Ti scaffolds fabricated using the 45 ppi template and sintered to 1200 °C, with varying porogen content and number of coats of the slurry, plotted on same y-scale as Figure 7.57

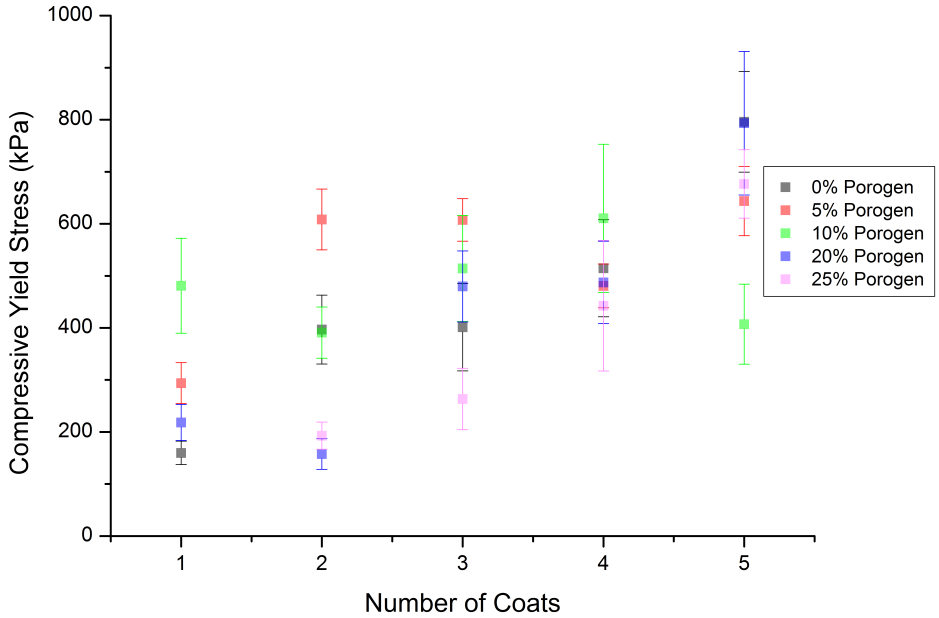

Figure 7.60: Theoretical compressive yield strength (kPa) of Ti scaffolds fabricated using the 45 ppi template and sintered to 1300 °C, with varying porogen content and number of coats of the slurry, plotted on same y-scale as Figure 7.57

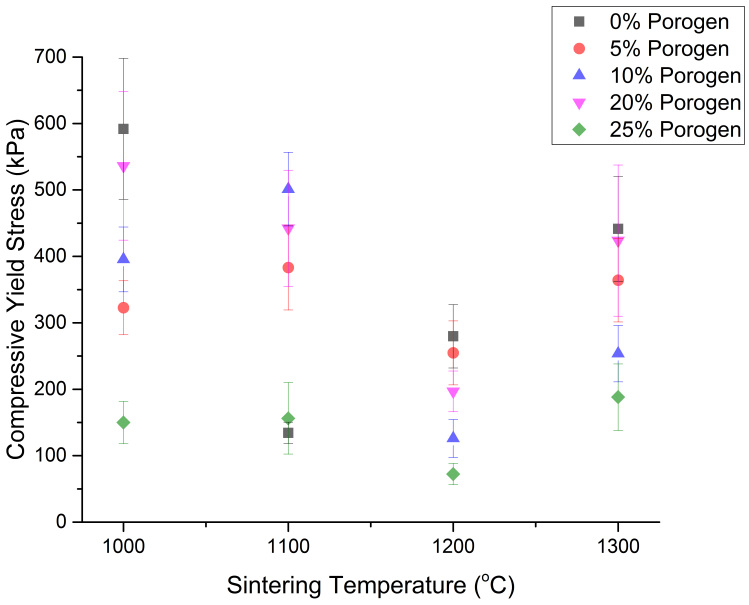

Figure 7.61: Theoretical compressive yield strength (kPa) of Ti scaffolds fabricated using 3 coats of the slurry on the 90 ppi template, with varying porogen content and sintering temperature

varying the number of coats and porogen content on Ti samples from the 90 ppi template and sintered to 1000, 1100, 1200 and 1300 °C are shown in Figures 7.62 - 7.65.

Samples fabricated from Ti-6Al-4V were generally much stronger in compression than those from either HA or Ti. The relationships between the compressive strength of Ti-6Al-4V samples from the 45 ppi template and the number of coats and porogen contents after sintering at 1200, 1250 and 1300 °C are shown in Figures 7.67, 7.68 and 7.69. Samples sintered to 1200 and 1300 °C exhibited similar strengths, of 238 ± 30 to 2147 ± 357 and 219 ± 43 to 2553 ± 456kPa respectively, however those sintered at 1250 °C exhibited much higher values, of 349 ± 34 to 7025 ± 1450kPa, as shown in Figure 7.66. The porogen content only had an effect when samples sintered to 1250 °C were coated multiple times, with the strength generally decreasing with increasing porogen content. However, the weakest sample for each number of coats was stronger than when all other conditions were unchanged apart from the sintering

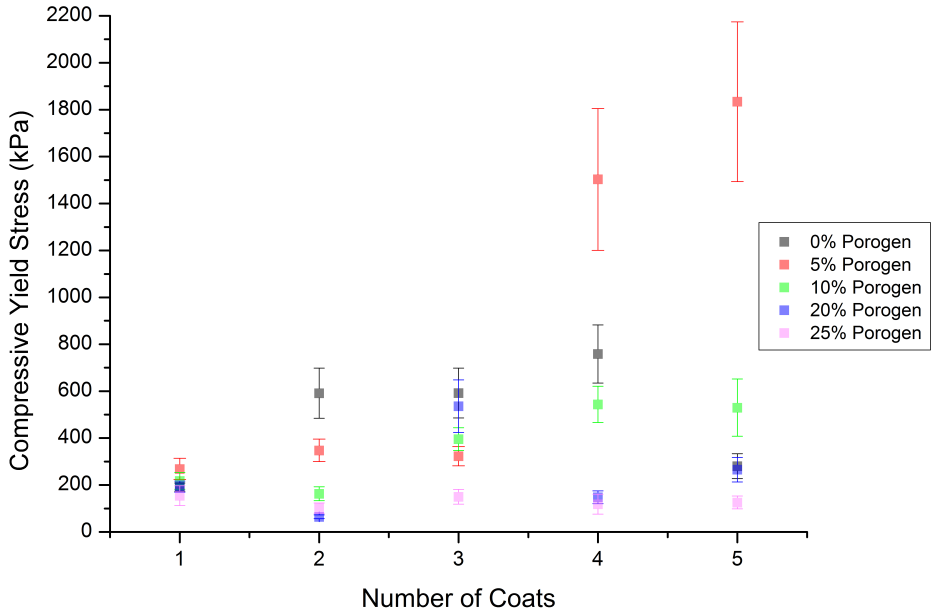

Figure 7.62: Theoretical compressive yield strength (kPa) of Ti scaffolds fabricated using the 90 ppi template and sintered to 1000 °C, with varying porogen content and number of coats of the slurry

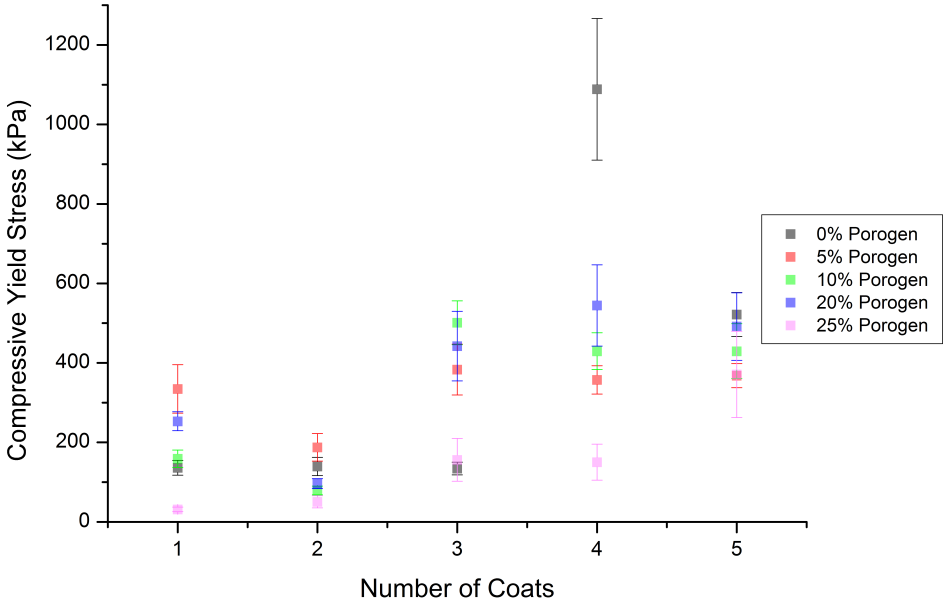

Figure 7.63: Theoretical compressive yield strength (kPa) of Ti scaffolds fabricated using the 90 ppi template and sintered to 1100 °C, with varying porogen content and number of coats of the slurry, plotted on same y-scale as Figure 7.62

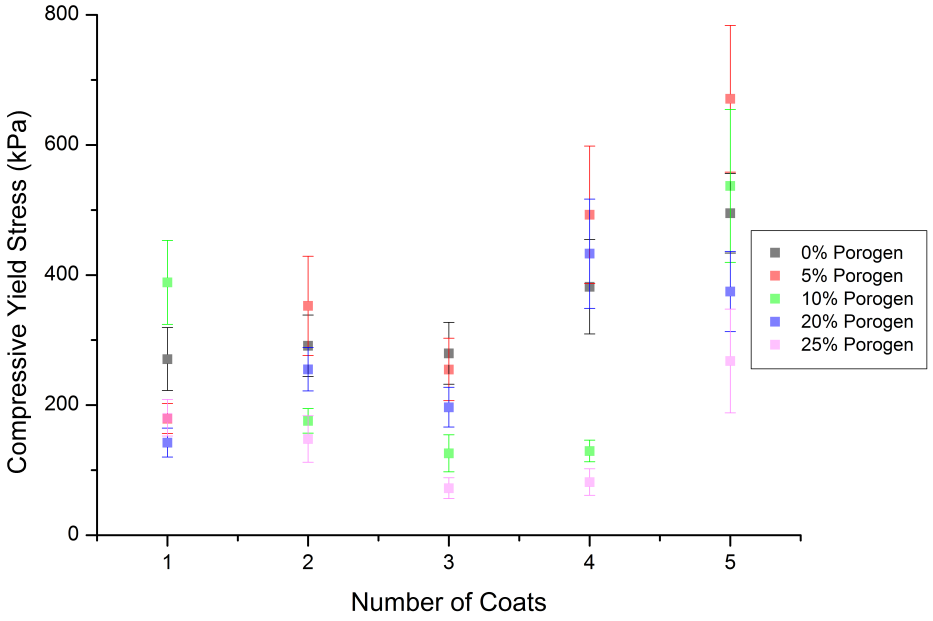

Figure 7.64: Theoretical compressive yield strength (kPa) of Ti scaffolds fabricated using the 90 ppi template and sintered to 1200 °C, with varying porogen content and number of coats of the slurry, plotted on same y-scale as Figure 7.62

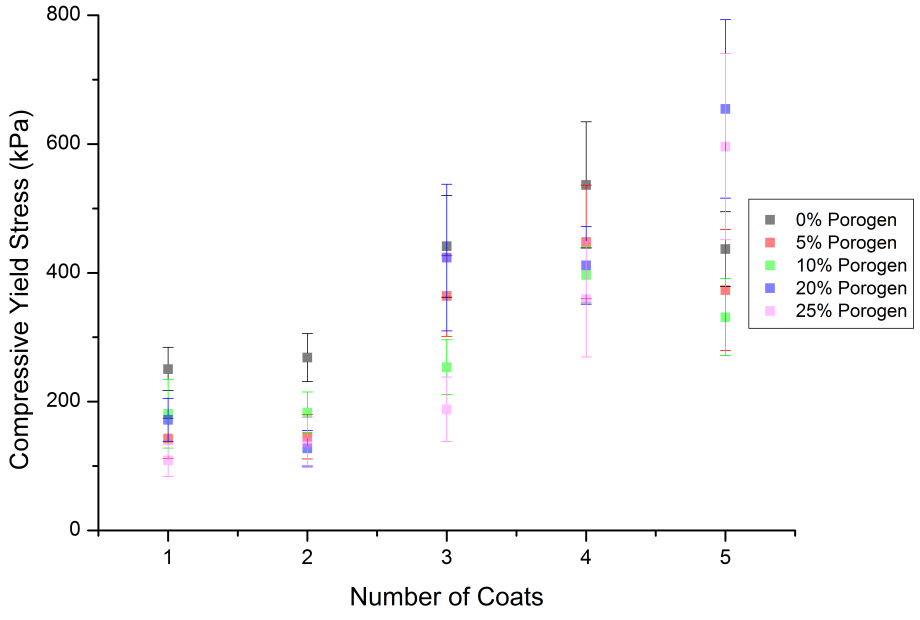

Figure 7.65: Theoretical compressive yield strength (kPa) of Ti scaffolds fabricated using the 90 ppi template and sintered to 1300 °C, with varying porogen content and number of coats of the slurry, plotted on same y-scale as Figure 7.62

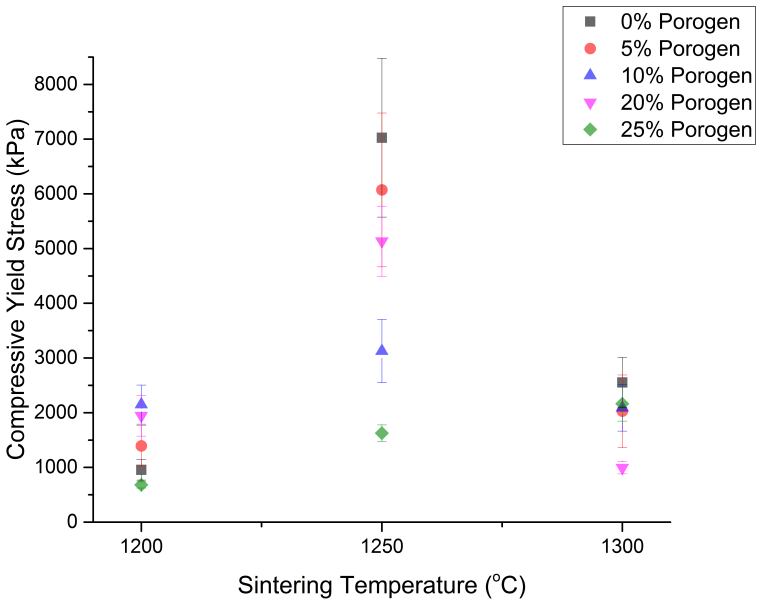

Figure 7.66: Theoretical compressive yield strength (kPa) of Ti scaffolds fabricated using 3 coats of the slurry on the 90 ppi template, with varying porogen content and sintering temperature

temperature. Finally, increasing the number of coats from one to five led to an increase in the compressive yield stress in all cases apart from the sample produced with 25% porogen and sintered to 1200 °C which decreased from 859 ± 176 to 680 ± 56kPa.

The mechanical properties of Ti-6Al-4V scaffolds from the 90 ppi template exhibited similar characteristics as to those already mentioned, with the relationships between the number of coats, porogen content and theoretical strength shown in Figures 7.71, 7.72 and 7.73 when sintered to 1200, 1250 and 1300 °C respectively. Increasing the sintering temperature did not have a great impact on the mechanical strength, however those sintered to 1200 and 1300 °C were stronger than those sintered to 1250 °C after multiple coats were added as shown in Figure 7.70. For example, the structures produced without porogen and coated five times had yield stresses of 13.6 ± 1.1 and 13.7 ± 2.7 MPa when sintered to 1200 and 1300 °C, whilst that of the sample sintered to 1250 °C was 7.9 ± 1.9MPa. There was some decrease to the

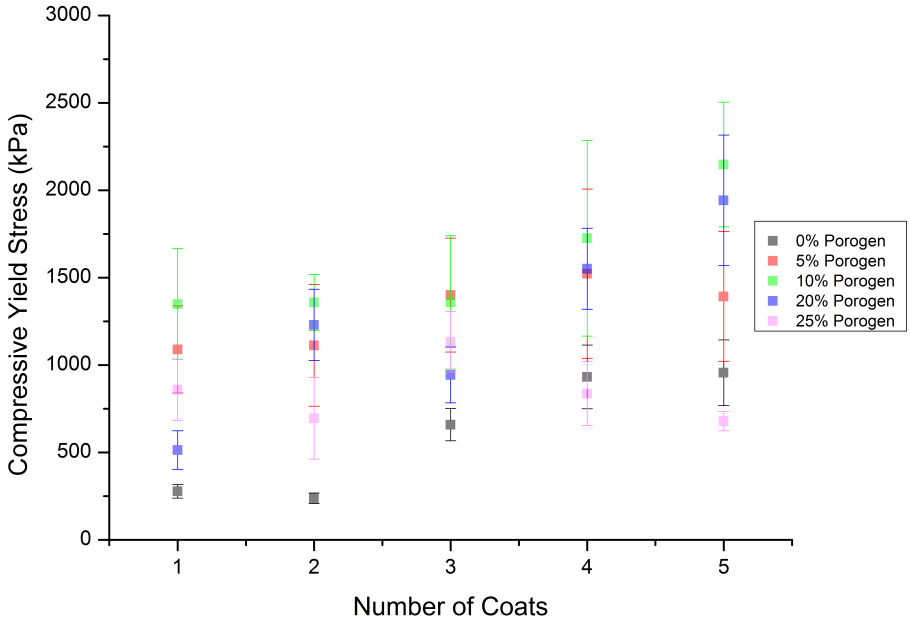

Figure 7.67: Theoretical compressive yield strength (kPa) of Ti-6Al-4V scaffolds fabricated using the 45 ppi template and sintered to 1200 °C, with varying porogen content and number of coats of the slurry

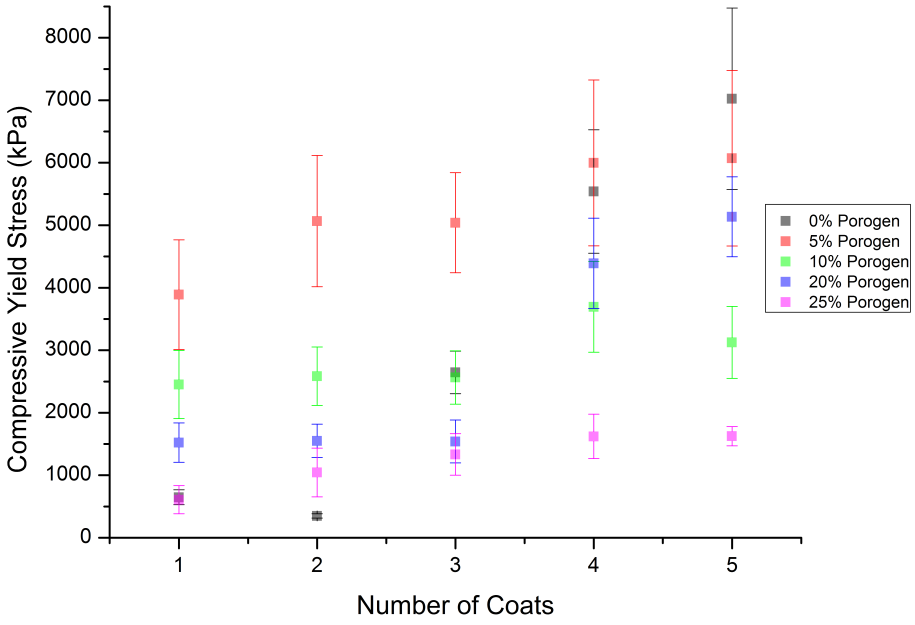

Figure 7.68: Theoretical compressive yield strength (kPa) of Ti-6Al-4V scaffolds fabricated using the 45 ppi template and sintered to 1250 °C, with varying porogen content and number of coats of the slurry, plotted on same y-scale as Figure 7.67

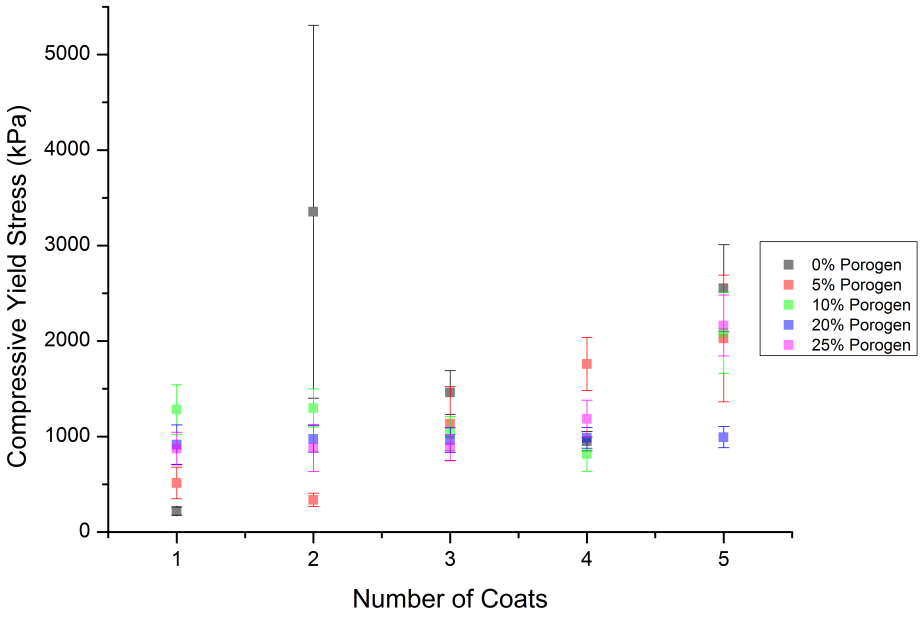

Figure 7.69: Theoretical compressive yield strength (kPa) of Ti-6Al-4V scaffolds fabricated using the 45 ppi template and sintered to 1300 °C, with varying porogen content and number of coats of the slurry, plotted on same y-scale as Figure 7.67

yield stress when the porogen was included with samples coated multiple times, with values decreasing from 13.6± 1.1 to 5.3 ± 0.5, 7.9 ± 1.9 to 6.0 ± 1.1 and 13.7 ± 2.7 to 6.0 ± 1.0MPa at 1200, 1250 and 1300 °C as the porogen content was increased from 0 to 25%. This was not a linear decrease, with the samples with 5% porogen marginally different than those with 0%, and those with 10, 20 and 25% having only slight variations. Finally, as with all AFR fabrications, increasing the number of coats led to an increase in the mechanical properties.

7.4.2 Discussion

The density measurements, combined with the macropore, micropore and strut sizes, were used to calculate the theoretical mechanical properties of Ti and Ti-6Al-4V scaffolds. As the theoretical calculations matched the experimentally obtained values for HA scaffolds, as detailed in Section 6.3, it was deemed appropriate to use Equation 4.10 with Equation 4.11 to determine the yield stress of scaffolds fabricated

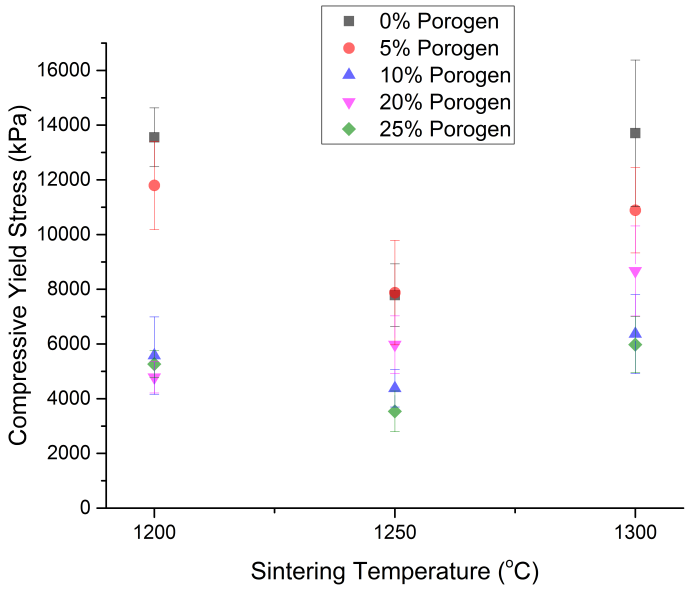

Figure 7.70: Theoretical compressive yield strength (kPa) of Ti scaffolds fabricated using 3 coats of the slurry on the 90 ppi template, with varying porogen content and sintering temperature

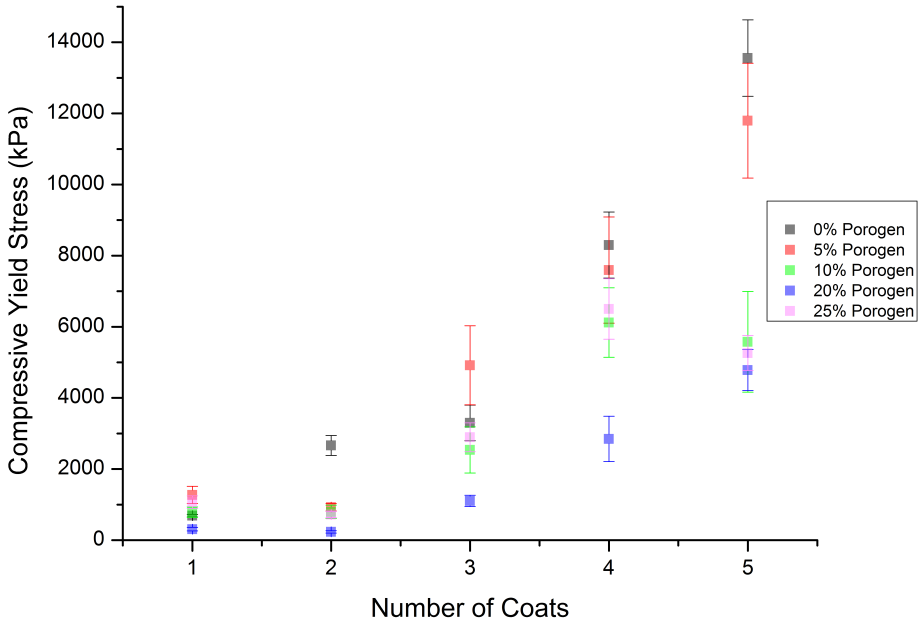

Figure 7.71: Theoretical compressive yield strength (kPa) of Ti-6Al-4V scaffolds fabricated using the 90 ppi template and sintered to 1200 °C, with varying porogen content and number of coats of the slurry

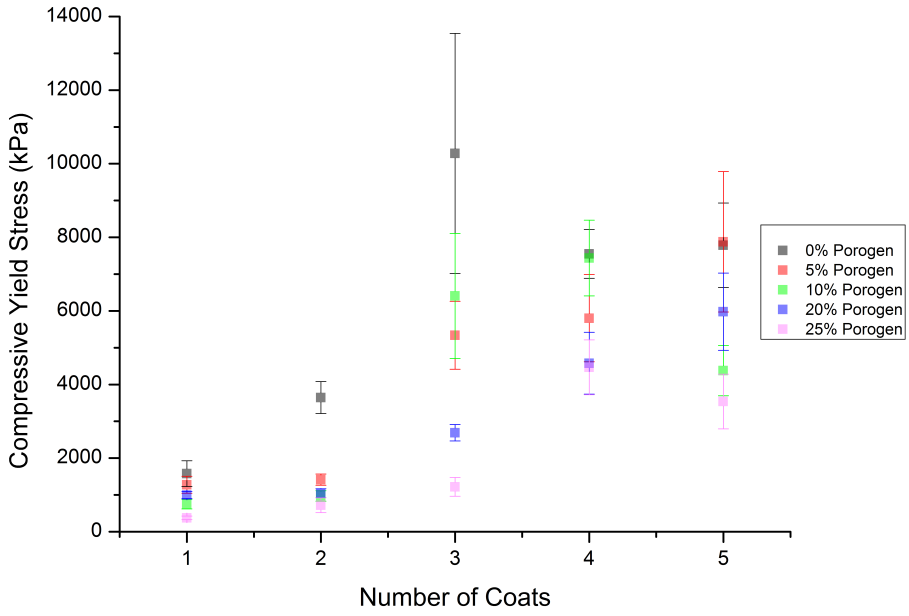

Figure 7.72: Theoretical compressive yield strength (kPa) of Ti-6Al-4V scaffolds fabricated using the 90 ppi template and sintered to 1250 °C, with varying porogen content and number of coats of the slurry, plotted on same y-scale as Figure 7.71

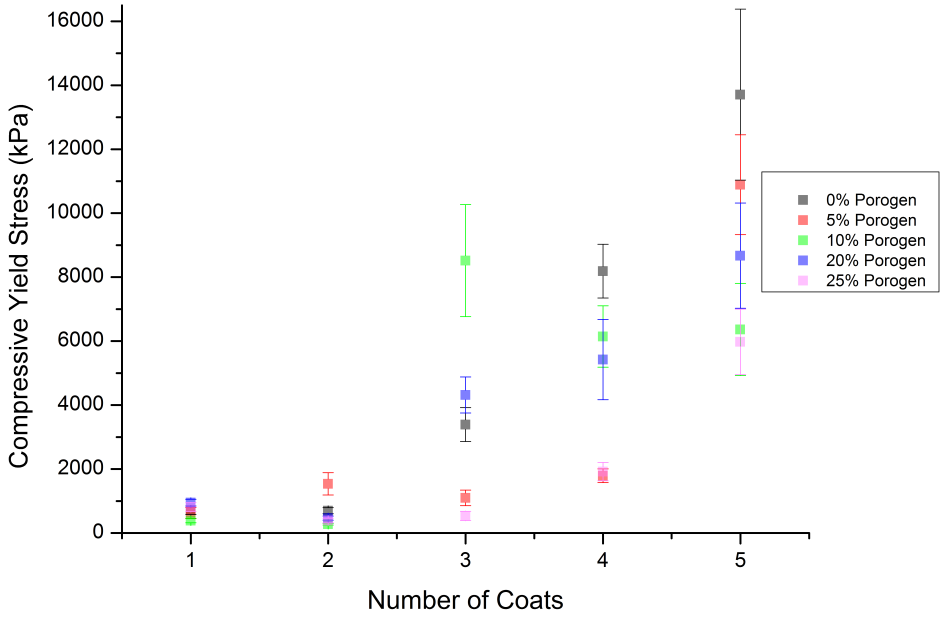

Figure 7.73: Theoretical compressive yield strength (kPa) of Ti-6Al-4V scaffolds fabricated using the 90 ppi template and sintered to 1300 °C, with varying porogen content and number of coats of the slurry, plotted on same y-scale as Figure 7.71

from Ti and Ti-6Al-4V.

As the sintering temperature and level of porogen inclusion did not have a significant impact upon the porosity or macrostructure of the scaffolds, a limited effect on the yield stress was expected. The shape factor incorporates the micropore size into strength calculations by allowing for microstructural characteristics [424, 425], however as they remain of a similar size regardless of the level of porogen the effect was again expected to be limited.

An increase in the number of coats of the slurry generally led to an increase in the yield stress of scaffolds from both materials. Decreasing the porosity is known to lead to improved mechanical properties [50,53,54,65,230,275,564,565]. As increasing the number of coats causes a reduction in the level of porosity, it was expected that the yield stress would increase, as observed. Also as a result of the increase in the number of coats, a reduced ratio of strut to pore size further limits the reduction compared to the yield stress of bulk structures. Finally, the differences in the porosity of the templates influences the mechanical strength as the 90 ppi template and subsequent scaffolds exhibit decreased porosity.

In most cases, the mechanical strength of Ti-6Al-4V scaffolds was much greater than those fabricated from Ti. The bulk yield stress of Ti-6Al-4V is over twice that of Ti (795 vs 328 MPa respectively [411]). Furthermore, Ti-6Al-4V samples underwent increased shrinkage and as such the ratio of pore to strut size was slightly decreased. The ratio of pore to strut size plays an important role in the theoretical mechanical strength as this value is raised by the power of 1.5. Furthermore, the increased shrinkage and resultant decrease in porosity, a variable which is cubed in Equation 4.10, has a significant influence on the final calculated strength of the samples.

Scaffolds produced from Ti using existing methodologies have yield stresses ranging from 1.2 MPa at 86% porosity to 24 MPa at 70% [50, 52–54, 67, 229, 230, 232, 565] whilst those from Ti-6Al-4V have yield stresses from 10 MPa at 90% porosity to 36 MPa at 80% [65, 230, 275] as shown in Table 7.10. Scaffolds fabricated via AFR

from Ti have a yield stress of between 0.002 and 1.8 MPa at 90 and 81% porosity respectively, whilst those from Ti-6Al-4V are between 0.21 and 13.6 MPa at 93 and 76%. The strength of Ti scaffolds is outside of the range of native cancellous bone (2-23 MPa [229]), and as such, although structurally similar, they are unsuitable for use as bone replacements. Furthermore, the values obtained are lower than those achieved by others [50, 52, 53, 67, 229, 230, 565] and as such other techniques such as powder metallurgy [50, 230] or space holder methodologies [227, 230, 231] could be more suited to bone regenerative medicine. However, decreasing the porosity could lead to Ti structures with suitable mechanical and structural properties and as such should be investigated. Ti-6Al-4V scaffolds with lower porosities have a yield stress similar to that of native bone and as such, coupled with the structural similarities could be suitable as bone scaffolds. The biological performance needs investigation however to confirm this.

Table 7.10: Mechanical strength and porosity of Ti-based materials

	Porosity (%)	Strength (MPa)	Ref
Ti	84	7.16	[67]
	78	8.6	[54]
	75	18	[50]
	75	23.72	[51, 232]
	70	18	[52]
	70	24.2	[53]
	81-94	0.002-1.8	This work
Ti-6Al-4V	90	10.3	[65, 275]
	80	36	[230]
	74-94	13.6-0.21	This work

All theoretical calculations have been made assuming that the scaffolds are pure Ti or Ti-6Al-4V. However XRD analysis (Section 7.1) has indicated that in most cases there has been some phase transformation to a multi-phase Ti, TiC and Ti-C-N material. The investigations into the different mechanical properties of TiC and Ti-C-N components has been based around their use as cutting tool heads. The major advantage of carbides over pure metals for that application is the decrease in the amount of wear seen with no discernible effect on the hardness [566] or fracture

strength [567]. However, Zhu et al [568] have shown a 15% composite of Ti and TiC to have a yield strength even greater than that of Ti-6Al-4V, although Liu et al [549] suggested that very high carbon content can lead to the formation of graphite and TiC, reducing the hardness. Furthermore, the corrosion resistance of Ti-6Al-4V alloys increased with C or N ion [549] implantation which may have an impact on the biological behaviour, particularly *in-vivo*. The final point to consider with regards to the mechanical properties of titanium carbide is that stoichiometric TiC has increased yield stress, wear resistance and hardness over non-stoichiometric TiC [546, 569]. The formation of the carbide was not intended, and although in this work stoichiometric TiC was generated, it cannot be guaranteed that this would always occur.

7.5 Summary

The AFR method has been successfully implemented to fabricate structures from both Ti and Ti-6Al-4V. The inert atmosphere generated for sintering of the constructs stopped the formation of any oxide, however some carbide and carbide-nitride was formed on both Ti and Ti-6Al-4V structures, with this particularly prevalent above 1100 °C. Although not desirable, this does not detrimentally affect the biocompatibility and so was not removed prior to the other analyses implemented in this work.

The trends observed whilst varying the processing parameters were similar to those observed when using HA as the biomaterial. The macrostructure of the final constructs closely replicated that of the template, albeit with some shrinkage. Whilst the sintering temperature had a limited effect on the pore and strut size, increasing the number of coats of the slurry on the template led to a decrease in the pore size and increase in strut size. Finally, varying the porogen content in the precursor slurry had no effect on the macroporous network, but instead led to the generation of micropores. Although the size was unchanged, the level and density of the

micropores increased with increasing camphene content.

Fabrications had high levels of porosity, which was independant within expected error of the sintering temperature or porogen content. However an increase to the number of coats generally led to a decrease in the porosity. The mechanical strength of Ti constructs was particularly weak, with theoretical values below that required for bone regeneration. However, the yield stress of Ti-6Al-4V constructs with lower porosities was within the limits outlined for bone reparative scaffolds.

Both Ti and Ti-6Al-4V structures are known to be biocompatible, hence biological evaluation has not been undertaken on structures from either material in this work. Thus, whilst it has not been verified, it is that that the enhanced viability observed with HA is likely to also be seen with Ti and Ti-6Al-4V constructs. Furthermore, structures from pure Ti and Ti-6Al-4V are required before biocompatibility can be assessed as, although biocompatible, the impurities observed in this work are likely to decrease the bioinductivity.

Chapter 8

Is AFR a Viable Alternative?

There are many existing methods capable of fabricating bioscaffolds. However none fulfill all of the wide range of requirements outlined in Section 1.1.1 which scaffolds should adhere to in order to be successful. Briefly, they must have a 3D interconnected porosity of suitable pore sizes: macropores and micropores as well as surface topography. Structures should also be biocompatible, bioactive and if possible bioresorbable, with mechanical properties matched to those of bone. Finally, the manufacturing technique should allow for controllability and repeatability at a suitable cost. This chapter discusses AFR as a whole and considers its suitability as a viable alternative to autografts and scaffolds fabricated using other methodologies.

8.1 Pore Size

One of the objectives was to develop a technique that offers a more viable alternative to autografts than preexisting methods. As has been previously discussed, Section 3.3, the existing techniques can all be used to produce structures with pore sizes within the limits specified for bone regeneration. The size of ALM fabrications is controlled by the user, and as such scaffolds have been produced with pores of suitable sizes [318, 319, 322, 324, 338]. Solvent cast structures have pore sizes which are determined by the size of the porogen [235], with possible pore sizes of up to 600 µm [570]. Porosity in sol-gel derived materials can be produced by foaming [295], porogen inclusion [305, 306], dip-coating onto scaffolds fabricated by other methods [300, 302] or sintering sol-gel microspheres together [307, 334]. This

allows for the large range obtainable, however foaming is difficult to control [12], and the inclusion of a porogen necessitates relatively small constructs to ensure the complete removal of the porogen.

The AFR method has been successfully implemented to produce structures with pore sizes within the prescribed limits for bone regeneration. Scaffolds were produced using templates with two different pore sizes (622 and 253 μm for the 45 and 90 ppi PU foam templates respectively), with constructs having pore sizes between 97.5± 7.4 and 546±38 μm depending on the processing parameters. Whilst the pore size of cancellous bone ranges from 1-3500 μm depending on the location within the body [3], the predetermined optimal range for scaffold pore sizes is 100-900 μm. Thus the size of constructs is suitable for bone regenerative applications, with the potential to use alternative templates, as has been demonstrated by others [273,276], which could extend the range observed here.

All scaffolds have a macroporous network of pore sizes within the prescribed limits for bone regenerative scaffolds. There is currently no consensus however as to a single size that optimises cell viability. The viability assays undertaken for this work, Section 6.4, seem to confirm this. When comparing scaffolds from both pore sizes to a commercially available porous disc, the MG63 cell number, shown in Figure 6.54, does not differ significantly between structures from the 45 and 90 ppi templates, although both offer enhanced viability over the CellSupports disc. When considering the average 3T3 cell numbers from all the scaffolds produced on each template, Figure 6.58, there is again no significant difference. The only instance where there is a significant difference between the templates is when MC3T3 cells were seeded on constructs with 25% porogen, where those from the 45 ppi template offered greater viability than scaffolds from the 90 ppi template, particularly after 7 days culture, as shown in Figure 6.59. In this case, a decrease in the number of viable cells is seen on the 90 ppi constructs between 4 and 7 days, a phenomenon which needs further investigations. If, however, as described in Section 6.4.6, it is due to certain cells undergoing the physiological changes to become more osteoblastic, then

the 45 ppi template may actually be inferior to the 90 ppi template.

One consideration regarding the controllability of pore size production however is the amount of shrinkage. In most cases, pore and struts underwent approximately 50% shrinkage compared to the templates. Nevertheless, the size of the macrostructural features was controllable and repeatable, as discussed further in Sections 8.6 and 8.7. Thus, although the final structure is within the range described, this should be accounted for in future scaffold production. It may be suitable to use templates with even greater pore sizes to obtain structures with pores closer to the upper limits of the prescribed range such that their porosity, mechanical properties and cell viability can be determined. However, decreasing the pore size and increasing the relative strut size, particularly when this has been obtained by coating the templates multiple times with the slurry, led to a significant increase in the mechanical properties of the scaffolds. When using HA or Ti as the biomaterial, as detailed in Sections 6.3 and 7.4, this is imperative in ensuring the compressive yield stress is as similar as possible to that of bone.

Of particular importance is that both macro and microporosity can be produced. Although further investigations should be made to determine the behaviour of cells with respect to macroporous structures with microporous struts, the initial analyses undertaken here, Section 6.4, and previous work by Woodard et al [333], suggests that this may have a positive effect on cell viability. The results of this work suggest that the most important feature of microporosity within the struts is that cells can fully infiltrate the micropores, whilst pores that are smaller than the size of the cells results in little effect on *in-vitro* cell viability. Finally, as the presence of multi-scale porosity is present on all materials tested, the enhanced biological viability due to the presence of both types of porosity can be assumed to be translated across all materials, although this would require confirmation through suitable analyses.

8.2 Porosity

Structures from all materials exhibited a high degree of porosity of 74-96%. In all cases the macrostructure was interconnected and of a trabecular nature, as shown in SEM micrographs, such as Figures 6.5, 6.6, 7.12, 7.13, 7.16 and 7.17, and microCT images, as shown in Figures 6.38 and 6.39, similar to that found in cancellous bone. As such, it is suited to the flow of nutrients, metabolites and bodily fluids found *in-vivo*. The introduction of a porogen led to the controllable, simultaneous production of microporosity, considered essential for the attachment of cells and vascularisation of the constructs.

The level of porosity can be tailored with variations to the processing parameters. In particular, increasing the number of coats from 1 to 5 led to a decrease in porosity of up to 15%, whilst only increasing the sintering temperature for HA constructs led to further decreases, of up to 5%. Finally, the template used also affected the porosity, with structures from the 45 ppi template approximately 5% more porous than those from the 90 ppi template. The inclusion of a porogen and the use of different materials had only a small impact on the porosity, indicating that structures can be made to a desired value. The incorporation of microporosity had a small effect (<3%) on the overall porosity due to the dominance of the highly open macroporosity, and the shrinkage and densification of structures. Even after freezing of the scaffolds to different temperatures, the microporosity did not have a significant impact upon the porosity, indicating that the micropores were more likely to provide surface roughness.

The porosity of cancellous bone is location specific, and ranges from 10 to 90% [43, 571]. It is relatively simple to develop structures with specific porosities using ALM techniques, with the range obtainable dependent on the CAD model and sintering properties of the material [310, 312, 338]. Whilst solvent casting can generate structures with up to 90% porosity [570], this is limited to small structures due to potential issues with porogen removal. Sol-gel techniques have a narrow range of

50-70% [305,306], which although within the range of cancellous bone does not allow samples with the maximum amount of porosity observed in native bone. Freeze casting has been used previously to develop structures with up to 75% porosity [253,260], however it is extremely difficult to increase this significantly. Meanwhile foam reticulation can be used to generate structures with up to 95% porosity [267, 277]. As determination of the exact lower limits of potential porosities requires further investigations, it is not possible at this stage to explicitly state the range obtainable for AFR fabricated structures, however the work presented here suggests that there is a wide scope for different porosities suited to cancellous bone regenerative medicine. The total range of foam reticualted structures is dependant on the template and the processing conditions, hence further work needs to be undertaken to determine the minimum porosity obtainable using AFR whilst retaining the 3D interconnectivity.

8.3 Compressive Strength

For this work, a standard equation to predict the theoretical strength of porous constructs, Equation 4.10, has been combined with an equation facilitating the generation of a shape factor, Equation 4.11, to determine the compressive yield stress of macroporous structures with microporous struts. The strength of constructs with such features has not been investigated previously, however combining the two equations relates closely to the experimentally determined values in most cases. However, there is a discrepancy with one of the sets of samples, as outlined in Table 6.5, where the theoretical values are much lower than the experimental. Thus, further investigations are necessary to determine the reasons behind this and whether there is a more appropriate shape factor that could be used.

All theoretical values have been calculated assuming that there is no phase transformation during processing. The crystallographic analysis of HA, Section 6.1, and Ti and Ti-6Al-4V, Section 7.1, indicates that there has been at least a partial phase transformation in all cases to either whitlockite for HA, or to Ti-C or Ti-C-N for

the titanium-based materials. These have different mechanical properties and as such it is possible that the yield stress may be different to that reported. However, the amount of material undergoing phase transformation is not predictable, and XRD would need to be undertaken on all scaffolds to determine their individual compositions and hence their strength. Furthermore, the interactions between the phases may not fit with a standard `rule of mixtures´ analysis and experimental determination of each scaffold may be necessary. Finally, no analysis has been undertaken using FEA of microCT scans, which could offer an alternative. However, this would require extensive further work to analyse the exact structure and composition of each sample. Nevertheless, the theoretical calculations have provided a suitable base for analysis.

The main issue with foam reticulation techniques in general is the weak mechanical properties the fabrications exhibit [277,355,372]. Structures fabricated via AFR have similar mechanical properties to foam reticulated constructs with similar porosity [355]. However, AFR fabrications have, in general, a higher porosity than most foam reticulated scaffolds, as shown in Table 8.1, and as such the comparison is relatively limited. This work has shown that the compressive properties can be varied with changes to the processing parameters. In particular, as the theoretical mechanical strength is proportional the the third power of the porosity, significant improvements to the yield stress have been obtained by varying paramaters to decrease the porosity.

The theoretical calculations matched the experimental observations in most cases, enabling the non-destructive estimation of the sample strength. Decreases to the porosity led to significant increases in the yield stress. For example, decreasing the porosity of HA samples by 11% from 96% to 85% led to an almost 50 fold increase in the mechanical strength, from 2.7kPa to 133kPa. This is particularly important with respect to HA and Ti samples as no scaffold produced using those materials in this work had a yield stress similar to the lower limit of native cancellous bone (2MPa) [3].

A higher number of coats, increased shrinkage and densification with higher sintering temperatures, use of the less porous template and limiting the size and amount of microporosity increased the yield stress of constructs. Nevertheless, the compressive strength of HA scaffolds was still only 0.002 - 0.14 MPa, of Ti components was 0.002 - 1.8 MPa and of Ti-6Al-4V constructs was 0.22-13.7 MPa. With the compressive strength of cancellous bone between 2 - 23 MPa depending on the location with the body [3], the only material of those analysed that could currently offer a suitable alternative to autografts is Ti-6Al-4V, without further optimisation of the porosity or macrostructure.

Table 8.1: Porosity and compressive yield stress of foam reticulated structures from HA, Ti and Ti-6Al-4V, including data obtained in this work

Material	Porosity (%)	Compressive Strength (MPa)	Ref
HA	76-82	1.7-3.8	[276]
	50-90	<0.5-2.3	[269]
	82.6	n/a	[224]
	66-82	1.5-3.4 (excluding additives)	[268]
	89-91	0.05-0.15	[355]
	43.3	3.56	[274]
	89	0.95	[277]
	77	0.9	[372]
	82-96	0.002-0.139	This Work
Ti	75	23.7	[51]
	45-75	18-121	[50]
	78	8.6	[54]
	70	18	[52]
	70-84	7-24.2	[53]
	81-94	0.002-1.8	This Work
Ti-6Al-4V	90	10.3	[275]
	74-94	0.22-13.7	This Work

The problem of the weak mechanical properties of AFR fabricated structures is further highlighted when other methodologies are considered. As outlined in Table 3.1, almost all other techniques have the potential to produce scaffolds with a yield stress similar to that of cancellous bone. However, due to the possible effects on

the structure and hence bioactivity of the scaffolds, compromising the porosity of as fabricated structures is not necessarily a suitable solution. As such, Woodard et al [333] found the improved in-growth of microporous robocast structures led to enhanced pull out strength *in-vivo* over non-microporous structures.

Even with their weak compressive strength, there may still be some potential options for using the HA and Ti scaffolds fabricated in this work. Coating highly porous, interconnected structures with a biodegradable material, particularly with polymers such as PLA or PGA, can provide structures with a suitable reinforcement for implantation [572, 573]. Due to the high level of open porosity observed in AFR structures, they could be suitable for being coating, however further investigations are required to confirm this. Alternatively, other materials with a bulk yield stress similar or greater than that of Ti-6Al-4V could be used. Finally, variations to the template may enable the fabrication of structures with suitable mechanical properties. The use of templates that are not removed during sintering could provide a suitable alternative. For example, Cunningham et al [273, 277] have implemented coral as a template to significantly improve the mechanical properties from 0.95 to 8.4 MPa. Alternatively, templates with an elongated pore morphology may render structures with suitable anisotropic compressive strength such as has been shown by Jo et al [276]. One last consideration is that Deville et al [260] fabricated scaffolds with extremely high mechanical properties by freeze casting in such a way as to have different zones of porosity depending on the processing conditions. The development of a suitable template to enable structures with graded porosities, from dense to highly porous, could offer exciting possibilities for improving the strength of foam reticulated structures.

8.4 Biological Performance

As cell viability analyses have only been undertaken using HA scaffolds, this section only considers cases where HA has been used unless otherwise stated.

The different potential manufacturing techniques have varying cell viabilities. Freeze-dried scaffolds can be suited to bone growth, with for example, Fu et al [264] showing that lamellar and cellular pores enhance cell viability compared to a tissue plastic control. Foam reticulation has also been shown to enhance the cell viability compared to controls [277, 372] with scaffolds exhibiting significant growth *in-vivo* [15]. Sepulveda et al [283] showed gel-cast scaffolds to have enhanced behavior compared to a cytotoxic material, however it was not as high as on a non-cytotoxic alumina surface. Woodard et al [333] have shown microporosity to have an important effect on macroporous robocast structures, and enable the formation of new bone *in-vivo* which did not otherwise occur. Meanwhile, there are conflicting results regarding the viability of 3DP scaffolds: Will et al [324] found good revascularisation *in-vivo*, while Leukers et al [319] found only similar results to plastic controls *in-vitro*. This work has shown that AFR produced structures exhibit suitable cell viability *in-vitro*.

The viability of AFR scaffolds has been analysed using 3 cell types, MG63, 3T3 and MC3T3 cells as shown in Section 6.4. When evaluated against a commercially available porous HA disc using MG63 cells, AFR scaffolds fabricated without any porogen exhibited a greater viability, demonstrated through a higher cell number at all time points, Figure 6.54. As such all other analyses compared scaffolds with varying amounts of porogen to those fabricated without. In most cases, the inclusion of the porogen had a negligible positive effect and generally caused a slight drop in viability. However, scaffolds produced with 25% porogen in the precursor slurry exhibited an increased viability, particularly when seeded with the pre-osteoblastic MC3T3 cells, shown in Figure 6.59. This is believed to be due to the size of the micropores being slightly larger than that of the cells and as such the scaffolds offered a greater surface area for attachment.

The pore and strut size has a relatively limited effect on the biological performance of scaffolds, as discussed previously in Section 8.1. There is little significant difference between structures fabricated from the 45 and 90 ppi templates except when the MC3T3 cells are seeded on scaffolds produced with a slurry incorporating 25%

porogen. The effect of smaller changes to the macrostructure, obtained through varying the number of coats or sintering temperature, has not been investigated, however the limited effect seen with the significant differences in pore sizes obtained on scaffolds from different templates suggests this will also have a limited effect. Furthermore, the effect of varying the microstructure on the cell viability has also not been investigated. Particularly when frozen to -20 °C, the micropores became elongated and exhibited a general increase in size. Thus they were generally greater in length than the size of the individual cells, although their width was not significantly different. Although this may not have a significant effect on *in-vitro* investigations, it may facilitate greater *in-vivo* vascularisation, however this would need confirmation.

As the AFR produces scaffolds with enhanced viability over a commercially available porous disk of similar material (Section 6.4), it therefore follows that the structures could be suitable for replacing autografts, subject to *in-vivo* investigations. As the viability of structures produced using other techniques have not been compared to the same standard, it is not possible to say which is the optimal technique to instigate regrowth. However, the AFR does produce constructs with a promising biological performance which require further *in-vivo* investigation.

The main reason for the use of Ti and Ti-6Al-4V has been the ability they have to instigate bony regrowth on the surface of scaffolds [3, 44]. It is assumed that the enhanced viability seen with HA scaffolds can be translated to these materials which would lead to greater *de-novo* growth. However, this needs confirmation through *in-vitro* and *in-vivo* investigations.

8.5 Potential Materials

The AFR has been successfully implemented to fabricate HA, Ti and Ti-6Al-4V scaffolds in this PhD, whilst previous work [279] has shown that Bioglass structures

can also be produced. Due to the similarities in the methodologies, it is expected that most, if not all, materials that have been fabricated by foam reticulation techniques can be incorporated into the AFR. As such, it should be possible to fabricate structures from other calcium phosphates, bioinert ceramics, such as those outlined in Section 2.2.1, and other metals. Polymeric scaffolds cannot be fabricated via AFR due to the high temperatures involved in pyrolysis of the template, however the open porosity of the constructs facilitates the incorporation of polymeric coatings after sintering. Furthermore, other than in the case of ceramic or metallic constructs subjected to coatings, the method is not suited to conventional composite materials (e.g. carbon fibre reinforced polymer). Finally, when considering the final material, any potential interactions between the biomaterial and the porogen should first be considered, as this could affect the final structure.

Not only are there a wide range of potential biomaterials, there are also many different porogens that could be implemented to vary the microporous structure. This PhD has only investigated the effects of including camphene as a porogen, whilst Lee et al [268] and Yang et al [355] have implemented TBA, although without a freezing stage. Outlined in Table 3.3 are some of the porogens used when freeze casting structures, including dioxane [250, 264], NaCl [255], and gelatine [255]. Although some porogens are chosen to overcome the issues with the limited pore size of freeze cast structures, others produce pores of 10-20 μm and thus may positively affect the cell viability. However, candidate structures should be subjected to a similar *in-vitro* protocol as implemented in this work to confirm their viability.

8.6 Controllability

As previously detailed in Section 3.1, foam reticulation is the only conventional technique with a high degree of control over the size and location of the macroporous network, as well as the total porosity. Although for most other techniques the amount of porosity and size of the pores is controllable, the exact location cannot

be predetermined. Meanwhile, as outlined in Section 3.2, ALM based techniques have a high degree of controllability.

Control over both the size and location of the pores, as well as the total porosity, is important with respect to the mechanical properties of the scaffolds as well as their viability. The macrostructure is controlled by the foam reticulation part of the technique and is the dominant feature controlling the mechanical properties. Thus, the ability to vary this enables the production of scaffolds with a compressive yield stress closer to that of native bone. The AFR also enables the production of scaffolds with a 3D interconnected porous network of pore sizes that facilitate the movement of biological media throughout the structure [2, 5, 6, 12–15], whilst concurrently producing microporosity which is essential for vascularisation [17–19] and cell development [2].

As has been shown for HA, and Ti and Ti-6Al-4V in Sections 6.2.1 and 7.2.1 respectively, the nature, size and location of the pores can be produced with a great deal of control. The structures closely mimic the template as shown in the figures in these sections (e.g. Figures 6.5 and 6.6 for HA; Figures 7.8 and 7.9 for Ti; and Figures 7.10 and 7.11 for Ti-6Al-4V), although there is a significant amount of shrinkage of up to 50% in all cases. This is regardless of the other processing parameters used, although variation of these enables the final structure to be altered slightly as outlined in Sections 8.1 and 8.2. Thus, with consideration as to the effects of the processing parameters it is possible to predetermine the structure of AFR fabrications, as it is with those produced via foam reticulation [15,50,273,275,276,372]. In particular, the shrinkage of structures during sintering [224,280] and the decrease in pore size and increase in strut size with an increasing number of coats of the slurry on the template [270] requires careful forethought. However, this is no different to foam reticulated structures and thus the level of control over the macrostructure is similar between the two techniques.

The major advantage with AFR is that it allows the simultaneous fabrication of macro and microporosity. Furthermore, the generation of micropores is achieved by

the incorporation of the freeze drying technique which allows for significant control over the number and size of the pores within the structure [97,244,250,253,254,259, 260]. This control has been demonstrated in Sections 6.2.2 and 7.2.2 for structures from HA, and Ti and Ti-6Al-4V respectively. The amount of microporosity can be controlled through the amount of porogen incorporated into the precursor slurry, whilst variations to the size of the micropores can be achieved with changes to the freezing temperature, as shown in Figures 6.22 - 6.27.

The final consideration lies with ALM fabrications. The macrostructure for fabrications produced using ALM is highly controllable, and closely resembles the CAD model from which it is produced. Although it has not yet been tested, there is no reason that models produced from patient specific CT data could not be used. Whilst the outer dimensions can be readily controlled [326, 574], only recently have scaffolds with a trabecular porous network been produced [575]. Furthermore, it has hitherto been difficult to induce microporosity into the macroporous struts [576,577]. This PhD has demonstrated that the inclusion of a porogen into the precursor slurry can be used to generate microporosity, which could be of interest with regards to colloidal-ink based techniques in particular (Section 3.2.3).

8.7 Repeatability

As has been previously mentioned, the structures produced by AFR closely mimic the template. Thus, provided a suitable template is used for all scaffolds, the final macroporous network can be produced repeatably, as has been demonstrated previously for foam reticulated fabrications [15, 50, 273, 275, 276, 372]. Dip-coating the templates has an element of unpredictability, causing some scope for variability. However, pre-soaking the foams in water reduces the hydrophobicity of the polymer and thus the random nature of slurry attachment to the template. Furthermore, the standard error of the mean of the macropore and strut size is generally within 10% of the mean, demonstrating that there is little variability outside of normal

experimental variations.

Excluding foam reticulation techniques, AFR offers an improvement in the repeatability obtainable over other conventional techniques as in these the exact structure cannot be produced repeatably [310, 312]. Meanwhile, all ALM methodologies produce fabrications that closely mimic the CAD model and as such have a high degree of repeatability. For example, Dellinger et al [335] found the standard deviation of robocast scaffolds to be between 3.5 and 11.5% of the mean and Seitz et al [322] had a standard deviation of 4.7 - 8.2% of the mean for 3DP structures. Although others (e.g. [318, 319, 329, 338]) have not stated the range, the figures provided in the articles show that structures have pores of similar sizes.

Although the macrostructure of AFR-produced scaffolds has reasonably good repeatability, the microstructure is less readily reproducible under given conditions. Although the size of individual micropores was controlled by the freezing temperature and as such is repeatable, the location is not. This led to the agglomeration of the porogen to produce larger micropores. Despite the slurries being thoroughly mixed by ball milling for 24 hours as described in Section 4.1.1, this phenomenon was still observed. Therefore there should be further investigations to determine the optimal slurry conditions, with systematic variations to the quantity and type of dispersant and binders used.

Finally, considering the longer term implications with a new technique such as that investigated here, there is likely to be a degree of user error. Although the AFR implements a relatively simple methodology, there are areas of the technique within which errors can be introduced, particularly with respect to the coating of the slurry on the templates. Avoiding this would involve suitable training, which would be associated with further costs, as discussed further in Section 8.8.

8.8 Cost

The costs involved with AFR fabrications are similar to those seen with foam reticulation. Thus, the manufacturing costs are associated with the raw materials required, the templates, a suitable pump set-up and a high temperature furnace, dependant on the biomaterial used. Compared to foam reticulated structures, the additional costs only relate to that of the porogen. For example, the cost (as of 12 January 2015) of 1 kg of camphene is £86.00 (Sigma Aldrich, UK), whilst 1.5 l of DMC is £57.30 (Sigma Aldrich, UK). Considering the amount incorporated in a scaffold weighing approximately 2 g, this would relate to an additional cost of up to £0.07 at 25% porogen inclusion. The dimensions of such scaffolds (12 ± 1.0 mm diameter by 15 ± 2.7 mm height) are similar to those used in *in-vivo* analyses [2] (rabbit critical sized defect 15 mm; rat critical sized defect 8 mm), however the exact dimensions of final scaffolds would need tailoring to patients needs. Although these dimensions are not reported in the literature, it is not expected that the diameter would increase. As such, increases would only be required for the length, and therefore the additional material costs would not be significant. Furthermore, the values given here are not for bulk production, which generally allow for cheaper wholesale prices.

The greater costs with implementing such a technique would involve training of manufacturers. The AFR is a relatively labour intensive technique: the slurry needs to be prepared, the template coated, the exact freeze drying protocol developed, exact sintering procedures determined and final variations to the template size and shape decided. Training needs to be provided for each stage, with the final user(s) expert(s) in each area. However, all manufacturing techniques that could be implemented for bioscaffolds require significant training, whether it be in the physical manufacture with conventional techniques, or the CAD model design for ALM techniques. Until an in-depth analysis of the various costs involved has been undertaken, it cannot be stated which would involve lower costs. As such, at this point it is only suitable to compare the costs of the materials and technologies required, which, for AFR, are

similar to those of foam reticulation techniques.

8.9 Summary

This chapter discusses the viability of implementing the AFR as an alternative to autografts by comparing it to other existing scaffold manufacturing techniques. As such, the comparison is made against the scaffold requirements previously outlined: namely that the pore size of scaffolds from each material was of a suitable size similar to that seen in cancellous bone, as is the porosity; the mechanical strength was only similar to that of natural bone for Ti-6Al-4V constructs, however increases could be made to HA or Ti structures using variations to the template or by incorporating coatings; structures exhibited suitable biological capabilities when compared to a commercially available porous HA disc, which was improved with 25% porogen in the slurry; and fabrications can be produced controllably, repeatably and cost effectively for a range of materials.

Table 3.2 ranked the various scaffold manufacturing techniques considering their performance against the requirements, with this extended to include the AFR in Table 8.2, with the rankings based on the analyses given in this chapter. The AFR has shown promising results for most of these requirements, with the only significant limitation caused by the weak compressive strength they exhibit. There have been numerous reports on improving the compressive strength of foam reticulation fabrications, which have led to the potential routes to structures with the appropriate mechanical properties. Such methodologies should be implemented to AFR to determine whether the poor strength of AFR constructs can be improved to be within a simlar range as foam reticulated structures. Only if this is possible does AFR offer a suitable alternative methodology of fabricating bone regenerative scaffolds.

Table 8.2: Ranking of the different techniques against key performance factors, with AFR included for comparison against other methodologies. ✓✓ denotes ranks best, ✓ denotes ranks good, ◦ denotes ranks average, ✗ denotes ranks poor, ✗✗ denotes ranks worst

Technique	Pore Size	Porosity	Compressive Strength	Biological Perform-ance	Potential Materials	Control (pore size)	Repeatability	Cost	Adaptability
Dry Methods	n/a	n/a	✗✗	n/a	✓✓	✗✗	✗✗	✓✓	◦
Freeze casting	✗	✓	✓✓	✓	✓	✗	✗	✓	✓✓
Replication	✓	✓	✗	✓✓	✓	✓	✓	✓	✓✓
Gelcasting	✓	✓	✓✓	✓✓	◦	✗	◦	◦	✓
Sol-Gel	✓✓	✓	◦	✓	◦	✗	◦	◦	✗
Solvent Casting	✗	✓	✗	✓✓	✓	✗	✗	✓	✓
3DP	◦	✓	◦	✗	◦	✓	✓	✗✗	✗
SLS	◦	✓	✓✓	◦	◦	✓	✓	✗✗	✗
SLA	✓	✓	◦	◦	✗✗	✓	✓	✗✗	✗✗
Robocasting	✗	✓	✓✓	n/a	✗	✓	✓	✗✗	✗
Ink-Jet Printing	✗✗	✓	✗✗	n/a	✗	✓	✓	✗✗	✗
FDM	✗✗	✓	◦	✓	✗✗	✓	✓	✗✗	✗
AFR	✓✓	✓✓	✗✗	✓✓	✓	✓✓	✓	✓	n/a

Part IV

Concluding Remarks

Chapter 9

Further Work and Conclusions

9.1 Further Work

Work with the AFR has, as yet, been restricted to selected materials, with camphene the sole porogen. Nevertheless, it has shown promise as a technique, however this PhD has shown there to be limitations with the production of impurities in titanium-based structures and weak mechanical strength of, particularly HA, scaffolds.

The formation of Ti-C and Ti-C-N was not predicted and, although biocompatible, not desired. As such, investigations into either the removal of the carbide, or the production of scaffolds without such impurities are necessary. The removal is possible, as previously detailed in Section 7.1, as is the production of pure Ti and Ti-6Al-4V constructs. Whether these methodologies can be extended to AFR fabrications should be determined. In particular, the implementation of a vaccuum furnace should be investigated as this is likely to enable a more complete removal of any natural atmosphere and hydrocarbons generated by the pyrolysis of the PU template. Additionally, the effect of the flow rate of the gases generating teh inert atmosphere should be considered. As it is thought that the impurities remained after the polymer burnout stage due to the flow rate not being high enough, this should be confirmed and the optimal flow rate determined.

The main problem with AFR scaffolds is that the mechanical strength is very weak, particularly on scaffolds with the highest level of porosity. To improve this, a wider

range of templates could be investigated. These could be of a wider range of porosities, of different materials, or of an elongated nature to add anisotropy to the structures. Alternatively, the structures could be coated with biodegradable polymers to add reinforcement. Furthermore, although theoretical compressive values closely matched experimentally obtained values for the yield strength, there was some degree of variation. Therefore for a more complete understanding of the mechanical properties of the scaffolds, experimental values should be measured for all scaffolds.

The controllable production of microporous struts within macroporous structures is of considerable importance as this improves the biological performance of structures, even compared to those with biological agents incorporated [333]. Thus, further investigations into this should involve varying the parameters used to induce microporosity such as the porogen and freezing temperatures used. There is a large difference between structures fabricated using freezing temperatures of 10 and -20 ^{o}C and a thorough investigation of the effect of the freezing temperature on the microstructure should be undertaken. This will enable for a greater level of control over the micropore size and as such this can be optimised for cell attachment.

The production of a structure with a minimally porous shell surrounding a highly porous interior would result in a truly hierarchical structure that more closely mimics a complete section of bone. AFR offers a suitable method of producing the interior structure, of a trabecular nature similar to that of natural bone. However, investigations into fabricating this simultaneously with a dense shell are required to realise such structures.

Finally, a more complete investigation should be undertaken on the biological activity of scaffolds produced via AFR. The in-vitro analysis should be extended to human osteoblasts (hOBs) and to osteogenic markers such as osteocalcin. Further investigations into where cells attach to the scaffolds could also provide important information. One possible method could be to microCT scan scaffolds prior to seeding, and then rescan the scaffolds after a fixed period of incubation. Thus the nature of cell attachment and pore infiltration could be determined. If these

analyses exhibit promising results, further *in-vivo* testing would be required.

9.2 Conclusions

Autografts are the gold standard for assisting bone reparation. However they are associated with many limitations, that are exacerbated when considering auto and xenografts as alternatives. Synthetic scaffold structures offer an alternative, however they must fulfill a range of requirements in order to be successful, particularly with respect to bone reparation. These include producing structures with a 3D interconnected porosity of suitable pore sizes within different ranges similar to that seen in native bone, inherent biocompatibility, bioactivity and if possible bioresorbability, and similar properties, such as porosity and compressive strength to existing bone.

The use of synthetic structures in hard tissue replacement is not new. Stainless steels, Co-Cr alloys and transition metals are all used clinically whilst there is a large body of research into the potential uses of ceramics. These can be bioinert, such as transition metal oxides, semi-inert, such as apatite or glass-based bulk structures, or resorbable, such as apatitic or glass-based scaffolds. Furthermore, such scaffolds can be produced using a range of methodologies however each is associated with specific limitations. Thus, there still lacks one ultimate technique that enables the optimised production of bioscaffolds suited to hard tissue repair.

One new methodology that could facilitate the production of structures that fulfill the many requirements is the adaptive foam reticulation technique. This combines two preexisting techniques, the foam reticulation and freeze casting methodologies, to produce scaffolds with a 3D porous network similar to that seen in cancellous bone, constructed of microporous struts. The technique follows that of the foam reticulation, however with a freeze drying stage to produce microporosity. Briefly, the biomaterial is mixed into a slurry that is then coated onto a polymeric template. The slurry is then frozen, and subjected to a freeze drying protocol stage to remove

the ice dendrites. The structure is then fired to remove the template and ensure suitable densification of the scaffold. There is little available literature surrounding this technique, and many of the processing parameters that can be varied to optimise the structure have not been investigated.

The aim of this PhD was to investigate the AFR technique and thus determine whether it is a viable alternative to other techniques capable of producing hard tissue replacement scaffolds. Variations to the macrostructure were achieved by varying the template from which the scaffold was produced, using 45 and 90 ppi polyurethane foams, varying the number of coats of the slurry on the template, from one through five, varying the amount of porogen included in the slurry, at 0, 5, 10, 20 and 25% and varying the sintering temperature the structure was fired to, depending on the material. Furthermore, the freezing temperature for selected samples was varied, at 20, 10, and -20 °C to determine the effect this has on the microstructure. Finally, the scaffolds and precursor materials were characterised using a range of techniques including STA, XRD, SEM, microCT, porosimetry, mechanical testing and cell viability assays.

Structures were fabricated from three different materials, hydroxyapatite, titanium and titanium-aluminium-vanadium. During sintering, all HA structures underwent at least a partial phase change to whitlockite. Whitlockite is more similar to the natural mineral phase of bone due to the incorporation of metal ions, such as magnesium and iron, found in native bone. Thus this change does not detrimentally affect structures. When fabricating structures from Ti and Ti-6Al-4V, both materials exhibited some carbide and carbonitride formation due to incomplete polymer removal from the furnace during firing. Although biocompatible, TiC has not been used for bone replacement structures and as such investigations into a more complete method of removing the carbon from the furnace, such as using a vacuum as opposed to flowing gas, are required.

Scaffolds from all materials exhibited a macrostructure within the prescribed limits, 100-900 μm, for bone regenerative structures that closely mimiced the template used.

The pore sizes HA of structures from the 45 and 90 ppi template were of 216 ± 12 to 514 ± 36 µm and 94 ± 6 to 196 ± 5 µm respectively, whilst Ti pore sizes were of 238 ± 11 to 546 ± 38 µm and 114 ± 7 to 240 ± 10 µm and Ti-6Al-4V constructs had pores of 206 ± 20 to 510 ± 23 µm and 98 ± 7 to 299 ± 6 µm. Meanwhile, strut sizes were of 41 ± 2 to 108 ± 7 µm and 17 ± 1 to 55 ± 3 µm, 54± 3 to 101 ± 6 µm and 20 ± 1 to 65 ± 4, and 54 ± 3 to 118 ± 13 µm and 27 ± 2 to 83 ± 5 µm respectively. The sintering temperature only affected the size of HA constructs, with increased shrinkage observed with higher temperatures. Increasing the number of coats in all cases led to decreased pore sizes and increased strut size, whilst varying the porogen content and freezing temperature had no significant effect on the macrostructure. Thus the technique allows for the controllable, repeatable production of a suitable macroporous network.

The AFR includes a porogen, which for this work was camphene, to produce microporosity. Whilst this had no effect on the macrostructure, it led to the controllable production of micropores of 2-5 µm when frozen at room temperature. The size of the micropores was similar accross all scaffolds, irrespective of the amount included in the slurry, when frozen to the same temperature, although some agglomeration was observed resulting in larger micropores of up to 20-30 µm at the highest levels of camphene inclusion. However, decreasing the freezing temperature, particularly to -20 °C led to the production of larger, elongated pores, of 2-5 µm width with up 20-30 µm length. Thus the technique allows for the controllable production of microporosity within the struts of the macroporous network.

All scaffolds exhibited at least 76% porosity, with maximum values of up to 96% depending on the processing parameters. Using the 45 ppi template increased the porosity by approximately 5% compared to the 90 ppi template. Whilst variations to the sintering temperature, freezing temperature and porogen content had little effect on the porosity, increasing the number of coats from one to five led to a general decrease of up to 15%. The lack of any significant differences between those produced with and without porogen is due to the shrinkage of constructs from all

materials compared to the template, which was up to 50%, as well as the dominance of the macroporosity.

The lack of evaluation of the mechanical strength of macroporous structures with microporous struts led to the incorporation of a shape factor into a standard equation used to calculate the yield stress of porous structures. Thus it was possible to calculate the theoretical mechanical strength of all scaffolds produced in this PhD. In most cases this closely mimicked that observed for the selected samples where the yield stress was determined experimentally, however the discrepancies observed should be considered and as such further work is required for a more rigourous calculation. The mechanical strength of foam reticulated structures is generally weak, a problem also observed in this work. As such, with values from 0.002 to 0.18 MPa and 0.002 to 1.8 MPa for HA and Ti structures respectively, they are not suitable for bone reparation, however it may be possible to implement coatings to reinforce the scaffold due the open nature of the porosity, a possibility that requires further investigations. Particularly for Ti structures, the values are weaker than observed using other techniques, and thus may not be as applicable as such techniques. However, Ti-6Al-4V scaffolds exhibited compressive yield stresses of 0.21-13.7MPa within the range for cancellous bone (2-23MPa), and thus could be suitable as scaffolds.

The viability of selected HA samples demonstrated that AFR produced scaffolds fabricated without any porogen offered greater potential than a commercially available porous HA disc. Further investigations thus involved determination of the cell number, ALP activity and dissolution of the scaffolds. Structures produced with 5, 10 and 20% porogen exhibited similar behaviours as seen on scaffolds produced without any porogen, however those fabricated using 25% camphene offered a slight increase in viability. This is because the agglomeration of the porogen led to pores that were greater than the size of the cells and as such generated a larger area onto which cells could attach.

The AFR technique offers the ability to controllably produce scaffolds with a 3D

interconnected porous network of pore sizes predetermined as suitable for bone regeneration. The replication of a template ensures that the structure can be produced repeatably from a range of materials. Furthermore, structures from HA have been shown to be biocompatible, bioactive and bioresorbable. Although the porosity is similar to that seen in native cancellous bone, the mechanical strength, in most cases, is not and as such further work is required to improve this. However, should this be achieved, this work has demonstrated that the AFR could be viable alternative to the other manufacturing techniques capable of producing porous structures suited to bone reparation, subject to further *in-vivo* analyses.

References

[1] C. J. Damien, J. R. Parsons, Bone-Graft and Bone-Graft Substitutes - a Review of Current Technology and Applications, Journal of Applied Biomaterials 2 (3) (1991) 187–208.

[2] A. J. Salgado, O. P. Coutinho, R. L. Reis, Bone tissue engineering: state of the art and future trends, Macromolecular Bioscience 4 (8) (2004) 743–65.

[3] J. Planell, S. Best, D. Lacroix, A. Merolli, Bone repair biomaterials, 1st Edition, Vol. 1, Woodhead Publishing, Cambridge, UK, 2009, pp. xiv, 464.

[4] A. Mahendra, A. Maclean, Available biological treatments for complex non-unions, Injury-International Journal of the Care of the Injured 38 (2007) S7–S12.

[5] K. J. L. Burg, S. Porter, J. F. Kellam, Biomaterial developments for bone tissue engineering, Biomaterials 21 (23) (2000) 2347–59.

[6] J. I. Dawson, R. O. C. Oreffo, Bridging the regeneration gap: Stem cells, biomaterials and clinical translation in bone tissue engineering, Archives of Biochemistry and Biophysics 473 (2) (2008) 124–31.

[7] P. X. Ma, J. H. Elisseeff, Scaffolding in tissue engineering, Taylor&Francis, Boca Raton, 2005, pp. xvi, 638 p.

[8] U. G. Longo, A. Lamberti, N. Maffulli, V. Denaro, Tendon augmentation grafts: a systematic review, British Medical Bulletin 94 (2010) 165–88.

[9] S. F. Badylak, The extracellular matrix as a biologic scaffold material, Biomaterials 28 (25) (2007) 3587–93.

[10] M. Parker, Fractures of the hip, Surgery (Oxford) 25 (10) (2007) 424–9.

[11] R. Media, http://www.rkm.com.au/anatomy/anatomical-illustrations/femur.jpg, Retrieved December 2011.

[12] I. Sopyan, M. Mel, S. Ramesh, K. Khalid, Porous hydroxyapatite for artificial bone applications, Science and Technology of Advanced Materials 8 (2006) 116–23.

[13] T. J. Flatley, K. L. Lynch, M. Benson, Tissue response to implants of calcium phosphate ceramic in the rabbit spine, Clinical Orthopaedics and Related Research (179) (1983) 246–52.

[14] K. Hing, W. Bonfield, Foamed ceramics, Apatech Limited US 12/216,710 (2013) 6.

[15] B.-S. Chang, C.-K. Lee, K.-S. Hong, H.-J. Youn, H.-S. Ryu, S.-S. Chung, K.-H. Park, Osteoconduction at porous hydroxyapatite with various pore configurations, Biomaterials 21 (2000) 1291–8.

[16] B. Annaz, K. A. Hing, M. Kayser, T. Buckland, L. Di Silvio, Porosity variation in hydroxyapatite and osteoblast morphology: a scanning electron microscopy study, Journal of Microscopy 215 (Pt 1) (2004) 100–10.

[17] D. Perizzolo, W. R. Lacefield, D. M. Brunette, Interaction between topography and coating in the formation of bone nodules in culture for hydroxyapatite- and titanium-coated micromachined surfaces, Journal of Biomedical Materials Research 56 (4) (2001) 494–503.

[18] B. Chehroudi, D. McDonnell, D. M. Brunette, The effects of micromachined surfaces on formation of bonelike tissue on subcutaneous implants as assessed by radiography and computer image processing, Journal of Biomedical Materials Research 34 (3) (1997) 279–90.

[19] X. Lu, Y. Leng, Quantitative analysis of osteoblast behavior on microgrooved hydroxyapatite and titanium substrata, Journal of Biomedical Materials Research Part A 66 (3) (2003) 677–87.

[20] B. Chehroudi, E. Soorany, N. Black, L. Weston, D. M. Brunette, Computer-assisted three-dimensional reconstruction of epithelial cells attached to per-

cutaneous implants, Journal of Biomedical Materials Research 29 (3) (1995) 371–9.

[21] A. Curtis, C. Wilkinson, Topographical control of cells, Biomaterials 18 (24) (1997) 1573–83.

[22] R. Singhvi, G. Stephanopoulos, D. I. Wang, Effects of substratum morphology on cell physiology, Biotechnology and Bioengineering 43 (8) (1994) 764–71.

[23] J. R. Jones, R. C. Atwood, G. Poologasundarampillai, S. Yue, P. D. Lee, Quantifying the 3D macrostructure of tissue scaffolds, Journal of Materials Science: Materials in Medicine 20 (2) (2009) 463–71.

[24] S. Weiner, W. Traub, H. D. Wagner, Lamellar bone: structure-function relations, Journal of Structural Biology 126 (3) (1999) 241–55.

[25] J. Y. Rho, L. Kuhn-Spearing, P. Zioupos, Mechanical properties and the hierarchical structure of bone, Medical Engineering and Physics 20 (2) (1998) 92–102.

[26] S. Weiner, H. D. Wagner, The material bone: Structure mechanical function relations, Annual Review of Materials Science 28 (1998) 271–98.

[27] H. R. Dudley, D. Spiro, The Fine Structure of Bone Cells, Journal of Biophysical and Biochemical Cytology 11 (3) (1961) 627–49.

[28] E. Beniash, Biominerals - hierarchical nanocomposites: the example of bone, Wiley Interdisciplinary Reviews-Nanomedicine and Nanobiotechnology 3 (1) (2011) 47–69.

[29] R. Lakes, Materials with structural hierarchy, Nature 361 (6412) (1993) 511–5.

[30] H. S. Gupta, P. Zioupos, Fracture of bone tissue: The 'hows' and the 'whys', Medical Engineering & Physics 30 (10) (2008) 1209–26.

[31] M. Wettergreen, The Effect of Material Organization on the Structural Properties of Porous Architectures, Rice University, Ph.D. thesis (2008).

[32] K. Choi, J. L. Kuhn, M. J. Ciarelli, S. A. Goldstein, The Elastic-Moduli of Human Subchondral, Trabecular, and Cortical Bone Tissue and the Size-Dependency of Cortical Bone Modulus, Journal of Biomechanics 23 (11) (1990) 1103–13.

[33] D. T. Reilly, A. H. Burstein, Elastic and Ultimate Properties of Compact Bone Tissue, Journal of Biomechanics 8 (6) (1975) 393–405.

[34] H. M. Frost, The Utah paradigm of skeletal physiology: an overview of its insights for bone, cartilage and collagenous tissue organs, Journal of Bone and Mineral Metabolism 18 (6) (2000) 305–16.

[35] D. B. Burr, M. R. Forwood, D. P. Fyhrie, B. Martin, M. B. Schaffler, C. H. Turner, Bone microdamage and skeletal fragility in osteoporotic and stress fractures, Journal of Bone and Mineral Research 12 (1) (1997) 6–15.

[36] Binderma.I, D. Duksin, A. Harell, E. Katzir, L. Sachs, Formation of Bone Tissue in Culture from Isolated Bone-Cells, Journal of Cell Biology 61 (2) (1974) 427–39.

[37] J. E. Davies, Bone bonding at natural and biomaterial surfaces, Biomaterials 28 (34) (2007) 5058–67.

[38] R. Huiskes, Stress Patterns, Failure Modes and Bone Remodeling, Raven Press, New York, 1988, Ch. 24, pp. 283–302.

[39] H. M. Frost, Bone Mass and the Mechanostat - a Proposal, Anatomical Record 219 (1) (1987) 1–9.

[40] H. M. Frost, From Wolff's law to the Utah paradigm: Insights about bone physiology and its clinical applications, Anatomical Record 262 (4) (2001) 398–419.

[41] H. M. Frost, Bone's mechanostat: A 2003 update, Anatomical Record Part A-Discoveries in Molecular Cellular and Evolutionary Biology 275A (2) (2003) 1081–101.

[42] H. M. Frost, A 2003 update of bone physiology and Wolff's Law for clinicians, Angle Orthodontist 74 (1) (2004) 3–15.

[43] J. Y. Rho, M. C. Hobatho, R. B. Ashman, Relations of mechanical properties to density and CT numbers in human bone, Medical Engineering and Physics 17 (5) (1995) 347–55.

[44] J. Y. Wong, J. D. Bronzino, Biomaterials, CRC Press, Boca Raton, 2007, p. 296.

[45] L. J. Gibson, Mechanical behavior of metallic foams, Annual Review of Materials Science 30 (2000) 191–227.

[46] G. J. Davies, S. Zhen, Metallic Foams - Their Production, Properties and Applications, Journal of Materials Science 18 (7) (1983) 1899–911.

[47] J. Banhart, Manufacturing routes for metallic foams, JOM-Journal of the Minerals Metals & Materials Society 52 (12) (2000) 22–7.

[48] F. Simancik, Reproducibility of aluminium foam properties, Verlag MIT publishing (1999) 235–40.

[49] S. W. Yook, B. H. Yoon, H. E. Kim, Y. H. Koh, Y. S. Kim, Porous titanium (Ti) scaffolds by freezing TiH2/camphene slurries, Materials Letters 62 (30) (2008) 4506–8.

[50] B. Dabrowski, W. Swieszkowski, D. Godlinski, K. J. Kurzydlowski, Highly porous titanium scaffolds for orthopaedic applications, Journal of Biomedical Materials Research Part B-Applied Biomaterials 95B (1) (2010) 53–61.

[51] S. C. P. Cachinho, R. N. Correia, Titanium scaffolds for osteointegration: mechanical, in vitro and corrosion behaviour, Journal of Materials Science-Materials in Medicine 19 (1) (2008) 451–7.

[52] J. H. Lee, H. E. Kim, Y. H. Koh, Highly porous titanium (Ti) scaffolds with bioactive microporous hydroxyapatite/TiO(2) hybrid coating layer, Materials Letters 63 (23) (2009) 1995–8.

[53] J. H. Lee, H. E. Kim, K. H. Shin, Y. H. Koh, Improving the strength and biocompatibility of porous titanium scaffolds by creating elongated pores coated with a bioactive, nanoporous TiO(2) layer, Materials Letters 64 (22) (2010) 2526–9.

[54] J. Zhao, X. Lu, J. Weng, Macroporous Ti-based composite scaffold prepared by polymer impregnating method with calcium phosphate coatings, Materials Letters 62 (17-18) (2008) 2921–4.

[55] M. H. Fathi, M. Salehi, A. Saatchi, V. Mortazavi, S. B. Moosavi, In vitro corrosion behavior of bioceramic, metallic, and bioceramic-metallic coated stainless steel dental implants, Dental Materials 19 (3) (2003) 188–98.

[56] S. D. F. Mariotto, V. Guido, L. Y. Cho, C. P. Soares, K. R. Cardoso, Porous Stainless Steel for Biomedical Applications, Materials Research-Ibero-American Journal of Materials 14 (2) (2011) 146–54.

[57] J. C. Galvan, L. Saldana, M. Multigner, A. Calzado-Martin, M. Larrea, C. Serra, N. Vilaboa, J. L. Gonzalez-Carrasco, Grit blasting of medical stainless steel: implications on its corrosion behavior, ion release and biocompatibility, Journal of Materials Science: Materials in Medicine 23 (3) (2012) 657–66.

[58] M. Niinomi, Recent metallic materials for biomedical applications, Metallurgical and Materials Transactions a-Physical Metallurgy and Materials Science 33 (3) (2002) 477–86.

[59] L. O. Bailey, S. Lipplatt, F. S. Biancanello, S. D. Ridder, N. R. Washburn, The quantification of cellular viability and inflammatory response to stainless steel alloys, Biomaterials 26 (26) (2005) 5296–302.

[60] T. Eliades, H. Pratsinis, D. Kletsas, G. Eliades, M. Makou, Characterization and cytotoxicity of ions released from stainless steel and nickel-titanium orthodontic alloys, American Journal of Orthodontics and Dentofacial Orthopedics 125 (1) (2004) 24–9.

[61] A. J. Ortiz, E. Fernandez, A. Vicente, J. L. Calvo, C. Ortiz, Metallic ions released from stainless steel, nickel-free, and titanium orthodontic alloys: Toxicity and DNA damage, American Journal of Orthodontics and Dentofacial Orthopedics 140 (3) (2011) E115–E22.

[62] A. Parsapour, S. Khorasani, M. H. Fathi, Effect of Surface Treatment and Metallic Coating on Corrosion Behavior and Biocompatibility of Surgical 316L Stainless Steel Implant, Journal of Materials Science & Technology 28 (2) (2012) 125–31.

[63] C. C. Shih, C. M. Shih, Y. Y. Su, L. H. J. Su, M. S. Chang, S. J. Lin, Effect of surface oxide properties on corrosion resistance of 316L stainless steel for biomedical applications, Corrosion Science 46 (2) (2004) 427–41.

[64] D. M. Brunette, Titanium in medicine : material science, surface science, engineering, biological responses, and medical applications, Engineering materials, Springer, Berlin ; New York, 2001, pp. xiii, 1019 p.

[65] J. P. Li, J. R. Wijn, C. A. Van Blitterswijk, K. De Groot, Comparison of porous Ti6Al4V made by sponge replication and direct 3D fiber deposition and cancellous bone, Bioceramics 19, Pts 1 & 2 (330-332) (2007) 999–1002.

[66] Y. Suzuki, N. Nomura, S. Hanada, S. Kamakura, T. Anada, T. Fuji, Y. Honda, T. Masuda, K. Sasaki, S. Kokubun, O. Suzuki, Osteoconductivity of porous titanium having Young's modulus similar to bone and surface modification by OCP, Bioceramics 19, Pts 1 and 2 (330-332) (2007) 951–4.

[67] S. Ahmad, N. Muhamad, A. Muchtar, J. Sahari, M. Ibrahim, K. Jamaludin, N. Nor, Development and Characterization of Titanium Alloy Foams, International Journal of Mechanical and Materials Engineering 5 (2) (2010) 244–50.

[68] M. Takemoto, S. Fujibayashi, M. Neo, K. So, N. Akiyama, T. Matsushita, T. Kokubo, T. Nakamura, Bone ingrowth into porous bioactive titanium implant for load-bearing use: Experimental study using a novel canine anterior interbody fusion model, Bioceramics 19, Pts 1 & 2 (330-332) (2007) 987–90.

[69] T. Albrektsson, H. A. Hansson, B. Ivarsson, Interface analysis of titanium and zirconium bone implants, Biomaterials 6 (2) (1985) 97–101.

[70] L. V. Branzoi, M. Iordoc, M. Codescu, Electrochemical studies on the stability and corrosion resistance of new zirconium-based alloys for biomedical applications, Surface and Interface Analysis 40 (3-4) (2008) 167–73.

[71] L. Saldana, A. Mendez-Vilas, L. Jiang, M. Multigner, J. L. Gonzalez-Carrasco, M. T. Perez-Prado, M. L. Gonzalez-Martin, L. Munuera, N. Vilaboa, In vitro biocompatibility of an ultrafine grained zirconium, Biomaterials 28 (30) (2007) 4343–54.

[72] M. Uchida, H. M. Kim, F. Miyaji, T. Kokubo, T. Nakamura, Apatite formation on zirconium metal treated with aqueous NaOH, Biomaterials 23 (1) (2002) 313–7.

[73] J. D. Bobyn, R. A. Poggie, J. J. Krygier, D. G. Lewallen, A. D. Hanssen, R. J. Lewis, A. S. Unger, T. J. O'Keefe, M. J. Christie, S. Nasser, J. E. Wood, S. D. Stulberg, M. Tanzer, Clinical validation of a structural porous tantalum biomaterial for adult reconstruction, Journal of Bone and Joint Surgery-American Volume 86A (2004) 123–9.

[74] L. D. Zardiackas, D. E. Parsell, L. D. Dillon, D. W. Mitchell, L. A. Nunnery, R. Poggie, Structure, metallurgy, and mechanical properties of a porous tantalum foam, Journal of Biomedical Materials Research 58 (2) (2001) 180–7.

[75] X. Zou, H. Li, M. Bunger, N. Egund, M. Lind, C. Bunger, Bone ingrowth characteristics of porous tantalum and carbon fiber interbody devices: an experimental study in pigs, The Spine Journal 4 (1) (2004) 99–105.

[76] A. K. Tsao, J. R. Roberson, M. J. Christie, D. A. Heck, D. D. Robertson, R. A. Poggie, Biomechanical and clinical evaluations of a porous tantalum implant for the treatment of early-stage osteonecrosis, Journal of Bone and Joint Surgery-American Volume 87A (2005) 22–7.

[77] B. Levine, C. J. Della Valle, J. J. Jacobs, Applications of porous tantalum in total hip arthroplasty, Journal of the American Academy of Orthopaedic Surgeons 14 (12) (2006) 646–55.

[78] B. R. Levine, S. Sporer, R. A. Poggie, C. J. Della Valle, J. J. Jacobs, Experimental and clinical performance of porous tantalum in orthopedic surgery, Biomaterials 27 (27) (2006) 4671–81.

[79] N. Patil, K. Lee, S. B. Goodman, Porous Tantalum in Hip and Knee Reconstructive Surgery, Journal of Biomedical Materials Research Part B-Applied Biomaterials 89B (1) (2009) 242–51.

[80] J. D. Bobyn, K. K. Toh, S. A. Hacking, M. Tanzer, J. J. Krygier, Tissue response to porous tantalum acetabular cups - A canine model, Journal of Arthroplasty 14 (3) (1999) 347–54.

[81] S. A. Hacking, J. D. Bobyn, K. K. Toh, M. Tanzer, J. J. Krygier, Fibrous tissue ingrowth and attachment to porous tantalum, Journal of Biomedical Materials Research 52 (4) (2000) 631–8.

[82] C. B. Johansson, H. A. Hansson, T. Albrektsson, Qualitative Interfacial Study between Bone and Tantalum, Niobium or Commercially Pure Titanium, Biomaterials 11 (4) (1990) 277–80.

[83] G. Mohandas, N. Oskolkov, M. T. McMahon, P. Walczak, M. Janowski, Porous tantalum and tantalum oxide nanoparticles for regenerative medicine, Acta Neurobiologiae Experimentalis (Wars) 74 (2) (2014) 188–96.

[84] M. P. Staiger, A. M. Pietak, J. Huadmai, G. Dias, Magnesium and its alloys as orthopedic biomaterials: A review, Biomaterials 27 (9) (2006) 1728–34.

[85] H. Zreiqat, C. R. Howlett, A. Zannettino, P. Evans, G. Schulze-Tanzil, C. Knabe, M. Shakibaei, Mechanisms of magnesium-stimulated adhesion of osteoblastic cells to commonly used orthopaedic implants, Journal of Biomedical Materials Research 62 (2) (2002) 175–84.

[86] F. Witte, J. Fischer, J. Nellesen, H. A. Crostack, V. Kaese, A. Pisch, F. Beckmann, H. Windhagen, In vitro and in vivo corrosion measurements of magnesium alloys, Biomaterials 27 (7) (2006) 1013–8.

[87] Y. Yamada, K. Shimojima, Y. Sakaguchi, M. Mabuchi, M. Nakamura, T. Asahina, T. Mukai, H. Kanahashi, K. Higashi, Processing of cellular magnesium materials, Advanced Engineering Materials 2 (4) (2000) 184–7.

[88] F. Witte, V. Kaese, H. Haferkamp, E. Switzer, A. Meyer-Lindenberg, C. J. Wirth, H. Windhagen, In vivo corrosion of four magnesium alloys and the associated bone response, Biomaterials 26 (17) (2005) 3557–63.

[89] Y. Zhang, L. L. Ren, M. Li, X. Lin, H. Zhao, K. Yang, Preliminary Study on Cytotoxic Effect of Biodegradation of Magnesium on Cancer Cells, Journal of Materials Science & Technology 28 (9) (2012) 769–72.

[90] Q. Wang, S. Jin, X. Lin, Y. Zhang, L. L. Ren, K. Yang, Cytotoxic Effects of Biodegradation of Pure Mg and MAO-Mg on Tumor Cells of MG63 and KB, Journal of Materials Science & Technology 30 (5) (2014) 487–92.

[91] S. Schumacher, I. Roth, J. Stahl, W. Baumer, M. Kietzmann, Biodegradation of metallic magnesium elicits an inflammatory response in primary nasal epithelial cells, Acta Biomaterialia 10 (2) (2014) 996–1004.

[92] J. B. Park, Bioceramics : properties, characterizations, and applications, Springer, New York, 2008, pp. xii, 359 p.

[93] P. K. Chu, X. Liu, Biomaterials fabrication and processing handbook, CRC Press/Taylor & Francis, Boca Raton, 2008, pp. xv, 701 p.

[94] M. Vallet-Regi, Ceramics for medical applications, Journal of the Chemical Society-Dalton Transactions (2) (2001) 97–108.

[95] A. J. Salinas, M. Vallet-Regi, Evolution of ceramics with medical applications, Zeitschrift Fur Anorganische Und Allgemeine Chemie 633 (11-12) (2007) 1762–73.

[96] H. S. Costa, M. M. Pereira, G. I. Andrade, E. F. B. Stancioli, H. S. Mansur, Characterization of calcium phosphate coating and zinc incorporation on the porous alumina scaffolds, Materials Research 10 (2007) 27–9.

[97] Y. H. Koh, J. H. Song, E. J. Lee, H. E. Kim, Freezing dilute ceramic/camphene slurry for ultra-high porosity ceramics with completely interconnected pore networks, Journal of the American Ceramic Society 89 (10) (2006) 3089–93.

[98] H. X. Peng, Z. Fan, J. R. G. Evans, J. J. C. Busfield, Microstructure of ceramic foams, Journal of the European Ceramic Society 20 (7) (2000) 807–13.

[99] C. Tuck, J. R. G. Evans, Porous ceramics prepared from aqueous foams, Journal of Materials Science Letters 18 (13) (1999) 1003–5.

[100] Y. S. Han, J. B. Li, Y. J. Chen, Fabrication of bimodal porous alumina ceramics, Materials Research Bulletin 38 (2) (2003) 373–9.

[101] M. Karlsson, E. Palsgard, P. R. Wilshaw, L. Di Silvio, Initial in vitro interaction of osteoblasts with nano-porous alumina, Biomaterials 24 (18) (2003) 3039–46.

[102] J. Cao, C. R. Rambo, H. Sieber, Preparation of porous Al2O3 - Ceramics by biotemplating of wood, Journal of Porous Materials 11 (3) (2004) 163–72.

[103] J. Y. Yu, X. D. Sun, Q. Li, X. D. Li, Preparation of Al2O3 and Al2O3-ZrO2 ceramic foams with adjustable cell structure by centrifugal slip casting, Materials Science and Engineering Part A: Structural Materials Properties, Microstructure and Processing 476 (1-2) (2008) 274–80.

[104] B. H. Yoon, W. Y. Choi, H. E. Kim, J. H. Kim, Y. H. Koh, Aligned porous alumina ceramics with high compressive strengths for bone tissue engineering, Scripta Materialia 58 (7) (2008) 537–40.

[105] R. Khattab, M. Wahsh, N. Khalil, Preparation and Characterization of Porous Alumina Ceramics through Starch Consolidation Casting Technique, Ceramics International.

[106] Y. M. Soon, K. H. Shin, Y. H. Koh, W. Y. Choi, H. E. Kim, Assembling unidirectionally frozen alumina/camphene bodies for aligned porous alumina ceramics with larger dimensions, Journal of the European Ceramic Society 31 (3) (2011) 415–9.

[107] Y. W. Moon, K. H. Shin, Y. H. Koh, W. Y. Choi, H. E. Kim, Production of highly aligned porous alumina ceramics by extruding frozen alumina/camphene body, Journal of the European Ceramic Society 31 (11) (2011) 1945–50.

[108] H. Comas, V. Laporte, F. Borcard, P. Mieville, F. Krauss Juillerat, M. A. Caporini, U. T. Gonzenbach, L. Juillerat-Jeanneret, S. Gerber-Lemaire, Surface functionalization of alumina ceramic foams with organic ligands, ACS Applied Materials & Interfaces 4 (2) (2012) 573–6.

[109] H. S. Costa, A. A. P. Mansur, E. F. Barbosa-Stancioli, M. M. Pereira, H. S. Mansur, Morphological, mechanical, and biocompatibility characterization of macroporous alumina scaffolds coated with calcium phosphate/PVA, Journal of Materials Science 43 (2) (2008) 510–24.

[110] M. Andreiotelli, H. J. Wenz, R. J. Kohal, Are ceramic implants a viable alternative to titanium implants? A systematic literature review, Clinical Oral Implants Research 20 (2009) 32–47.

[111] C. Piconi, G. Maccauro, Zirconia as a ceramic biomaterial, Biomaterials 20 (1) (1999) 1–25.

[112] F. Di Carlo, L. Prosper, F. Ripari, A. Scarano, Bone response to zirconia ceramic implants: an experimental study in rabbit, Bioceramics 192-1 (2000) 403–7.

[113] F. Carinci, F. Pezzetti, S. Volinia, F. Francioso, D. Arcelli, E. Farina, A. Piattelli, Zirconium oxide: analysis of MG63 osteoblast-like cell response by means of a microarray technology, Biomaterials 25 (2) (2004) 215–28.

[114] P. F. Manicone, P. R. Iommetti, L. Raffaelli, An overview of zirconia ceramics: Basic properties and clinical applications, Journal of Dentistry 35 (11) (2007) 819–26.

[115] H. W. Kim, S. Y. Lee, C. J. Bae, Y. J. Noh, H. E. Kim, H. M. Kim, J. S. Ko, Porous ZrO2 bone scaffold coated with hydroxyapatite with fluorapatite intermediate layer, Biomaterials 24 (19) (2003) 3277–84.

[116] I. K. Jun, Y. H. Koh, J. H. Song, S. H. Lee, H. E. Kim, Improved compressive strength of reticulated porous zirconia using carbon coated polymeric sponge as novel template, Materials Letters 60 (20) (2006) 2507–10.

[117] J. Han, C. Hong, X. Zhang, J. Du, W. Zhang, Highly porous ZrO2 ceramics fabricated by a camphene-based freeze-casting route: Microstructure and properties, Journal of the European Ceramic Society 30 (1) (2010) 53–60.

[118] C. Q. Hong, X. H. Zhang, J. C. Han, J. C. Du, W. B. Han, Ultra-high-porosity zirconia ceramics fabricated by novel room-temperature freeze-casting, Scripta Materialia 60 (7) (2009) 563–6.

[119] C. R. Rambo, J. Cao, H. Sieber, Preparation and properties of highly porous, bimorphic YSZ ceramics, Materials Chemistry and Physics 87 (2004) 345–52.

[120] T. von Schewelov, L. Sanzén, I. Önsten, Å. Carlsson, J. Besjakov, Total hip replacement with a zirconium oxide ceramic femoral head, Journal of Bone & Joint Surgery, British Volume 87-B (12) (2005) 1631–5.

[121] S. A. Guelcher, J. O. Hollinger, An introduction to biomaterials, Biomedical engineering series, CRC/Taylor & Francis, Boca Raton, FL, 2006, p. 553 p.

[122] R. Hannink, M. Swain, Progress in Transformation Toughening of Ceramics, Annual reviews in Materials Science 24 (1994) 359–408.

[123] R. Hannink, P. Kelly, B. Muddle, Transformation Toughening in Zirconia-Coated Ceramics, Journal of the American Ceramic Society 83 (3) (2000) 461–487.

[124] I. Denry, J. R. Kelly, State of the art of zirconia for dental applications, Dental Materials 24 (3) (2008) 299–307.

[125] P. J. Li, C. Ohtsuki, T. Kokubo, K. Nakanishi, N. Soga, K. Degroot, The Role of Hydrated Silica, Titania, and Alumina in Inducing Apatite on Implants, Journal of Biomedical Materials Research 28 (1) (1994) 7–15.

[126] J. G. Li, Behavior of Titanium and Titania-Based Ceramics Invitro and Invivo, Biomaterials 14 (3) (1993) 229–32.

[127] M. P. Casaletto, G. M. Ingo, S. Kaciulis, G. Mattogno, L. Pandolfi, G. Scavia, Surface studies of in vitro biocompatibility of titanium oxide coatings, Applied Surface Science 172 (1-2) (2001) 167–77.

[128] B. Fartash, H. Liao, J. Li, N. Fouda, L. Hermansson, Long-term evaluation of titania-based ceramics compared with commercially pure titanium in-vivo, Journal of Materials Science-Materials in Medicine 6 (8) (1995) 451–4.

[129] F. Escalas, J. Galante, W. Rostoker, P. Coogan, Biocompatibility of Materials for Total Joint Replacement, Journal of Biomedical Materials Research 10 (2) (1976) 175–95.

[130] T. Kokubo, T. Matsushita, H. Takadama, Titania-based bioactive materials, Journal of the European Ceramic Society 27 (2-3) (2007) 1553–.

[131] G. X. Tang, R. J. Zhang, Y. N. Yan, Z. X. Zhu, Preparation of porous anatase titania film, Materials Letters 58 (12-13) (2004) 1857–60.

[132] Y. X. Leng, N. Huang, P. Yang, J. Y. Chen, H. Sun, J. Wang, G. J. Wan, Y. Leng, P. K. Chu, Influence of oxygen pressure on the properties and biocompatibility of titanium oxide fabricated by metal plasma ion implantation and deposition, Thin Solid Films 420 (2002) 408–13.

[133] S. Areva, H. Paldan, T. Peltola, T. Narhi, M. Jokinen, M. Linden, Use of sol-gel-derived titania coating for direct soft tissue attachment, Journal of Biomedical Materials Research Part A 70A (2) (2004) 169–78.

[134] B. Li, X. Y. Liu, C. Cao, C. X. Ding, Biocompatibility and antibacterial activity of plasma sprayed titania coating grafting collagen and gentamicin, Journal of Biomedical Materials Research Part A 83A (4) (2007) 923–30.

[135] L. Zhu, X. Ye, G. Tang, N. Zhao, Y. Gong, Y. Zhao, J. Zhao, X. Zhang, Biomimetic coating of compound titania and hydroxyapatite on titanium, Journal of Biomedical Materials Research Part A 83A (4) (2007) 1165–75.

[136] P. Huang, K. W. Xu, Y. Han, Formation mechanism of biomedical apatite coatings on porous titania layer, Journal of Materials Science-Materials in Medicine 18 (3) (2007) 457–63.

[137] M. Brama, N. Rhodes, J. Hunt, A. Ricci, R. Teghil, S. Migliaccio, C. Della Rocca, S. Leccisotti, A. Lioi, M. Scandurra, G. De Maria, D. Ferro, F. R. Pu, G. Panzini, L. Politi, R. Scandurra, Effect of titanium carbide coating on the osseointegration response in vitro and in vivo, Biomaterials 28 (4) (2007) 595–608.

[138] J. W. Park, Increased bone apposition on a titanium oxide surface incorporating phosphate and strontium, Clinical Oral Implants Research 22 (2) (2011) 230–4.

[139] X. L. Xiao, L. X. Yang, M. L. Guo, C. F. Pan, Q. Y. Cai, S. Z. Yao, Biocompatibility and in vitro antineoplastic drug-loaded trial of titania nanotubes prepared by anodic oxidation of a pure titanium, Science in China Series B-Chemistry 52 (12) (2009) 2161–5.

[140] K. C. Popat, L. Leoni, C. A. Grimes, T. A. Desai, Influence of engineered titania nanotubular surfaces on bone cells, Biomaterials 28 (21) (2007) 3188–97.

[141] T. Lopez, E. Ortiz, P. Quintana, R. D. Gonzalez, A nanostructured titania bioceramic implantable device capable of drug delivery to the temporal lobe of the brain, Colloids and Surfaces A-Physicochemical and Engineering Aspects 300 (1-2) (2007) 3–10.

[142] L. Xie, X. M. Liao, G. F. Yin, Z. B. Huang, D. H. Yan, Y. D. Yao, W. L. Liu, X. C. Chen, J. W. Gu, Preparation, characterization, in vitro bioactivity, and osteoblast adhesion of multi-level porous titania layer on titanium by two-step anodization treatment, Journal of Biomedical Materials Research Part A 98A (2) (2011) 312–20.

[143] T. Kokubo, H. Kushitani, S. Sakka, T. Kitsugi, T. Yamamuro, Solutions able to reproduce in vivo surface-structure changes in bioactive glass-ceramic a-w, Journal of Biomedical Materials Research 24 (6) (1990) 721–34.

[144] H. Tiainen, M. Monjo, J. Knychala, O. Nilsen, S. P. Lyngstadaas, J. E. Ellingsen, H. J. Haugen, The effect of fluoride surface modification of ceramic TiO2 on the surface properties and biological response of osteoblastic cells in vitro, Biomedical Materials 6 (4) (2011) 045006.

[145] M. Vallet-Regi, Revisiting ceramics for medical applications, Dalton Transactions (44) (2006) 5211–20.

[146] Z. Amjad, Calcium phosphates in biological and industrial systems, Kluwer Academic Publishers, Boston, 1998, pp. xiv, 515 p.

[147] C. D. Friedman, P. D. Costantino, S. Takagi, L. C. Chow, BoneSource (TM) hydroxyapatite cement: A novel biomaterial for craniofacial skeletal tissue engineering and reconstruction, Journal of Biomedical Materials Research 43 (4) (1998) 428–32.

[148] M. Nilsson, E. Fernandez, S. Sarda, L. Lidgren, J. A. Planell, Characterization of a novel calcium phosphate/sulphate bone cement, Journal of Biomedical Materials Research 61 (4) (2002) 600–7.

[149] T. Yuasa, Y. Miyamoto, K. Ishikawa, M. Takechi, Y. Momota, S. Tatehara, M. Nagayama, Effects of apatite cements on proliferation and differentiation of human osteoblasts in vitro, Biomaterials 25 (7-8) (2004) 1159–66.

[150] Y. Miyamoto, K. Ishikawa, M. Takechi, T. Toh, T. Yuasa, M. Nagayama, K. Suzuki, Histological and compositional evaluations of three types of calcium phosphate cements when implanted in subcutaneous tissue immediately after mixing, Journal of Biomedical Materials Research 48 (1) (1999) 36–42.

[151] L. L. Hench, R. J. Splinter, W. C. Allen, T. K. Greenlee, Bonding mechanisms at the interface of ceramic prosthetic materials, Journal of Biomedical Materials Research 5 (6) (1971) 117–41.

[152] J. M. Gomez-Vega, A. Hozumi, E. Saiz, A. P. Tomsia, H. Sugimura, O. Takai, Bioactive glass-mesoporous silica coatings on Ti6Al4V through enameling and triblock-copolymer-templated sol-gel processing, Journal of Biomedical Materials Research 56 (3) (2001) 382–9.

[153] S. Lopez-Esteban, E. Saiz, S. Fujino, T. Oku, K. Suganuma, A. P. Tomsia, Bioactive glass coatings for orthopedic metallic implants, Journal of the European Ceramic Society 23 (15) (2003) 2921–30.

[154] P. Tormala, J. Vasenius, S. Vainionpaa, J. Laiho, T. Pohjonen, P. Rokkanen, Ultra-High-Strength Absorbable Self-Reinforced Polyglycolide (Sr-Pga) Composite Rods for Internal-Fixation of Bone-Fractures - Invitro and Invivo Study, Journal of Biomedical Materials Research 25 (1) (1991) 1–22.

[155] K. Koskikare, T. Toivonen, P. Rokkanen, Tissue response to bioabsorbable self-reinforced polylevolactide and polyglycolide pins implanted intra-articularly and directly into the bone on different levels - An experimental study on rats, Archives of Orthopaedic and Trauma Surgery 118 (3) (1998) 149–55.

[156] H. Pihlajamaki, O. Tynninen, P. Karjalainen, P. Rokkanen, Enveloping bioabsorbable polyglycolide membrane and immobilization in Achilles tendon repair: A comparative experimental study on rabbits, Journal of Orthopaedic Research 26 (2) (2008) 264–70.

[157] S. Gogolewski, Bioresorbable polymers in trauma and bone surgery, Injury-International Journal of the Care of the Injured 31 (2000) S28–S32.

[158] O. Bostman, U. Paivarinta, E. Partio, J. Vasenius, M. Manninen, P. Rokkanen, Degradation and Tissue Replacement of an Absorbable Polyglycolide Screw in the Fixation of Rabbit Femoral Osteotomies, Journal of Bone and Joint Surgery-American Volume 74A (7) (1992) 1021–31.

[159] H. K. Pihlajamaki, S. T. Salminen, O. Tynninen, O. M. Bostman, O. Laitinen, Tissue Restoration After Implantation of Polyglycolide, Polydioxanone, Polylevolactide, and Metallic Pins in Cortical Bone: An Experimental Study in Rabbits, Calcified Tissue International 87 (1) (2010) 90–8.

[160] F. Baumchen, R. Smeets, D. Koch, H. G. Graber, The impact of defined polyglycolide scaffold structure on the proliferation of gingival fibroblasts in vitro: a pilot study, Oral Surgery, Oral Medicine, Oral Pathology, Oral Radiology, and Endodontology 108 (4) (2009) 505–13.

[161] G. Q. Zhao, S. Yin, G. P. Liu, L. Cen, J. Sun, H. Zhou, W. Liu, L. Cui, Y. L. Cao, In vitro engineering of fibrocartilage using CDMP1 induced dermal fibroblasts and polyglycolide, Biomaterials 30 (19) (2009) 3241–50.

[162] K. Schwarz, M. Epple, Hierarchically structured polyglycolide - a biomaterial mimicking natural bone, Macromolecular Rapid Communications 19 (12) (1998) 613–7.

[163] N. Y. C. Yu, A. Schindeler, D. G. Little, A. J. Ruys, Biodegradable Poly(alpha-hydroxy acid) Polymer Scaffolds for Bone Tissue Engineering, Journal of Biomedical Materials Research Part B-Applied Biomaterials 93B (1) (2010) 285–95.

[164] J. O. Hollinger, K. Leong, Poly(alpha-hydroxy acids): Carriers for bone morphogenetic proteins, Biomaterials 17 (2) (1996) 187–94.

[165] E. N. Antonov, A. V. Popova, I. I. Selezneva, V. V. Trofimov, A. Y. Fedotov, A. S. Fomin, Mechanical characteristics of composites of polylactide and nanosized calcium phosphates formed in supercritical carbon dioxide, Russian Journal of Physical Chemistry B 5 (8) (2011) 1189–94.

[166] K. M. Nampoothiri, N. R. Nair, R. P. John, An overview of the recent developments in polylactide (PLA) research, Bioresource Technology 101 (22) (2010) 8493–501.

[167] J. S. Son, S. G. Kim, J. S. Oh, M. Appleford, S. Oh, J. L. Ong, K. B. Lee, Hydroxyapatite/polylactide biphasic combination scaffold loaded with dexamethasone for bone regeneration, Journal of Biomedical Materials Research Part A 99A (4) (2011) 638–47.

[168] J. J. Blaker, S. N. Nazhat, V. Maquet, A. R. Boccaccini, Long-term in vitro degradation of PDLLA/bioglass (r) bone scaffolds in acellular simulated body fluid, Acta Biomaterialia 7 (2) (2011) 829–40.

[169] E. A. Abou Neel, V. Salih, P. A. Revell, A. M. Young, Viscoelastic and biological performance of low-modulus, reactive calcium phosphate-filled, degradable, polymeric bone adhesives, Acta Biomaterialia 8 (1) (2012) 313–20.

[170] C. Gaball, S. Lovald, B. Baack, G. Olson, Minimally Invasive Bioabsorbable Bone Plates for Rigid Internal Fixation of Mandible Fractures, Archives of Facial Plastic Surgery 13 (1) (2011) 31–5.

[171] J. A. Roether, A. R. Boccaccini, L. L. Hench, V. Maquet, S. Gautier, R. Jerome, Development and in vitro characterisation of novel bioresorbable and bioactive composite materials based on polylactide foams and Bioglass (R) for tissue engineering applications, Biomaterials 23 (18) (2002) 3871–8.

[172] A. Kolk, C. Haczek, C. Koch, S. Vogt, M. Kullmer, C. Pautke, H. Deppe, C. Plank, A strategy to establish a gene-activated matrix on titanium using gene vectors protected in a polylactide coating, Biomaterials 32 (28) (2011) 6850–9.

[173] H. Pistner, R. Gutwald, R. Ordung, J. Reuther, J. Muhling, Poly(L-Lactide) - a Long-Term Degradation Study in-Vivo .1. Biological Results, Biomaterials 14 (9) (1993) 671–7.

[174] P. Mainil-Varlet, R. Rahm, S. Gogolewski, Long-term in vivo degradation and bone reaction to various polylactides .1. one-year results, Biomaterials 18 (3) (1997) 257–66.

[175] V. Maquet, D. Martin, B. Malgrange, R. Franzen, J. Schoenen, G. Moonen, R. Jerome, Peripheral nerve regeneration using bioresorbable macroporous polylactide scaffolds, Journal of Biomedical Materials Research 52 (4) (2000) 639–51.

[176] C. Martin, H. Winet, J. Y. Bao, Acidity near eroding polylactide-polyglycolide in vitro and in vivo in rabbit tibial bone chambers, Biomaterials 17 (24) (1996) 2373–80.

[177] J. Tiainen, Y. Soini, P. Tormala, T. Waris, N. Ashammakhi, Self-reinforced polylactide/polyglycolide 80/20 screws take more than 1 1/2 years to resorb in rabbit cranial bone, Journal of Biomedical Materials Research Part B-Applied Biomaterials 70B (1) (2004) 49–55.

[178] J. Tiainen, Y. Soini, E. Suokas, M. Veiranto, P. Tormala, T. Waris, N. Ashammakhi, Tissue reactions to bioabsorbable ciprofloxacin-releasing polylactide-polyglycolide 80/20 screws in rabbits' cranial bone, Journal of Materials Science-Materials in Medicine 17 (12) (2006) 1315–22.

[179] C. Bertoldi, D. Zaffe, U. Consolo, Polylactide/polyglycolide copolymer in bone defect healing in humans, Biomaterials 29 (12) (2008) 1817–23.

[180] E. Makela, E. A. Makela, E. K. Partio, T. Juutilainen, K. Lahteenkorva, P. Tormala, P. Rokkanen, Fixation of experimental osteotomies with bioabsorbable SR-polylactide-polyglycolide (80/20) polymeric rods, Journal of Materials Science-Materials in Medicine 19 (3) (2008) 1061–7.

[181] J. O. Hollinger, Preliminary report on the osteogenic potential of a biodegradable copolymer of polyactide (PLA) and polyglycolide (PGA), Journal of Biomedical Materials Research 17 (1) (1983) 71–82.

[182] D. Dziedzic, I. Bertoja, J. Zielak, Initial endosseous healing response to lactide/glycolide copolymer, Revista Sul-Brasileira de Odontologia 6 (2) (2009) 176–84.

[183] A. Bansal, S. Prakash, Evaluation of the polylactide-polyglycolide copolymer Fisiograft (R) in the treatment of intrabony defects. Clinical and radiographic results of a pilot study, Brazilian Journal of Oral Sciences 10 (2) (2011) 98–104.

[184] H. Winet, J. O. Hollinger, Incorporation of polylactide-polyglycolide in a cortical defect: neoosteogenesis in a bone chamber, Journal of Biomedical Materials Research 27 (5) (1993) 667–76.

[185] G. Serino, W. Rao, G. Iezzi, A. Piattelli, Polylactide and polyglycolide sponge used in human extraction sockets: bone formation following 3 months after its application, Clinical Oral Implants Research 19 (1) (2008) 26–31.

[186] S. H. Lee, H. Shin, Matrices and scaffolds for delivery of bioactive molecules in bone and cartilage tissue engineering, Advanced Drug Delivery Reviews 59 (4-5) (2007) 339–59.

[187] C. M. Agrawal, R. B. Ray, Biodegradable polymeric scaffolds for musculoskeletal tissue engineering, Journal of Biomedical Materials Research 55 (2) (2001) 141–50.

[188] M. H. Sheridan, L. D. Shea, M. C. Peters, D. J. Mooney, Bioadsorbable polymer scaffolds for tissue engineering capable of sustained growth factor delivery, Journal of Controlled Release 64 (1-3) (2000) 91–102.

[189] I. Engelberg, J. Kohn, Physico-mechanical properties of degradable polymers used in medical applications: a comparative study, Biomaterials 12 (3) (1991) 292–304.

[190] J. C. Middleton, A. J. Tipton, Synthetic biodegradable polymers as orthopedic devices, Biomaterials 21 (23) (2000) 2335–46.

[191] D. W. Hutmacher, T. Schantz, I. Zein, K. W. Ng, S. H. Teoh, K. C. Tan, Mechanical properties and cell cultural response of polycaprolactone scaffolds designed and fabricated via fused deposition modeling, Journal of Biomedical Materials Research 55 (2) (2001) 203–16.

[192] H. Kweon, M. K. Yoo, I. K. Park, T. H. Kim, H. C. Lee, H. S. Lee, J. S. Oh, T. Akaike, C. S. Cho, A novel degradable polycaprolactone network for tissue engineering, Biomaterials 24 (5) (2003) 801–8.

[193] A. G. A. Coombes, S. C. Rizzi, M. Williamson, J. E. Barralet, S. Downes, W. A. Wallace, Precipitation casting of polycaprolactone for applications in tissue engineering and drug delivery, Biomaterials 25 (2) (2004) 315–25.

[194] D. Rohner, D. W. Hutmacher, T. K. Cheng, M. Oberholzer, B. Hammer, In vivo efficacy of bone-marrow-coated polycaprolactone scaffolds for the reconstruction of orbital defects in the pig, Journal of Biomedical Materials Research Part B: Applied Biomaterials 66B (2) (2003) 574–80.

[195] P. S. Tan, S. H. Teoh, Effect of stiffness of polycaprolactone (PCL) membrane on cell proliferation, Materials Science & Engineering C-Biomimetic and Supramolecular Systems 27 (2) (2007) 304–8.

[196] L. Averous, L. Moro, P. Dole, C. Fringant, Properties of thermoplastic blends: starch-polycaprolactone, Polymer 41 (11) (2000) 4157–67.

[197] Y. M. Wang, M. A. Rodriguez-Perez, R. L. Reis, J. F. Mano, Thermal and thermomechanical behaviour of polycaprolactone and starch/polycaprolactone

blends for biomedical applications, Macromolecular Materials and Engineering 290 (8) (2005) 792–801.

[198] K. J. Wu, C. S. Wu, J. S. Chang, Biodegradability and mechanical properties of polycaprolactone composites encapsulating phosphate-solubilizing bacterium Bacillus sp PG01, Process Biochemistry 42 (4) (2007) 669–75.

[199] S. Fuchs, S. Ghanaati, C. Orth, M. Barbeck, M. Kolbe, A. Hofmann, M. Eblenkamp, M. Gomes, R. L. Reis, C. J. Kirkpatrick, Contribution of outgrowth endothelial cells from human peripheral blood on in vivo vascularization of bone tissue engineered constructs based on starch polycaprolactone scaffolds, Biomaterials 30 (4) (2009) 526–34.

[200] P. Wutticharoenmongkol, N. Sanchavanakit, P. Pavasant, P. Supaphol, Preparation and characterization of novel bone scaffolds based on electrospun polycaprolactone fibers filled with nanoparticles, Macromolecular Bioscience 6 (1) (2006) 70–7.

[201] Y. Lei, B. Rai, K. H. Ho, S. H. Teoh, In vitro degradation of novel bioactive polycaprolactone-20engineering, Materials Science & Engineering C-Biomimetic and Supramolecular Systems 27 (2) (2007) 293–8.

[202] L. Shor, S. Guceri, X. J. Wen, M. Gandhi, W. Sun, Fabrication of three-dimensional polycaprolactone/hydroxyapatite tissue scaffolds and osteoblast-scaffold interactions in vitro, Biomaterials 28 (35) (2007) 5291–7.

[203] M. C. Phipps, W. C. Clem, S. A. Catledge, Y. Xu, K. M. Hennessy, V. Thomas, M. J. Jablonsky, S. Chowdhury, A. V. Stanishevsky, Y. K. Vohra, S. L. Bellis, Mesenchymal Stem Cell Responses to Bone-Mimetic Electrospun Matrices Composed of Polycaprolactone, Collagen I and Nanoparticulate Hydroxyapatite, Plos One 6 (2).

[204] K. R. Duan, H. L. Chen, J. Huang, J. H. Yu, S. Y. Liu, D. X. Wang, Y. P. Li, One-step synthesis of amino-reserved chitosan-graft-polycaprolactone as

a promising substance of biomaterial, Carbohydrate Polymers 80 (2) (2010) 498–503.

[205] N. Kumar, R. S. Langer, A. J. Domb, Polyanhydrides: an overview, Advanced Drug Delivery Reviews 54 (7) (2002) 889–910.

[206] S. El-Amin, M. Kwon, T. Starnes, H. R. Allcock, C. T. Laurencin, The biocompatibility of biodegradable glycine containing polyphosphazenes: A comparative study in bone, Journal of Inorganic and Organometallic Polymers and Materials 16 (2006) 387–96.

[207] T. Akagi, X. Wang, T. Uto, M. Baba, M. Akashi, Protein direct delivery to dendritic cells using nanoparticles based on amphiphilic poly(amino acid) derivatives, Biomaterials 28 (23) (2007) 3427–36.

[208] T. Elzein, M. Nasser-Eddine, C. Delaite, S. Bistac, P. Dumas, FTIR study of polycaprolactone chain organization at interfaces, Journal of Colloid and Interface Science 273 (2) (2004) 381–7.

[209] A. M. A. Ambrosio, H. R. Allcock, D. S. Katti, C. T. Laurencin, Degradable polyphosphazene/poly(alpha-hydroxyester) blends: degradation studies, Biomaterials 23 (7) (2002) 1667–72.

[210] A. D. Cook, J. S. Hrkach, N. N. Gao, I. M. Johnson, U. B. Pajvani, S. M. Cannizzaro, R. Langer, Characterization and development of RGD-peptide-modified poly(lactic acid-co-lysine) as an interactive, resorbable biomaterial, Journal of Biomedical Materials Research 35 (4) (1997) 513–23.

[211] A. Coda, R. Lamberti, S. Martorana, Classification of prosthetics used in hernia repair based on weight and biomaterial, Hernia 16 (1) (2011) 9–20.

[212] S. J. Lee, G. J. Lim, J. W. Lee, A. Atala, J. J. Yoo, In vitro evaluation of a poly(lactide-co-glycolide)-collagen composite scaffold for bone regeneration, Biomaterials 27 (18) (2006) 3466–72.

[213] S. Sethuraman, L. S. Nair, S. El-Amin, M. T. Nguyen, A. Singh, N. Krogman, Y. E. Greish, H. R. Allcock, P. W. Brown, C. T. Laurencin, Mechanical properties and osteocompatibility of novel biodegradable alanine based polyphosphazenes: Side group effects, Acta Biomaterialia 6 (6) (2010) 1931–7.

[214] K. S. Soppimath, T. M. Aminabhavi, A. R. Kulkarni, W. E. Rudzinski, Biodegradable polymeric nanoparticles as drug delivery devices, Journal of Controlled Release 70 (1-2) (2001) 1–20.

[215] Z. Zhang, R. Kuijer, S. K. Bulstra, D. W. Grijpma, J. Feijen, The in vivo and in vitro degradation behavior of poly(trimethylene carbonate), Biomaterials 27 (9) (2006) 1741–8.

[216] K. J. Zhu, R. W. Hendren, K. Jensen, C. G. Pitt, Synthesis, Properties, and Biodegradation of Poly(1,3-Trimethylene Carbonate), Macromolecules 24 (8) (1991) 1736–40.

[217] D. H. Dan, D. C. Lee, Synthesis and molecular characterization of bisphenol A poly(iminocarbonate), Korea Polymer Journal 3 (2) (1995) 94–100.

[218] C. Li, J. Kohn, Synthesis of Poly(Iminocarbonates) - Degradable Polymers with Potential Applications as Disposable Plastics and as Biomaterials, Macromolecules 22 (5) (1989) 2029–36.

[219] J. Kohn, R. Langer, Poly(Iminocarbonates) as Potential Biomaterials, Biomaterials 7 (3) (1986) 176–82.

[220] H. Seeherman, J. M. Wozney, Delivery of bone morphogenetic proteins for orthopedic tissue regeneration, Cytokine & Growth Factor Reviews 16 (3) (2005) 329–45.

[221] S. Bose, A. Banerjee, S. Dasgupta, A. Bandyopadhyay, Synthesis, Processing, Mechanical, and Biological Property Characterization of Hydroxyapatite Whisker-Reinforced Hydroxyapatite Composites, Journal of the American Ceramic Society 92 (2) (2009) 323–30.

[222] D. Singh, M. D. Lorenzo-Martin, F. Gutierrez-Mora, J. L. Routbort, E. D. Case, Self-joining of zirconia/hydroxyapatite composites using plastic deformation process, Acta Biomaterialia 2 (6) (2006) 669–75.

[223] N. Koc, M. Timucin, F. Korkusuz, Fabrication and characterization of porous tricalcium phosphate ceramics, Ceramics International 30 (2) (2004) 205–11.

[224] J. Zhao, S. G. Xiao, X. Lu, J. X. Wang, J. Weng, A study on improving mechanical properties of porous HA tissue engineering scaffolds by hot isostatic pressing, Biomedical Materials 1 (4) (2006) 188–92.

[225] A. Rapacz-Kmita, C. Paluszkiewicz, A. Slosarczyk, Z. Paskiewicz, FTIR and XRD investigations on the thermal stability of hydroxyapatite during hot pressing and pressureless sintering processes, Journal of Molecular Structure 744-747 (2005) 653–6.

[226] M. Nanko, K. Ishizaki, T. Fujiawa, Porous ceramic filters produced by hot isostatic pressing, Journal of the American Ceramic Society 77 (1994) 2437–342.

[227] Y. Chino, D. C. Dunand, Creating Aligned, Elongated Pores in Titanium Foams by Swaging of Preforms with Ductile Space-Holder, Advanced Engineering Materials 11 (1-2) (2009) 52–5.

[228] C. E. Wen, Y. Yamada, K. Shimojima, Y. Chino, H. Hosokawa, M. Mabuchi, Novel titanium foam for bone tissue engineering, Journal of Materials Research 17 (10) (2002) 2633–9.

[229] C. E. Wen, M. Mabuchi, Y. Yamada, K. Shimojima, Y. Chino, T. Asahina, Processing of biocompatible porous Ti and Mg, Scripta Materialia 45 (10) (2001) 1147–53.

[230] D. C. Dunand, Processing of titanium foams, Advanced Engineering Materials 6 (6) (2004) 369–76.

[231] L. M. de Vasconcellos, F. N. Oliveira, O. Leite Dde, L. G. de Vasconcellos, R. F. do Prado, C. J. Ramos, M. L. Graca, C. A. Cairo, Y. R. Carvalho, Novel production method of porous surface Ti samples for biomedical application, Journal of Materials Science Materials in Medicine 23 (2) (2012) 357–64.

[232] S. C. P. Cachinho, R. N. Correia, Titanium porous scaffolds from precursor powders: rheological optimization of TiH2 slurries, Powder Technology 178 (2) (2007) 109–13.

[233] A. Mikos, J. Temenoff, Formation of highly porous biodegradable scaffolds for tissue engineering, Electronic Journal of Biotechnology 3 (2) (2000) 1995–2000.

[234] J. M. Cordell, M. L. Vogl, A. J. Wagoner Johnson, The influence of micropore size on the mechanical properties of bulk hydroxyapatite and hydroxyapatite scaffolds, Journal of Mechanical Behaviour of Biomedical Materials 2 (5) (2009) 560–70.

[235] B. Chuenjitkuntaworn, W. Inrung, D. Damrongsri, K. Mekaapiruk, P. Supaphol, P. Pavasant, Polycaprolactone/Hydroxyapatite composite scaffolds: Preparation, characterization, and in vitro and in vivo biological responses of human primary bone cells, Journal of Biomedical Materials Research Part A 94A (1) (2010) 241–51.

[236] A. M. Le Ray, H. Gautier, J. M. Bouler, P. Weiss, C. Merle, A new technological procedure using sucrose as porogen compound to manufacture porous biphasic calcium phosphate ceramics of appropriate micro- and macrostructure, Ceramics International 36 (1) (2010) 93–101.

[237] Y. X. Liu, J. H. Kim, D. Young, S. Kim, S. K. Nishimoto, Y. Z. Yang, Novel template-casting technique for fabricating beta-tricalcium phosphate scaffolds with high interconnectivity and mechanical strength and in vitro cell responses, Journal of Biomedical Materials Research Part A 92A (3) (2010) 997–1006.

[238] L. Lu, S. J. Peter, M. D. Lyman, H. L. Lai, S. M. Leite, J. A. Tamada, S. Uyama, J. P. Vacanti, R. Langer, A. G. Mikos, In vitro and in vivo degradation of porous poly(DL-lactic-co-glycolic acid) foams, Biomaterials 21 (18) (2000) 1837–45.

[239] C. J. Liao, C. F. Chen, J. H. Chen, S. F. Chiang, Y. J. Lin, K. Y. Chang, Fabrication of porous biodegradable polymer scaffolds using a solvent merging/particulate leaching method, Journal of Biomedical Materials Research 59 (4) (2002) 676–81.

[240] Q. Yang, L. Chen, X. Y. Shen, Z. Q. Tan, Preparation of polycaprolactone tissue engineering scaffolds by improved solvent casting/particulate leaching method, Journal of Macromolecular Science Part B-Physics 45 (6) (2006) 1171–81.

[241] V. P. Shastri, I. Martin, R. Langer, Macroporous polymer foams by hydrocarbon templating, Proceedings of the National Academy of Science of the United States of America 97 (5) (2000) 1970–5.

[242] A. S. Goldstein, G. Zhu, G. E. Morris, R. K. Meszlenyi, A. G. Mikos, Effect of osteoblastic culture conditions on the structure of poly(DL-lactic-co-glycolic acid) foam scaffolds, Tissue Engineering 5 (5) (1999) 421–34.

[243] R. C. Thomson, M. J. Yaszemski, J. M. Powers, A. G. Mikos, Hydroxyapatite fiber reinforced poly(alpha-hydroxy ester) foams for bone regeneration, Biomaterials 19 (21) (1998) 1935–43.

[244] L. L. Ren, Y. P. Zeng, D. L. Jiang, Preparation of porous TiO2 by a novel freeze casting, Ceramics International 35 (3) (2009) 1267–70.

[245] Y. Suetsugu, Y. Hotta, M. Iwasashi, M. Sakane, M. Kikuchi, T. Ikoma, T. Higaki, N. Ochiai, J. Tanaka, Structural and tissue reaction properties of novel hydroxyapatite ceramics with unidirectional pores, Bioceramics 19, Pts 1 and 2 (330-332) (2007) 1003–6.

[246] S. C. Schneid, H. Gieseler, W. J. Kessler, S. A. Luthra, M. J. Pikal, Optimization of the secondary drying step in freeze drying using TDLAS technology, AAPS PharmSciTech 12 (1) (2011) 379–87.

[247] M. J. Pikal, S. Shah, M. L. Roy, R. Putman, The secondary stage of freeze drying: drying kinetics as a function of temperature and chamber pressure, International Journal of Pharmaceutics 60 (3) (1990) 203–7.

[248] X. Tang, M. J. Pikal, Design of freeze-drying processes for pharmaceuticals: practical advice, Pharmaceutical Research 21 (2) (2004) 191–200.

[249] W. Abdelwahed, G. Degobert, S. Stainmesse, H. Fessi, Freeze-drying of nanoparticles: formulation, process and storage considerations, Advanced Drug Delivery Reviews 58 (15) (2006) 1688–713.

[250] Q. Fu, M. N. Rahaman, F. Dogan, B. S. Bal, Freeze casting of porous hydroxyapatite scaffolds. 1. processing and general microstructure, Journal of Biomedical Materials Research Part B: Applied Biomaterials 86 (1) (2008) 125–35.

[251] C. Q. Hong, X. H. Zhang, J. C. Han, J. C. Du, W. Zhang, Camphene-based freeze-cast ZrO(2) foam with high compressive strength, Materials Chemistry and Physics 119 (3) (2010) 359–62.

[252] H. D. Jung, S. W. Yook, H. E. Kim, Y. H. Koh, Fabrication of titanium scaffolds with porosity and pore size gradients by sequential freeze casting, Materials Letters 63 (17) (2009) 1545–7.

[253] K. K. Mallick, Freeze Casting of Porous Bioactive Glass and Bioceramics, Journal of the American Ceramic Society 92 (1) (2009) S85–S94.

[254] A. Macchetta, I. G. Turner, C. R. Bowen, Fabrication of HA/TCP scaffolds with a graded and porous structure using a camphene-based freeze-casting method, Acta Biomaterialia 5 (4) (2009) 1319–27.

[255] E. Munch, E. Saiz, A. P. Tomsia, S. Deville, Architectural Control of Freeze-Cast Ceramics Through Additives and Templating, Journal of the American Ceramic Society 92 (7) (2009) 1534–9.

[256] S. Deville, Ice-templating, freeze casting: Beyond materials processing, Journal of Materials Research 28 (17) (2013) 2202–19.

[257] S. Deville, Freeze-Casting of Porous Ceramics: A Review of Current Achievements and Issues, Advanced Engineering Materials 10 (3) (2008) 155–69.

[258] U. G. Wegst, M. Schecter, A. E. Donius, P. M. Hunger, Biomaterials by freeze casting, Philosophical Transactions. Series A, Mathematical, Physical and Engineering Science 368 (1917) (2010) 2099–121.

[259] S. Deville, Freeze-Casting of Porous Biomaterials: Structure, Properties and Opportunities, Materials 3 (3) (2010) 1913–27.

[260] S. Deville, E. Saiz, A. P. Tomsia, Freeze casting of hydroxyapatite scaffolds for bone tissue engineering, Biomaterials 27 (32) (2006) 5480–9.

[261] C. M. Murphy, M. G. Haugh, F. J. O'Brien, The effect of mean pore size on cell attachment, proliferation and migration in collagen-glycosaminoglycan scaffolds for bone tissue engineering, Biomaterials 31 (3) (2010) 461–6.

[262] K. Scoffin, Scaling the Scaffolds: Control of Pore Size in Tissue Engineering Scaffolds, Labcompare 2012.

[263] B. Ambasta, Phase Equilibria (Phase Rule), 4th Edition, University Science Press, India, 2012, Ch. 2, pp. 47–81.

[264] Q. Fu, M. N. Rahaman, B. S. Bal, R. F. Brown, Proliferation and function of MC3T3-E1 cells on freeze-cast hydroxyapatite scaffolds with oriented pore architectures, Journal of Materials Science-Materials in Medicine 20 (5) (2009) 1159–65.

[265] J. H. Song, Y. H. Koh, H. E. Kim, L. H. Li, H. J. Bahn, Fabrication of a porous bioactive glass-ceramic using room-temperature freeze casting, Journal of the American Ceramic Society 89 (8) (2006) 2649–53.

[266] S. I. Roohani-Esfahani, S. Nouri-Khorasani, Z. F. Lu, R. Appleyard, H. Zreiqat, The influence hydroxyapatite nanoparticle shape and size on the properties of biphasic calcium phosphate scaffolds coated with hydroxyapatite-PCL composites, Biomaterials 31 (21) (2010) 5498–509.

[267] K. K. Mallick, J. Winnett, Porous Biodegradable Scaffolds for Hard Tissue Engineering, John Wiley & Sons, Inc., 2011, pp. 57–66.

[268] J. Lee, H. Choi, S. Yoon, B. Kim, H. Park, Processing of porous hydroxyapatite scaffolds containing calcium phosphate glass-ceramics for bone tissue engineering, Ceramic Processing Research 14 (4) (2013) 544–8.

[269] N. Bakunova, V. Komlev, A. Y. Fedotov, I. Fadeeva, V. Smirnov, L. Shvorneva, A. Gurin, S. Barinov, A method of fabrication of porous carbonated hydroxyapatite scaffolds for bone tissue engineering, Powder Metallurgy Progress 8 (4) (2008) 336–42.

[270] S. Kwon, Y. Jun, S. Hong, I. Lee, H. E. Kim, Calcium Phosphate Bioceramics with Various Porosities and Dissolution Rates, Journal of the American Ceramic Society 85 (12) (2002) 3129–31.

[271] S. Teixeira, M. Rodriguez, P. Pena, A. De Aza, S. De Aza, M. Ferraz, F. Monteiro, Physical characterization of hydroxyapatite porous scaffolds for tissue engineering, Materials Science and Engineering: C 29 (5) (2009) 1510–4.

[272] G. Tripathi, B. Basu, A porous hydroxyapatite scaffold for bone tissue engineering: Physico-mechanical and biological evaluations, Ceramics International 38 (2012) 341–9.

[273] E. Cunningham, N. Dunne, G. Walker, C. Maggs, R. Wilcox, F. Buchanan, Hydroxyapatite bone substitutes developed via replication of natural marine

sponges, Journal of Materials Science-Materials in Medicine 21 (8) (2010) 2255–61.

[274] J. Kim, D. Lim, Y. H. Kim, Y. H. Koh, M. H. Lee, I. Han, S. J. Lee, O. S. Yoo, H. S. Kim, J. C. Park, A Comparative Study of the Physical and Mechanical Properties of Porous Hydroxyapatite Scaffolds Fabricated by Solid Freeform Fabrication and Polymer Replication Method, International Journal of Precision Engineering and Manufacturing 12 (4) (2011) 695–701.

[275] J. P. Li, S. H. Li, C. A. Van Blitterswijk, K. de Groot, A novel porous Ti6Al4V: Characterization and cell attachment, Journal of Biomedical Materials Research Part A 73A (2) (2005) 223–33.

[276] I. H. Jo, K. H. Shin, Y. M. Soon, Y. H. Koh, J. H. Lee, H. E. Kim, Highly porous hydroxyapatite scaffolds with elongated pores using stretched polymeric sponges as novel template, Materials Letters 63 (20) (2009) 1702–4.

[277] E. Cunningham, N. Dunne, S. Clarke, S. Choi, G. Walker, R. Wilcox, R. Unger, F. Buchanan, C. Kirkpatrick, Comparative Characterisation of 3-D Hydroxyapatite Scaffolds Developed Via Replication of Synthetic Polymer Foams and Natural Marine Sponges, Tissue Science and Engineering S1 (001).

[278] J. Winnett, Development of a Novel Foam Reticulation Method for the Fabrication and Characterisation of Ceramic Scaffolds, Dissertation.

[279] K. K. Mallick, J. Winnett, Preparation and Characterization of Porous Bioglass (R) and PLLA Scaffolds for Tissue Engineering Applications, Journal of the American Ceramic Society 95 (9) (2012) 2680–6.

[280] G. Muralithran, S. Ramesh, The effects of sintering temperature on the properties of hydroxyapatite, Ceramics International 26 (2000) 221–30.

[281] J. Lee, H. Choi, S. Yoon, B. Kim, H. Park, Porous mullite ceramics derived from coal fly ash using a freeze-gel casting/polymer sponge technique, Journal of Porous Materials 20 (1).

[282] A. G. A. Coombes, J. D. Heckman, Gel Casting of Resorbable Polymers .1. Processing and Applications, Biomaterials 13 (4) (1992) 217–24.

[283] P. Sepulveda, J. G. P. Binner, S. O. Rogero, O. Z. Higa, J. C. Bressiani, Production of porous hydroxyapatite by the gel-casting of foams and cytotoxic evaluation, Journal of Biomedical Materials Research 50 (1) (2000) 27–34.

[284] S. Dhara, R. K. Kamboj, M. Pradhan, P. Bhargava, Shape forming of ceramics via gelcasting of aqueous particulate slurries, Bulletin of Materials Science 25 (6) (2002) 565–8.

[285] B. Chen, T. Zhang, J. Zhang, Q. Lin, D. Jiang, Microstructure and mechanical properties of hydroxyapatite obtained by gel-casting process, Ceramics International 34 (2) (2008) 359–64.

[286] S. P. Jiang, L. Z. Ab, Y. Zhang, Lanthanum strontium manganese chromite cathode and anode synthesized by gel-casting for solid oxide fuel cells, Journal of Materials Chemistry 17 (25) (2007) 2627–35.

[287] J. Yang, J. Yu, Y. Huang, Recent developments in gelcasting of ceramics, Journal of the European Ceramic Society 31 (14) (2011) 2569–91.

[288] J. A. Puertolas, J. L. Vadillo, S. Sanchez-Salcedo, A. Nieto, E. Gomez-Barrena, M. Vallet-Regi, Compression behaviour of biphasic calcium phosphate and biphasic calcium phosphate-agarose scaffolds for bone regeneration, Acta Biomaterialia 7 (2) (2011) 841–7.

[289] Y. Jia, Y. Kanno, Z. P. Xie, New gel-casting process for alumina ceramics based on gelation of alginate, Journal of the European Ceramic Society 22 (12) (2002) 1911–6.

[290] J. Ha, Effect of atmosphere type on gelcasting behavior of Al2O3 and evaluation of green strength, Ceramics International 26 (2000) 251–4.

[291] M. Kokabi, A. Babaluo, A. Barati, Gelation process in low-toxic gelcasting systems, Journal of the European Ceramic Society 26 (15) (2006) 3083–90.

[292] K. Cai, Y. Huang, J. Yang, Alumina gelcasting by using HEMA system, Journal of the European Ceramic Society 25 (7) (2005) 1089–93.

[293] L. L. Hench, J. K. West, The Sol-Gel Process, Chemical Reviews 90 (1) (1990) 33–72.

[294] M. Vallet-Regi, Nanostructured mesoporous silica matrices in nanomedicine, Journal of International Medicine 267 (1) (2010) 22–43.

[295] D. Arcos, M. Vallet-Regi, Sol-gel silica-based biomaterials and bone tissue regeneration, Acta Biomaterialia 6 (8) (2010) 2874–88.

[296] W. Zeng, X. F. Qian, Y. B. Zhang, J. Yin, Z. K. Zhu, Organic modified mesoporous MCM-41 through solvothermal process as drug delivery system, Materials Research Bulletin 40 (5) (2005) 766–72.

[297] D. Avnir, T. Coradin, O. Lev, J. Livage, Recent bio-applications of sol-gel materials, Journal of Materials Chemistry 16 (11) (2006) 1013–30.

[298] J. Zarzycki, Past and present of sol-gel science and technology, Journal of Sol-Gel Science and Technology 8 (1-3) (1997) 17–22.

[299] T. Coradin, M. Boissiere, J. Livage, Sol-gel chemistry in medicinal science, Current Medicinal Chemistry 13 (1) (2006) 99–108.

[300] R. Gupta, A. Kumar, Bioactive materials for biomedical applications using sol-gel technology, Biomedical Materials 3 (3).

[301] S. Lin, C. Ionescu, K. J. Pike, M. E. Smith, J. R. Jones, Nanostructure evolution and calcium distribution in sol-gel derived bioactive glass, Journal of Materials Chemistry 19 (9) (2009) 1276–82.

[302] H. Podbielska, A. Ulatowska-Jarza, Sol-gel technology for biomedical engineering, Bulletin of the Polish Academy of Sciences 53 (3) (2005) 261–71.

[303] A. Nieto, S. Areva, T. Wilson, R. Viitala, M. Vallet-Regi, Cell viability in a wet silica gel, Acta Biomaterialia 5 (9) (2009) 3478–87.

[304] A. Balamurugan, G. Sockalingum, J. Michel, J. Faure, V. Banchet, L. Wortham, S. Bouthors, D. Laurent-Maquin, G. Balossier, Synthesis and characterisation of sol gel derived bioactive glass for biomedical applications, Materials Letters 60 (29-30) (2006) 3752–7.

[305] A. Garcia, I. Izquierdo-Barba, M. Colilla, C. L. de Laorden, M. Vallet-Regi, Preparation of 3-D scaffolds in the SiO(2)-P(2)O(5) system with tailored hierarchical meso-macroporosity, Acta Biomaterialia 7 (3) (2011) 1265–73.

[306] M. G. Raucci, V. Guarino, L. Ambrosio, Hybrid composite scaffolds prepared by sol-gel method for bone regeneration, Composites Science and Technology 70 (13) (2010) 1861–8.

[307] B. Lei, X. F. Chen, Y. J. Wang, N. R. Zhao, G. H. Miao, Z. M. Li, C. Lin, Fabrication of porous bioactive glass particles by one step sintering, Materials Letters 64 (21) (2010) 2293–5.

[308] M. Ferrer, Z. Garcia-Carvajal, L. Yuste, F. Rojo, F. del Monte, Bacteria Viability in Sol-Gel Materials Revisited: Cryo-SEM as a Suitable Tool To Study the Structural Integrity of Encapsulated Bacteria, Chemistry of Materials 18 (6) (2006) 1458–63.

[309] G. Kuncova, O. Podrazky, S. Ripp, J. Trogl, K. Demnerova, R. Vankova, Monitoring of the Viability of Cells Immobilized by Sol-Gel Process, Journal of Sol-Gel Science and Technology 31 (2004) 335–42.

[310] E. Sachlos, J. T. Czernuszka, Making tissue engineering scaffolds work. review: the application of solid freeform fabrication technology to the production of tissue engineering scaffolds, European Cells and Materials 5 (2003) 29–40;.

[311] S. M. Peltola, F. P. Melchels, D. W. Grijpma, M. Kellomaki, A review of rapid prototyping techniques for tissue engineering purposes, Annals of Medicine 40 (4) (2008) 268–80.

[312] K. F. Leong, C. M. Cheah, C. K. Chua, Solid freeform fabrication of three-dimensional scaffolds for engineering replacement tissues and organs, Biomaterials 24 (13) (2003) 2363–78.

[313] A. Butscher, M. Bohner, S. Hofmann, L. Gauckler, R. Muller, Structural and material approaches to bone tissue engineering in powder-based three-dimensional printing, Acta Biomaterialia 7 (3) (2011) 907–20.

[314] F. P. W. Melchels, J. Feijen, D. W. Grijpma, A poly(D,L-lactide) resin for the preparation of tissue engineering scaffolds by stereolithography, Biomaterials 30 (23-24) (2009) 3801–9.

[315] F. P. W. Melchels, J. Feijen, D. W. Grijpma, A review on stereolithography and its applications in biomedical engineering, Biomaterials 31 (24) (2010) 6121–30.

[316] G. T. M. Chu, G. A. Brady, W. G. Miao, J. W. Halloran, S. J. Hollister, D. Brei, Ceramic SFF by direct and indirect stereolithography, Solid Freeform and Additive Fabrication 542 (1999) 119–23.

[317] J. Jansen, F. P. Melchels, D. W. Grijpma, J. Feijen, Fumaric acid monoethyl ester-functionalized poly(D,L-lactide)/N-vinyl-2-pyrrolidone resins for the preparation of tissue engineering scaffolds by stereolithography, Biomacromolecules 10 (2) (2009) 214–20.

[318] B. Leukers, H. Gulkan, S. H. Irsen, S. Milz, C. Tille, M. Schieker, H. Seitz, Hydroxyapatite scaffolds for bone tissue engineering made by 3D printing, Journal of Materials Science: Materials in Medicine 16 (12) (2005) 1121–4.

[319] B. Leukers, H. Gulkan, S. H. Irsen, S. Milz, C. Tille, H. Seitz, M. Schieker, Biocompatibility of ceramic scaffolds for bone replacement made by 3D printing, Materialwissenschaft Und Werkstofftechnik 36 (12) (2005) 781–7.

[320] C. T. Wu, Y. X. Luo, G. Cuniberti, Y. Xiao, M. Gelinsky, Three-dimensional printing of hierarchical and tough mesoporous bioactive glass scaffolds with a

controllable pore architecture, excellent mechanical strength and mineralization ability, Acta Biomaterialia 7 (6) (2011) 2644–50.

[321] E. Sachs, C. Cima, J. Cornie, Three-Dimensional Printing: Rapid tooling and prototypes Directly from a CAD Model, Journal of Engineering for Industry 114 (4) (1992) 481–8.

[322] H. Seitz, W. Rieder, S. Irsen, B. Leukers, C. Tille, Three-dimensional printing of porous ceramic scaffolds for bone tissue engineering, Journal of Biomedical Materials Research Part B: Applied Biomaterials 74 (2) (2005) 782–8.

[323] B. Y. Nan, X. W. Yin, L. T. Zhang, L. F. Cheng, Three-Dimensional Printing of Ti(3)SiC(2)-Based Ceramics, Journal of the American Ceramic Society 94 (4) (2011) 969–72.

[324] J. Will, R. Melcher, C. Treul, N. Travitzky, U. Kneser, E. Polykandriotis, R. Horch, P. Greil, Porous ceramic bone scaffolds for vascularized bone tissue regeneration, Journal of Materials Science-Materials in Medicine 19 (8) (2008) 2781–90.

[325] C. K. Chua, K. F. Leong, K. H. Tan, F. E. Wiria, C. M. Cheah, Development of tissue scaffolds using selective laser sintering of polyvinyl alcohol/hydroxyapatite biocomposite for craniofacial and joint defects, Journal of Materials Science-Materials in Medicine 15 (10) (2004) 1113–21.

[326] J. M. Williams, A. Adewunmi, R. M. Schek, C. L. Flanagan, P. H. Krebsbach, S. E. Feinberg, S. J. Hollister, S. Das, Bone tissue engineering using polycaprolactone scaffolds fabricated via selective laser sintering, Biomaterials 26 (23) (2005) 4817–27.

[327] F. E. Wiria, K. F. Leong, C. K. Chua, Y. Liu, Poly-epsilon-caprolactone/hydroxyapatite for tissue engineering scaffold fabrication via selective laser sintering, Acta Biomaterialia 3 (1) (2007) 1–12.

[328] K. H. Tan, C. K. Chua, K. F. Leong, C. M. Cheah, P. Cheang, M. S. Abu Bakar, S. W. Cha, Scaffold development using selective laser sintering of polyetheretherketone-hydroxyapatite biocomposite blends, Biomaterials 24 (18) (2003) 3115–23.

[329] W. Y. Zhou, S. H. Lee, M. Wang, W. L. Cheung, W. Y. Ip, Selective laser sintering of porous tissue engineering scaffolds from poly(l)/carbonated hydroxyapatite nanocomposite microspheres, Journal of Materials Science-Materials in Medicine 19 (7) (2008) 2535–40.

[330] S. Das, S. J. Hollister, C. Flanagan, A. Adewunmi, K. Bark, C. Chen, K. Ramaswamy, D. Rose, E. Widjaja, Freeform fabrication of Nylon-6 tissue engineering scaffolds, Rapid Prototyping Journal 9 (1) (2003) 43–9.

[331] Y. Shanjani, Y. X. Hu, R. M. Pilliar, E. Toyserkani, Mechanical characteristics of solid-freeform-fabricated porous calcium polyphosphate structures with oriented stacked layers, Acta Biomaterialia 7 (4) (2011) 1788–96.

[332] Y. Shanjani, J. N. A. De Croos, R. M. Pilliar, R. A. Kandel, E. Toyserkani, Solid freeform fabrication and characterization of porous calcium polyphosphate structures for tissue engineering purposes, Journal of Biomedical Materials Research Part B-Applied Biomaterials 93B (2) (2010) 510–9.

[333] J. R. Woodard, A. J. Hilldore, S. K. Lan, C. J. Park, A. W. Morgan, J. A. Eurell, S. G. Clark, M. B. Wheeler, R. D. Jamison, A. J. Wagoner Johnson, The mechanical properties and osteoconductivity of hydroxyapatite bone scaffolds with multi-scale porosity, Biomaterials 28 (1) (2007) 45–54.

[334] M. N. Rahaman, W. Xiao, B. S. Bal, Development of Implants Composed of Hollow Hydroxyapatite Microspheres for Bone Regeneration, Vol. 251 of Ceramic Transactions, John Wiley & Sons, USA, 2014.

[335] J. G. Dellinger, J. Cesarano, R. D. Jamison, Robotic deposition of model hydroxyapatite scaffolds with multiple architectures and multiscale porosity

for bone tissue engineering, Journal of Biomedical Materials Research Part A 82A (2) (2007) 383–94.

[336] F. J. Martinez-Vazquez, F. H. Perera, P. Miranda, A. Pajares, F. Guiberteau, Improving the compressive strength of bioceramic robocast scaffolds by polymer infiltration, Acta Biomaterialia 6 (11) (2010) 4361–8.

[337] P. Miranda, A. Pajares, E. Saiz, A. P. Tomsia, F. Guiberteau, Mechanical properties of calcium phosphate scaffolds fabricated by robocasting, Journal of Biomedical Materials Research Part A 85A (1) (2008) 218–27.

[338] J. Russias, E. Saiz, S. Deville, K. Gryn, G. Liu, R. K. Nalla, A. P. Tomsia, Fabrication and in vitro characterization of three-dimensional organic/inorganic scaffolds by robocasting, Journal of Biomedical Materials Research Part A 83A (2) (2007) 434–45.

[339] A. Mukherjee, B. Maiti, A. Das Sharma, R. N. Basu, H. S. Maiti, Correlation between slurry rheology, green density and sintered density of tape cast yttria stabilised zirconia, Ceramics International 27 (7) (2001) 731–9.

[340] J. A. Lewis, J. E. Smay, J. Stuecker, J. Cesarano, Direct ink writing of three-dimensional ceramic structures, Journal of the American Ceramic Society 89 (12) (2006) 3599–609.

[341] S. J. Polak, S. K. Levengood, M. B. Wheeler, A. J. Maki, S. G. Clark, A. J. Johnson, Analysis of the roles of microporosity and BMP-2 on multiple measures of bone regeneration and healing in calcium phosphate scaffolds, Acta Biomaterialia 7 (4) (2011) 1760–71.

[342] J. A. Lewis, Direct-write assembly of ceramics from colloidal inks, Current Opinion in Solid State & Materials Science 6 (3) (2002) 245–50.

[343] J. A. Lewis, Direct ink writing of 3D functional materials, Advanced Functional Materials 16 (17) (2006) 2193–204.

[344] J. T. Schantz, A. Brandwood, D. W. Hutmacher, H. L. Khor, K. Bittner, Osteogenic differentiation of mesenchymal progenitor cells in computer designed fibrin-polymer-ceramic scaffolds manufactured by fused deposition modeling, Journal of Materials Science-Materials in Medicine 16 (9) (2005) 807–19.

[345] M. H. Too, K. F. Leong, C. K. Chua, Z. H. Du, S. F. Yang, C. M. Cheah, S. L. Ho, Investigation of 3D non-random porous structures by fused deposition modelling, International Journal of Advanced Manufacturing Technology 19 (3) (2002) 217–23.

[346] S. J. Kalita, S. Bose, H. L. Hosick, A. Bandyopadhyay, Development of controlled porosity polymer-ceramic composite scaffolds via fused deposition modeling, Materials Science & Engineering C-Biomimetic and Supramolecular Systems 23 (5) (2003) 611–20.

[347] C. Liu, Z. Xia, J. T. Czernuszka, Design and development of three-dimensional scaffolds for tissue engineering, Chemical Engineering Research & Design 85 (A7) (2007) 1051–64.

[348] H. W. Kim, H. E. Kim, J. C. Knowles, Bioactive porous bone scaffold coated with biphasic calcium phosphates, Bioceramics 16 254-2 (2004) 1103–6.

[349] E. Ebaretonbofa, J. R. G. Evans, High porosity hydroxyapatite foam scaffolds for bone substitute, Journal of Porous Materials 9 (4) (2002) 257–63.

[350] Y. Gao, W. L. Cao, X. Y. Wang, Y. D. Gong, J. M. Tian, N. M. Zhao, X. F. Zhang, Characterization and osteoblast-like cell compatibility of porous scaffolds: bovine hydroxyapatite and novel hydroxyapatite artificial bone, Journal of Materials Science-Materials in Medicine 17 (9) (2006) 815–23.

[351] X. Li, D. C. Li, L. Wang, B. H. Lu, Z. Wang, Osteoblast cell response to beta-tricalcium phosphate scaffolds with controlled architecture in flow perfusion culture system, Journal of Materials Science-Materials in Medicine 19 (7) (2008) 2691–7.

[352] S. C. Dieudonne, J. van den Dolder, J. E. de Ruijter, H. Paldan, T. Peltola, M. A. van't Hof, R. P. Happonen, J. A. Jansen, Osteoblast differentiation of bone marrow stromal cells cultured on silica gel and sol-gel-derived titania, Biomaterials 23 (14) (2002) 3041–51.

[353] A. Balamurugan, G. Balossier, S. Kannan, J. Michel, A. H. S. Rebelo, J. M. F. Ferreira, Development and in vitro characterization of sol-gel derived CaO-P2O5-SiO2-ZnO bioglass, Acta Biomaterialia 3 (2) (2007) 255–62.

[354] S. S. Kim, M. S. Park, O. Jeon, C. Y. Choi, B. S. Kim, Poly(lactide-co-glycolide)/hydroxyapatite composite scaffolds for bone tissue engineering, Biomaterials 27 (8) (2006) 1399–409.

[355] T. Y. Yang, J. M. Lee, S. Y. Yoon, H. C. Park, Hydroxyapatite scaffolds processed using a TBA-based freeze-gel casting/polymer sponge technique, Journal of Materials Science: Materials in Medicine 21 (5) (2010) 1495–502.

[356] S. J. Hollister, Porous scaffold design for tissue engineering, Nature Materials 4 (7) (2005) 518–24.

[357] L. Hieu, N. Zlatov, J. Vander Sloten, E. Bohez, L. Khanh, P. Binh, P. Oris, Y. Toshev, Medical rapid prototyping applications and methods, Assembly Automation 25 (4) (2005) 284–92.

[358] P. Bartolo, H. Almeida, T. Laoui, Rapid prototyping and manufacturing for tissue engineering scaffolds, International Journal of Computer Applications in Technology 36 (1) (2009) 1–9.

[359] W. Y. Yeong, C. K. Chua, K. F. Leong, M. Chandrasekaran, Rapid prototyping in tissue engineering: challenges and potential, Trends in Biotechnology 22 (12) (2004) 643–52.

[360] H. Wiehler, C. Korner, R. Singer, High pressure integral foam moulding of aluminium - process technology, Advanced Engineering Materials 10 (3) (2008) 171–8.

[361] Y. W. Gu, M. S. Yong, B. Y. Tay, C. S. Lim, Synthesis and bioactivity of porous Ti alloy prepared by foaming with TiH2, Materials Science & Engineering C-Biomimetic and Supramolecular Systems 29 (5) (2009) 1515–20.

[362] J. F. Wang, X. Y. Liu, B. Luan, Fabrication of Ti/polymer biocomposites for load-bearing implant applications, Journal of Materials Processing Technology 197 (1-3) (2008) 428–33.

[363] U. Muller, T. Imwinkelried, M. Horst, M. Sievers, U. Graf-Hausner, Do human osteoblasts grow into open-porous titanium?, European Cells & Materials 11 (2006) 8–15.

[364] M. Dewidar, H. F. Mohamed, J. K. Lim, A New Approach for Manufacturing a High Porosity Ti-6Al-4V Scaffolds for Biomedical Applications, Journal of Materials Science & Technology 24 (6) (2008) 931–5.

[365] E. Hong, B. Y. Ahn, D. Shoji, J. A. Lewis, D. C. Dunand, Microstructure and Mechanical Properties of Reticulated Titanium Scrolls, Advanced Engineering Materials 13 (12) (2011) 1122–7.

[366] D. Jorgensen, D. C. Dunand, Structure and mechanical properties of Ti-6Al-4V with a replicated network of elongated pores, Acta Materialia 59 (2011) 640–50.

[367] A. Barbas, A. S. Bonnet, P. Lipinski, R. Pesci, G. Dubois, Development and mechanical characterization of porous titanium bone substitutes, Journal of Mechanical Behaviour of Biomedical Materials 9 (2012) 34–44.

[368] A. H. Brothers, D. C. Dunand, Amorphous metal foams, Scripta Materialia 54 (4) (2006) 513–20.

[369] S. Deville, E. Saiz, A. P. Tomsia, Ice-templated porous alumina structures, Acta Materialia 55 (6) (2007) 1965–74.

[370] F. C. Buciuman, B. Kraushaar-Czarnetzki, Ceramic foam monoliths as catalyst carriers. 1. Adjustment and description of the morphology, Industrial & Engineering Chemistry Research 42 (9) (2003) 1863–9.

[371] H. Mahdjoub, P. Roy, C. Filiatre, G. Bertrand, C. Coddet, The effect of the slurry formulation upon the morphology of spray-dried yttria stabilised zirconia particles, Journal of the European Ceramic Society 23 (10) (2003) 1637–48.

[372] J.-H. Sung, K.-H. Shin, Y. H. Koh, W. Y. Choi, Y. Jin, H. E. Kim, Preparation of the reticulated hydroxyapatite ceramics using carbon-coated polymeric sponge with elongated pores as a novel template, Ceramics International 37 (2011) 2591–6.

[373] Y. Zhang, M. Q. Zhang, Three-dimensional macroporous calcium phosphate bioceramics with nested chitosan sponges for load-bearing bone implants, Journal of Biomedical Materials Research 61 (1) (2002) 1–8.

[374] L. Nie, J. Suo, P. Zou, S. Feng, Preparation and Properties of Biphasic Calcium Phosphate Scaffolds Multiply Coated with HA/PLLA Nanocomposites for Bone Tissue Engineering Applications, Journal of Nanomaterials 2012 (2012) 11.

[375] D. Bellucci, V. Cannillo, A. Sola, Shell Scaffolds: A new approach towards high strength bioceramic scaffolds for bone regeneration, Materials Letters 64 (2) (2010) 203–6.

[376] D. Bellucci, F. Chiellini, G. Ciardelli, M. Gazzarri, P. Gentile, A. Sola, V. Cannillo, Processing and characterization of innovative scaffolds for bone tissue engineering, Journal of Materials Science-Materials in Medicine 23 (6) (2012) 1397–409.

[377] Z. K. Hong, A. X. Liu, L. Chen, X. S. Chen, X. B. Jing, Preparation of bioactive glass ceramic nanoparticles by combination of sol-gel and coprecipitation method, Journal of Non-Crystalline Solids 355 (6) (2009) 368–72.

[378] N. C. for Biotechnology Information, Pubchem compound database: Camphene, Retrieved 23 June 2015 CID 6616 (2015) http://pubchem.ncbi.nlm.nih.gov/compound/6616.

[379] H. Sandim, B. Morante, P. Suzuki, Kinetics of thermal decomposition of titanium hydride powder using in situ high-temperature X-ray diffraction (HTXRD), Materials Research 8 (3) (2005) 293–7.

[380] D. Schur, Y. Zaginaichenko, V. Adejev, V. Voitovich, A. Lyashenko, V. Trefilov, Phase Transformations in Titanium Hydrides, International Journal of Hydrogen Energy 21 (11/12) (1996) 1121–4.

[381] K. Erk, D. C. Dunand, K. Shull, Titanium with controllable pore fractions by thermoreversible gelcasting of TiH2, Acta Materialia 56 (2008) 5147–57.

[382] P. P. Ewald, Fifty years of X-ray diffraction. Dedicated to the International Union of Crystallography on the occasion of the commemoration meeting in Munich, July 1962, Published for the International Union of Crystallography by A. Oosthoek's Uitgeversmij., Utrecht„ 1962, pp. ix, 720 p.

[383] B. D. Cullity, S. Stock, Elements of X-Ray Diffraction, 3rd Edition, Prentice-Hall, Inc„ USA, 2001, p. 664.

[384] P. E. J. Flewitt, R. K. Wild, Physical methods for materials characterisation, 2nd Edition, Series in materials science and engineering, Institute of Physics Pub., Bristol ; Philadelphia, 2003, pp. xii, 602 p.

[385] J. Loizeau, D. Arbouille, S. Santiago, J. Vernet, Evaluation of a wide range laser diffraction grain size analyser for use with sediments, Sedimentology 41 (1994) 353–361. doi:10.1111/j.1365-3091.1994.tb01410.x.

[386] D. Black, M. McQuay, M. Bonin, Laser-baser techniques for particle-size measurement: A review of sizing methods and their industrial applications, Progress in Energy and Combustion Science 22 (3) (1996) 267–306. doi:10.1016/S0360-1285(96)00008-1.

[387] M. Konert, J. Vandenberghe, Comparison of laser grain size analysis with pipette and sieve analysis: a solutionf for the underestimation of the clay fraction, Sedimentology 44 (3) (1997) 523–535. doi:10.1046/j.1365-3091.1997.d01-38.x.

[388] B. Davis, N. Cho, Theory and Application of X-Ray Diffraction Compound Analysis to High-Volume Filter Samples, Atmospheric Environment 11 (73-85).

[389] B. Davis, "Standardless" X-ray diffraction quantitative analysis, Atmospheric Environment 14 (1980) 217–20.

[390] L. Guo, H. Li, X. Gao, Phase transformations and structure characterization of calcium polyphosphate during sintering process, Journal of Materials Science 39 (23) (2004) 7041–7.

[391] M. E. Brown, Introduction to thermal analysis : techniques and applications, Chapman and Hall, London ; New York, 1988, pp. viii, 211 p.

[392] T. Ozawa, Thermal analysis - review and prospect, Thermochimica Acta 355 (1-2) (2000) 35–42.

[393] H. Horowitz, G. Metzger, A New Analysis of Thermogravimetric Traces, Analytical Chemistry 35 (10) (1963) 1464–8.

[394] R. C. Mackenzie, Origin and Development of Differential Thermal-Analysis, Thermochimica Acta 73 (3) (1984) 307–67.

[395] Mackenzi.Rc, C. J. Keattch, Dollimor.D, Forreste.Ja, A. A. Hodgson, J. P. Redfern, Differential Thermal Analysis, Chemistry & Industry (2) (1971) 57–&.

[396] C. B. Murphy, Differential Thermal Analysis, Analytical Chemistry 30 (4) (1958) 867–72.

[397] W. Symkatz-Kloss, Application of Differential Thermal Analysis in Mineralogy, Journal of Thermal Analysis 23 (1982) 15–44.

[398] G. Hohne, W. Hemminger, H. J. Flammersheim, Differential scanning calorimetry : an introduction for practitioners, 2nd Edition, Springer, Berlin ; New York, 2003, pp. xii, 298 p.

[399] H. K. Yuen, G. W. Mappes, W. A. Grote, An Automated-System for Simultaneous Thermal-Analysis and Mass-Spectrometry .1., Thermochimica Acta 52 (1-3) (1982) 143–53.

[400] J. W. S. Hearle, J. T. Sparrow, P. M. Cross, The use of the scanning electron microscope, 1st Edition, Pergamon Press, Oxford, New York„ 1972, pp. xi, 278 p.

[401] O. C. Wells, Scanning electron microscopy, McGraw-Hill, New York„ 1974, pp. xviii, 421 p.

[402] M. L. Bouxsein, S. K. Boyd, B. A. Christiansen, R. E. Guldberg, K. J. Jepsen, R. Muller, Guidelines for Assessment of Bone Microstructure in Rodents Using Micro-Computed Tomography, Journal of Bone and Mineral Research 25 (7) (2010) 1468–86.

[403] S. K. Boyd, S. Moser, M. Kuhn, R. J. Klinck, P. L. Krauze, R. Musser, J. S. Gasser, Evaluation of three-dimensional image registration methodologies for in vivo micro-computed tomography, Annals of Biomedical Engineering 34 (10) (2006) 1587–99.

[404] E. L. Ritman, Micro-computed tomography-current status and developments, Annual Review of Biomedical Engineering 6 (2004) 185–208.

[405] L. Wachsmuth, K. Engelke, High-Resolution Imaging of Osteoarthritis Using Microcomputed Tomography, Vol. 2 of Methods in molecular medicine, Humana Press, Totowa, N.J., 2004, Ch. 12, pp. 231–48.

[406] K. Girstmair, G. Kirchner, Towards a completion of Archimedes' treatise on floating bodies, Expositones Mathematicae 26 (3) (2008) 219–36.

[407] J. C. Rice, S. C. Cowin, J. A. Bowman, On the dependence of the elasticity and strength of cancellous bone on apparent density, Journal of Biomechanics 21 (2) (1988) 155–68.

[408] D. J. Sharp, K. E. Tanner, W. Bonfield, Measurement of the density of trabecular bone, Journal of Biomechanics 23 (8) (1990) 853–7.

[409] L. Zou, R. D. Bloebaum, K. N. Bachus, Reproducibility of techniques using Archimedes' principle in measuring cancellous bone volume, Medical Engineering and Physics 19 (1) (1997) 63–8.

[410] C. S. Chang, Measuring density and porosity of grain kernels using a gas pyconometer, Cereal Chemistry 65 (1) (1988) 13–5.

[411] G. Welsch, R. Boyer, E. W. Collings, Materials properties handbook : titanium alloys, ASM International, Materials Park, OH, 1994, pp. xxii, 1176 p.

[412] P. Miranda, A. Pajares, E. Saiz, A. P. Tomsia, F. Guiberteau, Fracture modes under uniaxial compression in hydroxyapatite scaffolds fabricated by robocasting, Journal of Biomedical Materials Research Part A 83 (3) (2007b) 646–55.

[413] D. Woo, Y. Won, H. Kim, D. Lim, A Biomechanical Study of Osteoporotic Vertebral Trabecular Bone: The Use of Micro-CT and High-Resolution Finite Element Analysis, Journal of Mechanical Science and Technology 21 (2007) 593–601.

[414] S. J. Shefelbine, U. Simon, L. Claes, A. Gold, Y. Gabet, I. Bab, R. Muller, P. Augat, Prediction of fracture callus mechanical properties using micro-CT images and voxel-based finite element analysis, Bone 36 (3) (2005) 480–8.

[415] R. Muller, P. Ruegsegger, Micro-Tomographic Imaging for the Nondestructive Evaluation of Trabecular Bone Architecture, Technology and Informatics, IOS Press, Netherlands, 1997, pp. 61–80.

[416] B. Van Rietbergen, H. Weinans, R. Huiskes, Prospects of computer models for the prediction of osteoporotic bone fracture risk, Technology and Informatics, IOS Press, Netherlands, 1997, pp. 25–33.

[417] D. Ulrich, T. Hildebrand, B. Van Rietbergen, R. Muller, P. Ruegsegger, The quality of trabecular bone evaluated with micro-computed tomography, FEA and mechanical testing, Technology and Informatics, IOS Press, Netherlands, 1997, pp. 97–112.

[418] M. Luxner, Finite element modeling concepts and linear analyses of 3D regular open cell structures, Journal of Materials Science 40 (2005) 5859–66.

[419] C. Chua, K. Leong, C. S. Lim, Rapid Prototyping: Pinciples and Applications, 3rd Edition, World Scientific Publishing Co. Pte. Ltd., Singapore, 2010, p. 512.

[420] B. Borah, G. J. Gross, T. E. Dufresne, T. Smith, M. Cockman, P. A. Chmielewski, M. Lundy, J. Hartke, E. Sod, Three-dimensional Microimaging (MRuI and uCT), Finite Element Modeling, and Rapid Prototyping Provide Unique Insights Into Bone Architecture in Osteoporosis, The Anatomical Record 265 (2) (2001) 101–10.

[421] L. J. Gibson, M. F. Ashby, Cellular solids : structure & properties, 1st Edition, Pergamon Press, Oxford Oxfordshire ; New York, 1988, pp. ix, 357 p.

[422] L. J. Gibson, M. F. Ashby, B. A. Harley, Cellular materials in nature and medicine, Cambridge University Press, Cambridge ; New York, 2010, pp. x, 309 p., 14 p. of col. plates.

[423] L. J. Gibson, M. F. Ashby, Cellular solids : structure and properties, 2nd Edition, Cambridge solid state science series, Cambridge University Press, Cambridge ; New York, 1997, pp. xviii, 510 p.

[424] L. F. Nielsen, Strength and Stiffness of Porous Materials, Journal of the American Ceramic Society 73 (1990) 2684–9.

[425] L. F. Nielsen, On strength of porous material: Simple systems and densified systems, Materials and Structures 31 (1998) 651–61.

[426] D. Tadic, F. Beckmann, K. Schwarz, M. Epple, A novel method to produce hydroxyapatite objects with interconnecting porosity that avoids sintering, Biomaterials 25 (16) (2004) 3335–40.

[427] G. Squires, Practical Physics, 3rd Edition, Cambridge University Press, UK, 1985, p. 213.

[428] T. Mosmann, Rapid Colorimetric Assay for Cellular Growth and Survival - Application to Proliferation and Cyto-Toxicity Assays, Journal of Immunological Methods 65 (1-2) (1983) 55–63.

[429] D. Gerlier, N. Thomasset, Use of MTT Colorimetric Assay to Measure Cell Activation, Journal of Immunological Methods 94 (1-2) (1986) 57–63.

[430] M. Ferrari, M. C. Fornasiero, A. M. Isetta, MTT Colorimetric Assay for Testing Macrophage Cytotoxic Activity In-vitro, Journal of Immunological Methods 131 (2) (1990) 165–72.

[431] Y. F. Shi, B. S. Kornovski, R. Savani, E. A. Turley, A Rapid, Multiwell Colorimetric Assay for Chemotaxis, Journal of Immunological Methods 164 (2) (1993) 149–54.

[432] D. Vanhee, M. Joseph, H. Vorng, A. B. Tonnel, A Colorimetric Assay to Evaluate the Immune Reactivity of Blood-Platelets Based on the Reduction of a Tetrazolium Salt, Journal of Immunological Methods 159 (1-2) (1993) 253–9.

[433] C. J. Goodwin, S. J. Holt, S. Downes, N. J. Marshall, Microculture Tetrazolium Assays - a Comparison between 2 New Tetrazolium Salts, XTT and MTS, Journal of Immunological Methods 179 (1) (1995) 95–103.

[434] J. A. Barltrop, T. C. Owen, A. H. Cory, J. G. Cory, 5-(3-Carboxymethoxyphenyl)-2-(4,5-Dimethylthiazolyl)-3-(4-

Sulfophenyl)Tetrazolium, Inner Salt (MTS) and Related Analogs of 3-(4,5-Dimethylthiazolyl)-2,5-Diphenyltetrazolium Bromide (MTT) Reducing to Purple Water-Soluble Formazans as Cell-Viability Indicators, Bioorganic & Medicinal Chemistry Letters 1 (11) (1991) 611–&.

[435] T. M. Buttke, J. A. Mccubrey, T. C. Owen, Use of an Aqueous Soluble Tetrazolium Formazan Assay to Measure Viability and Proliferation of Lymphokine-Dependent Cell-Lines, Journal of Immunological Methods 157 (1-2) (1993) 233–40.

[436] M. I. Patel, R. Tuckerman, Q. H. Dong, A pitfall of the 3-(4,5-dimethylthiazol-2-yl)-5(3-carboxymethonyphenol)-2-(4-sulfophenyl)-2H-tetrazolium (MTS) assay due to evaporation in wells on the edge of a 96 well plate, Biotechnology Letters 27 (11) (2005) 805–8.

[437] C. Pannecouque, D. Daelemans, E. De Clercq, Tetrazolium-based colorimetric assay for the detection of HIV replication inhibitors: revisited 20 years later, Nature Protocols 3 (3) (2008) 427–34.

[438] S. L. Voytik-Harbin, A. O. Brightman, B. Waisner, C. H. Lamar, S. F. Badylak, Application and evaluation of the alamarBlue assay for cell growth and survival of fibroblasts, In Vitro Celular & Developmental Biology - Animal 34 (3) (1998) 239–46.

[439] A. Schreer, C. Tinson, J. P. Sherry, K. Schirmer, Application of Alamar blue/5-carboxyfluorescein diacetate acetoxymethyl ester as a noninvasive cell viability assay in primary hepatocytes from rainbow trout, Analytical Biochemistry 344 (1) (2005) 76–85.

[440] M. M. Nociari, A. Shalev, P. Benias, C. Russo, A novel one-step, highly sensitive fluorometric assay to evaluate cell-mediated cytotoxicity, Journal of Immunological Methods 213 (2) (1998) 157–67.

[441] S. A. Ahmed, J. Gogal, R. M., J. E. Walsh, A new rapid and simple non-radioactive assay to monitor and determine the proliferation of lymphocytes:

an alternative to [3H]thymidine incorporation assay, Journal of Immunological Methods 170 (2) (1994) 211–24.

[442] S. A. Back, R. Khan, X. D. Gan, P. A. Rosenberg, J. J. Volpe, A new Alamar Blue viability assay to rapidly quantify oligodendrocyte death, Journal of Neuroscience Methods 91 (1-2) (1999) 47–54.

[443] S. Al-Nasiry, N. Geusens, M. Hanssens, C. Luyten, R. Pijnenborg, The use of Alamar Blue assay for quantitative analysis of viability, migration and invasion of choriocarcinoma cells, Human Reproduction 22 (5) (2007) 1304–9.

[444] M. R. Slaughter, P. J. Bugelski, P. J. O'Brien, Evaluation of Alamar Blue reduction for the in vitro assay of hepatocyte toxicity, Toxicology in Vitro 13 (4-5) (1999) 567–9.

[445] H. Puchtler, S. N. Meloan, M. S. Terry, On the history and mechanism of alizarin and alizarin red S stains for calcium, Journal of Histochemistry and Cytochemistry 17 (2) (1969) 110–24.

[446] C. M. Stanford, P. A. Jacobson, E. D. Eanes, L. A. Lembke, R. J. Midura, Rapidly forming apatitic mineral in an osteoblastic cell line (UMR 106-01 BSP), Journal of Biological Chemistry 270 (16) (1995) 9420–8.

[447] K. Basavaiah, SriLatha, J. M. Swamy, Spectrophotometric determination of ceterizine hydrochloride with Alizarin Red S, Talanta 50 (4) (1999) 887–92.

[448] G. Springsteen, B. H. Wang, Alizarin Red S. as a general optical reporter for studying the binding of boronic acids with carbohydrates, Chemical Communications (17) (2001) 1608–9.

[449] C. A. Gregory, W. G. Gunn, A. Peister, D. J. Prockop, An Alizarin red-based assay of mineralization by adherent cells in culture: comparison with cetylpyridinium chloride extraction, Analytical Biochemistry 329 (1) (2004) 77–84.

[450] J. Bowers, G. N., R. B. McComb, A continuous spectrophotometric method for measuring the activity of serum alkaline phosphatase, Clinical Chemistry 12 (2) (1966) 70–89.

[451] R. B. McComb, J. Bowers, G. N., Study of optimum buffer conditions for measuring alkaline phosphatase activity in human serum, Clinical Chemistry 18 (2) (1972) 97–104.

[452] Bernstin.Eg, M. L. Hooper, Grandcha.S, B. Ephrussi, Alkaline-Phosphatase Activity in Mouse Teratoma, Proceedings of the National Academy of Sciences of the United States of America 70 (12) (1973) 3899–903.

[453] A. A. Monte, C. Chiang, Alkaline Phosphatase Assay, Mallinckrodt, Inc. Patent No.: 3,926,765 (467,319) (1975) 14.

[454] S. Manolagas, D. Burton, L. Deftos, 1,25-Dihydroxyvitamin D3 Stimulates the Alkaline Phosphatase Activity of Osteoblast-like Cells, The Journal of Biological Chemistry 256 (14) (1981) 7115–7.

[455] C. Self, Enzyme Amplification - A General Method Applied to Provide an Immunoassisted Assay for Placental Alkaline Phosphatase, Journal of Immunological Methods 76 (1985) 389–93.

[456] I. Bronstein, J. Voyta, G. Thorpe, L. Kricks, G. Armstrong, Chemiluminescent Assay of Alkaline Phosphatase Applied in an Ultrasensitive Enzyme Immunoassay of Thyrotropin, Clinical Chemistry 35 (7) (1989) 1441–6.

[457] Y. Takuwa, C. Ohse, E. A. Wang, J. M. Wozney, K. Yamashita, Bone morphogenetic protein-2 stimulates alkaline phosphatase activity and collagen synthesis in cultured osteoblastic cells, MC3T3-E1, Biochemical and Biophysical Research Communications 174 (1) (1991) 96–101.

[458] J. Gomez, B., S. Ardakani, J. Ju, D. Jenkins, M. J. Cerelli, G. Y. Daniloff, V. T. Kung, Monoclonal antibody assay for measuring bone-specific alkaline phosphatase activity in serum, Clinical Chemistry 41 (11) (1995) 1560–6.

[459] Y. W. Wang, Q. Wu, G. Q. Chen, Attachment, proliferation and differentiation of osteoblasts on random biopolyester poly(3-hydroxybutyrate-co-3-hydroxyhexanoate) scaffolds, Biomaterials 25 (4) (2004) 669–75.

[460] U. Karsten, A. Wollenberger, Determination of DNA and RNA in homogenized cells and tissues by surface fluorometry, Analytical Biochemistry 46 (1) (1972) 135–48.

[461] G. J. Boer, A simplified microassay of DNA and RNA using ethidium bromide, Analytical Biochemistry 65 (1-2) (1975) 225–31.

[462] J. S. Lai, W. Herr, Ethidium bromide provides a simple tool for identifying genuine DNA-independent protein associations, Proceeding of the National Academy of Science of the United States of America 89 (15) (1992) 6958–62.

[463] A. J. Geall, I. S. Blagbrough, Rapid and sensitive ethidium bromide fluorescence quenching assay of polyamine conjugate-DNA interactions for the analysis of lipoplex formation in gene therapy, Journal of Pharmaceutical and Biomedical Analysis 22 (5) (2000) 849–59.

[464] J. D. de Bruijn, C. P. Klein, K. de Groot, C. A. van Blitterswijk, The ultrastructure of the bone-hydroxyapatite interface in vitro, Journal of Biomedical Materials Research 26 (10) (1992) 1365–82.

[465] F. Barrere, C. A. van Blitterswijk, K. de Groot, Bone regeneration: molecular and cellular interactions with calcium phosphate ceramics, International Journal of Nanomedicine 1 (3) (2006) 317–32.

[466] P. Ducheyne, S. Radin, L. King, The effect of calcium phosphate ceramic composition and structure on in vitro behavior. I. Dissolution, Journal of Biomedical Materials Research 27 (1) (1993) 25–34.

[467] Y. F. Chou, W. Huang, J. C. Dunn, T. A. Miller, B. M. Wu, The effect of biomimetic apatite structure on osteoblast viability, proliferation, and gene expression, Biomaterials 26 (3) (2005) 285–95.

[468] C. S. Adams, K. Mansfield, R. L. Perlot, I. M. Shapiro, Matrix regulation of skeletal cell apoptosis. role of calcium and phosphate ions, Journal of Biological Chemistry 276 (23) (2001) 20316–22.

[469] J. D. de Bruijn, C. A. van Blitterswijk, J. E. Davies, Initial bone matrix formation at the hydroxyapatite interface in vivo, Journal of Biomedical Materials Research 29 (1) (1995) 89–99.

[470] H. Yuan, H. Fernandes, P. Habibovic, J. de Boer, A. Barradas, A. de Ruiter, W. Walsh, C. A. Van Blitterswijk, J. D. De Bruijn, Osteoinductive ceramics as a synthetic alternative to autologous bone grafting, Proceedings of the National Academy of Sciences of the United States of America 107 (31) (2010) 13614–9.

[471] P. Ducheyne, Q. Qiu, Bioactive ceramics: the effect of surface reactivity on bone formation and bone cell function, Biomaterials 20 (23-24) (1999) 2287–303.

[472] J. D. De Bruijn, Y. Bovell, C. A. Van Blitterswijk, Structural arrangements at the interface between plasma sprayed calcium phosphates and bone, Biomaterials 15 (7) (1994) 543–50.

[473] M. M. Dvorak, A. Siddiqua, D. T. Ward, D. H. Carter, S. L. Dallas, E. F. Nemeth, D. Riccardi, Physiological changes in extracellular calcium concentration directly control osteoblast function in the absence of calciotropic hormones, Proceedings of the National Academy of Science of the United States of America 101 (14) (2004) 5140–5.

[474] Z. Meleti, I. M. Shapiro, C. S. Adams, Inorganic phosphate induces apoptosis of osteoblast-like cells in culture, Bone 27 (3) (2000) 359–66.

[475] C. G. Bellows, J. N. Heersche, J. E. Aubin, Inorganic phosphate added exogenously or released from beta-glycerophosphate initiates mineralization of osteoid nodules in vitro, Bone and Mineral 17 (1) (1992) 15–29.

[476] J. Beck, G. R., E. Moran, N. Knecht, Inorganic phosphate regulates multiple genes during osteoblast differentiation, including Nrf2, Experimental Cell Research 288 (2) (2003) 288–300.

[477] X. Wu, N. Itoh, T. Taniguchi, T. Nakanishi, K. Tanaka, Requirement of calcium and phosphate ions in expression of sodium-dependent vitamin C transporter 2 and osteopontin in MC3T3-E1 osteoblastic cells, Biochimica et Biophysica Acta 1641 (1) (2003) 65–70.

[478] J. Beck, G. R., B. Zerler, E. Moran, Phosphate is a specific signal for induction of osteopontin gene expression, Proceedings of the National Academy of Sciences of the United States of America 97 (15) (2000) 8352–7.

[479] J. W. Robinson, Atomic Absorption Spectroscopy, Analytical Chemistry 32 (8) (1960) 17A–29A.

[480] T. V. Ramakrishna, J. W. Robinson, P. W. West, The determination of calcium and magnesium by atomic absorption spectroscopy, Analytica Chimica Acta 36 (1) (1966) 57–64.

[481] G. Kessler, M. Wolfman, An Automated Procedure for the Simultaneous Determination of Calcium and Phosphorus, Clinical Chemistry 10 (1964) 686–703.

[482] B. C. Sarkar, U. P. Chauhan, A new method for determining micro quantities of calcium in biological materials, Analytical Biochemistry 20 (1) (1967) 155–66.

[483] D. H. Meun, K. C. Smith, A micro phosphate method, Analytical Biochemistry 26 (3) (1968) 364–8.

[484] P. Kaewruang, S. Benjakul, T. Prodpran, Characteristics and gelling property of phosphorylated gelatin from the skin of unicorn leatherjacket, Food Chemistry 146 (2014) 591–6.

[485] P. S. Chen, Microdetermination of Phosphorus, Analytical Chemistry 28 (11) (1956) 1756–8.

[486] Y. Chen, J.-B. Fan, L. Du, H. Xu, Q.-H. Zhang, Y.-Q. He, The application of phosphate solubilizing endophyte Pantoea dispersa triggers the microbial community in red acidic soil, Applied Soil Ecology 84 (2014) 235–44.

[487] S. Crouch, H. Malmstadt, A Mechanistic Investigation of Molybdenum Blue Method for Determination of Phosphate, Analytical Chemistry 39 (10) (1967) 1084–9.

[488] J. W. Lichtman, J. A. Conchello, Fluorescence microscopy, Nature Methods 2 (12) (2005) 910–9.

[489] P. T. So, C. Y. Dong, B. R. Masters, K. M. Berland, Two-photon excitation fluorescence microscopy, Annual Review of Biomedical Engineering 2 (2000) 399–429.

[490] D. Shotton, N. White, Confocal scanning microscopy: three-dimensional biological imaging, Trends in Biochemical Science 14 (11) (1989) 435–9.

[491] J. B. Pawley, Handbook of biological confocal microscopy, rev. Edition, Plenum Press, New York, 1990, pp. xiii, 232 p.

[492] S. Wright, D. Wright, Introduction to Confocal Microscopy, Vol. 70, Academic Press, USA, 2002, Ch. 1, pp. 2–87.

[493] F.-Z. Schmid, Biological Macromolecules: UV-Visible Spectophotometry, Encyclopedia of Life Sciences.

[494] F. Sanchez Rojas, C. Bosch Ojeda, Recent development in derivative ultraviolet/visible absorption spectophotometry: 2004-2008 A review, Analytica Chimica Acta 635 (2009) 22–44.

[495] A. Gelman, Analysis of Variance - Why it is More Important than Ever, The Annals of Statistics 33 (1) (2005) 1–53.

[496] R. Miller Jr., Beyond ANOVA: Basics of Statistics, 2nd Edition, CRC Press LLC, USA, 1997, p. 336.

[497] C. Hoyt, Test Reliability Estimated by Analysis of Variance, Psychometrika 6 (3) (1941) 153–60.

[498] W. Shallow, J. Monahan, Monte Carlo Comparison of ANOVA, MIVQUE, REML, and ML Estimators of Variance Components, Technometrics 26 (1) (1984) 47–57.

[499] Student, The Probable Error of a Mean, Biometrika 6 (1) (1908) 1–25.

[500] Q. Shao, A Cramer Type Large Deviation Result for Student's t-Statistic, Journal of Theoretical Probability 12 (2) (1999) 385–98.

[501] G. Ruxton, The unequeal variance t-test is an underused alternative to Student's t-test and the Mann-Whitney U test, Behavioral Ecology 17 (4) (2006) 688–90.

[502] A. K. Gayen, The distribution of Student's t in random samples of any size drawn from non-normal universes, Biometrika 36 (3-4) (1949) 353–69.

[503] P. Ramsay, Exact Type 1 Error Rates for Robustness of Student's t Test with Unequal Variances, Journal of Educational and Behavioural Statistics 5 (4) (1980) 337–49.

[504] N. Johnson, Modified t Tests and Confidence Intervals for Asymmetrical Populations, Journal of the American Statistical Association 73 (363) (1978) 536–44.

[505] J. Tukey, The problem of Multiple Comparisons, Chapman and Hall, New York, 1953, Ch. Unpublished Manuscript, pp. 1–300.

[506] A. Hayter, A Proof of the Conjecture that the Tukey-Kramer Multiple Comparisons Procedure is Conservative, The Annals of Statistics 12 (1) (1984) 61–75.

[507] C. Dunnett, Pairwise Multiple Comparisons in the Homogenous Variance, Unequal Sample Size Case, Journal of the American Statistical Association 75 (372) (1980a) 789–95.

[508] C. Dunnett, Pairwise Multiple Comparisons in the Unequal Variance Case, Journal of the American Statistical Association 75 (372) (1980b) 796–800.

[509] T. Sheo, S. Mano, Y. Fujikoshi, A Generalized Tukey Conjecture for Multiple Comparisons among Mean Vectors, Journal of the American Statistical Association 89 (426) (1994) 676–9.

[510] Y. Benjamini, H. Braun, John W. Tukey's contributions to multiple comparisons, The Annals of Statistics 30 (6) (2002) 1576–94.

[511] S. Maxwell, Pairwise Multiple Comparisons in Repeated Measures Designs, Journal of Educational and Behavioural Statistics 5 (3) (1980) 269–87.

[512] H. Keselman, J. Rogan, A Comparison of the Modified-Tukey and Scheffe Methods of Multiple Comparisons for Pairwise Contrasts, Journal of the American Statistical Association 73 (361) (1978) 47–52.

[513] H. Lilliefors, On the Kolmogorov-Smirnov Test for Normality with Mean and Variance Unknown, Journal of the American Statistical Association 62 (318) (1967) 399–402.

[514] H. Lilliefors, On the Kolmogorov-Smirnov Test for the Exponential Distribution with Mean Unknown, Journal of the American Statistical Association 64 (325) (1969) 387–9.

[515] A. Justel, D. Pena, R. Zamar, A multivariate Kolmogorov-Smirnov test of goodness of fit, Statistics and Probability Letters 35 (1997) 251–9.

[516] F. Massay Jr., The Kolmogorov-Smirnov test for goodness of fit, Journal of the American Statistical Association 46 (253) (1951) 68–78.

[517] J. Doob, Heuristic Approach to the Kolmogorov-Smirnov Theorems, The Annals of Mathematical Statistics 20 (3) (1949) 393–403.

[518] D. Darling, The Kolmogorov-Smirnov, Cramer-von Mises Tests, The Annals of Mathematical Statistics 28 (4) (1957) 823–38.

[519] W. Feller, On the Kolmogorov-Smirnov Limit Theorems for Empirical Distributions, The Annals of Mathematical Statistics 19 (2) (1948) 177–89.

[520] J. Kiefer, K-sample analogues of the Kolmogorov-Smirnov and Cramer-V. Mises tests, The Annals of Mathematical Statistics 30 (2) (1959) 420–47.

[521] P. B.V., Semi-quantitative Algorithm, 3rd Edition, Panalytical B.V., UK, 2011, Ch. 9.

[522] R. Snyder, The Use of Reference Intensity Ratios in X-Ray Quantitative Analysis, Powder Diffraction 7 (1992) 186–93.

[523] C. J. Liao, F. H. Lin, K. S. Chen, J. S. Sun, Thermal decomposition and reconstitution of hydroxyapatite in air atmosphere, Biomaterials 20 (19) (1999) 1807–13.

[524] R. Gopal, C. Calvo, Structural Relationship of Whitlockite and betaCa3(PO4)2, Nature 237 (1972) 30–2.

[525] R. Gopal, C. Calvo, J. Ito, W. Sabine, Crystal Structure of Synthetic Mg-Whitlockite, Ca18Mg2H2(PO4)14, Canadian Journal of Chemistry 52 (1973) 1155–64.

[526] I. Fadeev, L. Shvorneva, S. Barinov, V. Orlovski, Synthesis and Structure of Magnesium-Substituted Hydroxyapatite, Inorganic Materials 39 (9) (2003) 947–50.

[527] S. C. Liou, S. Y. Chen, Transformation mechanism of different chemically precipitated apatitic precursors into beta-tricalcium phosphate upon calcination, Biomaterials 23 (23) (2002) 4541–7.

[528] K. A. Gross, C. C. Berndt, Thermal processing of hydroxyapatite for coating production, Journal of Biomedical Materials Research 39 (4) (1998) 580–7.

[529] S. Nakamura, R. Ostsuka, H. Aoki, M. Akao, N. Miura, T. Yamamoto, Thermal Expansion of Hydroxyapatite-beta-Tricalcium Phosphate Ceramics, Thermochimica Acta 165 (57-72).

[530] H. Newesely, High temperature behaviour of hydroxy- and fluorapatite. Crystalchemical implications of laser effects on dental enamel, Journal of Oral Rehabilitation 4 (1) (1977) 97–104.

[531] F. Rouquerol, J. Rouquerol, K. S. W. Sing, Adsorption by powders and porous solids : principles, methodology, and applications, Academic Press, San Diego, 1999, pp. xvi, 467 p.

[532] S. Westermarck, Use of Mercury Porosimetry and Nitrogen Adsorption in Characterisation of the Pore Structure of Mannitol and Microcrystalline Cellulose Powders, Granules and Tablets, University of Helsinki, Ph.D. thesis (2000).

[533] H. R. Ramay, M. Zhang, Preparation of porous hydroxyapatite scaffolds by combination of the gel-casting and polymer sponge methods, Biomaterials 24 (19) (2003) 3293–302.

[534] H. D. Jung, H. E. Kim, Y. H. Koh, Production and evaluation of porous titanium scaffolds with 3-dimensional periodic macrochannels coated with microporous TiO2 layer, Materials Chemistry and Physics (2012) 1–6.

[535] A. Ben-Ze'ev, Animal Cell Shape Changes and Gene Expression, BioEssays 13 (5) (2005) 207–12.

[536] F. Levi-Schaffer, K. Austen, P. Gravallese, R. Stevens, Coculture of interleukin 3-dependent mouse mast cells with fibroblasts results in a phenotypic change of the mast cells, Proceedings of the National Academy of Sciences of the United States of America 83 (17) (1986) 6485–8.

[537] P. Clark, P. Connolly, A. S. Curtis, J. A. Dow, C. D. Wilkinson, Topographical control of cell behaviour: II. Multiple grooved substrata, Development 108 (4) (1990) 635–44.

[538] L. I. Huschtscha, F. C. Lucibello, W. F. Bodmer, A rapid micro method for counting cells "in situ" using a fluorogenic alkaline phosphatase enzyme assay, In Vitro Cellular Devevelopment and Biology 25 (1) (1989) 105–8.

[539] H. Sudo, H. A. Kodama, Y. Amagai, S. Yamamoto, S. Kasai, In vitro differentiation and calcification in a new clonal osteogenic cell line derived from newborn mouse calvaria, Journal of Cellular Biology 96 (1) (1983) 191–8.

[540] L. Charles, D. Yohay, L. Lever, R. Caton, R. Wenstrup, Distinct proliferative and differentiated stages of murine MC3T3-E1 cells in culture: An in vitro model of osteoblast development, Journal of Bone and Mineral Research 7 (6) (1992) 683–92.

[541] H. A. Kodama, Y. Amagai, H. Koyama, S. Kasai, Hormonal responsiveness of a preadipose cell line derived from newborn mouse calvaria, Journal of Cellular Physiology 112 (1) (1982) 83–8.

[542] M. Hurley, C. Abreu, J. Harrison, A. Lichtler, L. Raisz, B. Kream, Basic Fibroblastic Growth Factor Inhibits Type I Collagen Gene Expression in Osteoblastic MC3T3-E1 Cells, The Journal of Biological Chemistry 268 (8) (1993) 5588–93.

[543] Y. Itakura, In vitro study on biocompatibility of implant materials using MC3T3-E1 osteogenic cell line, Nihon Hotetsu Shika Gakkai Zasshi 31 (1) (1987) 21–9.

[544] D. Wang, K. Christensen, K. Chawla, G. Xiao, P. H. Krebsbach, R. T. Franceschi, Isolation and characterization of MC3T3-E1 preosteoblast subclones with distinct in vitro and in vivo differentiation/mineralization potential, Journal of Bone and Mineral Research 14 (6) (1999) 893–903.

[545] N. Kinto, M. Iwamoto, M. Enomoto-Iwamoto, S. Noji, H. Ohuchi, H. Yoshioka, H. Kataoka, Y. Wada, G. Yuhao, H. E. Takahashi, S. Yoshiki, A. Yamaguchi, Fibroblasts expressing Sonic hedgehog induce osteoblast differentiation and ectopic bone formation, Federation of European Biochemical Societies Letters 404 (2-3) (1997) 319–23.

[546] G. Hollox, Microstructure and mechanical behavior of carbides, Materials Science and Engineering 3 (3) (1968) 121–37.

[547] E. Gemelli, N. Camargo, Oxidation kinetics of commercially pure titanium, Materia (Rio de Janeiro) 12 (3) (2007) 525–31.

[548] B. Wendler, K. Jakubowski, Vacuum annealing studies of thin TiC layers on steels, Journal of Vacuum Science and Technology 6 (1988) 93–8.

[549] X. Liu, P. K. Chu, C. X. Ding, Surface modification of titanium, titanium alloys, and related materials for biomedical applications, Materials Science and Engineering Part R: Reports 47 (3-4) (2004) 49–121.

[550] I. Halevy, G. Zamir, M. Winterrose, G. Sanjit, C. Grandini, A. Moreno-Gobbi, Crystallographic structure of Ti-6Al-4V, Ti-HP and Ti-CP under High-Pressure, Journal of Physics: Conference Series 215 (2010) 9.

[551] A. Swarnakar, O. Van der Biest, B. Baufeld, Thermal expansion and lattice parameters of shaped metal deposited Ti-6Al-4V, Journal of Alloys and Compounds 509 (6) (2011) 2723–8.

[552] R. Valiev, V. Gertsman, O. Kaibyshev, The role of non-equilibrium grain boundary structure in strain induced grain boundary migration (recrystallization after small strains), Scripta Materialia 17 (1983) 853–6.

[553] A. Hasnaoui, H. Van Swygenhoven, P. Derlet, On non-equilibrium grain boundaries and their effect on thermal and mechanical behaviour: a molecular dynamics computer simulation, Acta Materialia 50 (2002) 3927–39.

[554] S. Grazulis, D. Chateigner, R. Downs, A. Yokochi, M. Quiros, L. Lutterotti, E. Manakova, J. Butkus, P. Moeck, A. LeBail, Crystallography Open Database - an open-access collection of crystal structures, Journal of Applied Crystallography 42 (2009) 726–9.

[555] S. Grazulis, A. Daskevic, A. Merkys, D. Chateigner, L. Lutterotti, M. Quiros, N. Serebryanaya, P. Moeck, R. Downs, A. LeBail, Crystallography Open Database (COD): an open-access collection of crystal structures and platform for world-wide collaboration, Nucleic Acids Research 40 (2012) D420–D7.

[556] R. Downs, M. Hall-Wallace, The American Mineralogist Crystal Structure, American Mineralogist 88 (2003) 247–50.

[557] S. Bhattarai, K. Khalil, M. Dewidar, P. Hwang, H. Yi, H. Kim, Novel production method and in-vitro cell compatibility of porous Ti-6Al-4V alloy disk for hard tissue engineering, Journal of Biomedical Materials Research Part A 86A (8) (2007) 289–99.

[558] M. Dewidar, J. K. Lim, Properties of solid core and porous surface Ti-6Al-4V implants manufactured by powder metallurgy, Journal of Alloys and Compounds 454 (1-2) (2008b) 442–6.

[559] M. Avrami, Kinetics of phase change. I general theory, The Journal of Chemical Physics 7 (1939) 1103–12.

[560] S. Banerjee, P. Mukhopadhyay, Phase transformations : examples from titanium and zirconium alloys, Pergamon materials series, Elsevier/Pergamon, Amsterdam ; Oxford, 2007, pp. xxii, 813 p.

[561] T. Inoue, Z. Wang, Coupling between stress, temperature, and metallic structures during processes involving phase transformations, Materials Science and Technology 1 (10) (1985) 845–50.

[562] P. Withers, H. Bhadeshia, Residual Stress. Part 2 - Nature and origins, Materials Science and Technology 17 (4) (2001) 366–75.

[563] J. Lettow, Y. Han, P. Schmidt-Winkel, P. Yang, D. Zhao, G. Stucky, J. Ying, Hexagonal to Mesocellular Foam Phase Transition in Polymer-Templated Mesoporous Silicas, Langmuir 16 (22) (2000) 8291–5.

[564] J. P. Li, C. Wilson, J. R. Wijn, C. A. Van Blitterswijk, K. De Groot, Fabrication of porous Ti6Al4V with designed structure by rapid prototyping technology, Bioceramics 19, Pts 1 & 2 (330-332) (2007) 1293–6.

[565] K. H. Shin, Y. M. Soon, Y. H. Koh, J. Lee, W. Y. Choi, H. E. Kim, Fabrication of highly porous titanium (Ti) scaffolds with two interlaced periodic pores, Materials Letters 63 (2009) 1341–3.

[566] B. Powell, D. Tabor, The fracture of titanium carbide under static and sliding conditions, Journal of Physics D: Applied Physics 3 (5) (1970) 783–8.

[567] P. Jindal, A. Santhanam, U. Schleinkofer, A. Shuster, Performance of PVD TiN TiCN and TiAlN coated cemented carbide tools in turning, International Journal of Refractory Metals and Hard Materials 17 (1-3) (1999) 163–70.

[568] S. Zhu, D. Mukherji, W. Chen, Y. Lu, Z. Wang, R. Wahi, Steady state creep behaviour of TiC particulate reinforced Ti-6Al-4V composite, Materials Science and Engineering: A 256 (1-2) (1998) 301–7.

[569] S. Ramalingam, Stoichiometry of TiC and its Significance to the Performance of Hard Metal Compacts, Materials Science and Engineering 29 (1977) 123–30.

[570] E. Pamula, E. Filova, L. Bacakova, V. Lisa, D. Adamczyk, Resorbable polymeric scaffolds for bone tissue engineering: the influence of their microstructure on the growth of human osteoblast-like MG 63 cells, Journal of Biomedical Materials Research Part A 89 (2) (2009) 432–43.

[571] P. Zioupos, R. B. Cook, J. R. Hutchinson, Some basic relationships between density values in cancellous and cortical bone, Journal of Biomechanics 41 (9) (2008) 1961–8.

[572] B. S. Kim, H. J. Kang, J. Lee, Improvement of the compressive strength of a cuttlefish bone-derived porous hydroxyapatite scaffold via polycaprolactone coating, Journal of Biomedical Materials Research Part B: Applied Biomaterials 101 (7) (2013) 1302–9.

[573] B. S. Kim, S. S. Yang, J. Lee, A polycaprolactone/cuttlefish bone-derived hydroxyapatite composite porous scaffold for bone tissue engineering, Journal of Biomedical Materials Research Part B: Applied Biomaterials 102 (5) (2014) 943–51.

[574] J. Li, L. Zhang, S. Lv, S. Li, N. Wang, Z. Zhang, Fabrication of individual scaffolds based on a patient-specific alveolar bone defect model, Journal of Biotechnology 151 (1) (2011) 87–93.

[575] A. Cheng, A. Humayun, D. J. Cohen, B. D. Boyan, Z. Schwartz, Additively manufactured 3D porous Ti-6Al-4V constructs mimic trabecular bone structure and regulate osteoblast proliferation, differentiation and local factor production in a porosity and surface roughness dependent manner, Biofabrication 6 (4) (2014) 045007.

[576] B. Thavornyutikarn, N. Chantarapanich, K. Sitthiseripratip, G. Thouas, Q. Chen, Bone tissue engineering scaffolding: computer-aided scaffolding techniques, Progress in Biomaterials 3 (2-4) (2014) 61–102.

[577] M. Cicuendez, M. Malmsten, J. Doadrio, M. Portoles, I. Izquierdo-Barba, M. Vallet-Regi, Tailoring hierarchical meso-macroporous 3D scaffolds: from nano to macro, Journal of Materials Chemistry B 2 (2014) 49–58.

Part V

Appendices

Appendix A

Tables of Raw Data of Scaffolds

A.1 XRD Data

A.1.1 HA

Table A.1: COD reference pattern of HA expressed as a percentage of the maximum peak

2theta (°)	COD reference HA (96-230-0274)
12.565	10.6
31.117	47.8
33.658	22.9
37.002	100
37.518	72.5
38.329	45.8
39.717	16.3
46.475	25.6
54.717	43.5
56.381	11.2
58.088	36.4
59.255	14.1
62.612	22.0
77.065	11.6

Table A.2: COD reference pattern of whitlockite expressed as a percentage of the maximum peak

2theta (°)	COD reference whitlockite (96-230-2137)
12.636	22.7
15.874	21.3
19.738	28.5
25.430	20.9
30.178	28.1
32.397	67.5
36.321	100
37.936	22.4
40.094	75.6
52.233	15.1
55.201	28.6
60.538	10.5
62.751	34.7

Table A.3: Relative peak intensity and relative area of XRD peaks of sample sintered to 1250 °C, compared to maximum

2theta (°)	Peak Intensity (%)	Area Intensity (%)
19.735	13.6	8.5
29.975	23.2	25.9
32.369	49.1	43.0
34.543	11.4	8.6
36.154	100	100
37.836	21.8	16.3
40.098	67.9	84.0
40.197	46.0	37.9
41.534	12.8	18.5
46.548	10.7	17.6
48.065	13.0	10.7
56.828	14.9	24.5
62.352	33.7	48.7
63.053	10.3	21.2
70.309	11.3	23.2
70.458	14.7	18.2

Table A.4: Relative peak intensity and relative area of XRD peaks of sample sintered to 1300 °C, compared to maximum

2theta (°)	Peak Intensity (%)	Area Intensity (%)
19.726	12.4	11.0
25.370	10.3	5.7
29.961	22.0	17.1
32.350	50.5	56.1
34.502	11.2	6.2
36.146	100	100
37.812	21.1	18.7
40.068	72.2	56.1
41.508	12.1	16.1
46.536	11.7	9.1
48.046	14.3	9.6
48.752	12.6	9.8
52.137	10.5	11.7
55.063	25.2	28.2
56.299	17.6	13.7
56.797	15.9	14.1
60.523	10.3	9.1
62.320	37.3	24.9
63.026	12.2	9.5
70.370	17.7	34.3

Table A.5: Relative peak intensity and relative area of XRD peaks of sample sintered to 1350 °C, compared to maximum

2theta (°)	Peak Intensity (%)	Area Intensity (%)
30.095	27.5	16.7
33.715	14.5	7.0
36.175	15.4	9.3
37.058	100	100
37.150	47.4	19.0
37.531	48.4	38.7
37.626	22.7	13.6
38.403	60.9	48.7
38.497	29.1	17.5
39.739	23.0	23.0
39.835	12.2	7.4
46.572	28.3	28.3
63.683	15.2	9.1
54.793	40.9	40.9
54.922	22.2	19.8
56.465	18.3	18.3
58.124	43.9	52.6
58.266	22.9	18.3
59.380	22.3	22.3
59.524	12.0	9.6
60.334	16.9	16.9
61.300	17.8	17.8
62.597	17.8	28.2
74.711	14.0	14.0
75.908	10.4	14.6
76.161	13.0	20.9
77.252	13.4	16.1

A.1.2 Ti

Table A.6: COD reference pattern of TiH_2 expressed as a percentage of the maximum peak

2theta (°)	ICDD reference TiH_4 (04-001-6850)
40.683	100.0
47.331	41.4
69.174	25.1
83.462	22.6
88.091	5.8

Table A.7: COD reference pattern of Ti_2 expressed as a percentage of the maximum peak

2theta (°)	COD reference Ti_2 (96-900-8518)
40.991	25.1
44.888	25.6
473.005	100
62.399	13.3
74.666	14.5
84.323	14.5
91.55	15
93.073	10.7

Table A.8: COD reference pattern of Ti_4 expressed as a percentage of the maximum peak

2theta (°)	COD reference Ti_4 (96-901-1601)
40.702	98
44.547	100
61.915	52.4
74.078	57
90.745	58.9

Table A.9: COD reference pattern of Ti-C expressed as a percentage of the maximum peak

2theta (°)	COD reference Ti-C (96-591-0092)
42.342	89.6
49.293	100
72.279	54.1
87.505	28.2
92.489	16

Table A.10: COD reference pattern of Ti-C-N expressed as a percentage of the maximum peak

2theta (°)	COD reference Ti-C-N (96-101-0872)
42.834	73.3
49.876	100
73.209	53.1
88.727	23.9
93.823	15.6

Table A.11: COD reference pattern of silicon expressed as a percentage of the maximum peak (96-901-1657)

2theta (°)	COD Reference Si (96-901-1657)
37.959	70.1
40.022	59.7
10.128	14.6
10.629	100
46.341	40.9
56.811	70.0
73.110	15.8
80.877	11.6
85.470	20.5

Table A.12: ICDD reference pattern of Ti_2 expressed as a percentage of the maximum peak

2theta (°)	ICDD Ti_2 (04-002-5207)
34.853	25.7
38.101	26.0
39.883	100
52.587	12.3
62.493	12.3
70.049	11.6
73.592	1.6
75.594	11.3
79.750	8.1
81.505	1.4
86.020	1.8

Table A.13: ICDD reference pattern of Ti_4 expressed as a percentage of the maximum peak

2theta (°)	ICDD Ti_4 (01-071-3947)
35.470	25.8
38.269	26.9
40.474	100
53.163	12.4
63.687	12.0
70.675	11.7
75.066	1.5
76.798	11.3
78.230	7.9
81.926	1.5
87.547	1.7

Table A.14: ICDD reference pattern of Ti-C expressed as a percentage of the maximum peak

2theta (°)	ICDD Ti-C (04-002-0789)
36.239	92.3
42.092	100
61.043	46.7
73.100	21.9
76.925	12.0

Table A.15: ICDD reference pattern of Ti_2-C-N expressed as a percentage of the maximum peak

2theta (°)	ICDD Ti_2-C-N (03-065-9875)
36.362	82.2
42.236	100
61.265	45.3
73.378	19.3
77.224	11.6

Table A.16: ICDD reference pattern of Ti-N expressed as a percentage of the maximum peak

2theta (°)	ICDD Ti-N (04-007-4803)
36.666	71.4
42.594	100
61.814	45.9
74.070	17.9
77.965	11.6

Table A.17: ICDD reference pattern of Ti_2-N expressed as a percentage of the maximum peak

2theta (°)	ICDD Ti_2-N (04-004-3072)[1]
25.452	11.9
34.657	3.6
36.303	36.9
39.281	100
40.767	28.6
51.063	12.2
52.281	14.4
61.027	7.4
64.256	14.1
63.305	11.8
68.337	1.8
73.125	5.7
76.01	6.1
76.098	6.2
77.081	1.2
79.918	6.0
82.732	1.6
84.481	4.1

Table A.18: ICDD reference pattern of Ti_2-O expressed as a percentage of the maximum peak

2theta (°)	ICDD Ti_2-O (04-009-8171)[2]
18.403	6.6
34.897	10.4
37.304	17.9
39.732	100
52.003	20.8
62.577	15.3
68.906	12
75.168	8.2
76.727	7.8
79.529	1.9
85.631	2.7

Table A.19: ICDD reference pattern of Ti_3-O expressed as a percentage of the maximum peak

2theta (°)	ICDD Ti_3-O (04-005-4376)[3]
20.876	1.1
34.840	14.7
37.691	19.7
39.800	100
52.283	18.2
64.142	14.2
69.457	10.8
75.364	8.9
76.724	7.9
80.488	1.6
85.807	2.4

Table A.20: ICDD reference pattern of Ti_6-O expressed as a percentage of the maximum peak

2theta (°)	ICDD Ti_6-O (001-072-1807)[4]
19.969	2.2
27.494	1.6
34.953	20.1
37.934	23.2
39.932	100
52.530	14.8
62.684	13.0
69.864	11.3
70.121	6.0
73.829	1.3
75.664	9.9
76.956	7.7
81.089	1.5
86.145	2.0

Table A.21: Relative peak intensity and relative area of XRD peaks of sample sintered to 1000 °C, compared to maximum

2theta (°)	Peak Intensity (%)	Area Intensity (%)
14.2063	8.9	12.4
40.77331	20.0	21.7
12.45658	2.2	12.9
44.27183	20.4	26.0
46.65028	100	100
61.73575	20.6	24.5
74.23112	23.0	20.8
83.18739	21.2	54.0

Table A.22: Relative peak intensity and relative area of XRD peaks of sample sintered to 1100 °C, compared to maximum

2theta (°)	Peak Intensity (%)	Area Intensity (%)
14.23484	11.2	26.6
40.81182	20.6	24.5
42.32904	6.2	14.9
42.88749	4.8	11.4
44.27391	18.3	38.0
46.67707	100	89.3
49.23422	6.5	28.2
49.87902	5.8	20.8
61.82264	19.5	52.3
72.21755	4.9	23.5
74.2779	19.31	34.5
83.35765	21.0	100

Table A.23: Relative peak intensity and relative area of XRD peaks of sample sintered to 1200 °C, compared to maximum

2theta (°)	Peak Intensity (%)	Area Intensity (%)
40.67267	15.8	6.4
42.38813	59.6	35.1
43.95893	13.6	10.0
45.66448	9.0	7.9
46.5046	100	29.4
49.10358	53.1	31.3
49.3628	71.2	62.9
61.43031	23.0	20.4
72.40794	45.5	100
74.04359	19.7	14.5
82.71497	14.6	17.2
87.80075	16.9	34.8

Table A.24: Relative peak intensity and relative area of XRD peaks of sample sintered to 1300 °C, compared to maximum

2theta (°)	Peak Intensity (%)	Area Intensity (%)
40.66911	14.9	21.0
42.15713	66.0	46.4
13.9968	18.6	17.4
46.50929	100	93.7
49.08454	94.9	100
61.4736	18.9	22.1
71.9646	57.0	80.1
74.04836	20.6	28.9
82.77781	17.9	33.6
87.10741	25.7	49.5

A.1.3 Ti-6Al-4V

Table A.25: ICDD reference pattern of Ti_2-Al-N expressed as a percentage of the maximum peak

2theta (°)	ICDD Ti_2-Al-N (04-001-6325)[5]
12.999	32.4
34.565	15.9
35.207	4.9
39.704	19.0
40.020	100
43.865	4.1
53.641	16.3
59.366	1.2
61.936	15.6
63.588	1.1
72.269	10.4
72.906	1.2
76.124	9.8
76.333	8.9
85.558	1.4
86.371	2.4

Table A.26: ICDD reference pattern of Ti_3-Al expressed as a percentage of the maximum peak

2theta (°)	ICDD Ti_3-Al (04-015-7850)[6]
17.754	2.5
26.127	5.7
31.005	2.3
35.953	25.3
38.576	26.9
40.980	100
52.261	1.1
53.752	12.5
64.628	12.0
71.428	11.9
76.232	1.5
77.861	11.4
79.430	7.6
82.696	1.5
88.867	1.7

Table A.27: ICDD reference pattern of Ti_3-Al-C expressed as a percentage of the maximum peak

2theta (°)	ICDD Ti_3-Al-C (04-001-6068)[7]
21.394	15.5
30.437	1.1
37.507	100
43.583	57.5
49.044	3.8
63.336	27.3
67.676	1.1
75.993	21.6
80.030	7.2

Table A.28: ICDD reference pattern of V_2-C expressed as a percentage of the maximum peak

2theta (°)	ICDD V_2-C (04-077-7210)
35.863	16.2
39.321	20.9
41.078	100
54.266	16.5
64.452	14.1
72.481	11.1
76.015	1.1
78.178	9.3
79.334	7.8
84.582	1.6
89.124	2.3

Table A.29: ICDD reference pattern of V_7-O_3 expressed as a percentage of the maximum peak

2theta (°)	ICDD V_7-O_3 (04-007-0520)[8]
34.684	1.9
39.583	100
39.805	33.9
43.654	96.4
44.549	8.6
47.760	13.1
48.201	1.4
50.692	14.8
50.984	5.2
57.840	5.5
62.797	5.0
63.300	11.6
63.592	11.3
68.921	8.5
69.247	8.3
73.076	1.1
75.279	1.5
77.133	3.1
77.279	7.8
77.402	10.3
77.714	5.4
78.457	1.7
80.679	1.5
82.131	1.9
85.250	4.8
85.477	1.4
85.818	1.8

Table A.30: ICDD reference pattern of V-N expressed as a percentage of the maximum peak

2theta (°)	ICDD V-N (04-008-7244)
37.638	77.2
43.738	100
63.575	44.6
76.296	18.2
80.356	11.4

Table A.31: Relative peak intensity and relative area of XRD peaks of sample sintered to 1200 °C, compared to maximum

2theta (°)	Peak Intensity (%)	Area Intensity (%)
42.32619	81.9	44.7
44.82292	6.5	9.5
47.67501	28.9	21.0
49.30105	100	100
62.98524	4.9	10.6
72.38855	65.0	65.0
73.31107	4.8	7.0
87.67596	37.3	30.5

Table A.32: Relative peak intensity and relative area of XRD peaks of sample sintered to 1250 °C, compared to maximum

2theta (°)	Peak Intensity (%)	Area Intensity (%)
41.29759	16.2	16.7
42.38308	93.4	42.1
44.67266	22.7	23.3
47.21547	86.3	100
47.69373	37.4	28.9
49.33712	100	51.5
62.46232	14.2	29.2
72.35832	30.0	46.3

Table A.33: Relative peak intensity and relative area of XRD peaks of sample sintered to 1300 °C, compared to maximum

2theta (°)	Peak Intensity (%)	Area Intensity (%)
41.26851	11.2	8.4
12..38338	89.5	67.1
44.58604	15.8	15.8
47.1688	58.5	40.2
47.6711	23.2	23.2
49.34835	100	100
62.3963	10.1	12.6
72.4064	60.9	60.9
72.23608	9.6	14.4
84.10948	11.1	16.6
87.68816	38.3	47.9

A.2 Pore/Strut Sizes

A.2.1 HA

Table A.34: Average $\pm\sigma_{er}$ (n=10) pore and strut sizes (μm) for HA samples produced using AFR using the 45 ppi template, with up to 5 coats, sintered to 1250 °C and with camphene loadings of 0, 5, 10, 20 and 25 wt.%

	1 coat		2 coat		3 coat		4 coat		5 coat	
	Pore size	Strut Size	Pore size	Strut Size	Pore size	Strut Size	Pore size	Strut Size	Pore size	Strut Size
0% porogen	514 ± 36	87.3 ± 5.8	488 ± 26	93.2 ± 3.7	394 ± 22	95.6 ± 7.1	375 ± 15	106 ± 4.8	329 ± 21	108 ± 7.1
5% porogen	299 ± 12	49.7 ± 4.3	256 ± 14	52.0 ± 3.0	299 ± 14	68.6 ± 3.7	298 ± 21	71.0 ± 2.8	279 ± 21	87.4 ± 4.0
10% porogen	325 ± 15	53.9 ± 3.3	281 ± 10	59.3 ± 3.1	257 ± 8	60.3 ± 2.6	254 ± 13	65.6 ± 2.7	241 ± 14	68.1 ± 3.2
20% porogen	271 ± 15	47.5 ± 2.5	254 ± 13	53.8 ± 2.1	249 ± 13	57.8 ± 2.8	228 ± 10	55.3 ± 2.6	219 ± 14	56.2 ± 3.5
25% porogen	330 ± 19	52.0 ± 2.8	240 ± 12	47.1 ± 2.7	223 ± 11	56.2 ± 1.9	230 ± 10	58.3 ± 2.3	230 ± 16	62.3 ± 2.1

Table A.35: Average $\pm\sigma_{er}$ (n=10) pore and strut sizes (µm) for HA samples produced using AFR using the 45 ppi template, with up to 5 coats, sintered to 1300 °C and with camphene loadings of 0, 5, 10, 20 and 25 wt.%

	1 coat		2 coat		3 coat		4 coat		5 coat	
	Pore size	Strut Size	Pore size	Strut Size	Pore size	Strut Size	Pore size	Strut Size	Pore size	Strut Size
0% porogen	400 ± 40	73.3 ± 5.5	325 ± 28	82.3 ± 5.6	319 ± 28	88.2 ± 6.5	331 ± 24	86.1 ± 8.0	302 ± 26	94.6 ± 5.0
5% porogen	330 ± 21	59.0 ± 2.9	282 ± 10	60.7 ± 1.6	296 ± 18	60.4 ± 1.8	291 ± 25	66.5 ± 3.3	260 ± 20	68.4 ± 3.4
10% porogen	262 ± 11	40.6 ± 2.2	259 ± 18	52.2 ± 3.1	258 ± 18	54.3 ± 2.2	239 ± 15	55.2 ± 3.5	234 ± 15	60.4 ± 1.8
20% porogen	247 ± 13	49.1 ± 2.7	249 ± 13	49.4 ± 1.5	241 ± 12	47.2 ± 1.8	227 ± 9	49.2 ± 2.0	219 ± 7	54.9 ± 2.6
25% porogen	303 ± 13	46.0 ± 2.4	278 ± 11	53.0 ± 3.5	269 ± 19	58.5 ± 1.3	234 ± 12	59.5 ± 1.1	229 ± 4	66.5 ± 1.6

Table A.36: Average $\pm\sigma_{er}$ (n=10) pore and strut sizes (µm) for HA samples produced using AFR using the 45 ppi template, with up to 5 coats, sintered to 1350 °C and with camphene loadings of 0, 5, 10, 20 and 25 wt.%

	1 coat		2 coat		3 coat		4 coat		5 coat	
	Pore size	Strut Size	Pore size	Strut Size	Pore size	Strut Size	Pore size	Strut Size	Pore size	Strut Size
0% porogen	363 ± 21	64.7 ± 5.4	348 ± 23	80.4 ± 4.9	313 ± 23	80.0 ± 6.6	300 ± 26	81.0 ± 4.4	267 ± 20	89.0 ± 8.2
5% porogen	274 ± 12	55.9 ± 2.7	257 ± 12	57.8 ± 3.0	251 ± 16	63.3 ± 5.2	246 ± 20	64.2 ± 3.4	212 ± 15	72.9 ± 3.3
10% porogen	269 ± 18	51.3 ± 3.2	258 ± 17	48.7 ± 1.4	247 ± 11	52.8 ± 2.0	243 ± 20	60.6 ± 3.1	230 ± 18	60.6 ± 2.2
20% porogen	259 ± 9	53.4 ± 2.6	252 ± 16	56.4 ± 3.4	240 ± 14	56.3 ± 1.8	227 ± 11	55.7 ± 1.9	223 ± 10	55.6 ± 0.7
25% porogen	266 ± 12	46.3 ± 2.3	243 ± 7	52.1 ± 2.4	235 ± 10	45.5 ± 2.4	239 ± 12	58.5 ± 2.7	216 ± 12	54.9 ± 2.0

Table A.37: Average $\pm\sigma_{er}$ (n=10) pore and strut sizes (μm) for HA samples produced using AFR using the 90 ppi template, with up to 5 coats, sintered to 1250 °C and with camphene loadings of 0, 5, 10, 20 and 25 wt.%

	1 coat		2 coat		3 coat		4 coat		5 coat	
	Pore size	Strut Size	Pore size	Strut Size	Pore size	Strut Size	Pore size	Strut Size	Pore size	Strut Size
0% porogen	148 ± 9	32.4 ± 3.0	146 ± 4	41.3 ± 2.4	140 ± 9	44.9 ± 2.7	136 ± 8	49.7 ± 4.2	130 ± 10	52.3 ± 7.1
5% porogen	156 ± 10	41.0 ± 1.5	152 ± 8	47.1 ± 5.7	149 ± 11	49.0 ± 2.9	149 ± 11	49.2 ± 5.6	150 ± 7	49.9 ± 3.8
10% porogen	156 ± 5	24.1 ± 1.0	153 ± 4	30.3 ± 1.3	151 ± 8	30.6 ± 1.9	149 ± 8	35.8 ± 1.3	142 ± 5	35.0 ± 2.7
20% porogen	175 ± 4	24.6 ± 1.1	154 ± 8	26.3 ± 1.0	148 ± 5	28.6 ± 1.6	152 ± 7	31.7 ± 2.1	141 ± 5	34.6 ± 2.4
25% porogen	161 ± 7	23.8 ± 1.0	161 ± 7	23.6 ± 1.2	155 ± 7	30.8 ± 1.4	156 ± 6	28.1 ± 1.1	139 ± 4	27.9 ± 1.3

Table A.38: Average $\pm\sigma_{er}$ (n=10) pore and strut sizes (μm) for HA samples produced using AFR using the 90 ppi template, with up to 5 coats, sintered to 1300 °C and with camphene loadings of 0, 5, 10, 20 and 25 wt.%

	1 coat		2 coat		3 coat		4 coat		5 coat	
	Pore size	Strut Size	Pore size	Strut Size	Pore size	Strut Size	Pore size	Strut Size	Pore size	Strut Size
0% porogen	119 ± 10	37.3 ± 2.3	116 ± 10	47.1 ± 3.2	113 ± 10	48.5 ± 4.7	110 ± 6	50.2 ± 2.6	108 ± 4	55.4 ± 3.2
5% porogen	146 ± 9	32.5 ± 1.2	145 ± 5	47.3 ± 2.7	146 ± 8	44.8 ± 1.1	126 ± 4	45.1 ± 1.6	125 ± 8	44.0 ± 1.4
10% porogen	153 ± 8	20.6 ± 1.9	152 ± 5	22.3 ± 1.2	146 ± 8	29.0 ± 2.2	143 ± 6	30.1 ± 1.5	144 ± 6	37.5 ± 2.1
20% porogen	137 ± 11	18.6 ± 1.6	136 ± 7	25.0 ± 1.6	131 ± 5	29.7 ± 1.9	127 ± 4	35.8 ± 1.9	129 ± 8	37.5 ± 2.0
25% porogen	156 ± 4	25.7 ± 3.4	146 ± 5	23.7 ± 1.2	123 ± 7	25.9 ± 2.2	124 ± 3	27.0 ± 1.7	117 ± 5	28.0 ± 1.6

Table A.39: Average $\pm\sigma_{er}$ (n=10) pore and strut sizes (μm) for HA samples produced using AFR using the 90 ppi template, with up to 5 coats, sintered to 1350 °C and with camphene loadings of 0, 5, 10, 20 and 25 wt.%

	1 coat		2 coat		3 coat		4 coat		5 coat	
	Pore size	Strut Size	Pore size	Strut Size	Pore size	Strut Size	Pore size	Strut Size	Pore size	Strut Size
0% porogen	135 ± 10	29.6 ± 1.4	117 ± 8	34.6 ± 3.3	103 ± 6	34.9 ± 2.0	102 ± 5	43.2 ± 3.5	100 ± 5	42.7 ± 2.7
5% porogen	143 ± 8	29.9 ± 1.3	142 ± 5	26.9 ± 2.6	131 ± 7	48.5 ± 3.1	123 ± 5	39.6 ± 2.0	120 ± 3	37.1 ± 2.1
10% porogen	154 ± 6	20.6 ± 1.1	129 ±	24.0 ± 1.2	122 ± 7	28.7 ± 1.0	123 ± 7	28.5 ± 1.3	114 ± 7	35.0 ± 1.4
20% porogen	145 ± 3	20.3 ± 2.5	146 ± 6	22.2 ± 1.1	132 ± 5	25.7 ± 2.5	135 ± 5	29.2 ± 2.7	134 ± 5	31.0 ± 1.9
25% porogen	135 ± 8	20.0 ± 0.6	140 ± 6	26.2 ± 1.7	126 ± 4	28.8 ± 1.4	133 ± 6	28.5 ± 1.4	126 ± 4	30.2 ± 1.6

Table A.40: Average $\pm\sigma_{er}$ (n=10) pore and strut sizes (μm) for HA samples produced using AFR with freeze casting to 10 °C, from both templates, with 1 coat, sintered to 1350 °C and with camphene loadings of 0, 5, 10, 20 and 25 wt.%

Template (ppi)	Porogen Content (%)	Pore size (μm)	Strut Size (μm)
45	0	324 ± 14	60.7 ± 2.6
	5	253 ± 8	55.6 ± 4.4
	10	304 ± 24	55.2 ± 2.2
	20	356 ± 17	67.6 ± 3.4
	25	311 ± 7	61.2 ± 2.5
90	0	196 ± 5	28.4 ± 1.5
	5	96 ± 7	20.7 ± 0.9
	10	94 ± 56	20.0 ± 0.7
	20	158 ± 10	21.8 ± 1.4
	25	149 ± 10	21.6 ± 1.0

Table A.41: Average $\pm\sigma_{er}$ (n=10) pore and strut sizes (µm) for HA samples produced using AFR with freeze casting to -20 °C, from both templates, with 1 coat, sintered to 1350 °C and with camphene loadings of 0, 5, 10, 20 and 25 wt.%

Template (ppi)	Porogen Content (%)	Pore size (µm)	Strut Size (µm)
45	0	366 ± 31	53.8 ± 2.5
	5	344 ± 31	57.6 ± 2.4
	10	401 ± 34	56.6 ± 2.6
	20	378 ± 43	64.4 ± 3.2
	25	396 ± 29	65.8 ± 2.9
90	0	153 ± 9	17.1 ± 1.0
	5	143 ± 11	23.5 ± 2.3
	10	154 ± 16	21.2 ± 1.4
	20	142 ± 9	19.4 ± 1.3
	25	139 ± 9	19.9 ± 1.1

A.2.2 Ti

Table A.42: Average $\pm\sigma_{er}$ (n=10) pore and strut sizes (µm) for Ti samples produced using the 45 ppi template, with up to 5 coats, sintered to 1000 °C and with camphene loadings of 0, 5, 10, 20 and 25 wt.%

	1 coat		2 coat		3 coat		4 coat		5 coat	
	Pore size	Strut Size	Pore size	Strut Size	Pore size	Strut Size	Pore size	Strut Size	Pore size	Strut Size
0% porogen	528 ± 45	74.1 ± 3.7	431 ± 31	80.4 ± 2.9	349 ± 18	72.0 ± 3.7	321 ± 15	79.1 ± 4.5	322 ± 27	79.1 ± 5.3
5% porogen	493 ± 34	66.8 ± 4.7	480 ± 19	85.4 ± 6.3	378 ± 25	76.7 ± 4.7	400 ± 20	77.5 ± 4.9	395 ± 35	101 ± 5.5
10% porogen	434 ± 21	62.3 ± 7.0	378 ± 28	71.6 ± 5.1	364 ± 18	77.7 ± 7.6	336 ± 18	86.5 ± 5.6	347 ± 18	82.8 ± 7.0
20% porogen	397 ± 19	71.2 ± 4.3	404 ± 25	66.2 ± 4.4	394 ± 37	85.6 ± 4.4	370 ± 26	83.6 ± 6.3	341 ± 20	84.8 ± 5.1
25% porogen	240 ± 12	58.0 ± 3.0	296 ± 18	62.2 ± 5.0	348 ± 28	60.8 ± 2.3	342 ± 27	75.8 ± 3.9	285 ± 19	99.3 ± 4.6

Table A.43: Average $\pm\sigma_{er}$ (n=10) pore and strut sizes (µm) for Ti samples produced using the 45 ppi template, with up to 5 coats, sintered to 1100 °C and with camphene loadings of 0, 5, 10, 20 and 25 wt.%

	1 coat		2 coat		3 coat		4 coat		5 coat	
0% porogen	449 ± 34	66.6 ± 3.9	393 ± 23	83.2 ± 3.5	330 ± 20	80.4 ± 3.0	450 ± 23	74.7 ± 2.8	439 ± 26	87.9 ± 5.5
5% porogen	417 ± 22	62.7 ± 3.5	421 ± 20	61.6 ± 4.7	400 ± 23	74.7 ± 2.6	330 ± 22	80.0 ± 2.8	383 ± 32	80.8 ± 3.1
10% porogen	396 ± 16	47.6 ± 3.9	417 ± 22	74.0 ± 5.2	352 ± 23	73.4 ± 4.1	319 ± 11	77.3 ± 5.9	357 ± 23	61.8 ± 5.1
20% porogen	369 ± 29	62.3 ± 5.6	378 ± 15	63.6 ± 4.0	394 ± 14	79.4 ± 3.9	362 ± 14	74.2 ± 5.6	349 ± 14	76.6 ± 4.1
25% porogen	363 ± 20	85.9 ± 2.3	331 ± 15	58.6 ± 3.2	293 ± 18	60.2 ± 2.5	337 ± 23	84.4 ± 5.6	267 ± 15	74.4 ± 4.4

Table A.44: Average $\pm\sigma_{er}$ (n=10) pore and strut sizes (µm) for Ti samples produced using the 45 ppi template, with up to 5 coats, sintered to 1200 °C and with camphene loadings of 0, 5, 10, 20 and 25 wt.%

	1 coat		2 coat		3 coat		4 coat		5 coat	
	Pore size	Strut Size	Pore size	Strut Size	Pore size	Strut Size	Pore size	Strut Size	Pore size	Strut Size
0% porogen	546 ± 38	81.7 ± 4.4	438 ± 29	83.8 ± 7.6	422 ± 22	85.4 ± 5.4	372 ± 30	69.2 ± 4.0	371 ± 12	83.5 ± 8.2
5% porogen	442 ± 20	34.1 ± 3.5	450 ± 18	85.5 ± 6.2	423 ± 16	80.9 ± 5.1	414 ± 41	96.9 ± 6.0	421 ± 22	76.6 ± 5.4
10% porogen	301 ± 22	72.3 ± 4.4	357 ± 20	49.5 ± 1.9	315 ± 18	49.5 ± 3.7	311 ± 11	64.2 ± 4.6	303 ± 13	65.0 ± 4.0
20% porogen	385 ± 23	81.7 ± 7.0	400 ± 16	72.2 ± 5.9	382 ± 21	73.7 ± 4.6	365 ± 18	83.6 ± 5.9	346 ± 20	97.0 ± 6.3
25% porogen	316 ± 21	84.3 ± 1.3	245 ± 16	73.7 ± 2.2	323 ± 21	55.4 ± 2.3	349 ± 18	64.8 ± 4.3	255 ± 20	71.9 ± 4.0

Table A.45: Average $\pm\sigma_{er}$ (n=10) pore and strut sizes (µm) for Ti samples producedusing the 45 ppi template, with up to 5 coats, sintered to 1300 °C and with camphene loadings of 0, 5, 10, 20 and 25 wt.%

	1 coat		2 coat		3 coat		4 coat		5 coat	
	Pore size	Strut Size	Pore size	Strut Size	Pore size	Strut Size	Pore size	Strut Size	Pore size	Strut Size
0% porogen	238 ± 11	54.3 ± 2.5	419 ± 24	72.7 ± 2.9	358 ± 23	74.4 ± 7.0	332 ± 20	75.9 ± 4.6	347 ± 14	79.4 ± 2.6
5% porogen	477 ± 15	57.3 ± 5.2	486 ± 15	59.6 ± 1.1	443 ± 10	60.7 ± 1.1	431 ± 11	54.9 ± 2.6	426 ± 14	87.9 ± 3.8
10% porogen	418 ± 26	63.0 ± 4.3	423 ± 17	78.4 ± 3.8	364 ± 25	88.8 ± 3.5	350 ± 27	70.8 ± 5.0	355 ± 23	90.4 ± 3.5
20% porogen	413 ± 22	74.8 ± 3.8	430 ± 24	70.0 ± 6.3	407 ± 16	75.1 ± 6.1	375 ± 20	81.6 ± 4.7	356 ± 21	99.8 ± 4.9
25% porogen	380 ± 9	46.7 ± 2.2	302 ± 13	48.5 ± 2.7	294 ± 17	57.2 ± 7.6	263 ± 26	64.7 ± 3.0	273 ± 6	63.1 ± 4.3

Table A.46: Average $\pm\sigma_{er}$ (n=10) pore and strut sizes (µm) for Ti samples produced using the 90 ppi template, with up to 5 coats, sintered to 1000 °C and with camphene loadings of 0, 5, 10, 20 and 25 wt.%

	1 coat		2 coat		3 coat		4 coat		5 coat	
	Pore size	Strut Size	Pore size	Strut Size	Pore size	Strut Size	Pore size	Strut Size	Pore size	Strut Size
0% porogen	240 ± 10	40.2 ± 3.7	218 ± 13	42.3 ± 2.6	205 ± 12	40.6 ± 2.7	198 ± 9	44.3 ± 4.1	187 ± 9	44.5 ± 4.1
5% porogen	204 ± 10	52.6 ± 4.7	176 ± 8	43.2 ± 2.7	189 ± 8	31.1 ± 4.6	216 ± 13	46.4 ± 4.5	183 ± 11	49.0 ± 3.9
10% porogen	155 ± 8	27.5 ± 2.1	180 ± 10	31.4 ± 2.1	171 ± 6	36.1 ± 2.5	166 ± 8	47.7 ± 2.4	123 ± 8	38.8 ± 4.4
20% porogen	204 ± 7	32.2 ± 2.3	173 ± 7	32.0 ± 1.3	168 ± 11	38.7 ± 3.4	151 ± 10	44.8 ± 2.1	165 ± 11	42.2 ± 2.3
25% porogen	165 ± 14	27.3 ± 3.1	129 ± 9	24.8 ± 1.9	149 ± 11	27.8 ± 1.1	140 ± 17	40.3 ± 3.5	138 ± 10	47.4 ± 3.2

Table A.47: Average $\pm\sigma_{er}$ (n=10) pore and strut sizes (µm) for Ti samples produced using the 90 ppi template, with up to 5 coats, sintered to 1100 °C and with camphene loadings of 0, 5, 10, 20 and 25 wt.%

	1 coat		2 coat		3 coat		4 coat		5 coat	
	Pore size	Strut Size	Pore size	Strut Size	Pore size	Strut Size	Pore size	Strut Size	Pore size	Strut Size
0% porogen	172 ± 8	32.5 ± 1.8	174 ± 10	37.1 ± 2.1	164 ± 6	25.8 ± 1.2	169 ± 8	37.1 ± 3.0	167 ± 5	51.0 ± 3.3
5% porogen	114 ± 7	29.1 ± 1.5	161 ± 9	38.4 ± 3.5	157 ± 9	52.8 ± 2.3	153 ± 5	43.2 ± 1.6	141 ± 2	44.3 ± 2.8
10% porogen	143 ± 6	28.3 ± 1.6	174 ± 7	37.7 ± 2.7	151 ± 5	34.9 ± 2.3	139 ± 3	44.5 ± 3.7	148 ± 6	45.6 ± 4.4
20% porogen	188 ± 6	31.8 ± 1.1	159 ± 6	34.0 ± 2.5	155 ± 7	43.5 ± 5.7	158 ± 10	41.7 ± 3.0	161 ± 10	57.4 ± 2.6
25% porogen	159 ± 10	18.7 ± 1.5	146 ± 15	25.9 ± 1.8	142 ± 16	35.2 ± 3.7	129 ± 13	33.8 ± 2.8	121 ± 12	64.6 ± 4.2

Table A.48: Average $\pm\sigma_{er}$ (n=10) pore and strut sizes (µm) for Ti samples produced using the 90 ppi template, with up to 5 coats, sintered to 1200 °C and with camphene loadings of 0, 5, 10, 20 and 25 wt.%

	1 coat		2 coat		3 coat		4 coat		5 coat	
	Pore size	Strut Size	Pore size	Strut Size	Pore size	Strut Size	Pore size	Strut Size	Pore size	Strut Size
0% porogen	162 ± 9	33.6 ± 2.7	170 ± 8	46.5 ± 4.3	149 ± 8	35.9 ± 2.3	165 ± 11	43.2 ± 1.5	155 ± 5	40.6 ± 3.0
5% porogen	199 ± 8	34.8 ± 1.7	173 ± 13	44.8 ± 1.7	177 ± 11	39.1 ± 2.3	162 ± 11	52.5 ± 4.5	160 ± 8	60.5 ± 4.8
10% porogen	153 ± 7	32.8 ± 3.0	131 ± 4	40.2 ± 2.7	142 ± 11	43.6 ± 2.3	137 ± 5	46.1 ± 3.5	137 ± 10	42.4 ± 2.6
20% porogen	202 ± 10	35.1 ± 2.6	163 ± 6	36.3 ± 2.6	161 ± 8	40.4 ± 2.9	147 ± 9	41.2 ± 3.3	152 ± 8	52.9 ± 3.0
25% porogen	240 ± 10	40.2 ± 3.7	152 ± 12	24.4 ± 1.9	131 ± 10	25.8 ± 1.2	133 ± 11	39.6 ± 2.9	125 ± 13	38.0 ± 1.7

Table A.49: Average $\pm\sigma_{er}$ (n=10) pore and strut sizes (µm) for Ti samples produced using the 90 ppi template, with up to 5 coats, sintered to 1300 °C and with camphene loadings of 0, 5, 10, 20 and 25 wt.%

	1 coat		2 coat		3 coat		4 coat		5 coat	
	Pore size	Strut Size	Pore size	Strut Size	Pore size	Strut Size	Pore size	Strut Size	Pore size	Strut Size
0% porogen	186 ± 7	22.4 ± 1.7	184 ± 9	37.0 ± 1.2	161 ± 10	37.1 ± 2.1	159 ± 10	33.0 ± 2.2	158 ± 7	35.7 ± 1.6
5% porogen	206 ± 15	35.3 ± 2.3	189 ± 15	40.5 ± 2.7	172 ± 10	49.5 ± 3.4	165 ± 11	44.7 ± 2.5	165 ± 14	52.5 ± 3.7
10% porogen	168 ± 8	31.9 ± 7.1	166 ± 8	34.3 ± 3.6	165 ± 8	40.6 ± 3.9	142 ± 5	35.4 ± 2.1	154 ± 10	42.3 ± 1.7
20% porogen	189 ± 12	30.0 ± 2.0	163 ± 11	38.7 ± 3.5	169 ± 15	51.9 ± 4.2	169 ± 8	48.1 ± 3.3	161 ± 11	52.9 ± 4.2
25% porogen	146 ± 10	28.1 ± 3.1	134 ± 13	19.6 ± 1.3	133 ± 12	25.0 ± 1.6	131 ± 11	42.5 ± 2.8	126 ± 10	50.1 ± 4.0

A.2.3 Ti-6Al-4V

Table A.50: Average $\pm\sigma_{er}$ (n=10) pore and strut sizes (µm) for Ti-6Al-4V scaffolds produced using the 45 ppi template, with up to 5 coats, sintered to 1200 °C and with camphene loadings of 0, 5, 10, 20 and 25 wt.%

	1 oat		2 coat		3 coat		4 coat		5 coat	
	Pore size	Strut size	Pore size	Strut size	Pore size	Strut size	Pore size	Strut size	Pore size	Strut size
0% porogen	268 ± 11	105 ± 8.3	369 ± 14	92.2 ± 5.7	510 ± 23	101 ± 5.6	464 ± 25	118 ± 13	374 ± 22	104 ± 9.7
5% porogen	387 ± 25	73.3 ± 8.8	387 ± 39	80.7 ± 8.7	380 ± 25	76.4 ± 9.4	343 ± 33	95.3 ± 13	432 ± 29	81.6 ± 13
10% porogen	405 ± 33	82.5 ± 3.8	344 ± 12	77.5 ± 4.9	283 ± 27	68.7 ± 4.6	257 ± 29	68.7 ± 2.9	281 ± 15	75.9 ± 4.8
20% porogen	312 ± 21	46.1 ± 4.0	379 ± 20	76.8 ± 5.0	317 ± 17	66.3 ± 4.7	300 ± 14	75.7 ± 5.1	302 ± 19	80.6 ± 5.4
25% porogen	255 ± 16	69.0 ± 6.3	357 ± 40	80.5 ± 7.1	294 ± 15	77.7 ± 3.9	275 ± 20	62.2 ± 3.9	320 ± 8	75.0 ± 2.6

Table A.51: Average $\pm\sigma_{er}$ (n=10) pore and strut sizes (µm) for Ti-6Al-4V scaffolds produced using the 45 ppi template, with up to 5 coats, sintered to 1250 °C and with camphene loadings of 0, 5, 10, 20 and 25wt.%

	1 oat		2 coat		3 coat		4 coat		5 coat	
	Pore size	Strut size	Pore size	Strut size	Pore size	Strut size	Pore size	Strut size	Pore size	Strut size
0% porogen	417 ± 26	75.3 3.8	274 ± 8	65.0 ± 2.9	403 ± 16	72.1 ± 2.9	338 ± 12	83.6 ± 4.1	357 ±23	71.6 ± 5.9
5% porogen	275 ± 18	71.2 ± 8.0	376 ± 26	73.7 ± 4.6	301 ± 14	31.0 ± 4.9	316 ± 24	71.5 ± 3.8	253 ± 19	63.0 ± 5.2
10% porogen	326 ± 24	64.4 ± 4.7	281 ± 15	73.7 ± 6.7	271 ± 14	70.3 ± 5.2	253 ± 15	69.9 ± 6.5	290 ± 16	77.2 ± 6.7
20% porogen	395 ± 28	73.8 ± 3.7	369 ± 21	79.7 ± 4.7	317 ± 28	77.2 ± 4.4	360 ± 20	64.9 ± 3.4	360 ± 13	72.6 ± 4.8
25% porogen	214 ± 27	53.6 ± 4.1	280 ± 35	56.1 ± 5.3	290 ± 24	61.6 ± 4.7	225 ± 17	62.8 ± 3.0	237 ± 6	71.1 ± 2.2

Table A.52: Average $\pm\sigma_{er}$ (n=10) pore and strut sizes (µm) for Ti-6Al-4V scaffolds produced using the 45 ppi template, with up to 5 coats, sintered to 1300 °C and with camphene loadings of 0, 5, 10, 20 and 25 wt.%

	1 oat		2 coat		3 coat		4 coat		5 coat	
	Pore size	Strut size	Pore size	Strut size	Pore size	Strut size	Pore size	Strut size	Pore size	Strut size
0% porogen	481 ± 30	79.0 ± 6.2	461 ± 32	93.1 ± 7.8	385 ± 20	80.7 ± 4.1	333 ± 11	92.6 ± 4.7	277 ± 16	90.0 ± 5.6
5% porogen	269 ± 30	82.5 ± 5.1	277 ± 19	69.3 ± 4.2	376 ± 31	67.0 ± 7.0	234 ± 10	55.0 ± 4.9	259 ± 30	89.6 ± 1.9
10% porogen	381 ± 25	59.7 ± 4.2	334 ± 15	61.6 ± 4.9	304 ± 17	61.5 ± 4.1	299 ± 22	68.9 ± 4.6	303 ± 20	71.7 ± 5.5
20% porogen	385 ± 29	53.5 ± 3.4	291 ± 13	74.7 ± 4.5	276 ± 12	70.4 ± 3.8	340 ± 12	82.0 ± 3.2	266 ± 10	77.3 ± 3.7
25% porogen	321 ± 22	72.0 ± 2.4	206 ± 20	72.8 ± 3.4	278 ± 20	76.0 ± 4.0	285 ± 16	88.5 ± 3.8	264 ± 13	82.6 ± 4.0

Table A.53: Average $\pm\sigma_{er}$ (n=10) pore and strut sizes (µm) for Ti-6Al-4V scaffolds produced using the 90 ppi template, with up to 5 coats, sintered to 1200 °C and with camphene loadings of 0, 5, 10, 20 and 25 wt.%

	1 coat		2 coat		3 coat		4 coat		5 coat	
	Pore size	Strut size	Pore size	Strut size	Pore size	Strut size	Pore size	Strut size	Pore size	Strut size
0% porogen	299 ± 6	73.1 ± 3.5	182 ± 4	66.1 ± 5.3	153 ± 8	58.2 ± 1.8	147 ± 5	67.0 ± 2.9	142 ± 3	73.0 ± 2.9
5% porogen	161 ± 10	60.2 ± 4.2	169 ± 6	55.7 ± 3.3	185 ± 14	63.5 ± 3.9	159 ± 11	71.6 ± 2.3	152 ± 7	72.9 ± 3.8
10% porogen	187 ± 11	41.8 ± 3.5	195 ± 16	50.3 ± 2.5	159 ± 11	50.2 ± 7.0	162 ± 8	41.1 ± 2.6	153 ± 13	46.1 ± 3.4
20% porogen	139 ± 6	26.7 ± 2.4	152 ± 6	35.0 ± 2.3	147 ± 7	47.5 ± 3.2	164 ± 12	43.5 ± 3.4	142 ± 6	33.9 ± 1.5
25% porogen	212 ± 12	65.8 ± 1.9	152 ± 6	46.2 ± 2.5	149 ± 6	47.7 ± 3.7	167 ± 6	60.4 ± 3.9	169 ± 4	66.7 ± 3.9

Table A.54: Average $\pm\sigma_{er}$ (n=10) pore and strut sizes (µm) for Ti-6Al-4V scaffolds produced using the 90 ppi template, with up to 5 coats, sintered to 1250 °C and with camphene loadings of 0, 5, 10, 20 and 25 wt.%

	1 coat		2 coat		3 coat		4 coat		5 coat	
	Pore size	Strut size	Pore size	Strut size	Pore size	Strut size	Pore size	Strut size	Pore size	Strut size
0% porogen	141 ± 11	41.1 ± 1.6	159 ± 6	50.5 ± 3.0	176 ± 18	70.5 ± 7.4	174 ± 3	48.5 ± 3.3	138 ± 6	72.4 ± 3.0
5% porogen	133 ± 8	52.1 ± 2.1	151 ± 5	41.5 ± 2.1	168 ± 9	49.3 ± 3.8	141 ± 10	52.4 ± 2.0	144 ± 12	68.8 ± 3.4
10% porogen	172 ± 9	38.9 ± 3.2	157 ± 6	67.4 ± 3.2	157 ± 14	62.9 ± 4.6	152 ± 6	63.2 ± 4.2	145 ± 8	68.2 ± 3.4
20% porogen	139 ± 4	35.5 ± 1..6	161 ± 5	40.3 ± 2.3	138 ± 3	37.6 ± 1.6	165 ± 9	45.3 ± 4.2	174 ± 10	44.2 ± 2.8
25% porogen	142 ± 3	34.7 ± 3.6	176 ± 13	41.9 ± 6.6	158 ± 10	53.2 ± 5.1	139 ± 7	61.6 ± 4.8	140 ± 10	53.1 ± 2.8

Table A.55: Average $\pm\sigma_{er}$ (n=10) pore and strut sizes (μm) for Ti-6Al-4V scaffolds produced using the 90 ppi template, with up to 5 coats, sintered to 1300 °C and with camphene loadings of 0, 5, 10, 20 and 25 wt.%

	1 coat		2 coat		3 coat		4 coat		5 coat	
	Pore size	Strut size	Pore size	Strut size	Pore size	Strut size	Pore size	Strut size	Pore size	Strut size
0% porogen	208 ± 12	57.7 ± 4.4	216 ± 9	56.3 ± 3.7	187 ± 4	47.2 ± 6.1	198 ± 5	67.8 ± 4.9	190 ± 12	82.6 ± 5.4
5% porogen	111 ± 9	31.7 ± 4.2	97.5 ± 7	19.3 ± 1.3	111 ± 7	32.5 ± 3.6	111 ± 4	35.1 ± 1.7	125 ± 5	52.8 ± 3.5
10% porogen	136 ± 6	28.6 ± 2.6	139 ± 3	30.9 ± 1.8	139 ± 9	46.6 ± 3.9	129 ± 6	38.6 ± 2.6	142 ± 10	43.8 ± 4.7
20% porogen	154 ± 5	52.7 ± 1.2	151 ± 6	38.1 ± 2.4	165 ± 7	36.5 ± 1.2	165 ± 13	49.3 ± 3.1	155 ± 10	45.2 ± 2.8
25% porogen	153 ± 8	39.3 ± 5.5	146 ± 5	38.1 ± 5.0	155 ± 14	40.6 ± 2.6	134 ± 6	58.7 ± 4.1	131 ± 7	72.7 ± 4.6

A.3 Porosity

A.3.1 HA

Table A.56: Average $\pm\sigma_{er}$ (n=3) porosity (%) for HA samples produced using AFR using the 45 ppi template, with up to 5 coats, sintered to 1250, 1300 and 1350 °C and with camphene loadings of 0, 5, 10, 20 and 25 wt.%

		1 coat	2 coat	3 coat	4 coat	5 coat
1250 °C	0% porogen	96 ± 0.2	95 ± 0.3	95 ± 0.2	95 ± 0.3	95 ± 0.6
	5% porogen	96 ± 0.3	95 ± 0.2	90 ± 0.4	92 ± 0.2	91 ± 0.4
	10% porogen	95 ± 0.3	93 ± 0.5	94 ± 0.3	93 ± 0.2	91 ± 0.1
	20% porogen	96 ± 0.6	90 ± 0.4	93 ± 0.2	92 ± 0.2	93 ± 0.4
	25% porogen	91 ± 0.2	90 ± 0.5	93 ± 0.1	93 ± 0.4	90 ± 0.2
1300 °C	0% porogen	88 ± 0.2	89 ± 0.1	87 ± 0.1	86 ± 0.2	88 ± 0.3
	5% porogen	85 ± 0.3	87 ± 0.5	83 ± 0.5	85 ± 0.5	85 ± 0.3
	10% porogen	85 ± 0.5	85 ± 0.6	82 ± 0.5	89 ± 0.1	85 ± 0.4
	20% porogen	90 ± 0.1	90 ± 0.4	91 ± 0.1	90 ± 0.4	92 ± 0.1
	25% porogen	92 ± 0.1	95 ± 0.2	93 ± 0.2	91 ± 0.2	89 ± 0.1
1350 °C	0% porogen	92 ± 0.3	93 ± 0.4	94 ± 0.3	94 ± 0.1	92 ± 0.4
	5% porogen	92 ± 0.1	91 ± 0.6	95 ± 0.5	93 ± 0.1	94 ± 0.2
	10% porogen	91 ± 0.1	91 ± 0.4	92 ± 0.1	89 ± 0.5	95 ± 0.2
	20% porogen	90 ± 0.1	87 ± 0.1	92 ± 0.4	93 ± 0.1	94 ± 0.1
	25% porogen	93 ± 0.2	94 ± 0.1	96 ± 0.3	95 ± 0.1	94 ± 0.4

Table A.57: Average $\pm\sigma_{er}$ (n=3) porosity (%) for HA samples produced using AFR using the 90 ppi template, with up to 5 coats, sintered to 1250, 1300 and 1350 °C and with camphene loadings of 0, 5, 10, 20 and 25 wt.%

		1 coat	2 coat	3 coat	4 coat	5 coat
1250 °C	0% porogen	93 ± 0.5	92 ± 0.4	91 ± 0.1	90 ± 0.2	90 ± 0.2
	5% porogen	91 ± 0.5	92 ± 0.6	90 ± 0.5	89 ± 0.3	90 ± 0.2
	10% porogen	96 ± 0.3	90 ± 0.1	88 ± 0.1	87 ± 0.1	91 ± 0.1
	20% porogen	96 ± 0.1	95 ± 0.2	94 ± 0.1	87 ± 0.3	85 ± 0.3
	25% porogen	93 ± 0.4	94 ± 0.1	91 ± 0.1	90 ± 0.1	85 ± 0.5
1300 °C	0% porogen	94 ± 0.1	92 ± 0.5	90 ± 0.1	91 ± 0.1	89 ± 0.3
	5% porogen	91 ± 0.4	92 ± 0.3	91 ± 0.1	90 ± 0.5	90 ± 0.6
	10% porogen	95 ± 0.1	94 ± 0.5	90 ± 0.4	85 ± 0.1	87 ± 0.6
	20% porogen	90 ± 0.1	93 ± 0.4	88 ± 0.1	88 ± 0.4	88 ± 0.1
	25% porogen	91 ± 0.3	91 ± 0.3	88 ± 0.4	90 ± 0.6	87 ± 0.2
1350 °C	0% porogen	91 ± 0.4	90 ± 0.4	89 ± 0.2	88 ± 0.5	85 ± 0.3
	5% porogen	92 ± 0.6	91 ± 0.1	92 ± 0.2	91 ± 0.1	88 ± 0.6
	10% porogen	91 ± 0.1	92 ± 0.6	90 ± 0.5	91 ± 0.1	91 ± 0.2
	20% porogen	89 ± 0.3	90 ± 0.5	87 ± 0.1	88 ± 0.2	91 ± 0.4
	25% porogen	88 ± 0.1	87 ± 0.4	91 ± 0.3	91 ± 0.2	86 ± 0.2

Table A.58: Average $\pm\sigma_{er}$ (n=3) porosity (%) of scaffolds freeze dried during production. All scaffolds were coated once with the slurry and sintered to 1350 °C

Template	Freezing Temperature	Porogen Content	Porosity (%)
45 ppi	10 °C	0 %	89 ± 0.3
		5 %	89 ± 0.1
		10 %	91 ± 0.1
		20 %	91 ± 0.1
		25 %	91 ± 0.3
	-20 °C	0 %	94 ± 0.3
		5 %	94 ± 0.5
		10 %	94 ± 0.4
		20 %	89 ± 0.5
		25 %	91 ± 0.6
90 ppi	10 °C	0 %	93 ± 0.3
		5 %	88 ± 0.3
		10 %	87 ± 0.2
		20 %	91 ± 0.3
		25 %	92 ± 0.6
	-20 °C	0 %	93 ± 0.3
		5 %	93 ± 0.4
		10 %	94 ± 0.4
		20 %	88 ± 0.5
		25 %	91 ± 0.6

A.3.2 Ti

Table A.59: Average $\pm\sigma_{er}$ (n=3) porosity (%) for Ti samples produced using the 45 ppi template, with up to 5 coats, sintered to 1000, 1100, 1200 and 1300 °C and with camphene loadings of 0, 5, 10, 20 and 25 wt.%

		1 coat	2 coat	3 coat	4 coat	5 coat
1000 °C	0% porogen	94 ± 1	93 ± 1	92 ± 0.9	90 ± 1	87 ± 1
	5% porogen	92 ± 0.2	92 ± 0.5	94 ± 2	89 ± 0.7	88 ± 2
	10% porogen	90 ± 1	91 ± 0.2	93 ± 0.4	86 ± 0.2	86 ± 0.7
	20% porogen	91 ± 1	90 ± 0.1	93 ± 1	93 ± 0.3	93 ± 1
	25% porogen	87 ± 0.5	91 ± 1	89 ± 2	90 ± 1	85 ± 0.2
1100 °C	0% porogen	91 ± 0.8	90 ± 0.6	90 ± 0.3	88 ± 0.7	88 ± 2
	5% porogen	91 ± 1	91 ± 1	87 ± 0.9	89 ± 1	85 ± 0.2
	10% porogen	91 ± 1	92 ± 1	92 ± 0.4	87 ± 1	87 ± 0.9
	20% porogen	92 ± 1	87 ± 0.2	91 ± 0.6	87 ± 0.5	86 ± 0.4
	25% porogen	90 ± 0.9	85 ± 0.7	86 ± 0.8	87 ± 0.8	86 ± 0.8
1200 °C	0% porogen	88 ± 1	92 ± 1	90 ± 0.8	85 ± 1	85 ± 0.1
	5% porogen	91 ± 0.8	91 ± 1	86 ± 1	86 ± 0.9	85 ± 0.2
	10% porogen	91 ± 0.1	89 ± 0.5	88 ± 0.4	87 ± 0.8	86 ± 1
	20% porogen	92 ± 0.5	92 ± 1	92 ± 2	89 ± 0.7	88 ± 0.6
	25% porogen	94 ± 2	91 ± 2	90 ± 0.3	90 ± 0.9	87 ± 0.9
1300 °C	0% porogen	91 ± 1	88 ± 1	88 ± 0.1	87 ± 0.3	85 ± 1.5
	5% porogen	89 ± 0.9	86± 0.8	86 ± 1	87 ± 0.5	86 ± 0.1
	10% porogen	87 ± 0.3	88 ± 1	87 ± 1	86 ± 1	88 ± 2
	20% porogen	90 ± 0.5	90 ± 1	88 ± 1	89 ± 0.9	88 ± 0.6
	25% porogen	81 ± 0.1	90 ± 0.9	89 ± 1	87 ± 0.1	85 ± 0.3

Table A.60: Average $\pm\sigma_{er}$ (n=3) porosity (%) for Ti samples produced using the 90 ppi template, with up to 5 coats, sintered to 1000, 1100, 1200 and 1300 °C and with camphene loadings of 0, 5, 10, 20 and 25 wt.%

		1 coat	2 coat	3 coat	4 coat	5 coat
1000 °C	0% porogen	91 ± 0.4	87 ± 0.8	87 ± 0.2	86 ± 1	90 ± 1
	5% porogen	90 ± 0.3	89 ± 0.4	89 ± 0.8	82 ± 0.1	81 ± 0.3
	10% porogen	90 ± 1	91 ± 1	88 ± 1	87 ± 1	87 ± 1
	20% porogen	90 ± 0.2	93 ± 1	86 ± 0.1	91 ± 1	89 ± 1
	25% porogen	90 ± 0.1	91 ± 1	90 ± 0.9	91 ± 0.3	91 ± 0.7
1100 °C	0% porogen	92 ± 0.3	92 ± 0.2	92 ± 2	84 ± 0.3	88 ± 1
	5% porogen	89 ± 1	91 ± 0.3	89 ± 1	89 ± 2	89 ± 1
	10% porogen	91 ± 0.7	93 ± 1	87 ± 0.3	88 ± 0.2	88 ± 1
	20% porogen	89 ± 1	92 ± 0.8	87 ± 2	86 ± 1	87 ± 1
	25% porogen	94 ± 0.1	93 ± 1	90 ± 0.9	90 ± 0.1	88 ± 2
1200 °C	0% porogen	90 ± 0.9	90 ± 1	90 ± 0.9	89 ± 0.3	88 ± 1
	5% porogen	91 ± 1	89 ± 1	90 ± 2	88 ± 0.8	87 ± 0.2
	10% porogen	88 ± 2	91 ± 1	92 ± 0.8	92 ± 1	87 ± 2
	20% porogen	91 ± 1	91 ± 1	90 ± 1	87 ± 1	88 ± 1
	25% porogen	90 ± 1	90 ± 1	92 ± 0.9	92 ± 2	88 ± 0.2
1300 °C	0% porogen	89 ± 0.8	89 ± 0.5	87 ± 1	86 ± 0.1	87 ± 0.6
	5% porogen	91 ± 0.2	91 ± 1	88 ± 0.4	87 ± 0.1	88 ± 0.8
	10% porogen	90 ± 1	90 ± 0.9	89 ± 0.2	87 ± 0.3	88 ± 1
	20% porogen	90 ± 1	91 ± 1	87 ± 1	87 ± 0.5	85 ± 0.2
	25% porogen	91 ± 0.4	90 ± 0.5	89 ± 1	87 ± 1	85 ± 1

A.3.3 Ti-6Al-4V

Table A.61: Average $\pm\sigma_{er}$ (n=3) porosity (%) for Ti-6Al-4V samples produced using the 45 ppi template, with up to 5 coats, sintered to 1200, 1350 and 1300 °C and with camphene loadings of 0, 5, 10, 20 and 25 wt.%

		1 coat	2 coat	3 coat	4 coat	5 coat
1200 °C	0% porogen	93 ± 1	93 ± 0.4	90 ± 0.6	89 ± 0.5	89 ± 1
	5% porogen	88 ± 0.9	88 ± 0.4	87 ± 0.2	87 ± 0.6	87 ± 0.9
	10% porogen	87 ± 0.4	87 ± 0.2	87 ± 1	86 ± 1	85 ± 1
	20% porogen	90 ± 1	89 ± 1	88 ± 0.5	86 ± 0.1	87 ± 0.9
	25% porogen	88 ± 0.7	89 ± 2	87 ± 0.1	88 ± 1	89 ± 0.8
1250 °C	0% porogen	90 ± 0.6	92 ± 1	84 ± 1	80 ± 0.8	78 ± 1
	5% porogen	82 ± 1	80 ± 0.1	80 ± 1	79 ± 0.3	79 ± 0.5
	10% porogen	84 ± 0.3	84 ± 0.7	84 ± 0.7	82 ± 0.5	83 ± 1
	20% porogen	86 ± 0.6	86 ± 0.7	86 ± 1	80 ± 0.5	79 ± 0.8
	25% porogen	89 ± 1	87 ± 0.6	86 ± 0.9	85 ± 1	80 ± 1
1300 °C	0% porogen	93 ± 0.9	86 ± 0.7	87 ± 1	89 ± 0.1	86 ± 2
	5% porogen	91 ± 0.4	92 ± 1	88 ± 0.6	86 ± 2	86 ± 0.6
	10% porogen	87 ± 1	87 ± 0.7	88 ± 0.2	89 ± 1	85 ± 0.3
	20% porogen	88 ± 2	88 ± 0.9	88 ± 0.3	88 ± 1	88 ± 0.2
	25% porogen	88 ± 0.7	88 ± 1	88 ± 0.6	87 ± 1	84 ± 0.4

Table A.62: Average $\pm\sigma_{er}$ (n=3) porosity (%) for Ti-6A;-4V samples produced using the 90 ppi template, with up to 5 coats, sintered to 1200, 1250 and 1300 °C and with camphene loadings of 0, 5, 10, 20 and 25 wt.%

		1 coat	2 coat	3 coat	4 coat	5 coat
1200 °C	0% porogen	90 ± 0.2	85 ± 0.9	84 ± 0.7	79 ± 1	76 ± 0.6
	5% porogen	88 ± 1	89 ± 0.8	81 ± 2	77 ± 0.4	76 ± 0.1
	10% porogen	89 ± 0.1	89 ± 0.9	84 ± 2	78 ± 1	79 ± 0.3
	20% porogen	91 ± 0.7	92 ± 0.2	87 ± 0.7	82 ± 0.1	78 ± 0.3
	25% porogen	87 ± 2	88 ± 0.8	87 ± 1	79 ± 1	78 ± 1
1250 °C	0% porogen	87 ± 0.1	86 ± 1	77 ± 0.5	78 ± 0.4	78 ± 0.2
	5% porogen	88 ± 1	87 ± 0.4	80 ± 0.7	80 ± 1	79 ± 1
	10% porogen	89 ± 2	88 ± 2	79 ± 0.6	78 ± 0.5	82 ± 0.7
	20% porogen	87 ± 1	87 ± 2	82 ± 2	79 ± 2	77 ± 0.6
	25% porogen	90 ± 0.6	88 ± 2	86 ± 1	79 ± 1	80 ± 0.1
1300 °C	0% porogen	90 ± 2	90 ± 0.1	83 ± 0.8	78 ± 0.9	75 ± 2
	5% porogen	90 ± 0.9	86 ± 0.9	88 ± 0.6	86 ± 2	75 ± 1
	10% porogen	91 ± 0.4	92 ± 1	76 ± 0.6	78 ± 2	78 ± 0.6
	20% porogen	87 ± 0.7	90 ± 0.6	79 ± 1	78 ± 0.8	74 ± 1
	25% porogen	88 ± 2	90 ± 1	89 ± 2	84 ± 0.5	78 ± 1

A.4 Compressive Strength

A.4.1 HA

Table A.63: Mean $\pm\sigma_{er}$ theoretical yield stress (kPa) of HA samples under compression, produced using the 45 ppi template, with up to 5 coats, sintered to 1250, 1300, 1350 °C and with camphene loadings of 0, 5, 10, 20 and 25 wt.%

		1 coat	2 coat	3 coat	4 coat	5 coat
1250 °C	0% porogen	2.7 ± 0.6	3.4 ± 0.5	4.7 ± 0.8	5.0 ± 0.6	4.5 ± 0.9
	5% porogen	2.0 ± 0.3	4.1 ± 0.7	41 ± +6	18 ± 4	35 ± 8
	10% porogen	5.0 ± 0.7	11 ± 1	5.7 ± 0.6	13 ± 2	24 ± 4
	20% porogen	1.7 ± 0.3	32 ± 6	8.4 ± 1.3	14 ± 2	10 ± 2
	25% porogen	17 ± 3	63 ± 9	7.2 ± 1.0	11 ± 1	26 ± 5
1300 °C	0% porogen	62 ± 18	51 ± 8	91 ± 16	121 ± 28	67 ± 17
	5% porogen	111 ± 21	86 ± 9	180 ± 29	11 ± 2	138 ± 31
	10% porogen	110 ± 14	94 ± 19	11 ± 3	50 ± 10	118 ± 22
	20% porogen	29 ± 5	27 ± 4	23 ± 3	27 ± 3	13 ± 1
	25% porogen	11 ± 3	12 ± 2	11 ± 2	18 ± 3	11 ± 2
1350 °C	0% porogen	17 ± 4	13 ± 3	6.8 ± 1.8	8.9 ± 2	17 ± 5
	5% porogen	22 ± 3	29 ± 4	4.5 ± 0.9	13 ±	13 ± 3
	10% porogen	28 ± 6	22 ± 4	15 ± 2	42 ± 10	11 ± 3
	20% porogen	30 ± 3	70 ± 13	15 ± 3	11 ± 2	15 ± 2
	25% porogen	9.5 ± 1.3	5.5 ± 0.5	1.7 ± 0.2	3.2 ± 0.5	3.7 ± 0.7

Table A.64: Mean $\pm\sigma_{er}$ theoretical yield stress (kPa) of HA samples under compression, produced using the 90 ppi template, with up to 5 coats, sintered to 1250, 1300, 1350 °C and with camphene loadings of 0, 5, 10, 20 and 25 wt.%

		1 coat	2 coat	3 coat	4 coat	5 coat
1250 °C	0% porogen	11 ± 2	18 ± 2	36 ± 7	45 ± 9	43 ± 12
	5% porogen	24 ± 5	22 ± 4	42 ± 9	58 ± 14	45 ± 7
	10% porogen	2.9 ± 0.2	33 ± 3	59 ± 10	72 ± 11	24 ± 3
	20% porogen	1.1 ± 0.1	4.0 ± 0.6	6.0 ± 0.6	53 ± 8	94 ± 11
	25% porogen	7.5 ± 1.0	5.3 ± 0.7	13 ± 2	22 ± 2	61 ± 3
1300 °C	0% porogen	9.6 ± 2.3	26 ± 7	44 ± 12	36 ± 6	48 ± 6
	5% porogen	23 ± 4	23 ± 3	30 ± 4	45 ± 4	42 ± 7
	10% porogen	2.6 ± 0.4	5.3 ± 0.5	11 ± 2	100 ± 12	72 ± 9
	20% porogen	24 ± 6	6.5 ± 1.1	46 ± 6	38 ± 4	35 ± 7
	25% porogen	17 ± 3	11 ± 3	29 ± 5	26 ± 3	38 ± 5
1350 °C	0% porogen	23 ± 5	42 ± 10	50 ± 8	84 ± 14	134 ± 22
	5% porogen	15 ± 2	22 ± 3	22 ± 4	28 ± 3	50 ± 4
	10% porogen	18 ± 2	15 ± 2	31 ± 5	25 ± 4	20 ± 4
	20% porogen	29 ± 4	23 ± 3	47 ± 7	46 ± 7	26 ± 3
	25% porogen	36 ± 6	41 ± 5	15 ± 2	13 ± 2	17 ± 2

Table A.65: Mean $\pm\sigma_{er}$ theoretical yield stress (kPa) of scaffolds freeze dried during production. All scaffolds were coated once with the slurry and sintered to 1350 °C

Template	Freezing Temperature	Porogen Content	Compressive Strength
45 ppi	10 °C	0 %	31 ± 4
		5 %	30 ± 5
		10 %	16 ± 4
		20 %	21 ± 3
		25 %	16 ± 1
	-20 °C	0 %	6.1 ± 1.5
		5 %	5.4 ± 1.4
		10 %	4.3 ± 1.0
		20 %	30 ± 10
		25 %	20 ± 4
90 ppi	10 °C	0 %	7.8 ± 0.7
		5 %	22 ± 5
		10 %	29 ± 5
		20 %	14 ± 3
		25 %	10 ± 2
	-20 °C	0 %	5.1 ± 0.9
		5 %	4.7 ± 1.2
		10 %	3.8 ± 1.1
		20 %	22 ± 4
		25 %	13 ± 2

A.4.2 Ti

Table A.66: Mean $\pm\sigma_{er}$ theoretical yield stress (kPa) of Ti samples produced using the 45 ppi template, with up to 5 coats, sintered to 1000, 1100, 1200 and 1300 °C and with camphene loadings of 0, 5, 10, 20 and 25 wt.%

		1 coat	2 coat	3 coat	4 coat	5 coat
1000 °C	0% porogen	56 ± 14	92 ± 19	140 ± 22	285 ± 41	627 ± 156
	5% porogen	2.0 ± 0.4	2.1 ± 0.3	57 ± 11	347 ± 54	482 ± 125
	10% porogen	241 ± 45	181 ± 40	87 ± 15	724 ± 119	711 ± 123
	20% porogen	166 ± 25	225 ± 42	81 ± 22	81 ± 19	81.7 ± 15
	25% porogen	427 ± 64	147 ± 29	270 ± 63	212 ± 49	789 ± 152
1100 °C	0% porogen	189 ± 42	275 ± 47	284 ± 49	455 ± 68	471 ± 85
	5% porogen	186 ± 29	277 ± 134	570 ± 94	362 ± 69	896 ± 214
	10% porogen	171 ± 36	127 ± 32	129 ± 25	567 ± 73	535 ± 109
	20% porogen	114 ± 28	491 ± 64	169 ± 19	504 ± 68	636 ± 89
	25% porogen	218 ± 34	678 ± 95	547 ± 98	478 ± 98	577 ± 98
1200 °C	0% porogen	450 ± 92	138 ± 30	273 ± 44	906 ± 215	942 ± 132
	5% porogen	183 ± 26	191 ± 27	716 ± 92	744 ± 216	874 ± 144
	10% porogen	187 ± 40	314 ± 51	409 ± 74	544 ± 69	430 ± 60
	20% porogen	120 ± 23	117 ± 17	117 ± 20	314 ± 50	428 ± 76
	25% porogen	47 ± 10	153 ± 29	198 ± 37	205 ± 33	457 ± 105
1300 °C	0% porogen	160 ± 23	397 ± 66	401 ± 84	515 ± 94	796 ± 98
	5% porogen	294 ± 39	608 ± 58	608 ± 41	481 ± 42	644 ± 67
	10% porogen	481 ± 91	391 ± 49	514 ± 102	611 ± 142	407 ± 77
	20% porogen	218 ± 35	158 ± 29	480 ± 68	487 ± 79	793 ± 138
	25% porogen	136 ± 11	193 ± 26	263 ± 59	431 ± 126	677 ± 66

Table A.67: Mean $\pm\sigma_{er}$ theoretical yield stress (kPa) of Ti samples produced using the 90 ppi template, with up to 5 coats, sintered to 1000, 1100, 1200 and 1300 °C and with camphene loadings of 0, 5, 10, 20 and 25 wt.%

		1 coat	2 coat	3 coat	4 coat	5 coat
1000 °C	0% porogen	191 ± 18	591 ± 107	592 ± 106	759 ± 124	280 ± 53
	5% porogen	269 ± 45	348 ± 48	323 ± 41	1503 ± 302	1834 ± 340
	10% porogen	217 ± 35	163 ± 30	395 ± 49	544 ± 77	530 ± 122
	20% porogen	193 ± 24	65 ± 8	536 ± 112	148 ± 27	266 ± 52
	25% porogen	155 ± 42	102 ± 22	150 ± 32	118 ± 43	126 ± 27
1100 °C	0% porogen	136 ± 19	140 ± 23	134 ± 16	1088 ± 178	522 ± 55
	5% porogen	335 ± 61	188 ± 35	383 ± 64	357 ± 36	368 ± 30
	10% porogen	159 ± 22	79 ± 11	501 ± 55	429 ± 46	429 ± 69
	20% porogen	253 ± 24	96.4 ± 13	442 ± 88	544 ± 102	492 ± 85
	25% porogen	32 ± 6	51 ± 15	1557 ± 54	150 ± 45	371 ± 108
1200 °C	0% porogen	271 ± 48	291 ± 47	280 ± 48	382 ± 73	495 ± 61
	5% porogen	179 ± 23	353 ± 76	255 ± 48	493 ± 106	671 ± 113
	10% porogen	389 ± 65	176 ± 19	126 ± 28	130 ± 17	537 ± 117
	20% porogen	142 ± 22	255 ± 33	197 ± 31	433 ± 84	375 ± 62
	25% porogen	180 ± 28	148 ± 36	72 ± 16	82 ± 20	268 ± 80
1300 °C	0% porogen	251 ± 34	269 ± 37	441 ± 79	537 ± 98	437 ± 58
	5% porogen	143 ± 31	145 ± 34	364 ± 63	448 ± 88	373 ± 94
	10% porogen	181 ± 53	183 ± 32	254 ± 42	397 ± 43	331 ± 60
	20% porogen	172 ± 33	128 ± 28	424 ± 114	412 ± 60	655 ± 138
	25% porogen	109 ± 25	137 ± 39	188 ± 50	359 ± 90	596 ± 145

A.4.3 Ti-6Al-4V

Table A.68: Mean $\pm\sigma_{er}$ theoretical yield stress (kPa) for Ti-6Al-4V samples produced using the 45 ppi template, with up to 5 coats, sintered to 1200, 1350 and 1300 °C and with camphene loadings of 0, 5, 10, 20 and 25 wt.%

		1 coat	2 coat	3 coat	4 coat	5 coat
1200 °C	0% porogen	278 ± 39	238 ± 30	659 ± 92	932 ± 182	956 ± 188
	5% porogen	1090 ± 249	1113 ± 348	1401 ± 326	1523 ± 484	1393 ± 371
	10% porogen	1349 ± 316	1358 ± 161	1359 ± 382	1725 ± 560	2147 ± 357
	20% porogen	514 ± 110	1230 ± 204	943 ± 160	1551 ± 232	1943 ± 373
	25% porogen	859 ± 176	695 ± 234	1133 ± 173	837 ± 183	680 ± 56
1250 °C	0% porogen	647 ± 119	349 ± 34	2646 ± 341	5541 ± 988	7025 ± 1450
	5% porogen	3890 ± 877	5066 ± 1050	5040 ± 802	5998 ± 1327	6072 ± 1040
	10% porogen	2452 ± 546	2585 ± 468	2564 ± 427	3695 ± 726	3126 ± 576
	20% porogen	1523 ± 315	1551 ± 267	1540 ± 343	4391 ± 722	5134 ± 640
	25% porogen	608 ± 226	1044 ± 390	1333 ± 332	1621 ± 355	1625 ± 154
1300 °C	0% porogen	219 ± 43	3355 ± 1953	1462 ± 228	952 ± 101	2553 ± 456
	5% porogen	514 ± 166	338 ± 69	1097 ± 389	1790 ± 278	2027 ± 633
	10% porogen	1284 ± 258	1299 ± 200	1031 ± 178	817 ± 180	2088 ± 425
	20% porogen	915 ± 206	975 ± 138	963 ± 129	988 ± 109	993 ± 111
	25% porogen	874 ± 171	881 ± 246	885 ± 135	1185 ± 196	2164 ± 318

Table A.69: Mean $\pm\sigma_{er}$ theoretical yield stress (kPa) for Ti-6A;-4V samples produced using the 90 ppi template, with up to 5 coats, sintered to 1200, 1250 and 1300 °C and with camphene loadings of 0, 5, 10, 20 and 25 wt.%

		1 coat	2 coat	3 coat	4 coat	5 coat
1200 °C	0% porogen	688 ± 35	2663 ± 280	3297 ± 501	8298 ± 927	13557 ± 1075
	5% porogen	1272 ± 244	927 ± 106	4919 ± 1112	7596 ± 1494	11797 ± 1613
	10% porogen	787 ± 145	794 ± 189	2537 ± 649	6121 ± 977	5577 ± 1415
	20% porogen	309 ± 51	234 ± 32	1105 ± 159	2848 ± 637	4784 ± 574
	25% porogen	1070 ± 176	721 ± 88	2893 ± 405	6502 ± 852	5262 ± 494
1250 °C	0% porogen	1578 ± 352	3647 ± 433	10281 ± 3259	7552 ± 664	7784 ± 1146
	5% porogen	1275 ± 231	1415 ± 151	5339 ± 923	5801 ± 1184	7878 ± 1908
	10% porogen	751 ± 130	971 ± 142	6407 ± 1699	7438 ± 1028	4379 ± 685
	20% porogen	997 ± 93	1047 ± 122	2690 ± 224	4579 ± 839	5978 ± 1050
	25% porogen	377 ± 49	719 ± 202	1220 ± 745	4467 ± 745	3539 ± 743
1300 °C	0% porogen	711 ± 131	698 ± 94	3389 ± 531	8189 ± 840	13707 ± 2673
	5% porogen	630 ± 169	1537 ± 349	1097 ± 244	1790 ± 214	10889 ± 1561
	10% porogen	386 ± 65	276 ± 26	8517 ± 1752	6144 ± 960	6366 ± 1443
	20% porogen	949 ± 104	467 ± 64	4315 ± 564	5423 ± 1257	8672 ± 1645
	25% porogen	809 ± 142	390 ± 71	535 ± 143	1920 ± 286	5975 ± 1024